Advances in Experimental Medicine and Biology 812

Harold M. Swartz
David K. Harrison
Duane F. Bruley *Editors*

Oxygen Transport to Tissue XXXVI

Springer

Advances in Experimental Medicine and Biology

For further volumes:
http://www.springer.com/series/5584

Harold M. Swartz • David K. Harrison
Duane F. Bruley
Editors

Oxygen Transport to Tissue XXXVI

Springer

Editors
Harold M. Swartz
EPR Center for the Study of Viable Systems
The Geisel School of Medicine
at Dartmouth
Lebanon, NH, USA

David K. Harrison
Microvascular Measurements
St. Lorenzen, Italy

Duane F. Bruley
Synthesizer Inc.
Ellicott City, MD, USA

ISSN 0065-2598 ISSN 2214-8019 (electronic)
ISBN 978-1-4939-0583-6 ISBN 978-1-4939-0620-8 (eBook)
DOI 10.1007/978-1-4939-0620-8
Springer New York Heidelberg Dordrecht London

Library of Congress Control Number: 2014935881

Printed on acid-free paper

Springer is part of Springer Science+Business Media (www.springer.com)

The 41st ISOTT Conference President, Harold M. Swartz, would like to dedicate this volume in memory of David Maguire.

David James Maguire (1945–2012) leaves behind a legacy of discovery, service, and friendship. The consummate scientist, artist, sailor, and community servant, David was truly beloved by those he touched. His unparalleled kindness, generosity of spirit, and genuine openness to all that life offers led him to live an enviable existence of adventure and camaraderie. Forever and forever, farewell David. If we do meet again, why we shall smile. If not, why then this parting was well made.

Preface

This volume consists of papers submitted, reviewed, and accepted from presentations at the 41st Annual Meeting of ISOTT that was held on June 22–26, 2013 at Dartmouth College in Hanover, NH, USA. 210 scientists from 14 countries attended the meeting. A major focus of the meeting was to discuss the clinical aspects of oxygen and methods related to its measurement, and the presentation format was planned to facilitate and promote discussions, with extensive discussion time allocated for oral presentations. There were more than 180 lectures on a variety of topics. The conference featured 2 days with a clinical focus with presentations of clinical relevance related to tissue oxygenation in cancer, cerebral, cardiovascular, muscular, and renal pathophysiology and treatment.

There were several special features at this meeting, including an emphasis on the "Wisdom of ISOTT" in which special invitations and speaking opportunities were extended to members who have had a prominent role in the development of the society and the field. The contributions from these members are featured in the first ten articles in this volume. Another special feature was a conference on the application of Electron Paramagnetic Resonance (EPR) with an emphasis on oxygen measurements in both preclinical and clinical settings and which was held in concert with the ISOTT meeting. Finally, a special feature was a tribute to David Maguire, a former President of ISOTT, who prematurely passed away prior to the meeting.

The scientific communications were enhanced by a schedule that included brief oral presentations of the highlights of every poster presentation, participation by young scholars in co-chairing most sessions, and a social program that kept the participants together for all meals while enjoying the traditional ample drink, food, and entertainment each evening that is a hallmark of the ISOTT conferences.

All articles in this volume were derived from presentations at ISOTT-2013 and were subject to rigorous review by a minimum of two knowledgeable referees and the editors. Virtually all articles required at least one revision and several of the submissions were not able to meet the criteria for inclusion. As a result the articles in this volume should have a high degree of scientific validity.

This book is dedicated to the senior members of ISOTT who continue to guide us, including those who have passed away but whose scientific contributions continue to illuminate and lead us. In particular we dedicate this book to David Maguire, whose last publication is the first article in this book.

Lebanon, NH, USA Harold M. Swartz

Acknowledgements

As President of the 2013 Meeting of the International Society on Oxygen Transport to Tissue, held from June 22–26, 2013 in Hanover, New Hampshire, USA, I would like to gratefully acknowledge the support of our sponsors:

www.bruker.com

http://global.oup.com

http://cancer.dartmouth.edu/

http://www.dartmouth-hitchcock.org/

http://www.springer.com

Panel of Reviewers

Reviewer	Affiliation
Allann Al-armaghany	University College London, UK
Clifford Belden	The Geisel School of Medicine at Dartmouth, USA
Duane F. Bruley	Synthesizer, Inc., Ellicott City, USA
Alexander Caicedo	Katholieke Universiteit Leuven, Belgium
Eunice Y. Chen	Dartmouth-Hitchcock Medical Center, Lebanon, USA
Chris E. Cooper	University of Essex, Colchester, UK
Jeff F. Dunn	University of Calgary, Canada
Gareth Eaton	University of Denver, USA
Clare E. Elwell	University College London, UK
Boris Epel	University of Chicago, USA
Malou Friederich-Persson	Uppsala University, Sweden
Bernard Gallez	University of Louvain, Belgium
Oleg Grinberg	The Geisel School of Medicine at Dartmouth, USA
Howard J. Halpern	University of Chicago, USA
David K. Harrison	Microvascular Measurements, St. Lorenzen, Italy
Alan C. Hartford	Dartmouth-Hitchcock Medical Center, Lebanon, USA
David Highton	University College London, UK
Hitoshi Hori	University of Tokushima Institute of Technology and Science, Japan
Huagang Hou	The Geisel School of Medicine at Dartmouth, USA
Mark A. Israel	Norris Cotton Cancer Center, Lebanon, USA
Lesley Jarvis	Dartmouth-Hitchcock Medical Center, Lebanon, USA
Peter E. Keipert	Keipert Corp., San Diego, USA
Valery V. Khramtsov	Ohio State University, USA

Periannan Kuppusamy	The Geisel School of Medicine at Dartmouth, USA
Joseph C. LaManna	Case Western Reserve University, Cleveland, USA
Terence Leung	University College London, UK
Lin Z. Li	University of Pennsylvania, USA
Per Liss	University of Uppsala, Sweden
Shingo Matsumoto	National Cancer Institute, NIH, Bethesda, USA
Andreas J. Metz	University Hospital Zurich, Switzerland
Nassim Nasseri	University Hospital Zurich, Switzerland
Edwin M. Nemoto	University of New Mexico, USA
Paul Okunieff	University of Florida, USA
Fredrik Palm	University of Uppsala, Sweden
Brian W. Pogue	Thayer School of Engineering at Dartmouth, Hanover, USA
Kaoru Sakatani	Nihon University, Japan
Felix Scholkmann	University of Zurich, Switzerland
John W. Severinghaus	University of California, San Francisco, USA
Nannan Sun	University of Pennsylvania, USA
Harold M. Swartz	The Geisel School of Medicine at Dartmouth, USA
IliasTachtsidis	University College London, UK
Eiji Takahashi	Saga University, Japan
Oliver Thews	University of Halle, Germany
Iuliana Toma-Dasu	Stockholm University and Karolinska Institute, Sweden
Peter Vaupel	University Medical Center, Mainz, Germany
William Welch	Georgetown University, USA
Martin Wolf	University of Zurich, Switzerland
Ursula Wolf	University of Bern, Switzerland
He Xu	University of Pennsylvania, USA
Kui Xu	Case Western Reserve University, Cleveland, USA
Mei Zhang	University of Florida, USA
Technical Reviewers	
Laraine Visser-Isles	Rotterdam, The Netherlands
Eileen Harrison	St. Lorenzen, Italy

Local Organizing Committee: The Geisel School of Medicine at Dartmouth

Harold M. Swartz
Periannan Kuppusamy
Ann B. Flood
Traci Rosenbaum
Catherine C. Lindsay
Jennifer Thody
Denise Smith
Rachel Meyer
Izzy Alexander

Scientific Advisory Committee

Dr. Duane F. Bruley
(Synthesizer, Inc., USA)
Dr. Chris Cooper
(University of Essex, UK)
Dr. Andras Eke
(Semmelweis University, Hungary)
Dr. Jerry D. Glickson
(University of Pennsylvania, USA)
Dr. David K. Harrison
(Microvascular Measurements, Italy)
Dr. Kyung A. Kang
(University of Louisville, USA)
Dr. Joseph C. LaManna
(Case Western Reserve University, USA)
Dr. Per Liss
(Uppsala University, Sweden)
Dr. Edwin M. Nemoto
(University of New Mexico, USA)

Dr. Karel Rakusan
(Ottawa University, Canada)

Dr. Giuseppe Cicco
(University of Bari, Italy)
Dr. Clare Elwell
(University College of London, UK)
Dr. Wilhelm Erdmann
(Erasmus University, The Netherlands)
Dr. Howard J. Halpern
(University of Chicago, USA)
Dr. Anthony G. Hudetz
(Medical College of Wisconsin, USA)
Dr. Peter E. Keipert
(Sangart Inc., USA)
Dr. Edwin N. Lightfoot
(University of Wisconsin-Madison, USA)
Dr. Avraham Mayevsky
(Bar-Ilan University, Israel)
Dr. Paul Okunieff
(University of Florida College of Medicine, USA)
Dr. John W. Severinghaus
(University of California-Los Angles, USA)

ISOTT Officers and Executive Committee

President

Name: Dr. Harold M. Swartz
Country: USA
Telephone: (+1) 603-650-1955
Fax: (+1) 603-650-1717
Email: harold.m.swartz
@dartmouth.edu

President-Elect

Name: Dr. Clare Elwell
Country: United Kingdom
Telephone: (+44) 20-7679-0270
Fax: (+44) 20-7679-0255
Email: celwell@medphys.ucl.ac.uk

Treasurer

Name: Dr. Peter E. Keipert
Country: USA
Telephone: (+1) 858-699-4789
Fax: (+1) 858-792-7489
Email: peterkeipert@gmail.com

Executive Committee
Chris Cooper (UK)
Jerry D. Glickson (USA)
Howard J. Halpern (USA)
Terence Leung (USA)
Rammohan Maikala (USA)
Kazuto Masamoto (Japan)
Masaomi Nangaku (Japan)
Frederik Palm (Sweden)
Ursula Wolf (Switzerland)

Past President

Name: Dr. Sabine Van Huffel
Country: Belgium
Telephone: (+32) 16-32-1703
Fax: (+32) 16-32-1970
Email: sabine.vanhuffel
@esat.kuleuven.ac.be

Secretary

Name: Dr. Oliver Thews
Country: Germany
Telephone: (+49) 345 557 4048
Fax: (+49) 345 557 4019
Email: oliver.thews@medizin.uni-halle

Chairman, **Knisely Award Committee**

Name: Dr. Duane F. Bruley
Country: USA
Telephone: (+1) 410-313-9939
Fax: (+1) 410-313-9939
Email: bruley33@verizon.net.

ISOTT Award Winners

The Melvin H. Knisely Award

The Melvin H. Knisely Award was established in 1983 to honor Dr. Knisely's accomplishments in the field of the transport of oxygen and other metabolites and anabolites in the human body. Over the years, he has inspired many young investigators and this award is to honor his enthusiasm for assisting and encouraging young scientists and engineers in various disciplines. The award is to acknowledge outstanding young investigators. This award was first presented during the banquet of the 1983 annual conference of ISOTT in Ruston, Louisiana. The award includes a Melvin H. Knisely plaque and a cash prize.

Melvin H. Knisely Award Recipients

1983 Antal G. Hudetz (Hungary)
1984 Andras Eke (Hungary)
1985 Nathan A. Bush (USA)
1986 Karlfried Groebe (Germany)
1987 Isumi Shibuya (Japan)
1988 Kyung A. Kang (Korea/USA)
1989 Sanja Batra (Canada)
1990 Stephen J. Cringle (Australia)
1991 Paul Okunieff (USA)
1992 Hans Degens (The Netherlands)
1993 David A. Benaron (USA)
1994 Koen van Rossem (Belgium)
1995 Clare E. Elwell (UK)
1996 Sergei A. Vinogradov (USA)
1997 Chris Cooper (UK)

1998 Martin Wolf (Switzerland)
1999 Huiping Wu (USA)
2000 Valentina Quaresima (Italy)
2001 Fahmeed Hyder (Bangladesh)
2002 Geofrey De Visscher (Belgium)
2003 Mohammad Nadeem Khan (USA)
2004 Fredrick Palm (Sweden)
2005 Nicholas Lintell (Australia)
2006 –
2007 Ilias Tachtsidis (UK)
2008 Kazuto Masamoto (Japan)
2009 Rossana Occhipinti (USA)
2010 Sebatiano Cicco (Italy)
2011 Mei Zhang (USA)
2012 Takahiro Igarashi (Japan)
2013 Malou Friederich-Persson (Sweden)

The Dietrich W. Lübbers Award

The Dietrich W. Lübbers Award was established in honor of Professor Lübbers's long-standing commitment, interest, and contributions to the problems of oxygen transport to tissue and to the society. This award was first presented in 1994 during the annual conference of ISOTT in Istanbul, Turkey.

Dietrich W. Lübbers Award Recipients

1994 Michael Dubina (Russia)
1995 Philip E. James (UK/USA)
1996 Resit Demit (Germany)
1997 Juan Carlos Chavez (Peru)
1998 Nathan A. Davis (UK)
1999 Paola Pichiule (USA)
2000 Ian Balcer (USA)
2001 Theresa M. Busch (USA)
2002 Link K. Korah (USA)
2003 James J. Lee (USA)
2004 Richard Olson (Sweden)
2005 Charlotte Ives (UK)
2006 Bin Hong (China/USA)
2007 Helga Blockx (Belgium)
2008 Joke Vanderhaegen (Belgium)
2009 Matthew Bell (UK)

2010 Alexander Caicedo Dorado (Belgium)
2011 Malou Friedrich (Sweden)
2012 Maria Papademetriou (UK)
2013 Nannan Sun (China/USA)

The Britton Chance Award

The Britton Chance Award was established in honor of Professor Chance's long-standing commitment, interest, and contributions to the science and engineering aspects of oxygen transport to tissue and to the society. This award was first presented in 2004 during the annual conference of ISOTT in Bari, Italy.

Britton Chance Award Recipients

2004 Derek Brown (Switzerland)
2005 James Lee (USA)
2006 Hanzhu Jin (China/USA)
2007 Eric Mellon (USA)
2008 Jianting Wang (USA)
2009 Jessica Spires (USA)
2010 Ivo Trajkovic (Switzerland)
2011 Alexander Caicedo Dorado (Belgium)
2012 Felix Scholkmann (Switzerland)
2013 Tharindi Hapuarachchi (UK)

The Duane F. Bruley Travel Awards

The Duane F. Bruley Travel Awards were established in 2003 and first presented by ISOTT at the 2004 annual conference in Bari, Italy. This award was created to provide travel funds for student researchers in all aspects of areas of oxygen transport to tissue. The awards signify Dr. Bruley's interest in encouraging and supporting young researchers to maintain the image and quality of research associated with the society. As a co-founder of ISOTT in 1973, Dr. Bruley emphasizes cross-disciplinary research among basic scientists, engineers, medical scientists, and clinicians. His pioneering work constructing mathematical models for oxygen and other anabolite/metabolite transport in the microcirculation, employing computer solutions, was the first to consider system nonlinearities, time dependence, including multidimensional diffusion, convection, and reaction kinetics. It is hoped that receiving the Duane F. Bruley Travel Award will inspire students to excel in their research and will assist in securing future leadership for ISOTT.

Duane F. Bruley Award Recipients

2004 Helga Blocks (Belgium), Jennifer Caddick (UK), Charlotte Ives (UK), Nicholas Lintell (Australia), Leonardo Mottola (Italy), Samin Rezania (USA/Iran), Ilias Tachtsidis (UK), Liang Tang (USA/China), Iyichi Sonoro (Japan), Antonio Franco (Italy)

2005 Robert Bradley (UK), Harald Oey (Australia), Kathy Hsieh (Australia), Jan Shah (Australia)

2006 Ben Gooch (UK), Ulf Jensen (Germany), Smruta Koppaka (USA), Daya Singh (UK), Martin Tisdall (UK), Bin Wong (USA), and Kui Xu (USA)

2007 Dominique De Smet (Belgium), Thomas Ingram (UK), Nicola Lai (USA), Andrew Pinder (UK), Joke Vanderhaegen (Belgium)

2008 Sebastiano Chicco (Italy)

2009 Lei Gao (UK), Jianting Wang (USA), Obinna Ndubuizu (USA), Joke Vanderhaegen (Belgium)

2010 Zareen Bashir (UK), Tracy Moroz (UK), Mark Muthalib (Australia), Catalina Meßmer (USA), Takashi Eriguchi (Japan), Yoshihiro Murata (Japan), Jack Honeysett (UK), Martin Biallas (Switzerland)

2011 Catherine Hesford (UK), Luke S. Holdsworth (UK), Andreas Metz (Switzerland), Maria D. Papademetriou (UK), Patrik Persson (Sweden), Felix Scholkmann (Switzerland), Kouichi Yoshihara (Japan)

2012 Allann Al-Armaghany(UK), Malou Friederich-Persson (Sweden), Tharindi Hapuarachchi (UK), Benjamin Jones (UK), Rebecca Re (Italy), Yuta Sekiguchi (Japan), Ebba Sivertsson (Sweden), André Steimers (Germany)

2013 Allann Al-Armaghany (UK), Gemma Bale (UK), Alexander Caicedo Dorado (Belgium), Luke Dunne (UK)

Kovach Lecture

The Kovach Lecture is presented periodically to honor a career dedicated to oxygenation research. Arisztid Kovach was a world-renowned cardiovascular physiologist and one of the early leaders of ISOTT. This lecture is dedicated to his remarkable scientific and teaching career.

Kovach Lecture Recipients

2011 John Severinghaus

2012 Peter Vaupel

2013 No recipient

Contents

The original version of this book was revised. An erratum to this book can be found at DOI 10.1007/978-1-4939-0620-8_49

Chapter 1
Mitochondrial Genetic Abnormalities After Radiation Exposure

David Maguire, Steven B. Zhang, and Paul Okunieff

Abstract Because mitochondria are prone to oxidative stress, damage to their DNA might provide a record of radiation exposure. We measured the effect of gamma radiation on mitochondrial DNA (mtDNA) copy number and common deletion (mito-CD) mutations using Beas-2B and HFL-1 cells lines and C3H/HeJ mice exposed to total-body irradiation (TBI) and sub-TBI. DNA was extracted 5 days after cell irradiation or 12 months after animal exposure. We found that: (1) natural ratios of mtDNA/nDNA and mito-CD/mtDNA varied between cell lines; (2) mtDNA copy number decreased in Beas-2B and increased in HFL-1 following 2 Gy; (3) mito-CD in both cell lines increased after 2 Gy; (4) in aged mice, the natural ratios of mtDNA/nDNA varied from 0.723 to 8.146 in different tissues; (5) in kidney tissue, TBI and sub-TBI mildly increased mtDNA copy number but substantially increased mtDNA-CD; and (6) in liver tissue, TBI and sub-TBI induced a slight increase in mtDNA copy number and a larger increase in mtDNA-CD. These findings indicate that mtDNA copy number varies in time by cell type, but there is a substantial and sustained increase in mtDNA mutations that occurs to different degrees in different tissues and cells following irradiation.

Keywords Mitochondrial DNA • Irradiation • Reactive oxygen species • Common deletion • Mitochondrial copy number

---

David Maguire deceased at the time of publication.

S.B. Zhang, Ph.D., D.V.M. • P. Okunieff, M.D. (✉)
Department of Radiation Oncology, College of Medicine, University of Florida,
2033 Mowry Road, Suite 145, P.O. Box 103633, Gainesville, FL 32610, USA
e-mail: pokunieff@ufl.edu

H.M. Swartz et al. (eds.), *Oxygen Transport to Tissue XXXVI*, Advances in Experimental Medicine and Biology 812, DOI 10.1007/978-1-4939-0620-8_1,

1 Introduction

Mitochondria perform major roles in metabolism, cellular energy production, apoptosis, and reactive oxygen species (ROS) generation. The best-characterized function of mitochondria is the production of adenosine triphosphate (ATP) through oxidative phosphorylation, which supplies over 90 % of cellular energy [1]. In addition to their critical role in the fulfilment of cellular energy requirements, mitochondria are essential to the processing of important metabolic intermediates for various pathways involved in the metabolism of carbohydrates, amino acids, and fatty acids [2–4]. Mitochondria are also involved in signalling, cellular differentiation, cell death, controlling the cell cycle, and cell growth [5].

Ionizing radiation can lead to DNA damage directly by ionizing or breaking DNA molecules or indirectly through the formation of hydroxyl (OH) radicals [6]. Although DNA damage is expected to occur with similar frequency in nuclear DNA (nDNA) and mtDNA, nDNA repair is extremely efficient, with ≈98 % of double-strand breaks repaired within a few hours; mtDNA is less efficient, with at most 60–80 % repair. Thus, radiation can lead to mtDNA and functional abnormalities.

Within hours of exposure, ionizing radiation causes a compensatory increase in mtDNA copy number in murine brains, spleens, small bowels, and bone marrow [7–9]. In the late stage (6 months), mtDNA copy number changes (increase or decrease) depend on tissue type, murine strain (radiosensitive or radioresistant), radiation dose, and exposure volume (TBI or sub-TBI).

To determine if mtDNA copy number and mutation frequency change over time following irradiation, we studied the *in vitro* and *in vivo* effects of ionizing radiation on mtDNA in two normal human cell lines (Beas-2B and HFL-1) and in C3H/HeJ mice.

2 Methods

Beas-2B (derived from adenovirus 12-SV40-transformed normal human bronchial epithelium) and HFL-1 (human lung fibroblast) cell lines were purchased from American Type Culture Collection (ATCC, Manassas, VA) and were maintained in DMEM/F-12 with 10 % FBS, 100 U/ml of penicillin, and 100 µg/ml of streptomycin (Invitrogen, Carlsbad, CA) at 37 °C under 5 % CO_2. Following the tenth passage, cells were dissociated using trypsin and cultured in 100-mm dishes. After culturing for 24 h, cells were exposed to radiation via a 137-caesium gamma source at a dose rate of 0.95 Gy/min. Cells were then cultured for 5 days with medium changes every other day. On day 5, the cells were harvested at approximately 80–90 % confluence through the cell scraper method and frozen immediately at −70 °C until use.

Male C3H/HeJ mice, 7–8 weeks old, were purchased from the National Cancer Institute's Mouse Repository (Frederick, MD). Care and use procedures were approved by the Institutional Animal Care and Use Committee. Five days after arriving, the mice were immobilized in plastic boxes and shaved (control) and sham irradiated (i.e., immobilized and stored in the irradiation room for the same length of time as TBI mice without receiving radiation) or administrated a single dose of

TBI or sub-TBI (TBI with shielding of the left hind-leg) via a 137-caesium gamma source at a dose rate of 1.75 Gy/min. Twelve months after treatment, the mice were euthanized for brain, small bowel, liver, skeletal, muscle, and bone marrow tissue collection. The collected tissues were frozen immediately at −70 °C until use.

Total genomic DNA (nuclear and mitochondrial DNA) from these cells and tissues was extracted by standard proteolytic digestion, followed by phenol/chloroform/isoamyl alcohol purification. The extracted DNA was diluted in polymerase chain reaction (PCR) water at a pH of 7.8 and measured in an ultraviolet (UV) spectrometer using 260- and 280-nm absorbance for quantifying and qualifying the DNA. Human nuclear actin gene (forward: 5′-TGACATTAAGGAGAAGCTG TGC-3′; reverse: 5′-TGAAGGTAGTTTCGTGGATGC-3′) and the mtDNA 16S rRNA gene (forward: 5′-CACAGCAAGACGAGAAGACC-3′; reverse: 5′-GAGT ATAGTAGTTCGCTTTGACTGGTG-3′) as well as a probe detecting the 4,977-bp common deletion region (forward: 5′-ATGGCCCACCATAATTACCC-3′ located at mitochondrial 8,391–8,410 bp; reverse: 5′-TCGATGATGTGGTCTTTGGA-3′ located at mitochondrial 13,528–13,509 bp) were used. The murine mtDNA copy number and common deletion primer sets were developed in our laboratory [9]. The real-time quantitative PCR was carried out using the SYBR Green PCR Master Mix (Affymetrix, Santa Clara, CA) and the Bio-Rad iQ5 program (Hercules, CA). Conditions for real-time PCR were as follows: 5 min at 50 °C and 10 min at 95 °C for initial denaturation, 15 s melting at 95 °C, 20 s annealing at 60 °C, and 30 s amplification at 72 °C. Forty-five cycles were performed. We recorded the threshold cycle value (Ct). The calculations were based on the 2-ΔΔCt value [10]. To verify the size of the amplification product, PCR reactions were analysed on an ethidium bromide-stained 2.0 % agarose gel.

Each DNA sample was run in duplicate or triplicate by PCR assay. The recorded Ct was used as the basis for the quantification of relative nDNA and mtDNA copy numbers and mutations (common deletion frequency). A *t*-test was used to determine if a statistically significant difference existed between the groups. Differences were considered significant for P values of <0.05.

3 Results

Beas-2B and HFL-1 were exposed to 2 Gy and then examined 5 days later. Figure 1.1a shows the natural ratios of mtDNA copy number and common deletion frequency. The relative ratio of mtDNA to nDNA in HFL-1 cells was slightly lower than in Beas-2B cells (1.0 ± 0.09 SD vs. 0.822 ± 0.04, $P = 0.067$). The 4,977-bp common deletion frequency was also significantly lower in HFL-1 than in Beas-2B (1.0 vs. 0.428, $P = 0.0058$). Five days after irradiation, mtDNA abnormalities occurred (Fig. 1.1b–c). The Beas-2B cells had a significantly lower mtDNA copy number (1.0 vs. 0.197) after irradiation, while the common deletion frequency was stable or slightly increased (1.0 vs. 1.352). By contrast, the mtDNA copy number and the common deletion in HFL-1 cells significantly increased (1.0 vs. 5.823 and 1.0 vs. 20.08, respectively).

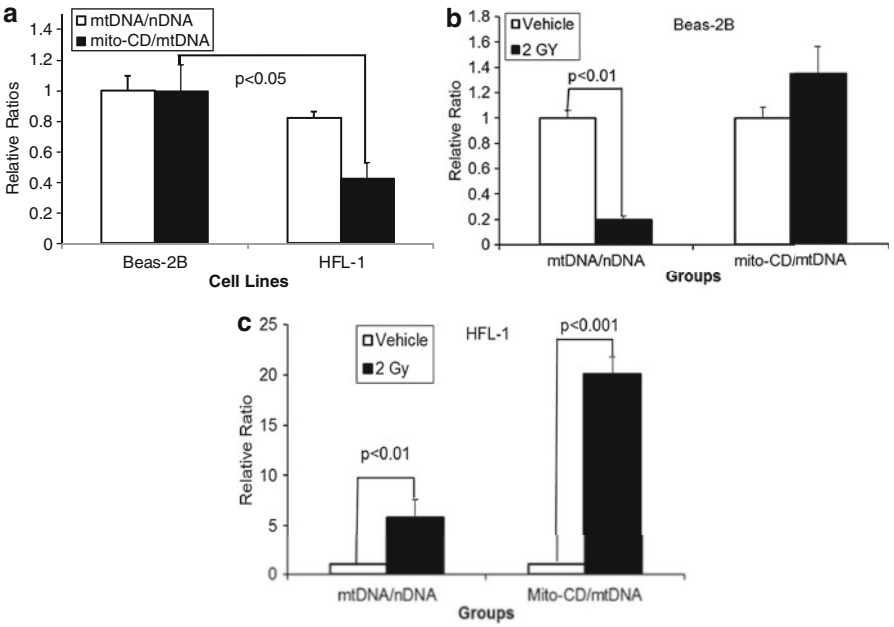

Fig. 1.1 Effect of radiation on mitochondrial copy number and common deletion frequency *in vitro*. Natural ratios of mtDNA/nDNA and mito-CD/mtDNA between Beas-2 and HFL-1 cells were slightly different (**a**). Radiation significantly decreased mtDNA copy number in the Beas-2B cell line (**b**). However, radiation resulted in a significant increase in both mtDNA copy number and common deletion frequency in HFL-1 (**c**)

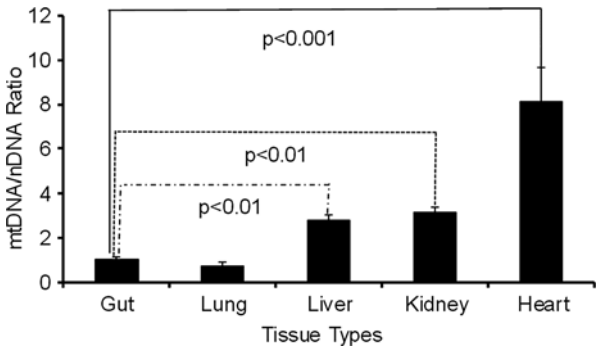

Fig. 1.2 The natural ratio of mtDNA/nDNA was tissue dependent. Values are mean ± SD (five mice)

Small bowel (gut), lung, liver, kidney, and heart tissues from C3H/HeJ mice were collected 12 months after the sham irradiation procedure. The total genomic DNA was extracted from each sample and subjected to real-time PCR. Figure 1.2 shows the ratios of mtDNA to nDNA in the five organs. The highest ratio of mtDNA to nDNA was seen in heart tissue, followed by kidney–liver and gut–lung (varying from 0.723 to 8.146). No significant differences were seen between the gut and lung (1.0 vs. 0.723) or the kidney and liver (2.818 vs. 3.13).

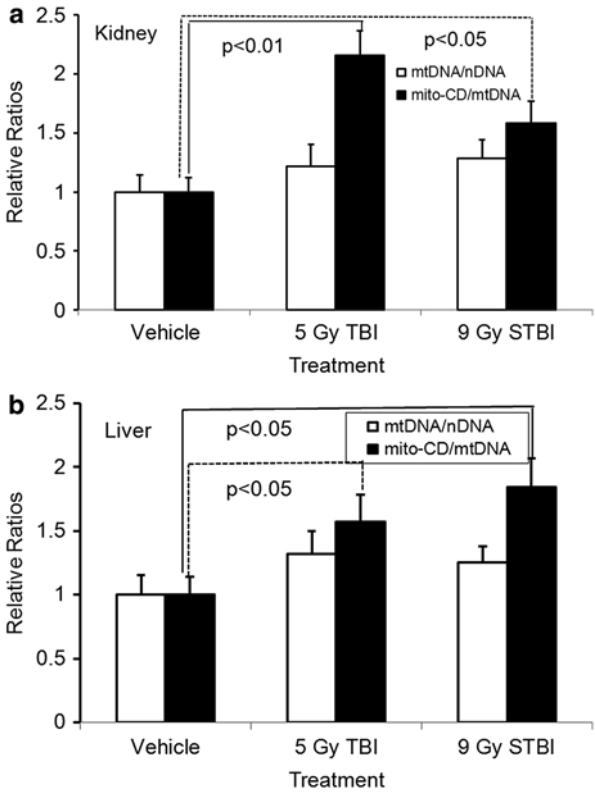

Fig. 1.3 Dose-dependent and tissue-dependent changes in mitochondrial copy number and common deletion. Mice were exposed to 5 Gy TBI or 9 Gy Sub-TBI. Twelve months later, the kidneys (**a**) and livers (**b**) were harvested. Values are mean ± SD (five mice)

Twelve months after mice were exposed to 5 Gy TBI or 9 Gy sub-TBI, kidney and liver tissues were harvested. The genomic DNA was extracted from the two tissues and subjected to real-time PCR. A similar trend existed in ratios of mtDNA to nDNA and mito-CD to mtDNA, independent of tissue type and dose. In the kidneys, the mtDNA copy number was stable or slightly increased (1.0 vs. 1.216–1.285) after irradiation; the 3,860-bp common deletion significantly increased after both 5 Gy TBI and 9 Gy sub-TBI (1.0 vs. 1.570–1.844; Fig. 1.3a). In the liver, the mtDNA copy number was slightly increased (1.0 vs. 1.253–1.317), while the 3,860-bp common deletion was substantially higher (1.0 vs. 1.570–1.844) after irradiation (Fig. 1.3b).

4 Discussion

We investigated the *in vitro* and *in vivo* effects of gamma radiation on mtDNA. As expected, radiation-induced mtDNA alterations, including mtDNA copy number and the mtDNA 4,977-bp common deletion for humans or the 3,860-bp common deletion for mice, are cell, tissue, and dose dependent. We speculate that these variations might partly explain the range of late side effects seen after radiation exposure of different organs or of different mouse strains.

Because mitochondria are the major producers of ROS in mammalian cells, mtDNA is prone to oxidative damage [11, 12]. Therefore, mtDNA alterations (copy number, mutation, and deletion) are expected to increase with aging. Accumulation of mtDNA mutations can lead to dysfunction, higher ROS, and more rapid accumulation of mutations. Ionizing radiation induces ROS generation throughout the cell, including damage to the mtDNA [13, 14], potentially accelerating age-related mtDNA damage.

Findings similar to those in mice have been seen in humans. Wen et al. found that mtDNA copy numbers were elevated in lymphocytes in over 80 % of cases following TBI for acute lymphoblastic leukemia, and mtDNA content of irradiated peripheral blood lymphocytes was elevated with a dose response [15]. In our previous murine studies, we saw proliferation of mtDNA shortly after irradiation and continued elevations for 6 months in some organs [8, 16]. In this study, we found that mild elevations persisted for 12 months.

However, *in vitro* results varied compared to *in vivo* results. We found that mtDNA copy number increased only in HFL-1 cells (Fig. 1.1b). In contrast, mtDNA content in BEAS-2B significantly decreased. Similar cell type-specific mtDNA changes were seen by Yamamori et al. and Tang et al. [13, 17]. Others have also seen increases in mtDNA mutations in radiation-damaged tissues. For example, radiation-associated human thyroid tumors have increased mtDNA content and deletion mutations [18].

This study further emphasizes the intrinsic role of mtDNA copy number in cell-dependent and tissue-dependent radiosensitivity. Our *in vitro* model potentially mimics *in vivo* mtDNA biogenesis in response to irradiation. The relation between mtDNA change and cell or tissue function should be investigated.

5 Conclusion

We found that the change in mtDNA copy number following irradiation is cell type dependent, independent of time frame. In all systems studied, there was a more rapid temporal accumulation of the common deletion mutation in irradiated cells or tissues. The data suggest that the analysis of mtDNA (content and mutations) has promise in helping us to better understand and predict radiation-induced late organ and tissue dysfunction and perhaps oncogenesis. Mitochondrial DNA change is an important biomarker for radiation exposure. Mitochondrial dysfunction related to mtDNA change is a promising area of research that should be further investigated.

Acknowledgments This paper was prepared in honor of the final work performed by David Maguire during his time in our laboratory shortly before his passing. We would also like to thank Kate Casey-Sawicki for expert editorial guidance and insights.

References

1. Campbell NA, Williamson B, Heyden RJ (2006) Biology: exploring life. Pearson Prentice Hall, Boston
2. Krebs HA (1970) The history of the tricarboxylic acid cycle. Perspect Biol Med 14:154–170
3. Kornburg HL (1987) Tricarboxylic acid cycles. Bioessays 7:236–238
4. Watford M (1991) The urea cycle: a two-compartment system. Essays Biochem 26:49–58
5. McBride HM, Neuspiel M, Wasiak S (2006) Mitochondria: more than just a powerhouse. Curr Biol 16:R551–R560
6. Zaider M, Bardash M, Fung A (1994) Molecular damage induced directly and indirectly by ionizing radiation in DNA. Int J Radiat Biol 66:459–465
7. Malakhova L, Bezlepkin VG, Antipova V et al (2005) The increase in mitochondrial DNA copy number in the tissues of gamma-irradiated mice. Cell Mol Biol Lett 10:721–732
8. Zhang H, Zhang SB, Sun W et al (2009) B1 sequence-based real-time quantitative PCR: a sensitive method for direct measurement of mouse plasma DNA levels after gamma irradiation. Int J Radiat Oncol Biol Phys 74:1592–1599
9. Zhang SB, Maguire D, Zhang M et al (2013) Maternal bias in mouse radiosensitivity: the role of the mitochondrial PTP. Adv Exp Med Biol 789:251–256
10. Livak KJ, Schmittgen TD (2001) Analysis of relative gene expression data using real-time quantitative PCR and the 2(-Delta Delta C(T)) Method. Methods 25:402–408
11. Harman D (1972) The biologic clock: the mitochondria? J Am Geriatr Soc 20:145–147
12. Larsen NB, Rasmussen M, Rasmussen LJ (2005) Nuclear and mitochondrial DNA repair: similar pathways? Mitochondrion 5:89–108
13. Yamamori T, Yasui H, Yamazumi M et al (2012) Ionizing radiation induces mitochondrial reactive oxygen species production accompanied by upregulation of mitochondrial electron transport chain function and mitochondrial content under control of the cell cycle checkpoint. Free Radic Biol Med 53:260–270
14. Leach JK, Van Tuyle G, Lin PS et al (2001) Ionizing radiation-induced, mitochondria-dependent generation of reactive oxygen/nitrogen. Cancer Res 61:3894–3901
15. Wen Q, Hu Y, Ji F et al (2011) Mitochondrial DNA alterations of peripheral lymphocytes in acute lymphoblastic leukemia patients undergoing total body irradiation therapy. Radiat Oncol 6:133
16. Zhang SB, Zhang M, Cao Y et al (2012) Delayed effects of radiation on mitochondrial DNA in radiation-sensitive organs. Adv Exp Med Biol 737:139–145
17. Tang JT, Yamazaki H, Inoue T et al (1999) Mitochondrial DNA influences radiation sensitivity and induction of apoptosis in human fibroblasts. Anticancer Res 19:4959–4964
18. Rogounovitch TI, Saenko VA, Shimizu-Yoshida Y et al (2002) Large deletions in mitochondrial DNA in radiation-associated human thyroid tumors. Cancer Res 62:7031–7041

Chapter 2
Crediting Six Discoverers of Oxygen

John W. Severinghaus

Abstract Recent events have called long-overdue attention to one of the first investigators to discover the roles of something in air changing the color of the pulmonary blood flowing through the lung.

Keywords Oxygen • Michael Servetus • Robert Boyle • Joseph Priestley • Henry Cavendish

More than two centuries before Joseph Priestley, recent historic research has found that the mixing of venous blood and inspired air in the pulmonary circulation was discovered and published by Michael Servetus (Fig. 2.1). He was a Spanish-French precocious, brilliant anatomist and physician, a liberal renaissance humanist, versed in pharmacology, mathematics, astronomy, geography and jurisprudence. Fourteen years after Luther posted his 95 theses, Servetus started critically examining the bible. Influenced by Erasmus and other reformation scholars, from 1531 to 1553, he wrote books and essays claiming there was no support in the Bible for the Christian doctrines of the trinity and infant baptism. In 1553, he published a diatribe against church doctrines titled *Christianismi Restitutio*. Like the Czech liberal early reformer hero Jan Hus 140 years earlier, Servetus was declared a heretic, captured, imprisoned for months and burned at the stake by the Calvinist reformation authorities in Geneva in 1553. They burned all available copies of his book.

In a surviving copy of that book, hidden among the theology scholarship, was his claim that blood flows through the lung where it disposes of waste products and where air causes passing blood to become a bright red color. This was written 75 years before William Harvey published discovery of the circulation in *De Motu Cordis*.

J.W. Severinghaus (✉)
Professor Emeritus Anesthesiology and Cardiovascular Research Institute, University of California at San Francisco, San Francisco, CA 94957, USA
e-mail: jwseps@comcast.net

H.M. Swartz et al. (eds.), *Oxygen Transport to Tissue XXXVI*, Advances in Experimental Medicine and Biology 812, DOI 10.1007/978-1-4939-0620-8_2,

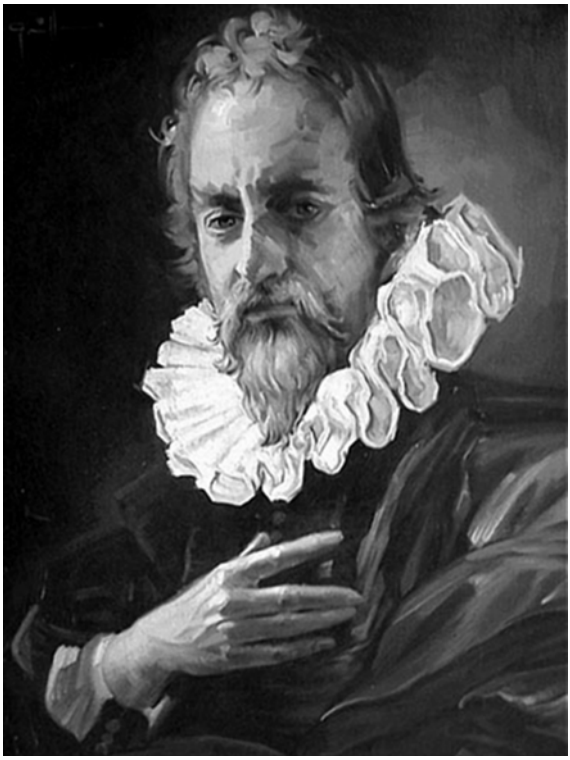

Fig. 2.1 Michael Servetus

In 1668, after working for several years in Robert Boyle's Oxford laboratory, John Mayow published two books of his research (Fig. 2.2). He showed that air was a mixture of two components of which 1/5th was essential for life, consumed during breathing, and in fire, and thus was used to provide both body heat and energy. He named that part of air "spiritus igneo-aereus". He had no way to isolate it or further study its chemistry. His writings were ignored when science adopted the false theory of fire called phlogiston, first described in 1667 by a German alchemist-physician J. J. Becher, and then widely promoted by a famous physician Georg Ernst Stahl in Halle. In that idea, the function of breathing was to eliminate phlogiston released from food within the body. Although some faults in that theory were found, it became the universally accepted chemistry until 1784.

In 1771, Carl Wilhelm Scheele (Fig. 2.3, possible portrait), a brilliant Swedish apothecary and research chemist in Torbern Bergman's chemistry department in Uppsala, generated an unknown gas by heating the calc (oxide) of manganese or mercury. He named it "Ilds Luft" (fire air) because it supported combustion better than air. Unable to understand how it fit into the phlogiston theory, he delayed publication. In 1775 he finally finished writing a book about it and his many discoveries of elements and compounds, but its publication, at first in Swedish and then in

Fig. 2.2 John Mayow

German, was delayed until 1777 by Bergman's 1 year delay in writing a preface, and another year by the German printer. As the book neared publication, he became aware that Priestley had independently described the same method of making this new air. Not able to claim priority, he added a note that he had described his methods and findings to Lavoisier in a letter he said he had posted in September 1774. He stated that Lavoisier had never responded nor acknowledged the letter.

Most commonly credited with discovery of O_2 was Joseph Priestley (Fig. 2.4, by Gilbert Stuart), an English Unitarian (non-conforming) minister. Several churches had fired him as too liberal, so he became a self-trained scientist and teacher, making Warrington the finest academy in England. With Benjamin Franklin's help he wrote a textbook about electricity that became very popular. In 1768, he was awarded the Copley medal, for that book and for having invented and discovered how to make soda water from brewery gas much cheaper than importing pyramont water from France. By 1772, he had discovered seven new gases, N_2O, NO_2, NO, HCl, SO_2, SO_3, and SiF_4 (and later CO). In 1773, the 2nd Earl Shelburne attracted Priestley as a tutor for his sons. He provided a laboratory and funds for his research in his Bowood palace in Calne, Wiltshire, and homes in London and Calne.

Priestley discovered how to generate oxygen in his new laboratory on August 1, 1774, independently of Scheele, but also by heating mercuric calc. It caused a glowing splinter to burst into flames. He named it dephlogisticated air. He showed that mice

Fig. 2.3 Carl Wilhelm Scheele

could live in it longer than in a similar volume of air. He reported that its ability to support life returned after a few weeks following the death of a mouse in it when he included a sprig of mint in the closed space. He immediately sent notes to the Royal Society and friends.

Two months later, while in Paris, Priestley later wrote that he had demonstrated to the world's best chemist Antoine Lavoisier and associates his method of making dephlogisticated air. Priestley wrote that Lavoisier never acknowledged his visit and demonstration. Joseph Black, discoverer of CO_2, repeatedly, in print, accused Lavoisier of failing to credit him. Much evidence has survived that Lavoisier tended to claim credit for work by others.

In 1775, after the Royal Society published several of Priestley's letters, Lavoisier began studying the new gas. He may have failed to discover it earlier because he added charcoal to remove impurities, causing all the O_2 to be consumed. In 1777, he named it principe oxigen, Greek 'oxi' for acid or sharp, incorrectly believing that all acids contain oxygen. He extensively studied its chemistry over the next 10 years, but was unable to prove whether oxygen was a new element.

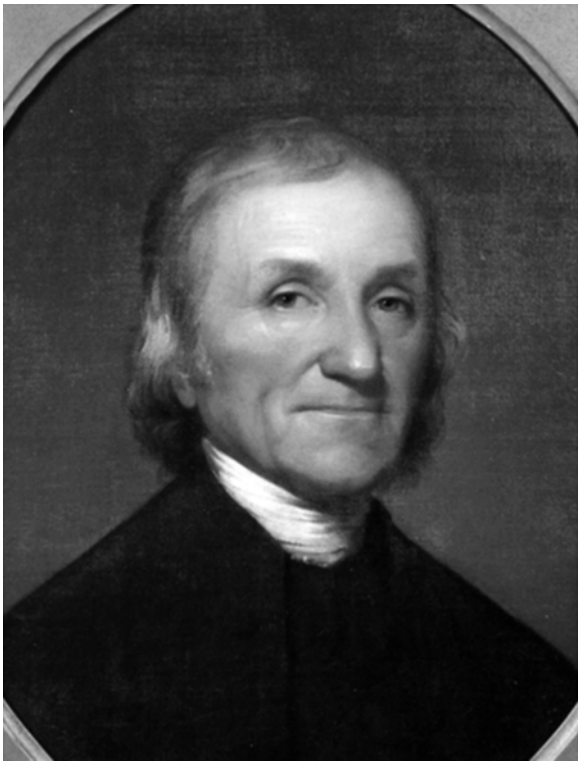

Fig. 2.4 Joseph Priestley

The final proof came from an old experiment. In 1766, Henry Cavendish (Fig. 2.5), by mixing iron filings with acid, had made a new gas he called "inflammable air" (hydrogen). He wrote that when it was burned, pure water appeared on the vessel walls. He was ignored because no scientist, including Lavoisier could believe that burning a gas could generate water. Since antiquity water had been assumed to be an element.

In 1783, 17 years later, the Royal Society invited Cavendish to review, at a Society meeting, his still mysterious, incredible finding. A few weeks later, Cavendish's assistant, Dr. Charles Blagden, traveling to Paris, told Lavoisier about the renewed interest at the Society meeting of Cavendish's 1766 claim of generating water. Lavoisier had read the 1766 paper but was sure that Cavendish was wrong. The Royal Society's invitation and presentation stimulated Lavoisier to prove or disprove the Cavendish experiment.

The final decisive event occurred on June 24, 1783. Lavoisier with eight chemist observers repeated the Cavendish experiment. They were astonished to confirm that, when inflammable air was burned, water appeared. Lavoisier then, suddenly, realized the implication of this experiment. He promptly stated and reported to the Academie: "Inflammable air and oxygen are elements. Water is not an element but a compound made of them!" He forthwith named inflammable air *hydrogen*. With this new insight, he demolished the phlogiston theory and founded modern chemistry.

Fig. 2.5 Henry Cavendish

Lavoisier had become the world's best-known chemist by 1770. His much younger wife Marie-Anne became a skilled draftsman, his secretary, lab assistant, and business manager. In 1789 she commissioned a huge painting by France's celebrated artist Jacques Louis David (Fig. 2.6). It now hangs in the major gallery at the top of the grand staircase at the Metropolitan Museum in New York City.

Lavoisier became very rich as a tax collector, banker and gunpowder manufacturer. He was hated for building a wall around Paris to force incoming merchants to pay taxes on their goods for sale. When the physician-writer Jean-Paul Marat presented inadequate scientific research reports to the *Académie des Sciences* in the 1770s, Lavoisier, the editor, rejected the papers and his several applications for membership. During the terror, Marat's writings based on his residual hatred of Lavoisier, influenced the Revolutionary Tribunal to try, convict and behead him on May 8, 1794.

The French revolution also ended Priestley's safety. Church, Crown and press repeatedly attacked him for speaking and writing in support of the French and

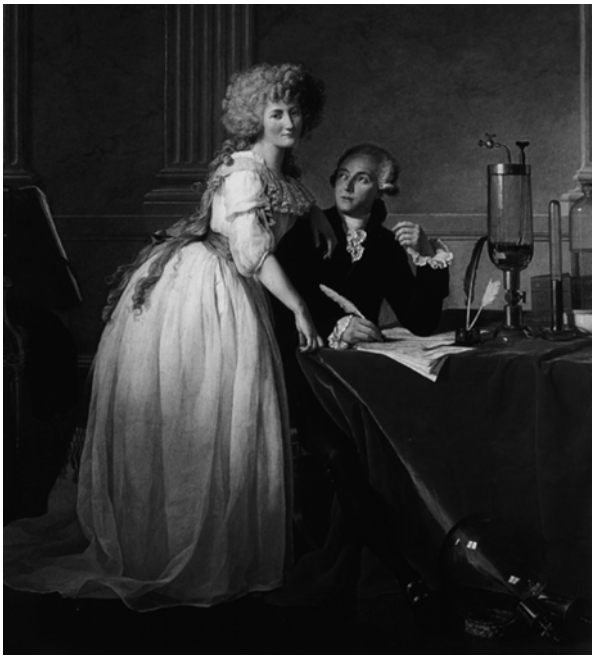

Fig. 2.6 Marie-Anne and Antoine Lavoisier

American revolutions. On the third Bastille day in 1791, drunken rioters destroyed his Birmingham home and laboratory, and many homes and churches of the Unitarian dissenters. Priestley and his family fled to London, then to Philadelphia in 1793. There he persuaded Jefferson, who attended his sermons, to establish liberal education in the American form as we know it.

In 1795, Priestley built a home and laboratory in Northumberland, PA on the Susquehanna River. He wrote in defense of the phlogiston theory 16 years after it was demolished by Lavoisier and abandoned by all scientists. Near his life's end, in 1803 he described himself as an exhausted volcano. He died in 1804 in Northumberland. The American Chemical Society was founded there in 1874, the centenary of Priestley's discovery.

In 1890, the French historian, Edouard Grimaux, claimed that he had been shown Scheele's letter to Lavoisier. He published the text, but said he was unable to show it to any other scholar, claiming that it had disappeared. His publication led to erection of a Scheele sculpture by John Börjeson in Stockholm's Skulpturparken, in Humlegården. But for many scientists, inability to see Scheele's letter led to doubt.

Now jumping ahead another century to 1993, some personal properties of Marie-Anne Lavoisier were donated to the French Academy of Science when the government threatened to tax them. Among these personal belongings was the letter written by Scheele to Lavoisier, dated 30 Sept 1774. Descendants of Marie Anne Lavoisier's

Fig. 2.7 Servetus sculpture

brother had hid it for 219 years, presumably because it established that Lavoisier failed to credit other scientists for their help.

I began this discovery story with Michael Servetus and now will end with recent news about him. At the end of the nineteenth century, a famous author, Auguste Dide, published a book on heretics and revolutionaries, with special praise for Servetus. In 1903, he was elected as a French Senator. He proposed to erect a Servetus honorary monument in Geneva. Servetus supporters then commissioned Rodin's student Clothilde Roch to sculpt Servetus suffering in Geneva's prison. It was finished in 1907. The Geneva town council, still Calvinists, found excuses to refuse to mount it. Instead they named a nearby dingy alley "rue Michel-Servet". Dide then got it mounted in France on the Annemasse town hall square across the border 4 km east of Geneva, taunting the Calvinist Swiss. In 1942 during WW II, because Servetus had promoted freedom of conscience, the French Vichy (Nazi) rulers melted it down.

Finally, in 2011, on Servetus' 500th birthday, with approval of Geneva's now-secular town council, the Roch sculpture, recast from new molds of the century-old plaster original, was erected in the Champel district near the site of his execution, beside Geneva University Hospital (Fig. 2.7). The local Calvinist officials refused to attend the ceremony!

It has taken four and a half centuries to appropriately credit the contributions of these six scientists to the discovery of oxygen. The first five published experiments while the sixth, although a brilliant experimental chemist, found nothing by experiment leading to discovery of oxygen but deserves credit as first to comprehend, after 18 years of denying it, that Cavendish had proved experimentally that water was a compound of oxygen and hydrogen!

Chapter 3
Hypoxia in Tumors: Pathogenesis-Related Classification, Characterization of Hypoxia Subtypes, and Associated Biological and Clinical Implications

Peter Vaupel and Arnulf Mayer

Abstract Hypoxia is a hallmark of tumors leading to (mal-)adaptive processes, development of aggressive phenotypes and treatment resistance. Based on underlying mechanisms and their duration, two main types of hypoxia have been identified, coexisting with complex spatial and temporal heterogeneities. Chronic hypoxia is mainly caused by diffusion limitations due to enlarged diffusion distances and adverse diffusion geometries (e.g., concurrent vs. countercurrent microvessels, Krogh- vs. Hill-type diffusion geometry) and, to a lesser extent, by hypoxemia (e.g., in anemic patients, HbCO formation in heavy smokers), and a compromised perfusion or flow stop (e.g., due to disturbed Starling forces or intratumor solid stress). Acute hypoxia mainly results from transient disruptions in perfusion (e.g., vascular occlusion by cell aggregates), fluctuating red blood cell fluxes or short-term contractions of the interstitial matrix. In each of these hypoxia subtypes oxygen supply is critically reduced, but perfusion-dependent nutrient supply, waste removal, delivery of anticancer or diagnostic agents, and repair competence can be impaired or may not be affected. This detailed differentiation of tumor hypoxia may impact on our understanding of tumor biology and may aid in the development of novel treatment strategies, tumor detection by imaging and tumor targeting, and is thus of great clinical relevance.

Keywords Tumor hypoxia • Acute hypoxia • Chronic hypoxia • Hypoxia subtypes • Hypoxia classification

---

Dedicated to the memory of Dr. Britton Chance on the occasion of his 100th birthday (July 24, 2013), and remembering many exciting discussions on the inadequate and heterogeneous oxygenation of breast cancer.

P. Vaupel (✉) • A. Mayer
Department of Radiooncology and Radiotherapy,
University Medical Center, Langenbeckstrasse 1, 55131 Mainz, Germany
e-mail: vaupel@uni-mainz.de

H.M. Swartz et al. (eds.), *Oxygen Transport to Tissue XXXVI*, Advances in Experimental Medicine and Biology 812, DOI 10.1007/978-1-4939-0620-8_3,

1 Introduction

Approximately 50–60 % of human tumors contain hypoxic regions which show complex spatial and temporal heterogeneities [1–3]. Tumor hypoxia is known to trigger (mal-)adaptive processes, increased tumor aggressiveness and resistance to O_2-dependent therapies (e.g., standard radiotherapy, some forms of chemotherapy, photodynamic therapy, immunotherapy and hormonal therapy), all together leading to a poor clinical prognosis [4–6]. Based on underlying mechanisms and their duration, two main types have been identified: chronic and acute hypoxia. This traditional classification is based on empirical observations and generally overlooks the multiple pathogenetic processes involved.

Chronic hypoxia is mainly caused by diffusion limitations [7], whereas acute hypoxia has been thought to preferentially result from temporary flow stops [8, 9]. In each of these hypoxia subtypes, oxygen supply is critically reduced, but perfusion-dependent delivery of diagnostic and therapeutic agents, supply of nutrients and removal of waste products, and repair competence can vary or may be unaffected [10]. Thus, detailed differentiation of tumor hypoxia may impact on our understanding of tumor biology and may aid in the development of novel treatment strategies (e.g., modulation of fractionation schedules), in tumor detection by imaging and tumor targeting, and is thus of upmost clinical importance far beyond an academic discussion. In this chapter, an updated review of the pathogenesis of hypoxia subtypes and their biological/clinical implications is therefore presented. Eventually, this updated classification of tumor hypoxia may also result in a better understanding of mismatches between perfusion and hypoxia in tumor imaging.

2 Chronic Hypoxia

According to a recent quantification of hypoxia in vital tumor tissue of xenografted squamous cell carcinomas of the head and neck, chronic hypoxia is the dominating subtype (mean = 77 % of total hypoxia [range: 65–86 %], total hypoxia covering 45 % of vital tumor tissue [range: 27–57 %]), with pronounced heterogeneity between individual tumors and between tumor lines [11].

Causes, the estimated time frame, major biological consequences, the therapeutic relevance and the prognostic power of chronic hypoxia are listed in Table 3.1. By definition, a reduced or abolished oxygen supply is inherent in each of these different pathogenetic mechanisms leading to chronic hypoxia. Perfusion- (convection-) dependent nutrient supply, waste removal, delivery of anticancer agents (e.g., chemotherapeutic drugs, antibodies or immune cells) or diagnostic agents for tumor imaging can be impaired or may not be affected, depending on the causative mechanism (Table 3.2).

Table 3.1 Causes and major consequences of chronic hypoxia (selection, updated from [10])

Synonyms used	Continuous h., diffusion-limited h., sustained h., long-term h.
Causes (pathogenesis)	1. Diffusion-limited hypoxia due to – Enlarged diffusion distances – Adverse diffusion geometries (concurrent vs. countercurrent tumor microvessels, Krogh- vs. Hill-type diffusion geometry) – Extreme longitudinal intravascular oxygen gradients – Shunt perfusion 2. Hypoxemic hypoxia – Tumor-associated anemia – Therapy-induced anemia – Small liver tumors supplied by portal vein – HbCO-formation in heavy smokers 3. Compromised perfusion of microvessels – Disturbed Starling forces due to high interstitial fluid pressure (transmural coupling) – Solid-phase stress by non-fluid components (compression) – Intratumor thrombosis
Time frame	Hours→weeks (under experimental conditions)
Major biological consequences	Slowing of proliferation rate, regressive changes (apoptosis, necrosis), HIF-destabilization
Therapeutic relevance	Resistance to O_2-dependent therapies (RX, O_2-dependent CX, photodynamic therapy, immunotherapy, hormonal therapy)
Prognostic power	Strong adverse and independent prognostic factor (e.g., for overall survival in cervix cancer, for local control in head and neck cancer)

Table 3.2 Subtypes of chronic hypoxia according to causative mechanisms and associated transport capacities via blood flow/convection and extravascular diffusion

Causes	Diffusion limitations	Hypoxemia	Interstitial hypertension or solid stress
Blood flow	Maintained	Maintained	Reduced/abolished[b]
Nutrient supply (e.g., glucose, glutamine), waste removal	Reduced/abolished[a]	Maintained	Reduced/abolished[b]
Delivery of growth factors etc.	Reduced/abolished[a]	Maintained	Reduced/abolished[b]
Delivery of anti-cancer agents	Reduced/abolished[a]	Maintained	Reduced/abolished[b]
Delivery of imaging agents	Reduced/abolished[a]	Maintained	Reduced/abolished[b]

[a]Dependent on distance away from tumor microvessel
[b]Pressure-dependent

3 Acute Hypoxia

Pathophysiologically speaking, acute hypoxia can be divided into two further subgroups: ischemic and hypoxemic hypoxia, the latter being characterized by plasma flow only (Table 3.3). In fluctuating or intermittent hypoxia caused by spontaneous fluctuations of red blood cell fluxes, hypoxia levels during the temporary

Table 3.3 Causes and major consequences of acute hypoxia (selection, updated from [10])

Synonyms used	Transient h., short-term h., perfusion-limited h., cyclic h., fluctuating h., intermittent h.
Causes (pathogenesis)	1. Temporary flow stop in microvessels – Due to tumor or blood cell aggregates, fibrin plugs – Ischemic hypoxia due to vascular remodeling 2. Transient hypoxemia – Temporal plasma flow in microvessels – Fluctuating red blood cell fluxes
Time frame	Minutes→hour (not well defined; spontaneous hypoxia cycles show spatial and temporal irregularities)
Major biological consequences	Leads to HIF-activation, cyclic reoxygenation episodes (ROS formation), increases genomic instability promoting tumor cell survival, selection of aggressive and apoptosis-resistant cell clones
Therapeutic relevance	Acquired treatment resistance via changes in the transcriptome, gene expression, proteome and genome
Prognostic power	Adverse prognostic factor

Table 3.4 Subtypes of acute hypoxia according to causative mechanisms and associated transport capacities via blood flow/convection and extravascular diffusion

Causes	Flow stop	Transient hypoxemia
Perfusion	Abolished	Maintained
Nutrient supply, waste removal	Abolished	Maintained
Delivery of growth factors	Abolished	Maintained
Delivery of anti-cancer agents	Abolished	Maintained
Delivery of imaging agents	Abolished	Maintained

drop of intravascular hematocrit are often not reached (e.g., [12]). In these cases, effects preferentially triggered by the formation of reactive oxygen species have to be considered. Ischemic hypoxia is preferentially caused by transient flow stops or critically reduced perfusion due to physical obstructions, such as by aggregates of tumor cells, blood cells or fibrin clots in the vessel lumen. In analogy with Table 3.2, relevant supply conditions are listed for subtypes of acute hypoxia in Table 3.4.

4 Hypoxia-Associated Biological and Clinical Implications

Major biological and clinical implications of chronic and acute hypoxia are listed in Tables 3.1, 3.2, 3.3, and 3.4. Unfortunately, there is no clear consensus on the biological and clinical consequences of the different hypoxia subtypes [13]. For example, there is opposing in vivo experimental evidence that chronic hypoxia can lead to both regressive changes and tumor progression depending on the cell line used, whereas for acute hypoxia there is a general trend towards development of an invasive phenotype. This is most likely due to changes in the transcriptome, gene expression,

proteome and metabolome (metabolic reprogramming). In addition, experimental evidence has demonstrated that in vitro acute hypoxia leads to genomic instability due to reduced DNA damage repair or due to the generation of reactive oxygen species during hypoxia-reoxygenation episodes (for reviews see [14, 15]). A number of in vivo experimental studies have verified that acute hypoxia can cause accelerated tumor growth and metastasis. Based on so far inconsistent data, there seems to be a general trend towards development of a more aggressive phenotype upon acute hypoxia than after chronic hypoxia. Responses following acute hypoxia most probably are driven by a transient stabilization of HIF-1α, possibly the most important factor for hypoxia-induced signaling, whereas the expression and activity of HIF-2α is often less prominent in cancer cells but can be strong in macrophages [16]. HIF-2α may not stimulate the glycolytic pathway [17].

5 Conclusions

Biological and therapeutic consequences seem to be different for "static," chronic hypoxia and "dynamic," acute hypoxia. Thus, a distinction between and quantification of these subtypes may be mandatory. Acute and chronic hypoxia have been convincingly described for the experimental/preclinical setting. Direct evidence in clinical (radio-)oncology has so far not been provided, mainly due to the lack of valid detection and quantification methods. Thus translation of experimental findings into the clinical practice urgently needs more advanced technologies (e.g., imaging techniques, use of valid modeling) before modifications in currently used radiotherapy regimens are implemented [13].

Acknowledgments The authors thank Dr. Debra Kelleher for her valuable editorial help during preparation of this manuscript.

References

1. Vaupel P, Mayer A, Höckel M (2004) Tumor hypoxia and malignant progression. Methods Enzymol 381:335–354
2. Vaupel P, Höckel M, Mayer A (2007) Detection and characterization of tumor hypoxia using pO_2 histography. Antioxid Redox Signal 9:1221–1235
3. Vaupel P, Mayer A (2007) Hypoxia in cancer: significance and impact on clinical outcome. Cancer Metastasis Rev 26:225–239
4. Höckel M, Knoop C, Schlenger K et al (1993) Intratumoral pO_2 predicts survival in advanced cancer of the uterine cervix. Radiother Oncol 26:45–50
5. Höckel M, Schlenger K, Aral B et al (1996) Association between tumor hypoxia and malignant progression in advanced cancer of the uterine cervix. Cancer Res 56:4509–4515
6. Mayer A, Vaupel P (2013) Hypoxia, lactate accumulation, and acidosis: siblings or accomplices driving tumor progression and resistance to therapy? Adv Exp Med Biol 789:203–209
7. Thomlinson RH, Gray LH (1955) The histological structure of some human lung cancers and the possible implications for radiotherapy. Br J Cancer 9:539–549

8. Brown JM (1979) Evidence for acutely hypoxic cells in mouse tumours, and a possible mechanism of reoxygenation. Br J Radiol 52:650–656
9. Chaplin DJ, Durand RE, Olive PL (1986) Acute hypoxia in tumors: implications for modifiers of radiation effects. Int J Radiat Oncol Biol Phys 12:1279–1282
10. Bayer C, Shi K, Astner ST et al (2011) Acute versus chronic hypoxia: why a simplified classification is simply not enough. Int J Radiat Oncol Biol Phys 80:965–968
11. Maftei CA, Bayer C, Shi K et al (2011) Quantitative assessment of hypoxia subtypes in microcirculatory supply units of malignant tumors using (immuno-)fluorescence techniques. Strahlenther Onkol 187:260–266
12. Matsumoto S, Yasui H, Mitchell JB et al (2010) Imaging cycling tumor hypoxia. Cancer Res 70:10019–10023
13. Bayer C, Vaupel P (2012) Acute versus chronic hypoxia in tumors: controversial data concerning time frames and biological consequences. Strahlenther Onkol 188:616–627
14. Aguilera A, Gomez-Gonzalez B (2008) Genome instability: a mechanistic view of its causes and consequences. Nat Rev Genet 9:204–217
15. Bindra RS, Crosby ME, Glazer PM (2007) Regulation of DNA repair in hypoxic cancer cells. Cancer Metastasis Rev 26:249–260
16. Talks KL, Turley H, Gatter KC et al (2000) The expression and distribution of the hypoxia-inducible factors HIF-1alpha and HIF-2alpha in normal human tissues, cancers, and tumor-associated macrophages. Am J Pathol 157:411–421
17. Ratcliffe PJ (2007) HIF-1 and HIF-2: working alone or together in hypoxia? J Clin Invest 117:862–865

Chapter 4
Heterogeneity in Tissue Oxygenation: From Physiological Variability in Normal Tissues to Pathophysiological Chaos in Malignant Tumours

David K. Harrison and Peter Vaupel

Abstract Heterogeneity is a feature of both normal oxygen supply to tissue and of a supply that is disturbed due to a wide range of different pathologies. Here, the physiological importance of heterogeneity of tissue oxygenation is revisited. The anatomical and functional basis for heterogeneity of blood flow, local and regional regulatory mechanisms in normal tissues and the pathophysiology of the failure of regulation will be examined.

Under physiological conditions, regulation of blood flow distributions at global, regional and microregional levels play coordinated roles in ensuring adequate O_2 supply to all tissue cells. How this is achieved may be organ-/organ layer-specific, depending on its function and priorities to match local O_2 delivery to consumption. Examples where these regulatory mechanisms break down under conditions of ischaemia and shock will also be given.

In contrast, pathologic heterogeneity in tissue oxygenation resulting from uncontrolled, chaotic growth as seen in malignant tumours represents a pathophysiological status that is not predictable which, in general, is associated with chronic and acute hypoxia. This can have fatal consequences due to hypoxia- induced (mal-)adaptive processes, malignant tumour progression and treatment resistance.

Keywords Heterogeneity • Oxygenation • Normal Tissue • Tumour • Microflow • Microvasculature

D.K. Harrison (✉)
Microvascular Measurements, 39030 St Lorenzen, Italy
e-mail: Harrison.David.K@gmail.com

P. Vaupel
Department of Radiooncology & Radiotherapy, Klinikum rechts der Isar,
Technical University, 81675 Munich, Germany
e-mail: vaupel@uni-mainz.de

H.M. Swartz et al. (eds.), *Oxygen Transport to Tissue XXXVI*, Advances in Experimental Medicine and Biology 812, DOI 10.1007/978-1-4939-0620-8_4,

1 Heterogeneity of Blood Flow

The distribution of blood flow is heterogeneous at all levels: global, regional and microregional. At the global level, cardiac output is distributed to the various organs of the body according to an organ's specific oxygen demand (e.g. heart, brain) or an organ's need for high perfusion due to its bodily function (e.g. kidneys, spleen). This principle also applies at the regional level where individual layers of organs may have quite different tissue blood flows. Figure 4.1 shows examples of various tissue blood flow values at global and regional levels

Figure 4.2 shows a histogram of capillary blood flow values recorded in the resting skeletal muscle. Given the broad distribution of capillary segment lengths and diameters, heterogeneity of tissue blood flow at the microregional level is predictable, simply on the basis of the Hagen-Poiseuille equation. Indeed, analysis of capillary diameters alone indicates the existence of "high flow" and "low flow" compartments within the microcirculation of resting skeletal muscle [3].

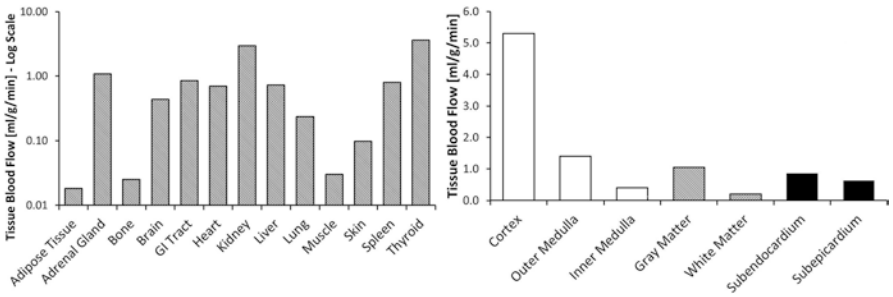

Fig. 4.1 *Left*: Distribution of cardiac output to various organs (data from [1]) *Right*: Regional blood flow in different layers of the kidney, brain and heart (data from [2])

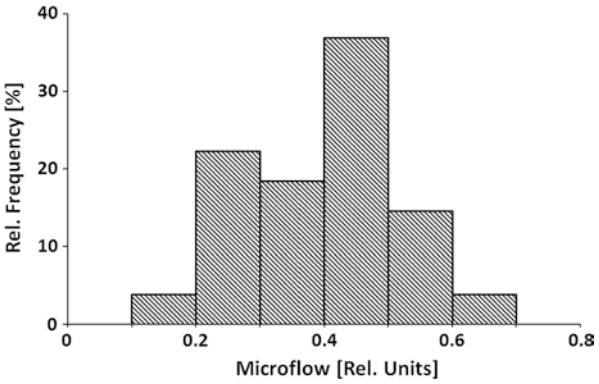

Fig. 4.2 Distribution of capillary blood flow (microflow) at the surface of resting sartorius muscle in the anaesthetised dog measured using the hydrogen clearance technique

2 Heterogeneity of Oxygen Supply: The Tissue pO_2 Histogram

Figure 4.3 shows pO_2 histograms measured in various organs [4–9], including skeletal muscle, and represent the real distribution of pO_2 within the tissue. With the exception of the heart and kidney, which differ for reasons associated with their function, it can be seen that the venous pO_2 values are clearly higher than the mean tissue pO_2 values. This reflects the microregional heterogeneity of blood flow discussed above. Despite this, the histograms are remarkably similar and Gaussian in all organs. Even if microregional blood flow were not heterogeneous, heterogeneity of tissue pO_2 was predicted by August Krogh, almost a century ago, in the form of the so-called "Krogh cylinder" model [10] which has been elaborated on in later versions, many developed by ISOTT members (e.g. [11]).

3 Physiological Response of Tissue O_2 Supply

The similarities of tissue pO_2 histograms from organ to organ and absence of anoxic values point towards a system of local regulation that ensures that the oxygen supply is always sufficient, even for those cells in the periphery of the tissue

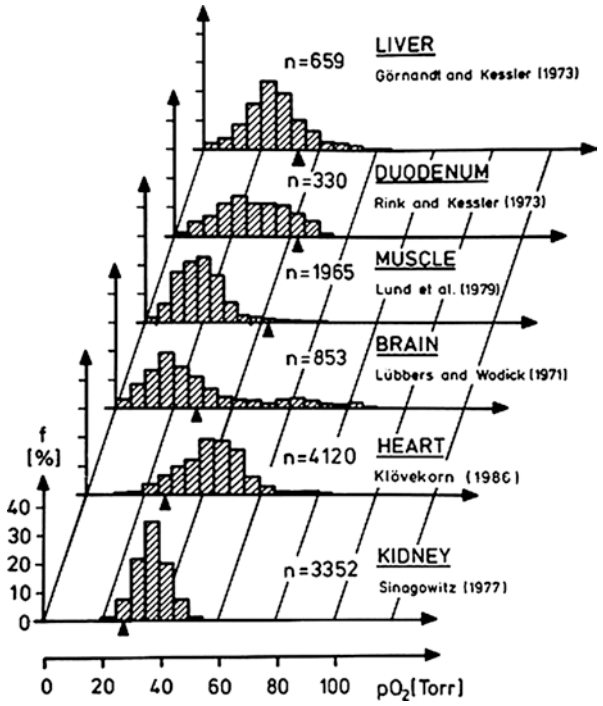

Fig. 4.3 pO_2 histograms measured in various organs [4–9]. The mean venous pO_2 values are indicated by *arrows*

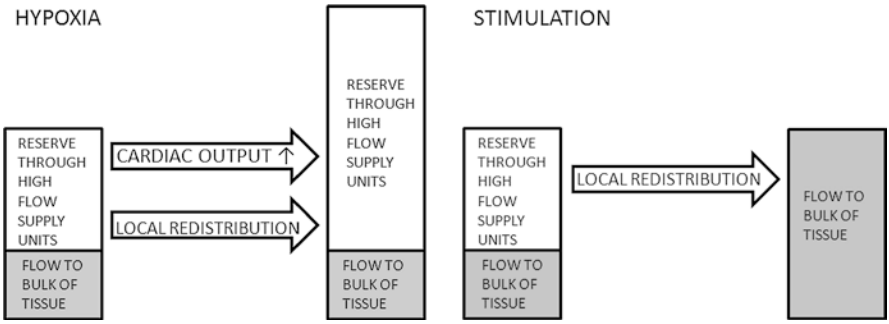

Fig. 4.4 Redistribution of capillary blood flow in skeletal muscle induced by hypoxaemia and stimulation

cylinder at the venous end of the capillaries. This has been demonstrated in the sartorius muscle in anaesthetised dogs during conditions of hypoxaemia [12] and muscle contraction [13], where in no cases were more than 5 % of pO_2 values found in the histogram class 0–5 mmHg. Maximal hypoxaemia (arterial pO_2 31 mmHg) induced an increase of 86 % in femoral artery blood flow, but a decrease in capillary flow of 6 %. Maximal direct stimulation of the muscle (20 Hz) produced no significant increase in femoral artery flow, but a 73 % increase in capillary flow. This physiological redistribution of blood flow is shown schematically in Fig. 4.4.

4 Pathological Responses of Tissue O_2 Supply in Normal Microvasculature and in Malignant Tumours

Two examples are presented of the effect of pathological conditions on local tissue oxygen supply: hypovolaemic shock and critical limb ischaemia. Under these conditions, although the microvasculature is anatomically normal, disturbances of global or regional blood flow mean that the local physiological mechanisms are unable to maintain an adequate tissue oxygen supply, particularly in peripheral organs such as skeletal muscle and skin (Fig. 4.5). In principle, because the microvasculature is intact, it is possible to reverse these conditions: in the first case by replacement of blood volume, in the second by surgical intervention to restore regional blood flow.

In malignant tumours, however, although the tissue pO_2 histograms (see Fig. 4.6) are also shifted to the left, the images of the microvasculatures in the tumours show chaotically heterogeneous arrangements of the microvessels which means that the disturbance to local tissue oxygen supply is irreversible. Although the histograms in solid tumours generally reveal significant anoxia, the pattern of heterogeneity of tissue oxygen supply is not always predictable. The histograms In some tumours, although not usually Gaussian, may even be right-shifted [17–19].

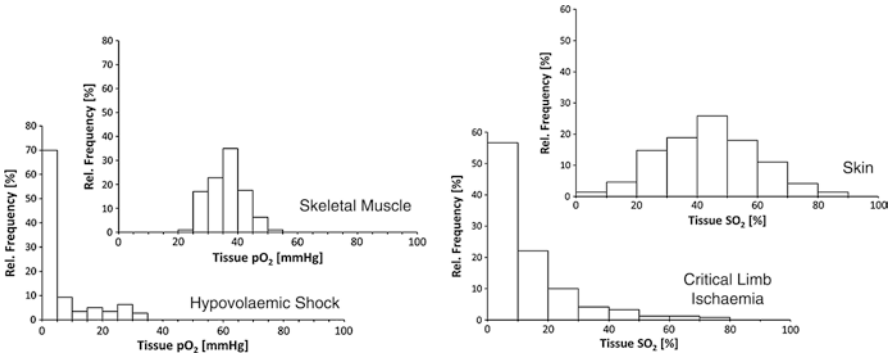

Fig. 4.5 *Left*: pO_2 histograms in skeletal muscle under normal conditions (*top*) and hypovolaemic shock (*bottom*) [14]; *Right*: tissue oxygen saturation (SO_2) histograms in normal (*top*) and critically ischaemic skin (*bottom*) [15]

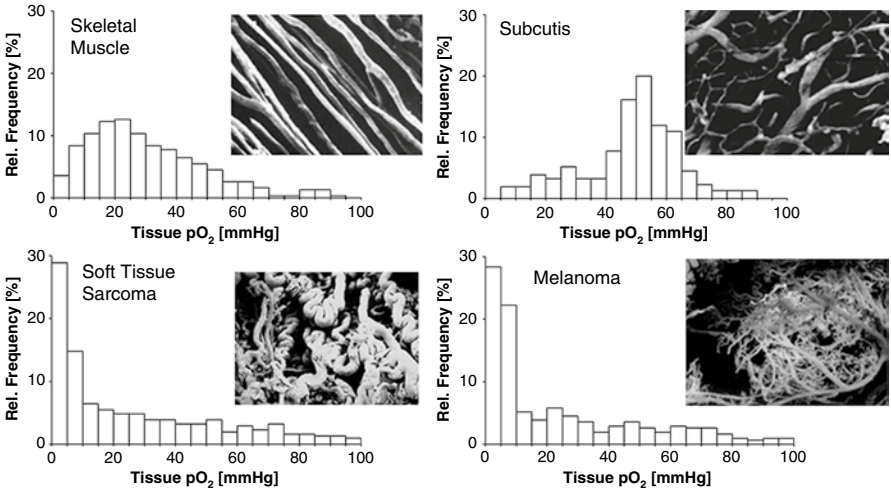

Fig. 4.6 Compilation of pO_2 histograms and microvasculatures of normal tissues (*upper panels*) and of malignant tumours growing in the respective tissue site (*lower panels*). Adapted from [16]

Histograms can vary within the same and different types of tumours, and between patients with the same cancers at the same clinical stage [17–19]. Figure 4.7 shows examples of tumour heterogeneities in breast cancer caused by different expression of the stromal compartment. In stroma-rich cancers the pO_2 histogram becomes increasingly bimodal due to the vasculature-carrying stroma. The greater the stromal compartment, the more bimodal is the distribution. The left part of the histograms show the low pO_2 values in the cancer cell compartment whereas the right part stands for the supporting tumour stroma with "normal" pO_2 values [20].

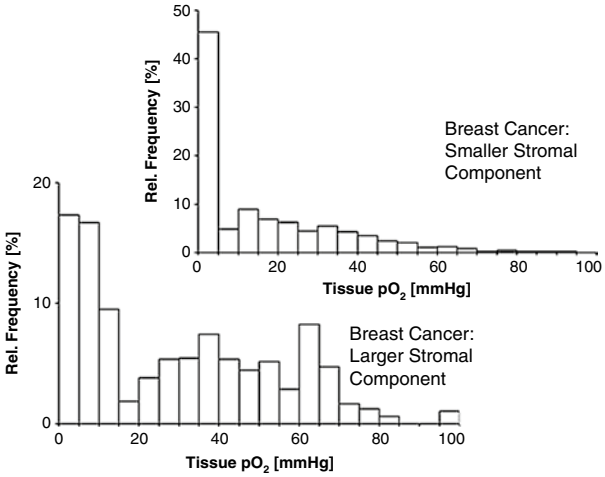

Fig. 4.7 pO_2 histograms of breast cancers with moderate development of the microvasculature carrying stromal compartment (median $pO_2 = 10$ mmHg, *upper panel*) and of stroma-rich breast cancers (median $pO_2 = 25$ mmHg, *lower panel*). Data redrawn from [20]

5 Conclusions

Heterogeneity is a feature of both normal oxygen supply to tissue and of a supply that is disturbed due to a wide range of different pathologies.

The physiological heterogeneity of blood flow at all levels, and local regulation of microcirculatory flow patterns are vital elements in the maintenance of adequate oxygen supply to all tissues, irrespective of local demand.

Pathophysiological disruption of regulation, such as shock or critical ischaemia, or chaotic heterogeneity of microcirculatory patterns found most prominently in malignant tumours, can have fatal consequences. Such consequences are not confined to local tissues, but can prove extremely serious to the whole organism.

References

1. Williams LR, Leggett RW (1989) Reference values for resting blood flow to organs of man. Clin Phys Physiol Meas 10:187–217
2. Thews G, Vaupel P (2005) Vegetative Physiologie. Springer, Heidelberg
3. Harrison DK, Birkenhake S, Knauf S, Hagen N, Beier I, Kessler M (1988) The role of high flow capillary channels in the local oxygen supply to skeletal muscle. Adv Exp Med Biol 222:623–630
4. Görnandt L, Kessler M (1973) Tissue pO_2 in regenerating liver tissue. In: Kessler M, Bruley DF, Clark LC et al (eds) Oxygen supply. Urban & Schwarzenberg, Munich, pp 288–289
5. Rink R, Kessler M (1973) Signs of hypoxia in the small intestine of the rat during haemorrhagic shock. Adv Exp Med Biol 37A:469–475

6. Lund N (1979) Studies on skeletal muscle surface oxygen pressure fields. Dissertation no. 71, Linköping University, Linköping
7. Lübbers DW, Wodick R (1971) Sauerstofftransport im Warmblüterorganismus. Umschau Wiss Techn 13:486–492
8. Klövekorn WP (1986) Das Verhalten der regionalen myokardialen Sauerstoffversorgung unter normalen und pathologishen Bedingungen: Tierexperimentelle Untersuchumgen am schlagenden Herzen. Habilitationsschrift, Ludwig-Maximillians University, Munich
9. Sinagowitz E (1977) Die lokale Sauerstoffversorgung der Nierenrinde bei Hydronephrose und Nierenischämie; ihre klinische Bedeutung in der Urologie. Habilitationsschrift, University of Freiburg, Freiburg im Breisgau
10. Krogh A (1919) The number and distribution of capillaries in muscles with calculations of oxygen pressure head necessary for supplying the tissues. J Physiol (Lond) 52:409–415
11. Hoofd L, Degens H (2013) Statistical treatment of oxygenation-related data in muscle tissue. Adv Exp Med Biol 789:137–142
12. Harrison DK, Kessler M, Knauf SK (1990) Regulation of capillary blood flow and oxygen supply in skeletal muscle in dogs during hypoxaemia. J Physiol (Lond) 420:431–446
13. Harrison DK, Kessler M, Birkenhake S, Knauf SK (1990) Local oxygen supply and blood flow regulation in contracting muscle in dogs and rabbits. J Physiol (Lond) 422:227–243
14. Beier I (1987) Die Verteilung des Sauerstoffpartialdruckes an der Oberfläche des Musculus gracilis der Ratte. Dissertation, Friederich-Alexander University, Erlangen
15. Harrison DK, McCollum PT, Newton DJ, Hickman P, Jain AS (1995) Amputation level assessment using lightguide spectrophotometry. Prosthet Orthot Int 19:139–147
16. Vaupel P, Thews O, Kelleher DK, Höckel M (1998) Current status of knowledge and critical issues in tumor oxygenation. Adv Exp Med Biol 454:591–602
17. Höckel M, Schlenger K, Knoop C, Vaupel P (1991) Oxygenation of carcinomas of the uterine cervix: evaluation by computerized O_2 tension measurements. Cancer Res 51:6098–6102
18. Vaupel P, Schlenger K, Knoop C, Höckel M (1991) Oxygenation of human tumors: evaluation of tissue oxygen distribution in breast cancers by computerized O_2 tension measurements. Cancer Res 51:3316–3322
19. Wendling P, Manz R, Thews G, Vaupel P (1984) Heterogeneous oxygenation of rectal carcinomas in humans: a critical parameter for preoperative irradiation? Adv Exp Med Biol 180:293–300
20. Vaupel P, Höckel M (2001) Blood supply, oxygenation status and metabolic micromilieu of breast cancers: characterization and therapeutic relevance. Int J Oncol 17:869–879

Chapter 5
Oxygen Diffusion: An Enzyme-Controlled Variable Parameter

Wilhelm Erdmann and Stefan Kunke

Abstract Previous oxygen microelectrode studies have shown that the oxygen diffusion coefficient (DO_2) increases during extracellular PO_2 decreases, while intracellular PO_2 remained unchanged and thus cell function (spike activity of neurons). Oxygen dependency of complex multicellular organisms requires a stable and adequate oxygen supply to the cells, while toxic concentrations have to be avoided. Oxygen brought to the tissue by convection diffuses through the intercellular and cell membranes, which are potential barriers to diffusion. In gerbil brain cortex, PO_2 and DO_2 were measured by membrane-covered and by bare gold microelectrodes, as were also spike potentials. Moderate respiratory hypoxia was followed by a primary sharp drop of tissue PO_2 that recovered to higher values concomitant with an increase of DO_2. A drop in intracellular PO_2 recovered immediately. Studies on the abdominal ganglion of aplysia californica showed similar results.

Heterogeneity is a feature of both normal oxygen supply to tissue and supply due to a wide range of disturbances in oxygen supply. Oxygen diffusion through membranes is variable thereby ensuring adequate intracellular PO_2. Cell-derived glucosamine oxidase seems to regulate the polymerization/depolymerisation ratio of membrane mucopolysaccharides and thus oxygen diffusion.

Variability of oxygen diffusion is a decisive parameter for regulating the supply/demand ratio of oxygen supply to the cell; this occurs in highly developed animals as well as in species of a less sophisticated nature. Autoregulation of oxygen diffusion is as important as the distribution/perfusion ratio of the capillary meshwork and as the oxygen extraction ratio in relation to oxygen consumption of the cell. Oxygen diffusion resistance is the cellular protection against luxury oxygen supply (which can result in toxic oxidative species leading to mutagenesis).

W. Erdmann (✉) • S. Kunke
Erasmus University Rotterdam, Goilberdingerdijk 2a, Gelderland,
Culemborg 4105 LA, The Netherlands
e-mail: cbladt@ziggo.nl

H.M. Swartz et al. (eds.), *Oxygen Transport to Tissue XXXVI*, Advances in Experimental Medicine and Biology 812, DOI 10.1007/978-1-4939-0620-8_5,

Keywords Oxygen diffusion • Glucosamine oxidase • Enzyme controlled O_2 diffusion • Mucopolysaccharides • Tissue O_2 autoregulation

1 Introduction

Abiogenetic synthesis in the surface water of quite complex organic molecules occurred in the early development of the earth, the energy deriving from ultra-violet light and ionizing radiation. This was followed by aggregation of these organic compounds in primitive membranes about ±3 billion years ago. This development under anaerobic conditions was important for the formation of nucleotides by the 'first spark,' a process that was probably the origin of life since it led to the development of DNA and RNA, the carriers of genetic information. Photosynthesis, reproduction capacity and endosymbiosis as well as enzyme formation started. The newly developed cells engulfed chloroplasts, including their own DNA, followed by release of oxygen as a waste product. Oxygen escaped into the atmosphere where it blocked damaging UV solar radiation and made it possible for living organisms to leave the protective shielding of water while changing to an oxidative metabolism in which the oxygen consumed by the cells is fully reduced in the terminal cytochrome chain.

However, to exist in an environment with high concentrations of the very reactive and toxic oxygen there had to be a mechanism to limit the amount of oxygen diffusing into the cell while allowing enough oxygen to reach the cell furnace, the mitochondria. Our dependence on oxygen is especially precarious because of the reactive nature of oxygen. In choosing for oxygen as an energy source, nature not only had to develop a means to supply the cells with oxygen at all times, but also to develop a whole spectrum of enzymes and naturalizing reactions to detoxify oxidative intermediates that occur as a normal product of metabolism [1]. There are two main conditions under which the production of mutagenic (cancer precursors) oxidative species may overwhelm the natural defense system: (1) increased oxidative metabolism (e.g. sepsis), and (2) high concentrations and partial pressures of oxygen (luxury O_2 supply).

Oxygen dependency of complex multicellular organisms requires secure adequate oxygen supply to the cells while toxic concentrations have to be avoided. Oxygen brought to the tissue by convection diffuses throughout the intercellular and cell membranes (which can be diffusion barriers).

Previous oxygen microelectrode studies have shown that oxygen diffusion coefficient (DO_2) increases when extracellular PO_2 decreases, while intracellular PO_2 remained unchanged. The aim of our studies was to learn more about the DO_2 regulating mechanism.

2 Methods

PO_2 and DO_2 were measured by membrane-covered (PO_2) and by bare gold microelectrodes (DO_2), as were also spike potentials (Fig. 5.1). The electronic feedback circuit [4] maintaining the polarisation voltage at a desired constant value, permitted separate registration of PO_2, DO_2 and spike potentials (Fig. 5.2). The experiments were performed in the brain cortex of rats, gerbils, monkeys and in the abdominal ganglion of aplysia californensis [2–6].

3 Results

The frequency of measured PO_2 values in the rat brain and the gerbil brain cortex showed that ≥50 % of the values were below 5 mmHg [5]. Simultaneous spike interval measurements showed that active neurons are present in well-supplied areas with tissue PO_2 values of 30 mmHg or more, as well as in areas where cells have to survive with tissue PO_2 values of 5 mmHg, or perhaps even less. Graded hypoxia revealed that

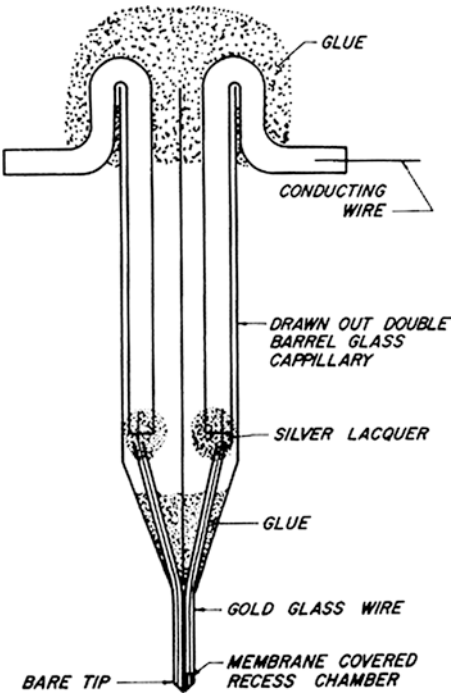

Fig. 5.1 Electrode with two gold in glass microelectrodes (5 µm diameter each) one with recess chamber membrane covered (Clark electrode), one bare gold surface for diffusion and action potential (spike) measurement [2]. Reproduced from [3] by permission

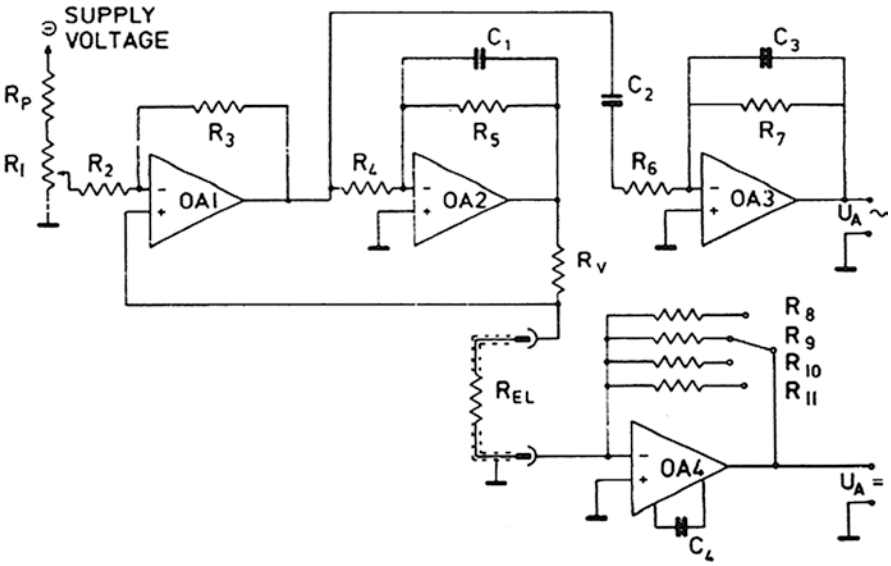

Fig. 5.2 Electronic feedback circuit maintaining polarization voltage constant at a desired value. Polarization voltage is measured by operational amplifier OA1. OA2: inverting amplifier; OA3: amplifier for AC amplification; OA4: O_2 amplifier. List of resistance and capacitance values: $R_p = 4.7$ kΩ, $R_1 = 500$ Ω, $R_2 = 10$ kΩ, $R_3 = 50$ kΩ, $R_4 = 10$ kΩ, $R_5 = 1$ MΩ, $R_6 = 10$ kΩ, $R_7 = 1.2$ MΩ, $R_8 = 10$ MΩ, $R_9 = 80$ MΩ, $R_{10} = 680$ MΩ, $R_{11} = 1$ GΩ, $R_v = 100$ MΩ, $C_1 = 100$ nf, $C_2 = 220$ nf, $C_3 = 8$ pf, $C_4 = 1$ nf. Reproduced from [5] by permission

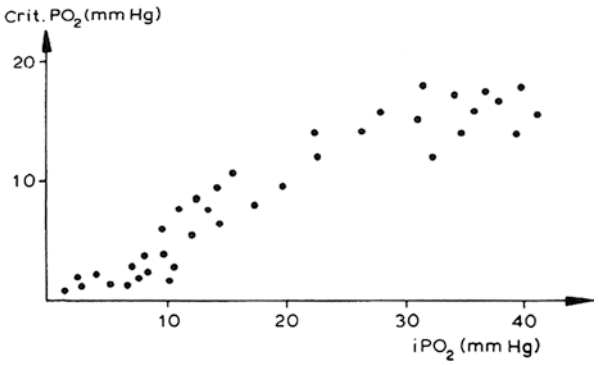

Fig. 5.3 Critical PO_2 values for neuronal function: cells usually functioning in a high PO_2 environment cease cell function at 15–20 mmHg; other cells can stand PO_2 values of 2 mmHg, remaining fully and normally active (environmental adaptation of neuronal cells). Reproduced from [5] by permission

the tissue critical PO_2 for an active pacemaker function of neurons has a broad range of PO_2 of between 20 and 5 mmHg, or even less (Fig. 5.3). Oxygen diffusion coefficients (DO_2) in neuronally active grey matter with high oxygen consumption rates are clearly higher than those in the white matter with low consumption rates [3].

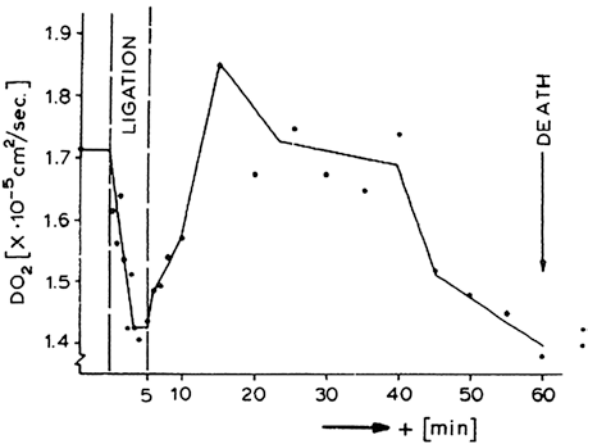

Fig. 5.4 Oxygen diffusion (DO_2) in gerbil brain during reperfusion after a 5-min carotid ligation period. A primary increase of the oxygen diffusion coefficient is followed by a constant decrease until death occurs. Reproduced from [5] by permission

This demonstrates adjustment of DO_2 to the different needs of the various tissues. When oxygen supply to the tissue is lowered, the oxygen transport capacity of the blood lowers (e.g. decreased hematocrit) and there is an autoregulative response with unchanged PO_2 values at hematocrit values of 40 to ±25 [5].

Severe tissue hypoxia only starts at hematocrit values below 25. This autoregulation of tissue PO_2 has been interpreted to be a result of an increase in capillary perfusion, reduction of viscosity, and increase of perfusion pressure. The possibility of regulative changes of oxygen diffusion as a contributing factor was never discussed.

Figure 5.4 shows that, during a 5-min carotid ligation (in gerbils) tissue PO_2 immediately drops to 0, as does the DO_2 from 1.7 to 1.4. During reperfusion DO_2 increases to values above the preligation values and returns to the preligation values, from there it drops continuously to values below 1.4 with PO_2 near 0, until finally death is unavoidable (±60 min later) (Fig. 5.4). Application of hyaluronidase (a glucosamine oxidase) during the post-ischemic period reverses the process of DO_2 with concomitant decrease in tissue PO_2 with full recovery (Fig. 5.5). Measurements of DO_2 and tissue PO_2 before, during and after ligation of the middle cerebral artery in the monkey demonstrated a close relationship between the oxygen diffusion and tissue oxygenation, a decrease during ligation, a post-ischemic high DO_2, followed by a hyperoxic phase and recovery to normal [5, 6].

The abdominal ganglion of aplysia californensis (a mollusc from the early chain of development and a relic of the first phase of development of about one billion years ago) was an ideal model to measure extracellular versus intracellular PO_2. Moving the microelectrode (diameter ±10 µm) into the pacemaker neurons (R6) with a diameter of 500 µm shows a steep gradient of PO_2 from the surrounding oxygen supplying endolymph (40–60 mmHg) extracellular to penetrating the cell membrane and 5–20 mmHg intracellular PO_2 (Figs. 5.6 and 5.7). Stepwise reduction of the

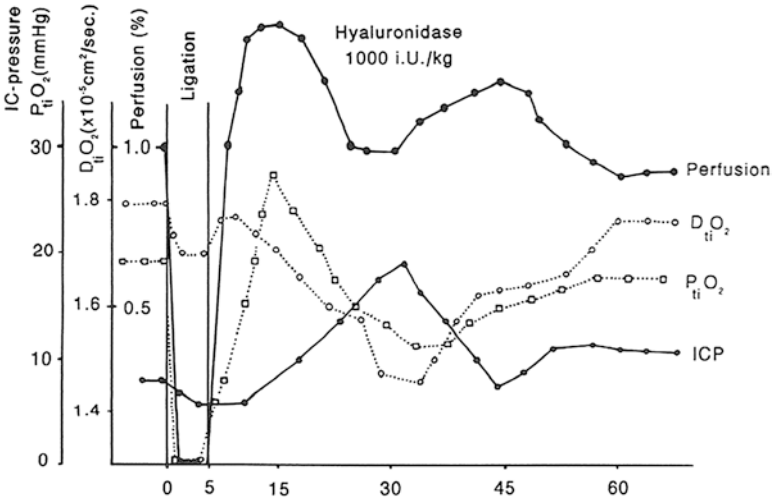

Fig. 5.5 Postischemic changes of microphysiologic parameters determining cellular oxygen supply—treatment with hyaluronidase administration at point of deterioration of $D_{ti}O_2$ (tissue oxygen diffusion coefficient). Reproduced from [5] by permission

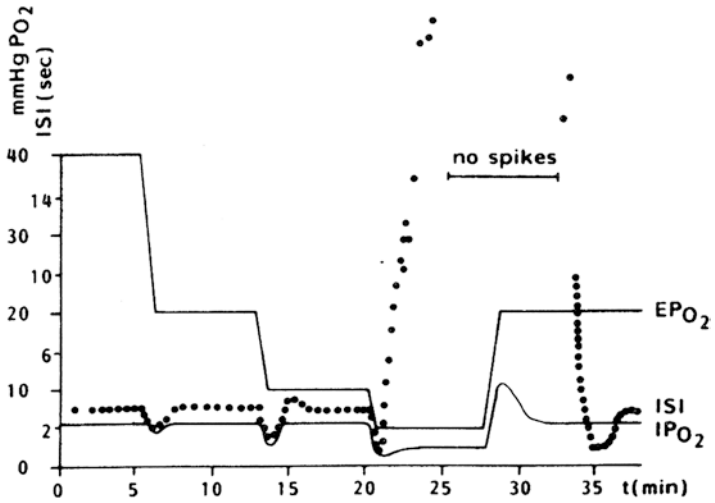

Fig. 5.6 Responses of IPO_2 (intracellular PO_2) to changes of EPO_2 (extracellular PO_2) and effects on bioelectronic function of aplysia giant neurons. The intermittent spike interval (ISI) is registered. ISI changes are closely related and very sensitive to IPO_2 changes, but not to changes of EPO_2. Regarding only the intracellular PO_2 there is no hypoxic-hyperoxic tolerance of cellular neurogenic function to be seen. Reproduced from [5] by permission

extracellular PO_2 (EPO_2) from 40 to ±20 mmHg is first followed by a slight drop of intracellular PO_2 with a slight drop of the intermittent spike interval (ISI), both then returning to normal, and then a further decrease in EPO_2 to ±10 mmHg is followed by a similar transient drop in IPO_2-ISI, recovering to normal within ±1 min. In this

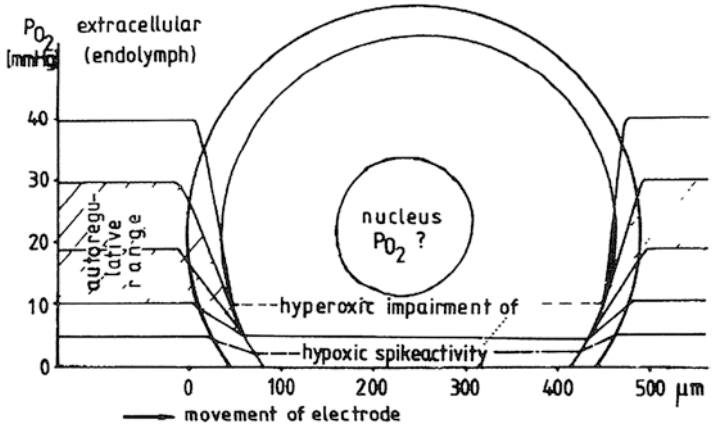

Fig. 5.7 Oxygen gradient through the cell wall of a neuron in the abdominal ganglion of aplysia californensis. These cells are pacemaker cells and have a diameter of 500 µm. The cell membrane changes the diffusion resistance for oxygen by autoregulation and keeps the intracellular PO_2 constant over a broad range of extracellular PO_2 values. Slight reaction of intracellular PO_2 beyond this range, however, results in severe changes of the spike pattern. Reproduced from [5] by permission

special neuron, EPO_2 adjusted to the value before measured intracellular PO_2 leads to a severe hypoxic state of IPO_2 after a slight autoregulative response; this decrease to below normal leads to an abrupt stop of neuronal activity (no further spikes). After a 7-min hypoxic phase. EPO_2 is restored to 20 mmHg immediately followed by an increase of intracellular PO_2 to 10 mmHg and secondary to prehypoxic IPO_2 values (hyperoxic state autoregulated to the original IPO_2 of this cell). The spike activity returns with a delay after a short period of overshoot–undershoot (Figs. 5.6 and 5.7).

4 Discussion

Microelectrode studies have demonstrated huge PO_2 gradients from the oxygen supply medium (blood or endolymph) to the tissue, and from the tissue across the cell membrane into the cell. Thus two membrane diffusion barriers from the capillary into the tissue and from the extracellular tissue into the cell are present.

Moderate changes of oxygen supply (hypoxia of the supplying medium or reduction of transport capacity) changes the gradients after a short transient hypoxic reaction of the supplied tissue or cell. The same happens in response to hyperoxia (thus avoiding luxury oxygen supply). Swartz and colleagues [9–11] using electron paramagnetic resonance, found similar gradients between the intra- and extra-cellular compartments. Incorporation of additional cholesterol in the plasma membrane increased the oxygen gradient, and depletion of cholesterol decreased the gradient, indicating the changeable character of the intracellular PO_2 and the cell interior protecting membranes. The oxygen diffusion and oxygen-regulating barriers seem to be of utmost importance to sustain life; this is demonstrated by the reactivity of

cellular function (e.g. neurogenic function of the pacemaker neurons) to slight changes of intracellular PO_2.

Cells from the earliest phase of existence have an enormous spectrum of enzyme-controlled functions, as well as protection systems with countless nucleus-regulated functions [12]. Regarding the phenomenon of diffusion as a changeable parameter between the membranes as well as between interstitium and the cell interior, the main conclusion can only be the structure of the membrane. The membrane components (e.g. mucopolysaccharides) are either polymerized (high O_2 diffusion resistance) or depolymerised (low diffusion resistance). Glucose oxidase (e.g. hyaluronidase) (Fig. 5.5) depolarises (increase of oxygen diffusion) and vice versa polymerises (increase of diffusion resistance) which occurs due to low glucose amino-oxidase levels. Probably there are various other regulators of membrane diffusibility involved, such as cholesterol, as demonstrated by Swartz and his research team [9–11].

5 Conclusion

Shortly after the 'first spark,' before leaving the protective water environment, cells (aplysia californica) developed a cell nucleus and enzyme-controlled regulation of membrane oxygen diffusibility according to the changing state of the constituents of the membrane of polymerization versus depolymerization, which persists in each cell and tissue, irrespective of its degree of development.

References

1. Erdmann W (1992) Origin of oxygen. Adv Exp Med Biol 317:7–17
2. Erdmann W, Krell (1976) Measurement of diffusion parameters with noble metal electrodes. Adv Exp Med Biol 75:225–228
3. Clark DK, Erdmann W, Halsey JH, Strong E (1978) Oxygen diffusion, conductivity and solubility coefficients in the microarea of the brain. Adv Exp Med Biol 94:697–704
4. Kunke S, Erdmann W, Metzger H (1972) A new method for simultaneous PO2 and action potential measurement in microareas of tissue. J Appl Physiol 32:436–438
5. Erdmann W, Fennema M, van Kesteren R (1992) Factors that determine the oxygen supply of the cell and their possible disruption. Adv Exp Med Biol 317:607–622
6. Nemoto EM, Erdmann W, Strong E, Rao GR, Moosy J (1977) Regional brain PO2 after global ischemia in monkeys: evidence for regional differences in critical perfusion pressures. Stroke 8:558–564
7. Morawetz R, Strong E, Clark DK, Erdmann W (1978) Effects of ischemia on the diffusion coefficients in the brain cortex. Adv Exp Med Biol 94:629–632
8. Chen C, Erdmann W, Halsey J (1978) The sensitivity of applysia giant neurons to changes in extracellular and intracellular PO2. Adv Exp Med Biol 94:691–696
9. Swartz HM (1994) Measurement of intracellular concentrations of oxygen: Experimental results and conceptual implications of an observed gradient between intracellular and extracellular concentrations of oxygen. Adv Exp Med Biol 345:799–806

10. Khan N, Shen J, Chang TY, Chang CC, Swartz H et al (2003) Plasma membranes cholesterol: a possible barrier to intracellular oxygen in normal and mutant CHO cells defective cholesterol metabolism. Biochemistry 42:23–29
11. Chen K, Ng CE, Zweier JL, Kuppusamy P, Glickson JD, Schwartz HM (1994) Measurement of the intracellular concentrations of oxygen in a cell perfusion system. Magn Reson Med 31:668–672
12. de Duve C (1984) A guided tour of the living cell. Scientific American Books, New York

Chapter 6
Role of Microvascular Shunts in the Loss of Cerebral Blood Flow Autoregulation

Edwin M. Nemoto, Denis E. Bragin, Gloria Statom, Mark Krasberg, Suguna Pappu, Bobby Sena, Tracey Berlin, Kim Olin, and Howard Yonas

Abstract Historically, determination of the critical cerebral perfusion pressure (CPP) was done in animals by a progressive lowering of arterial pressure yielding a nominal critical CPP of 60 mmHg. Subsequently, it was shown that if the CPP was decreased by increasing intracranial pressure (ICP), critical CPP fell to 30 mmHg. This discrepancy was unexplained. We recently provided evidence that the decrease in critical CPP was due to microvascular shunting resulting in maintained cerebral blood flow (CBF) at a lower CPP. We demonstrated by a progressive increase in ICP in rats using two-photon laser scanning microscopy (2PLSM) that the transition from capillary to microvascular shunt flow is a pathological process. We surmise that the loss of CBF autoregulation revealed by decreasing arterial pressure occurs by dilation of normal cerebral blood vessels whereas that which occurs by increasing ICP is due to microvascular shunting. Our observations indicate that the loss of CBF autoregulation we observed in brain injured patients that changes on an hourly or daily basis reflects an important pathophysiological process impacting on outcome that remains to be determined.

Keywords Brain • Cerebral blood flow • Edema • Intracranial pressure • Microvascular shunts • Thoroughfare channels

E.M. Nemoto (✉) • G. Statom • M. Krasberg • S. Pappu • B. Sena
T. Berlin • K. Olin • H. Yonas
Department of Neurosurgery, University of New Mexico, 1101 Yale Blvd, NE, Domenici Hall, Brain Center, RM 1131B, Albuquerque, NM 87131, USA
e-mail: enemoto@salud.unm.edu

D.E. Bragin
Department of Neurosurgery, University of New Mexico, 1101 Yale Blvd, NE, Domenici Hall, Brain Center, RM 1131B, Albuquerque, NM 87131, USA

BRaIN Imaging Center, University of New Mexico, Albuquerque, NM 87106, USA

H.M. Swartz et al. (eds.), *Oxygen Transport to Tissue XXXVI*, Advances in Experimental Medicine and Biology 812, DOI 10.1007/978-1-4939-0620-8_6,

1 Introduction

Intracranial pressure (ICP) was first measured clinically more than 60 years ago [1]. With the measurement of ICP, the concept of cerebral perfusion pressure (CPP) or mean arterial pressure minus ICP evolved [2]. Simultaneously, methods to measure cerebral blood flow (CBF) were developed along with the concept of CBF autoregulation [3]. With these developments, the question arose as to the minimum cerebral perfusion pressure (CPP) or the "critical CPP" where CBF would begin to fall and brain perfusion compromised. This was especially relevant to brain injured patients in whom CPP may fall due to either a *decrease* in mean arterial pressure (MAP) or an *increase* in ICP.

Historically, critical CPP has been determined in animals by a progressive reduction of arterial pressure in the *normal*, *uninjured*, brain to decrease CPP while measuring CBF yielding a value of about 60 mmHg [3, 4]. This was applied clinically. The recommended CPP in the Brain Trauma guidelines is 50–70 mmHg [5].

However, Miller et al. [6] showed in dogs, that when CPP was reduced by *increasing ICP* as opposed to *decreasing arterial pressure*, the critical CPP fell to 30 mmHg (Fig. 6.1). Their observations were subsequently reproduced in non-human primates [7, 8] and rats [9]. The reason for the decrease in CPP to 30 mmHg by increasing ICP remained unexplained. We recently tested the *hypothesis* that the reduction in critical CPP by high ICP was due to microvascular shunting resulting in a sustained high CBF at a lower CPP by using two-photon laser scanning microscopy (2PLSM) [10] and examined the effect of increasing CPP on the transition from capillary to microvascular shunt flow [11].

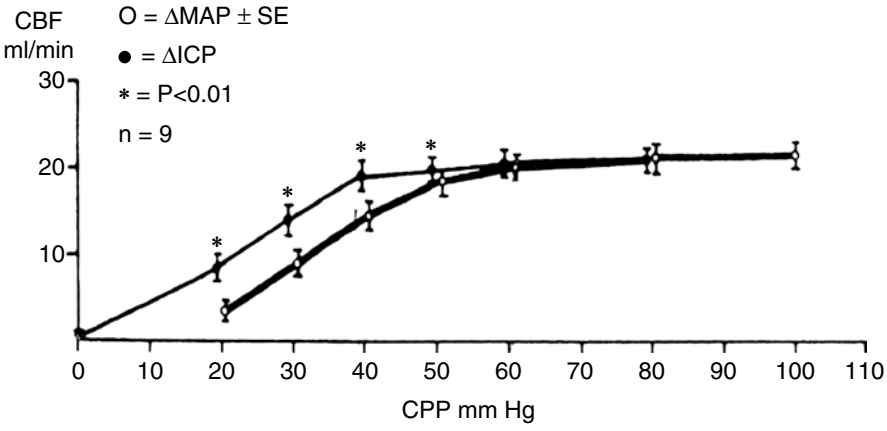

Fig. 6.1 Effect of altering cerebral perfusion pressure (CPP) by decreasing arterial pressure (*thick line*) and by increasing intracranial pressure (*thin line*) in dogs with intact autoregulation on cerebral blood flow (CBF). Significance between changes assessed by paired *t*-test [11]. $*P<0.05$ [11]. Reproduced with permission of the Editor of Elsevier Press

2 Methods

2.1 Two Photon Laser Scanning Microscopy Studies

All procedures used in these studies were previously described [10]. Briefly, laboratory acclimated, male, Sprague-Dawley rats weighing 250–300 g body weight were studied by 2PLSM under 2 % isoflurane/70 % nitrous oxide/28 % oxygen anesthesia via a craniotomy over the left parietal cortex.

Fluorescent serum was visualized using an Olympus BX 51WI upright microscope and water-immersion LUMPlan FL/IR 20×/0.50 W objective. Excitation was provided by a PrairieView Ultima multiphoton microscopy laser scan unit powered by a Millennia VI 6 W diode laser source pumping a Tsunami Ti:sapphire laser (Spectra-Physics, Mountain View, CA) tuned to 810-nm center wavelength. Band-pass-filtered epifluorescence (560–660 nm) was collected by the photomultiplier tubes of the Prairie View Ultima system. Images (512×512 pixels, 0.15 μm/pixel in the x- and y-axes) or line scans were acquired using Prairie View software. Red blood cell flow velocity was measured in microvessels ranging from 3 to 25 μm diameter up to 500 μm below the surface of the parietal cortex as previously described [8].

Tissue hypoxia was assessed by measurement of NADH concentration by autofluorescence and blood brain barrier (BBB) permeability by fluorescein dye transcapillary extravasation. In offline analyses using NIH ImageJ software, three dimensional anatomy of the vasculature in regions of interest was reconstructed from two-dimensional (planar) scans of the fluorescence intensity obtained at successive focal depths in the cortex (XYZ stack). Attenuation of the signal along the Z-direction was corrected by multiplication of each XY image by factors determined empirically from plots of the intensity variation of background fluorescence as a function of depth.

Doppler flux was measured via a lateral temporal window using a 0.9 mm diameter probe (DRT4, Moor Inst., Axminster, UK) in the same region of the brain studied by 2PLSM. Brain and rectal temperatures were monitored and controlled at 38 ± 0.5 °C. Arterial blood gases and pH were monitored intermittently.

2.1.1 Microvascular Shunting by Increasing Intracranial Pressure

The rats were studied at CPP of 70 (baseline), 50 and 30 mmHg by increasing ICP or decreasing arterial pressure as previously described [10]. Arterial blood gases and all monitored variables were recorded during the 30 min duration at each CPP and ICP or mean arterial pressure (MAP). ICP was increased by the height of a fluid reservoir of artificial CSF at different levels through a catheter sealed into the cisterna magna. Arterial pressure was decreased by phlebotomy through a femoral venous catheter.

2.1.2 Increasing CPP Attenuates the Transition from Capillary Flow to Microvascular Shunts with Increasing ICP

In a second series of studies with the aim of studying the effects of increasing CPP on microvascular shunting with increasing ICP, rats were subjected to a 10 mmHg stepwise increase in ICP from a baseline normal of 10–60 mmHg with CPP maintained at 50, 60, 70 and 80 mmHg by titrated i.v. dopamine infusion throughout the increase in ICP [11].

2.2 Multimodal Monitoring System in Patients

We also report on the results of our multimodality monitoring system in our Neurosurgical Intensive Care Unit (NSICU) using the Component Neuromonitoring System (CNS) (Moberg Research, Inc., Philadelphia, PA). The CNS monitor enables the simultaneous acquisition of brain monitored variables such as tissue PO_2 (Licox), cerebral blood flow (CBF) (Bowman, Inc.), near infrared cerebral oximetry, temperature and intracranial pressure time-locked with vital signs including arterial pressure, pulse oximetry, and EKG. The data are collected de-identified and stored on a server. We currently have data from about 300 patients and are in the process of analyzing these data to explore for significant correlations and relationships that may reveal useful predictors of adverse patterns in these physiological variables to correlate with patient outcome. One of these variables is the correlation between pulsatile arterial pressure and pulsatile changes in CBF and ICP with respect to phase and amplitude both of which would provide information on CBF and ICP autoregulation.

3 Results

Increasing ICP to decrease CPP resulted in increased microvascular shunt flow at higher velocity and larger microvessel diameters of 8–25 μm (Fig. 6.2) which did not occur when CPP was decreased by reducing arterial pressure [10].

Progressively increasing ICP from baseline to 60 mmHg was accompanied by a decrease in the ratio of capillary (CAP)/microvascular shunt (MVS) reflecting a gradual transition from capillary to MVS shunt flow (Fig. 6.3) [11].

The loss of CBF autoregulation observed clinically is especially important if ICP is increased which would lead to a pressure-passive relationship between arterial pressure and ICP. With the development of clinical multimodality monitoring with the Component Neuromonitoring System (CNS) developed by Moberg and colleagues and with the development of various brain tissue monitors such as brain tissue PO_2 ($PbtO_2$), blood flow (CBF), temperature, and intracranial pressure all time locked with vital signs, has enabled the acquisition of data to illustrate

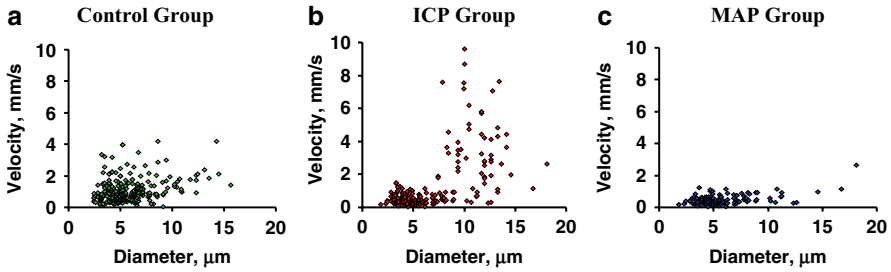

Fig. 6.2 (**a**) normal CPP (70 mmHg) and by (**b**) decreased CPP to 30 mmHg by increasing ICP. (**c**) Decreased MAP to reduce the CPP to 30 mmHg [10]. Reproduced with the permission of the Editor of J Neurotrauma

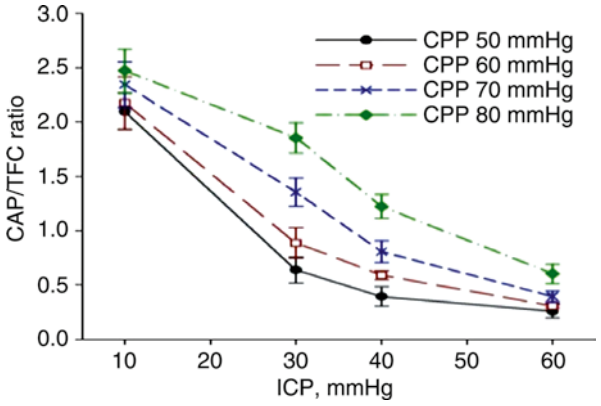

Fig. 6.3 Ratio of capillary (CAP) and thoroughfare channel (TFC) shunt flow with increasing intracranial pressure (ICP) and different cerebral perfusion pressure (CPP) in rats. Increasing ICP increases TFC flow [11]. Reprinted with the permission of the Editor of Stroke Journal

variations in CBF and ICP autoregulation with spontaneous fluctuations in arterial pressure. Acquisition of pulsatile waveforms by AD converters of arterial pressure, intracranial pressure and high frequency CBF allows the continuous assessment of CBF and ICP autoregulation by CVRx and PRx, respectively.

The relationships between CBF and arterial pressure in patients in whom arterial pressure, CBF and ICP were monitored showed CBF and ICP autoregulation varied on a daily if not an hourly basis (Fig. 6.4).

4 Discussion

Our observation of a progressive increase in microvascular shunting with increasing ICP suggests that the decrease in critical CPP is due to microvascular shunting resulting in a sustained high CBF at a lower CPP. In stark contrast, microvascular

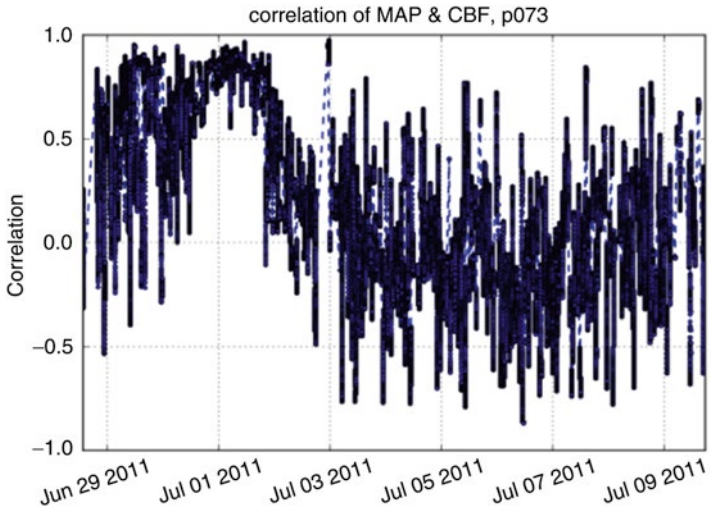

Fig. 6.4 Correlation coefficient plot of mean arterial pressure (MAP) and thermal diffusion cerebral blood flow (CBF) showing daily variations in correlation coefficients reflecting loss and return of CBF autoregulation

shunting did *not* occur when CPP was decreased by reducing arterial pressure. These results suggest that the loss of CBF autoregulation where CPP is manipulated by increasing ICP or decreasing arterial pressure likely differ in the fundamental mechanisms involved.

We surmise that the reduction in CPP by decreasing arterial pressure results in a pressure passive decrease in flow through cerebral capillaries whereas that observed by increasing ICP occurs through a transition from capillary to microvascular shunt flow, i.e. two entirely different processes. This mechanism is supported by the observation of capillary rarefaction in stroke in animal models [11].

These results for the first time show the gradual transition from capillary to microvascular shunt flow where previously only two stable states of capillary and microvascular shunts were known.

5 Conclusions

The loss of CBF autoregulation in the injured brain represents pathological microvascular shunt flow whereas that observed by a passive decrease in CPP represents a simple vasodilation of normal cerebrovasculature.

Acknowledgments Supported in part by: NIH Grants NS061216, NS051639 and UNM HSC COBRE program (P20 RR15636).

References

1. Guillaume J, Janny P (1951) Continuous intracranial manometry; physiopathologic and clinical significance of the method. Presse Med 59(45):953–955
2. Ingvar DH (1964) The regulation of cerebral circulation. Acta Anaesthesiol Scand Suppl 15(15):43–46
3. Jennett WB, Harper AM, Miller JD et al (1970) Relation between cerebral blood-flow and cerebral perfusion pressure. Br J Surg 57(5):390
4. Waltz AG, Yamaguchi T (1970) Pressure-flow relationships of the cerebral vasculature: autoregulatory responses to changes of perfusion pressure produced without drugs or hemorrhage. Trans Am Neurol Assoc 95:326–327
5. Brain Trauma Foundation, American Association of Neurological Surgeons, Congress of Neurological Surgeons, Joint Section on Neurotrauma and Critical Care, AANS/CNS, Bratton SL, Chestnut RM, Ghajar J et al (2007) Guidelines for the management of severe traumatic brain injury. IX. Cerebral perfusion thresholds. J Neurotrauma 24(1):S1–S116
6. Miller JD, Stanek A, Langfitt TW (1972) Concepts of cerebral perfusion pressure and vascular compression during intracranial hypertension. Prog Brain Res 35:411–432
7. Grubb RL Jr, Raichle ME, Phelps ME et al (1975) Effects of increased intracranial pressure on cerebral blood volume, blood flow, and oxygen utilization in monkeys. J Neurosurg 43(4):385–398
8. Johnston IH, Rowan JO, Harper AM, Jennett WB (1972) Raised intracranial pressure and cerebral blood flow: I. Cisterna magna infusion in primates. J Neurol Neurosurg Psychiat 35:285–296
9. Hauerberg J, Juhler M (1994) Cerebral blood flow autoregulation in acute intracranial hypertension. J Cereb Blood Flow Metab 14:519–525
10. Bragin DE, Bush RC, Müller WS et al (2011) High intracranial pressure effects on cerebral cortical microvascular flow in rats. J Neurotrauma 28(5):775–785
11. Bragin DE, Bush RC, Nemoto EM (2013) Effect of cerebral perfusion pressure on cerebral cortical microvascular shunting at high intracranial pressure in rats. Stroke 44(1):177–181

Chapter 7
Impact of Hypoxia-Related Tumor Acidosis on Cytotoxicity of Different Chemotherapeutic Drugs *In Vitro* and *In Vivo*

Oliver Thews, Anne Riemann, Martin Nowak, and Michael Gekle

Abstract Extracellular acidosis in tumors leads to an activation of the p-glycoprotein (Pgp) drug transporter. In the present study the cytotoxicity of different chemotherapeutic drugs and its dependence on the Pgp activity during acidosis were analyzed *in vitro* and *in vivo*. Treating R3327-AT1, Pgp-positive tumor cells at pH 7.4 with daunorubicin, cisplatin or docetaxel led to marked apoptosis induction and cell death. Under acidic (pH 6.6) conditions cytotoxicity of daunorubicin or docetaxel was significantly reduced whereas cisplatin-induced cell death was almost pH-independent. Inhibiting Pgp with verapamil reversed the acidosis-induced chemoresistance against daunorubicin and docetaxel. The Pgp expression was unaffected by pH. *In vivo* the cytotoxicity of daunorubicin and docetaxel was also pH dependent. When acidifying the tumors by forcing glycolytic metabolism, apoptosis induction decreased significantly indicating a reduced chemosensitivity. The cytotoxic effect of cisplatin *in vivo* was unaffected by the tumor pH. Since daunorubicin and docetaxel (but not cisplatin) are substrates of the Pgp, these results underline the influence of the tumor acidosis on the Pgp-mediated chemoresistance which can be counteracted by inhibition of the drug transporter.

Keywords Multi-drug resistance • Chemotherapy • Acidosis • p-Glycoprotein • Pgp expression

O. Thews (✉) • A. Riemann • M. Gekle
Julius-Bernstein-Institute of Physiology, University of Halle, Halle (Saale), Germany
e-mail: oliver.thews@medizin.uni-halle.de

M. Nowak
Institute of Physiology and Pathophysiology, University of Mainz, Mainz, Germany

H.M. Swartz et al. (eds.), *Oxygen Transport to Tissue XXXVI*, Advances in Experimental Medicine and Biology 812, DOI 10.1007/978-1-4939-0620-8_7,

1 Introduction

Hypoxic tumors are known to be resistant to numerous chemotherapeutic drugs [1] with various mechanisms responsible for this. For instance, several drugs are interacting with molecular oxygen resulting in ROS and cytotoxic oxidative stress [2] or hypoxia might induce a cell cycle arrest limiting the cytotoxicity of drugs acting in specific cell cycle phases [3, 4]. However, previous studies have also shown that indirect effects of hypoxia might contribute to chemoresistance.

Hypoxia-induced extracellular acidosis activates drug transporters which extrude cytotoxic drugs out of the tumor cells resulting in a chemoresistant phenotype. This effect is most prominent for the p-glycoprotein (Pgp) [5, 6]. These studies also showed that the chemotherapeutic drug daunorubicin (DNR) became less effective in an acidotic environment [5]. Since DNR is a substrate of the Pgp, it was proposed that the loss in cytotoxicity is the result of the increased Pgp transport rate leading to a reduced intracellular drug concentration. However, also other mechanisms of a pH-dependent reduction in chemosensitivity have to be considered. Since daunorubicin is a weak base ($pK_a = 8.46$) [7] the uptake of the drug may be reduced by the extracellular acidosis, since passive diffusion into the cell takes place only in the undissociated form of the molecule [3]. In this case the diminished cytotoxicity under acidotic conditions may also result from a reduced cellular uptake and not from Pgp.

For this reason, the aim of the present study was to analyze the cytotoxic effect of different chemotherapeutics (daunorubicin, cisplatin, docetaxel) under acidic conditions (pH 6.6). Besides daunorubicin, docetaxel is also a substrate of the Pgp whereas the cisplatin transport is independent from the Pgp expression or activity [8]. For this reason the present experiment is suitable to show whether the pH-dependent Pgp activity is responsible for the reduced cytotoxicity or whether other mechanisms have to be considered. All experiments were performed *in vitro* with isolated Pgp-positive tumor cells but also *in vivo* using experimental tumors in which the glycolytic metabolism was intensified leading to pronounced extracellular acidosis.

2 Material and Methods

2.1 Cell Lines

The subline AT1 of the R-3327 Dunning-prostate carcinoma of the rat was used in all experiments. In cell culture experiments (*in vitro*) cells were incubated either in HEPES (20 mM)-buffered Ringer solution adjusted to pH 7.4 or in 20 mM MES (morpholinoethanesulfonic acid) + 4.51 mM $NaHCO_3$ resulting in a pH of 6.6 for 3 or 6 h. These solutions were also containing the chemotherapeutic drugs (see below).

For the *in vivo* experiments the same cell line was implanted subcutaneously in male Copenhagen rats (body weight 180–260 g) by injection of AT1 cells

(0.4 ml approx. 10^4 cells/µl) into the dorsum of the hind foot. Tumors grew as flat, spherical segments and replaced the subcutis and corium completely. Experiments were performed when tumors reached a target volume of 0.5–1.5 ml, approx. 10–14 days after tumor cell inoculation. Studies were approved by the regional ethics committee and conducted according to UKCCCR guidelines [9] and the German Law for Animal Protection.

2.2 Chemotherapy

Tumor cells as well as solid tumors *in vivo* were treated with daunorubicin (DNR), cisplatin (CIS) or docetaxel (DOC). *In vitro* the drugs were used at concentrations of 10 µM(DNR), 150 µM (CIS) or 1 µM (DOC) and cells were incubated for 3 (DNR, CIS) or 6 (DOC) hours. Afterwards caspase 3-activity was measured. Additionally, cells were allowed to regrow (by replacing the Ringer solution with FCS-containing medium) for 42 h and the number of surviving cells was determined. *In vivo* tumor bearing rats received a single i.p. dose of DNR (50 mg/kg b.w.), CIS (10 mg/kg b.w.) or DOC (15 mg/kg b.w.), respectively. The drugs were dissolved either in isotonic saline or in EtOH which was further diluted in isotonic saline. Three hours after chemotherapy tumors were surgically removed and caspase 3-activity was determined.

2.3 Forcing Glycolytic Metabolism

In order to induce a more pronounced extracellular acidosis in solid tumors *in vivo*, rats were treated with a combination of inspiratory hypoxia (inspiratory O_2-fraction 8 %, starting 30 min prior to chemotherapy), hyperglycaemia (3 g/kg b.w., i.v., 15 min prior to the chemotherapy) and an injection of meta-iodo-benzylguanidine (MIBG, 20 mg/kg b.w., i.v. 4 h prior to chemotherapy) [10] in order to force anaerobic glycolysis in the tumor cells. Previous measurements revealed that this treatment reduces the extracellular tumor pH from 7.04 ± 0.05 (control) to 6.65 ± 0.04 (acidotic) [5].

2.4 Measurement of Apoptosis Induction and Cell Survival

Caspase 3-activity was determined as described previously [11] using the caspase 3-substrate DEVD-AFC. In the *in vitro* experiments cells were directly lysed whereas for the *in vivo* experiments cryosections of the tumors were used, which were then lysed. The lysates were incubated with DEVD-AFC and cleaved AFC-fluorescence was measured in a fluorescence multi-well reader at 405 nm excitation

and 535 nm emission wavelengths. All measurements were normalized with respect to the protein content in each sample.

The number of surviving cells after treating the cells *in vitro* was determined using a Casy cell counter (Innovatis, Reutlingen, Germany).

3 Results

Treating R3327-AT1, Pgp-positive tumor cells *in vitro* at pH 7.4 with daunorubicin (DNR), cisplatin (CIS) or docetaxel (DOC) led to marked apoptosis induction and cell death (Fig. 7.1). The cytotoxic effect under these control conditions was most pronounced with CIS whereas DOC induced distinct lower apoptosis and cell kill. When adding verapamil (VPL), an inhibitor of the p-glycoprotein, cytotoxicity of DNR and CIS was not altered, whereas the cytotoxic effect of DOC was significantly increased. Since docetaxel is a substrate of the Pgp [8] it can be proposed that VPL treatment leads to an increase in intracellular drug concentration resulting in a higher anti-tumoral effect.

Exposing AT1 cells to an acidic extracellular pH of 6.6 for 3 or 6 h (without chemotherapy) led only to a minor induction of apoptosis. However, treating the cells with the three chemotherapeutics at pH 6.6 resulted in a significant reduction in apoptosis induction as compared to pH 7.4 (which was less pronounced with docetaxel) (Fig. 7.1a). With daunorubicin and docetaxel the reduction in apoptosis was reflected in a higher number of surviving cells compared to pH 7.4 (Fig. 7.1b) whereas with cisplatin the cell survival remained almost unchanged. An additional incubation of the cells with verapamil at pH 6.6 resulted in a significant increased apoptosis and decreased cell survival after DNR and DOC but not after CIS treatment. In summary, extracellular acidosis reduced the cytotoxicity (measured by caspase 3-activity) of daunorubicin by 84 ± 2 %, of cisplatin by 70 ± 1 % and of docetaxel by 50 ± 4 %. With additional VPL incubation the respective values were 43 ± 4, 72 ± 2 and 24 ± 4 %. Obviously, the cytotoxicity of drugs which are substrates of the Pgp (daunorubicin, docetaxel) was reduced at low pH, an effect which was reversed by a Pgp inhibitor, indicating a higher Pgp transport rate under acidic conditions. However, analyzing the Pgp expression revealed that the acidotic environment did not lead to a higher Pgp expression (Fig. 7.2).

The cytotoxicity *in vivo* was assessed by measuring apoptosis in the tumor tissue. All three drugs led to a significant increase in caspase 3-activity most pronounced for DNR and CIS whereas DOC showed the least cytotoxicity (Fig. 7.3). With daunorubicin a linear correlation between intratumoral drug level (which was measured by its own fluorescence in the tumor tissue) and caspase 3-activity was seen ($r = 0.636$). When forcing glycolytic metabolism in these tumors ("acidosis treatment") leading to a reduced tumor pH, the cytotoxicity of DNR and DOC was significantly reduced (Fig. 7.3) whereas the cytotoxicity of CIS remained almost independent from the tumor pH. The normalized cytotoxicity at an acidotic pH of 6.65 ± 0.04 compared to control tumors with a pH of 7.04 ± 0.05 was 74 ± 5 % for daunorubicin, 103 ± 5 % for cisplatin and 89 ± 3 % for docetaxel.

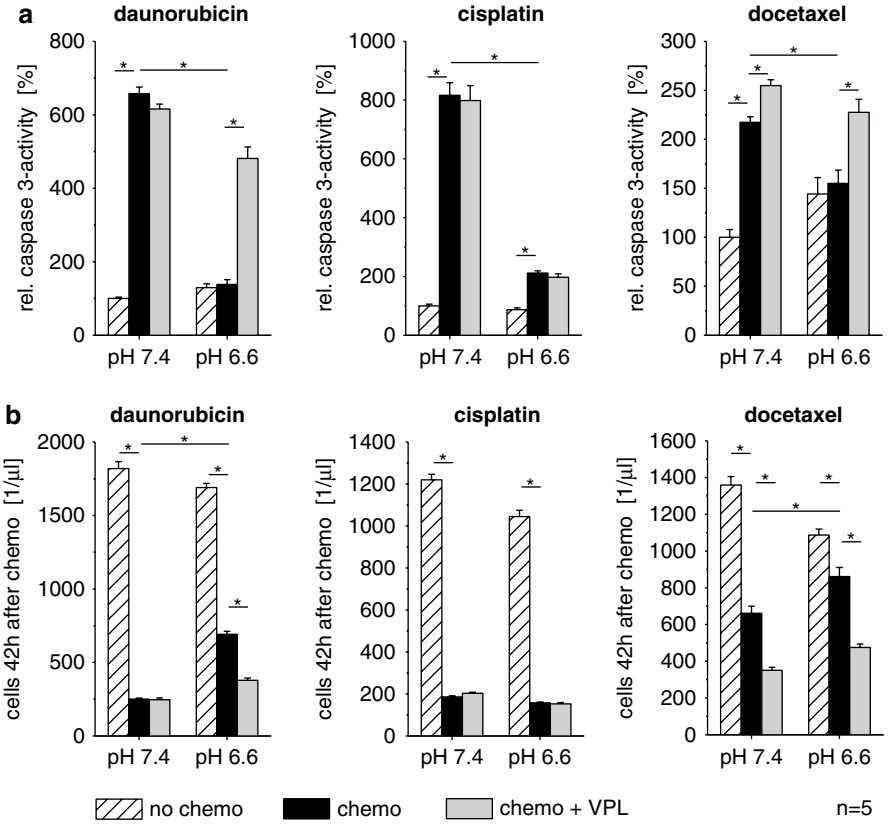

Fig. 7.1 *In vitro* cytotoxicity of daunorubicin, cisplatin and docetaxel measured by (**a**) apoptosis induction and (**b**) cell survival under control conditions (pH = 7.4) and during extracellular acidosis. Measurements were performed without and with additional inhibition of the Pgp by verapamil (VPL). *$p < 0.05$; n = 5

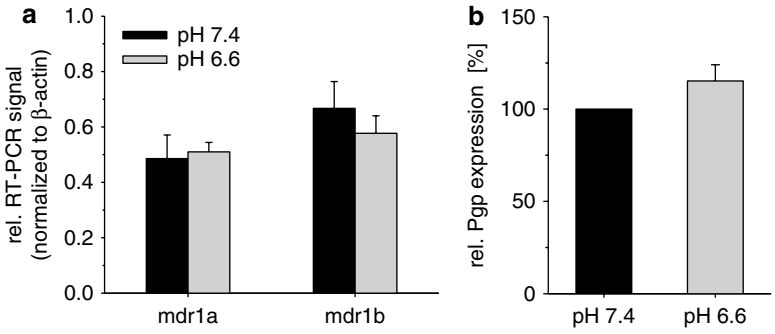

Fig. 7.2 Impact of extracellular pH on p-glycoprotein expression. (**a**) Mdr1 transcription (PCR) and (**b**) Pgp protein expression (Western blot) under control and acidotic conditions. n = 5

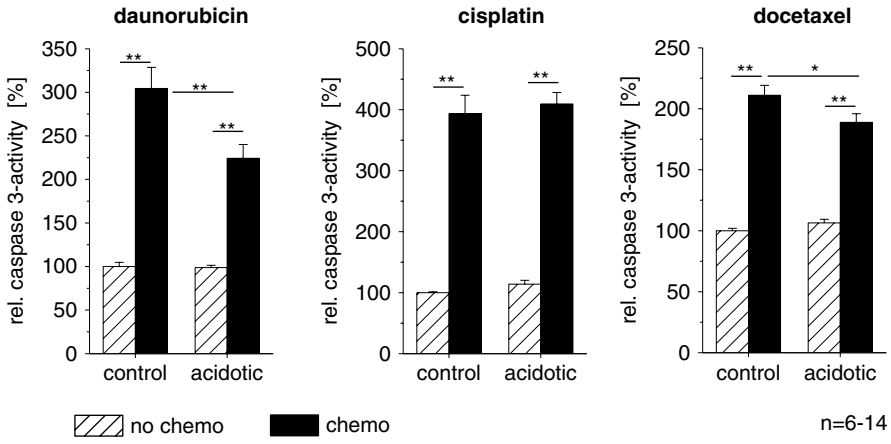

Fig. 7.3 Impact of tumor pH on cytotoxicity *in vivo*. Apoptosis induction after treating tumors with daunorubicin, cisplatin and docetaxel in control (pH 7.04 ± 0.05) and acidotic (pH 6.65 ± 0.04) tumors; *$p < 0.05$, **$p < 0.01$; n = 6–14 tumors

4 Discussion

Extracellular acidosis with a pH of 6.6 has been shown to significantly increase the transport activity of the p-glycoprotein. In the AT1 cell line used in the present study the transport rate was more than doubled in isolated cells [6] but also in experimental solid growing tumors [12]. This increase in transport was not associated with changes in expression of the transport protein (Fig. 7.2) and has therefore been attributed to a functional modulation.

In the *in vitro* experiments, apoptosis induction by the three drugs (daunorubicin, cisplatin, docetaxel) was significantly reduced in the acidic extracellular medium (Fig. 7.1), an effect which was most prominent with DNR and CIS. Reichert et al. [13] also described a reduced cytotoxicity of vincristine, teniposide, gemcitabine and cisplatin, which was cell line specific for cisplatin. These data are therefore in good accordance with the present result (Fig. 7.1). Other studies described a reduction in doxorubicin cytotoxicity (consistent with the present study) but an increase in cisplatin efficacy by acidosis [14]. Therefore it seems likely that the effect of cisplatin is strongly cell line dependent showing marked differences in the sensitivities to cisplatin. The AT1 cell line clearly showed a strong reduction in cisplatin-induced apoptosis induction. However, the number of surviving cells after chemotherapy was almost pH-independent (Fig. 7.1b) indicating that cytotoxicity did not only rely on apoptosis induction. Besides apoptosis necrotic cell death may contribute. Release of lactate dehydrogenase (LDH) from the cells can be used as a measure of necrosis. In the present study the release during cisplatin treatment at pH 7.4 was only 5.6 ± 2.4 % of the total LDH whereas under acidotic conditions (with cisplatin) it reached 32.8 ± 12.2 %.

These data indicate that necrosis markedly increased during cisplatin treatment at pH 6.6 which could explain the constant number of surviving cells even though apoptosis was reduced significantly (Fig. 7.1).

When adding the Pgp-inhibitor verapamil, the impact of Pgp-dependent drug extrusion for chemoresistance becomes measurable. With DNR and DOC which are Pgp-substrates the pH-dependent reduction of cytotoxicity became at least partially reversible, indicating that the previously described Pgp-activation is responsible for the reduction of the cytotoxicity under acidotic conditions. However, with cisplatin (which is no Pgp substrate) the loss of chemosensitivity is not induced by Pgp activity (VPL-independent) (Fig. 7.1). Here, other mechanisms, for instance alterations of the cell cycle, may be responsible for reduced apoptosis induction under acidotic conditions.

These cell experiments lead to the question whether the observed loss in chemosensitivity by acidosis also takes place *in vivo*. Therefore, the glycolytic metabolism was intensified as described before [5] leading to a drop of extracellular pH from 7.04 to 6.65 which was associated with a reduction of apoptosis induced by daunorubicin and docetaxel. However, the reduction was smaller than *in vitro* which may be due to the fact that even under control conditions the extracellular pH was lower than in cell culture, probably leading to a Pgp activation even under control conditions. In contrast to the *in vitro* experiments cisplatin did not show a pH-dependent reduction in apoptosis induction. Since the reason for the pH-dependency of cisplatin *in vitro* remains unclear, the differences between *in vitro* and *in vivo* experiments need to be further investigated, especially the question whether the observed differences are cell line specific.

In conclusion, the present data underline the impact of extracellular acidosis on the activity of the p-glycoprotein and the resulting chemoresistance against drugs which are substrates of the Pgp (daunorubicin and docetaxel but not cisplatin) which can be counteracted by inhibition of the drug transporter. The results with cisplatin reveal that also Pgp-independent effects of the pH on the chemosensitivity have to be taken into account and need further investigation.

Acknowledgments This study was supported by Deutsche Krebshilfe (grants 106774/106906).

References

1. Teicher BA, Holden SA, al Achi A et al (1990) Classification of antineoplastic treatments by their differential toxicity toward putative oxygenated and hypoxic tumor subpopulations in vivo in the FSaIIC murine fibrosarcoma. Cancer Res 50:3339–3344
2. Fang J, Nakamura H, Iyer AK (2007) Tumor-targeted induction of oxystress for cancer therapy. J Drug Target 15:475–486
3. Chaplin DJ, Horsman MR, Trotter MJ et al (1998) Therapeutic significance of microenvironmental factors. In: Molls M, Vaupel P (eds) Blood perfusion and microenvironment of human tumors. Springer, Berlin, pp 131–143
4. Teicher BA (1994) Hypoxia and drug resistance. Cancer Metastasis Rev 13:139–168

5. Sauvant C, Nowak M, Wirth C et al (2008) Acidosis induces multi-drug resistance in rat prostate cancer cells (AT1) in vitro and in vivo by increasing the activity of the p-glycoprotein via activation of p38. Int J Cancer 123:2532–2542
6. Thews O, Gassner B, Kelleher DK et al (2006) Impact of extracellular acidity on the activity of p-glycoprotein and the cytotoxicity of chemotherapeutic drugs. Neoplasia 8:143–152
7. Di Marco A, Casazza AM, Dasdia T et al (1977) Changes of activity of daunorubicin, adriamycin and stereoisomers following the introduction or removal of hydroxyl groups in the amino sugar moiety. ChemBiol Interact 19:291–302
8. Chan LM, Lowes S, Hirst BH (2004) The ABCs of drug transport in intestine and liver: efflux proteins limiting drug absorption and bioavailability. Eur J Pharm Sci 21:25–51
9. Workman P, Aboagye EO, Balkwill F et al (2010) Guidelines for the welfare and use of animals in cancer research. Br J Cancer 102:1555–1577
10. Kalliomäki T, Hill RP (2004) Effects of tumour acidification with glucose+MIBG on the spontaneous metastatic potential of two murine cell lines. Br J Cancer 90:1842–1849
11. Schwerdt G, Freudinger R, Schuster C et al (2003) Inhibition of mitochondria prevents cell death in kidney epithelial cells by intra- and extracellular acidification. Kidney Int 63:1725–1735
12. Thews O, Dillenburg W, Fellner M et al (2010) Activation of P-glycoprotein (Pgp)-mediated drug efflux by extracellular acidosis: in vivo imaging with ^{68}Ga-labelled PET tracer. Eur J Nucl Med Mol Imaging 37:1935–1942
13. Reichert M, Steinbach JP, Supra P et al (2002) Modulation of growth and radiochemosensitivity of human malignant glioma cells by acidosis. Cancer 95:1113–1119
14. Atema A, Buurman KJ, Noteboom E et al (1993) Potentiation of DNA-adduct formation and cytotoxicity of platinum-containing drugs by low pH. Int J Cancer 54:166–172

Chapter 8
The Founding of ISOTT: The Shamattawa of Engineering Science and Medical Science

Duane F. Bruley

Abstract The founding of ISOTT was based upon the blending of Medical and Engineering sciences. This occurrence is portrayed by the Shamattawa, the joining of the Chippewa and Flambeau rivers. Beginning with Carl Scheele's discovery of oxygen, the medical sciences advanced the knowledge of its importance to physiological phenomena. Meanwhile, engineering science was evolving as a mathematical discipline used to define systems quantitatively from basic principles. In particular, Adolf Fick's employment of a gradient led to the formalization of transport phenomena. These two rivers of knowledge were blended to found ISOTT at Clemson/Charleston, South Carolina, USA, in 1973.

The establishment of our society with a mission to support the collaborative work of medical scientists, clinicians and all disciplines of engineering was a supporting step in the evolution of bioengineering. Traditional engineers typically worked in areas not requiring knowledge of biology or the life sciences. By encouraging collaboration between medical science and traditional engineering, our society became one of the forerunners in establishing bioengineering as the fifth traditional discipline of engineering.

Keywords Carl Scheele • Adolf Fick • ISOTT • Medical and engineering sciences • Clemson/Charleston meeting

1 The Merging of Engineering and Medical Sciences

The wise man Confucius once said, "Study the past if you would define the future." In consideration of this insight, I have thought back to days in Northern Wisconsin where I have spent a great part of my life hunting and fishing. I think about the

D.F. Bruley (✉)
Synthesizer, Inc., 2773 Westminster Road, Ellicott City, MD 21043, USA
e-mail: bruley33@verizon.net

H.M. Swartz et al. (eds.), *Oxygen Transport to Tissue XXXVI*, Advances in Experimental Medicine and Biology 812, DOI 10.1007/978-1-4939-0620-8_8,

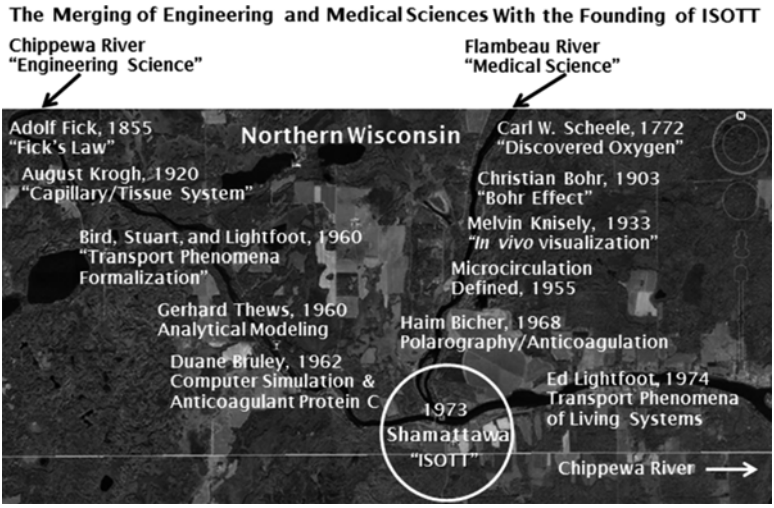

Fig. 8.1 ISOTT, a formal, focused merging of engineering science and medical science in oxygen transport to tissue

Chippewa River and the Flambeau River (Fig. 8.1) and how they meet at what is called the "Shamattawa" (the confluence of two rivers). Similarly, I view the founding of ISOTT as the merging of engineering science and medical science. While there are many important players on both sides, we can only highlight a few due to space limitations. A historical review of this development starts with the discovery of oxygen by Scheele in 1777 [1] (Flambeau River), while on the engineering science side, the concept of transport phenomena started with Adolf Fick in 1855 [2] (Chippewa River). Following the discovery of oxygen, scientists such as Christian Bohr [3] and Melvin Knisely [4] evolved the medical sciences through their studies and observations. On the engineering science side, with the concept of Fick's Law, August Krogh applied Fick's Law involving the oxygen gradient in tissue [5]. At a later date, Professors of Chemical Engineering at the University of Wisconsin, Madison, Bird, Stewart, and Lightfoot formalized the discipline of transport phenomena in inanimate objects [6]. Gerhard Thews, employing linear analytical mathematics, expanded on Krogh's conceptualization of a tissue cylinder [7], which was further refined by Duane F. Bruley using complex computer simulations to study the Krogh capillary tissue cylinder (unsteady state, non-linear, multi-component, convection, diffusion, and reaction kinetics) [8]. Following this research, Haim I. Bicher used micro-electrodes and polarography on the grey matter of the brain to validate the mathematical simulations which had demonstrated that oxygen and component gradients existed in the tissue [9]. In these early days, the microcirculation was formally defined (1955). ISOTT was then established at the Clemson/Charleston, South Carolina founding meeting in 1973 [10, 11], which was then followed by Ed Lightfoot's 1974 book, which applied transport phenomena to living systems [12].

This paper is an enhancement of the presentations and papers prepared for the 1997, 2006, and 2010 *International Society on Oxygen Transport to Tissue* meetings [13–15]. Similar to most successful research projects the development of ISOTT has been a serendipitous process. Prior to the founding of this society, there were many meetings, internationally, related to oxygen transport in tissue as well as several societies that promoted sessions on the subject. ISOTT became one of the first societies to form with the specific focus of promoting collaboration between the medical sciences and engineering.

A significant byproduct of the establishment of ISOTT has been its major contribution to the evolution of today's bioengineer. Prior to the 1970s, all of the traditional disciplines of engineering education focused on inanimate systems and the discipline of bioengineering was not recognized and even ridiculed in engineering education.

The evolution of modern engineering began in the early eighteenth century. We all know that engineering applications were promoted back hundreds of years before Napoleon. However, Napoleon's need for engineering structures, roads, bridges, pure water, etc., motivated him to establish special corps of engineers assigned to these tasks. After the wars, these people returned to their villages and carried out those duties in a civilian capacity. This evolved into the first formal traditional discipline of engineering—the civil engineer. The civil engineers were educated primarily in mathematics and the basic science of physics. From this beginning the traditional discipline of mechanical engineering evolved and again it was based primarily on mathematics and physics. The next step in the progression was the formalization of the electrical engineering discipline, also based primarily on mathematics and physics. Chemical engineering came out of World War II, when Hitler used the chemical industry to his advantage to produce necessary gasoline, rocket fuels, poisonous gases, etc., for his military. The chemists in that operation who were primarily involved with process design and development became the backbone of the formalization of the traditional discipline of chemical engineering. It is obvious that the formal background and training of the chemical engineer required not just mathematics and physics, but also a strong background in chemistry, utilizing a second basic science.

These steps in the engineering progression have led to what I call the fifth traditional discipline in engineering [16]. Bioengineering (biomedical and biological engineering) stands as a traditional discipline primarily because of the necessity of formal education in mathematics and all three basic sciences—physics, chemistry, and *biology*. It is fully understood that all of the traditional disciplines of engineering are interacting so that a total knowledge base might be necessary for any engineering endeavor. However, it is essential that the modern bioengineer has a formal education in the biological and life sciences. We all know that traditional civil, mechanical, electrical and chemical engineers can and do make contributions in the biological and medical sciences. However, it is well understood in this day and age that the definition of bioengineering includes formal education in the biological sciences. Because the mission of ISOTT includes the importance of interdisciplinary and cross disciplinary interactions, it has brought traditional engineers in close

collaboration with medical scientists and clinicians, supporting and promoting the establishment of a formal bioengineering discipline.

In a historical sense, bioengineering has been with us for thousands of years. Mummies have even been discovered with wooden prosthetic body parts [17]. In 1816, a French physician used a rolled up newspaper next to a young woman's chest to listen to the heartbeat, triggering the idea that led to the development of the stethoscope. Engineering has provided enhancements that have led to improvements in disease diagnosis, probably as long as man has been around. The formal roots of bioengineering reach back two hundred years or so to early developments in electrophysiology. Early in this century, bioengineering's unique mix of engineering, medicine, and science evolved with biophysics and medical physics with no formal educational programs. The first training programs for physics in medicine were established in Germany in 1921, and a biophysics Ph.D. program was established in 1940. A biophysical society was formed in Germany in 1943. Throughout the world during that era, there were many conferences and meetings that brought together engineering and medical science. The diversity of work and background of people contributing made it difficult for a single organization to represent everyone. Since there were many professional groups, several umbrella organizations were established to facilitate cooperation. In 1968, the Biomedical Engineering Society was founded to recognize bioengineering and its applications. From further research, it appears that ISOTT founded in 1973, was the second organized effort to formally advance the interaction between disciplines in an effort to solve medical problems in a very narrow application area, oxygen transport to tissue. Hence our society became a real entity and has advanced to our present status.

Our charter was established to define a high level research society without a desire to grow large, but to focus mainly on quality research, presenting and publishing incremental studies on an annual basis. During the years of our society, we have established such honors as the Knisely, Lübbers, Chance, and Bruley Awards, and the Kovach Lecturer. The recipients and presenters can be found on the ISOTT website, www.isott.org. These goals of high quality research still remain our focus, which fuels our contributions to the future.

The remainder of the story can be found in previously published ISOTT history papers as mentioned above, as well as on the ISOTT website. I would be happy to take further questions with discussion at any convenient time.

The future of ISOTT will be determined by our young and new members, with the dedicated mentoring of our old time membership. It will be important to stay current with new technology and be flexible enough to embrace new directions in the area of oxygen transport to tissue. The vision of ISOTT members will be critical in guiding this very special international scientific and engineering society through the troubled waters created by politics, religion, and other outside influences.

Referring back to Fig. 8.1, the flow of the Chippewa River after the Shamattawa represents the future of the society. Technologies in sensing and measuring oxygen in normal physiology and pathology in combination with theoretical predictions and analysis are major components. Further studies in the pathology of blood and exploring modern technologies to prevent or diminish the harmful impact of oxygen deprivation to tissue are worthy goals.

Acknowledgments Dr. Bruley is most grateful for the expert and professional assistance of Eileen Thiessenin the preparation of this paper and supporting presentation.

References

1. Scheele CW (1964) "Discovery of oxygen, part 2, experiments by Carl Wilhelm Scheele (1777)," reissue edition, published for The Alembic Club. E&S Livingstone, Edinburgh
2. Tyrrell HJV (1964) The origin and present status of Fick's Diffusion Law. J Chem Ed 41(7):397–400
3. Bohr C, Hasselbalch K, Krogh A (1904) Skand Arch Physiol 16:402
4. Goro FW (1948) Blood sludge. Life Magazine 24(22):49–59
5. Krogh A (1918/1919) J Physiol (Lond) 52:409
6. Bird RB, Stewart WE, Lightfoot EN (1960) Transport phenomena. John Wiley & Sons, New York
7. Thews G (1960) Oxygen diffusion in the brain. A contribution to the question of the oxygen supply of the organs. Pflugers Arch 271:197–226
8. Reneau DD, Bruley DF, Knisely MH (1967) "A mathematical simulation of oxygen release, diffusion and consumption in the human brain," chemical engineering in medicine and biology. Plenum, New York, pp 135–241
9. Bicher HI, Bruley DF, Knisely MH (1973) Anti-adhesive drugs and tissue oxygenation. In: Bruley DF, Bicher HI (eds) Advances in experimental medicine and biology, vol 37. Plenum, New York, pp B657–B667
10. (1973) Oxygen transport to tissue-instrumentation, methods, and physiology. In: Bicher HI, Bruley DF (eds) Advances in experimental medicine and biology, vol 37A. Plenum, New York
11. (1973) Oxygen transport to tissue-pharmacology, mathematical studies, and nematology. In: Bruley DF, Bicher HI (eds) Advances in experimental medicine and biology, vol 37B, Plenum, New York
12. Lightfoot EN (1974) Transport phenomena and living systems: biomedical aspects of momentum and mass transport. John Wiley & Sons, New York
13. Bruley DF (1998) The genesis of ISOTT. In: Hudetz AG, Bruley DF (eds) Oxygen transport to tissue XX. Plenum, New York
14. Bruley DF (2008) ISOTT: roots, founding, and beyond. In: Kang KA, Harrison DK, Bruley DF (eds) Oxygen transport to tissue XXIX, advances in experimental medicine and biology, vol 614. Springer, New York
15. Bruley DF (2010) The history of ISOTT. In: Wolf M et al (eds) Oxygen transport to tissue XXXIII, advances in experimental medicine and biology, vol 737. Springer, New York
16. Bruley DF (1992) Bioengineering: the fifth traditional engineering discipline. In: Erdmann W, Bruley DF (eds) Advances in experimental medicine and biology, vol 317. Plenum, New York, pp 3–6
17. http://www.bmesphotos.org/WhitakerArchives/glance/history.html

Chapter 9
A Tale of Two Methods: Combining Near-Infrared Spectroscopy with MRI for Studies of Brain Oxygenation and Metabolism

Jeff F. Dunn, Nabeela Nathoo, and Runze Yang

Abstract Combining magnetic resonance imaging (MRI) with near-infrared spectroscopy (NIRS) leads to excellent synergies which can improve the interpretation of either method and can provide novel data with respect to measuring brain oxygenation and metabolism. MRI has good spatial resolution, can detect a range of physiological parameters and is sensitive to changes in deoxyhemoglobin content. NIRS has lower spatial resolution, but can detect, and with specific technologies, quantify, deoxyhemoglobin, oxyhemoglobin, total hemoglobin and cytochrome oxidase. This paper reviews the application of both methods, as a multimodal technology, for assessing changes in brain oxygenation that may occur with changes in functional activation state or metabolic rate. Examples of hypoxia and ischemia are shown. Data support the concept of reduced metabolic rate resulting from hypoxia/ischemia and that metabolic rate in brain is not close to oxygen limitation during normoxia. We show that multimodal MRI and NIRS can provide novel information for studies of brain metabolism.

Keywords MRI • Near-infrared • Brain • Hypoxia • Multimodal imaging

J.F. Dunn (✉)
Hotchkiss Brain Institute, University of Calgary, Calgary, AB, Canada

Department of Radiology, University of Calgary, 3330 Hospital Drive, N.W., Calgary, AB, Canada T2N 4 N1

Experimental Imaging Centre, University of Calgary, Calgary, AB, Canada
e-mail: dunnj@ucalgary.ca

N. Nathoo • R. Yang
Hotchkiss Brain Institute, University of Calgary, Calgary, AB, Canada

Department of Radiology, University of Calgary, 3330 Hospital Drive, N.W., Calgary, AB, Canada T2N 4 N1

H.M. Swartz et al. (eds.), *Oxygen Transport to Tissue XXXVI*, Advances in Experimental Medicine and Biology 812, DOI 10.1007/978-1-4939-0620-8_9,

1 Introduction

Hypoxia (low oxygen conditions) in brain can be both a cause and an effect of brain disorders. An obvious case of this is ischemia, or stroke, which reduces perfusion and brain oxygenation, eventually leading to neuronal death. Many disorders including Alzheimer's disease [1], multiple sclerosis [2], stroke [3], birth asphyxia, and sudden infant death syndrome [4], to name a few, are also associated with altered brain metabolic rate, reduced functional activation or with hypoxia.

Changes in metabolic rate also impact brain oxygenation. An increase in metabolic rate associated with increased functional activity leads to an increase in both perfusion and oxygenation [5, 6]. Conversely, a decrease in metabolic rate results in increased deoxyhemoglobin (HHb) and decreased oxygenation. The basis of blood-oxygen level dependent (BOLD) magnetic resonance imaging (MRI) is that the activation decreases HHb, a paramagnetic contrast agent, leading to an increase in signal on MRI [6].

Alterations in oxygenation may be the cause of a brain disorder, such as in acute hypoxia, or may reflect changes in functional activation or metabolic rate. Measurements of brain oxygenation and metabolism can provide novel information in terms of identifying the cause of a disorder, or for monitoring disease progression or treatment.

As the brain is encased within the skull, non-invasive imaging methods which can assess metabolism and oxygenation over repeated measurements are required. Both MRI and NIRS have been used extensively for this purpose. The combination of NIRS and MRI can provide a new multimodal tool that allows for improved calibration of MRI (Fig. 9.1), improved spatial resolution of NIRS and novel datasets linking metabolism with oxygenation.

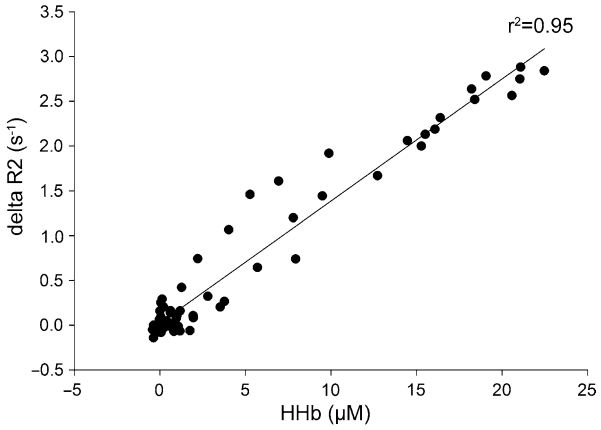

Fig. 9.1 Calibration of ΔR_2 using Δdeoxyhemoglobin (HHb). The slope of the best fit line is 0.14. Data are obtained from rat cortex during a pulse of low oxygen at 9.4 T using a T2 weighted sequence to measure ΔR_2, and a broadband NIRS system to quantify HHb. Although many factors contribute to the slope [21], R_2 can be used to estimate the changes in microvascular hemoglobin saturation and tissue oxygenation [22]

Possibly the first to actually use MRI and NIRS in combination as a multimodal tool performed functional MRI and NIRS simultaneously while subjects performed a unilateral sequential finger opposition task, with the key finding being that a task-related decrease in HHb was seen using both MRI and NIRS [7].

2 Fiber Optics and MRI, the Issues and Solutions to Multimodality Imaging

The main problem with undertaking multimodal imaging relates to the quality and location of the fiber optics. The components that are placed within the MRI need to be magnet-compatible. This means that the technology must be safe to put inside the MRI. One must also consider whether the presence of the technology will adversely impact the image quality. Most non-magnetic materials are safe, but different plastics and glass may still cause susceptibility artifacts. Probes with plastic caps may or may not be MRI-compatible.

The location of the probes can also be an issue. Since subjects are laying down in the MRI, it can be difficult to place fibers onto the back of the head. Also, many studies use an RF coil that fits closely to the head. In order for the tip of the probe to fit tightly onto the scalp and still fit inside the RF coil, the bend radius has to be very small or the fiber requires a prism to turn the light path, allowing the fibers to be positioned parallel to the skin. The requirement for a small turn radius makes fiber bundles more versatile than solid fibers.

3 Advantages of Combining NIRS and MRI

One clear advantage of the multimodal technique is the use of MRI to provide structural information that can then be applied in the reconstruction and localization of NIRS data [8, 9]. NIRS mapping data can be projected onto the surface of the cortex [10]. This provides depth information and allows 3D reconstruction of NIRS images. A second major advantage is the ability to obtain data on tissue oxygenation with NIRS at the same time as obtaining anatomical, physiological, biochemical and metabolic data from MRI. The following are examples of how multimodal MRI/NIRS provides novel data in brain.

4 Studying Cellular Redox Potential

The cellular redox potential describes the equilibrium that involves the ratio of nicotinamide adenine dinucleotide (NAD)/NADH. This, in turn, relates to the potential for mitochondria to produce adenosine triphosphate (ATP) [11].

In brain, the ratio of phosphocreatine (PCr) to inorganic phosphate (Pi) has been reported to be a non-invasive measure of intracellular redox potential and correlates with NADH [12]. In NIRS, the absorption spectrum of the copper (a) component (Cu_A) of cytochrome oxidase (cytOx) will change with oxidation state, and therefore, will also relate to redox potential [11]. However, each method has its own assumptions. For instance, the PCr/Pi ratio argument is based on a model and requires other metabolic factors to be constant, such as pH. The cytOx signal is small, making it difficult to differentiate this signal from changes associated with oxyhemoglobin (HbO_2) [13]. Combining ^{31}P NMR and NIRS allows one to study the relationship between the PCr/Pi ratio and cellular redox potential.

5 Measuring Brain Oxidative State in Hypoxia

A combined ^{31}P NMR and NIRS study was conducted to determine if the redox state of the electron transport chain is dependent on cerebral oxygenation during normoxia and normal brain function. Piglets were anesthetized with isoflurane and ventilated [11]. Broadband NIRS was undertaken with the sensitive volume in the cortex. Quantification of NIRS was carried out using second differential spectroscopy [14] in conjunction with an anoxia pulse. ^{31}P NMR was done at 7 T with non-localized spectroscopy. A repeated anoxia of 105 s was used to reduce blood oxygenation.

This paradigm resulted in significant brain hypoxia. However, HbO_2 declined well before Cu_A showed a change, supporting the argument that levels of oxygen in mitochondria are normally above a limiting concentration. Also, PCr content only began to decline when Cu_A began to change, after which there was a linear relationship between the two parameters.

A similar type of study was done in piglets using a graded hypoxia paradigm. Inspired oxygen was reduced while obtaining ^{31}P NMR spectroscopy on a 4.7 T MRI and NIRS data using a NIRO-500. Changes in cytOx did not relate to changes in HbO_2 or HHb directly, providing evidence that cytOx data was independent of hemoglobin. PCr correlated best with Cu_A but neither declined immediately with reduction in oxygenation [15]. A study of cardiopulmonary bypass showed a linear relationship between cytOx redox state and relative ^{31}P concentration [16].

These multimodal studies confirm that changes in cytoplasmic PCr/Pi provide a reasonable approximation of changes in mitochondrial redox potential in brain. Additionally, the fact that the reduction in oxidation state was delayed relative to the reduction in oxygenation supports the premise that oxygen levels in the brain are not close to limiting for metabolism under normal conditions. A previous paper using electron paramagnetic resonance to quantify brain tissue PO_2 and ^{31}P NMR to quantify energetics came to a similar conclusion—oxygen levels have to drop significantly before affecting PCr or pH [17].

6 Measuring Cerebral Metabolic Rate for Oxygen ($CMRO_2$) in Hypoxia-Ischemia

In studies of hypoxia/ischemia (or stroke), NIRS/MRI can provide information on brain physiology, including cell swelling, while monitoring oxygenation and energy metabolism. A study of the metabolic effects of hypoxia-ischemia (HI) was performed on the newborn piglet brain using a broadband NIRS system in combination with 3 T MRI [18]. Metabolic energy substrates were assessed with ^{31}P NMR, ^{1}H spectroscopy was used to study lactate, and diffusion weighted MRI was used to study edema. $CMRO_2$ was calculated using the Fick principle using NIRS.

There was a significant decline in $CMRO_2$ after HI (Fig. 9.2). This decline had been observed previously [19]. The decline was progressive, with a low plateau occurring about 1.5 h post-HI. The apparent diffusion content (ADC) declined significantly

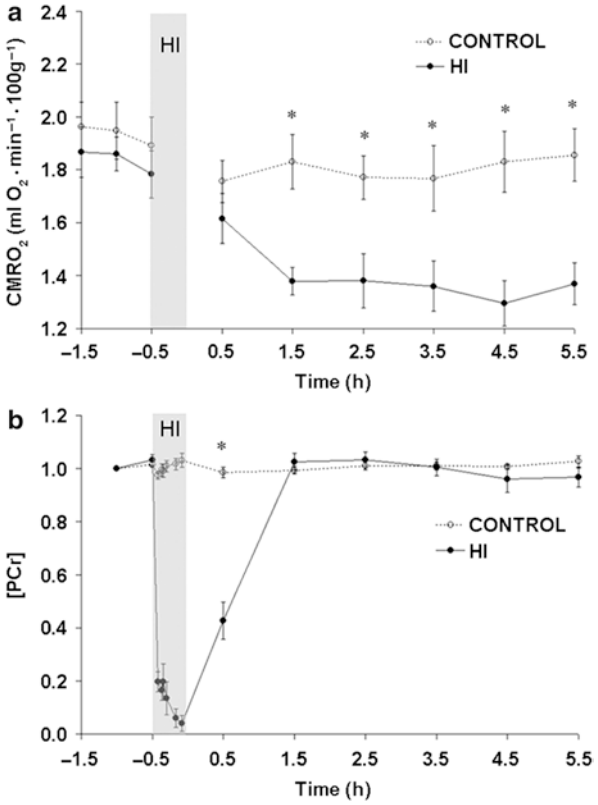

Fig. 9.2 Multimodal studies of stroke (hypoxia/ischemia, HI) in a piglet model. (**a**) metabolic rate for oxygen ($CMRO_2$) and (**b**) phosphocreatine (PCr) with time. $CMRO_2$ was calculated from NIRS data on hemoglobin saturation. Perfusion was measured with NIRS and an ICG bolus. Data show continuous reduction in $CMRO_2$ while PCr, and therefore mitochondrial redox ratios, recover; adapted from [18]

by 3.5 h post-HI. By that time, energy metabolites including PCr and Pi had totally recovered while nucleoside triphosphate remained approximately 8 % lower than pre-HI conditions. Proton spectroscopy showed that lactate increased after HI, but had largely recovered by 1.5 h post-HI. The recovery of metabolites and oxygenation occurred in conjunction with reduced $CMRO_2$. The reduced $CMRO_2$ is consistent with a controlled reduction in metabolic rate rather than a condition where metabolic rate is inhibited by deficient substrate or direct effects of hypoxia [18].

Another group also using a piglet model combined a four wavelength NIRS system outside the MRI with alternating measurements of ^{31}P NMR obtained at 4.7 T. Although the study was not strictly simultaneous, it shows that relevant multimodal data can be obtained when NIRS is undertaken before and after MRI. HI was induced by blocking both carotid arteries and reducing inspired O_2 until the PCr/Pi ratio was reduced to approximately 30 % of pre-hypoxia values for 1 h [20]. It was suggested that when energy utilization was drastically reduced, and the cells were in an energy failure condition, there could actually be an increase in cytOx oxidation state. When energy production is moderately reduced, then cytOx can decline. Low PCr/Pi ratios reflect reduced energy status in both cases. Increased neuronal death was confirmed with histology. This suggests that measurements of PCr and cytochrome oxidation state may predict post-HI damage.

7 Conclusion

In this review, we have demonstrated that multimodal NIRS/MRI provides added capability for brain studies where there are changes in oxygenation and/or functional activation and metabolic rate. Among other things, this multimodal configuration has shown that brain metabolism is not oxygen-limited and that it is possible for metabolic rate to decline with hypoxia/ischemia. The studies described illustrate how NIRS/MRI can be applied to monitor brain metabolism in various physiological settings.

Acknowledgments Work was supported by NSERC, CIHR, endMS, the MS Society of Canada and AIHS.

References

1. Ishii K, Kitagaki H, Kono M, Mori E (1996) Decreased medial temporal oxygen metabolism in Alzheimer's disease shown by PET. J Nucl Med 37(7):1159–1165
2. Brooks DJ, Leenders KL, Head G, Marshall J, Legg NJ, Jones T (1984) Studies on regional cerebral oxygen utilisation and cognitive function in multiple sclerosis. J Neurol Neurosurg Psychiatry 47(11):1182–1191
3. Heiss WD, Podreka I (1993) Role of PET and SPECT in the assessment of ischemic cerebrovascular disease. Cerebrovasc Brain Metab Rev 5(4):235–263

4. Oehmichen M, Woetzel F, Meissner C (2009) Hypoxic-ischemic changes in SIDS brains as demonstrated by a reduction in MAP2-reactive neurons. Acta Neuropathol 117(3):267–274
5. Buxton RB, Frank LR (1997) A model for the coupling between cerebral blood flow and oxygen metabolism during neural stimulation. J Cereb Blood Flow Metab 17(1):64–72
6. Ogawa S, Lee TM, Kay AR, Tank DW (1990) Brain magnetic resonance imaging with contrast dependent on blood oxygenation. Proc Natl Acad Sci U S A 87(24):9868–9872
7. Kleinschmidt A, Obrig H, Requardt M, Merboldt KD, Dirnagl U, Villringer A, Frahm J (1996) Simultaneous recording of cerebral blood oxygenation changes during human brain activation by magnetic resonance imaging and near-infrared spectroscopy. J Cereb Blood Flow Metab 16(5):817–826. doi:10.1097/00004647-199609000-00006
8. Gagnon L, Yucel MA, Dehaes M, Cooper RJ, Perdue KL, Selb J, Huppert TJ, Hoge RD, Boas DA (2012) Quantification of the cortical contribution to the NIRS signal over the motor cortex using concurrent NIRS-fMRI measurements. Neuroimage 59(4):3933–3940. doi:S1053-8119(11)01218-3 [pii]. 10.1016/j.neuroimage.2011.10.054
9. Xu H, Deghani H, Pogue BW, Springett R, Paulsen KD, Dunn JF (2003) Feasibility of NIR tomographic reconstruction with multispectral continuous wave data by mapping into frequency domain data. Proc of SPIE 4955
10. Chuang CC, Chen CM, Hsieh YS, Liu TC, Sun CW (2012) Brain structure and spatial sensitivity profile assessing by near-infrared spectroscopy modeling based on 3D MRI data. J Biophotonics 6(3):267–274. doi:10.1002/jbio.201200025
11. Springett R, Wylezinska M, Cady EB, Cope M, Delpy DT (2000) Oxygen dependency of cerebral oxidative phosphorylation in newborn piglets. J Cereb Blood Flow Metab 20(2):280–289
12. Mayevsky A, Nioka S, Subramanian VH, Chance B (1988) Brain oxidative metabolism of the newborn dog: correlation between 31P NMR spectroscopy and pyridine nucleotide redox state. J Cereb Blood Flow Metab 8(2):201–207
13. Matcher SJ, Elwell CE, Cooper CE, Cope M, Delpy DT (1995) Performance comparison of several published tissue near-infrared spectroscopy algorithms. Anal Biochem 227(1):54–68. doi:S0003-2697(85)71252-3 [pii]. 10.1006/abio.1995.1252
14. Matcher SJ, Cooper CE (1994) Absolute quantification of deoxyhaemoglobin concentration in tissue using near infrared spectroscopy. Phys Med Biol 39:1295
15. Tsuji M, Naruse H, Volpe J, Holtzman D (1995) Reduction of cytochrome aa3 measured by near-infrared spectroscopy predicts cerebral energy loss in hypoxic piglets. Pediatr Res 37(3):253–259. doi:10.1203/00006450-199503000-00001
16. Shin'oka T, Nollert G, Shum-Tim D, du Plessis A, Jonas RA (2000) Utility of near-infrared spectroscopic measurements during deep hypothermic circulatory arrest. Ann Thorac Surg 69(2):578–583
17. Rolett EL, Azzawi A, Liu KJ, Yongbi MN, Swartz HM, Dunn JF (2000) Critical oxygen tension in rat brain: a combined (31)P-NMR and EPR oximetry study. Am J Physiol Regul Integr Comp Physiol 279(1):R9–R16
18. Winter JD, Tichauer KM, Gelman N, Thompson RT, Lee TY, St Lawrence K (2009) Changes in cerebral oxygen consumption and high-energy phosphates during early recovery in hypoxic-ischemic piglets: a combined near-infrared and magnetic resonance spectroscopy study. Pediatr Res 65(2):181–187
19. Tichauer KM, Brown DW, Hadway J, Lee TY, St Lawrence K (2006) Near-infrared spectroscopy measurements of cerebral blood flow and oxygen consumption following hypoxia-ischemia in newborn piglets. J Appl Physiol 100(3):850–857
20. Peeters-Scholte C, van den Tweel E, Groenendaal F, van Bel F (2004) Redox state of near infrared spectroscopy-measured cytochrome aa(3) correlates with delayed cerebral energy failure following perinatal hypoxia-ischaemia in the newborn pig. Exp Brain Res 156(1):20–26. doi:10.1007/s00221-003-1761-5
21. Dunn JF, Zaim-Wadghiri Y, Pogue BW, Kida I (1998) BOLD MRI vs. NIR spectrophotometry. Will the best technique come forward? Adv Exp Med Biol 454:103–113
22. Punwani S, Cooper CE, Clemence M, Penrice J, Amess P, Thornton J, Ordidge RJ (1997) Correlation between absolute deoxyhaemoglobin [dHb] measured by near infrared spectroscopy (NIRS) and absolute R2' as determined by magnetic resonance imaging (MRI). Adv Exp Med Biol 413:129–137

Chapter 10
Advances in Probes and Methods for Clinical EPR Oximetry

Harold M. Swartz, Huagang Hou, Nadeem Khan, Lesley A. Jarvis, Eunice Y. Chen, Benjamin B. Williams, and Periannan Kuppusamy

Abstract EPR oximetry, which enables reliable, accurate, and repeated measurements of the partial pressure of oxygen in tissues, provides a unique opportunity to investigate the role of oxygen in the pathogenesis and treatment of several diseases including cancer, stroke, and heart failure. Building on significant advances in the *in vivo* application of EPR oximetry for small animal models of disease, we are developing suitable probes and instrumentation required for use in human subjects. Our laboratory has established the feasibility of clinical EPR oximetry in cancer patients using India ink, the only material presently approved for clinical use. We now are developing the next generation of probes, which are both superior in terms of oxygen sensitivity and biocompatibility including an excellent safety profile for use in humans. Further advances include the development of implantable oxygen sensors linked to an external coupling loop for measurements of deep-tissue oxygenations at any depth, overcoming the current limitation of 10 mm. This paper presents an overview of recent developments in our ability to make meaningful measurements of oxygen partial pressures in human subjects under clinical settings.

H.M. Swartz (✉)
EPR Center for the Study of Viable Systems, The Geisel School of Medicine at Dartmouth, Lebanon, NH 03766, USA
e-mail: harold.m.swartz@dartmouth.edu

H. Hou • N. Khan • B.B. Williams • P. Kuppusamy
EPR Center for the Study of Viable Systems, Department of Radiology, Norris Cotton Cancer Center, Geisel School of Medicine, Dartmouth College, 48 Lafayette Street, HB 7785, Lebanon, NH 03766, USA

L.A. Jarvis
Department of Medicine, Norris Cotton Cancer Center, Geisel School of Medicine, Dartmouth College, Lebanon, NH, USA

E.Y. Chen
Department of Surgery, Norris Cotton Cancer Center, Geisel School of Medicine, Dartmouth College, Lebanon, NH, USA

H.M. Swartz et al. (eds.), *Oxygen Transport to Tissue XXXVI*, Advances in Experimental Medicine and Biology 812, DOI 10.1007/978-1-4939-0620-8_10,

Keywords EPR • In vivo • Oximetry • pO_2 • Clinical • Cancer

1 Introduction

Considering currently available methodology to measure partial pressure of oxygen (pO_2) in tissues *in vivo*, EPR (electron paramagnetic resonance) oximetry uniquely has the potential to provide direct, reliable, and accurate measurements on a temporal basis (repeated measurements) over long periods of time [1]. At present, EPR technologies and methodologies have been developed thoroughly for use in laboratory animals. However, translation of this capability for useful clinical applications is faced with some constraints and challenges with respect to instrumentation, probe administration, and regulatory issues [2, 3]. Scaling up the magnet and positioning systems to comfortably and safely accommodate human subjects within the active region of measurement has been accomplished. There is also concern that clinical EPR oximetry requires the placement of an exogenous probe in the tissue. The probe, once implanted using a minimally invasive surgical procedure, will stay in the tissue for a desired length of period or left permanently enabling subsequent measurements of pO_2 noninvasively and repeatedly, a unique capability that no other technique can match. However, from a regulatory point of view, if the tissues are directly exposed to the probe, this procedure raises safety concerns for use in humans and thus necessitates elaborate studies, which are both expensive and time-consuming in order to get FDA clearance. This paper gives an update of the development of EPR oximetry as a viable clinical tool for measurement of oxygen concentration in humans.

2 Probes for Clinical EPR Oximetry

2.1 India Ink

The potential of India ink as a probe for clinical EPR oximetry has been recognized for some time [4, 5]. India ink has very high sensitivity to oxygen, high stability in tissues, and no clinically significant toxicity. Moreover, it has been approved for clinical use as a tissue marker, which makes it immediately usable for clinical measurements. Pre-clinical and clinical measurements have shown the feasibility and safety of India ink for repeated measurements of pO_2 from easily-accessible, subcutaneous sites [6]. Despite the advantage that it is readily usable for clinical applications, India ink has some limitations, including a tendency to diffuse, reducing spatial resolution, and only moderate EPR detection sensitivity. We have therefore focused considerable effort, and made significant progress, on developing complementary alternatives to India ink, using highly oxygen-sensitive materials in biocompatible coatings that can be used in human subjects.

2.2 High-Sensitive Crystalline Probes

Synthetic materials based on lithium phthalocyanine and derivatives [7–10] possess many desirable properties to make them ideally-suited for clinical EPR oximetry. These are well-characterized crystalline particulates that exhibit substantially greater sensitivity to oxygen than India ink. We have developed an array of useful materials having a range of oxygen sensitivity and applicability to a broader range of oxygen levels. We have extensively used these probes in animal models of cancer, heart disease, and wound healing [11–15]. The results show substantially high oxygen sensitivity, spatial resolution, tissue stability, and biocompatibility, which gives these probes great potential and makes them highly promising for use in humans. However, regulatory approvals are required before testing them in humans.

2.3 Polymer-Encapsulated High-Sensitive Crystalline Probes for Safe Use in Humans

The most notable drawback and potential limitation to the use of the crystalline materials for clinical applications is the need to leave them permanently in the tissue, which may present practical barriers for obtaining approval for use in human subjects. Therefore, we are developing an alternative approach for their clinical use. The raw particulates (of 10–100 μm size) are embedded in biocompatible materials that have high oxygen permeability [16, 17]. The probes are effectively shielded from interaction with the biological *milieu* that could result in biochemical degradation and breakdown, as well as limiting the probability of local and/or systemic toxicity effects from interactions of the probe with the tissues. The implants could be left in the tissue or removed when no longer needed. We have especially used polydimethylsiloxane (PDMS), a silicone polymer with properties desirable for encapsulation of oximetry probes. PDMS is biocompatible, highly flexible, oxygen permeable, and has been used in a wide range of medical device and health-care applications. Furthermore, PDMS has been approved for use in human subjects and is one of the reference materials provided by the National Heart Lung and Blood Institute for standardized biocompatibility testing. We have used PDMS to encapsulate LiNc-BuO and developed the implants in the form of thin films (OxyChip). The efficacy and safety of OxyChip have been well characterized in animal models [17, 18]. We have taken steps to obtain investigational device exemption (IDE) status from FDA for testing the OxyChips in human subjects. The OxyChip implants will be used for oxygen measurements up to a depth of 10 mm.

2.4 Implantable Oxygen Sensors (ImOS) for Deep-Tissue Oximetry

The penetration depth of conventional resonators at L-band frequencies (approximately 1.2 GHz) is limited due to non-resonant absorption of microwave energy and

hence they are not capable of making measurements deeper than 10 mm in tissues. To overcome this limitation, we have developed a new class of resonators called implantable resonators capable of deep-tissue pO_2 measurements anywhere in the body, and at multiple sites, simultaneously [19–21]. The implantable resonator-based oxygen sensors (ImOS) are assembled with thin twisted enameled copper wires (thickness: 0.15 mm) as transmission lines and contain two sets of loops, a sensory loop of 0.2- to 0.3-mm diameter at one end and a coupling loop of about 10-mm diameter at the other end [21]. The sensory loop is loaded with the oximetry probe embedded in a gas-permeable polymer material. The entire ImOS is coated with a biocompatible polymer. The sensory tip is surgically implanted in the desired tissue and the coupling loop is placed subcutaneously and coupled inductively to an external loop resonator of the EPR spectrometer during measurements. The total length of the transmission line can be anywhere from a few mm to more than 20 cm, depending on measurement depth that is needed. The ImOS can also be prepared to have multiple sensory tips to enable oximetry from multiple sites, simultaneous. Results using animals have shown substantial advantages of the ImOS with respect to EPR signal intensity and repeated measurements at deep sites when compared to traditional oximetry [19, 21]. FDA clearance for the use of implantable resonators in humans is expected to be less problematic.

2.5 Multisite Oximetry

Traditional EPR oximetry provides average pO_2 estimates based on the summed signals detected from spins within the sensitive volume of the resonator. In order to provide additional spatial resolution of pO_2 within the tissues, we have developed procedures for simultaneous spatially-resolved measurements from multiple implants, as well as implantable resonators with multiple sensory tips that are spatially distributed within the tissue [19, 20]. The multi-site measurement technique uses magnetic field gradients to spectrally distinguish their respective signals. Multisite oximetry has been demonstrated in a number of applications including rodent models of brain tumor and stroke [19, 20].

3 First Clinical Oximetry Data

We have demonstrated that oxygen measurements can be made in human subjects in superficial tumors using India ink, the only currently approved material for use in human subjects [6]. Extensive pre-clinical and clinical developments have shown the feasibility and safety of repeated oxygen measurements for easily-accessible, subcutaneous sites. EPR oximetry measurements in human subjects are performed using the clinical whole-body EPR spectrometer consisting of a 420-Gauss permanent magnet, magnetic field modulation and sweep coils, RF detection system

including surface-loop resonators, and computer control [6]. The spectrometer operates at an L-band frequency (approximately 1.2 GHz), where a practical compromise between RF penetration depth and EPR sensitivity is achieved. At this frequency RF penetration depths of approximately 10 mm are achieved. So far, we have obtained pO_2 data in superficial tumors at different sites in 14 patients, in subcutaneous foot tissues of nine normal volunteers, and one patient in a post-operative irradiated field [22].

The experimental procedure was purposely simple, using an approach to make the measurements under conditions that could readily be incorporated into normal clinical processes [6]. The India ink was inserted into the tumors or other tissues of interest in the outpatient clinic, with optional local anesthesia and using sterile procedures. A 21- to 23-gauge hypodermic needle and 30-gauge tuberculin syringe were used to insert 10–25 μl of sterilized India ink (a slurry of 200 mg/ml of Printex-U carbon black in 0.9 % NaCl and 1.25 % carboxymethylcellulose), whose response to oxygen had been well calibrated *in vitro* and *in vivo* in animals. One to five days later, a baseline measurement was made and then the subject was given 100 % oxygen to breathe through a regular simple face mask. EPR measurements were made continuously while breathing 100 % oxygen and then when the patient returned to breathing room air. For foot measurements in normal subjects, an additional period was included where compression was applied to temporarily suspend blood supply to the tissue and induce hypoxia [6]. These procedures took less than an hour in total and were very well tolerated by all subjects. The data obtained from the small number of tumor types led to the following conclusions: (1) The tumors varied considerably in their baseline pO_2, which ranged from 0 to 10 Torr; (2) The subjects varied considerably as to whether their tumors responded to increased oxygen in the breathing gas (4 out of 14 did not respond); (3) The amount of the increase in tumor oxygen varied widely among the responders (3–100 Torr). Even with such a limited amount of data, these results indicate that the ability to make repeated measurements of oxygen in tumors could be quite useful clinically.

These studies demonstrate that the measurements can be made under conditions compatible with usual clinical practice. The observation that a number of tumors did not respond at all to increases in the amount of oxygen in the inspired gas illustrates how misleading it could be to try to evaluate the ability of hyperoxygenation strategies to improve outcomes without being able to detect whether the treatment did actually change pO_2 in the tumor [22]. The EPR-based measurements of tumor pO_2 values and their variable response to hyperoxygenation treatments also agree with the computerized Eppendorf pO_2 histogram data obtained from several studies in human [23].

Foot measurements demonstrated variations in the baseline levels between volunteers and during repeated measurements [6]. Such variations are likely due to acute and gradual changes in the local tissue pO_2. In the days immediately following ink injection, near anoxic pO_2 levels were observed, which may be due to trauma and acute inflammation associated with the injection. The pO_2 values, however, gradually increased to levels near 30 Torr over the following weeks. Compression of the thigh led to near anoxia within the foot tissue, followed immediately by full recovery to the

baseline pO_2 level as soon as the compression was released. A significant increase in the tissue pO_2 was consistently observed during repeated experiments with oxygen breathing in each volunteer. The changes in the tissue oxygenation observed during hyperoxygenation and compression are likely to be useful, as it will provide information not only about the tissue oxygen status, but also functional information about perfusion, diffusion of oxygen into the tissues, and oxygen consumption.

4 Conclusion

The development of *in vivo* EPR oximetry as a viable clinical tool for repeated, direct measurements of tumor pO_2 and other tissues in human subjects in compatibility with clinical practice has continued successfully. With the availability of high-sensitive, bio-safe probes, instrumentation and procedures for multiple site, and deep-tissue measurements it will soon be possible to obtain regulatory approvals and begin to make routine clinical measurements of pO_2 in human subjects. These new approaches should significantly expand the applicability of clinical EPR oximetry.

Acknowledgments The development and applications of EPR oximetry reported in this manuscript was supported by the following grants from the National Institutes of Health (NIH): P01 EB002180 (HMS), R21 CA121593 (HMS), R21DK072112 (NK), and R01 EB004031 (PK).

References

1. Ahmad R, Kuppusamy P (2010) Theory, instrumentation, and applications of electron paramagnetic resonance oximetry. Chem Rev 110:3212–3236
2. Swartz HM, Khan N, Buckey J, Comi R, Gould L, Grinberg O, Hartford A, Hopf H, Hou H, Hug E, Iwasaki A, Lesniewski P, Salikhov I, Walczak T (2004) Clinical applications of EPR: overview and perspectives. NMR Biomed 17:335–351
3. Swartz HM, Walczak T (1998) Developing in vivo EPR oximetry for clinical use. Adv Exp Med Biol 454:243–252
4. Swartz HM, Liu KJ, Goda F, Walczak T (1994) India ink: a potential clinically applicable EPR oximetry probe. Magn Reson Med 31:229–232
5. Goda F, Liu KJ, Walczak T, O'Hara JA, Jiang J, Swartz HM (1995) In vivo oximetry using EPR and india ink. Magn Reson Med 33:237–245
6. Williams BB, Khan N, Zaki B, Hartford A, Ernstoff MS, Swartz HM (2010) Clinical electron paramagnetic resonance (EPR) oximetry using india ink. Adv Exp Med Biol 662:149–156
7. Liu KJ, Gast P, Moussavi M, Norby SW, Vahidi N, Walczak T, Wu M, Swartz HM (1993) Lithium phthalocyanine: a probe for electron paramagnetic resonance oximetry in viable biological systems. Proc Natl Acad Sci U S A 90:5438–5442
8. Ilangovan G, Manivannan A, Li H, Yanagi H, Zweier JL, Kuppusamy P (2002) A naphthalocyanine-based EPR probe for localized measurements of tissue oxygenation. Free Radic Biol Med 32:139–147
9. Pandian RP, Parinandi NL, Ilangovan G, Zweier JL, Kuppusamy P (2003) Novel particulate spin probe for targeted determination of oxygen in cells and tissues. Free Radic Biol Med 35:1138–1148

10. Pandian RP, Dolgos M, Marginean C, Woodward PM, Hammel PC, Manoharan PT, Kuppusamy P (2009) Molecular packing and magnetic properties of lithium naphthalocyanine crystals: hollow channels enabling permeability and paramagnetic sensitivity to molecular oxygen. J Mater Chem 19:4138–4147
11. Bratasz A, Pandian RP, Ilangovan G, Kuppusamy P (2006) Monitoring oxygenation during the growth of a transplanted tumor. Adv Exp Med Biol 578:375–380
12. Eubank TD, Roberts RD, Khan M, Curry JM, Nuovo GJ, Kuppusamy P, Marsh CB (2009) Granulocyte macrophage colony-stimulating factor inhibits breast cancer growth and metastasis by invoking an anti-angiogenic program in tumor-educated macrophages. Cancer Res 69:2133–2140
13. Khan M, Kutala VK, Vikram DS, Wisel S, Chacko SM, Kuppusamy ML, Mohan IK, Zweier JL, Kwiatkowski P, Kuppusamy P (2007) Skeletal myoblasts transplanted in the ischemic myocardium enhance in situ oxygenation and recovery of contractile function. Am J Physiol Heart Circ Physiol 293:H2129–H2139
14. Khan M, Meduru S, Mohan IK, Kuppusamy ML, Wisel S, Kulkarni A, Rivera BK, Hamlin RL, Kuppusamy P (2009) Hyperbaric oxygenation enhances transplanted cell graft and functional recovery in the infarct heart. J Mol Cell Cardiol 47:275–287
15. Selvendiran K, Bratasz A, Kuppusamy ML, Tazi MF, Rivera BK, Kuppusamy P (2009) Hypoxia induces chemoresistance in ovarian cancer cells by activation of signal transducer and activator of transcription 3. Int J Cancer 125:2198–2204
16. Meenakshisundaram G, Eteshola E, Pandian RP, Bratasz A, Lee SC, Kuppusamy P (2009) Fabrication and physical evaluation of a polymer-encapsulated paramagnetic probe for biomedical oximetry. Biomed Microdevices 11:773–782
17. Meenakshisundaram G, Pandian RP, Eteshola E, Lee SC, Kuppusamy P (2010) A paramagnetic implant containing lithium naphthalocyanine microcrystals for high-resolution biological oximetry. J Magn Reson 203:185–189
18. Meenakshisundaram G, Eteshola E, Pandian RP, Bratasz A, Selvendiran K, Lee SC, Krishna MC, Swartz HM, Kuppusamy P (2009) Oxygen sensitivity and biocompatibility of an implantable paramagnetic probe for repeated measurements of tissue oxygenation. Biomed Microdevices 11:817–826
19. Hou H, Dong R, Li H, Williams B, Lariviere JP, Hekmatyar SK, Kauppinen RA, Khan N, Swartz H (2012) Dynamic changes in oxygenation of intracranial tumor and contralateral brain during tumor growth and carbogen breathing: a multisite EPR oximetry with implantable resonators. J Magn Reson 214:22–28
20. Hou H, Li H, Dong R, Mupparaju S, Khan N, Swartz H (2011) Cerebral oxygenation of the cortex and striatum following normobaric hyperoxia and mild hypoxia in rats by EPR oximetry using multi-probe implantable resonators. Adv Exp Med Biol 701:61–67
21. Li H, Hou H, Sucheta A, Williams BB, Lariviere JP, Khan MN, Lesniewski PN, Gallez B, Swartz HM (2010) Implantable resonators: a technique for repeated measurement of oxygen at multiple deep sites with in vivo EPR. Adv Exp Med Biol 662:265–272
22. Swartz HM, Williams BB, Zaki BI, Hartford AC, Jarvis LA, Chen EY, Comi RJ, Ernstoff MS, Hou H, Khan N, Swartz SG, Flood AB, Kuppusamy P (2013) Clinical EPR: unique opportunities and some challenges. Acad Radiol 21:197–206
23. Vaupel P, Hockel M, Mayer A (2007) Detection and characterization of tumor hypoxia using pO_2 histography. Antioxid Redox Signal 9:1221–1235

Chapter 11
Real-Time, In Vivo Determination of Dynamic Changes in Lung and Heart Tissue Oxygenation Using EPR Oximetry

Brian K. Rivera, Shan K. Naidu, Kamal Subramanian, Matthew Joseph, Huagang Hou, Nadeem Khan, Harold M. Swartz, and Periannan Kuppusamy

Abstract The use of electron paramagnetic resonance (EPR) oximetry for oxygen measurements in deep tissues (>1 cm) is challenging due to the limited penetration depth of the microwave energy. To overcome this limitation, implantable resonators, having a small (0.5 mm diameter) sensory loop containing the oxygen-sensing paramagnetic material connected by a pair of twisted copper wire to a coupling loop (8–10 mm diameter), have been developed, which enable repeated measurements of deep-tissue oxygen levels (pO_2, partial pressure of oxygen) in the brain and tumors of rodents. In this study, we have demonstrated the feasibility of measuring dynamic changes in pO_2 in the heart and lung of rats using deep-tissue implantable oxygen sensors. The sensory loop of the resonator contained lithium octa-n-butoxynaphthalocyanine (LiNc-BuO) crystals embedded in polydimethylsiloxane (PDMS) polymer and was implanted in the myocardial tissue or lung pleura. The external coupling loop was secured subcutaneously above chest. The rats were exposed to different breathing gas mixtures while undergoing EPR measurements. The results demonstrated that implantable oxygen sensors provide reliable measurements of pO_2 in deep tissues such as heart and lung under adverse conditions of cardiac and respiratory motions.

B.K. Rivera • S.K. Naidu • K. Subramanian • M. Joseph
Department of Internal Medicine, Davis Heart and Lung Research Institute,
The Ohio State University Wexner Medical Center, Columbus, OH 43210, USA

H. Hou • N. Khan
EPR Center for the Study of Viable Systems, Department of Radiology, Geisel School of Medicine at Dartmouth, 48 Lafayette Street, Lebanon, NH 03766, USA

H.M. Swartz
EPR Center for the Study of Viable Systems, The Geisel School of Medicine at Dartmouth, Lebanon, NH, USA

P. Kuppusamy (✉)
EPR Center for the Study of Viable Systems, Department of Radiology, Geisel School of Medicine at Dartmouth, 48 Lafayette Street, Lebanon, NH 03766, USA
e-mail: Periannan.Kuppusamy@Dartmouth.edu

H.M. Swartz et al. (eds.), *Oxygen Transport to Tissue XXXVI*, Advances in Experimental Medicine and Biology 812, DOI 10.1007/978-1-4939-0620-8_11,

Keywords Oximetry • Electron paramagnetic resonance (EPR) • Implantable oxygen sensors • Myocardial tissue • Lung pleura

1 Introduction

Electron paramagnetic resonance (EPR) oximetry enables measurement of partial pressure of oxygen (pO_2) in biological tissues [1]. However, use of EPR oximetry for in vivo measurements, particularly in deep-seated tissues is limited by the depth of penetration of microwave energy. This limitation was addressed by the Swartz group through the development of implantable resonators consisting of an oxygen-sensory loop linked to a coupling loop [2–4]. The implantable oxygen sensors have been demonstrated for temporal oximetry measurements in tumors and brain in various animal models, as well as single time-point measurements in the heart [2–4]. As yet, temporal studies of heart and lung tissue pO_2 using the implantable oxygen sensors have not been reported. Measurements of dynamic changes in cardiac or lung tissue pO_2 on exposure to hyperoxia including hyperbaric therapy or periodic administration of oxygen (oxygen cycling) also present a significant challenge. The goal of this study was to test the implantable oxygen sensors for reliable and repeated measurements of oxygen concentration in the heart and lung, in a rodent model.

2 Methods

2.1 Fabrication of Implantable Resonators

The implantable resonators were fabricated in-house using 34-gauge copper wires (Fig. 11.1). One end of the copper wire was used to create a sensory loop (0.2–0.5 mm diameter) while the other end was rounded to create coupling loop (9 mm diameter). The distance between the sensory loop and coupling loop was 7–10 cm. The sensory element of the tip was created by mixing LiNc-BuO (lithium octa-n-butoxynaphthalocyanine) oxygen-sensing crystals [5] in uncured polydimethylsiloxane (PDMS; 1 part cure accelerant: 10 parts base, w/w; Factor II, Inc.) and dipping the sensory loop of the implantable resonator in the mixture. The resonator/sensor was then placed in an oven at 80 °C to cure overnight. The following day, the unit was removed, and coated by immersing in a PDMS:heptane (1:3 w/w) dispersion with an additional overnight cure at 80 °C.

2.2 Implantation of Resonators for Heart and Lung Oximetry

Sprague-Dawley rats were anesthetized and a thoracotomy was performed using the procedures reported previously [6]. As the sensory loop/tip of the implantable oxygen sensors is not sharp, approximately 1-mm long pilot channels were created

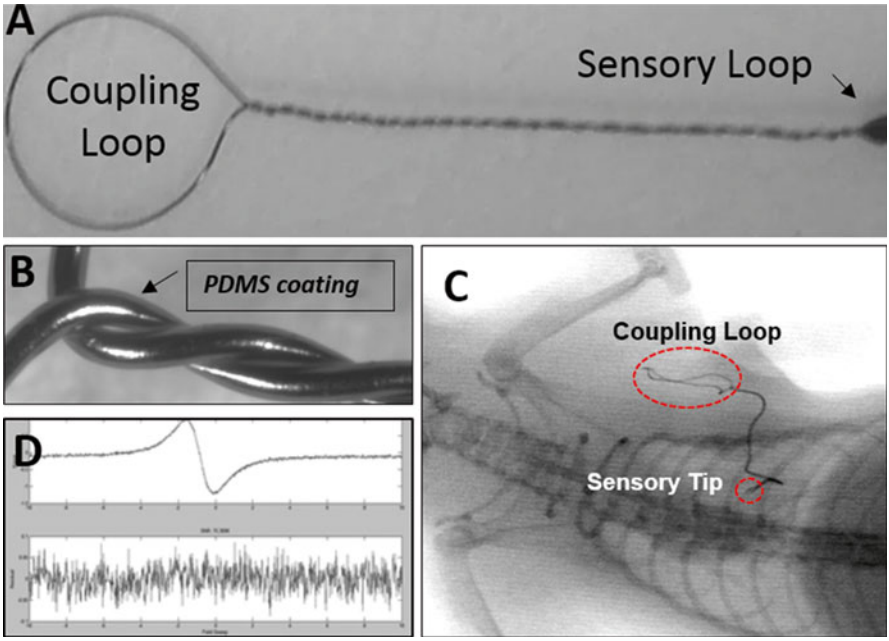

Fig. 11.1 Measurement of myocardial pO_2 in rat using implantable resonator (oxygen sensor). (**a**) Photo of an implantable resonator made of twisted copper wire (34 AWG) showing the coupling loop and sensory loop/tip holding the oxygen-sensing LiNc-BuO crystals, embedded in PDMS. (**b**) An expanded view of the resonator showing PDMS coating of the wire. (**c**) Fluoroscopy image of implantable resonator in the heart of a rat taken 10 days post-implantation. The coupling loop is buried under the skin (chest). (**d**) A typical EPR spectrum obtained using implantable resonator. Spectral fitting and residuals are shown at 8× amplification

in the myocardium or lung by gently inserting the bevel of a sterile, 23-gauge needle at 45° angle to the surface of the organ. The sensory loop was then placed inside this channel at the level of mid-myocardium of left ventricle or the parenchyma of left lung lobe. Care was taken to avoid perforation of the wall or organ and associated vasculature. A suture was placed around the juncture between the sensory loop and the surface of the tissue to prevent the sensory loop from becoming dislodged due to cardiac or respiratory motion. The thoracotomy was closed and the coupling loop was secured in the subcutaneous pouch with sutures prior to final closure (Fig. 11.1). For comparative purposes, in a separate group of rats, un-encapsulated LiNc-BuO crystals were implanted using a 25-gauge needle adapted as a positive-displacement delivery device.

2.3 EPR Oximetry Measurements

Rats were anesthetized using 2–2.5 % isoflurane mixed with breathing gas using an induction chamber. Rats with LiNc-BuO probe in the tissues were tested on day 3 post-implant while those with implantable oxygen sensors were tested on day 4

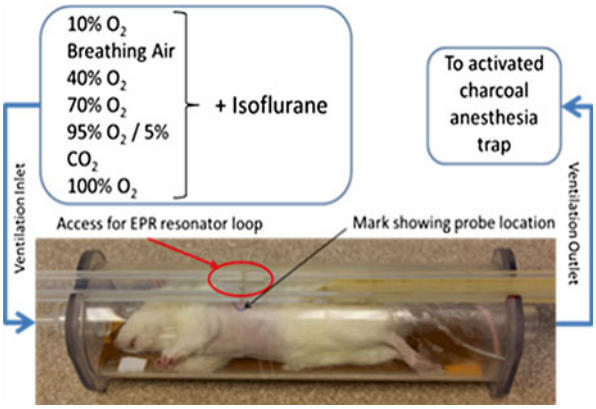

Fig. 11.2 Experimental scheme for *in vivo* EPR measurements in rats with bare LiNc-BuO particulates or implantable resonator. The rat is exposed to gases with different concentrations of oxygen in the chamber during EPR oximetry

post-implant. Once anesthetized, the rats were moved to a custom-fabricated chamber to breathe normally while being exposed to different oxygen concentrations mixed with isoflurane gas (1.25 %) to maintain anesthesia. Gas mixtures included 100 % oxygen, 95 % oxygen + 5 % CO_2 (carbogen), 70 % oxygen, 40 % oxygen, 21 % O_2 (room air), and 10 % oxygen balanced with nitrogen. The experimental scheme is shown in Fig. 11.2.

The chamber was designed to permit inductive coupling with the external loop resonator of the EPR unit. The rats were carefully positioned beneath the resonator of a Magnettech L-band (1.2 GHz) EPR unit such that the surface loop of the external loop resonator was located approximately above the coupling loop of the implanted resonator. Spectra were collected while the rats were breathing different gas mixture. The breathing gas was quickly changed using a simple valve system. The line-width of the EPR signal was analyzed by using a curve-fitting program (OxyScope) and a standard calibration curve for the probe was used to obtain the pO_2 values. The procedure was repeated for myocardial tissue oximetry measurements on day 7 post-implantation. One rat having an implantable oxygen sensor for myocardial measurements was imaged on day 10 post-implant by fluoroscopy (GE OEC 9800) to confirm that the implanted sensor was intact and ascertain the location of the sensory tip and coupling loop (Fig. 11.1).

3 Results and Discussion

The pO_2 data obtained from the heart and lung are shown in Fig. 11.3. Each point represents a single pO_2 value that was calculated using OxyScope curve-fitting program. Two observations are worth noting: (a) the measured values of tissue pO_2

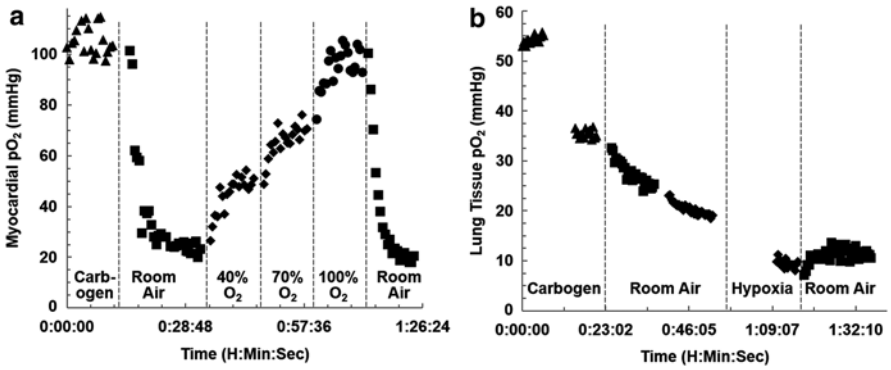

Fig. 11.3 Tissue pO_2 values in the rats exposed to gases with different oxygen concentrations. Data were obtained using (**a**) implantable resonator in the heart (day 4 post-implantation); (**b**) implantable resonator in the lung (day 4 post-implantation). The breathing gases used were: carbogen (95 % O_2/5 % CO_2), room air (21 % O_2), hypoxia (10 % O_2), 40 % O_2, 70 % O_2, and 100 % O_2

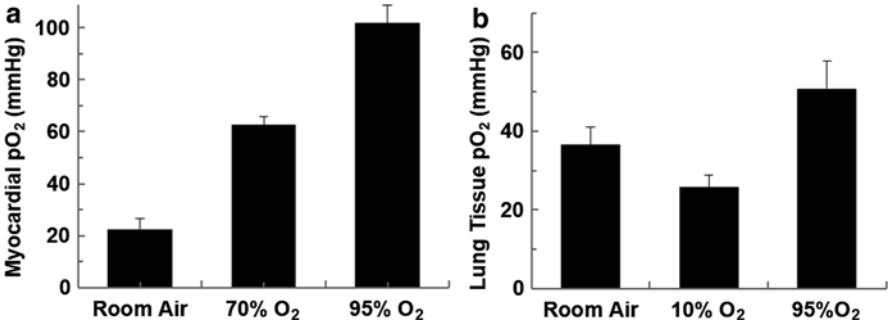

Fig. 11.4 Peak values of myocardial (**a**) and lung tissue (**b**) pO_2 values obtained using an implantable resonator during different inhaled oxygen mixtures, room air (21 % O_2), 70 % O_2, 10 % O_2, and carbogen (95 % O_2). Data are expressed as mean ± SD (N = 4)

changed, as expected, when the inhaled gas mixture was varied; (b) it was not possible to acquire EPR signal from the bare probes implanted in the rat heart or lung under these conditions in the animals. Because the sensory tip of the implantable sensor moves with the tissues of interest (lung and heart), there is minimal motional artifact by respiration or heartbeat. Figure 11.4 shows the peak pO_2 values collected from the heart and lung on day 4 post-implant under the conditions of changes in breathing-gas. The results indicate an increase in tissue pO_2 in the heart and lung on exposure to hyperoxic gases. It should be noted that, although the myocardial pO_2 in room air-breathing animal was normal, its response to hyperoxygenation was substantially greater compared to that of lung. This could be attributed to the effect of rigidity of the resonator which potentially could affect heartbeat and pO_2 measurement including some local perturbation at the sensory tip of the implant.

4 Conclusion

We have demonstrated the feasibility of dynamic oximetry in the lung and myocardial tissues of animals using implantable resonator technology with L-band EPR spectroscopy. The EPR acquisition had minimal physiologic artifacts due to the heartbeat and respiration. By increasing the length of the implantable resonator, and with the advent of clinical EPR spectrometers, it should be possible to use these devices in large animal models and humans for deep-tissue measurements of oxygen. The implantable oxygen sensors technology could also be applied to pulse oximetry.

Acknowledgments This work was supported by National Institutes of Health (NIH) grant 5R01EB004031.

References

1. Ahmad R, Kuppusamy P (2010) Theory, instrumentation, and applications of electron paramagnetic resonance oximetry. Chem Rev 110:3212–3236
2. Hou H, Dong R, Li H, Williams B, Lariviere JP, Hekmatyar SK, Kauppinen RA, Khan N, Swartz H (2012) Dynamic changes in oxygenation of intracranial tumor and contralateral brain during tumor growth and carbogen breathing: a multisite EPR oximetry with implantable resonators. J Magn Reson 214:22–28
3. Hou H, Li H, Dong R, Mupparaju S, Khan N, Swartz H (2011) Cerebral oxygenation of the cortex and striatum following normobaric hyperoxia and mild hypoxia in rats by EPR oximetry using multi-probe implantable resonators. Adv Exp Med Biol 701:61–67
4. Li H, Hou H, Sucheta A, Williams BB, Lariviere JP, Khan MN, Lesniewski PN, Gallez B, Swartz HM (2010) Implantable resonators – a technique for repeated measurement of oxygen at multiple deep sites with in vivo EPR. Adv Exp Med Biol 662:265–272
5. Pandian RP, Parinandi NL, Ilangovan G, Zweier JL, Kuppusamy P (2003) Novel particulate spin probe for targeted determination of oxygen in cells and tissues. Free Radic Biol Med 35:1138–1148
6. Chacko SM, Khan M, Kuppusamy ML, Pandian RP, Varadharaj S, Selvendiran K, Bratasz A, Rivera BK, Kuppusamy P (2009) Myocardial oxygenation and functional recovery in infarct rat hearts transplanted with mesenchymal stem cells. Am J Physiol Heart Circ Physiol 296:H1263–H1273

Chapter 12
Modulation of Hypoxia by Magnetic Nanoparticle Hyperthermia to Augment Therapeutic Index

Eunice Y. Chen, Kimberley S. Samkoe, Sassan Hodge, Katherine Tai, Huagang Hou, Alicia A. Petryk, Rendall Strawbridge, P. Jack Hoopes, and Nadeem Khan

Abstract A hypoxic microenvironment in solid tumors has been known to cause resistance to standard therapies and to increase the malignant potential of tumors. The utilization of magnetic nanoparticle hyperthermia (mNPH) has shown promise in improving therapeutic outcome by (1) killing of hypoxic tumor cells directly and (2) increasing tumor oxygenation and therefore susceptibility to therapies. In this study, the interaction of a hypoxic microenvironment with mNPH efficacy was investigated in a human breast cancer orthotopic xenograft model. Using electron paramagnetic resonance (EPR) to assess *in vivo* oxygen concentration in tumors

E.Y. Chen, M.D., Ph.D. (✉)
Department of Surgery, Geisel School of Medicine, Hanover, NH, USA

Section of Otolaryngology–Head and Neck Surgery, Department of Surgery, Dartmouth Hitchcock Medical Center, 1 Medical Center Drive, Lebanon, NH 03756, USA
e-mail: Eunice.Y.Chen@hitchcock.org

K.S. Samkoe • P.J. Hoopes
Department of Surgery, Geisel School of Medicine, Hanover, NH, USA

Department of Surgery, Dartmouth Hitchcock Medical Center, 1 Medical Center Drive, Lebanon, NH 03756, USA

Thayer School of Engineering, Dartmouth College, Hanover, NH, USA

S. Hodge • R. Strawbridge
Department of Surgery, Geisel School of Medicine, Hanover, NH, USA

Department of Surgery, Dartmouth Hitchcock Medical Center, 1 Medical Center Drive, Lebanon, NH 03756, USA

K. Tai
Dartmouth College, Hanover, NH, USA

H. Hou • N. Khan
Department of Radiology, Geisel School of Medicine, Hanover, NH, USA

A.A. Petryk
Thayer School of Engineering, Dartmouth College, Hanover, NH, USA

H.M. Swartz et al. (eds.), *Oxygen Transport to Tissue XXXVI*, Advances in Experimental Medicine and Biology 812, DOI 10.1007/978-1-4939-0620-8_12,

repeatedly and non-invasively, we found that mNPH increased tumor pO_2 from 3.5 to 68.8 mmHg on average for up to 10 days. Tumors treated once with mNPH showed growth delay. On Transmission Electron Microscopy, magnetic nanoparticles (mNPs) were localized intracellularly in multiple vesicles in the cytoplasm of cells within tumors 48 h after incubation of mNP. In conclusion, mNPH increased tumor oxygenation *in vivo* and resulted in decreased growth of hypoxic tumors. Future studies will establish tumor pO_2-guided multimodal therapies, such as mNPH and radiation, to improve therapeutic efficacy.

Keywords Tumor hypoxia • Magnetic nanoparticle hyperthermia (mNPH) • Electron paramagnetic resonance (EPR) oximetry

1 Introduction

Although hyperthermia to treat cancer has been investigated for centuries, its clinical use has been limited because of its poor selectivity for tumor cells [1]. The development of nanoparticles (NP) to target tumor cells has revitalized interest in hyperthermia as a cancer treatment [2, 3]. In magnetic nanoparticle hyperthermia (mNPH) treatments, magnetic iron oxide NP can be injected directly into the tumor or administered systemically and excited with alternating magnetic field (AMF) to produce selective cytotoxic heat. Iron oxide mNPs have excellent biocompatibility and high specific absorption rate (SAR) values and can be localized in specific tissues. In addition, the exciting AMF can be applied locally or to anywhere in the body, making mNPH a highly versatile and potentially effective treatment regardless of the tumor size or location [4].

Magnetic NPH is rapidly evolving as a promising adjuvant modality for the treatment of various malignancies. A number of investigators at Dartmouth as part of its Center for Cancer Nanotechnology Excellence (CCNE) award are focusing on the use of mNPH for breast cancer, as over 230,000 new cases of breast cancer in women in the United States are expected in 2013 with an estimated 39,620 deaths [5]. Using a syngeneic mouse breast cancer model, Hoopes and colleagues have investigated intratumoral as well as systemic administration of magnetic NP (untargeted and targeted) and have shown effective NP uptake and mNPH treatments, alone and with radiation and chemotherapy [2, 6]. This study examines the interaction of the tumor microenvironment (i.e. tumor hypoxia) and mNP uptake and mNPH efficacy.

Hyperthermia has been shown to enhance the effectiveness of radiation therapy [7] and to kill chronically hypoxic cells preferentially [8, 9], although direct and serial oxygen measurement of tumors and tissue has not been done during hyperthermia treatment. In this study, electron paramagnetic resonance (EPR) oximetry is used as the method of choice for direct, quantitative oxygen measurements. Due to its repeatable and non-invasive nature, EPR oximetry is a unique and powerful tool in the study of tumor and tissue hypoxia [10, 11]. It is known that hypoxic tumors

are difficult to treat because they are resistant to radio- and chemo-therapies and have increased malignant potential [12]. Targetted mNPH may enhance therapeutic outcome by directly killing hypoxic tumor cells and by increasing tumor oxygenation and hence susceptibility to adjuvant oxygen-dependent therapies, like radiation; however, conversely, the tumor hypoxia itself may affect mNP uptake and mNPH effectiveness. In this study, the interplay between the tumor oxygen microenvironment and mNPH was investigated.

2 Methods

2.1 Cell Lines and Culture

MCF-7 and MDA-MB-231 are human breast cancer cell lines obtained from the American Type Culture Collection (ATCC, Manassas, VA) and grown in Dulbecco's Modified Eagle's Medium (DMEM)/Ham's F12 50/50 Mix (Cellgro, Manassas, VA) with 1 % penicillin-streptomycin, 1 % L-glutamine and 10 % fetal bovine serum (FBS). Cells were plated to 75 % confluence and kept under 1 % O_2 in a hypoxia chamber (Bactron I, Sheldon Manufacturing, Cornelius, OR), or 21 or 95 % O_2 in tissue culture incubator. Iron oxide mNPs with average hydrodynamic diameter of 110–120 nm (Bionized NanoFerrite or BNF-Starch Plain particles, Micromod GmbH, Rostock, Germany) were incubated in cell media at the concentration of 0.2 mg Fe/ml for 4, 24, and 48 h.

2.2 Murine Model of Breast Cancer

All animal procedures were performed in accordance with the protocols approved by the Institutional Animal Care and Usage Committee. The mice were anesthetized using isoflurane. MDA-MB-231 cells (5×10^6 cells) were suspended in 0.2 ml media containing Matrigel (1 mg/ml) and injected into the mammary fat pad of female athymic nude mice (Charles River, Wilmington, MA). Tumors were measured with calipers and volumes calculated ($\text{volume} = \pi/6 \times \text{length} \times \text{width}$). Treatments started when the tumors reached 100–150 mm^3. Primary efficacy endpoint was when the tumor reached three times its initial volume post-treatment.

2.3 Magnetic NPH and Temperature Measurements

For mNPH treatments, Cumulative Equivalent Minutes (CEM) was used to quantify the amount of physiologically relevant heat deposited in a tissue by estimating equivalent cytotoxicity for various temperatures and heating times. While the mouse

was anesthetized, the tumor was directly injected with mNPs at 5–7.5 mg Fe/cm^3 of tumor. Immediately after injection, the mice were placed in the AMF coil. The mNP-injected tumors were treated to CEM 60 (n = 4) or CEM 30 (n = 12). For sham mNPH control (n = 10), tumors were injected with Phosphate Buffered Saline (PBS) and exposed to the AMF for 30 min. The mNP alone control (n = 9) were not exposed to AMF. The AMF of 450 Oe was generated by a water-cooled circular 4 cm diameter coil powered by a Huttinger TIG 10/300 10 kW generator operating at 165 kHz (Huttinger Elektronik GmbH, Freiburg, Germany) and maintained by a chiller (Tek-Temp Instruments, Croydon, PA). Ambient air and rectal temperatures were maintained with a heated air jacket surrounding the animal. Tumor, peritumoral, and rectal temperatures were recorded before, during, and after mNPH treatment with fiberoptic probes (Fiso, Quebec, Canada). Core temperatures of the mice were 36 ± 1 °C at the start of treatments, and tumors reached temperatures ranging from 41 to 49 °C during mNPH.

2.4 EPR Oximetry

Lithium phthalocyanine (LiPc) crystals were used as the oximetry probe. Under isoflurane anesthesia, two aggregates of the LiPc (40–60 μg each) were implanted into each tumor. Multi-site EPR oximetry was used to measure tumor pO_2 from two implants in each tumor repeatedly (every 1–5 days) for 4 weeks. No significant difference in the baseline pO_2 reported by the two LiPc aggregates in each tumor was observed. Therefore, the pO_2 values were pooled to determine the average pO_2 of each tumor. For the EPR measurements, the animals were anesthetized using 1–2 % isoflurane with FiO_2 of 30 %. The external loop resonator was placed close to the surface of where the LiPc implants were located. An L-band (1.2 GHz) EPR spectrometer was used. Two EPR spectra were collected with magnetic field gradients between 5 and 15 G/cm. The EPR spectra were recorded at optimal power to avoid power saturation with scan times varying from 10 to 30 s. The spectra acquired at each time point were accumulated for 5–7 min to increase the signal-to-noise ratio and improve the precision of the pO_2 measurement.

2.5 Inductively Coupled Plasma Mass Spectrometry (ICP-MS)

After incubation with mNPs, cells were washed with sterile PBS, harvested and counted manually by use of a hemocytometer. The cells were placed in 15 ml conical tubes and weighed with and without samples. One milliliter trace metal grade hydrochloric acid (HCl) was added to each tube, weighed and left at room temperature for digestion. Samples were sent out for ICP-MS analysis after they were completely digested (Agilent 7700x, Trace Element Lab, Dartmouth College). All conditions were performed in triplicate, using three sub-confluent T25 flasks, each yielding about 2–3 million cells.

2.6 Transmission Electron Microscopy (TEM)

Cells or tissues were fixed in 4 % glutaraldehyde in 0.1 M sodium cacodylate buffer. At least ten times volume of the buffer was added to a $10–12 \times 10^6$-cell pellet or 1–2 mm^3 tumor pieces, which were stored at 4 °C immediately until submission to the Dartmouth College Electron Microscopy Facility. Thin sections of 100 nm were cut using a Leica UltraCut Microtome (Leica Microsystems, GmbH, Wetzlar, Germany). TEM sections were imaged using a FEI company Tecnai F20 FEG TEM operating at 100 kV.

2.7 Statistical Analysis

The ICP-MS data and EPR data were expressed as median and range, and compared between hypoxic treatment and normoxic control groups using Student's t-test. Statistical software (Excel, Microsoft, Redmond, WA) was used for all analyses.

3 Results

Iron oxide mNP incubation under hypoxia (1 % O_2) conditions for 48 h resulted in decreased uptake of mNP compared with incubation in an aerobic (21 % O_2) environment for all of the breast cancer cell lines tested as assessed by ICP-MS (Fig. 12.1). mNP uptake after 4 and 24 h of incubation was minimal and did not

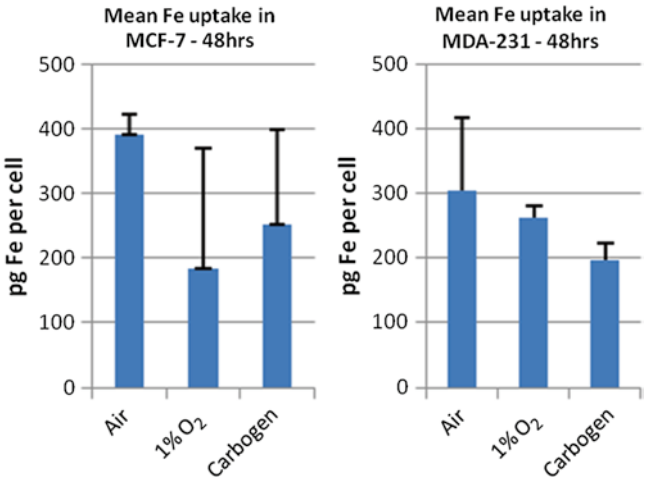

Fig. 12.1 ICP-MS quantification of iron in MCF-7 and MDA-MB-231 cells after 48 h of mNP incubation. Error bars represent standard deviation

differ between hypoxic and aerobic conditions. Interestingly, incubation under hyperoxic (carbogen 95 % O_2) conditions also resulted in decreased mNP uptake in the breast cancer cell lines.

At the cellular ultrastructural level, TEM of MDA-MB 231 breast cancer cells incubated with NP under normoxic and hypoxic conditions for 48 h also demonstrated decreased NP uptake in hypoxia as compared to normoxia. NP aggregates were found in vesicles within the cytoplasm more prominently in the cells incubated with mNP in a normoxic environment (Fig. 12.2a–d). In orthotopic MDA-MB 231 xenograft tumors, intratumorally-injected NPs can also be found in different stages of degeneration within vesicles in the cytoplasm of a tumor cell within a mNPH-treated tumor (Fig. 12.2e).

EPR oxygen measurements revealed baseline tumor pO_2 of less than 5 mmHg in all treatment (CEM 30 and CEM 60) and control (sham NPH with PBS and mNP alone) groups. Treatment of MDA-MB 231 tumors with mNPH to a CEM 60 resulted in a substantial increase in pO_2 from 3.46 to 68.6 mmHg on day 4. The increased pO_2 was sustained at least 8 days after mNPH treatment (Fig. 12.3). Tumor pO_2 after mNPH to a CEM 30 was similar to tumor O_2 after mNP administration alone. Increase in pO_2 in mNP alone is likely due to damage resulting from intratumoral injection or to disruption of the EPR signal by the iron oxide mNPs.

Tumors treated with CEM 60 revealed a nearly statistically significant delay in growth at 4 weeks as compared to sham NPH (PBS injection) (395 mm^3 vs 850 mm^3, $p = 0.08$). CEM 30 treatment did not show any difference in tumor growth compared to controls (Fig. 12.4). Although NPH to CEM 60 was a therapeutic thermal dose, it did result in notable burn injury at the tumor site (data not shown).

4 Conclusions

In this study, the uptake of magnetic mNPs by breast cancer cells, as assessed by ICP-MS and TEM, was decreased under hypoxic (1 % O_2) and hyperoxic (95 % O_2) conditions. MDA-MB 231 orthotopic tumors in nude mice were hypoxic (<5 mmHg) at a volume of 160–220 mm^3 yet showed adequate NP intracellular uptake. This difference in uptake highlights the ongoing debate about the utility of *in vitro* versus *in vivo* studies. NPH treatments to CEM 60 resulted in an immediate and sustained increase in tumor pO_2 as compared with sham treatment. The increase in pO_2 is likely due to a combination of several factors, including cell death which will lead to a decrease in oxygen consumption, decrease in tumor interstitial fluid pressure due to tumor shrinkage, and potential changes in blood flow due to hyperthermia. Tumors treated with mNPH to CEM 60 showed tumor growth delay as compared with those treated with mNPH to CEM 30 and sham mNPH, suggesting that a thermal dose threshold must be achieved for effective hyperthermia treatment. Additional studies are needed to optimize the therapeutic index of mNPH by finding the minimal thermal dose that will increase tumor pO_2 and thereby enhance radiation sensitivity and tumor cell killing but minimize injury to surrounding tissues.

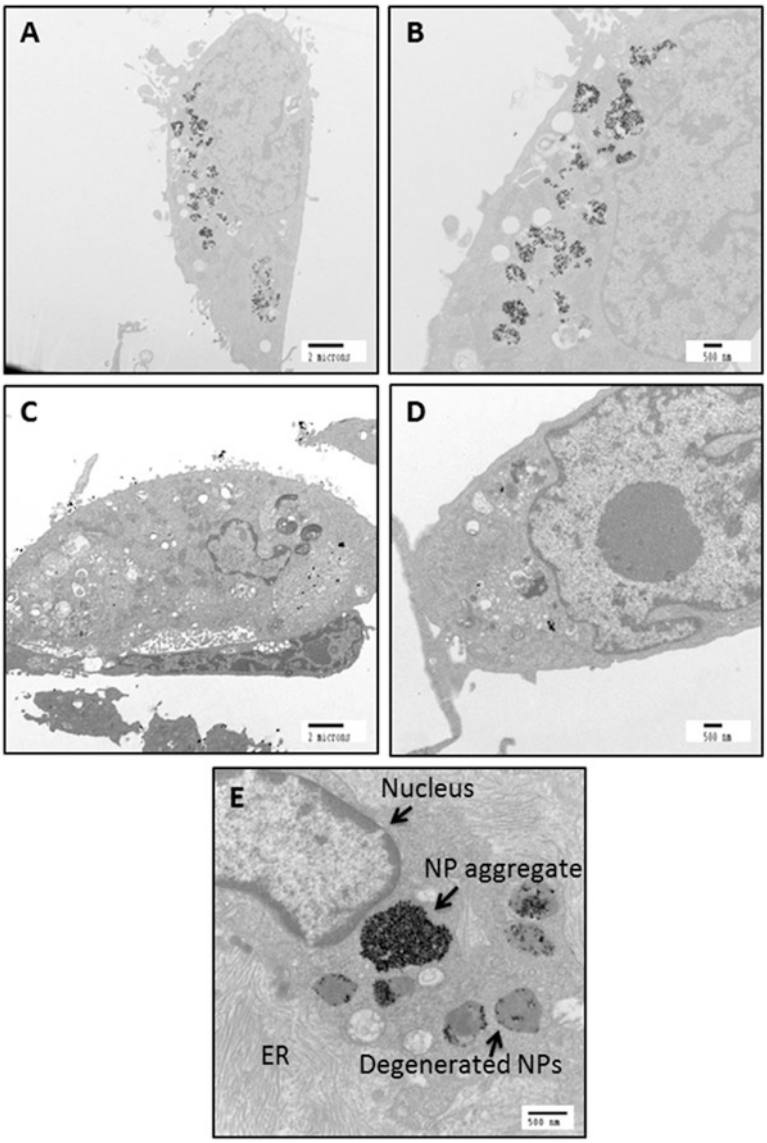

Fig. 12.2 TEM of MDA-MB 231 cells in normoxic (**a**, **b**) and hypoxic conditions (**c**, **d**) incubated with mNP for 48 h. Magnified view of mNP aggregates in an *ex vivo* MDA-MB 231 tumor specimen excised 4 weeks after mNP intratumoral injection and mNPH (**e**)

This project reinforces the need to measure the tumor oxygen microenvironment during any hypoxia-targeted therapies. Over the course of a treatment, tumor oxygenation likely changes, and tracking the oxygen dynamics is essential to optimize timing and dosing of adjuvant therapies. Future experiments will investigate the

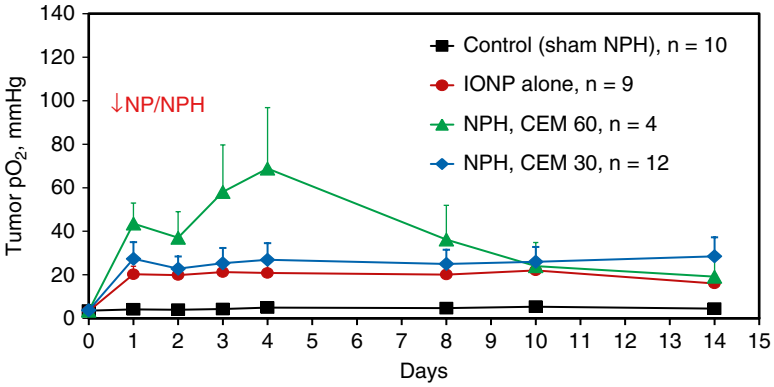

Fig. 12.3 Repeated measurements of MDA-MB 231 tumor pO_2 using *in vivo* EPR oximetry. Pre-NPH pO_2 of the tumors were <5 mmHg at a tumor volume of approximately 200 mm^3 (day 0)

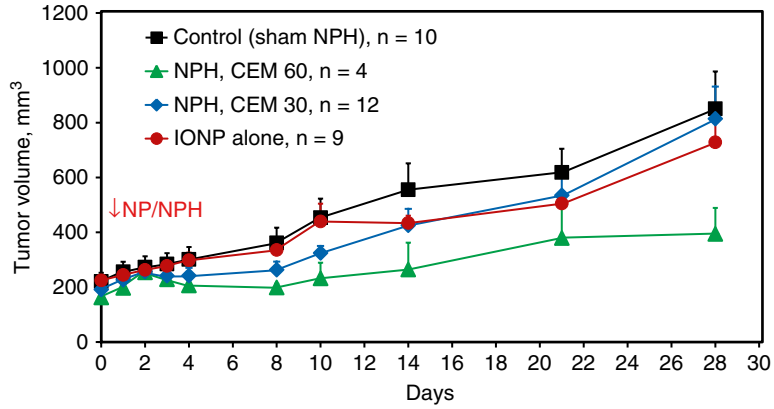

Fig. 12.4 Tumor volume of MDA-MB 231 tumors over 4 weeks

mechanisms of mNP uptake under varying tumor oxygen microenvironments *in vivo* and exploit these mechanisms to enhance mNP uptake of systemically-administered hypoxia-targeted NP. In addition, we aim to develop innovative protocols for tumor pO_2-guided multimodal approaches, such as combining magnetic hyperthermia with radiotherapy for the efficacious treatment of hypoxic tumors.

Acknowledgments This study is supported by the Dartmouth Center for Cancer Nanotechnology Excellence (DCCNE) and Dartmouth Center for Clinical and Translational Sciences (Synergy) Pilot Grants.

References

1. Oleson J, Dewhirst M (1983) Hyperthermia: an overview of current progress and problems. Curr Probl Cancer 8:1–62
2. Giustini A, Petryk A, Hoopes P (2012) Ionizing radiation increases systemic nanoparticle tumor accumulation. Nanomedicine 8:818–821
3. Peng X, Qian X, Mao H et al (2008) Targeted magnetic iron oxide nanoparticles for tumor imaging and therapy. Int J Nanomed 2:311–321
4. Dennis CL, Jackson AJ, Borchers JA et al (2009) Nearly complete regression of tumors via collective behavior of magnetic nanoparticles in hyperthermia. Nanotechnology 20:395103. doi:10.1088/0957-4484/20/39/395103
5. National Cancer Institute Breast Cancer Home Page. http://www.cancer.gov/cancertopics/types/breast. Accessed 23 July 2013
6. Guistini A, Ivkov R, Hoopes PJ (2011) Magnetic nanoparticle biodistribution following intratumoral administration. Nanotechnology 22:345101. doi:10.1088/0957-4484/22/34/345101
7. Overgaard J, Gonzalex D, Hulshof M et al (1995) Randomised trial of hyperthermia as adjuvant to radiotherapy for recurrent or metastatic malignant melanoma. European Society for Hyperthermic Oncology. Lancet 345:540–543
8. Horsman M, Chaplin D, Overgaard J (1990) Combination of nicotinamide and hyperthermia to eliminate radioresistant chronically and acutely hypoxic tumor cells. Cancer Res 50:7430–7434
9. Horsman M, Overgaard J (2007) Hyperthermia: a potent enhancer of radiotherapy. Clin Oncol 19:418–426
10. Hou H, Lariviere J, Demidenko E, Gladstone D, Swartz H, Khan N (2009) Repeated tumor pO_2 measurements by multi-site EPR oximetry as a prognostic marker for enhanced therapeutic efficacy of fractionated radiotherapy. Radiother Oncol 91:126–131
11. Swartz H, Khan N, Buckey J et al (2004) Clinical applications of EPR: overview and perspectives. NMR Biomed 17:335–351
12. Vaupel P (2008) Hypoxia and aggressive tumor phenotype: implications for therapy and prognosis. Oncologist 13:21–26

Chapter 13
Skeletal Muscle and Glioma Oxygenation by Carbogen Inhalation in Rats: A Longitudinal Study by EPR Oximetry Using Single-Probe Implantable Oxygen Sensors

Huagang Hou, Nadeem Khan, Jean Lariviere, Sassan Hodge, Eunice Y. Chen, Lesley A. Jarvis, Alan Eastman, Benjamin B. Williams, Periannan Kuppusamy, and Harold M. Swartz

Abstract The feasibility of EPR oximetry using a single-probe implantable oxygen sensor (ImOS) was tested for repeated measurement of pO_2 in skeletal muscle and ectopic 9L tumors in rats. The ImOS (50 mm length) were constructed using nickel–chromium alloy wires, with lithium phthalocyanine (LiPc, oximetry probe) crystals loaded in the sensor loop and coated with AF 2400® Teflon. These ImOS were implanted into the skeletal muscle in the thigh and subcutaneous 9L tumors. Dynamic changes in tissue pO_2 were assessed by EPR oximetry at baseline, during tumor growth, and repeated hyperoxygenation with carbogen breathing. The mean skeletal muscle pO_2 of normal rats was stable and significantly increased during carbogen inhalation in experiments repeated for 12 weeks. The 9L tumors were

H. Hou, M.D. (✉)
Department of Radiology, Geisel School of Medicine, Hanover, NH 03755, USA

Norris Cotton Cancer Center, Dartmouth-Hitchcock Medical Center, Lebanon, NH 03756, USA

EPR Center for Viable Systems, Department of Radiology, Geisel School of Medicine at Dartmouth, Hanover, NH 03755, USA
e-mail: Huagang.Hou@Dartmouth.Edu

N. Khan • B.B. Williams • P. Kuppusamy
Department of Radiology, Geisel School of Medicine, Hanover, NH 03755, USA

Norris Cotton Cancer Center, Dartmouth-Hitchcock Medical Center, Lebanon, NH 03756, USA

J. Lariviere
Department of Radiology, Geisel School of Medicine, Hanover, NH 03755, USA

S. Hodge
Department of Surgery, Geisel School of Medicine, Hanover, NH 03755, USA

E.Y. Chen
Norris Cotton Cancer Center, Dartmouth-Hitchcock Medical Center, Lebanon, NH 03756, USA

Department of Surgery, Geisel School of Medicine, Hanover, NH 03755, USA

H.M. Swartz et al. (eds.), *Oxygen Transport to Tissue XXXVI*, Advances in Experimental Medicine and Biology 812, DOI 10.1007/978-1-4939-0620-8_13,

hypoxic with a tissue pO_2 of 12.8 ± 6.4 mmHg on day 1; however, the response to carbogen inhalation varied among the animals. A significant increase in the glioma pO_2 was observed during carbogen inhalation on day 9 and day 14 only. In summary, EPR oximetry with ImOS allowed direct and longitudinal oxygen measurements in deep muscle tissue and tumors. The heterogeneity of 9L tumors in response to carbogen highlights the need to repeatedly monitor pO_2 to confirm tumor oxygenation so that such changes can be taken into account in planning therapies and interpreting results.

Keywords Carbogen • Electron paramagnetic resonance (EPR) oximetry • Glioma • Implantable oxygen sensor (ImOS) • Partial pressure of oxygen (pO_2)

1 Introduction

Tissue pO_2 is a key parameter in physiological and pathophysiological processes of biological systems and plays a key role in cancer therapy. For example, the efficacy of radiotherapy and chemotherapy dramatically depends on the level of oxygen in the tumors. Furthermore, tissue pO_2 varies in a temporal manner during disease progression and therapy. Accordingly, the assessment of tissue oxygenation is of great physiological and clinical interest.

In vivo electron paramagnetic resonance (EPR) oximetry is a powerful technique that provides repeated monitoring of tissue pO_2 as often as needed. In spite of successful applications in various pathologies, the sensitivity of EPR oximetry using particulate LiPc implants with direct detection has been limited to a depth of no more than 10 mm from the surface. To circumvent this problem, we have developed implantable oxygen sensors (ImOS) constructed with copper wires. However, these ImOS failed during rigorous testing in the skeletal muscle of rats and pigs due to mechanical damage. To overcome this problem, we have developed ImOS using nickel–chromium (Ni-Cr) alloy wires for pO_2 measurement in tissues such as skeletal muscle and 9L glioma.

L.A. Jarvis
Norris Cotton Cancer Center, Dartmouth-Hitchcock Medical Center, Lebanon, NH 03756, USA

Department of Medicine, Geisel School of Medicine, Hanover, NH 03755, USA

A. Eastman
Norris Cotton Cancer Center, Dartmouth-Hitchcock Medical Center,
Lebanon, NH 03756, USA

Department of Pharmacology, Geisel School of Medicine, Hanover, NH 03755, USA

H.M. Swartz
EPR Center for the Study of Viable Systems, The Geisel School of Medicine
at Dartmouth, Lebanon, NH, USA

2 Methods

2.1 Single-Probe Implantable Oxygen Sensors

Oxygen sensitive lithium phthalocyanine (LiPc) crystals were synthesized in our laboratory. The properties of LiPc have been reported earlier [1]. The ImOS of 50 mm in length was fabricated with Ni-Cr alloy and has two sets of loops, a large loop on one end and one small loop on the other end. These two loops are connected by a length of twisted wire. The small loop was loaded with LiPc aggregates (50–80 μg) and then the entire resonator was coated with a gas permeable biocompatible Teflon AF 2400® (Aldrich, Steinheim, Germany) (Fig. 13.1a).

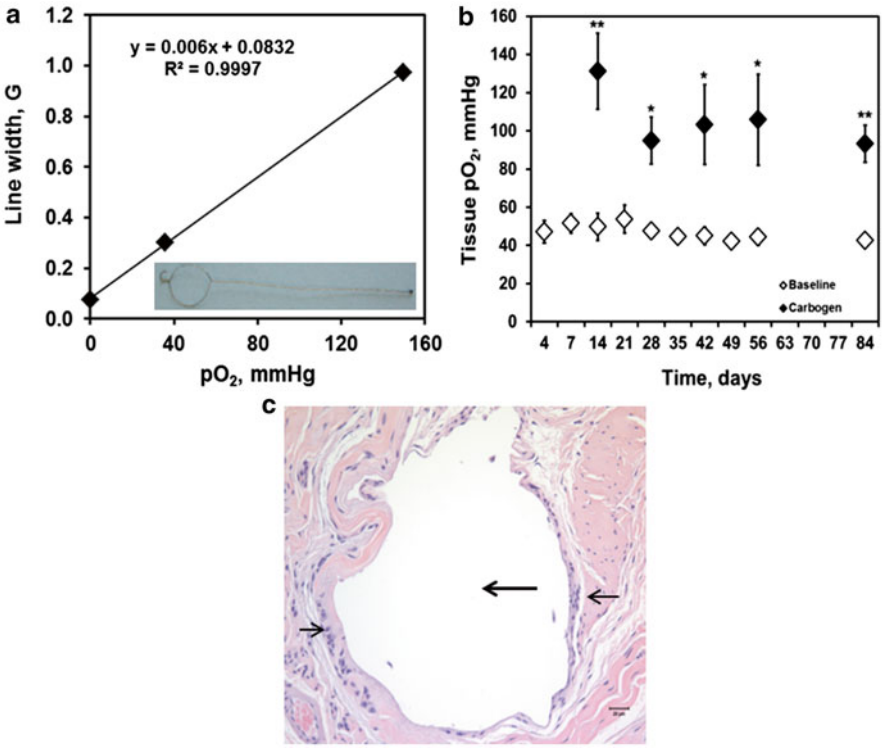

Fig. 13.1 (**a**) Calibration plot of an ImOS. The response of ImOS to different concentrations of perfused oxygen and regression coefficients (R^2). *Inset*: a sample of 50 mm length ImOS used in this study. (**b**) Mean skeletal muscle pO_2 prior to and during carbogen inhalation. Mean ± SE, N = 8. *p < 0.05, **p < 0.01, compared to baseline on the same day (paired t-test). (**c**) H&E stained sections of the skeletal muscle tissue obtained from a rat after 84 days of ImOS implantation. The *long arrows* indicate the track of the ImOS in the muscle and *short arrows* indicate the presence of a thin capsule formed by few layers of inflammatory cells around the track of the ImOS. The thickness of each section is 5 μm. Magnification: 40×

The small loop was implanted in the tissue of interest, and the large loop was placed below the skin for coupling with the external loop resonator of the EPR spectrometer [2].

2.2 Animal Preparation

All the animal procedures were approved by the Institutional Animal Care and Use Committee of Dartmouth Medical School. Fourteen male Fisher 344 rats, 200–250 g (Charles River Laboratories, Wilmington, MA) were used and divided into two groups: (i) Skeletal muscle group, N = 8; (ii) 9L tumor group, N = 6.

2.2.1 Tumor Model and Implantation of ImOS into the Skeletal Muscle and 9L Tumors

The 9L tumors were established by direct injection of 9L cells ($1–2 \times 10^6$ cells in 100 µl) into the subcutaneous tissue in the right thigh of the rats. One day or 4 days prior to the pO_2 measurement, the rats were anesthetized (2–2.5 % isoflurane in 30 % O_2) and the sensor loop was gently inserted into the skeletal muscle (5–6 mm depth, group i) or in the 9L tumor (2–3 mm depth, group ii) through a small skin incision, respectively. The reminder of the ImOS was inserted under the skin of the rats for the repeated measurement of pO_2 by EPR oximetry.

2.2.2 Hyperoxia Challenge

The rats were anesthetized (1.5 % isoflurane in 30 % oxygen) and baseline pO_2 was measured for 30 min and then the animals were allowed to breathe carbogen for 25 min. The inhaled gas was again switched back to 30 % O_2 for 25 min. This hyperoxia challenge was repeated either daily or weekly as shown in the results.

2.3 EPR Oximetry

EPR oximetry was performed with an L-band (1.2 GHz) EPR spectrometer using the method described earlier. Tissue pO_2 was determined by measuring the peak-to-peak line widths of the EPR spectra, which were converted to pO_2 by using appropriate calibration of the ImOS used in the study (Fig. 13.1a). The spectrometer parameters were: incident microwave power of 1–2 mW: modulation frequency 24 kHz; magnetic field 430 G; scan time 10 s and modulation amplitude not exceeding one third of the peak-to-peak line width.

2.4 Histological Analysis

At the end of the experiments, the rats were euthanized and muscle tissue surrounding the ImOS was excised and fixed with 10 % formalin, embedded in paraffin, and stained with hematoxylin–eosin for histological studies.

2.5 Statistical Analysis

Data were analyzed by Student's t-test. A paired t-test was used to compare pO_2 changes within the same group. The tests were two-sided, and a change with a p-value <0.05 was considered statistically significant. All data are expressed as mean ± SE. N is the number of animals in each group.

3 Results

The pO_2 measurements were started 4 days after the surgical implantation of the ImOS in the skeletal muscle and continued for up to 12 weeks (Fig. 13.1b). No significant difference in the skeletal muscle pO_2 was evident while breathing 30 % O_2 from day 4 to day 84. The mean skeletal muscle pO_2 increased significantly during carbogen inhalation (Fig. 13.1b). Histological examination showed no obvious blood cells along the track of the ImOS; however, the presence of a thin capsulate of inflammatory cells and fibroblasts was observed (Fig. 13.1c). These results demonstrate minimal histological changes around the ImOS and are similar to our earlier observation in the brain of the rats [2] and in the muscle of the rabbits [3].

A typical variation in the response of three ectopic 9L tumors to carbogen inhalation is shown in Fig. 13.2a–c. A small (Fig. 13.2a) to modest (Fig. 13.2b) and significant (Fig. 13.2c) response of the 9L tumor pO_2 to carbogen inhalation was evident in these individual tumors. The pO_2 data including these tumors were pooled to obtain mean baseline pO_2 and response to carbogen inhalation (Fig. 13.2d). The mean baseline pO_2 of the 9L tumors was 12.8 ± 6.4 mmHg on day 1 (Fig. 13.2d). A significant increase in the mean tumor pO_2 was observed during carbogen inhalation on day 9 and day 14 (Fig. 13.2d).

4 Discussion

The goal of current study was to test ImOS fabricated with Nickel–Chromium (Ni-Cr) alloy wires for a longitudinal measurement of skeletal muscle and 9L tumor pO_2 and the response to carbogen inhalation. Our results indicate that the ImOS fabricated

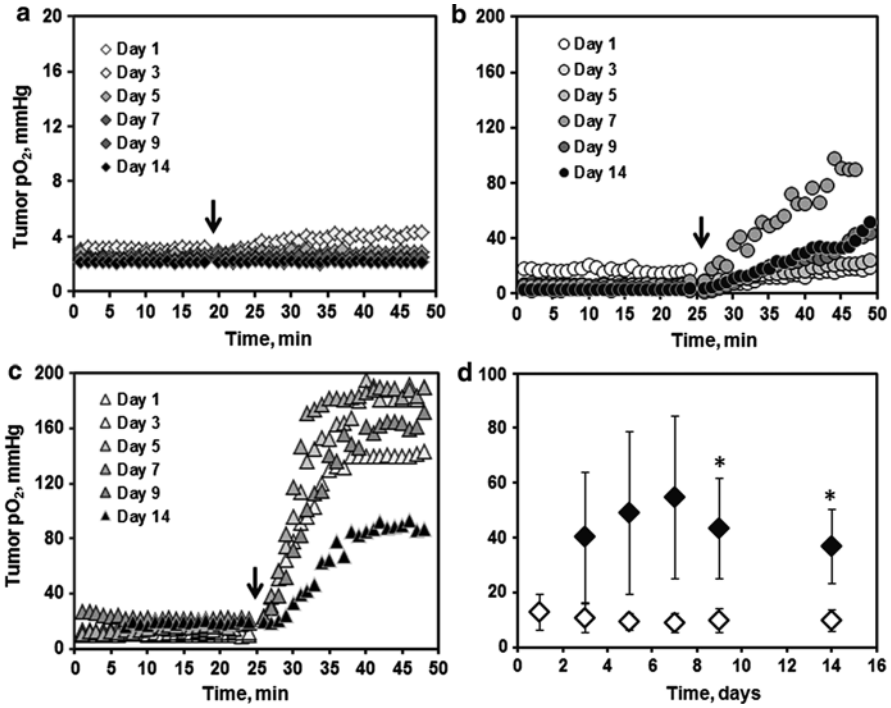

Fig. 13.2 Dynamic changes in ectopic 9L glioma pO_2 prior to and during carbogen inhalation in three typical rats (**a**: rat#4; **b**: rat#1; **c**: rat#6) and mean pO_2 observed from a group of six rats (**d**, *open diamond*: baseline tumor pO_2; *filled diamond*: tumor pO_2 during carbogen inhalation. mean ± SE, N = 6). *Black arrows* indicate the time to start carbogen inhalation. *$p < 0.05$, compared with baseline on same day (paired t-test)

with Ni-Cr alloy wires remained intact and thus enabled repeated measurement of tissue pO_2 in the skeletal muscle and ectopic 9L tumors for several weeks using EPR oximetry.

The mean baseline pO_2 values of the skeletal muscle were stable and a consistent response to carbogen inhalation was observed. The ectopic 9L tumors were hypoxic, which are consistent with the earlier reports [4]. However, the response of individual 9L tumors to carbogen varied among the animals. Lanzen et al. [5] used microelectrodes to detect the changes in tumor pO_2 in R3230Ac tumors transplanted in the quadriceps muscle or subcutis. The tumors in the muscle showed an increase in pO_2 from 14.6 ± 3.2 to 34.5 ± 8.2 mmHg with carbogen breathing; however, no significant change in the pO_2 of the subcutaneous tumor was observed. Bussink et al. used OxyLite to measure the changes in pO_2 on carbogen breathing in three human xenograft tumor lines and found that E102 and E106 tumors showed a significant increase in tumor pO_2. In an additional cell line (SCCNij3 tumor xenograft), 9 out of 17 tumors had an increase in pO_2 during carbogen breathing [6]. We speculate that the differences in response of individual 9L tumor pO_2 to carbogen

might be due to a different location of the sensor loop of the ImOS in each tumor. Additionally, differences in the status of tumor vasculature, blood flow and interstitial pressure among tumors can also lead to a difference in responses to carbogen inhalation over days. These variables should be further investigated.

The temporal changes in mean tumor pO_2 on carbogen inhalation varied over days with a statistically significant increase on days 9 and 14. These results signify the need for a repeated measurement of tumor pO_2 during interventions designed to improve the levels of oxygen for therapeutic intention.

In conclusion, temporal and longitudinal changes in skeletal muscle and glioma pO_2 can be measured using EPR oximetry with ImOS. The ability to repeatedly assess skeletal muscle and tumor pO_2 is likely to play a vital role in understanding the dynamics of tissue pO_2 during carbogen inhalation and other therapies designed to modulate tumor hypoxia. EPR oximetry with ImOS can provide this information to potentially optimize therapies by scheduling treatments at times of increase in tissue oxygenation.

Acknowledgments This work was partly supported by a Hitchcock Foundation Program Project Grant and PROUTY grant from the NCCC at Dartmouth-Hitchcock Medical Center.

References

1. Liu K, Gast P, Moussavi M (1993) Lithium phthalocyanine: a probe for electron paramagnetic resonance oximetry in viable biological systems. Proc Natl Acad Sci U S A 90:5438–5442
2. Hou H, Dong R, Li H, Williams B, Lariviere JP, Hekmatyar SK, Kauppinen RA, Khan N, Swartz H (2012) Dynamic changes in oxygenation of intracranial tumor and contralateral brain during tumor growth and carbogen breathing: a multisite EPR oximetry with implantable resonators. J Magn Reson 214(1):22–28. doi:10.1016/j.jmr.2011.09.043
3. Dinguizli M, Jeumont S, Beghein N, He J, Walczak T, Lesniewski PN, Hou H, Grinberg OY, Sucheta A, Swartz HM, Gallez B (2006) Development and evaluation of biocompatible films of polytetrafluoroethylene polymers holding lithium phthalocyanine crystals for their use in EPR oximetry. Biosensors Bioelectron 21(7):1015–1022
4. Hou H, Mupparaju SP, Lariviere JP, Hodge S, Gui J, Swartz HM, Khan N (2013) Assessment of the Changes in 9L and C6 Glioma pO_2 by EPR Oximetry as a Prognostic Indicator of Differential Response to Radiotherapy. Radiat Res 179(3):343–351
5. Lanzen JL, Braun RD, Ong AL, Dewhirst MW (1998) Variability in blood flow and pO2 in tumors in response to carbogen breathing. Int J Radiat Oncol Biol Phys 42(4):855–859
6. Bussink J, Kaanders JH, Strik AM, van der Kogel AJ (2000) Effects of nicotinamide and carbogen on oxygenation in human tumor xenografts measured with luminescense based fiber-optic probes. Radiother Oncol J Eur Soc Ther Radiol Oncol 57(1):21–30

Chapter 14
Recurrent Low-Dose Chemotherapy to Inhibit and Oxygenate Head and Neck Tumors

Nadeem Khan, Huagang Hou, Sassan Hodge, Muthulakshmi Kuppusamy, Eunice Y. Chen, Alan Eastman, Periannan Kuppusamy, and Harold M. Swartz

Abstract A lack of strategy to counteract hypoxia ($pO_2 < 10$–15 mmHg) and technique to repeatedly measure tumor pO_2 has restricted therapeutic optimization. We report the results obtained with an innovative anti-angiogenic strategy of recurrent low-dose (metronomic) chemotherapy to modulate hypoxia and growth of the Head and Neck tumor xenografts.

The FaDu tumors were established in the flank of immune deficient mice and EPR oximetry with lithium phthalocyanine crystals was used to follow the temporal changes in tumor pO_2 on treatment with gemcitabine including controls for three weeks. The FaDu tumors were hypoxic with a baseline (pre-treatment) pO_2 of 2–8 mmHg. A transient increase in the tumor pO_2 was evident on day 3 on treatment with a conventional schedule of gemcitabine (150 mg/kg, d1, d8, d15). No significant change in the tumor pO_2 on treatment with metronomic gemcitabine (25 mg/kg on d1, d3, d5 for 3 weeks) was observed. However, tumor pO_2 increased significantly on d15–d18 during treatment with a metronomic schedule of 15 mg/kg gemcitabine (d1, d3, d5 for 3 weeks). A modest decrease in the tumor growth was evident on treatment with conventional gemcitabine. Notably, tumor growth was significantly

N. Khan, Ph.D. (✉) • H. Hou • M. Kuppusamy • P. Kuppusamy
EPR Center for Viable Systems, Department of Radiology,
The Geisel School of Medicine, Hanover, NH 03755, USA

Norris Cotton Cancer Center, Lebanon, NH 03756, USA
e-mail: Nadeem.Khan@Dartmouth.Edu

S. Hodge • E.Y. Chen
Department of Surgery, Dartmouth-Hitchcock Medical Center,
One Medical Center Drive, Lebanon, NH 03756, USA

A. Eastman
Department of Pharmacology and Toxicology, The Geisel School of Medicine,
Hanover, NH 03755, USA

H.M. Swartz
EPR Center for the Study of Viable Systems, The Geisel School of Medicine
at Dartmouth, Lebanon, NH, USA

H.M. Swartz et al. (eds.), *Oxygen Transport to Tissue XXXVI*, Advances in Experimental Medicine and Biology 812, DOI 10.1007/978-1-4939-0620-8_14,

inhibited by metronomic (25 and 15 mg/kg) gemcitabine treatment. The immunohistochemistry (IHC) analyses of the tumor samples indicate a decrease in HIF-1α and TSP-1 on treatment with metronomic gemcitabine.

In conclusion, a significant inhibition of tumor growth on treatment with metronomic gemcitabine was observed; however, the increase in pO_2 was dose dependent. EPR oximetry can be used to follow the temporal changes in tumor pO_2 to identify a therapeutic window on treatment with metronomic chemotherapy for potential combination with radiotherapy.

Keywords Chemotherapy • Anti-angiogenesis • Vascular normalization • Head and neck cancer • Partial pressure of oxygen (pO_2) • Electron paramagnetic resonance (EPR) oximetry • Hypoxia inducible factor (HIF) • Thrombospondin (TSP)

1 Introduction

Atypical angiogenesis with leaky vasculature and abnormal blood flow in solid tumors often leads to hypoxic microenvironment, a major cause of resistance to most of the standard therapies, such as radiation and chemotherapy. Furthermore, tumor hypoxia is dynamic i.e. varies with tumor growth and as a consequence of various treatment. In spite of extensive research, a lack of a suitable strategy to effectively reduce tumor hypoxia and technique to measure the dynamic changes in tumor pO_2 has restricted the potential optimization of treatment outcome. We are investigating the efficacy of a recently proposed strategy of recurrent low-dose (metronomic) chemotherapy [1] on the pO_2 and growth of Head and Neck tumor xenografts. The metronomic schedule is expected to prune the immature neo-vasculature and then remodel the remaining vasculature, leading to the normalization of otherwise abnormal tumor vasculature [2, 3]. The vascular normalization is expected to restore the blood flow and thus oxygenate the tumors, thereby providing a therapeutic window which, if exploited, can improve treatment outcome.

We have successfully used in vivo EPR oximetry to repeatedly measure tissue pO_2 of Head and Neck tumor xenografts on treatment with conventional and metronomic schedules of gemcitabine. The results indicate a transient increase in the tumor pO_2 on treatment with metronomic gemcitabine; however the extent of increase in pO_2 was dose dependent. A significant decrease in the tumor growth was observed on treatment with metronomic gemcitabine as compared to the conventional schedule. Our overall goal is to establish metronomic regimens that can significantly oxygenate and inhibit tumor growth compared to the conventional regimen being tested in clinical trials

2 Methods

2.1 Head and Neck Tumor Xenografts and Experimental Groups

The FaDu tumors were established by injecting 100 μl suspension of $2–2.5 \times 10^6$ cells in each flank of 20–22 g NOD scid gamma (NSG) mice (inbred). The ectopic

tumors of 6–8 mm in length were obtained in 18–21 days after cell inoculation and then the animals were randomly assigned to four groups: (i) control, (ii) 150 mg/kg gemcitabine in a conventional schedule (d1, d8, d15), (iii) 25 mg/kg gemcitabine in a metronomic schedule (d1, d3, d5 for 3 weeks) and (iv) 15 mg/kg gemcitabine in a metronomic schedule (d1, d3, d5 for 3 weeks). The animals were treated by intraperitoneal injections of gemcitabine (Eli Lilly and Co., IN, USA). A baseline tumor pO_2 by EPR oximetry and tumor volume by a standard caliper method ($\text{volume} = \pi/6 \times \text{length} \times \text{width}^2$) was measured prior to any treatment on d1 and then the treatment was initiated along with the repeated measurement of tumor pO_2 and volume. At the end of the third week, the tumors were excised and IHC analysis was carried out to investigate the levels of HIF-1α and TSP-1 in the control, 150 mg/kg gemcitabine and 15 mg/kg gemcitabine groups.

2.2 *In Vivo EPR Oximetry*

A 1.2 GHz (L-band) EPR spectrometer was used to repeatedly measure tumor pO_2 during treatment with a different dose and schedule of gemcitabine. Two aggregates of LiPc (lithium phthalocyanine, oximetry probe) crystals synthesized in our laboratory were implanted using 25 G needles approximately 4 mm apart and at a depth of 2–3 mm from the surface in each tumor. The pO_2 was measured simultaneously from both implants using magnetic field gradients (multi-site EPR oximetry) for 15–20 min and pooled to obtain an average pO_2 on each day of the measurement [4, 5].

2.3 *Immunohistochemistry Analysis of the Tumors*

The HIF-1α (hypoxia marker) and TSP-1 (angiogenic inhibitor) staining was performed on formalin-fixed, paraffin-embedded sections of the FaDu tumors using the standard method [6]. Briefly, the primary antibodies were diluted 1:100 and incubated for 1 h. The sections were subsequently incubated with appropriate secondary antibody and staining was developed using diaminobenzidine solution. The images were acquired on Olympus BX50 microscope at different magnifications for analysis.

2.4 *Statistical Analysis*

A paired t-test was used to determine the statistical significance of the changes in tumor pO_2 compared to d1 in each group and an unpaired t-test was used to compare the tumor volume between groups. The tests were two-sided and a change with a $\text{p-value} < 0.05$ was considered statistically significant. All data are expressed as $\text{mean} \pm \text{SEM}$; N is the number of tumors in each group.

3 Results

The baseline pO_2 in the control, 150 mg/kg gemcitabine, 25 mg/kg gemcitabine and 15 mg/kg gemcitabine were 4.8±1.5, 2.3±0.6, 4.0±0.7 and 4.6±0.7 mmHg, respectively, and were not significantly different between the groups (Fig. 14.1a). In these experiments, a significant decline in the tumor pO_2 of the control group was evident on d10 but the pO_2 returned to baseline on subsequent days. On the other hand, a significant increase in the tumor pO_2 on treatment with 150 mg/kg gemcitabine was observed on d3, which declined to baseline in the subsequent measurements. No significant change in the tumor pO_2 was evident on metronomic treatment

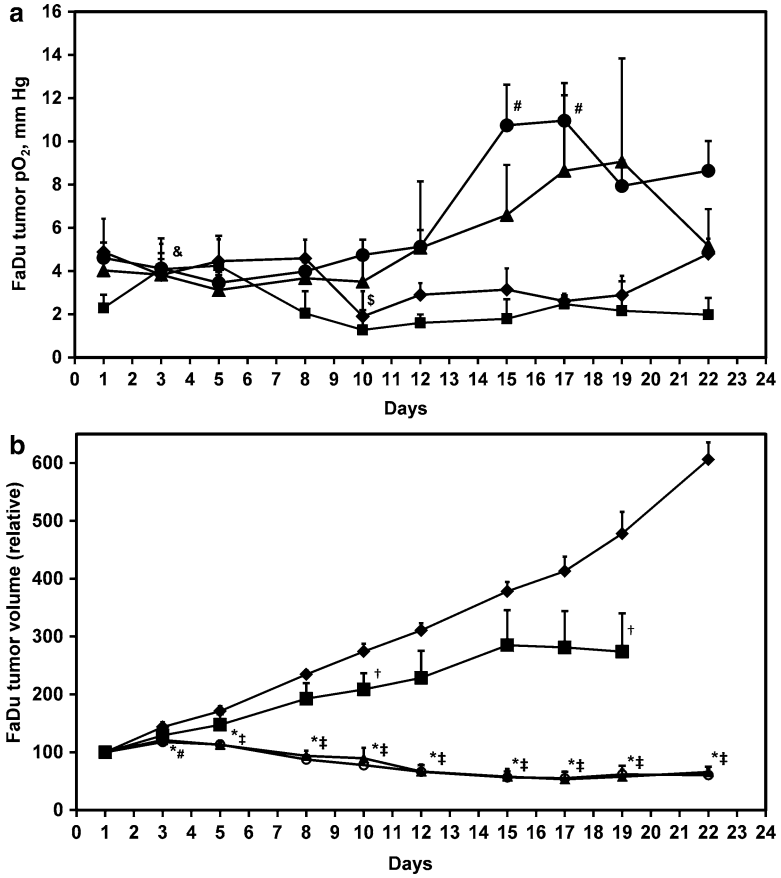

Fig. 14.1 (**a**).Temporal changes in the tumor pO_2, and (**b**). Tumor volume in the control (*diamond*, N=6–9), conventional chemotherapy (*square*, 150 mg/kg gemcitabine, d1, d8, d15, N=7–9) and metronomic chemotherapy (*triangle*, 25 mg/kg and *circle*, 15 mg/kg gemcitabine on d1, d3, d5 each week for 3 weeks, N=12–18). $, $p<0.05$ day 1 vs. d3–d22, control; &, $p<0.05$ day 1 vs. d3–d22, 150 mg/kg gemcitabine; #, $p<0.05$ day 1 vs. d3–d22, 15 mg/kg gemcitabine; †, $p<0.05$ 150 mg/kg gemcitabine vs. control; *, $p<0.05$ 25 mg/kg gemcitabine vs. control; ‡, $p<0.05$ 15 mg/kg gemcitabine vs. control

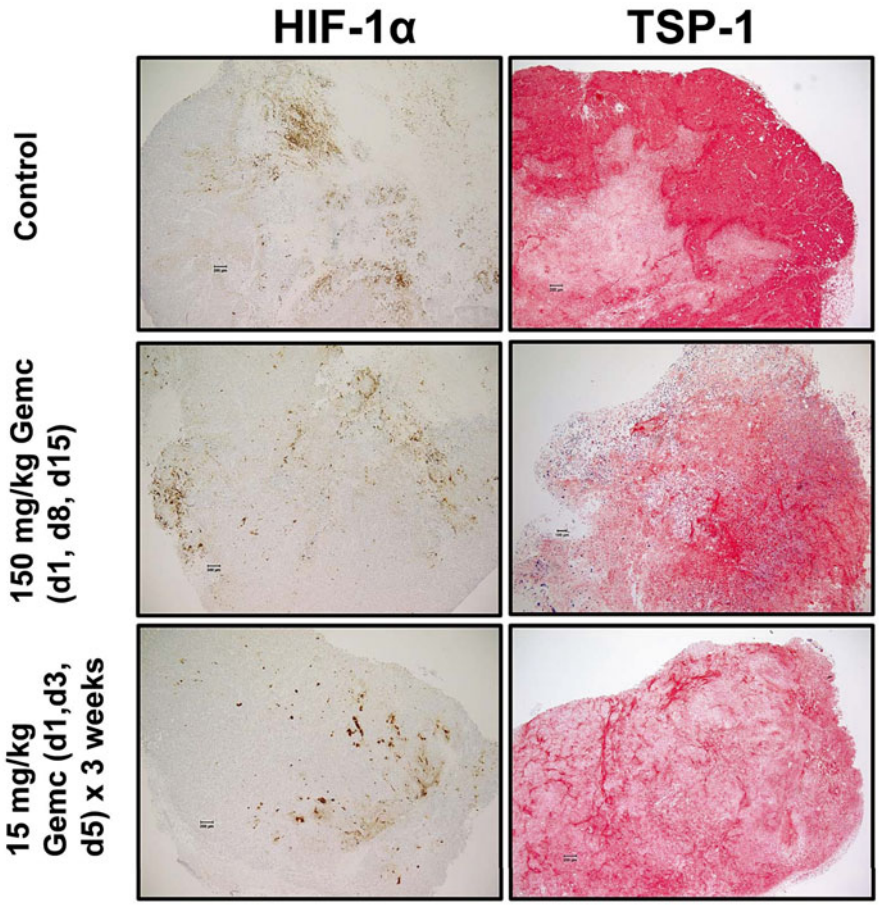

Fig. 14.2 Immunohistochemistry analysis of the tumor samples in the control, conventional (150 mg/kg gemcitabine, d1, d8, d15) and metronomic (15 mg/kg gemcitabine on d1, d3, d5 for 3 weeks) chemotherapy groups. The scale of magnification is 200 μm in the images

with 25 mg/kg gemcitabine; however, tumor pO_2 significantly increased on d15–d17 during treatment with 15 mg/kg gemcitabine.

The baseline tumor volume in the control, 150 mg/kg gemcitabine, 25 mg/kg gemcitabine and 15 mg/kg gemcitabine were 342.7 ± 23.8, 281.8 ± 18.6, 287.6 ± 16.6 and 321.3 ± 19 mm^3, respectively, and were not significantly different between the groups (Fig. 14.1b). A modest decrease in the tumor growth was observed on d10 and d19 on treatment with 150 mg/kg gemcitabine in the conventional schedule. However, a significant and consistent inhibition of tumor growth was observed from d3–d22 on metronomic treatment with 25 and 15 mg/kg gemcitabine. The IHC images indicate a relative decline in HIF-1α and TSP-1 on treatment with metronomic 15 mg/kg gemcitabine compared to the control and conventional 150 mg/kg gemcitabine schedule (Fig. 14.2).

4 Conclusions

The rationale for metronomic chemotherapy was proposed after the observation that treatment with some chemotherapeutics resulted in a mild and reversible anti-angiogenic effect on conventional schedule. Several pre-clinical studies have now confirmed a persistent anti-angiogenic effect using recurrent low-dose schedules, which led to the concept of vascular normalization [2, 3]. We hypothesize that vascular normalization induced by the metronomic approach should restore blood flow into the tumors and thus enhance tissue pO_2. We also hypothesize that the techniques that can provide repeated measurement of tumor pO_2 will be extremely useful in identifying a therapeutic window during which the tumors are oxygenated during metronomic treatment. Given the role of hypoxia in resistance to radiotherapy, this vital information can be used to schedule irradiations when the tumors are oxygenated (oxygen guided radiotherapy protocols) to improve the treatment outcome.

Our results indicate a significant increase in tumor pO_2 on treatment with metronomic gemcitabine compared to the conventional schedule; however, the efficacy was dose dependent. A significant inhibition of tumor growth was observed with both metronomic schedules (25 or 15 mg/kg gemcitabine) investigated in these experiments. The preliminary IHC results suggest a decrease in the levels of HIF-1α on treatment with 15 mg/kg gemcitabine in metronomic schedule, which is in agreement with the increase in tumor pO_2 observed in this group. However, a decrease in the levels of TSP-1 was also evident on treatment with metronomic gemcitabine compared to the conventional schedule. This is in contrary to the expected anti-angiogenic effect of metronomic gemcitabine, and warrants further investigation. The ability to repeatedly measure tumor pO_2 by EPR oximetry can be used to identify tumors that oxygenate during metronomic treatment for potential combination with radiotherapy. A direct assessment of tumor vasculature by mCT is ongoing to confirm vascular normalization on treatment with metronomic schedules.

Acknowledgments Pilot Program Project funded by the Norris Cotton Cancer Center, Department of Radiology, and the EPR Center, Geisel School of Medicine, Hanover, NH.

References

1. Pasquier E, Kavallaris M, Andre N (2010) Metronomic chemotherapy: new rationale for new directions. Nat Rev Clin Oncol 7(8):455–465
2. Goel S, Wong AH, Jain RK (2012) Vascular normalization as a therapeutic strategy for malignant and nonmalignant disease. Cold Spring Harbor Perspect Med 2(3):a006486
3. Carmeliet P, Jain RK (2011) Principles and mechanisms of vessel normalization for cancer and other angiogenic diseases. Nat Rev Drug Discov 10(6):417–427

4. Mupparaju S, Hou H, Lariviere JP, Swartz H, Jounaidi Y, Khan N (2011) Repeated tumor oximetry to identify therapeutic window during metronomic cyclophosphamide treatment of 9 L gliomas. Oncol Rep 26(1):281–286
5. Doloff JC, Khan N, Ma J, Demidenko E, Swartz HM, Jounaidi Y (2009) Increased tumor oxygenation and drug uptake during anti-angiogenic weekly low dose cyclophosphamide enhances the anti-tumor effect of weekly tirapazamine. Curr Cancer Drug Target 9(6):777–788
6. Shi ZR, Itzkowitz SH, Kim YS (1988) A comparison of three immunoperoxidase techniques for antigen detection in colorectal carcinoma tissues. J Histochem Cytochem 36(3):317–322

Chapter 15
How *In Vivo* EPR Measures and Images Oxygen

Boris Epel, Gage Redler, and Howard J. Halpern

Abstract The partial pressure of oxygen (pO_2) in tissues plays an important role in the pathophysiology of many diseases and influences outcome of cancer therapy, ischemic heart and cerebrovascular disease treatments and wound healing. Over the years a suite of EPR techniques for reliable oxygen measurements has been developed. This is a mini-review of pulse EPR in vivo oxygen imaging methods that utilize soluble spin probes. Recent developments in pulse EPR imaging technology have brought an order of magnitude increase in image acquisition speed, enhancement of sensitivity and considerable improvement in the precision and accuracy of oxygen measurements.

Keywords EPR • Imaging • Oxygen • Relaxation

1 Spin Probe

The oxygen molecule has two unpaired electrons in a triplet state that exhibits very fast relaxation. Upon interaction with a paramagnetic spin probe, oxygen enhances the relaxation rate of the probe via Heisenberg exchange [1]. The Smoluchowski

B. Epel • G. Redler
Center for EPR Imaging In Vivo Physiology, Chicago, IL, USA

Department of Radiation Oncology, University of Chicago, Chicago, IL, USA

H.J. Halpern (✉)
Center for EPR Imaging In Vivo Physiology, Chicago, IL, USA

Department of Radiation Oncology, University of Chicago, Chicago, IL, USA

MC1105, Department of Radiation and Cellular Oncology, University of Chicago Medical Center, 5841 S. Maryland Ave, Chicago, IL 60637, USA
e-mail: h-halpern@uchicago.edu

H.M. Swartz et al. (eds.), *Oxygen Transport to Tissue XXXVI*, Advances in Experimental Medicine and Biology 812, DOI 10.1007/978-1-4939-0620-8_15,

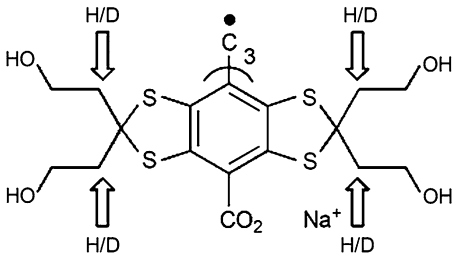

Fig. 15.1 Chemical structures of OX063 trityl

diffusion equation predicts a linear relationship between pO_2 and relaxation rates that is validated for multiple soluble radicals. This relationship allows a direct EPR measure of pO_2 with high precision [2].

The success of non-invasive oximetry in the last decade is strongly linked to triarylmethyl radicals or trityls (Fig. 15.1) developed by Nycomed Innovations (later acquired by GE Healthcare, Little Chalfont, Buckinghamshire, UK) possessing a narrow single EPR line [3]. The trityls that are commonly used for in vivo imaging are methyl-tris[8-carboxy-2,2,6,6-tetrakis[2-hydroxyethyl]benzo[1,2-d:4,5-d′]bis[1,3]dithiol-4-yl]-trisodium salt, OX063 (16 μT p-p) and its partially deuterated form Ox63H24D (8 μT p-p). These spin probes are distributed in the extracellular fluid compartment [2, 4]. In the blood stream of a mouse, the clearance halftime of these probes is approximately 9–10 min, whereas in tumors they remain and provide strong signals for about 40–50 min [5]. The lethal dose (LD50) of analogs of OX063 is very high, 8 mmol/kg, which allows high dose injections [6].

2 Imaging Methods

For imaging, the spatial position of a paramagnetic species is encoded by use of linear magnetic field gradients, **G**. The additional magnetic field experienced by a species at position **x** in the sample is then $\Delta B = \mathbf{G}\cdot\mathbf{x}$. The time evolution of signal from a sample after an RF pulse is

$$s(t) = \int_V f(x) exp\left(-\frac{t}{T_2^*(x)}\right) exp\left[-i2\pi k(t)x\right] dx \tag{15.1}$$

The time evolution of echoes can be treated in a similar way. Here, V describes an integral over the sample volume, and $\boldsymbol{f}(\boldsymbol{x})$ is the spatial distribution of the magnetization. The relaxation term $\exp\left(-\frac{t}{T_2^*(x)}\right)$ describes the attenuation of signal. The switching speed of the gradients achieved by EPR *in vivo* imaging hardware is slow in comparison to the relaxation rates of electrons (units of microseconds). Thus gradients constant on the time scale of spin probe relaxation are used in the definition of $\boldsymbol{k}$-space trajectories:

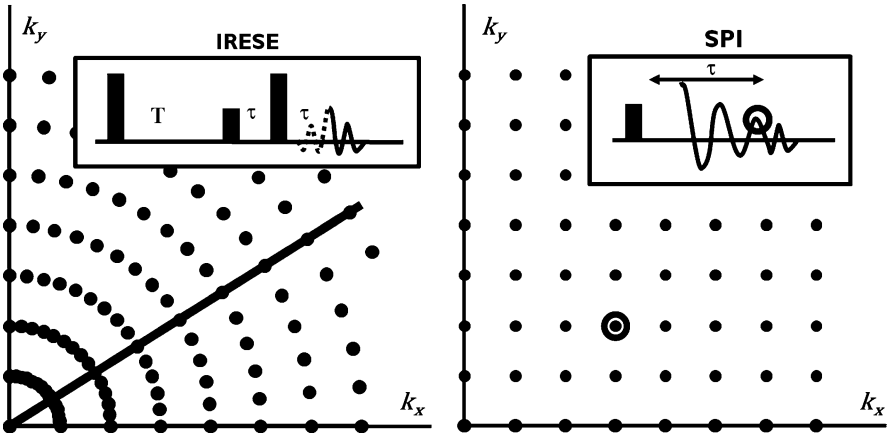

Fig. 15.2 Filling of two dimensional *k*-space by projection-based and single point imaging methods

$$k(t) == \frac{\gamma_e}{2\pi}\int_0^t G(t')dt' = \frac{\gamma_e}{2\pi}Gt. \tag{15.2}$$

For correct reconstruction of an image, sufficient *k*-space data must be acquired. Two general ways of filling *k*-space by using static gradients have been elaborated: projection-based and Fourier imaging.

2.1 Projection-Based Reconstruction

The gradient in (15.2) is a scaling factor between time and ***k***-values. By increasing of the gradient, the time, t, necessary to cover the desired k-space can be made small enough that the relaxation term in the (15.1) becomes negligible. In this case (15.1) describes the Radon transformation of an object in Fourier space along the direction defined by the gradient [7]. The ***k***-space trajectory of EPR signal detected under static gradient is a radial line passing through the origin of the *k*-space coordinates (Fig. 15.2). For spatial imaging, EPR projections are obtained while static gradients, **G**, with constant amplitude and different directions are applied. Different reconstruction algorithms have been developed for radially sampled data. Most of them fall into one of two categories: filtered back projection (FBP) [8, 9] or iterative reconstruction [10]. All reconstruction procedures on sparsely sampled data give inexact results: they represent a compromise between accuracy and the computation time required. FBP demands fewer computational resources, whereas iterative reconstruction generally produces fewer artifacts at a higher computing cost.

2.2 Single Point Imaging

The Single point imaging (SPI) method is based on phase encoding of spatial information. The method was originally used to overcome the influence of the EPR line width (or R_2*) on the imaging resolution [11]. Use of a single data point at delay $t=\tau$ (15.1) makes the relaxation term constant and allows for *k*-space sampling at will by choice of an appropriate static gradient. Typically, gradients are sampled on a rectangular grid (Fig. 15.2) and object [12, 13]. The object is then reconstructed by use of multidimensional Fourier transformation of *k*-space data.

SPI generates images free from artifacts at the expense of the necessity to repeat the measurement in every point of $\boldsymbol{k}$-space. Thus this method has higher spatial fidelity but somewhat lower SNR.

In the simplest form of SPI, free induction decay (FID) detection is used, and phase relaxation times are extracted from multiple images with different τ [12]. The disadvantage of this method is that, for a given set of gradients, the images reconstructed from different τ have different *k*-space samplings and, therefore, different spatial extents and resolutions. Resampling of these images to a common scale causes artifacts, especially around the edges of an object. More advanced sampling techniques that involve acquisition with use of multiple gradient grids have been suggested. This has led to the same *k*-space sampling for different τ and consequently the elimination of artifacts [13].

2.3 Pulse Sequences and 4D Images

Pulse sequences for measuring FID decay, spin-spin and spin-lattice (R_2^*, R_2 and R_1) relaxation are available. In all cases, the pulse sequence is chosen in a way that amplitude of the EPR signal time evolution becomes dependent on the relaxation time and sequence parameter (for example delay between pulses). Multiple 3D images with different values of this parameter are acquired and reconstructed independently. Then these images are stacked together to form 4D images, the additional dimension of which represents the evolution of signal amplitude in every voxel as a function of the sequence parameter. The final image of relaxation times is produced by fitting of this evolution to an appropriate dependence. This process is illustrated in Fig. 15.3 and resulting pO_2 image is presented in Fig. 15.4.

For SPI and single $\pi/2$-pulse, the fit of individual voxels to an exponential decay gives the FID decay rate R_2^*, related to R_2 as $R_2^* = \Sigma(R_2^i) + R_2$, where $\Sigma(R_2^i)$ is the sum of the known oxygen-independent contributions to R_2 [14].

For projection based imaging, the FID detection was not successful. Pulse imagers do not allow signal detection immediately after the excitation. The delay between excitation and opening of the detector (t_{dead}), leads to a missing volume in *k*-space, $\boldsymbol{k} < \gamma_e \mathbf{G} t_{dead,}$ and to image distortion.

To avoid incomplete coverage of *k*-space, projection-based pulse imaging techniques use dead time free spin echo sequences [15, 16]. The electron spin echo is detected by use of the two-pulse sequence $(\pi/2)$-τ-(π)-τ-echo; here, τ is the time

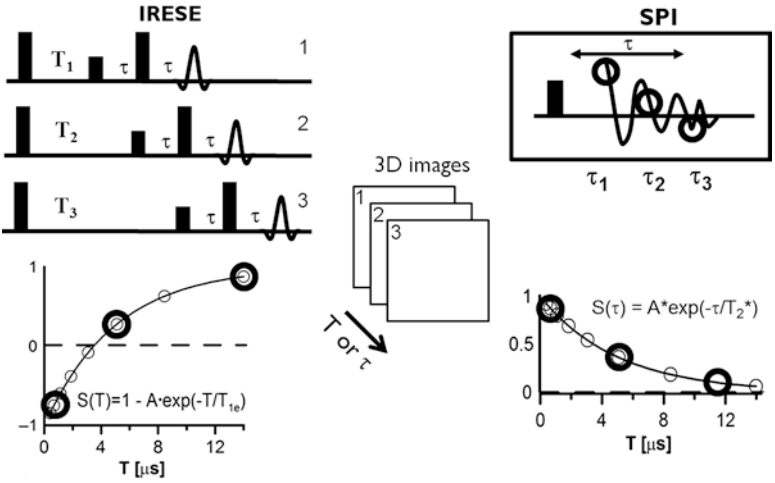

Fig. 15.3 Acquisition of 4D images

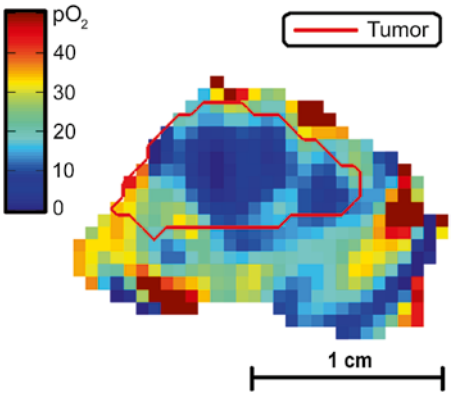

Fig. 15.4 R_1 pO_2 image of a murine leg with MCa4 F6 tumor. Sagittal slice with tumor outline obtained from MRI (*red*) is presented

delay between pulses. For acquiring of a phase relaxation image, separate images with different τ-delay values are obtained. These delays have to cover the range of times suitable for correct determination of the relaxation time. Logarithmically spaced delays yield a more precise determination of the relaxation time [16]. The echo sequence allow direct measurement of R_2, which results in higher pO_2 precision in comparison to R_2^* methods. Recently to obtain direct measurement of R_2 spin echo acquisition was introduced to SPI [17].

Finally, for generation of a spin-lattice relaxation (SLR) image, IRESE, the inversion recovery sequence (π)-T-(π/2)-τ-(π)-τ-echo can be used (Fig. 15.3) [18]. The first π-pulse inverts the populations of electron levels; the delay, T, allows this polarization to relax at the SLR rate. The detection sequence and imaging method are identical to that of the two pulse spin echo. The SLR images can be obtained using SPI as well.

3 Importance of Spin-Lattice Relaxation Imaging

Although oxygen-induced relaxation is the largest factor under physiologic conditions, other relaxation mechanisms can affect the accuracy of EPR oximetry. Some factors, such as temperature, viscosity, and salinity, are tightly controlled by a living body. Variations in these factors are relatively small and position-independent, so that their effects on relaxation rates can be accounted for. In contrast, spin-probe self-broadening, the effect of local spin-probe concentration on the relaxation rate, may be substantial and non-uniform and thus requires special treatment. Reducing trityl injection into the animal obviously reduces the trityl concentration *in vivo* and, thereby, the self-broadening. However, this strategy for reducing the self-broadening uncertainty in pO_2 also lowers the image SNR. These considerations stress the importance of a methodology that is less susceptible to concentration broadening. In trityls, the oxygen dependences of R_1 and R_2 are identical. However, the concentration dependence of R_2, especially at physiologic solvent salinity can be up to six times higher than that of R_1. Thus SLR measurement provides considerable improvement in the pO_2 image accuracy.

4 Conclusions

EPR oxygen imaging possesses the full suite of methods capable for accurate and precise imaging of small animals. This review is restricted to pulse EPR imaging. Continuous wave EPR also offers interesting oxygen imaging possibilities [19, 20].

Acknowledgments Supported by NIH grants P41 EB002034 and R01 CA98575.

References

1. Eastman PE, Kooser RG, Pas MR, Freed JH (1969) Studies of Heisenberg spin exchange in ESR spectra I. Linewidth and saturation effects. J Chem Phys 54(2690)
2. Tatum JL et al (2006) Hypoxia: Importance in tumor biology, noninvasive measurement by imaging, and value of its measurement in the management of cancer therapy. Int J Radiat Biol 82:699–757
3. Ardenkjaer-Larsen JH et al (1998) EPR and DNP properties of certain novel single electron contrast agents intended for oximetric imaging. J Magn Reson 133:1–12
4. Williams BB et al (2002) Imaging spin probe distribution in the tumor of a living mouse with 250 MHz EPR: correlation with BOLD MRI. Magn Reson Med 47:634–638
5. Matsumoto K et al (2004) Pharmacokinetics of a triarylmethyl-type paramagnetic spin probe used in EPR oximetry. Magn Reson Med 52:885–892
6. Krishna MC et al (2002) Overhauser enhanced magnetic resonance imaging for tumor oximetry: coregistration of tumor anatomy and tissue oxygen concentration. Proc Natl Acad Sci U S A 99:2216–2221

7. Williams BB, Pan XC, Halpern HJ (2005) EPR imaging: the relationship between CW spectra acquired from an extended sample subjected to fixed stepped gradients and the Radon transform of the resonance density. J Magn Reson 174:88–96
8. Deans SR (1983) The radon transformation and some of its applications. John Wiley & Sons, New York
9. Ahn KH, Halpern HJ (2007) Spatially uniform sampling in 4-D EPR spectral-spatial imaging. J Magn Reson 185:152–158
10. Ahmad R et al (2007) Enhanced resolution for EPR imaging by two-step deblurring. J Magn Reson 184:246–257
11. Maresch GG, Mehring M, Emid S (1986) High-resolution electron-spin-resonance imaging. Physica B C 138:261–263
12. Subramanian S et al (2002) Single-point (constant-time) imaging in radiofrequency Fourier transform electron paramagnetic resonance. Magn Reson Med 48:370–379
13. Devasahayam N et al (2007) Strategies for improved temporal and spectral resolution in in vivo oximetric imaging using time-domain EPR. Magn Reson Med 57:776–783
14. Matsumoto K et al (2006) Electron paramagnetic resonance imaging of tumor hypoxia: enhanced spatial and temporal resolution for in vivo pO(2) determination. Magn Reson Med 55:1157–1163
15. Mailer C, Sundramoorthy SV, Pelizzari CA, Halpern HJ (2006) Spin echo spectroscopic electron paramagnetic resonance imaging. Magn Reson Med 55:904–912
16. Epel B, Sundramoorthy SV, Mailer C, Halpern HJ (2008) A versatile high speed 250-MHz pulse imager for biomedical applications. Conc Magn Reson B 33B:163–176
17. Subramanian S et al (2012) Echo-based single point imaging (ESPI): a novel pulsed EPR imaging modality for high spatial resolution and quantitative oximetry (San Diego, CA: 1997). J Magn Reson 218:105–114
18. Epel B, Bowman MK, Mailer C, Halpern HJ (2013) Absolute oxygen R1e imaging in vivo with pulse electron paramagnetic resonance. Magnet Reson Med. Epub ahead of print
19. Gallez B, Baudelet C, Jordan BF (2004) Assessment of tumor oxygenation by electron paramagnetic resonance: principles and applications. NMR Biomed 17:240–262
20. Swartz HM, Clarkson RB (1998) The measurement of oxygen in vivo using EPR techniques. Phys Med Biol 43:1957–1975

Chapter 16
What We Learn from *In Vivo* EPR Oxygen Images

Gage Redler, Boris Epel, and Howard J. Halpern

Abstract Distributions of oxygen concentration (pO_2) are a critical determinant of normal tissue health as well as tumor aggressiveness and response to therapy. A number of studies show the value of normal tissue and tumor tissue oxygenation images and some of these will be discussed here. A strong correlation between tumor hypoxic fraction as measured with electron paramagnetic resonance oxygen imaging and radiation treatment success or failure has been found in two separate cancer types. Oxygen images of the torso of wild type mice show initial reduction of lung, liver, visceral, and muscle pO_2 with cyclic halving of fraction of inspired oxygen (FiO_2), but variation is blunted over an hour. Spontaneous breast cancers in Mouse Mammary Tumor Viral (MMTV) promoted-polyoma middle T antigen (PyMT) mice with BNIP3, a major factor in promotion of mitochondrial autophagy, knocked out will be compared with wild type animals. Preliminary studies for the BNIP3 knock out animals show extremely low pO_2. The wide variety of studies, in which oxygen images can play an integral role, serve to demonstrate the importance of oxygen images.

Keywords EPR • Oxygen imaging • Hypoxia • BNIP3 • Cancer • Microenvironment response

G. Redler • B. Epel
Center for EPR Imaging In Vivo Physiology, Chicago, IL, USA

Department of Radiation Oncology, University of Chicago, Chicago, IL, USA

H.J. Halpern (✉)
Center for EPR Imaging In Vivo Physiology, Chicago, IL, USA

Department of Radiation Oncology, University of Chicago, Chicago, IL, USA

MC1105, Department of Radiation and Cellular Oncology, University of Chicago Medical Center, 5841 S. Maryland Ave, Chicago, IL 60637, USA
e-mail: h-halpern@uchicago.edu

H.M. Swartz et al. (eds.), *Oxygen Transport to Tissue XXXVI*, Advances in Experimental Medicine and Biology 812, DOI 10.1007/978-1-4939-0620-8_16,

1 Introduction

In vivo oxygen concentration (pO_2) has been found to be crucially important in determining normal tissue health as well as the aggressiveness of tumors and their response to various forms of treatment [1–4]. Due to the ubiquitous influence of tissue pO_2 various methods for measuring and/or imaging pO_2 have been developed [5–8].

One such method is electron paramagnetic resonance (EPR) oxygen imaging (EPROI). EPROI is a particularly robust method of imaging in vivo tissue pO_2 distributions for several reasons. EPROI provides full 3D images of pO_2. These images have good spatial resolution (~1 mm^3 voxels) as well as pO_2 resolution (1–3 torr). The low electromagnetic wave excitation frequencies (e.g., 250 MHz) currently used in EPRI are comparable to those used in 6T whole body MRI and can penetrate deep in tissue (>7 cm) in animals as large as humans. EPROI images are obtained non-invasively, which means they can be used to study in vivo pO_2 distributions without perturbing the system. EPROI requires an intravenously injected, non-toxic spin probe, which distributes in the extracellular compartment of tumors, to report local pO_2 [9]. The accuracy of EPROI oxygen measurements has been established by correlating with well-established optical fiber based oxygen measurement techniques [10].The information provided by EPROI can be applied to help study myriad interesting oxygen related biologic and physiologic topics. A number of studies demonstrating the array of interesting applications of 3D EPR oxygen images of normal tissue and/or tumor tissue will be presented here.

2 Methods

EPROI is used to non-invasively determine the effect of tumor pO_2 on success of tumor treatment with radiation therapy. Two cancer models are used: fibrosarcoma (FSa) and murine mammary MCa4 carcinoma. Fraction of EPROI voxels with less than 10 torr pO_2 (HF10) is used as a measure of tumor hypoxia. The variable HF10 is then correlated to success or failure of radiotherapy to see what role, if any, hypoxia as determined by EPROI plays in tumor resistance to treatment.

EPROI has been used to provide insight into the effect of fraction of inspired oxygen (FiO_2) changes on the distribution of pO_2 in various organs of mice. The result of cyclic FiO_2 variation can also be observed in various organs using EPROI. This directly assesses levels of tissue pO_2 in models of important disorders such as sleep apnea to understand their biologic effects.

To examine the role of BNIP3 in tumor progression and regulation of oxygenation, changes in pO_2 levels and distributions in mouse mammary tumors are compared for BNIP3 null mice that have been crossed to the Mouse Mammary Tumor Viral (MMTV) promoted-polyoma middle T antigen (PyMT) mouse model of breast cancer and wild type mice. EPROI images are registered with anatomic CT images to analyse differences in oxygenation within these tumors.

3 Results

Using two cancer models (FSa and MCa4), we found that EPROI corroborates the theory that tumors exhibiting a higher degree of hypoxia tend to be more resistant to radiation therapy. A cohort of animals with either of the two tumor lines were treated to the previously determined 50 % tumor control dose (TCD_{50}) for each tumor type. The HF10 as determined by EPROI for each tumor was correlated with radiation therapy treatment outcome. For the FSa tumors, hypoxic tumors (HF10 > 10 %) 37 % were successfully controlled while for tumors with HF10 < 10 %, 90 % were successfully controlled ($p = 0.0138$) [11, 12]. For the MCa4 tumors, hypoxic tumors (HF10 > 10 %) 23 % were successfully controlled while for tumors with HF10 < 10 %, 90 % were successfully controlled ($p = 0.0072$) [12]. An example of the dramatic oxygenation difference observed in animals whose tumors were successfully controlled with radiotherapy versus those for which radiotherapy failed is shown in Fig. 16.1.

Significant differences in the overall pO_2 in three tissue types of a mouse breathing air versus a mouse breathing 12 % O_2 are seen in whole-body EPROI (Fig. 16.2). It is seen that significant variations in tissue pO_2 are observed with oscillating FiO_2, however the response becomes damped over time (Fig. 16.3). The direct assessment of tissue pO_2 responses in vivo provides data concerning the extent of hypoxia induced in these tissues and allows the development of models explaining the deleterious end organ effects.

Preliminary studies of BNIP3 knock out (KO) mice show extremely hypoxic breast tumors (Fig. 16.4). This is consistent with the fact that BNIP3 null tumor cells show increased invasive properties, suggesting that BNIP3 is a metastasis suppressor required to maintain mitochondrial integrity and mitigate against the metastasis promoting activities of reactive oxygen and hypoxia [13].

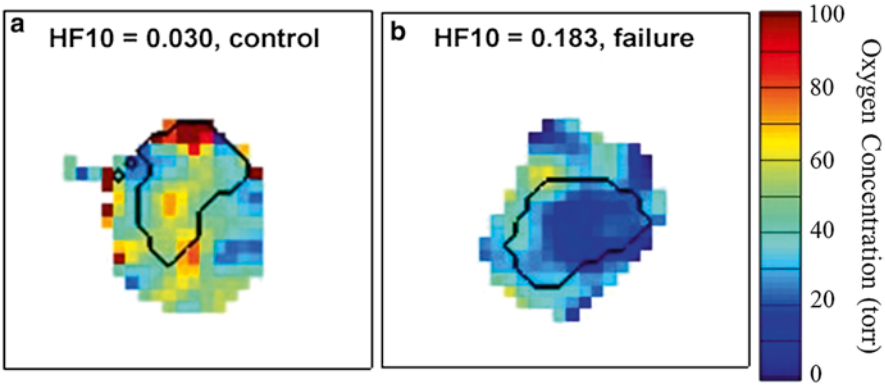

Fig. 16.1 Sample slices from representative EPROI of mouse legs bearing tumors (*black outline*) demonstrating the difference in tumor oxygenation observed in animals where treatment with radiation therapy eventually (**a**) successfully controlled the tumor or (**b**) failed to control the tumor

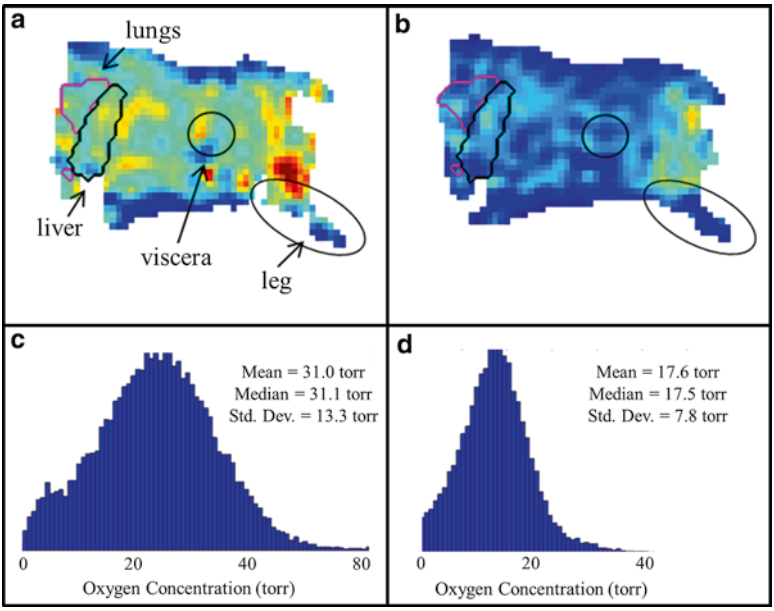

Fig. 16.2 Demonstration of the overall effect on the tissue pO_2 of a mouse when the breathing gas oxygen content is changed from 21 % O_2 to 12 % O_2 as measured with EPROI. Whole body EPROI of a mouse breathing (**a**) 21 % O_2 and (**b**) 12 % O_2, with labeled regions of interest. The pO_2 distributions for the whole body EPROI when the mouse is breathing (**c**) 21 % O_2 and (**d**) 12 % O_2

4 Discussion and Conclusions

With EPROI we can begin to develop quantitative assays of hypoxia induced in tumors and normal tissues. These, in turn will allow the development of quantitative models of the response of tumors and normal tissues to anti-cancer therapies and models of end-organ damage from disease processes such as the intermittent hypoxia induced by sleep apnea.

The hypoxic fraction of a tumor, as determined by EPROI, has been found to be quite a powerful determinant in the eventual outcome of treatment with radiation. This validates EPROI as a tool to analyze spatial distributions of pO_2 in vivo.

In preliminary studies EPROI has also proven to be a valuable tool for tracking tissue pO_2 response to changes in FiO_2. EPROI therefore has the potential to enhance studies investigating the biologic consequences of temporally fluctuating tissue oxygenations (e.g., sleep apnea conditions) by allowing noninvasive tracking of the response to FiO_2 changes of whole body pO_2 as well as pO_2 of individual organs and how this response changes over time.

EPR oxygen images can also help investigate the complicated effects of hypoxia on several aspects of tumor and tissue development. This is evidenced by preliminary results from a study investigating the effect of the BNIP3 protein, which limits

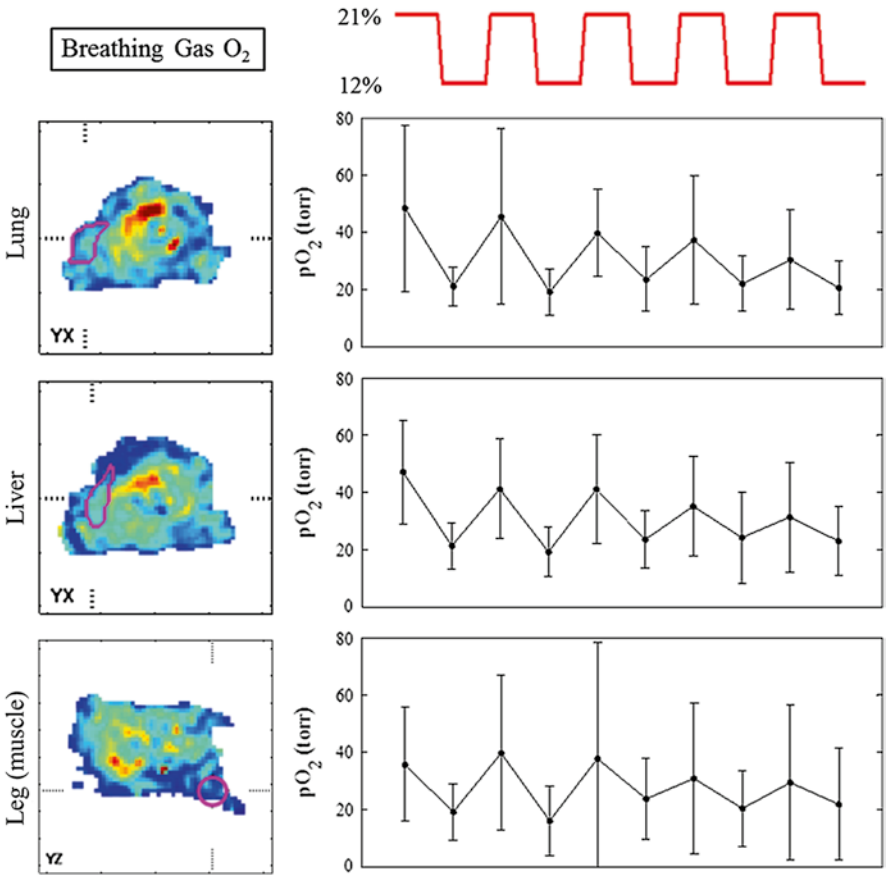

Fig. 16.3 Slices from an EPROI of a mouse are shown with regions of interest outlined in *magenta*. The breathing gas oxygenation for the mouse alternates from 21 % O_2 to 12 % O_2 (breathing gas O_2 changes shown in *red line*). Next to each image with a particular region of interest (lung, liver, or leg muscle) the change in mean oxygenation within that region of interest in response to the breathing gas change is shown

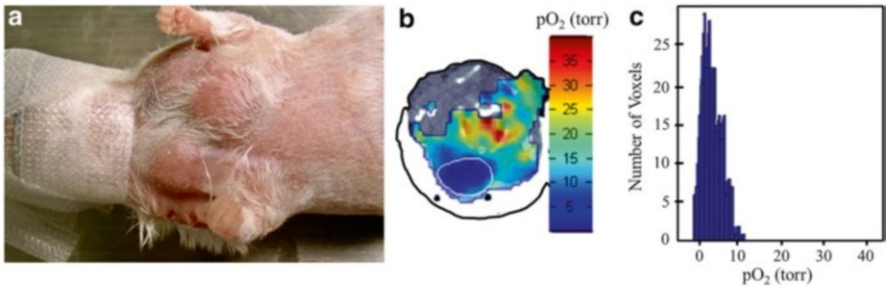

Fig. 16.4 (**a**) Photograph of MMTV-PyMT, BNIP3 null breast cancer tumors grown in the breast of a mouse. (**b**) Registered EPROI overlaid on an anatomical CT of the mouse, shown with the tumor outlined in *white*. (**c**) Distribution of pO_2 found within the BNIP3 null tumor demonstrating that the tumor is extremely hypoxic

production of reactive oxygen species by promoting mitochondrial degradation at the autophagosome, on tumor oxygenation. Initial results show that tumors in BNIP3 KO mice are extremely hypoxic, which may be due to dysfunctional mitochondria. EPROI will help in further studies to investigate the effect of BNIP3 on oxygenation as well as radiation resistance.

In general, oxygen images from EPROI provide an important tool in understanding the relationship between microenvironment oxygenation and a wide variety of crucial physiologic functions.

Acknowledgments Supported by NIH grants P41 EB002034 and R01 CA98575.

References

1. Hockel M, Schlenger K, Aral B et al (1996) Association between tumor hypoxia and malignant progression in advanced cancer of the uterine cervix. Cancer Res 56:4509–4515
2. Shannon AM, Bouchier-Hayes DJ, Condron CM et al (2003) Tumour hypoxia, chemotherapeutic resistance and hypoxia-related therapies. Cancer Treat Rev 29:297–307
3. Carmeliet P, Dor Y, Herbert JM et al (1998) Role of HIF-1alpha in hypoxia-mediated apoptosis. Nature 394:485–490
4. Rofstad EK (2000) Microenvironment-induced cancer metastasis. Int J Radiat Biol 76:589–605
5. Dewhirst MW, Klitzman B, Braun RD et al (2000) Review of methods used to study oxygen transport at the microcirculatory level. Int J Cancer 90:237–255
6. Zhao DW, Jiang L, Mason RP (2004) Measuring changes in tumor oxygenation. Methods Enzymol 386:378–418
7. Tatum JL (2006) Hypoxia: importance in tumor biology, noninvasive measurement by imaging, and value of its measurement in the management of cancer therapy. Int J Rad Biol 82:699–757
8. Bayer C, Vaupel P (2012) Acute versus chronic hypoxia in tumors: controversial data concerning time frames and biological consequences. Strahlenther Onkol 188:616–627
9. Golman K, Petersson JS, Ardenkjaer-Larsen JH et al (2000) Dynamic in vivo oxymetry using overhauser enhanced MR imaging. J Magn Reson Imaging 12:929–938
10. Elas M, Ahn KH, Parasca A et al (2006) Electron paramagnetic resonance oxygen images correlate spatially and quantitatively with oxylite oxygen measurements. Clin Cancer Res 12:4209–4217
11. Elas M, Bell R, Hleihel D et al (2008) Electron paramagnetic resonance oxygen image hypoxic fraction plus radiation dose strongly correlates with tumor cure in FSa fibrosarcomas. Int J Radiat Oncol Biol Phys 71:542–549
12. Elas M, Magwood JM, Butler B et al (2013) EPR oxygen images predict tumor control by a 50 percent tumor control radiation dose. Cancer Res (online and in press)
13. Tracy K, Macleod KF (2007) Regulation of mitochondrial integrity, autophagy and cell survival by BNIP3. Autophagy 3(6):616–619

Chapter 17
EPR Image Based Oxygen Movies for Transient Hypoxia

Gage Redler, Boris Epel, and Howard J. Halpern

Abstract Chronic hypoxia strongly affects the malignant state and resistance to therapy for tumors. Transient hypoxia has been hypothesized, but not proven to be more deleterious. Electron paramagnetic resonance imaging (EPRI) provides non-invasive, quantitative imaging of static pO_2 in vivo. Dynamic EPRI produces pO_2 movies, enabling non-invasive assessment of in vivo pO_2 changes, such as transient hypoxia. Recent developments have been made to enable Dynamic EPRI. Maximally spaced projection sequencing has been implemented to allow for more accurate and versatile acquisition of EPRI data when studying dynamic systems. Principal component analysis filtering has been employed to enhance SNR. Dynamic EPRI studies will provide temporally resolved oxygen movies necessary to perform in vivo studies of physiologically relevant pO_2 changes in tumors. These oxygen movies will allow for the localization/quantification of transient hypoxia and will therefore help to disentangle the relationship between chronic and transient hypoxia, in order to better understand their roles in therapeutic optimization and outcome.

Keywords Dynamic EPRI • Oxygen movies • PCA • Projection acquisition • Transient hypoxia

G. Redler • B. Epel
Center for EPR Imaging In Vivo Physiology, Chicago, IL, USA

Department of Radiation Oncology, University of Chicago, Chicago, IL, USA

H.J. Halpern (✉)
Center for EPR Imaging In Vivo Physiology, Chicago, IL, USA

Department of Radiation Oncology, University of Chicago, Chicago, IL, USA

MC1105, Department of Radiation and Cellular Oncology, University of Chicago Medical Center, 5841 S. Maryland Ave, Chicago, IL 60637, USA
e-mail: h-halpern@uchicago.edu

H.M. Swartz et al. (eds.), *Oxygen Transport to Tissue XXXVI*, Advances in Experimental Medicine and Biology 812, DOI 10.1007/978-1-4939-0620-8_17,

1 Introduction

The important prognostic implications related to the oxygenation status of tumors have been known for decades [1]. Chronic hypoxia, or chronically low oxygen concentration (pO_2), results in greater resistance to radiation therapy for cancer cells [2, 3] and therefore has been correlated with radiotherapy treatment failure in humans [4]. Additionally, tumors exhibiting chronic hypoxia are more resistant to chemotherapy [5], tend to grow more rapidly due to abnormal proliferation [6], and have increased potential for metastatic progression [7]. These implications have led to a high level of interest in methods for measuring/imaging pO_2 deep in tissues.

Diffusion limited chronic hypoxia was the first form of hypoxia found in tumors [8] and for many years was believed to be the only type of hypoxia present in tumors. However, more recent studies have found that perfusion limited transient hypoxia is present as well [9–12] and may even be the major cause of hypoxia in tumours [12, 13]. Studies suggest that transient hypoxia may be as important a determinant of cancer progression and patient prognosis as chronic hypoxia, if not more important. However, currently no definitive conclusions can be made due to inconsistencies in the data and methodological approaches from previous studies investigating the biologic effects of transient hypoxia versus those of chronic hypoxia. Furthermore, lack of data correlating a quantitative measure of transient hypoxia in vivo with treatment outcome currently precludes such a comparison [14].

Electron paramagnetic resonance imaging (EPRI) has proven to be a robust imaging modality for studying tissue pO_2 in vivo. EPRI noninvasively acquires highly-resolved, both spatially (~1 mm^3 voxels) and in pO_2 (1–3 torr), 3D images of pO_2 in vivo [15–19]. Acquisition time for our standard EPRI is on the order of 10 min, which is suitable for studying chronic hypoxia.

However, in order to use EPRI to study transient hypoxia, recent developments have been made to allow for improvements in temporal resolution (acquisition time on the order of 1 min) and accuracy. A novel acquisition method for maximally spaced projection sequencing has been implemented to allow for more accurate and versatile acquisition of EPRI data when studying dynamic systems (e.g., transient hypoxia). Principal component analysis (PCA) filtering has been employed as well to enhance SNR and thus allow for improved temporal resolution. These improvements enable Dynamic EPRI, which can provide 4D EPRI based oxygen movies and allow for the necessary non-invasive studies investigating transient hypoxia to eventually help determine its biologic implications.

2 Methods

2.1 Maximally Spaced Projection Sequencing

EPRI is a projection based imaging modality. Linear fixed magnetic field gradients are applied in a spherical geometry to spatially encode a 3D object. This enables the acquisition of projections of the object along the direction of the applied gradient.

With a sufficient number of these projections an image of the object can be reconstructed using an inverse radon transform. A series of 3D images with varying pulse sequence parameters is acquired, enabling a voxel-by-voxel fit of signal relaxation to determine T_1 and/or T_2, which provides a measure of local pO_2 at each voxel [22]. The rapidity with which these can be acquired is proportional to the number of projections acquired for each image and the speed at which each projection is acquired. Both the number and uniformity of acquired projections influence the image quality. More uniformly distributed projections provides more efficient data acquisition, i.e. relatively higher quality images can be reconstructed from smaller numbers of projections when they are more uniformly distributed. The influence of the uniformity of the spatial distributions of projections has been extensively studied [20, 21], but the uniformity with which the projections are acquired can still be optimized.

The directions through which projections are acquired can be represented as points on the unit sphere (unit hemisphere sufficient due to radon transform symmetry). Until now, a polar azimuthal raster (PAR) method has been used to acquire projections. The PAR method rasters through projection points on one side of the unit hemisphere and then back down the other, resulting in non-uniform distributions of projections throughout image acquisition. A new maximally spaced projection sequencing (MSPS) method has been implemented to achieve more uniform acquisition of projections. For the MSPS method, successive projections are acquired so that they are maximally spaced from projections that have already been acquired. In order to ensure uniformity for the final image, projection points are chosen from some final set of uniformly distributed points.

2.2 Principal Component Analysis Filtering

Principal component analysis (PCA) is a method for defining a new orthonormal basis on which to express some given n-D data set. The basis vectors, or principal components (PCs), are chosen to be the eigenvectors of the covariance matrix for the data. A subset of PCs span a smaller q-D space and contain mostly correlated features, while the space spanned by the other PCs contains mostly uncorrelated noise. Filtering of the data can be achieved with a low-order approximation by projection onto the subset of q PCs, thus selectively retaining relevant temporal patterns while discarding unwanted noise. PCA filtering is applied to dynamic EPRI studies as a pre-reconstruction spatiotemporal filter for projection data [22].

3 Results

3.1 Maximally Spaced Projection Sequencing

The distribution of projections at intermediate steps throughout imaging converge to uniformity more rapidly for the MSPS method as successive projections are acquired than for the PAR method. This yields intermediate images reconstructed

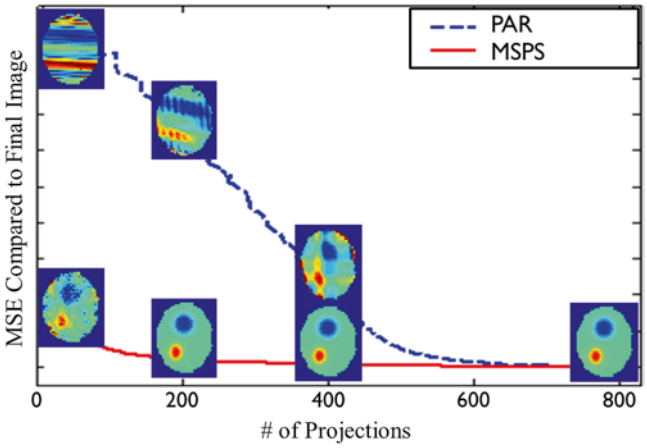

Fig. 17.1 Uniformly distributed projections throughout imaging for the MSPS method results in intermediate images that approximate the final image more rapidly than for the PAR method

from incomplete projection sets that approximate the final image more closely and earlier during imaging (Fig. 17.1).

The MSPS method affords the versatility to adjust temporal resolution to best fit the experiment and data following acquisition. This can be done simply by reconstructing temporally adjacent intermediate subsets of projections. These projection subsets are uniformly distributed enabling reconstruction of images of acceptable quality more rapidly than if a full set of projections is required. This allows for the visualization of important physiologic temporal changes that may not have been resolved with the temporal resolution of the original study (Fig. 17.2).

3.2 Principal Component Analysis Filtering

Simulation studies show that PCA filtering can significantly enhance SNR (by a factor of 3.8 ± 0.6) and allow for the order of magnitude improvement in temporal resolution necessary to obtain EPRI oxygen movies with 1 min frames (Fig. 17.3). PCA also helps to emphasize relevant temporal features. PCA is suited for data with large portions having common features and a small number of such features. Studies suggest that this is the case for tumors exhibiting transient hypoxia [22]. PCA filtering of Dynamic EPRI data is demonstrated in an experiment with a mouse breathing air (21 % O_2) followed by carbogen (95 % O_2) and then air again. One minute frames from this experiment are displayed and the tissue response to breathing gas changes can be clearly resolved.

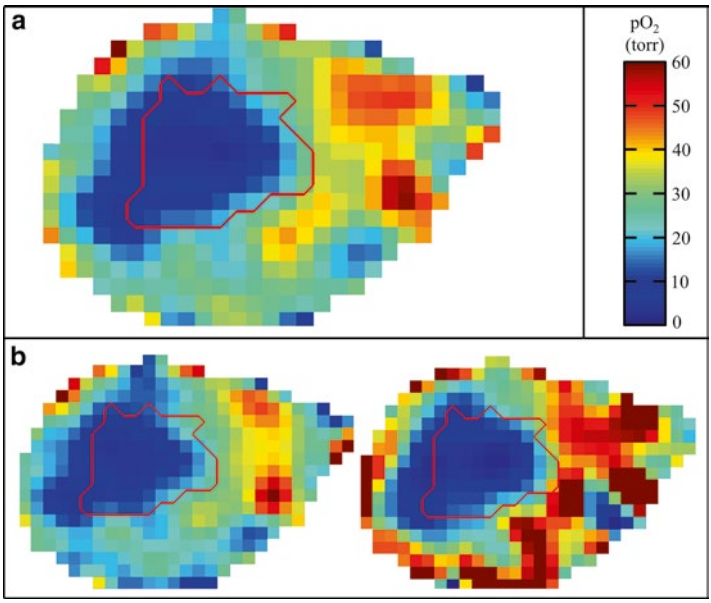

Fig. 17.2 (**a**) Single MSPS image acquired over 36 min with mouse breathing air for the first 18 min followed by carbogen for the second 18 min. (**b**) Two 18-min intermediate images that are subdivisions of the full image that now allow resolution of tissue response to increased breathing gas oxygen (tumor outlined in *red*)

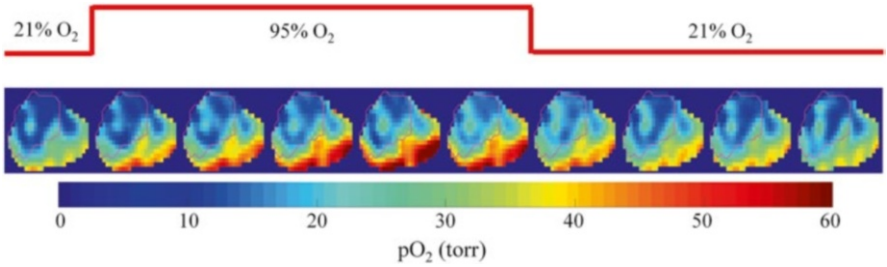

Fig. 17.3 One-minute frames from a PCA filtered Dynamic EPRI oxygen movie. Corresponding changes in breathing gas shown with *red line*. The mouse starts off breathing air and is switched to carbogen and then back to air. The temporal changes in tissue (tumor outlined in *red*) pO_2 are clearly resolved with such EPRI based oxygen movies

4 Discussion and Conclusions

Important tools such as the MSPS acquisition method and PCA filtering have been developed for EPRI in order to enable Dynamic EPRI with temporal resolution on the order of 1 min. PCA filtering of projection subsets acquired using the MSPS

method must be done carefully to avoid misrepresentation of projection differences due to varying projection views from subset to subset being considered as real pO_2 changes. PCA filtering of the full set of projections prior to subdivision can be done but may require a higher number of PCs to be included in the approximation, which will include more noise, and may not retain features with the higher temporal resolution afforded from reconstruction of sub-images. Another method requires a series of images acquired using MSPS, each of which can be subdivided to increase temporal resolution. The corresponding projection subsets can then each be grouped and separately PCA filtered.

The enhancements and versatility provided from the techniques discussed enable 4D EPRI based oxygen movies well resolved spatially, temporally, and in pO_2. Dynamic EPRI therefore is an ideal modality to study physiologically relevant temporal pO_2 changes in vivo without perturbing the system of interest. These oxygen movies will allow for the spatial localization as well as quantification (frequency, amplitude, etc.) of transient hypoxia in vivo and therefore enable the eventual determination of its clinical relevance.

Acknowledgments Supported by NIH grants P41 EB002034 and R01 CA98575.

References

1. Overgaard J (2007) Hypoxic radiosensitization: adored and ignored. J Clin Oncol 25:4066–4074
2. Schwarz G (1909) Uber Desensibilisierung gegen Rontgen-und Radiumstrahlen. Munch Med Wochenschr 56:1217
3. Hall EJ (2000) Radiobiology for the radiologist, 5th edn. Lippincott Williams & Wilkins, Philadelphia, PA
4. Hockel M, Schlenger K, Aral B et al (1996) Association between tumor hypoxia and malignant progression in advanced cancer of the uterine cervix. Cancer Res 56:4509–4515
5. Shannon AM, Bouchier-Hayes DJ, Condron CM et al (2003) Tumour hypoxia, chemotherapeutic resistance and hypoxia-related therapies. Cancer Treat Rev 29:297–307
6. Carmeliet P, Dor Y, Herbert JM et al (1998) Role of HIF-1alpha in hypoxia-mediated apoptosis, cell proliferation and tumour angiogenesis. Nature 394:485–490
7. Rofstad EK (2000) Microenvironment-induced cancer metastasis. Int J Radiat Biol 76:589–605
8. Thomlinson RH, Gray LH (1955) The histological structure of human lung cancers and the possible implications for radiotherapy. Br J Radiol 9:539–563
9. Brown JM (1979) Evidence for acutely hypoxic cells in mouse tumours, and a possible mechanism of reoxygenation. Br J Radiol 52:650–656
10. Chaplin DJ, Olive PL, Durand RE (1987) Intermittent blood-flow in a murine tumor – radiobiological effects. Cancer Res 47:597–601
11. Trotter MJ, Chaplin DJ, Olive PL (1991) Possible mechanisms for intermittent blood-flow in the murine SCCVII carcinoma. Int J Rad Biol 60:139–146
12. Durand RE, Lepard NE (1995) Contribution of transient blood-flow to tumor hypoxia in mice. Acta Oncol 34:317–323
13. Rofstad EK, Galappathi K, Mathiesen B et al (2007) Fluctuating and diffusion-limited hypoxia in hypoxia-induced metastasis. Clin Cancer Res 13:1971–1978
14. Bayer C, Vaupel P (2012) Acute versus chronic hypoxia in tumors: controversial data concerning time frames and biological consequences. Strahlenther Onkol 188:616–627

15. Elas M, Ahn KH, Parasca A et al (2006) Electron paramagnetic resonance oxygen images correlate spatially and quantitatively with oxylite oxygen measurements. Clin Cancer Res 12:4209–4217
16. Epel B, Sundramoorthy SV, Mailer C et al (2008) A versatile high speed 250 MHz pulse imager for biomedical applications. Concept Magn Reson B 33B:163–176
17. Epel B, Sundramoorthy SV, Barth ED et al (2011) Comparison of 250 MHz electron spin echo and continuous wave oxygen EPR imaging methods for in vivo applications. Med Phys 38:2045–2052
18. Epel B, Haney CR, Hleihel D et al (2010) Electron paramagnetic resonance oxygen imaging of a rabbit tumor using localized spin probe delivery. Med Phys 37:2553–2559
19. Elas M, Williams BB, Parasca A et al (2003) Quantitative tumor oxymetric images from 4D electron paramagnetic resonance imaging (EPRI): methodology and comparison with blood oxygen level-dependent (BOLD) MRI. Magn Reson Med 49:682–691
20. Ahmad R, Deng YM, Vikram DS et al (2007) Quasi Monte Carlo-based isotropic distribution of gradient directions for improved reconstruction quality of 3D EPR imaging. J Magn Reson 184:236–245
21. Ahmad R, Vikram DS, Clymer B et al (2007) Uniform distribution of projection data for improved reconstruction quality of 4D EPR imaging. J Magn Reson 187:277–287
22. Redler G, Epel B, Halpern HJ (2013) Principal component analysis enhances SNR for dynamic electron paramagnetic resonance oxygen imaging of cycling hypoxia in vivo. Magn Reson Med (unpublished)

Chapter 18
Repetitive Measurements of Intrarenal Oxygenation *In Vivo* Using L Band Electron Paramagnetic Resonance

Stephanie Franzén, Liselotte Pihl, Nadeem Khan, Fredrik Palm, and Håkan Gustafsson

Abstract Intrarenal oxygenation is heterogeneous with oxygen levels normally being highest in the superficial cortex and lowest in the inner medulla. Reduced intrarenal oxygenation has been implied in the pathology of several kidney diseases. However, there is currently no method available to repetitively monitor regional renal oxygenation using minimally invasive procedures. We therefore evaluated implantable lithium phthalocyanine (LiPc) probes, which display a close correlation between EPR line width and oxygen availability.

S. Franzén (✉)
Division of Drug Research, Experimental Renal Medicine, Department of Medical and Health Sciences, Linköping University, Linköping 58183, Sweden

Center of Medical Image Science and Visualization, Linköping University, Linköping, Sweden
e-mail: stephanie.franzen@liu.se

L. Pihl
Division of Drug Research, Experimental Renal Medicine, Department of Medical and Health Sciences, Linköping University, Linköping 58183, Sweden

N. Khan
EPR Center for Viable Systems, Department of Radiology, Geisel School of Medicine, Hanover, NH, USA

F. Palm
Division of Drug Research, Experimental Renal Medicine, Department of Medical and Health Sciences, Linköping University, Linköping 58183, Sweden

Center of Medical Image Science and Visualization, Linköping University, Linköping, Sweden

Division of Integrative Physiology, Department of Medical Cell Biology, Uppsala University, Uppsala, Sweden

H. Gustafsson
Center of Medical Image Science and Visualization, Linköping University, Linköping, Sweden

Department of Biomedical Engineering (MTÖ), County Council of Östergötland, Radiation Physics, Department of Medical and Health Sciences, Linköping University, Linköping, Sweden

H.M. Swartz et al. (eds.), *Oxygen Transport to Tissue XXXVI*, Advances in Experimental Medicine and Biology 812, DOI 10.1007/978-1-4939-0620-8_18,

LiPc probes were implanted in the kidney cortex and medulla in the same mouse and EPR spectra were acquired using a L band scanner during inhalation of air (21 % oxygen) or a mixture of air and nitrogen (10 % oxygen). In order to separate the signals from the two probes, a 1 G/cm gradient was applied and the signals were derived from 40 consecutive sweeps. Peak-to-peak comparison of the EPR line was used to convert the signal to an approximate oxygen tension in MATLAB. Kidney cortex as well as medullary oxygenation was stable over the 45 day period (cortex 56 ± 7 mmHg and medulla 43 ± 6 mmHg). However, 10 % oxygen inhalation significantly reduced oxygenation in both cortex (56 ± 6 to 34 ± 2 mmHg $n = 15$ $p < 0.05$) and medulla (42 ± 5 to 29 ± 3 mmHg $n = 7$ $p < 0.05$).

In conclusion, L band EPR using LiPc probes implanted in discrete intrarenal structures can be used to repetitively monitor regional renal oxygenation. This minimally invasive method is especially well suited for conditions of reduced intrarenal oxygenation since this increases the signal intensity which facilitates the quantification of the EPR signal to absolute oxygenation values.

Keywords Kidney • LiPc • L-Band EPR • NMRI mice • Oxygenation

1 Introduction

Intrarenal oxygenation is heterogeneous with oxygen levels normally being highest in the superficial cortex and lowest in the inner medulla [1]. Arterial and venous vessels are closely aligned causing oxygen to diffuse from the well-oxygenated arterial blood to the less oxygenated venous blood, constituting a functional arterial-venous shunting mechanism [2, 3]. A consequence of this arrangement is poor oxygenation of the inner parts of the renal medulla, making this structure work at the brink of hypoxia already during normal physiology.

Reduced intrarenal oxygenation has been proposed as common pathway to chronic kidney disease [4]. However, there is currently no method available to repetitively monitor regional renal oxygenation using minimally invasive procedures. A methodological problem has been to monitor changes in intrarenal oxygenation over time due to the lack of suitable methods. However, implantable lithium phthalocyanine (LiPc) oxygen probes have been used in tumor research to monitor such changes [5–7] and we therefore evaluated if this technique also can be used to study functionally relevant changes in intrarenal oxygenation. Longitudinal measurements were performed to determine long-term stability and acute interventions using reduced oxygen content in the inhaled air were used to demonstrate that rapid and reversible changes in intrarenal oxygenation could be detected.

2 Methods

All measurements were performed using a L band Elexsys II E540 (Bruker BioSpin GmbH, Rheinstetten, Germany).

2.1 Animals

Eight-week-old male NMRI mice were purchased from Taconic (Ryd, Denmark) and were housed two per cage at Linköping University's animal facility and all procedures were approved by the local Animal Use and Care Committee. Food and water were given *ad libitum*.

2.2 LiPc Probe Preparations

LiPc (Clin-EPR, NH, USA) oximetry probes were manufactured by loading aggregates of LiPc crystals into 23 G needles as previously described [6].

2.3 Insertion of Probes into Renal Tissue

Mice were anaesthetized with 2 % Isoflurane (Florene, Apoteket AB, Sweden) in air and 10–15 mm vertical incisions were made on both sides below the diaphragm. A 4 mm horizontal injection was made in the left kidney for placement of the cortical probe and 4 mm transversal injection in the right kidney for placement of the medullary probe. The incision was closed (6.0 Vicryl, AgnTho's AB, Lidingö, Sweden) and 5 mg/kg/24 h of Carprofen (Rimadyl Bovin, Apoteket, Sweden) was administered subcutaneously.

2.4 In Vivo Measurements with L Band EPR

Mice were measured at day 9, 13, 17, 21 and 45. Before measurements, mice were anaesthetized (2 % Isoflurane in air) and placed inside the resonator. For normal physiology, mice were allowed to breathe normal air (21 % oxygen) and for acute hypoxic measurements mice were breathing a mixture of equal amounts of air and nitrogen during 5 min, resulting in a final concentration of 10 % oxygen. Acute hypoxic measurements were performed after normal air. EPR measurements were performed using a Bruker Elexsys E540 L band EPR spectrometer equipped with an E540 GCL Triple axis coil set (gradient field strength up to 40 G/cm) and an E540 R36 L band Resonator (36 mm sample access) connected to an EPR 066L-AMC L band Microwave Bridge. The spectrometer settings were: 36 mW applied microwave power, 0.2 G modulation amplitude, 20 ms time constant, 5 s sweep time, 256 measurement points, 3 G sweep width and 40 sweep added together for each measurement. The EPR signals from the two probes in each mouse were then separated with 1 G/cm (gradient angle: $\Phi = 0$, $\theta = 0$ along B_0). No EPR signal could be detected for the empty resonator. The recorded EPR spectra were imported into MATLAB and peak-to-peak line width were analyzed using an in-house developed MATLAB

script. Oxygen tensions were calculated by comparison of the EPR line width for the two LiPc probes with spectra obtained from a calibration probe made from the same batch and measured at different oxygen tensions.

2.5 Statistical Analysis

All statistics were performed with Graphpad Prism 6.0. Student's t-test was used to compare cortical vs. medullary and 21 % oxygen vs. 10 % oxygen and one way ANOVA was used to analyze cortex and medulla over time. All data are displayed as mean ± SEM and $p < 0.05$ was considered significant.

3 Results

Two crystals placed in distinctively different intrarenal structures in the same mouse could easily be detected as two separate signals (Fig. 18.1) that can be converted into absolute oxygen tension values.

Rapid alterations in intrarenal oxygenation could easily be detected by the two crystals when altering the oxygen content in the inhaled air (Fig. 18.2). Estimation of cortical tissue measured from 56 ± 6 to 34 ± 2 mmHg (n = 15) and medullary tissue from 42 ± 5 to 29 ± 3 mmHg (n = 7).

Oxygenation monitored using LiPc crystals in both kidney cortex and medulla was stable over the 45 days at cortex 56 ± 7 mmHg and medulla 43 ± 6 mmHg, respectively. The optimal monitoring window seems to be around day 15–20 after installation of probes (Fig. 18.3).

4 Conclusions

Renal physiology is dependent on adequate oxygenation in order to fulfill the requirements to reabsorb and to secrete electrolytes and waste products. Insufficient oxygenation has been proposed as a common pathway to kidney disease [4]. In order to fully understand the role of deranged kidney oxygenation, we need methods allowing for repetitive and continuous monitoring of oxygen levels with the different anatomical structures of the kidney. The possibility to simultaneously measure cortical and medullary tissue improves our understanding of diminished oxygenation in different diseases. The results from the present study demonstrate that EPR oximetry using LiPc crystals is able to distinguish oxygenation in different parts of the kidney and also detect rapid and physiological relevant changes in intrarenal oxygenation. Thus, this method would be suitable to finally establish the role of deranged oxygenation as a pathway to kidney disease. In order to solidify such a

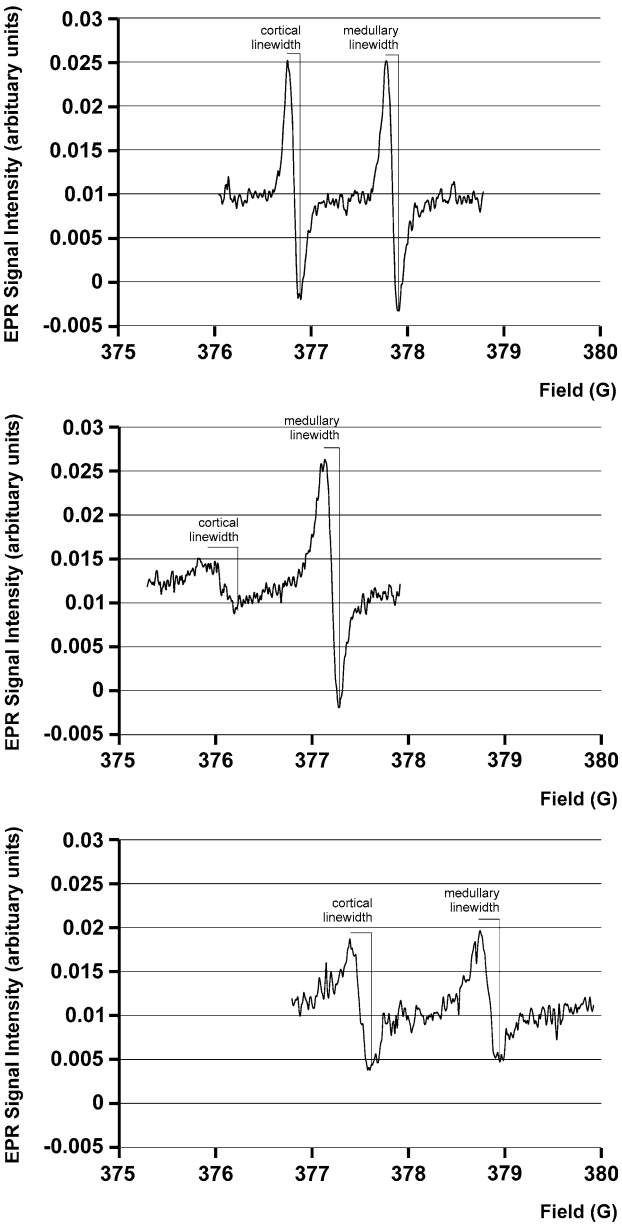

Fig. 18.1 *Upper panel*, spectra of two LiPc implanted in the kidney cortex (*left peak*) and medulla (*right peak*) of a euthanized mouse measured by L band EPR. *Middle* and *bottom panel*, representative L band EPR spectra of two LiPc implanted in the kidney cortex (*left peak*) and medulla (*right peak*) of a mouse during inhalation of air (21 % oxygen; *middle panel*) and a mixture of air and nitrogen (10 % oxygen; *bottom panel*). Kidney oxygen tensions during inhalation of air were 72 mmHg in cortex and 29 mmHg in medulla. Inhalation of 10 % oxygen resulted in reduced oxygen tensions in both cortex and medulla

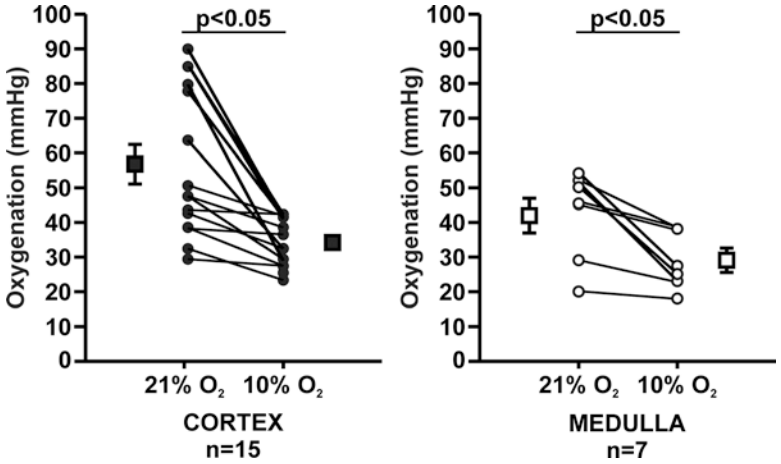

Fig. 18.2 Cortical and medullary oxygenation during inhalation of air (21 % oxygen) or a mixture of air and nitrogen (10 % oxygen). *p < 0.05 versus corresponding air inhalation

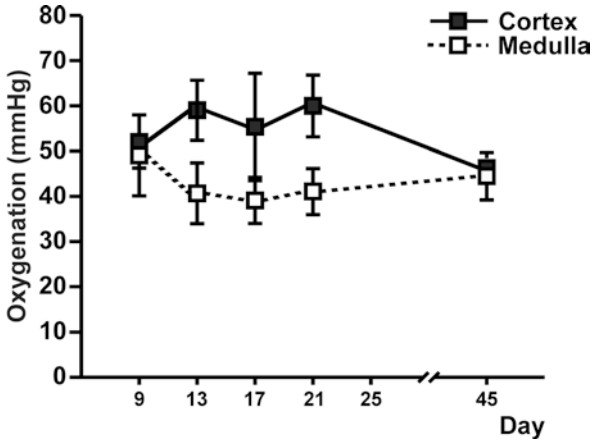

Fig. 18.3 Cortical and medullary (n = 5–10) oxygenation over time

common pathway, it is necessary to demonstrate that reduced oxygenation occurs before the onset of kidney disease and that interventions to correct pathologically low oxygenations are successful in preventing disease development. An obvious advantage of this technique is the increasing sensitivity as oxygenation decreases.

There are several limitations using EPR oximetry and LiPc probes to detect intrarenal oxygenation: the measurements are restricted to where the probes are placed. Fibrosis development may occur around the probes, which potentially could affect oxygen diffusion and we are currently restricted to using mice due to the limited space inside the resonator.

In conclusion, L band EPR using LiPc probes implanted in discrete intrarenal structures can be used to repetitively monitor regional renal oxygenation. This minimally invasive method is especially well suited for conditions of reduced intrarenal oxygenation since low oxygen increases the signal intensity.

Acknowledgments We are deeply grateful to Dr. Harold Swartz and the EPR Center, Hanover, New Hampshire, USA for technical assistance.

References

1. Palm F, Cederberg J, Hansell P, Liss P, Carlsson PO (2003) Reactive oxygen species cause diabetes-induced decrease in renal oxygen tension. Diabetologia 46(8):1153–1160
2. Wilcox CS, Palm F, Welch WJ (2013) Renal oxygenation and function of the rat kidney: effects of inspired oxygen and preglomerular oxygen shunting. Adv Exp Med Biol 765:329–334
3. LEVY MN, IMPERIAL ES (1961) Oxygen shunting in renal cortical and medullary capillaries. Am J Physiol 200:159–162
4. Fine LG, Bandyopadhay D, Norman JT (2000) Is there a common mechanism for the progression of different types of renal diseases other than proteinuria? Towards the unifying theme of chronic hypoxia. Kidney Int Suppl 75:S22–S26
5. Jiang J, Nakashima T, Liu KJ, Goda F, Shima T, Swartz HM (1996) Measurement of PO2 in liver using EPR oximetry. J Appl Physiol 80(2):552–558
6. Khan N, Mupparaju S, Hou H, Williams BB, Swartz H (2012) Repeated assessment of orthotopic glioma pO(2) by multi-site EPR oximetry: a technique with the potential to guide therapeutic optimization by repeated measurements of oxygen. J Neurosci Methods 204(1):111–117
7. Khan N, Li H, Hou H, Lariviere JP, Gladstone DJ, Demidenko E, Swartz HM (2009) Tissue pO_2 of orthotopic 9L and C6 gliomas and tumor-specific response to radiotherapy and hyperoxygenation. Int J Radiat Oncol Biol Phys 73(3):878–885

Chapter 19
Quantitative Hypoxia Imaging for Treatment Planning of Radiotherapy

Iuliana Toma-Dasu and Alexandru Dasu

Abstract Tumour oxygenation is an important determinant of radiotherapy outcome as it could modulate cellular radiation sensitivity. Advanced PET imaging able to characterise this microenvironmental aspect *in vivo* might be used to devise counteracting therapies as it could provide information on the severity and the spatial distribution of the hypoxic regions. This study reviews the advantages and limitations of PET for imaging and quantifying tumour hypoxia and proposes a novel approach to obtain absolute levels of hypoxia from PET images through the use of EPR oximetry. This would offer a significant advantage over proposals based on empirical conversions of the intensities in the PET images to relative radiosensitivities. Thus, tumour hypoxia must be taken into account at the stage of treatment planning for photons and particle therapy by accounting for its extent and severity through the use of PET imaging combined with absolute EPR measurements.

Keywords Tumour hypoxia • Oxygenation • PET imaging • Treatment planning • Treatment optimization

1 Introduction

One of the problems in the management of cancer resides in the characteristics of the tumour microenvironment in comparison to the normal tissues [1]. For radiation therapy in particular, tumour hypoxia has an important role to play since the

I. Toma-Dasu (✉)
Medical Radiation Physics, Stockholm University and Karolinska Institutet, Stockholm, Sweden
e-mail: Iuliana.Livia.Dasu@ki.se

A. Dasu
Department of Radiation Physics UHL, County Council of Östergötland, Linköping University, Linköping, Sweden

H.M. Swartz et al. (eds.), *Oxygen Transport to Tissue XXXVI*, Advances in Experimental Medicine and Biology 812, DOI 10.1007/978-1-4939-0620-8_19,

radiosensitivity of the cells is related to their oxygenation, as proposed more than 60 years ago by Gray and colleagues [2]. Thus, as hypoxic cells are less sensitive to radiation, they have increased probabilities of surviving at the end of curative radiotherapy. This has been supported by several clinical studies that have shown that impaired tumour oxygenation correlates with the failure of radiation treatment [3–5]. Consequently, several approaches have been proposed to overcome the resistance to treatment of the hypoxic tumours, including the use of radiation sensitisers, increasing the oxygen content of the tumours or targeting the hypoxic foci in tumours. The latter approach has seen increasing momentum in recent years due to technological developments of imaging methods capable of rendering the localisation and the extent of adverse metabolic processes.

This article presents a short review of available dose painting techniques based on PET hypoxia imaging and their limitations from the point of view of the ability to accurately map the target in terms of radiation resistance related to the tumour oxygenation. A solution for overcoming the most severe limitations has been identified and the conceptual approach will be presented here.

2 Treatment Planning Based on Tumour Oxygenation

Current practice in radiation therapy is based on physical optimisation of the dose distribution according to the anatomical information regarding the localisation and the extent of the tumour and the normal tissues. Routine planning in clinical radiation treatment does not generally take into account the particular radiation sensitivity of the tumour of an individual patient or the spatial and temporal heterogeneity of cellular radioresistance. However, it is well known that these aspects may be the cause of treatment failure for a considerable proportion of the non-responding patients, as the standard dose prescription does not ensure the dose levels needed to counteract the radiation resistance of the tumour cells.

The progress in imaging methods during the last decade has significantly improved cancer diagnosis and prognosis by increasing the accuracy of delineating target structures on a background of normal tissue anatomy and has formed the basis for 3D and 4D-based radiation treatment methods. Among the imaging techniques, positron emission tomography (PET) has the advantage of being almost non-invasive, using tracers that are usually metabolic substitutes and relatively sensitive, since quite low concentrations of tracers could be imaged.

Several tracers are now available for imaging tumour hypoxia with PET. Fluoromisonidazole (FMISO) was the first nitroimidazole derivative radiolabeled with ^{18}F proposed for hypoxia imaging with PET and currently is the most used hypoxia tracer [6, 7]. The relatively low uptake of FMISO in hypoxic lesions coupled with its slow clearance from the well oxygenated healthy tissue, has led to the development of other ^{18}F-labelled nitroimidazoles like Fluoroetanidazole (FETA) and Fluoroazomycinarabinofuranoside (FAZA) [8, 9] and non-imidazole tracers like Cu(II)-diacetyl-bis-N-(4)-methylthiosemicarbazone (Cu-ATSM) [10].

Several modelling studies have presented various approaches with different degrees of complexity to include the imaging information into treatment planning. A common approach is to delineate a hypoxic subtarget in the tumour and prescribe a more or less empirical escalation of the dose according to available radiation therapy techniques considering the tolerance of the normal tissues around the tumour [7, 11]. The risk, however, is that the prescribed dose is not large enough to counteract the hypoxic radioresistance and therefore the method might fail to achieve the expected results in clinical settings. Other approaches have recommended highly heterogeneous dose distributions based on a linear increase of the prescribed dose according to the signal intensity in the PET image [12] or as a result of redistributing the dose to the target, by increasing the dose to the hypoxic voxels while decreasing the prescribed dose to the remaining voxels in the tumour [13]. More complex approaches for heterogeneous dose prescription make use of dynamic PET information [14]. However, heterogeneous dose distributions are at risk of failing to provide the expected results for cases of dynamic hypoxia, as have indeed been seen in the clinic [15, 16].

Recently a paradigm shift in the biological prescription and adaptation of the treatment based on the quantitative analysis of the biological and functional information obtained by PET-CT imaging of tumour hypoxia was proposed [17, 18] and included in a research planning system for advanced studies. In order to devise a plan according to the proposed algorithm for treatment planning based on tumour hypoxia in Toma-Dasu et al. [17], the hypoxic compartments within the gross tumour volume (GTV) based on the uptake levels calculated relative to a well-oxygenated region in the patient are delineated. The hypoxic regions are defined according to a preset oxygenation threshold. The PET image is, therefore, first converted into oxygenation maps. The distribution of dose-modifying factors, calculated from the oxygenation map, is subsequently used for defining physical dose objectives for the subregions of the clinical target volume. These objectives are then delivered to the treatment planning module, together with additional objectives and constraints for the organs at risk. The feasibility of the proposed method for dose prescription and treatment planning based on FMISO-PET hypoxia was tested on several head-and-neck patients and the results were recently published [17].

3 Role of EPR Oximetry in PET Hypoxia Calibration for Treatment Planning Based on Tumour Oxygenation

The bioreductive markers used for imaging hypoxia with PET have selective retention in the hypoxic cells according to the inhibition of the chemical reaction of metabolizing the tracer in the presence of oxygen. Thus, the intensity in the PET image results from the differential uptake rate of the tracer according to the local tissue oxygenation. Therefore, the function used for converting the intensities in the PET image to oxygen partial pressures could be obtained by fitting experimental data of the tracer uptake under various hypoxic conditions with equations describing the

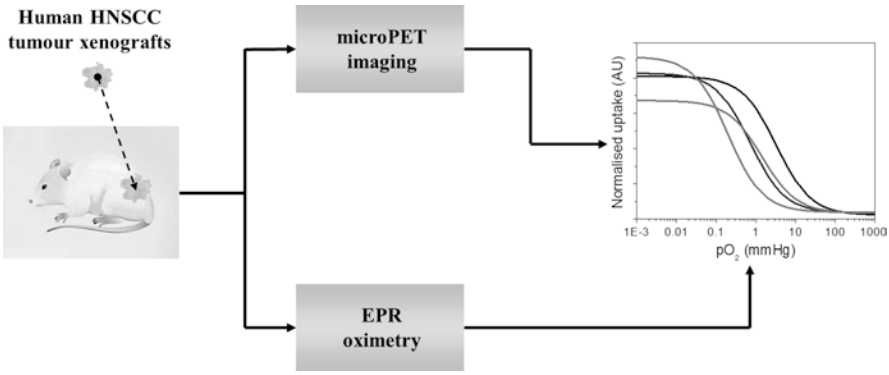

Fig. 19.1 Illustration of the experimental chain for calibration of the PET images taken with a hypoxic tracer based on absolute pO_2 EPR measurements

inhibition of chemical reactions. It is important to note that experimental data on tracer uptake *in vitro* showed that various tracers would provide different levels of uptake and discrimination between hypoxic levels [6, 10] and hence they will lead to different images according to their uptake characteristics. Consequently, they might impact differently on the treatment planning based on hypoxia tracer uptake [18, 19]. However, it is not known to what extent the uptake of cells *in vitro* can mimic the uptake in the complex environment *in vivo*. Therefore, the need for acquiring the calibration of the tracer uptake as function of pO_2 *in vivo* is warranted.

Electron Paramagnetic Resonance (EPR) oximetry is an interesting technique that allows the absolute determination of the oxygen partial pressure *in vivo*. It was recently shown that it could be used to qualify or disqualify other oxygen imaging methods and that good correlation was found between EPR oxygen measurements and PET hypoxia imaging with the ^{18}F-labelled nitroimidazole derivative FAZA [20]. The full potential of the technique could be further pursued for overcoming the most critical limitation of the current approach for treatment planning based on tumour hypoxia. The method for EPR oximetry—PET hypoxia calibration proposed in this paper is illustrated in Fig. 19.1. Thus, pre-clinical EPR oxygen measurements on human HNSCC tumour xenographs in mice as well as in well oxygenated normal tissues together with subsequent hypoxia imaging with a microPET could provide the *in vivo* relationship between tracer uptake and pO_2 that is needed for accurate quantification of tumour hypoxia. This calibration could be performed for several tracers that are available for PET hypoxia imaging.

The way these calibration curves are integrated in the dose planning chain going from the PET image to the dose distribution is illustrated in Fig. 19.2 for a head-and-neck cancer patient. However, the method has the potential to be used for other cancer types as long as suitable tumour xenografts are available for performing the pre-clinical EPR-based PET calibration.

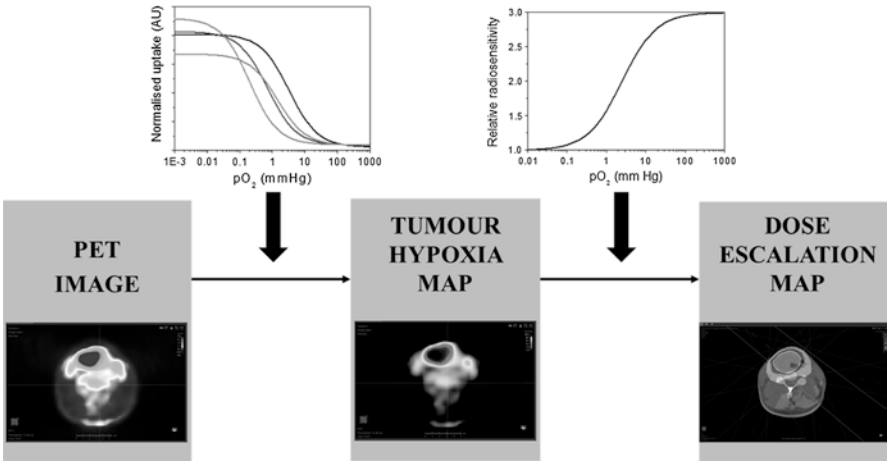

Fig. 19.2 Dose escalation factors for each voxel in the target relative to the homogeneous dose routinely prescribed could be determined if the relationship between the uptake of the tracer and the actual pO_2 is determined based on EPR calibration and subsequently the relationship between pO_2 and radiation sensitivity is employed

4 Conclusions

The proposed method for PET calibration with EPR would offer a significant advantage over proposals based on empirical conversions of the intensities in the PET images to relative radiosensitivities. Accurate quantification of PET hypoxia images would then be available and could provide an early identification of the clinical cases that might be suitable for dose escalation as well as the cases that could benefit from other counter-hypoxic measures.

Acknowledgments Financial support from the Cancer Research Funds of Radiumhemmet, Stockholm and the LiU Cancer research network at Linköping University and the County Council of Östergötland (Sweden) is gratefully acknowledged.

References

1. Vaupel P, Kallinowski F, Okunieff P (1989) Blood flow, oxygen and nutrient supply, and metabolic microenvironment of human tumors: a review. Cancer Res 49:6449–6465
2. Gray LH, Conger AD, Ebert M et al (1953) The concentration of oxygen dissolved in tissues at the time of irradiation as a factor in radiotherapy. Br J Radiol 26:638–648
3. Hockel M, Knoop C, Schlenger K et al (1993) Intratumoral pO2 predicts survival in advanced cancer of the uterine cervix. Radiother Oncol 26:45–50
4. Hockel M, Schlenger K, Aral B et al (1996) Association between tumor hypoxia and malignant progression in advanced cancer of the uterine cervix. Cancer Res 56:4509–4515

5. Brizel DM, Sibley GS, Prosnitz LR et al (1997) Tumor hypoxia adversely affects the prognosis of carcinoma of the head and neck. Int J Radiat Oncol Biol Phys 38:285–289
6. Rasey JS, Grunbaum Z, Magee S et al (1987) Characterization of radiolabeled fluoromisonidazole as a probe for hypoxic cells. Radiat Res 111:292–304
7. Lee ST, Scott AM (2007) Hypoxia positron emission tomography imaging with 18f-fluoromisonidazole. Semin Nucl Med 37:451–461
8. Piert M, Machulla HJ, Picchio M et al (2005) Hypoxia-specific tumor imaging with 18F-fluoroazomycin arabinoside. J Nucl Med 46:106–113
9. Krohn KA, Link JM, Mason RP (2008) Molecular imaging of hypoxia. J Nucl Med 49(Suppl 2):129S–148S
10. Lewis JS, McCarthy DW, McCarthy TJ et al (1999) Evaluation of 64Cu-ATSM in vitro and in vivo in a hypoxic tumor model. J Nucl Med 40:177–183
11. Grosu AL, Souvatzoglou M, Roper B et al (2007) Hypoxia imaging with FAZA-PET and theoretical considerations with regard to dose painting for individualization of radiotherapy in patients with head and neck cancer. Int J Radiat Oncol Biol Phys 69:541–551
12. Alber M, Paulsen F, Eschmann SM et al (2003) On biologically conformal boost dose optimization. Phys Med Biol 48:N31–N35
13. Flynn RT, Bowen SR, Bentzen SM et al (2008) Intensity-modulated x-ray (IMXT) versus proton (IMPT) therapy for theragnostic hypoxia-based dose painting. Phys Med Biol 53:4153–4167
14. Thorwarth D, Eschmann SM, Paulsen F et al (2007) Hypoxia dose painting by numbers: a planning study. Int J Radiat Oncol Biol Phys 68:291–300
15. Roels S, Slagmolen P, Nuyts J et al (2008) Biological image-guided radiotherapy in rectal cancer: is there a role for FMISO or FLT, next to FDG? Acta Oncol 47:1237–1248
16. Dasu A, Toma-Dasu I (2013) Dose painting by numbers – do the practical limitations of the technique decrease or increase the probability of controlling tumours? IFMBE Proc 39:1731–1734
17. Toma-Dasu I, Uhrdin J, Antonovic L et al (2012) Dose prescription and treatment planning based on FMISO-PET hypoxia. Acta Oncol 51:222–230
18. Toma-Dasu I, Dasu A (2013) Biologically-optimised IMRT based on molecular imaging of tumour hypoxia – the impact of the tracer used. IFMBE Proc 39:1742–1745
19. Toma-Dasu I, Uhrdin J, Dasu A et al (2009) Therapy optimization based on non-linear uptake of PET tracers versus "linear dose painting". IFMBE Proc 25(1):221–224
20. Tran LB, Bol A, Labar D et al (2012) Hypoxia imaging with the nitroimidazole 18F-FAZA PET tracer: a comparison with OxyLite, EPR oximetry and 19F-MRI relaxometry. Radiother Oncol 105:29–35

Chapter 20
A New Flavonoid Regulates Angiogenesis and Reactive Oxygen Species Production

Mei Zhang, Chaomei Liu, Zhenhuan Zhang, Shanmin Yang, Bingrong Zhang, Liangjie Yin, Steven Swarts, Sadasivan Vidyasagar, Lurong Zhang, and Paul Okunieff

Abstract The tumor vascular system, which is critical to the survival and growth of solid tumors, has been an attractive target for anticancer research. Building on studies that show that some flavonoids have anticancer vascular effects, we developed and analyzed the flavonoid derivative R24 [3, 6-bis (2-oxiranylmethoxy)-9*H*-xanthen-9-one]. A CAM assay revealed that R24 disrupted neovascular formation; fewer dendrites were detected and overall dendritic length was shorter in the R24-treated chicken embryos. The antiproliferative effect of R24 was measured by MTT assay in A549 (lung cancer), AsPC-1 (pancreatic cancer), HCT-116 (colorectal cancer), and PC-3 (prostate cancer) cell lines. R24 reduced proliferation with an IC_{50} of 3.44, 3.59, 1.22, and 11.83 μM, respectively. Cell-cycle analysis and Annexin-V/propidium iodide staining showed that R24 induced apoptosis. In addition, R24 regulated intracellular ROS production in a dose-dependent manner. CM-H_2DCFDA staining indicated that intracellular ROS production increased with the R24 dose. In summary, we found that R24 exhibits potent antiangiogenic and antiproliferative effects, induces apoptosis, and promotes ROS production.

Keywords Flavonoid • Angiogenesis • Reactive oxygen species • Tumor vasculature • Apoptosis

Mei Zhang and Chaomei Liu contributed equally to this work.

M. Zhang • C. Liu • Z. Zhang • S. Yang • B. Zhang • L. Yin • S. Swarts
S. Vidyasagar • L. Zhang • P. Okunieff (✉)
Department of Radiation Oncology, University of Florida, Cancer/Genetics Research Complex, 2033 Mowry Road, Suite 145, P.O. Box 103633, Gainesville, FL 32610, USA
e-mail: pokunieff@ufl.edu

H.M. Swartz et al. (eds.), *Oxygen Transport to Tissue XXXVI*, Advances in Experimental Medicine and Biology 812, DOI 10.1007/978-1-4939-0620-8_20,

1 Introduction

Development of a nutritive blood supply is critical for malignant tumor growth and progression. Tumors derive their blood supply either by displacing normal tissue and using its supply or through new angiogenesis. Antivascular agents address the former class of vessels, while antiangiogenic agents target the second vascular class. Limiting tumor-associated blood supply is a promising approach to control tumor growth and progression [1, 2].

Some natural flavonoids and their derivatives target tumor vessels, thereby providing antitumor, tumor static, or antimetastatic benefits [3, 4]. The flavonoids are polyphenolic compounds and integral components of the human diet that have displayed pharmacological activities in chemoprevention and treatment of cancer [4, 5]. Some of the most impressive effects relate to their specific toxicity to tumor vasculature, a phenomenon that can be seen after administration of the agent and suggests a rapid chemical response that occurs almost exclusively in the tumor.

Reactive oxygen species (ROS) are generally perceived as toxicants that induce various deleterious effects, including rapid cell dysfunction and death. Many ROS reactions are modified by oxygen levels, and aggressive and rapidly growing tumors commonly have intermittent hypoxia and reperfusion injury that potentiates those reactions. Thus, ROS is a reasonable potential mediator of the vascular toxicity seen after administration of these agents in animals with tumors.

Our aim was to study R24 (Fig. 20.1), a new flavonoid that we developed, as a potential modifier of angiogenesis, cancer cell proliferation, and ROS production.

2 Methods

Benzoic acid was used to prepare 2,4-dimethoxybenzoyl chloride, and thionyl chloride was reacted with 1,3-dimethoxybenzene, catalyzed by anhydrous aluminum chloride. Cyclization and demethylation were performed after the benzophenone precursor was formed. 2,6-Dihydroxyxanthenone was alkylated with epichlorohydrin, resulting in the final product 2,6-di(2,3-epoxypropoxy)xanthenone or R24.

A549 (lung cancer), AsPC-1 (pancreatic cancer), HCT-116 (colorectal cancer), and PC-3 (prostate cancer) cell lines were obtained from the American Type Culture Collection (Manassas, VA). The cells were maintained as monolayer cultures in

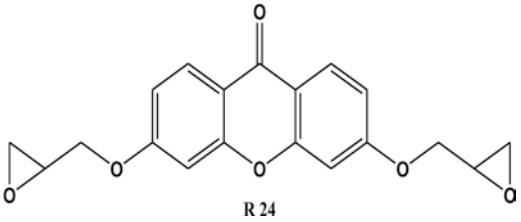

Fig. 20.1 The structure of R24

Dulbecco's Modified Eagle Medium (DMEM) supplemented with 10 % bovine calf serum (Invitrogen Life Technologies, Carlsbad, CA), 100 μg/mL of streptomycin, and 100 units/mL of penicillin. The cells were incubated at 37 °C in a humidified atmosphere of 5 % CO_2.

The effect of R24 on angiogenesis was investigated using a chicken embryo chorioallantoic membrane (CAM) assay (10–12 eggs/group). A window was made in the egg shell over the CAM on day 10 of incubation, and R24 (60 μg/egg) was added to the developing CAM and incubated for 48 h. The chorioallantoic membrane was fixed, and quantitative magnification was used to capture blood vessel images. The blood vessel length and number of branch points were quantified using Image-Pro (Media Cybernetics, Inc., Rockville, MD). Results were compared with a Student's *t*-test and were considered to be statistically significant at $P<0.05$. Values were represented as the mean ± 1 SD.

For the MTT assay to determine cell proliferation, A549, AsPC-1, HCT-116, and PC-3 cells were seeded into 96-well tissue culture plates. Various concentrations of R24 or genistein (control flavone) were added to the cells and incubated for 3 days. A yellow tetrazolium salt (3-(4,5-dimethylthiazol-2-yl)-2,5-diphenyltetrazolium bromide) was added, the cultures were incubated at 37 °C for 4 h, the supernatant was discarded, and 100 μL of dimethyl sulfoxide was added to each well. The absorbance was measured using a SpectraMax M2 plate reader (Molecular Devices LLC, Sunnyvale, CA) with a test wavelength of 560 nm. The concentration for 50 % cell growth inhibition (IC_{50}) was calculated.

AsPC-1 cells were treated with or without R24 for 48 h, and the cells were harvested and stained with Annexin V-PI for cell apoptosis. For cell-cycle analysis, the cells were fixed and stained with PI. The samples were then measured with an Accuri C6 flow cytometer (BD Biosciences, San Jose, CA).

To measure ROS production, A549 cells were loaded with ROS dye (CM-H_2DCFDA) and challenged with the control or R24 for 30 min at 37 °C. After cells were washed, the intensity of fluorescence was determined by flow cytometry.

3 Results

After R24 was delivered to the CAM and incubated for 48 h, the blood vessel structures were observed. As shown in Fig. 20.2, a normal vascular pattern with numerous branches was observed in the control group. The total number of blood vessel branches in the R24 group was significantly decreased. Likewise, the total vascular length was significantly shortened compared to the control group ($P<0.05$). The results indicated that R24 treatment disrupted angiogenesis *in vivo*.

MTT assays were used to assess the viability of the four cancer cell lines treated with R24 or genistein. Both treatments inhibited cancer cell growth. In A549, AsPC-1, HCT-116, and PC-3 cells, the IC_{50} was 3.44, 3.59, 1.22, and 11.83 μM, respectively. As Table 20.1 shows, R24 exhibited a lower IC_{50} than genistein.

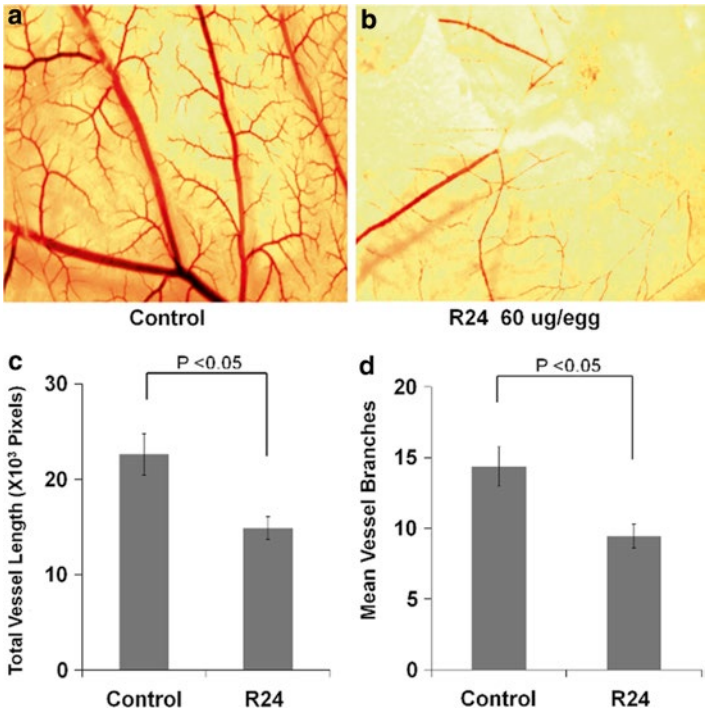

Fig. 20.2 The effect of R24 on chicken chorioallantoic membrane (CAM) angiogenesis. CAMs were treated with R24 for 48 h, and the blood vessels were photographed. (**a**) Control; (**b**) R24 (60 μg/egg); (**c**) length of the vascular tree; and (**d**) number of branches were analyzed and represented as mean ± SD from 10 to 12 eggs

Table 20.1 IC_{50} is the dose of agent that causes 50 % inhibition of proliferation

Compounds	IC_{50} (μM)			
	A549	AsPC-1	HCT-116	PC-3
R24	3.44	3.59	1.22	11.83
Genistein	82.14	88.89	93.27	65.04

The role that apoptosis plays in the antiproliferative activities of R24 was also addressed. As Fig. 20.3 shows, the early apoptosis of the Annexin V-stained population of A549 cells treated with R24 was significantly increased (49.7 % vs. 3.1 %), similarly necrosis and late apoptosis were also increased (10.8 % vs. 2.3 %). As Fig. 20.4 shows, cell-cycle analysis revealed increased cell accumulation in the sub-G1 phase, providing evidence for ongoing apoptosis.

To demonstrate the effect of R24 on ROS production, the CM-H_2DCFDA method was used. A rapid production of ROS occurred after A549 cells were exposed to R24. ROS production was R24-dose dependent (Fig. 20.5).

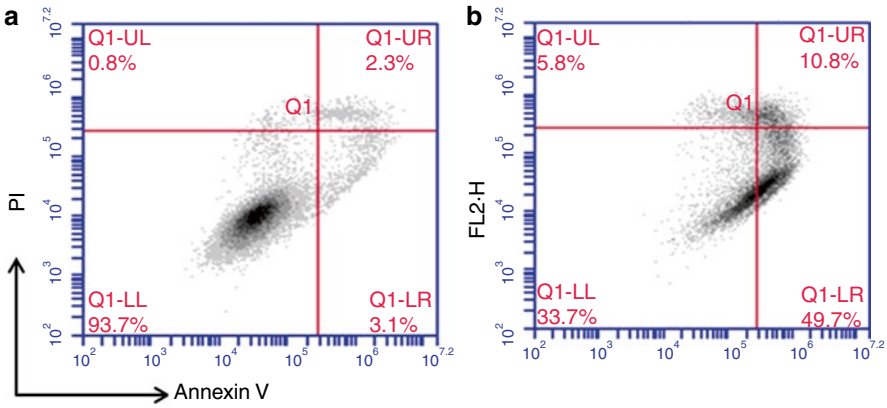

Fig. 20.3 R24-treated A549 cells exhibited increased apoptosis. (**a**) Control; (**b**) R24 (2.5 μM)

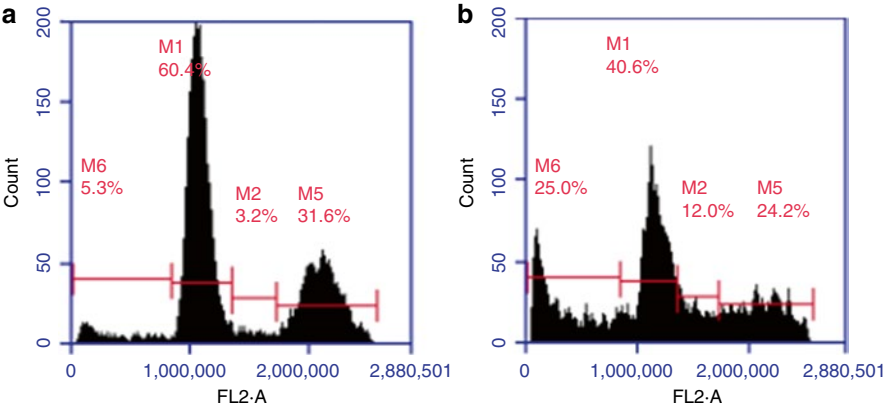

Fig. 20.4 The effect of R24 on A549 cell cycle. M6, M1, M2, and M5 in the figure represent sub-G1, G1, S, and G2/M phases, respectively. (**a**) Control; (**b**) R24 (2.5 μM)

4 Discussion

Angiogenesis is the formation of new blood vessels supplementing existing vasculature. The activation of angiogenic pathways is required for tumors to progress and metastasize [6]. New agents that target the angiogenic process are increasingly being used as a component of cancer care. Many of our current cancer therapies began as traditional medicines, which have been broadly investigated for their antitumor effects [7, 8]. Flavonoids are the most abundant polyphenols in our diet, and several groups have studied the role that these flavonoids might play in cancer therapy and prevention [9]. The antitumor activities of dietary flavonoids include the induction of apoptosis, suppression of proliferation, and antiangiogenesis [10].

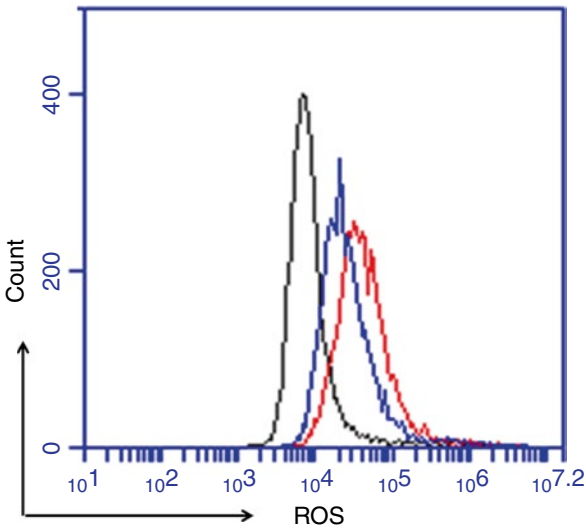

Fig. 20.5 R24 stimulated ROS production in A549 cells. The cells were incubated with either vehicle alone (as control, *black line*), 2.5 μM of R24 (*blue line*), or 10 μM of R24 (*red line*) for 30 min

R24 resulted in less vessel branch formation and shortened branch length in the CAM assay. Moreover, the MTT assay showed that IC_{50} values for the R24 groups were in the low μM range for all cancer cells types tested, indicating that R24 is a potent inhibitor of cancer cell viability and proliferation with promising translational potential.

Apoptosis is an important mechanism of cell death that can be mediated by ROS damage. R24 mediated regulation of cell-cycle progression and apoptosis in the A549 cell line, as indicated by the significantly increased apoptotic cell staining and cell-cycle arrest of the sub-G1 cell population. It also triggered cancer cell apoptosis. Thus, R24 likely reduced cell numbers through a combination of apoptosis and inhibition of proliferation, as evidenced by cell-cycle arrest.

The mitochondrial pathway is primarily responsible for ROS-induced apoptosis. Accumulation of ROS can lead to endoplasmic reticulum stress, mitochondrial dysfunction, and apoptosis [11]. This study demonstrated that R24 stimulates ROS production in A549 lung cancer cells in a dose-dependent manner, suggesting that R24-induced cancer cell toxicity could be partially due to elevated ROS levels.

5 Conclusion

R24, our new flavonoid derivative, disrupts CAM angiogenesis and induces ROS production in cancer cells. It also demonstrates a potent antiproliferative effect by promoting apoptosis. R24 exhibits great therapeutic potential for malignancies.

Acknowledgments This project is supported by UF Health Cancer Center startup funds (University of Florida). We thank Kate Casey-Sawicki for editing this manuscript.

References

1. Weis SM, Cheresh DA (2011) Tumor angiogenesis: molecular pathways and therapeutic targets. Nat Med 17(11):1359–1370
2. Vaupel P, Kallinowski F, Okunieff P (1989) Blood-flow, oxygen and nutrient supply, and metabolic microenvironment of human-tumors – a review. Cancer Res 49(23):6449–6465
3. Sagar SM, Yance D, Wong RK (2006) Natural health products that inhibit angiogenesis: a potential source for investigational new agents to treat cancer – part 2. Curr Oncol 13(3):99–107
4. Hill S, Williams KB, Denekamp J (1989) Vascular collapse after flavone acetic acid: a possible mechanism of its anti-tumour action. Eur J Cancer Clin Oncol 25(10):1419–1424
5. Middleton E Jr, Kandaswami C, Theoharides TC (2000) The effects of plant flavonoids on mammalian cells: implications for inflammation, heart disease, and cancer. Pharmacol Rev 52(4):673–751
6. Su JL, Yang PC, Shih JY et al (2006) The VEGF-C/Flt-4 axis promotes invasion and metastasis of cancer cells. Cancer Cell 9(3):209–223
7. Man SL, Gao WY, Wei CL et al (2012) Anticancer drugs from traditional toxic Chinese medicines. Phytother Res 26(10):1449–1465
8. Zhang M, Swarts SG, Yin LJ et al (2011) Antioxidant properties of quercetin. Oxygen Transp Tissue 701(Xxxii):283–289
9. Kuo SM (1997) Dietary flavonoid and cancer prevention: evidence and potential mechanism. Crit Rev Oncog 8(1):47–69
10. Kanadaswami C, Lee LT, Lee PPH et al (2005) The antitumor activities of flavonoids. In Vivo 19(5):895–909
11. Sanges D, Marigo V (2006) Cross-talk between two apoptotic pathways activated by endoplasmic reticulum stress: differential contribution of caspase-12 and AIF. Apoptosis 11(9):1629–1641

Chapter 21
Angiotensin II Reduces Transport-Dependent Oxygen Consumption but Increases Transport-Independent Oxygen Consumption in Immortalized Mouse Proximal Tubular Cells

Malou Friederich-Persson, William J. Welch, Zaiming Luo, Fredrik Palm, and Lina Nordquist

Abstract Oxidative stress is closely associated with renal dysfunction following diabetes and hypertension. Angiotensin II (Ang II) can activate the NADPH-oxidase, increasing oxidative stress that is thought to blunt proximal tubular electrolyte transport and thereby oxygen consumption (QO_2). We investigated the effect of Ang II on QO_2 in immortalized mouse proximal tubular cells over-expressing the NADPH oxidase subunit $p22^{phox}$; a model of increased oxidative stress. Cultured cells were exposed to either Ang II or H_2O_2 for 48 h. QO_2 was determined during baseline (113 mmol/l NaCl; transport-dependent QO_2) and during sodium-free conditions (transport-independent QO_2). Ang II reduced transport-dependent QO_2 in wild-types, but not in $p22^{phox}$ which also displayed increased QO_2 at baseline. Transport-independent QO_2 was increased in $p22^{phox}$ and Ang II had no additional effect, whereas it increased QO_2 in wild-type. Addition of H_2O_2 reduced transport-dependent QO_2 in wild-types, but not in $p22^{phox}$. Transport-independent QO_2 was unaffected by H_2O_2. The similar effects of Ang II and H_2O_2 to reduce transport-dependent QO_2 suggest a direct regulatory role of oxidative stress. In accordance, the

M. Friederich-Persson (✉)
Department of Medical Cell Biology, Uppsala University, Biomedical Center, Husargatan 3, Uppsala 751 23, Sweden
e-mail: Malou.Friederich@mcb.uu.se

W.J. Welch • Z. Luo
Department of Medicine, Georgetown University Medical Center, Washington DC, USA

F. Palm
Department of Medical Cell Biology, Uppsala University, Biomedical Center, Husargatan 3, Uppsala 751 23, Sweden

Department of Medical and Health Sciences, Linköping University, Linköping, Sweden

Center for Medical Image Science and Visualization, Linköping University, Linköping, Sweden

L. Nordquist
Department of Medical Cell Biology, Uppsala University, Uppsala, Sweden

H.M. Swartz et al. (eds.), *Oxygen Transport to Tissue XXXVI*, Advances in Experimental Medicine and Biology 812, DOI 10.1007/978-1-4939-0620-8_21,

transport-dependent QO_2 was reduced in $p22^{phox}$ already during baseline. The effects of Ang II on transport-independent QO_2 was not replicated by H_2O_2, indicating direct regulation via Ang II-receptors independently of oxidative stress. However, the Ang II effect was absent in $p22^{phox}$, suggesting that oxidative stress also modulates normal Ang II signaling. In conclusion, Ang II affects both transport-dependent and transport-independent QO_2 in proximal tubular cells and may be an important pathway modulating renal QO_2.

Keywords Proximal tubule cell • Oxidative stress • Angiotensin-II • Oxygen consumption • Electrolyte transport

1 Introduction

Development of nephropathy due to diabetes and hypertension is strongly connected with concurrent development of renal hypoxia [1]. Renal hypoxia may develop with increased metabolic demand, renal anemia, or when renal peritubular capillary blood flow is decreased due to glomerular injury or vasoactive substances constricting the arterioles. Angiotensin II (Ang II), a vasoactive substance known to be increased in both hypertensive and diabetic kidneys [2, 3], induces oxidative stress and constriction of afferent as well as efferent arteriole [4]. Both these effects reduce renal blood flow and therefore reduce oxygen delivery, contributing to renal hypoxia. The metabolic demand by the kidney is largely determined by electrolyte reabsorption, accounting for 80 % of total kidney oxygen consumption (QO_2) [5]. Interestingly, the energy-demanding Na^+/K^+-ATPase-activity is increased in diabetes [6], increasing QO_2 and possibly limiting renal oxygenation. Diabetes-induced increased QO_2 and development of renal hypoxia are closely linked to increased levels of oxidative stress, as demonstrated by the prevention of renal hypoxia using antioxidants [7]. Interestingly, Ang II activates the NADPH oxidase via the Ang II receptor subtype 1 (AT1-R), resulting in increased superoxide formation [8] and several studies have suggested a role for NADPH-oxidase in the development of both hypertension and nephropathy [9, 10].

In summary, renal QO_2 is affected by mitochondrial activity, electrolyte transport and cellular QO_2, all processes that are altered by oxidative stress. However, the detailed pathways of Ang II-mediated effects on proximal tubular QO_2 and their relation to increased oxidative stress are presently unknown. Therefore, the present study separated the effects of Ang II on electrolyte transport-dependent QO_2 from those on transport-independent QO_2 in immortalized wild-type and $p22^{phox}$ overexpressing mouse proximal tubular cells. The latter is a model of increased oxidative stress and was utilized to separate the effects of AT1-R signaling *per se* from those of Ang II-induced oxidative stress.

2 Material and Methods

Immortalized proximal tubular cells with and without a stable over-expression of the NADPH oxidase subunit $p22^{phox}$ were maintained at 37°C and 5 % CO_2 in Dulbecco's Modified Eagle Medium/F12 medium containing 5 % fetal bovine serum. At 50 % confluency, cell splitting was routinely performed using 2.5 % trypsin. Both cell types were grown with or without Ang II (10^{-7} mol/l, Sigma-Aldrich, St Louis, MO, USA replaced every 12 h) and H_2O_2 (2.5×10^{-5} mol/l, Sigma-Aldrich, St Louis, MO, USA replaced every 12 h) for 48 h. Before measurements, cells were placed in suspension with 2.5 % trypsin followed by triple rinsing by slow centrifugation ($100 \times g$, 4 min, 4°C) in ice-cold respiration buffer (in mmol/l: glucose 23.2; NaCl 113; KCl 4.0; $NaHCO_3$ 27.2; KH_2PO_4 1.0; $MgCl_2$ 1.2; $CaCl_2$ 1.0; HEPES 10.0; Ca^{2+}-lactate 0.5; glutamine 2.0 and streptomycin 50 U/ml; osmolality 298 ± 2 mOsm checked with a freezing point osmometer, Fiske laboratories; pH 7.4) with or without Na^+. In absence of NaCl and $NaHCO_3$, osmolality was kept constant with 280.4 mOsm mannitol. The cell-suspension was kept on ice until QO_2 was measured as described previously [11]. Briefly, a custom-made 1.1 ml gas-tight Plexiglas chamber thermostatically controlled at 37°C with continuous stirring from an air driven magnetic stirrer was used to determine QO_2 on free-floating cells in respiration buffer with or without Na^+ to evaluate transport-dependent QO_2 and transport-independent QO_2 respectively. QO_2 was determined as rate of oxygen disappearance as measured by a modified Unisense-500 O_2-sensor (Unisense A/S, Aarhus, Denmark) calibrated with the air-equilibrated buffer solution as 228 µmol/l O_2 and $Na_2S_2O_5$-saturated buffer as zero, and normalized to protein concentration. Statistical analyses were performed using GraphPad Prism software (GraphPad Software Inc., San Diego, CA, USA). Multiple comparisons between groups were performed using analysis of variance (ANOVA) followed by Sidak multiple comparisons test. All data are presented as mean ± standard error of the mean (SEM) and $p < 0.05$ was considered statistically significant.

3 Results

Cells overexpressing $p22^{phox}$ had reduced transport-dependent QO_2 compared to wild-type. Ang II reduced transport-dependent QO_2 in wild-type but not in $p22^{phox}$. During baseline conditions, transport-independent QO_2 was increased in $p22^{phox}$ compared to wild-type. Ang II displayed only a tendency to decrease transport-dependent oxygen consumption in $p22^{phox}$ whereas it increased transport-independent QO_2 in wild-type (Fig. 21.1). Addition of H_2O_2 reduced transport-dependent QO_2 in wild-type but only tended to reduce QO_2 in $p22^{phox}$. However, transport-independent QO_2 was unaffected by H_2O_2 in both cell types (Fig. 21.2).

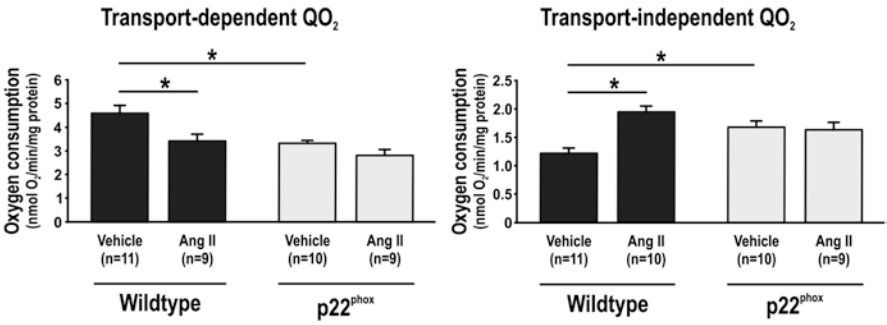

Fig. 21.1 Transport-dependent (left) and transport-independent oxygen consumption (QO_2, right) in immortalized wild-type mouse proximal tubular cells and corresponding cells overexpressing the NADPH oxidase subunit $p22^{phox}$ and the effect of 48 h exposure to angiotensin II. *Asterisk* denotes $p < 0.05$ and data are presented as mean ± SEM

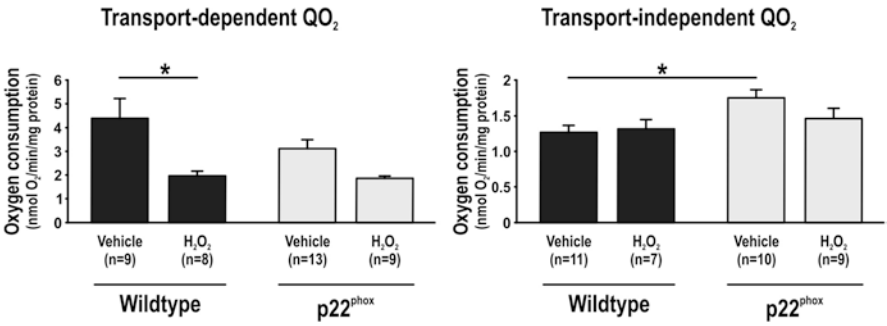

Fig. 21.2 Transport-dependent (left) and transport-independent oxygen consumption (QO_2, right) in immortalized wild-type mouse proximal tubular cells and corresponding cells overexpressing the NADPH oxidase subunit $p22^{phox}$ and the effect of 48 h exposure to H_2O_2. *Asterisk* denotes $p < 0.05$ and data are presented as mean ± SEM

4 Discussion

The present study demonstrates a role for Ang II in regulating transport-dependent as well as transport-independent QO_2 in mouse proximal tubular cells. It is likely that Ang-II decreases transport-dependent QO_2 by inducing oxidative stress, a hypothesis strengthened by the fact that the effect is mimicked by elevating oxidative stress via H_2O_2. Furthermore, the response to Ang II is reduced in cells with increased levels of oxidative stress during baseline, i.e. the $p22^{phox}$, further highlighting oxidative stress as a crucial component in the mechanism of Ang II.

However, as the effects on transport-independent QO_2 is not mimicked by H_2O_2 other mechanisms than oxidative stress may be involved.

It is known that Ang II increases superoxide formation by activating NADPH oxidase via AT-1R [8, 12]. Indeed, inhibition of AT-1R by olmesartan reduces oxidative stress independently of its blood pressure-lowering effect [13].

Several studies have suggested a role for NADPH oxidase in the development of hypertension and kidney disease [10, 14]. Oxidative stress is indeed increased in human hypertension [15] as well as in several hypertensive animal models [16]. AT_1-Receptor blockade with candesartan has been reported equally effective as the superoxide dismutase mimetic tempol in normalizing renal pO_2, implying that oxidative stress is directly involved [17]. Furthermore, inhibition of Ang II with angiotensin-converting enzyme (ACE) inhibitors and AT1-R blockers lowers renal QO_2 [18]. Ang II acting on AT_1-Receptors has been implied for the development in intrarenal hypoxia during hypertension, since 2 weeks of treatment with the AT1-R blocker candesartan to SHR rats normalize renal pO_2 [19]. Finally, Ang II-dependent hypertension in rats increases transport-dependent QO_2 in the thick ascending limb [20].

Cells with increased levels of oxidative stress displayed increased transport-independent QO_2. This may be due to mitochondrial uncoupling by uncoupling protein (UCP)-2, a phenomenon known to be induced during conditions of increased oxidative stress, resulting in increased QO_2 unrelated to ATP production [11, 21]. Importantly, diabetes-induced mitochondria uncoupling via UCP-2 is prevented by antioxidant treatment [22]. In the present study, addition of H_2O_2 to wildtype cells decreased transport-dependent oxygen consumption and did not affect transport-independent oxygen consumption, arguing against the presence of mitochondria uncoupling in these cells. However, it has been shown that mitochondria uncoupling is regulated by oxidative stress originating from the matrix side of the electron transport chain [23] and addition of H_2O_2 may therefore not be a strong enough signal to increase mitochondria uncoupling in cells with normal levels of oxidative stress. However, in cells with increased oxidative stress an increase in transport-independent oxygen consumption was evident, suggesting increased mitochondria uncoupling. Interestingly, the specific effect of Ang II on increasing transport-independent QO_2 may indeed be due to increased mitochondrial uncoupling. In a study by Doughan et al., addition of Ang II to cultured bovine aortic endothelial cells increased mitochondrial superoxide production and mitochondrial uncoupling [24]. Recently, Ang II receptors have been localized to the mitochondrial inner membrane [25]. In kidneys from SHR rats, oxidative stress was increased and the mitochondria displayed increased H_2O_2 generation, decreased membrane potential and increased UCP-2 expression [26]. Importantly, the effect of Ang II on transport-independent QO_2 was not replicated by increased oxidative stress *per se*, implying a crucial and specific role for AT1-R signaling. It is tempting to speculate that AT1-R located in the mitochondria are involved in these specific effects of Ang II. However, there was no effect of Ang II on transport-independent QO_2 in cells with increased levels of oxidative stress, demonstrating that oxidative stress may still have a regulatory role in mediating the observed effect on transport-independent QO_2 in wild-type cells. Reduced AT1-R expression or blunted receptor response in conditions with increased oxidative stress cannot be excluded.

In conclusion, the present study demonstrates that Ang II can affect both transport-dependent and transport-independent QO_2 in mouse proximal tubular cells and may be an important pathway modulating renal QO_2.

References

1. Nangaku M (2006) Chronic hypoxia and tubulointerstitial injury: a final common pathway to end-stage renal failure. J Am Soc Nephrol 17:17–25
2. Kobori H et al (2007) The intrarenal renin-angiotensin system: from physiology to the pathobiology of hypertension and kidney disease. Pharmacol Rev 59:251–287
3. Nagai Y et al (2005) Temporary angiotensin II blockade at the prediabetic stage attenuates the development of renal injury in type 2 diabetic rats. J Am Soc Nephrol 16:703–711
4. Arendshorst WJ, Brannstrom K, Ruan X (1999) Actions of angiotensin II on the renal microvasculature. J Am Soc Nephrol 10:149–161
5. Lassen NA, Munck O, Thaysen JH (1961) Oxygen consumption and sodium reabsorption in the kidney. Acta Physiol Scand 51:371–384
6. Korner A et al (1994) Increased renal metabolism in diabetes. Mechanism and functional implications. Diabetes 43:629–633
7. Palm F et al (2003) Reactive oxygen species cause diabetes-induced decrease in renal oxygen tension. Diabetologia 46:1153–1160
8. Chabrashvili T et al (2003) Effects of ANG II type 1 and 2 receptors on oxidative stress, renal NADPH oxidase, and SOD expression. Am J Physiol Regul Integr Comp Physiol 285:117–124
9. Cifuentes ME et al (2000) Upregulation of p67(phox) and gp91(phox) in aortas from angiotensin II-infused mice. Am J Physiol Heart Circ Physiol 279:2234–2240
10. Rey FE et al (2001) Novel competitive inhibitor of NAD(P)H oxidase assembly attenuates vascular O(2)(−) and systolic blood pressure in mice. Circ Res 89:408–414
11. Friederich M et al (2008) Diabetes-induced up-regulation of uncoupling protein-2 results in increased mitochondrial uncoupling in kidney proximal tubular cells. Biochim Biophys Acta 1777:935–940
12. Chabrashvili T et al (2002) Expression and cellular localization of classic NADPH oxidase subunits in the spontaneously hypertensive rat kidney. Hypertension 39:269–274
13. Fujimoto S et al (2008) Olmesartan ameliorates progressive glomerular injury in subtotal nephrectomized rats through suppression of superoxide production. Hypertens Res 31:305–313
14. Landmesser U et al (2002) Role of p47(phox) in vascular oxidative stress and hypertension caused by angiotensin II. Hypertension 40:511–515
15. Kumar KV, Das UN (1993) Are free radicals involved in the pathobiology of human essential hypertension? Free Radic Res Commun 19:59–66
16. Touyz RM (2000) Oxidative stress and vascular damage in hypertension. Curr Hypertens Rep 2:98–105
17. Welch WJ et al (2005) Angiotensin-induced defects in renal oxygenation: role of oxidative stress. Am J Physiol Heart Circ Physiol 288:22–28
18. Deng A et al (2005) Oxygen consumption in the kidney: effects of nitric oxide synthase isoforms and angiotensin II. Kidney Int 68:723–730
19. Welch WJ et al (2003) Renal oxygenation defects in the spontaneously hypertensive rat: role of AT1 receptors. Kidney Int 63:202–208
20. Silva GB, Garvin JL (2008) Angiotensin II-dependent hypertension increases Na transport-related oxygen consumption by the thick ascending limb. Hypertension 52:1091–1098
21. Echtay KS et al (2002) Superoxide activates mitochondrial uncoupling proteins. Nature 415:96–99
22. Persson MF et al (2012) Coenzyme Q10 prevents GDP-sensitive mitochondrial uncoupling, glomerular hyperfiltration and proteinuria in kidneys from db/db mice as a model of type 2 diabetes. Diabetologia 55:1535–1543
23. Echtay KS et al (2002) Superoxide activates mitochondrial uncoupling protein 2 from the matrix side. Studies using targeted antioxidants. J Biol Chem 277:129–135
24. Doughan AK, Harrison DG, Dikalov SI (2008) Molecular mechanisms of angiotensin II-mediated mitochondrial dysfunction: linking mitochondrial oxidative damage and vascular endothelial dysfunction. Circ Res 102:488–496

25. Abadir PM et al (2011) Identification and characterization of a functional mitochondrial angiotensin system. Proc Natl Acad Sci U S A 108:14849–14854
26. de Cavanagh EM et al (2006) Renal mitochondrial dysfunction in spontaneously hypertensive rats is attenuated by losartan but not by amlodipine. Am J Physiol Regul Integr Comp Physiol 290:1616–1625

Chapter 22
Investigation of Cerebral Autoregulation in the Newborn Piglet During Anaesthesia and Surgery

Gemma Bale, Aaron Oliver-Taylor, Igor Fierens, Kevin Broad, Jane Hassell, Go Kawano, Jamshid Rostami, Gennadij Raivich, Robert Sanders, Nicola Robertson, and Ilias Tachtsidis

Abstract The relationship between cerebral autoregulation (CA) and the neurotoxic effects of anaesthesia with and without surgery is investigated. Newborn piglets were randomly assigned to receive either 6 h of anaesthesia (isoflurane) or the same with an additional hour of minor surgery. The effect of the spontaneous changes in mean arterial blood pressure (MABP) on the cerebral haemodynamics (oxy- and deoxy-haemoglobin, HbO_2 and Hb) was measured using transverse broadband near-infrared spectroscopy (NIRS). A marker for impaired CA, concordance between MABP and intravascular oxygenation ($HbD = HbO_2 - Hb$) in the ultra-low frequency domain (0.0018–0.0083 Hz), was assessed using coherence analysis. Presence of CA impairment was not significant but found to increase with surgical exacerbation. The impairment did not correlate with histological outcome (presence of cell death, apoptosis and microglial activation in the brain).

Keywords Near-infrared spectroscopy • Ultra-low frequencies • Coherence • Neonatal • Histology

---

The original version of this chapter was revised. An erratum to this chapter can be found at DOI 10.1007/978-1-4939-0620-8_49

G. Bale (✉) • I. Tachtsidis
Biomedical Optics Research Laboratory, University College London,
Malet Place Engineering Building, Gower St., London WC1E6BT, UK
e-mail: gemma.bale.11@ucl.ac.uk

A. Oliver-Taylor • I. Fierens • K. Broad • J. Hassell • G. Kawano
J. Rostami • G. Raivich • N. Robertson
Institute for Women's Health, University College London, London, UK

R. Sanders
Wellcome Centre for Imaging Neuroscience, University College London, London, UK

H.M. Swartz et al. (eds.), *Oxygen Transport to Tissue XXXVI*, Advances in Experimental Medicine and Biology 812, DOI 10.1007/978-1-4939-0620-8_22,

1 Introduction

Neonatal exposure to anaesthesia has been associated with apoptotic death of neurons and long-term impairments in cognition in rodents and non-human primates [1, 2]. There is heightened vulnerability during the period of maximal growth, also known as the brain growth spurt period, which occurs perinatally in the human and piglet brain [3]. Research into the neurotoxicity of anaesthetic agents has previously been limited to rodent and primate models which are neurodevelopmentally different to humans; therefore we undertook the current study using a piglet model to gain further insight into the safety of human neonates subjected to anaesthesia.

From this preliminary study, we have found increased cell death and microglial activation in the newborn piglet following 6 h of anaesthesia compared to a naïve control, and that 1 h of minor surgery during the anaesthesia tended to increase injury further. However, the exact physiological mechanism of the injury remains unclear and needs investigation.

It was further observed that the range of mean arterial blood pressure (MABP) changes in the piglets that underwent surgery during anaesthesia was narrower than those that did not. In this paper we hypothesize that an impairment of the cerebral autoregulation (CA), the mechanism that protects the brain by limiting the cerebral blood flow (CBF) variation over a range of arterial blood pressures, may have effect on the histological outcome and will therefore help to explain the histological differences between the two populations (anaesthesia and anaesthesia with surgery).

Many different methods to assess CA impairment through analysis of MABP and markers of CBF using near-infrared (NIR) spectroscopy (NIRS) or transcranial Doppler (TCD) have been reported. The most widely performed is coherence analysis [4]; other methods include transfer function analysis that can assess the severity of the impairment [5]; partial coherence where the measured signals are broken down into smaller epochs and the percentage of epochs with significant coherence is then estimated [6]. Rowley and colleagues employed wavelet cross-correlation (WCC) analysis which can find temporal and frequency components of the CA [7]. Recently non-linear computational models were used to interpret measurements and increase understanding of physiological processes, including the level of CA [8]. The techniques that use frequency analysis typically look at the concordance in specific frequency bands ranging from 0.003 Hz up to 0.1 Hz [5]. The frequency bands relate to different physiological mechanisms so therefore can interpret different clinical features [5].

In this study, CA impairment was assessed by the level of coherence between cerebral intravascular oxygenation (HbD), the difference between oxy- and deoxy-haemoglobin (HbO_2 and Hb), and MABP. HbD is measured non-invasively using NIRS and reflects CBF if the oxygen saturation (SpO_2) remains constant. The level of CA impairment for each piglet was compared with the protocol (whether the piglet had anaesthesia or anaesthesia with surgery) and its histological outcome.

2 Methods

Experiments were conducted under UK Home Office Guidelines. The study was performed on 16 newborn piglets (less than 24 h old) in the Institute of Neurology, University College London. The piglets were randomized into two groups: (i) anaesthesia (ANA, n = 9) induced with IM midazolam followed by intubation and 2 % isoflurane and iv fentanyl (3–6 μg/kg/h) for 6 h (ii) anaesthesia plus surgery (SUR, n = 7), surgical tracheostomy and bilateral inguinal hernia surgery for 1 h followed by 5 h of anaesthesia. MABP, SpO_2 and cerebral HbD were measured simultaneously (i) during the anaesthesia and (ii) post-surgery during anaesthesia. The NIRS signals were measured on a broadband NIR spectrometer developed in-house that has been previously used to assess the cerebral function of piglets [9] and humans [10]. The emitter and detector optical fibres were co-linear over the ventromedial/temporal region with a line passing through the brain centre. Intensity spectra between 650 and 980 nm were collected continuously every 1 min (0.0167 Hz) and concentration changes in HbO_2 and Hb were determined using the UCLn algorithm. The systemic data (MABP and SpO_2) were measured by intravascular catheterisation (SA Instruments 1025L) and pulse oximetry on the hind hoof (Nonin 8600FO), respectively, at 1 Hz by a data acquisition system (NI USB 6343) and stored on a PC. Animals were sacrificed at 6 h and immunohistochemistry was performed on 9 of the 16 subjects (ANA, n = 5. SUR, n = 4) for TUNEL + (cell death [11]), IBA-1 (microglial activation [12]) and caspase-3 (apoptosis [13]). The histology counts were averaged across the brain for each subject.

3 Data Analysis

Spurious data with error values (e.g. −1 for MABP) were considered to be artefact. Artefacts occurring for 2 min or less were removed from the data and interpolated accordingly, artefacts longer than 2 min were truncated. Hence, a single continuous measurement was replaced by a set of continuous artefact-free segments. Figure 22.1 shows two typical examples of the processed signals. Due to problems with the data collection systems, the remaining data lengths range from 19 to 271 min per animal. Ideally only periods in which SpO_2 varies less than 5 % would be considered to minimize its influence on HbD [4]; however, problems with the data collection system gave insufficient SpO_2 data for 12 of the subjects. During the experiment, breathing rate and SpO_2 were well maintained and the SpO_2 data from the four other subjects was stable within 5 %. Hence, constant SpO_2 during the procedure has been assumed for all subjects. The 1 Hz systemic data was downsampled to the same time increment as the NIRS data (0.0167 Hz).

Autoregulation impairment was assessed by coherence analysis of the MABP-HbD signals using the Welch method for the estimation of the respective cross-power and auto-power spectral densities [14] implemented in MATLAB

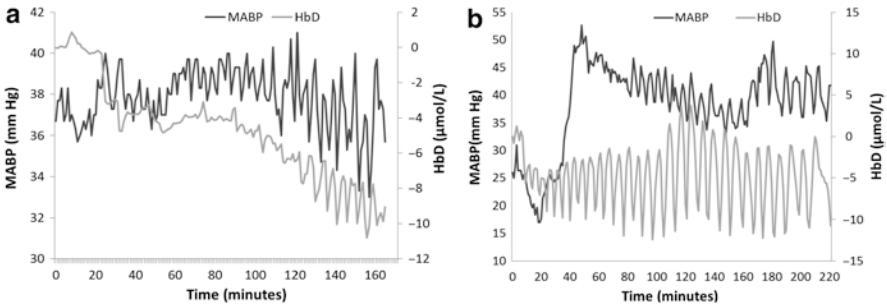

Fig. 22.1 Examples of simultaneous changes in MABP and HbD signals recorded from (**a**) piglet LWP 237 (SUR), $Coh_{ULF} = 0.20$ with a relatively high coherence as the general trend in MABP is reflected in the HbD and (**b**) piglet LWP 232 (SUR), $Coh_{ULF} = 0.06$ showing a much lower coherence between the two signals

(version R2013a, Mathworks). This method involves segmentation of the signals into 19-min epochs (of length equal to the shortest signal) with an overlap of 50 %. The average of the coherence coefficients in the lower end of the ultra-low frequency (ULF) range (0.0018–0.0083 Hz) was then calculated (Coh_{ULF}). The upper limit of this frequency range is determined by the Nyquist sampling theorem which avoids aliasing and the lower limit is taken from the window length. The window length is common across all subjects to ensure uniformity and avoid bias from signal length. The coherence coefficients range between 0 and 1 and a coefficient of greater than 0.5 was considered as significant CA impairment [4]. Short lengths of signal were noticed to correlate with higher Coh_{ULF} and so data lengths of less than 99 min were removed to avoid bias. Accordingly three subjects were removed from the study, leaving a remaining group of 13 subjects (ANA, n = 6. SUR, n = 7).

To compare the average Coh_{ULF} values in the two populations (ANA and SUR) a two-tailed Student's t-test was used. A nominal p-value of less than or equal to 0.05 was considered as statistically significant. The correlation between the histology counts and Coh_{ULF} were valued using R^2 linear regression and a R^2 value of greater than 0.5 was considered significant.

4 Results

Group Coh_{ULF} scores (mean ± standard deviation) for the ANA group were 0.08 ± 0.02 and for the SUR group 0.12 ± 0.05, and there is a significant difference between the sets (p = 0.050). No piglet showed significant Coh_{ULF} above 0.5 and thus CA was considered to be functioning satisfactorily in all piglets. Figure 22.2 shows the average coherence score for all frequencies across the ULF range for the ANA and SUR groups.The histological counts were plotted against the Coh_{ULF} for each of the seven subjects that had both histological and coherence data (ANA, n = 3. SUR, n = 4), shown in Fig. 22.3. No correlation was observed between any histological test and Coh_{ULF}.

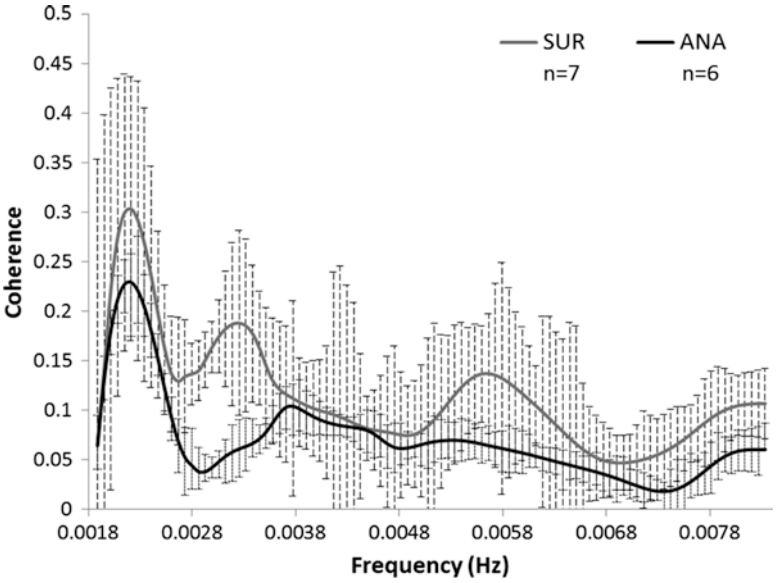

Fig. 22.2 Group average coherence data for anaesthesia (ANA) and anaesthesia plus surgery (SUR) piglets across the ULF range. Significant difference between the groups is observed ($p = 0.0498$)

5 Discussion

No significant levels of Coh_{ULF} between the MABP and HbD were observed in any of the 13 subjects. This suggests that in the ULF range the piglets were autoregulating. The piglets that had surgery with anaesthesia showed a small increase in the level of autoregulation impairment over the piglets that only had anaesthesia. There was no correlation between the histological data and level of CA impairment, suggesting that CA was not involved with the cellular damage. This is reinforced by the low Coh_{ULF} found in all subjects. This suggests that the failure of the CA mechanism was not involved in the apoptotic damage observed after anaesthesia.

These preliminary data suggest that we can eliminate the CA as a potential failing mechanism leading to increased apoptosis and that another physiological mechanism should be investigated. Previous studies [8] have also suggested that CA is not fully developed in newborn piglets and so any CA impairment may be unrelated to the presence of anaesthetic agents. However, the difference between the Coh_{ULF} ANA and SUR groups shows that surgery does stress the CA system, which correlates with the increase in cell death.

This study was limited by several factors. Firstly, the sampling frequency of the data is restricted by the transverse cranial NIRS exposure time and thus restricted the range of frequencies over which the coherence could be observed. Improved data collection methods could reduce the time between exposures and increase the frequency range over which we can test the CA impairment. Additionally, this experiment was not designed to challenge the CA system and thus the range of MABP remained within normal levels so it is possible that the system was not stressed enough to

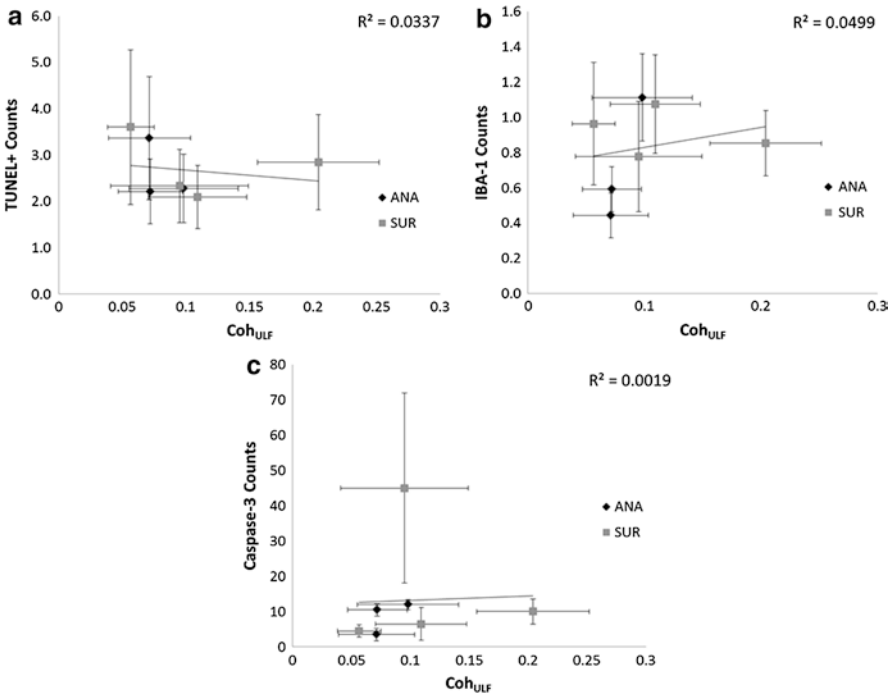

Fig. 22.3 Average Coh_{ULF} for each piglet compared with (**a**) TUNEL+counts, $R^2=0.0337$, (**b**) IBA-1 counts, $R^2=0.0499$ and (**c**) caspase-3 counts, $R^2=0.0019$. Error bars show standard deviation of the mean. The higher the number of counts, the higher the level of (**a**) cell death, (**b**) microglial activation and (**c**) apoptosis, respectively, in the tissue sample

observe CA. The lack of large fluctuations in the MABP results in a lower signal-to-noise ratio which can lower the precision of the Coh_{ULF} measurement [15]. These results are preliminary and more subjects are to be added to the study.

Acknowledgments Research was supported by the Centre for Doctoral Training in Photonic Systems Development (EP/G037256/1) and The Wellcome Trust (088429/Z/09/Z).

References

1. Brambrink AM et al (2010) Isoflurane-induced neuroapoptosis in the neonatal rhesus macaque brain. Anesthesiology 112:834–841
2. Paule MG et al (2012) Ketamine anesthesia during the first week of life can cause long-lasting cognitive defects in rhesus monkeys. Neurotoxical Teratol 33(2):220–230
3. Jelsing J et al (2006) The postnatal development of neocortical neurons and glial cells in the Gottingen minipig and the domestic pig brain. J Exp Biol 209:1454–1462
4. Tsuji M et al (2000) Cerebral intravascular oxygenation correlates with mean arterial pressure in critically ill premature infants. Pediatrics 106:625–632

5. Wong FY et al (2008) Impaired autoregulation in preterm infants identified by using spatially resolved spectroscopy. Pediatrics 121(3):604–611
6. Caicedo A et al (2011) Impaired cerebral autoregulation using near-infrared spectroscopy and its relation to clinical outcome in premature infants. Adv Exp Med Biol 701:233–239
7. Rowley AB et al (2006) Synchronization between arterial blood pressure and cerebral oxyhaemoglobin concentration investigated by wavelet cross-correlation. Physiol Meas 28:161–173
8. Moroz T et al (2012) Computational modelling of the piglet brain to simulate near-infrared spectroscopy and magnetic resonance spectroscopy data collected during oxygen deprivation. J R Soc Interface 9(72):1499–1509
9. Cooper CE et al (1997) Measurement of cytochrome oxidase and mitochondrial energetics by near-infrared spectroscopy. Phil Trans R Soc Lond Biol Sci 352:669–676
10. Tachtsidis I et al (2011) Analysis of the changes in the oxidation of brain tissue cytochrome-c-oxidase in traumatic brain injury patients during hypercapnea: a broadband NIRS study. Adv Exp Med Biol 701:9–14
11. Grasl-Kraupp K et al (1995) In situ detection of fragmented DNA (TUNEL assay) fails to discriminate among apoptosis, necrosis, and autolytic cell death: a cautionary note. Hepatology 21(5):1465–1468
12. Sasaki Y et al (2001) Iba1 is an action-cross-linking protein in macrophages/microglia. Biochem Bioph Res Com 286:292–297
13. Porter AG et al (1999) Emerging roles of caspase-3 in apoptosis. Cell Death Differ 6:99–104
14. Welch PD (1967) The use of fast Fourier transform for the estimation of power spectra: a method based on time averaging over short, modified periodograms. IEEE Trans Audio Electroacoust 15(2):70–73
15. Hahn G et al (2010) Precision of coherence analysis to detect cerebral autoregulation by near-infrared spectroscopy in preterm infants. J Biomed Opt 15(3):037002-1-10

Chapter 23
Influence of the Maternal Use of Labetalol on the Neurogenic Mechanism for Cerebral Autoregulation Assessed by Means of NIRS

Alexander Caicedo, Carolina Varon, Liesbeth Thewissen, Gunnar Naulaers, Petra Lemmers, Frank Van Bel, and Sabine Van Huffel

Abstract Labetalol is a drug used in the treatment of hypertensive disorders of pregnancy (HDP). In a previous study we investigated the influence of the maternal use of labetalol on the cerebral autoregulation (CA) mechanism of neonates. In that study, we found that labetalol induces impaired CA during the first day of life, with CA returning to a normal status by the third day after birth. This effect was hypothesized to be caused by labetalol-induced vasodilation. However, no strong evidence for this claim was found. In this study we aim to find stronger evidence for the vasodilation effect caused by labetalol, by investigating its effect on the neurogenic mechanism (NM) involved in CA. The status of the NM was assessed by means of transfer function analysis between the low frequency content of the autonomic control activity (LFA), obtained by processing of the heart rate (HR), and the regional cerebral oxygen saturation ($rScO_2$). We found that neonates from mothers treated with labetalol presented a lower LFA and an impaired NM response during the first day of life, with values returning to normal by the end of the third day. These results reflect a vasodilation effect caused by labetalol, and indicate that the impaired CA observed in the previous study is caused by vasodilation.

Keywords Labetalol • Hypertensive disorders of pregnancy • Vasodilation effect • Neurogenic mechanism • Cerebral autoregulation

A. Caicedo (✉) • C. Varon • S. Van Huffel
Department of Electrical Engineering (ESAT), STADIUS Center for Dynamical Systems, Signal Processing, and Data Analytics, KU Leuven, Kasteelpark Arenberg 10, Postbus 2446, Heverlee (Leuven), Vlaams-Brabant 3001, Belgium

iMinds Medical IT, KU Leuven, Belgium
e-mail: alexander.caicedodorado@esat.kuleuven.be; sabine.vanhuffel@esat.kuleuven.be

L. Thewissen • G. Naulaers
Neonatal Intensive Care Unit, University Hospitals Leuven, KU Leuven, Belgium

P. Lemmers • F. Van Bel
Department of Neonatology, Wilhelmina Children's Hospital, University Medical Center, Utrecht, The Netherlands

H.M. Swartz et al. (eds.), *Oxygen Transport to Tissue XXXVI*, Advances in Experimental Medicine and Biology 812, DOI 10.1007/978-1-4939-0620-8_23,

1 Introduction

Labetalol is an α_1 and non-selective β adrenergic antagonist that is normally used for the treatment of hypertensive disorders of pregnancy (HDP) [1]. Since labetalol easily passes the placental barrier, it accumulates in the neonate [2]. Therefore, its effects on the cerebral circulation of neonates should be studied. In the literature scarce information can be found about the influence of the maternal use of labetalol on the neonatal cerebral autoregulation (CA).

CA is a complex process that refers to the maintenance of a constant cerebral blood flow (CBF) over a broad range of arterial blood pressures. Several mechanisms are involved in CA; in the literature the myogenic, metabolic and neurogenic mechanisms have been described [3]. The myogenic mechanism is responsible for reactions to changes in MABP and has been extensively studied. The metabolic mechanism reacts to changes in the concentration of gases in the blood, especially to changes in CO_2 concentrations. Concerning the neurogenic mechanism (NM), only a few studies can be found in the literature where its influence on CA has been investigated. Purkayastha et al. studied the influence of the sympathetic activity on CA, which is related to the NM [4]. They conclude that increases in sympathetic activity have a role in establishing cerebral vascular tone in humans. In addition, they found that an α_1 adrenergic receptor blockade 'impairs' CA. Since labetalol is an α_1 adrenergic antagonist, we hypothesized that the maternal use of labetalol impairs the NM involved in CA. However, since labetalol is also a nonselective β adrenergic antagonist, it has a direct effect on the heart rate (HR), suppressing the influence of the autonomous system on heart activity. In this study we aimed to investigate the effect of maternal use of labetalol on the NM of neonates during the first 3 days of life.

2 Methods

Data. The study was performed in 49 infants from the Wilhelmina's Children's Hospital Utrecht (the Netherlands), with a gestational age of 29 (24.7–31.9) weeks and a birth weight of 960 (540–1585) g. In all infants, the peripheral oxygen saturation (SaO_2), MABP, HR, and the regional cerebral oxygen saturation ($rScO_2$) were continuously and noninvasively recorded using the INVOS4100 (Somanetics). All signals were simultaneously measured during the first 3 days of life and were resampled to 1 Hz. From the 49 infants, 14 correspond to control subjects, and 35 correspond to the group of mothers who were treated for HDP. From the HDP group, 19 neonates correspond to mothers treated with labetalol (HPD+Lab) and 16 correspond to mothers who followed other treatment (HPD−Lab). Among the other treatments we can find the use of Adalat, Aldomet, Ketanserine, Nepressol and Magnesium sulfate.

Signal Analysis. Artifacts shorter than 30 s were removed and corrected by interpolation using robust least squares support vector machines for function estimation [5]. Whereas artifacts longer than 30 s were removed from the signals. Only segments free of artifacts were used for further processing.

Mathematical Tools. The status of the neurogenic mechanism was assessed by means of transfer function analysis between the low frequency content of autonomic control activity (LFA) and $rScO_2$. The transfer function scores were calculated using a time-sliding window of length 15 min and overlapping time of 1 min. The cross-power and auto-power spectral densities needed for the estimation of transfer function values were computed using the Welch method. In this method a further segmentation of the signals into 5-min epochs with an overlap of 4.5 min was used.

In HR variability studies, the sympathetic activity (SA) and parasympathetic activity (PA) are quantified using the power contained in the low frequency (LF) and high frequency (HF) bands. The LF band contains information from the SA and PA, while the power in the HF is attributed mostly to PA. For neonates, these frequency bands are defined as follows: LF (0.04–0.24 Hz) and HF (0.24–1.0 Hz) [6]. According to [4], an increase in SA has a role in establishing cerebral muscular tone in humans; therefore, in this study we are interested in the information contained in the LF of the HR, which might reflect sympathetically mediated activity. To obtain a continuous estimation for the low frequency activity (LFA), we used the discrete wavelet transform [7]. In summary, LFA was estimated by decomposing the HR using a five level discrete wavelet transform, with Daubechies 4 as mother wavelet, and computing the root mean square value of the sum of the 2nd to the 4th level detail coefficients, using five samples for the mean average. The 2nd to the 4th level detail coefficients contain information on the HR located in the frequency range 0.031–0.25 Hz, which includes the LF range, as indicated in [6]. An approximation to the high frequency activity (HFA) was obtained as the root mean square value of the sum of the 1st level detail coefficients, which contains information in the frequency range 0.25–0.5 Hz. The upper frequency range was limited by the sampling frequency used to acquire the signals. The mean average of the transfer function gain in the LF range was used as a score to quantify the status of the NM. Figure 23.1 shows a representative set of measurements for a control subject where the MABP, $rScO_2$, HR and the estimated LFA and HFA are presented.

Statistical Analysis. Transfer function gain values, and the variance of the LFA and HFA for the three different populations were compared during the first, second and third day of life by means of the Kruskal–Wallis test. Statistical analysis was performed using the statistics toolbox from MATLAB. All reported p-values were two-tailed and a nominal p-value <0.05 was considered to be statistically significant.

3 Results

Figure 23.2 shows the median, 25 %, and 75 % percentiles of the LFA variance for the three different populations during the first 3 days of life. LFA was found to be significantly higher during the first day of life in the Control group than in the HDP+Lab group ($p=0.01$). In addition, higher values of LFA were found in the HDP+Lab population during the third day of life when compared to the first day ($p=0.01$). HFA values behave similarly to LFA (they are not shown here due to space limitations).

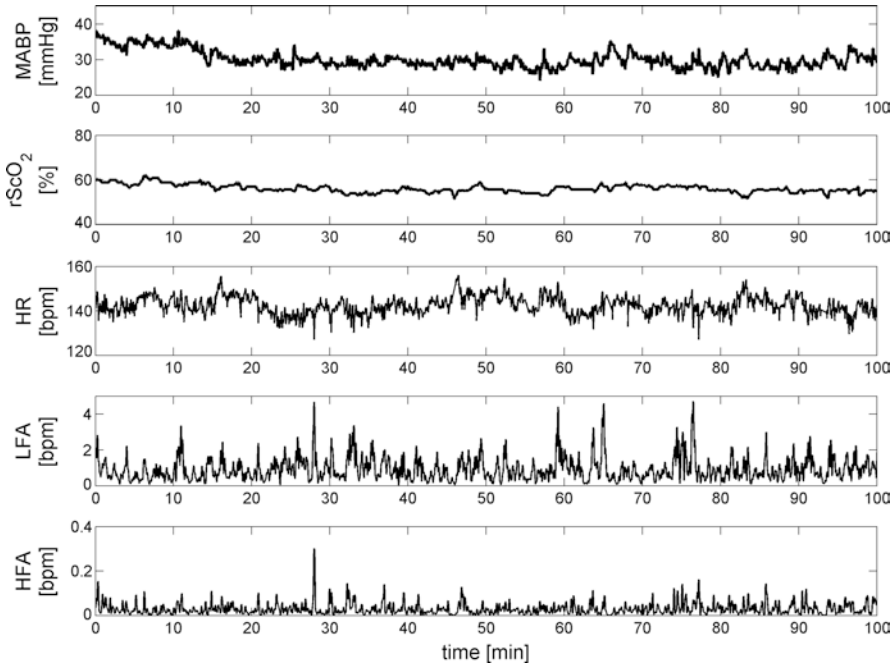

Fig. 23.1 Measurements of MABP, $rScO_2$, HR and the low frequency and high frequency autonomic control activity (LFA and HFA, respectively) for one control subject during the first day of life

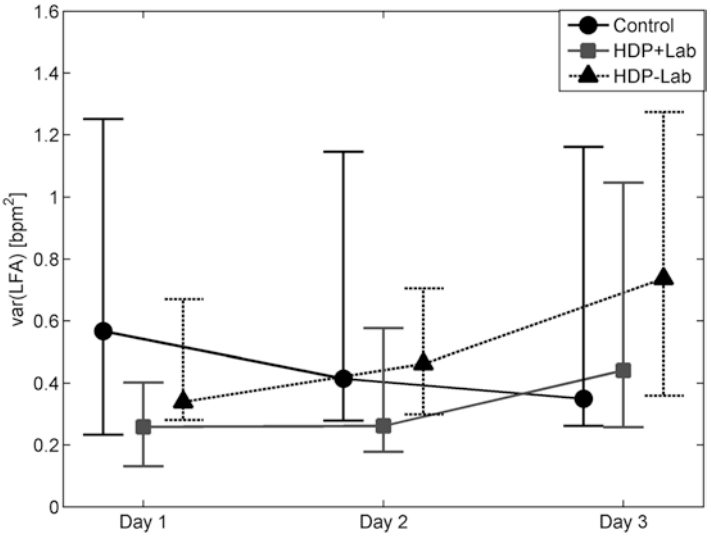

Fig. 23.2 Variance of the low frequency components in the autonomic control activity, var(LFA), for the three different populations during the first 3 days of life. The *solid circle*, *square* and *triangle* represent the median value for the control, HDP+Lab, and HDP−Lab populations, respectively. The *bar line* indicates the 25 and 75 % percentiles

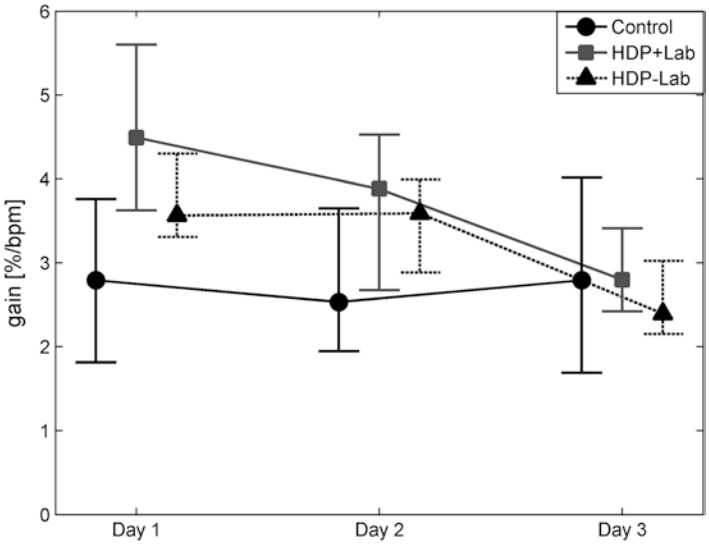

Fig. 23.3 Gain values indicating the status of the neurogenic mechanism for the three different populations during the first 3 days of life. The *solid circle*, *square* and *triangle* represent the median value for the control, HDP+Lab, and HDP−Lab populations, respectively. The *bar line* indicates the 25 and 75 % percentiles

Figure 23.3 shows the median, 25 %, and 75 % percentiles of the transfer function gain between LFA and $rScO_2$. When comparing the Control group with the HDP+lab group, significant differences were found during the first and second day ($p=0.001$, and $p=0.049$, respectively). In addition, when comparing the scores for the same population during the different days, in the HDP+Lab group the gain values during the first day and second day of life were significantly higher than the gain values during the third day of life ($p<0.001$ and $p=0.048$, respectively). Moreover, in the HDP−Lab group, the gain values during the first day and second day of life were significantly higher than the gain values during the third day of life ($p=0.009$, and $p=0.023$, respectively). No significant differences were found between the Control group and HDP−Lab group, or for the gain values in the Control group during the first 3 days of life.

4 Discussion and Conclusion

In this study we found that the activity in the low frequency and high frequency of the autonomic control, assessed by processing of the HR signals, was suppressed during the first day of life, with an increasing trend towards normality in the HDP+Lab group. In addition, we found that the gain values for the NM were higher during the first day of life in the same group, with a decreasing trend towards

normality. LFA, HFA and gain values in the HDP+Lab group were comparable to Controls by the third day of life.

Purkayastha et al. found that α_1 adrenergic receptor blockade reduced dynamic CA [4]. In [8], we performed a study with the same population analyzed in this paper; we found that the maternal use of labetalol impairs CA. In [8] the myogenic mechanism involved in CA was assessed by means of transfer function gain between MABP and $rScO_2$. By merging the results presented in this paper with the results published in [8], and using as support the results presented in [4], the effects of the maternal use of labetalol on the neonatal CA mechanisms can be summarized as follows: due to accumulation of labetalol in the neonates, the β and α_1 adrenergic receptors are blocked. On the one hand, β blockage produces as result a reduction of the influence of the autonomic nervous system in the heart, represented by a reduced LFA and HFA in the neonates. On the other hand, α_1 blockage reduces the muscular tone in the cerebral vascular bed, producing as a consequence vasodilation. Since the half-life time of labetalol in neonates is around 24 h [2], these effects are expected to disappear by the third day of life. Results provided in this paper indicate that as the LFA increases the NM is re-established, which corresponds to a concomitant reduction in α_1 and β adrenergic receptor blockade. In summary, in this paper we have found strong evidence that links the maternal use of labetalol with impaired CA caused by a vasodilation effect.

Acknowledgments Research supported by a postdoctoral mandate of the KU Leuven (BOF-KU Leuven) and: Research Council KUL: GOA MaNet, PFV/10/002 (OPTEC), IDO 08/013 Autism, several PhD/postdoc & fellow grants. Flemish Government: FWO: PhD/postdoc grants, projects: G.0427.10N (Integrated EEG-fMRI), G.0108.11 (Compressed Sensing) G.0869.12N (Tumor imaging) G.0A5513N (Deep brain stimulation); IWT: TBM070713-Accelero, TBM080658-MRI (EEG-fMRI), TBM110697-NeoGuard, PhD Grants; iMinds 2013; Flanders Care: Demonstratieproject Tele-Rehab III (2012–2014). Belgian Federal Science Policy Office: IUAP P719/(DYSCO, `Dynamical systems, control and optimization', 2012–2017); ESA AO-PGPF-01, PRODEX (CardioControl) C4000103224. EU: RECAP 209G within INTERREG IVB NWE programme, EU HIP Trial FP7-HEALTH/ 2007–2013 (n° 260777), EU MC ITN Transact 2012 # 316679 y carito linda.

References

1. Magee LA, Elran E et al (2000) Risks and benefits of beta-receptor blockers for pregnancy hypertension: overview of the randomized trials. Eur J Obstetr Gynecol Reproduct Biol 88(1):15–26
2. Haraldsson A, Geven W (1989) Half-life of maternal labetalol in a premature infant. Pharm Week Sci Ed 11(6):229–231
3. Peng T, Rowley A, Ainslie PN et al (2008) Multivariate system identification for cerebral autoregulation. Ann Biomed Eng 36(2):308–320
4. Purkayastha S, Saxena A et al (2012) α_1-Adrenergic receptor control of the cerebral vasculature in humans at rest and during exercise. Exp Physiol. doi:10.1113/expphysiol.2012.066118
5. Caicedo A and Van Huffel S (2010) Weighted LS-SVM for function estimation applied to artifact removal in biosignal processing. Proceedings of the 32nd annual international conference of the

IEEE Engineering in Medicine and Biology Society (EMBC 2010), Buenos Aires, Argentina, August 31–September 4, pp 988–991
6. Pichot V, Gaspoz JM et al (1999) Wavelet transform to quantify heart rate variability and to assess its instantaneous changes. J Appl Physiol 86:1081–1091
7. Schaffer L, Burkhardt T et al (2008) Cardiac autonomic balance in small-for-gestational-age neonates. Am J Physiol Heart Circ Physiol 294:H884–H890
8. Caicedo A, Thewissen L et al (2013) Effect of the maternal use of labetalol on the cerebral autoregulation in premature infants. Adv Exp Med Biol 789:105–111

Chapter 24
Development of a Near Infrared Multi-Wavelength, Multi-Channel, Time-Resolved Spectrometer for Measuring Brain Tissue Haemodynamics and Metabolism

Luke Dunne, Jem Hebden, and Ilias Tachtsidis

Abstract We present a novel time domain functional near infrared spectroscopy system using a supercontinuum laser allowing us to measure the coefficient of absorption and scattering of up to 16 multiplexed wavelengths in the near infrared region. This is a four detector system that generates up to 3 mW of light for each wavelength with a narrow 2–3 nm FWHM bandwidth between 650 and 890 nm; each measurement of 16 wavelengths per channel can be performed up to a rate of 1 Hz. We can therefore quantify absolute haemoglobin changes in tissue and are currently investigating which and how many wavelengths are needed to resolve additional chromophores in tissue, such as water and the oxidation state of cytochrome-c-oxidase.

Keywords NIRS • TRS • Cytochrome-c-oxidase • Supercontinuum laser • Haemoglobin

1 Introduction

Near infrared spectroscopy (NIRS) is commonly used for non-invasive measurements of the concentration changes of oxyhaemoglobin (HbO_2) and deoxyhaemoglobin (HHb) in tissue. Typically, continuous wave (CW) systems are used where a reflected/transmitted change in light attenuation through tissue is measured. If the scattering of light in the tissue is assumed constant and the differential path length factor estimated, the modified Beer–Lambert law can be used to calculate changes in chromophore concentrations [1]. CW systems have the benefit of requiring

The original version of this chapter was revised. An erratum to this chapter can be found at DOI 10.1007/978-1-4939-0620-8_49

L. Dunne (✉) • J. Hebden • I. Tachtsidis
Department of Medical Physics & Bioengineering, University College London, Malet Place Eng. Building, Gower Street, London WC1E 6BT, UK
e-mail: luke.dunne.10@ucl.ac.uk

H.M. Swartz et al. (eds.), *Oxygen Transport to Tissue XXXVI*, Advances in Experimental Medicine and Biology 812, DOI 10.1007/978-1-4939-0620-8_24,

relatively simple and inexpensive components, and can be made into easy to use compact devices.

Time-resolved spectroscopy operates by pulsing short picosecond pulses of light into the tissue through optical fibres. Fast single photon detectors and highly accurate timing electronics are then used to measure the time-of-flight (TOF) of each photon escaping the tissue surface. By repeating this TOF measurement many times a histogram called a temporal point spread function (TPSF) can be generated. We can obtain much more detailed information about the tissue from the TPSF than is possible using a CW technique, including mean path length and the absolute absorption and scattering coefficients [2].

Advances in technology have reduced the cost and size of the timing electronics needed for TOF measurements, making the technique reasonably accessible. Time-resolved systems are therefore becoming increasingly popular for tissue diagnostics.

In addition to haemoglobin, cytochrome-c-oxidase (CCO) the terminal electron accepter of the respiratory chain is a strong absorber of near infrared light [3]. The absorption spectrum of CCO depends on whether the enzyme is in its oxidised or reduced state; NIRS utilises this to measure the changes in its oxidation state (oxCCO). Although there is a clear optical signature in the difference between the reduced and oxidised forms of CCO, the measurement of oxCCO is considerably more difficult than haemoglobin as the concentration in tissue is of an order of magnitude less [4]. Therefore, in order to decouple the haemoglobin and oxCCO changes accurately it is necessary to enhance the spectroscopic resolution of the NIRS system and measure independently absorption and scattering in many wavelengths [5]. CW broadband [6] and recently hybrid broadband and frequency domain systems have been used to measure oxCCO [7]. Zhu and colleagues using computational techniques and data from a CW broadband system during severe hypoxic-ischaemia in piglets have found that not only is the number of wavelengths important but there is significant improvement in the estimation of chromophores if specific combinations of wavelengths are used [8].

In order to address these issues we have designed and built a near infrared time domain multiwavelength spectrometer using a supercontinuum laser source. This enables us to measure the coefficient of absorption (μ_a) and the reduced coefficient of scattering (μ_s') for 16 wavelengths between 650 and 890 nm. Here we describe the hardware of the system, discuss the theory of operation and present some preliminary results from the use of the system to monitor haemodynamic changes in the muscle during an arm cuff occlusion experiment.

2 Instrumentation and Methods

A custom designed supercontinuum laser (SC-480-6, Fianium, UK) with a repetition rate of 60 MHz producing white light over a range of 400–2,100 nm is used. The light is passed via optical fibre into a dual acoustic optic tunable filter (AOTF) system.

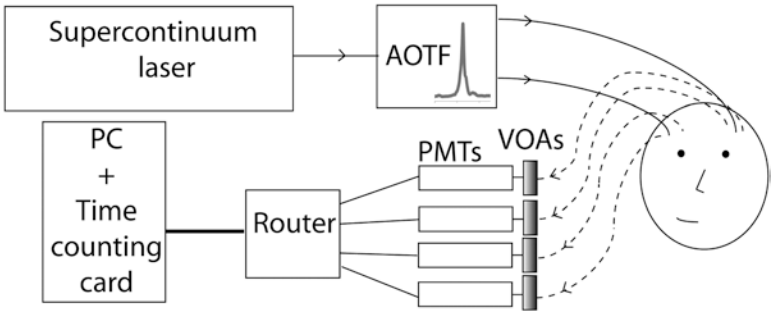

Fig. 24.1 Schematic of time resolved multiwavelength near infrared spectrometer. The light is tuned using acousto-optic tunable filters (AOTF) and detected with four photomultiplier tubes (PMTs) each protected by variable optical attenuators (VOAs)

As seen in Fig. 24.1, the light is collimated in free space and split by a polarising beam splitter. These beams are then passed through two AOTFs mounted at right angles to each other. As the devices only filter light in one plane this is the most efficient way of maximising the output power. The filters consist of piezo-electric transducers bonded to a birefringent quartz crystal that create a standing wave at a driven frequency. This modulates the refractive index of the crystal creating a phase grating, splitting the light from the laser into its different diffraction orders. A desired frequency can thus be directed and focused into an optical fibre. Custom AOTFs are used in the system to give narrow band filtered light of 2–3 nm FWHM in the region of 600–1,100 nm, these can provide an output power of 3 mW per wavelength.

For spectroscopy of tissue, each wavelength is multiplexed so that the TPSFs are averaged over the total desired measurement duration. The AOTF fast switches between 16 wavelengths at 160 Hz allowing time domain measurements with any combination of wavelengths between 650 and 890 nm. Two source fibres are used simultaneously when the detectors are placed on either hemisphere of the adult head. The light is passed into a 70 μm high NA single fibre which is attached to the patient via a custom designed 3D printed optode holder (Fig. 24.2d).

The light is collected by four glass fibre bundles (Loptek) with a diameter of 3 mm and is passed through custom made variable optical attenuators (VOAs) with a range of 0–3.7 OD to four Hamamatsu H7442-50P photomultiplier tube (PMT) modules. As the PMTs have a high gain the VOAs protect against over exposure during the experiment increasing the dynamic range. The signal from the PMTs is passed through a four way router (HRT-41) and the arrival time of each photon is measured with a Becker and Hickl SPC-130-EM time correlated single photon counting card.

The TSPF obtained in time resolved measurements contains information not only from the tissue but also the instrument itself. Therefore, a correction has to be made before the true optical properties of the tissue can be obtained. An instrument

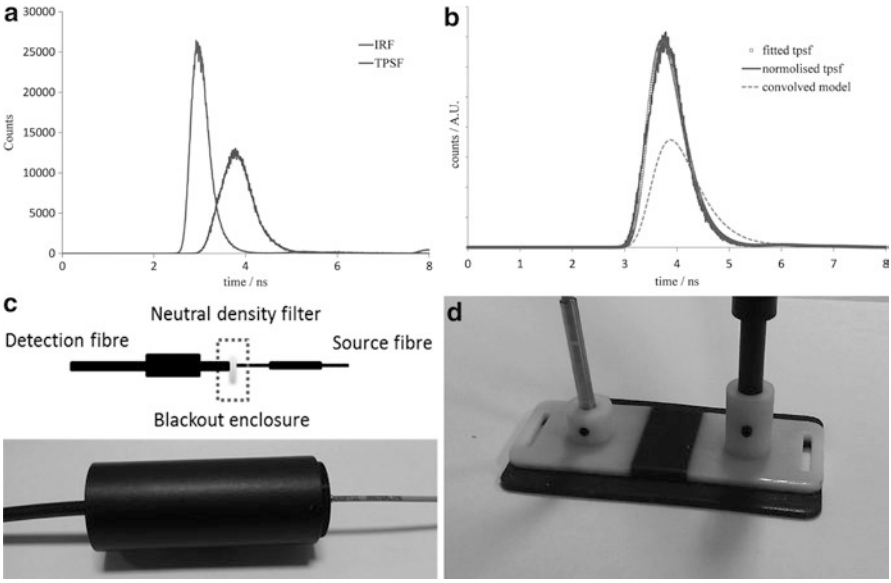

Fig. 24.2 (**a**) Raw TPSF (scaled) and IRF, (**b**) theoretical model convolved with the IRF, the real TPSF and fitted curve using the lsqcurvefit function returning μ_a and μ_s' as 0.0224 and 1.0655 mm^{-1}. (**c**) Method of measuring IRF. (**d**) 3D printed optode holder

response function (IRF, Fig. 24.2a) is recorded before each measurement using neutral density filters (Fig. 24.2c) in order to characterise the factors which contribute towards the broadening of the IRF (laser pulse, optical fibres, photon detectors, and timing electronics).

In order to quantify the optical properties of the tissue, the solution to the diffusion equation for a semi-infinite homogenous medium was convolved with the IRF (Fig. 24.2b) [9]. The convolved model is fitted to the measured TPSF using a non-linear curve fitting function and the absorption coefficient, μ_a and reduced scattering coefficient, μ_s' obtained. The Beer–Lambert law was then used to calculate chromophore concentrations [10]. To test the hardware and theory of operation we performed an arterial cuff-occlusion on the upper arm in one volunteer to induce flow and oxygenation changes in the forearm flexor muscles. The probe was placed on the forearm and measurements were done in reflection mode with source and detector fibres 3 cm apart. After 100 s of baseline measurements we inflated the cuff at 200 mmHg for 300 s, following cuff deflation we continue monitoring the muscle recovery for 5 min.

Data were collected every second for eight common wavelengths used in near infrared spectroscopy [690 750 761 790 801 834 850 870]. The average count rate over the experiment was kept at over 10^6/s to provide a good enough SNR for each wavelength. The diffusion equation model was then fitted to each TPSF to resolve absorption and scattering.

3 Results

Time series data for the changes in scattering and absorption for all eight wavelengths are shown in Fig. 24.3b, c, respectively. The standard deviation of the scattering and absorption during baseline was 0.0002 mm^{-1}. During the occlusion there were large changes in the absorption in some wavelengths, in particular there was a significant rise in absorption of 690 nm (sensitive to HHb) and significant decreases in 870 nm (sensitive to HbO_2). The scattering also demonstrated some hetereogeneous large changes and we are currently investigating whether these might be due to crosstalk or other factors. Finally, the absorption data were fitted for HbO_2 and HHb, the baseline total haemoglobin was 84.8 ± 0.3 μM l^{-1} and the absolute tissue saturation was 51.8 ± 0.5 %, comparable to previous studies in muscle [11]. Figure 24.3d shows the absolute concentration of oxyhaemoglobin and deoxyhaemoglobin during the study.

4 Conclusion

We have developed a four-channel NIR time-resolved spectrometer using a supercontinuum laser source and tunable narrow band filter system capable of measuring the TPSFs of 16 wavelengths between 650 and 890 nm every second in order to

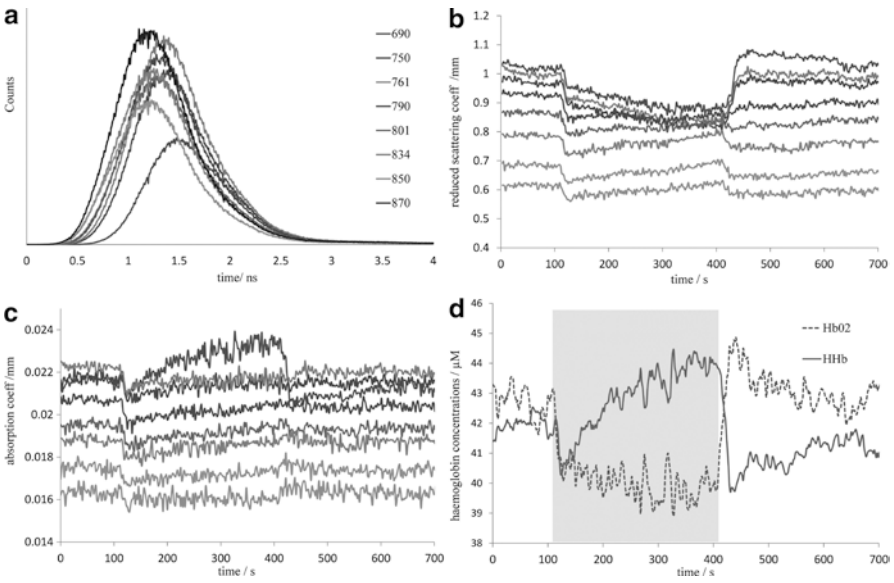

Fig. 24.3 (**a**) Example TPSFs for single measurement. (**b**) Reduced coefficient of scattering for eight wavelengths over course of cuff occlusion. (**c**) Coefficient of absorption for eight wavelengths over course of cuff occlusion. (**d**) Concentration changes for HbO_2 and HHb, cuff inflation time of 4 s

quantify the scattering and absorption independently for tissue. This offers us the ability to extract changes in haemoglobin and other chromophores in tissue such as CCO. We have presented preliminary results of the operation of the system for one channel and eight wavelengths during an arm cuff occlusion test. We are currently using the system to investigate wavelength selection optimisation for resolving HbO_2, HHb and oxCCO and will be carrying out a series of functional activation studies.

Acknowledgments The authors would like to thank The Wellcome Trust (088429/Z/09/Z) for the financial support of this work.

References

1. Delpy DT et al (1988) Estimation of optical pathlength through tissue from direct time of flight measurement. Phys Med Biol 33:1433–1442
2. Delpy DT (1997) Quantification in tissue near-infrared spectroscopy. Phil Trans Biol Sci 352:649–659
3. Lee J et al (2007) Non-invasive in vivo diffuse optical spectroscopy monitoring of cyanide poisoning in a rabbit model. Physiol Meas 28:1057–1066
4. Cooper CE (1997) Measurement of cytochrome oxidase redox state by near infrared spectroscopy. Opt Image Brain Funct Metab II:63–73
5. Matcher S (1995) Performance comparison of several published tissue near-infrared spectroscopy algorithms. Anal Biochem 227:54–68
6. Tisdall M et al (2007) Near-infrared spectroscopic quantification of changes in the concentration of oxidized cytochrome c oxidase in the healthy human brain during hypoxemia. J Biomed Opt 12:024002
7. Bevilacqua F et al (2000) Broadband absorption spectroscopy in turbid media by combined frequency-domain and steady-state methods. Appl Optics 39:6498–6507
8. T. Zhu et al (2012) Optimal wavelength combinations for resolving in-vivo changes of haemoglobin and cytochrome-c-oxidase concentrations with NIRS. Biomed Optics and 3-D Imaging, OSA Technical Digest. JM3A.6
9. Contini D et al (1997) Photon migration through a turbid slab described by a model based on diffusion approximation. I. Theory. Appl Optics 36:4587–4599
10. Matcher SJ et al (1994) Use of the water absorption spectrum to quantify tissue chromophore concentration changes in near-infrared spectroscopy. Phys Med Biol 39:177–196
11. Matcher SJ et al (1994) Absolute quantification of deoxyhaemoglobin concentration in tissue near infrared spectroscopy. Phys Med Biol 39:1295–1312

Chapter 25
Simulating NIRS and MRS Measurements During Cerebral Hypoxia-Ischaemia in Piglets Using a Computational Model

T. Hapuarachchi, T. Moroz, A. Bainbridge, S. Faulkner, D. Price, K.D. Broad, D. Thomas, E. Cady, X. Golay, Nicola Robertson, and Ilias Tachtsidis

Abstract We present a group analysis of the changes in cerebral haemodynamics, and the oxidation state of cytochrome-c-oxidase measured using broadband near-infrared spectroscopy (NIRS) and intracellular pH measured by phosphorous (^{31}P) magnetic resonance spectroscopy (MRS) during and after cerebral hypoxia-ischaemia (HI) in 15 piglets. We use a previously published computational model of cerebral metabolism in the piglet [1] to integrate these measurements and simulate HI. We successfully simulate changes in cellular metabolism including shifts in intracellular pH observed in the piglet brain during HI. In this process, we optimise physiological parameters in the model identified through sensitivity analysis (such as the rate of glucose metabolism and intracellular lactate concentration), to fit simulated and measured data. The model fits the data reasonably and suggests a 20 %

The original version of this chapter was revised. An erratum to this chapter can be found at DOI 10.1007/978-1-4939-0620-8_49

T. Hapuarachchi (✉)
CoMPLEX, University College London, London, UK

Department of Medical Physics and Bioengineering, University College London, Room 3.18, Malet Place Engineering Building, Gower Street, London WC1E 6BT, UK
e-mail: t.hapuarachchi@ucl.ac.uk

T. Moroz
CoMPLEX, University College London, London, UK

A. Bainbridge • D. Price • E. Cady
Medical Physics and Bioengineering, University College London Hospitals, London, UK

S. Faulkner • K.D. Broad • N. Robertson
Institute for Women's Health, University College London, London, UK

D. Thomas • X. Golay
Institute of Neurology, University College London, London, UK

I. Tachtsidis
Department of Medical Physics and Bioengineering, University College London, Room 3.18, Malet Place Engineering Building, Gower Street, London, WC1E 6BT, UK

H.M. Swartz et al. (eds.), *Oxygen Transport to Tissue XXXVI*, Advances in Experimental Medicine and Biology 812, DOI 10.1007/978-1-4939-0620-8_25,

drop in glucose consumption, a ~65 % increase in lactate concentration and ~35 % drop in the cerebral metabolic rate of oxygen ($CMRO_2$) during HI.

Keywords MRS • Neonatal • Mathematical modelling • Intracellular pH • Parameter optimisation

1 Introduction

Piglets are often used in pre-clinical studies to investigate the effect of physiological intra-partum cerebral HI in mammalian neonates. Using a mathematical and computational model of cerebral metabolism and blood flow, we aim to better understand the complex changes in the brain during these events. The neonatal piglet brain computational model (BrainPiglet) [1] incorporates and simulates NIRS and MRS measurements. These two non-invasive methods are used to monitor brain tissue oxygenation, haemodynamics and metabolism. BrainPiglet was developed from an earlier adult brain model (BrainSignals) [2]—extended to simulate MRS and adapted to the piglet brain. We have recently expanded our model to simulate intracellular pH, considered to be an important biomarker of cerebral pathology [3]. Brain functions are sensitive to changes in pH as the latter affects protein structure. We further optimise physiological parameters in our model to produce the best simulations that fit the measurements. This is vital when using the model with clinical data as biological parameters can vary with alterations in cerebral pathology. These modifications can convey some information about the physiological changes that occur during HI. In this paper we present averaged measurements of cerebral oxygenation, oxidised cytochrome-c-oxidase (oxCCO) level and intracellular pH from 15 piglets and compare these with optimised simulations from our BrainPiglet model.

2 Experimental Methods and Protocol

In this study, 15 1-day-old piglets were mechanically ventilated and anaesthetised. Inflatable occluders were surgically inserted around the carotid arteries. Normal levels of arterial oxygen and carbon dioxide, blood glucose and heart rate were maintained. Experiments were under UK Home Office Guidelines (Animals [Scientific Procedures] Act, 1986) and approved by the Institute of Neurology, University College London. Changes (Δ) in concentrations of oxy- and deoxy-haemoglobin (ΔHbO_2, ΔHHb) and brain oxCCO (ΔoxCCO) were monitored using broadband NIRS. We used ^{31}P-MRS to measure changes in concentrations of metabolites such as inorganic phosphate (Pi), phosphocreatine (PCr) and nucleotide triphosphate (NTP; mainly adenosine triphosphate (ATP)). We also estimated intracellular pH using the ^{31}P–MRS chemical shifts of Pi and phosphoethanolamine (PEt) [4]. Comparable with normal clinical practice, we continuously recorded

systemic variables: arterial blood pressure (P_a), arterial oxygen saturation (SaO_2), breathing rate and heart rate. Firstly baseline ^{31}P-MRS and NIRS were recorded. Transient HI was then induced (for ~1 h) by inflating the occluders and reducing fractional inspired oxygen (FiO_2) to 12 % from a normal value of 21 %. Once β-NTP had reduced to ~40 % of baseline, FiO_2 was gradually returned to normal. This titration was completed over 10–20 min and the carotid occluders were then released. ^{31}P-MRS and NIRS were acquired simultaneously every 1 min throughout HI and for a further ~2 h to monitor recovery from HI [4].

3 Group Analysis of Measurements

Measurements from experiments in 15 piglets that recovered following HI are presented in this paper. We examined ΔHbO_2, ΔHHb and ΔoxCCO and variations in intracellular pH. We used the difference between ΔHbO_2 and ΔHHb as a guide to manually divide the data into five phases: (i) baseline, (ii) start of HI to start of FiO_2 titration, (iii) FiO_2 titration period, (iv) release of occluders and recovery, and (v) post recovery from HI. Each phase was subsequently divided into ten sections and data in each section were averaged. The mean of each section across all piglets was calculated. This process was repeated for each measurement variable. The time period of each phase was also averaged across all piglets (Fig. 25.1a).

4 Model

BrainPiglet is focused on the physiology of the brain [1], and uses differential equations and algebraic relations to simulate cerebral metabolic activity. This model is complex, incorporating ~100 parameters and ~25 variables. It uses P_a, SaO_2, arterial carbon dioxide partial pressure (P_aCO_2) and the time of carotid occlusion as inputs to simulate NIRS measurements, such as ΔHbO_2, ΔHHb and ΔoxCCO, and MRS measurements such as Pi, PCr, ATP levels and intracellular pH. It also predicts changes in unmeasured quantities such as $CMRO_2$, CBF and intracellular lactate concentration. A simple schematic of the model is in Fig. 25.1b.

5 Results

Averaged data together with standard deviations are presented in Fig. 25.2. Averaged SaO_2 and Pa were input into the model. $PaCO_2$ was not recorded, however, as the piglets were ventilated, we assumed $PaCO_2$ remains constant at 40 mmHg. We used the Morris method [5] to identify the three most influential parameters for ΔHbO_2,

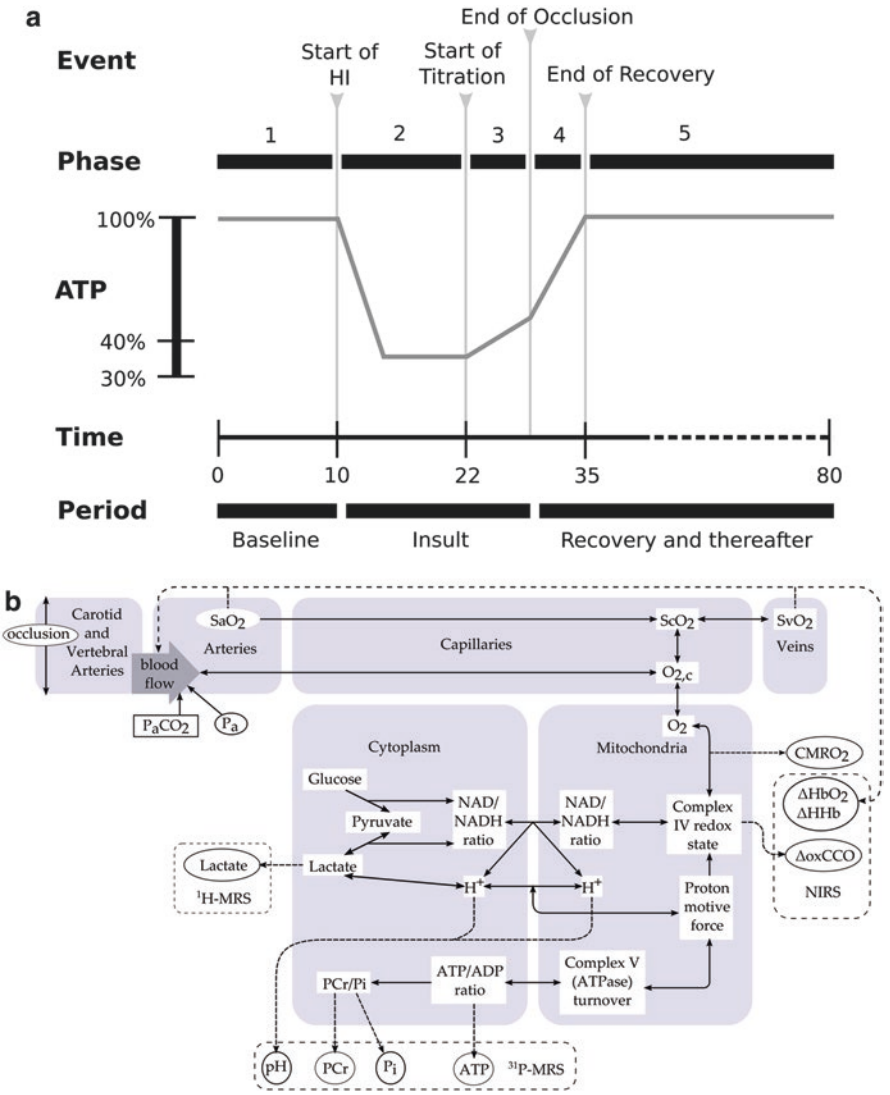

Fig. 25.1 (**a**) Method for averaging data from 15 piglets—the signals were manually divided into five phases. (**b**) Schematic of the BrainPiglet model

ΔHHb, ΔoxCCO and pH. These parameters were then optimised using the PSwarm method [6] to better fit the model to the data. Optimised parameters are presented in Table 25.1 with percentage change compared to their normal values. Also included is the Morris method ranking of influence for the variables we are investigating (1 = most influential). Optimised model simulations are presented in Fig. 25.2. Simulated $CMRO_2$ and cerebral blood flow (CBF) are illustrated in Fig. 25.3.

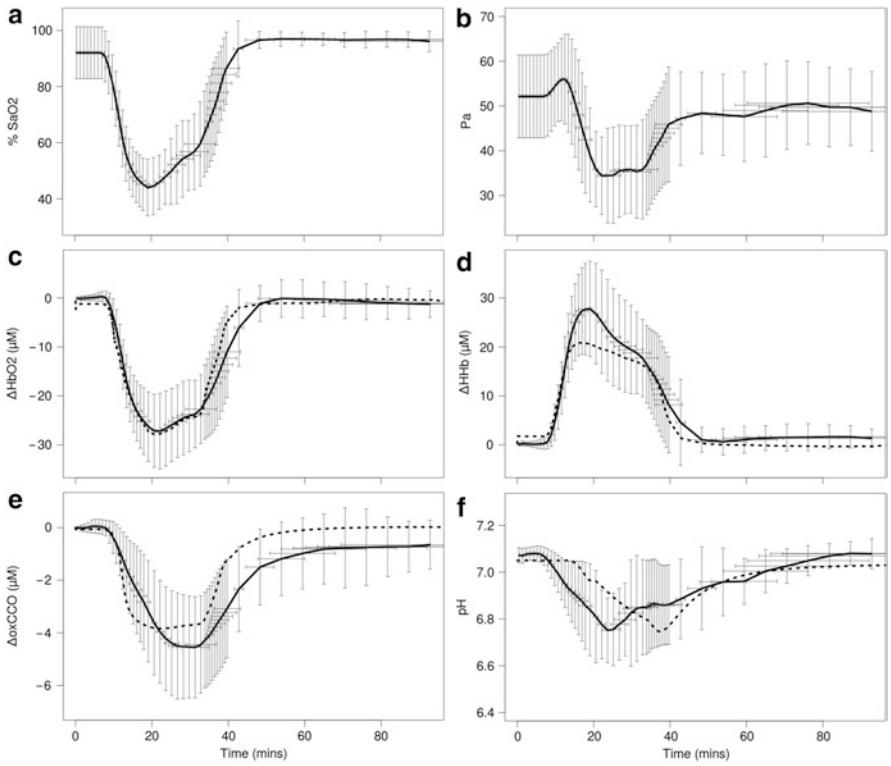

Fig. 25.2 Averaged arterial oxygen saturation (SaO_2, **a**) and blood pressure (P_a, **b**) measurements are used as inputs to the model; Averaged NIRS and MRS measurements (*solid line*) compared with modelled results (*dotted line*): oxyhaemoglobin (ΔHbO_2, **c**), deoxyhaemoglobin (ΔHHb, **d**), oxidised cytochrome-c-oxidase (ΔoxCCO, **e**) and intracellular pH (**f**). HI starts at ~10 min

Table 25.1 Optimised parameter values and their influence ranked by the Morris method

Parameter	Optimised value	Percentage change (%)	ΔHbO_2 rank	ΔHHb rank	ΔoxCCO rank	pH rank
Cytochrome-c-oxidase concentration	0.007 mM	+218			1	
Normal cytoplasm lactate concentration	5.00 mM	+66.7			3	2
Normal blood total haemoglobin	6.35 mM	+17.6	1	1	7	6
Normal arterial blood pressure	53.7 mmHg	+7.40	7	3		
Normal extra-mitochondrial pH	7.05	+0.007			6	1
Autoregulation constant	1.00	No change	3	4		
Special radius in the elastic tension relationship	0.0117 cm	−7.14	2	3		
Normal oxidised fraction of Cu_A	0.678	+1.19			2	
Normal blood fraction flowing through carotid arteries	0.64	−20.0		2	5	5
Normal glucose metabolism rate	0.00352 mM/s	−20.0			8	3

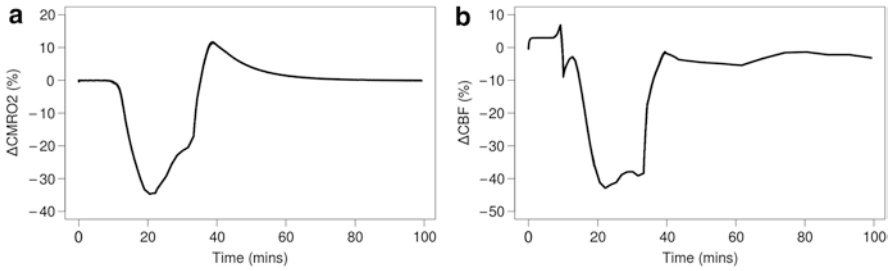

Fig. 25.3 Modelled changes in cerebral metabolic rate of oxygen ($\Delta CMRO_2$, **a**) and cerebral blood flow (ΔCBF, **b**). HI starts at ~10 min

6 Discussion

NIRS and MRS measurements offer a valuable insight into the haemodynamic and metabolic events that occur during cerebral HI. Although some large and significant standard deviations (Fig. 25.2) were observed in the measurements, especially during HI, the general trend in these signals is consistent. During HI we observe the expected drop in SaO_2 and ΔHbO_2 and rise in ΔHHb. These concentrations recover very well post HI and return to baseline levels. ΔoxCCO decreases during HI, but does not recover so well and fails to return to the baseline after the insult. Just after the start of HI there is a slight rise in Pa before the major drop during HI. Pa also exhibits significant variation during recovery. While the drop in pH during HI is consistent in all the piglets monitored, there is a lot of variation during both recovery and in the time at which recovery commences. In two piglets we observed an increase in the total haemoglobin concentration during HI. This may be due to back circulation of blood through the vertebral arteries during carotid occlusion. However, these piglets exhibited the same variations in the other metabolic quantities we monitored.

We optimised model parameters to get the best fit of model simulations to in-vivo measurements. We decreased the rate of glucose metabolism by 20 % and increased the normal concentration of cytoplasmic lactate by ~65 %. This suggests an increase in anaerobic respiration as expected during HI. We significantly increased the concentration of oxCCO. However, the normal model oxCCO concentration (0.0022 mM) is quite low and will be updated in future versions of the model. We increased the normal total haemoglobin concentration in blood and decreased the fraction of blood flowing through carotid arteries. This may well occur during HI as the carotid arteries are occluded and the vertebral arteries operate at full capacity. The autoregulation constant in the model represents the capacity of the brain to autoregulate, and ranges from 1.0 in a normal brain to 0.0 in the extreme case. The autoregulation capacity of the piglet remained at 1.00 with optimisation, suggesting that these piglets that recovered following HI are able to autoregulate. Small changes in other parameter values were insignificant. ΔHbO_2 and ΔHHb are simulated very well during HI. While ΔoxCCO compares well with the measurement, a steeper drop in ΔoxCCO is modelled. The model also simulates a better recovery to baseline than observed in vivo. Modelled intracellular pH reaches an acidity during HI similar to that observed in the

piglets, but has a more delayed response. This is caused by a buffering mechanism in the model which we are now investigating. Simulated $CMRO_2$ shows ~35 % drop during HI (Fig. 25.3a). This is contradictory to the long-term drop in $CMRO_2$ observed in piglets by others [7], suggesting that the current dynamics of our model do not account for the persistent reduction. The model has not taken into account cell death during HI, which may contribute to this effect. Simulated CBF also shows ~40 % drop during HI, and a recovery back to baseline (Fig. 25.3b). We must note that parameter optimisation was conducted on measurements over the complete experiment. However, as the physiological state of the brain before and after HI is quite different, we expect, and are currently attempting, to find distinct sets of parameters that suit each stage of the experiment. This will give us a better insight into the physiological changes that occur between these stages. Further, the distribution of the group data was not taken into account in the simulations.

The BrainPiglet model combines our knowledge of cerebral metabolism and experimental data to explore the effect of HI on brain physiology. It enables informed and practical predictions about patient outcome. The model is able to satisfactorily emulate changes in pH and concentrations of haemoglobin and oxCCO observed during HI. However, while recovery of cerebral haemodynamics and oxygenation is predicted in the model, the metabolic response is not well simulated. This may result from the differing spatial distribution and sensitivity of NIRS and MRS signals—involving cortical and deep white matter, respectively—and the presence of blood in addition to brain tissue in the interrogated tissue volume. Model simulations are also likely to improve with the optimisation techniques outlined above, which will provide more detailed information.

Acknowledgments We would like to thank the Wellcome Trust (088429/Z/09/Z) for financial support of this work. The first author is supported by her doctoral centre CoMPLEX, UCL.

References

1. Moroz T, Banaji M, Robertson NJ et al (2012) Computational modelling of the piglet brain to simulate near-infrared spectroscopy and magnetic resonance spectroscopy data collected during oxygen deprivation. J R Soc Interface. doi:10.1098/rsif.2011.0766
2. Banaji M, Mallet A, Elwell C et al (2008) A model of brain circulation and metabolism: NIRS signal changes during physiological challenges. PLoS Comput Biol 4(11):e1000212. doi:10.1371/journal.pcbi.1000212
3. Robertson NJ, Cowan FM, Cox IJ et al (2002) Brain alkaline intracellular pH after neonatal encephalopathy. Ann Neurol 52(6):732–742
4. Cady EB, Iwata O, Bainbridge A et al (2008) Phosphorus magnetic resonance spectroscopy 2 h after perinatal cerebral hypoxia-ischemia prognosticates outcome in the newborn piglet. J Neurochem 107(4):1027–1035
5. Morris MD (1991) Factorial sampling plans for preliminary computational experiments. Technometrics 33(2):161–174
6. Vaz AIF, Vincente LN (2007) A particle swarm pattern search method for bound constrained global optimization. J Global Optim 39:197–219
7. Tichauer KM et al (2005) Near-infrared spectroscopy measurements of cerebral blood flow and oxygen consumption following hypoxia-ischemia in newborn piglets. J Appl Physiol 100:850–857

Chapter 26
Analysis of Slow Wave Oscillations in Cerebral Haemodynamics and Metabolism Following Subarachnoid Haemorrhage

David Highton, Arnab Ghosh, Ilias Tachtsidis, Clare Elwell, and Martin Smith

Abstract Aneurysmal subarachnoid haemorrhage (SAH) causes the greatest loss of productive life years of any form of stroke. Emerging concepts of pathophysiology highlight early abnormalities of microvascular function, including impaired autoregulation of cerebral blood flow and flow-metabolism coupling, as key causes of cerebral ischaemia and poor outcome. Near infrared spectroscopy (NIRS) is a non-invasive optical technique which may help identify cerebral microvascular dysfunction. The aim of this research is to investigate the status of flow-metabolism coupling by examining phase relationships between NIRS-derived concentrations of oxy-haemoglobin ([HbO_2]), deoxy-haemoglobin ([HHb]) and cytochrome c oxidase oxidation ([oxCCO]). Eight sedated ventilated patients with SAH were investigated. A combined NIRS broadband and frequency domain spectroscopy system was used to measure [HbO_2], [HHb] and [oxCCO] alongside other multimodal neuromonitoring. Wavelet analysis of phase relationships revealed antiphase [HbO_2]-[oxCCO] and in-phase [HbO_2]-[HHb] oscillations between 0.1Hz-0.01Hz consistent with compromised flow-metabolism coupling. NIRS derived variables might offer unique insights into microvascular and metabolic dysfunction following SAH, and in the future identify therapeutic windows or targets.

Keywords Subarachnoid haemorrhage • Near infrared • Cerebral autoregulation • Ischaemia • Flow-metabolism coupling

---

The original version of this chapter was revised. An erratum to this chapter can be found at DOI 10.1007/978-1-4939-0620-8_49

D. Highton (✉)
Neurocritical Care, University College Hospitals, Queen Square, London, UK
e-mail: d.highton@ucl.ac.uk

A. Ghosh • M. Smith
Neurocritical Care, University College Hospitals, Queen Square, London, UK

I. Tachtsidis • C. Elwell
Medical Physics & Bioengineering, University College London, Malet Place, London, UK

H.M. Swartz et al. (eds.), *Oxygen Transport to Tissue XXXVI*, Advances in Experimental Medicine and Biology 812, DOI 10.1007/978-1-4939-0620-8_26,

1 Introduction

Aneurysmal subarachnoid haemorrhage (SAH) causes the greatest loss of productive life of all forms of stroke. Only 30 % of patients escape death or major complication [1]. Cerebral aneurysm rupture and extravasation of blood under high pressure leads to immediate and delayed neurological pathology. Emerging evidence highlights the critical role that early abnormalities in microvascular function may contribute to ischaemia; these may manifest as impaired autoregulation of cerebral blood flow (CBF) against blood pressure changes, and deranged flow-metabolism coupling [2].

Animal models of SAH fail to replicate human pathophysiology. Near infrared spectroscopy (NIRS) is a promising non-invasive optical technique which characterises cerebral haemodynamics and metabolism non-invasively, and thus may have widespread applicability investigating human pathophysiology following SAH. NIRS-derived concentration changes of oxy-haemoglobin ([HbO_2]) and deoxy-haemoglobin ([HHb]) reflect cerebral haemodynamics and may identify impaired pressure autoregulation, associated with vascular dysfunction and ischaemia [3].

Cytochrome c oxidase, the terminal electron acceptor in the mitochondrial respiratory chain reflects the balance between oxygen supply and demand, and its oxidation status [oxCCO] may be measured using NIRS [4, 5]. Intact flow-metabolism coupling results in a characteristic pattern of changes and oscillations in [HbO_2], [HHb] and [oxCCO] [6]. Typically this results in greater flow than is required by the metabolic demands leading to an increase in [HbO_2], [oxCCO] and fall in [HHb], a pattern which may be altered in pathology or with variation in flow-metabolism coupling [6, 7]. Slow oscillations (<0.1 Hz) of cerebral haemodynamics and metabolism are seen in neuromonitoring of brain injured patients and the frequency characteristics and phase relationships of these oscillations may be used to characterise cerebral haemodynamics and metabolism.

We hypothesise that the normal [HbO_2], [HHb] and [oxCCO] phase relationships will be disturbed in SAH patients, indicating impaired flow-metabolism coupling. The aim of this study is to characterise slow oscillations in cerebral haemodynamics and metabolism to investigate microvascular function (cerebral autoregulation and flow-metabolism coupling) within the first 48 h following SAH, where key interventions might be delivered to avoid or minimise ischaemia.

2 Methods

Analysis was performed on data from sedated, ventilated patients with SAH, a subset of patients from a larger study investigating [oxCCO] changes in brain injury. Patient characteristics and measured variables were summarised as mean (standard deviation) or median (interquartile range). Data were gathered over a 3-h period, within 48 h of ictus, following institutional Research Ethics Committee approval and representative consent.

Monitoring used for analysis included: invasive arterial blood pressure, transcranial Doppler measured flow velocity in the middle cerebral artery (Vmca; DWL DopplerBox, Compumedics, Germany), brain tissue oxygen tension (PbrO2; Licox, Integra Neurosciences, USA) and NIRS (hybrid optical spectrometer).

The hybrid optical spectrometer comprises two channels capable of simultaneous broadband and frequency domain spectroscopy, optimised for detection of [oxCCO] in brain injury, and has been described in detail elsewhere [4, 8]. [HbO_2], [HHb] and [oxCCO] were calculated using the UCLn algorithm, fitting NIR attenuation 780–900 nm. The differential pathlength factor (DPF) was calculated from absorption and scattering coefficients derived by the frequency domain system. Only concentration changes measured ipsilateral to invasive monitoring at 35 mm source detector separation was considered.

Transient artefacts were removed by interpolation. Systemic data, PbrO2 and Vmca, were synchronised (using a synchronisation signal at start and finish) and resampled to 1 Hz for analysis (*resample*, Matlab, Mathworks). NIRS data were analysed at its native sampling frequency (0.31 Hz). Autoregulation indices were derived from a moving continuous Pearson correlation coefficient between 30 epochs of 10 s time averaged data between arterial blood pressure and neuromonitoring (Vmca and $PbrO_2$), yielding the mean velocity index, and oxygen reactivity index respectively, as surrogate markers of pressure autoregulation and impaired vascular function [9]. These validated indices of autoregulation suggest impaired autoregulation when >0.3. NIRS phase difference and coherence measurements were calculated using a wavelet based approach (complex Morlet wavelet, Matlab, Mathworks) measuring the instantaneous phase difference and wavelet coherence [10] from scales 1 to 100 (frequency 0.3–0.003 Hz).

3 Results

Eight patients were studied, their characteristics and autoregulation indices are summarised in Table 26.1 and monitored variables in Table 26.2. Three patients showed evidence of impaired pressure autoregulation indicated by an oxygen reactivity index and/or mean velocity index above 0.3.

Table 26.1 Patients characteristics and autoregulation indices

Patient characteristics	
Age in years (range)	50.3 (23–74)
Sex	7 female, 1 male
Median Glasgow Coma Scale (IQR)	5.5 (3–8)
Mean Oxygen reactivity index (SD)	0.03 (0.21)
Mean velocity index (SD)	0.16 (0.15)

Table 26.2 Patients monitored variables

Monitored variables	Mean (SD)
Mean arterial pressure (mmHg)	93 (8)
PbrO2 (mmHg)	26 (12)
Vmca (cm/s)	56 (18)

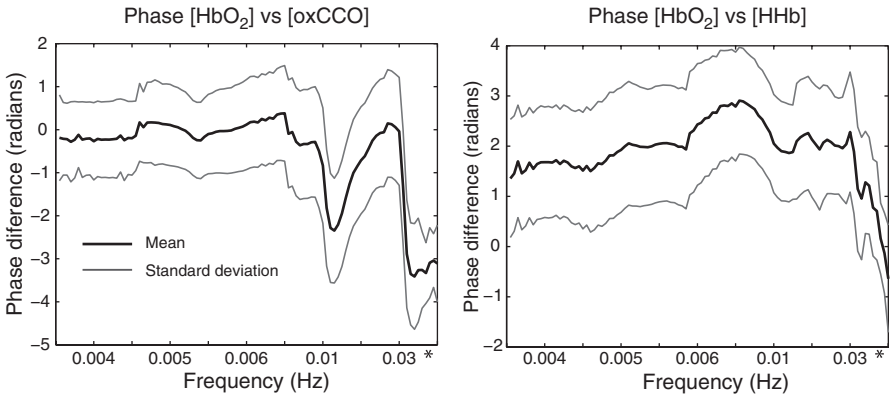

Fig. 26.1 These graphs demonstrate the group phase differences. Specific features are apparent between 0.1 and 0.01 Hz with anti phase [HbO_2] versus [CCO] activity. The *asterisk* marks 0.1 Hz. The pseudofrequency of wavelet scale is shown resulting in a non-linear x-axis

Phase difference, [HbO_2] versus [HHb] and [HbO_2] versus [oxCCO] are displayed in Fig. 26.1, demonstrating a key feature in the band 0.1–0.01 Hz where [oxCCO] approaches being antiphase to [HbO_2]. In contrast [HHb] is in phase with [HbO_2] at 0.1 Hz developing a phase lag (towards 1 radian) below 0.02 Hz. The time course of coherence and phase difference in a representative patient are displayed in Fig. 26.2.

4 Discussion

We have demonstrated evidence of impaired microvascular control of CBF in this group of critically ill patients with SAH, manifest as: (1) Impaired pressure autoregulation in 3/8 patients, and (2) NIRS phase relationships which suggest impaired flow-metabolism coupling of CBF to energy requirements.

Impaired pressure autoregulation is increasingly described in association with poor outcome following SAH, but it remains unclear whether this is due to ischaemia consequent to impaired autoregulation, or if this impairment is just a symptom of dysfunctional injured cerebral tissue [3]. The phase relationships between NIRS variables at 0.1 Hz are consistent with those observed in experimental models of ischaemia, and cortical spreading depression [10]. [oxCCO] reflects the dynamics of mitochondrial electron transport and presents a unique window into subcellular energetics. The observed occurrence of antiphase oscillations with [HbO_2] are consistent with suboptimal oxygen delivery in response to metabolic demand; this has previously been observed in animal models of cortical spreading depression [10], but also human functional activation [6, 11]. Crucially ischaemia results from failure of energy supply or utilisation—so the measurement of [oxCCO], a measure of cerebral oxygen utilisation, may provide valuable additional information over and above markers of haemodynamics.

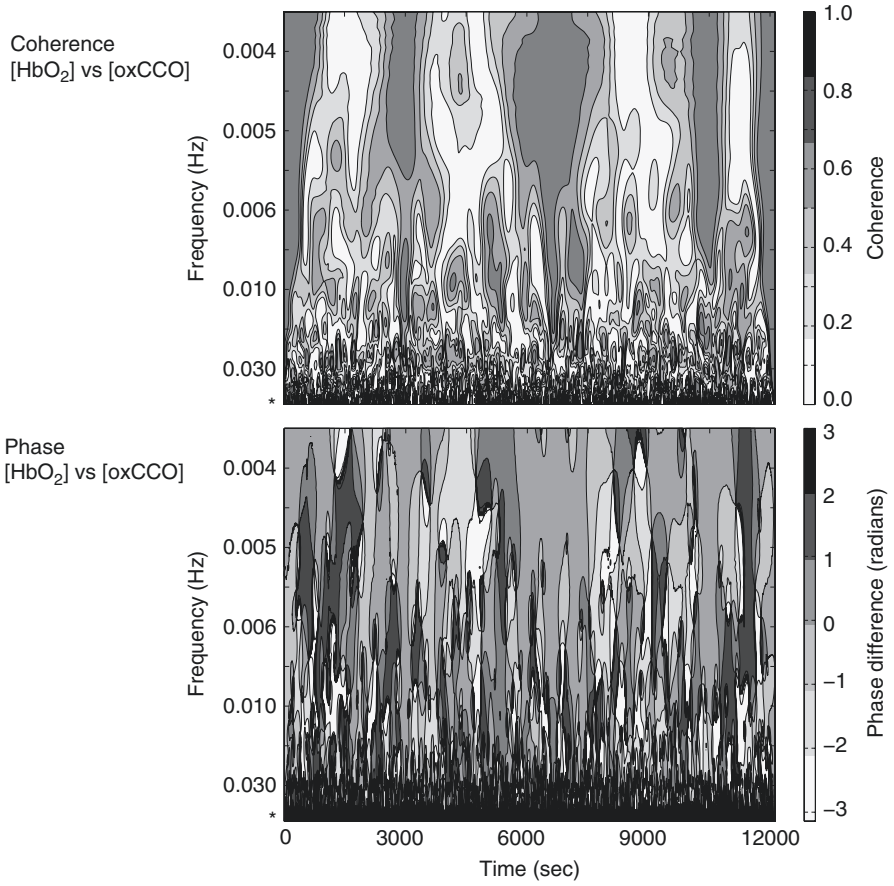

Fig. 26.2 Wavelet coherence and phase difference are shown for [HbO_2] versus [CCO] in an individual patient. Time is represented on the x axis and a non-linear representation of frequency on the y axis. Again a band of interest can be observed between 0.1 Hz (indicated by *asterisk*) and 0.03 Hz. A band of coherence in this frequency region (*dark grey*) indicates a strong relationship between the signals. The phase difference plot shows similar findings to the group data in this region—around 0.1 Hz [HbO_2] is antiphase to [CCO] indicated by *black*/*dark-grey*, at 0.01 Hz this changes to predominately *light grey* indicating phase difference close to 0. Some dynamic variation over time can be observed; however, these relationships remain considerably consistent over the 3-h period. The pseudofrequency of wavelet scale is shown resulting in a non-linear y-axis

The hybrid optical spectrometer has been specifically optimised for the detection of [oxCCO] in adult brain injury, combining broadband spectroscopy to aid separation of chromophores and frequency domain spectroscopy to calculate DPF. This robust solution reduces concerns that oscillations observed in [oxCCO] might be due to variation in DPF or crosstalk. Importantly we have observed distinct patterns of phase-relationship between [HbO_2], [HHb] and [oxCCO], and this adds weight to the argument that [oxCCO] is a distinct signal of relevance. However, quantifying

oscillations at 0.1 Hz is at the absolute limit of this device as the sampling period of each reading is 3.2 s. Wavelet methods of analysis also trade off between frequency resolution and time resolution, but are superior in that they discriminate important changes in the time domain. Despite these limitations the phase characteristics appear in broad bands, particularly within 0.1–0.01 Hz. Thus, we believe that the NIRS instrumentation and the analysis techniques described are both sufficient to demonstrate the key features of interest.

NIRS oscillations following SAH may reflect impaired autoregulation and flow metabolism coupling—consistent with proposed microvascular dysfunction mediated via nitric oxide or spreading cortical depression [2]. Monitoring the evolution of microvascular dysfunction in the first 48 h following SAH might identify pathological processes that allow for timely and targeted intervention [2]. Further work is required to elucidate the exact pathophysiology underpinning the haemodynamic and metabolic oscillations we have observed, and refine NIRS techniques in the optically complex injured brain. Importantly previous analyses of NIRS oscillations largely reflect vasomotion and haemodynamics [12, 13]. Monitoring [oxCCO] has unique potential to define metabolic compromise in SAH, and might be used in the future to guide neuroprotective strategies.

Acknowledgments This work was undertaken at University College London Hospitals and partially funded by the Department of Health's National Institute for Health Research Centres funding scheme via the UCLH/UCL Biomedical Research Centre. Support has also been provided by the Medical Research Council and IT was supported by Wellcome Trust (088429/Z/09/Z). The authors are indebted to the medical and nursing staff of the Neurocritical Care Unit at the National Hospital for Neurology & Neurosurgery, and to the study patients and their families.

References

1. Feigin VL, Lawes CM, Bennett DA et al (2009) Worldwide stroke incidence and early case fatality reported in 56 population-based studies: a systematic review. Lancet Neurol 8:355–369
2. Sehba FA, Pluta RM, Zhang JH (2010) Metamorphosis of subarachnoid hemorrhage research: from delayed vasospasm to early brain injury. Mol Neurobiol 43:27–40
3. Budohoski KP, Czosnyka M, Smielewski P et al (2012) Impairment of cerebral autoregulation predicts delayed cerebral ischemia after subarachnoid hemorrhage: a prospective observational study. Stroke 43:3230–3237
4. Kolyva C, Ghosh A, Tachtsidis I et al (2014) Cytochrome c oxidase response to changes in cerebral oxygen delivery in the adult brain shows higher brain-specificity than haemoglobin. NeuroImage, 85(0), 234–244. doi:10.1016/j.neuroimage.2013.05.070
5. Tisdall MM, Tachtsidis I, Leung TS et al (2008) Increase in cerebral aerobic metabolism by normobaric hyperoxia after traumatic brain injury. J Neurosurg 109:424–432
6. Kolyva C, Tachtsidis I, Ghosh A et al (2012) Systematic investigation of changes in oxidized cerebral cytochrome c oxidase concentration during frontal lobe activation in healthy adults. Biomed Opt Express BOE 3:2550–2566
7. Yin C, Zhou F, Wang Y et al (2013) Simultaneous detection of hemodynamics, mitochondrial metabolism and light scattering changes during cortical spreading depression in rats based on multi-spectral optical imaging. Neuroimage 76:70–80

8. Tachtsidis I, Leung TS, Ghosh A, Smith M, Cooper CE, Elwell CE (2010) Multi-wavelength, depth resolved, scattering and pathlength corrected in vivo near-infrared spectroscopy of brain tissue. Optical Society of America topical meeting: biomedical optics (BIOMED) (paper BTuB7), 11–14 Apr, Miami, FL. doi:10.1364/BIOMED.2010.BTuB7
9. Diedler J, Czosnyka M (2009) Merits and pitfalls of multimodality brain monitoring. Neurocrit Care 12:313–316
10. Torrence C, Compo GP (1998) A practical guide to wavelet analysis. Bull Am Meteorol Soc 79:61–78
11. Obrig H, Neufang M, Wenzel R et al (2000) Spontaneous low frequency oscillations of cerebral hemodynamics and metabolism in human adults. Neuroimage 12:623–639
12. Trajkovic I, Reller C, Wolf M (2012) Modelling and filtering of physiological oscillations in near-infrared spectroscopy by time-varying Fourier series. Adv Exp Med Biol 737:307–313
13. Caicedo Dorado A, De Smet D, Vanderhaegen J et al (2011) Impaired cerebral autoregulation using near-infrared spectroscopy and its relation to clinical outcomes in premature infants. Adv Exp Med Biol 701:233–239

Chapter 27
Effects of Enriched Environment on Hippocampal Neuronal Cell Death and Neurogenesis in Rat Global Ischemia

Tomokazu Kato, Takashi Eriguchi, Norio Fujiwara, Yoshihiro Murata, Atsuo Yoshino, Kaoru Sakatani, and Yoichi Katayama

Abstract Enriched environments reportedly show neuroprotective effects. Here, we evaluated the effect of an enriched environment prior to cerebral ischemia on neuronal cell death and neurogenesis in rats. Male SD rats were housed under standard conditions (SC) or in an enriched environment (EE), then subjected to global ischemia. The Y-maze test and novel object cognition test were used to evaluate cognitive function before and after ischemia. At 7 days post-ischemia, we evaluated hippocampal neuronal cell death with Fluoro-Jade B staining and neurogenesis with BrdU staining. Phosphorylated cAMP response element-binding protein (phospho-CREB) was also evaluated immunohistochemically. The EE + ischemia group showed a significant decrease of cell death post-ischemia compared with the SC + ischemia group. There was no difference in neurogenesis post-ischemia between SC + ischemia and EE + ischemia. The EE + ischemia group showed a significant increase of performance before and after ischemia compared with the SC + ischemia group. Phospho-CREB-positive cells were significantly increased post-ischemia in EE + ischemia

T. Kato • T. Eriguchi • N. Fujiwara • Y. Murata • A. Yoshino • Y. Katayama
Division of Neurosurgery, Department of Neurological Surgery,
Nihon University School of Medicine, 30-1 Oyaguchi-Kamimachi,
Itabashi-ku, Tokyo 173-8610, Japan
e-mail: tom_kato@rk9.so-net.ne.jp

K. Sakatani (✉)
Division of Neurosurgery, Department of Neurological Surgery, Nihon University School of Medicine, 30-1 Oyaguchi-Kamimachi, Itabashi-ku, Tokyo 173-8610, Japan

Department of Electrical and Electronics Engineering, Nihon University College of Engineering, NEWCAT Institute, Fukushima, Japan
e-mail: sakatani.kaoru@nihon-u.ac.jp

H.M. Swartz et al. (eds.), *Oxygen Transport to Tissue XXXVI*, Advances in Experimental Medicine and Biology 812, DOI 10.1007/978-1-4939-0620-8_27,

compared with SC + ischemia. EE suppressed hippocampal cell death due to global ischemia. Additionally, enhancement of cognitive function before and after ischemia and prevention of cognitive impairment associated with ischemia were observed compared with the controls (rats housed in SC without ischemia). The CREB pathway may play an important role in protection of cognitive ability.

Keywords Enriched environment • Cerebral ischemia • Neurogenesis • Neuronal cell death • Hippocampus

1 Introduction

Vulnerability of the hippocampus to cerebral ischemia has been established in numerous studies. Selective and delayed neuronal cell death after global ischemia occurs in the subgranular zone (SGZ) in rats [1]. It was also reported that neurogenesis proceeds constantly in the subventricular zone (SVZ) and SGZ [2]. Neurogenesis in SVZ and SGZ is deeply involved in memory, learning and mood disorders. In rat SGZ, neurogenesis is enhanced by learning [3] and neuronal damage, such as seizure and ischemic insult, and reduced by post-ischemic stress [4]. Thus, the environment influences hippocampal cell death and neurogenesis due to cerebral ischemia. We previously reported that a stress environment before cerebral ischemia increases neuronal cell death and impairs neurogenesis [5]. Effects of an enriched environment (EE) have been reported in some studies of cerebral ischemia. For example, EE after ischemia increases neuronal cell death [6] and enhances neurogenesis in rat hippocampus [7]. Here, we evaluated the influence of EE prior to cerebral ischemia on post-ischemic neuronal cell death in rats.

2 Methods

All experiments were performed following an institutionally approved protocol in accordance with the Nihon University School of Medicine Guide for the Care and Use of Laboratory Animals.

Twenty-four Sprague-Dawley male rats (250–300 g) were anesthetized with isoflurane (1–1.2 %) in 30 % oxygen/70 % nitrous oxide. Their temperature was maintained at 37 °C with a heating pad. Femoral arteries were cannulated to monitor arterial blood pressure, pH and blood gases. Rats were assigned into the following groups: controls housed under standard conditions (SC) (n = 6); EE (housed in an EE without ischemia) (n = 6); SC + ischemia (n = 6); ischemia following EE (EE + ischemia) (n = 6). Global ischemia was induced by bilateral carotid arterial occlusion combined with hypotension for 10 min [8]. The EE consisted of a

stainless steel cage (800 × 400 × 610 mm) containing wooden logs, tubes and shelves for climbing, and a running wheel. These rats were housed four per cage. On the other hand, in the SC group, rats were housed in pairs in standard laboratory cages (255 × 220 × 150 mm). All groups were housed SC or EE for 6 weeks.

Cognitive function was evaluated by means of the Y-maze test and a novel object recognition test (ORT) after 6 weeks SC or EE and after ischemia. Both tests have been used previously for cognitive assessment of rats [9–11]. Rats were euthanized at 7 days after ischemia. Reduction rates of Y-maze and ORT values were calculated as (pre-ischemia − post-ischemia)/pre-ischemia × 100 to assess differences between pre- and post-ischemia in the EE + ischemia group vs the corresponding differences in the SC + ischemia group. The brain was perfused with saline and 4 % paraformaldehyde, then 2 mm coronal sections were cut. Fluoro-Jade B staining and BrdU staining were used to evaluate hippocampal neuronal cell death and neurogenesis, respectively. Fluoro-Jade B-positive cells were counted in a 1 mm length of a horizontal section of the hippocampal CA1 area. BrdU-positive cells were counted in 1 mm^2 of hippocampal dentate gyrus. Staining of phosphorylated cAMP response element-binding protein (phospho-CREB) was also performed in the two groups subjected to ischemia, and positive cells were counted in the same manner as in the case of Fluoro-Jade B staining. Positively stained cells in each case were evaluated in a double-blind manner. Data were expressed as mean ± SD. The significance of differences in positive cell counts was assessed by means of ANOVA followed by Tukey-Kramer tests. Differences with $p \leq 0.05$ were considered significant.

3 Results

Hippocampal neuronal cell death in the two groups that had received global ischemia (SC + ischemia and EE + ischemia) was significantly increased compared with that in the two groups without ischemia (SC and EE) (Fig. 27.1a, b). Moreover, cell death in the EE + ischemia group was significantly decreased compared with that in the SC + ischemia group.

As for neurogenesis, BrdU-positive cells in the SC + ischemia and EE + ischemia groups were significantly increased compared with those in the SC and EE groups (Fig. 27.1c, d). However, no significant difference of BrdU-positive cells was observed between the SC + ischemia and EE + ischemia groups.

Phospho-CREB-positive cells in the SC + ischemia and EE + ischemia groups were also significantly increased compared with those in the SC and EE groups (Fig. 27.1e, f). Phospho-CREB-positive cells were significantly increased in EE + ischemia group compared with the SC + ischemia group.

Reduction rates in the two cognitive function tests in the EE + ischemia group were significantly lower than those in the SC + ischemia group (Fig. 27.2).In the case of ORT, there was no significant difference between before and after ischemia in the EE + ischemia group.

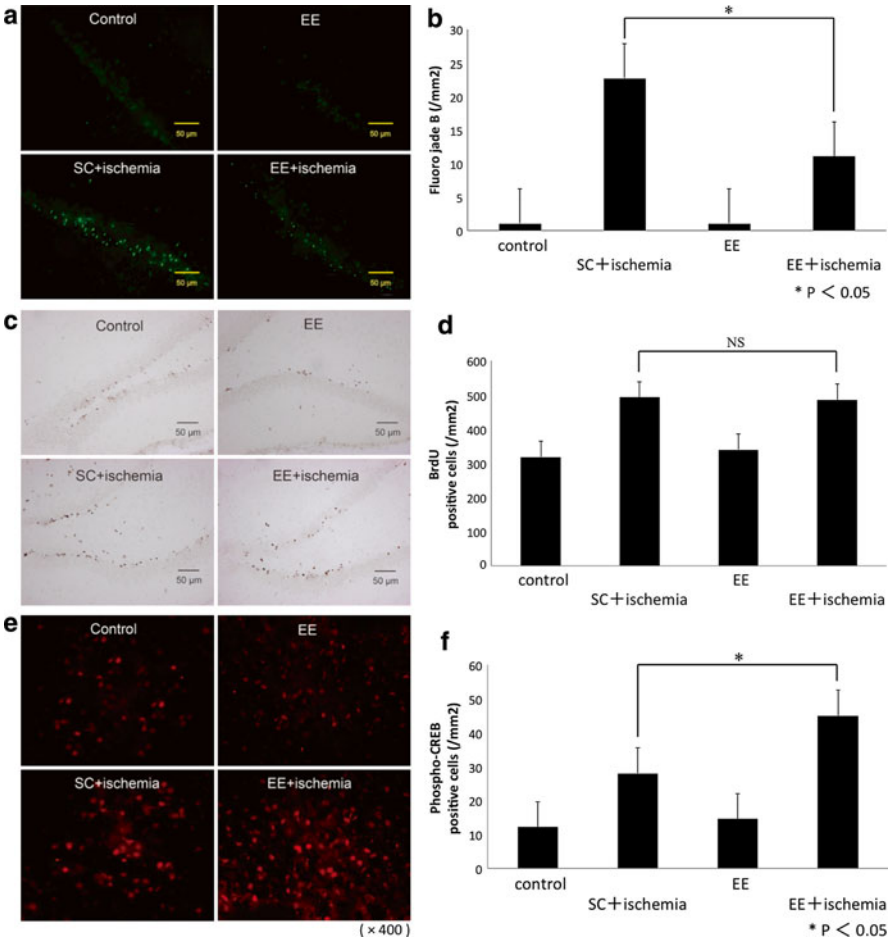

Fig. 27.1 Evaluation of neuronal cell death by Fluoro-Jade B staining (**a**), (**b**). (**a**) Hippocampal neuronal cell death in the EE + ischemia group was significantly decreased compared with that in the SC + ischemia group. (**b**) The results of statistical analysis of cell counts of Fluoro-Jade B-stained cells. Evaluation of neurogenesis by BrdU staining (**c**), (**d**). (**c**) BrdU-positive cells in the SC + ischemia and EE + ischemia groups were significantly increased compared with those in the SC and EE groups. There was no significant difference between the SC + ischemia and EE + ischemia groups. (**d**) The results of statistical analysis of cell counts of BrdU-stained cells. Evaluation of neurogenesis by phospho-CREB staining (**e**), (**f**). (**e**) Phospho-CREB-positive cells in the SC + ischemia and EE + ischemia groups were significantly increased compared with those in the SC and EE groups. Phospho-CREB-positive cells were significantly increased in the EE + ischemia group compared with the SC + ischemia group. (**f**) The results of statistical analysis of cell counts of phospho-CREB-stained cells

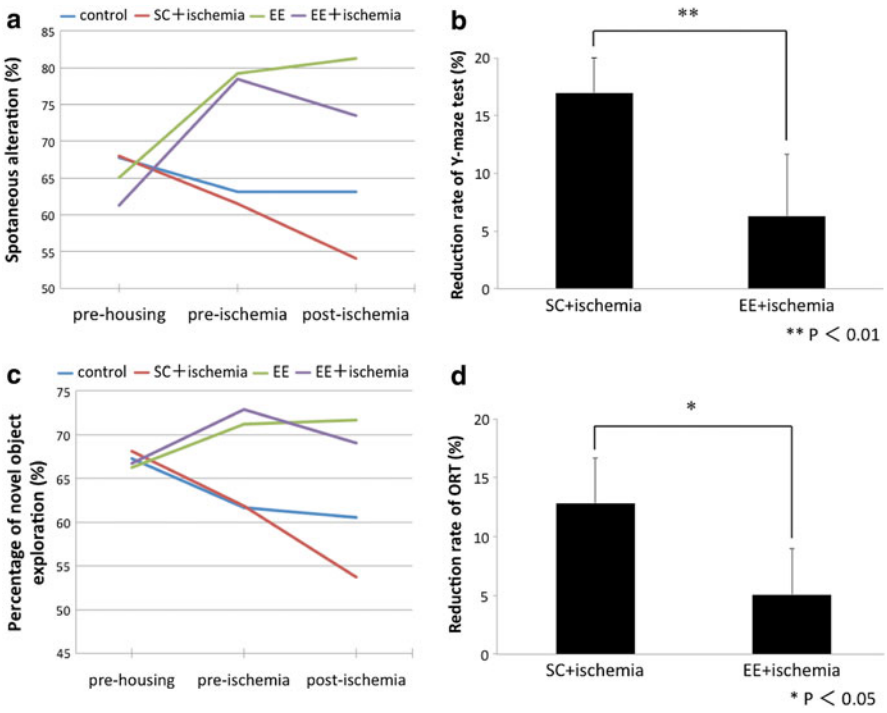

Fig. 27.2 Plots **a** (Y-maze test) and **c** (novel object recognition test (ORT)) show the results of cognitive function tests of all four groups. Significant enhancement of cognitive function before ischemia was observed in the EE + ischemia group compared with the SC + ischemia group in both tests ($p < 0.01$). Plots **b** (Y-maze test) and **d** (ORT) show the reduction rates of cognitive function. The reduction rates in the two cognitive function tests in the EE + ischemia group were significantly lower than those in the SC + ischemia group

4 Discussion

Exposure to EE after global cerebral ischemia leads to an increase in neuronal cell death and enhancement of neurogenesis in rat SGZ [6, 7]. However, little is known about whether EE prior to cerebral ischemia influences neuronal cell death and neurogenesis.

In the present study, exposure to EE prior to cerebral ischemia resulted in a decrease of neuronal cell death in the SGZ. This is a different response from that in rats exposed to EE after cerebral ischemia, because EE after cerebral ischemia increased neuronal cell death in rat hippocampus [6]. As regards neurogenesis, there was no difference between the EE + ischemia and SC + ischemia groups. The effect of EE prior to cerebral ischemia on neurogenesis may also be different from that of EE after ischemia. Expression of phospho-CREB in the SGZ was significantly increased in the EE + ischemia group compared with the SC + ischemia group.

It was reported that the CREB pathway is activated by ischemic insult [12], and the CREB pathway is related to cognitive function and anti-apoptotic effect through COX-2 and Bcl-2, respectively [13]. Our results suggest that activation of the CREB pathway may be related to enhancement of cognitive function before and after ischemia, prevention of cognitive impairment associated with ischemia and reduction of neuronal cell death associated with EE prior to ischemia. Additionally, the reduction of neuronal cell death itself may lead to the prevention of cognitive impairment associated with ischemia in the EE + ischemia group.

In conclusion, EE before global cerebral ischemia may reduce hippocampal cell death, enhance cognitive function before and after ischemia and prevent cognitive impairment associated with ischemia, compared with controls. The CREB pathway may play an important role in the neuronal cell death and enhancement and protection of cognitive ability associated with EE.

References

1. Kirino T (1982) Delayed neuronal death in the gerbil hippocampus following ischemia. Brain Res 239:57–69
2. Goldman SA, Nottebohm F (1983) Neuronal production, migration, and differentiation in a vocal control nucleus of the adult female canary brain. Proc Natl Acad Sci U S A 80(8): 2390–2394
3. Brown ES et al (1999) Hippocampal remodeling and damage by corticosteroids: implications for mood disorders. Neuropsychopharmacology 21(4):474–484
4. Parent JM (2003) Injury-induced neurogenesis in the adult mammalian brain. Neuroscientist 9:261–272
5. Eriguchi T (2012) Influence of stress preconditioning on hippocampal neuronal cell death and neurogenesis in rat cerebral ischemia. Adv Exp Med Biol 737:57–61
6. Farrell R (2001) Environmental enrichment enhances recovery of function but exacerebates ischemic cell death. Neuroscience 107(4):585–592
7. Komitova M (2002) Effects of cortical ischemia and postischemic environmental enrichment on hippocampal cell genesis and differentiation in the adult rat. J Cereb Blood Flow Metab 22(7):852–860
8. Smith ML, Auer RN, Siesjo BK (1984) The density and distribution of ischemic brain injury in the rat following 2–10 min forebrain ischemia. Acta Neuropathol (Berl) 64:319–332
9. Nakamura K (2013) Effects of single and repeated electroconvulsive stimulation on hippocampal cell proliferation and spontaneous behaviors in the rat. Brain Res 23(1491):88–97
10. Gaskin S (2003) Retrograde and anterograde object recognition in rats with hippocampal lesions. Hippocampus 13(8):962–969
11. Komitova M (2005) Postischemic exercise attenuates whereas enriched environment has certain enhancing effects on lesion-induced subventricular zone activation in the adult rat. Eur J Neurosci 21(9):2397–2405
12. Kitadawa K (2012) CREB activation is a key player for ischemic tolerance in the brain. Rinsho Shinkeigaku 52(11):904–907
13. Watanabe T (2006) Cilostazol protects against brain white matter damage and cognitive impairment in a rat model of chronic cerebral hypoperfusion. Stroke 37(6):1539–1545

Chapter 28
Automated Image Analysis for Diameters and Branching Points of Cerebral Penetrating Arteries and Veins Captured with Two-Photon Microscopy

Takuma Sugashi, Kouichi Yoshihara, Hiroshi Kawaguchi, Hiroyuki Takuwa, Hiroshi Ito, Iwao Kanno, Yukio Yamada, and Kazuto Masamoto

Abstract The present study was aimed to characterize 3-dimensional (3D) morphology of the cortical microvasculature (e.g., penetrating artery and emerging vein), using two-photon microscopy and automated analysis for their cross-sectional diameters and branching positions in the mouse cortex. We observed that both artery and vein had variable cross-sectional diameters across cortical depths. The mean diameter was similar for both artery (17 ± 5 μm) and vein (15 ± 5 μm), and there were no detectable differences over depths of 50–400 μm. On the other hand, the number of branches was slightly increased up to 400-μm depth for both the artery and vein. The mean number of branches per 0.1 mm vessel length was 1.7 ± 1.2 and 3.8 ± 1.6 for the artery and vein, respectively. This method allows for quantification of the large volume data of microvascular images captured with two-photon microscopy. This will contribute to the morphometric analysis of the cortical microvasculature in functioning brains.

T. Sugashi (✉) • K. Yoshihara • Y. Yamada
Department of Mechanical Engineering and Intelligent System, Graduate School of Informatics and Engineering, The University of Electro-Communications, 1-5-1 Chofugaoka, Chofu, Tokyo 182-8585, Japan
e-mail: t.sugashi@ymdlab.mce.uec.ac.jp

H. Kawaguchi • H. Takuwa • H. Ito • I. Kanno
Molecular Imaging Center, National Institute of Radiological Sciences, Chiba 263-8555, Japan

K. Masamoto, Ph.D. (✉)
Department of Mechanical Engineering and Intelligent System, Graduate School of Informatics and Engineering, The University of Electro-Communications, 1-5-1 Chofugaoka, Chofu, Tokyo 182-8585, Japan

Molecular Imaging Center, National Institute of Radiological Sciences, Chiba 263-8555, Japan

Brain Science Inspired Life Support Research Center, University of Electro-Communications, 1-5-1 Chofugaoka, Chofu, Tokyo 182-8585, Japan
e-mail: masamoto@mce.uec.ac.jp

H.M. Swartz et al. (eds.), *Oxygen Transport to Tissue XXXVI*, Advances in Experimental Medicine and Biology 812, DOI 10.1007/978-1-4939-0620-8_28,

Keywords Brain microcirculation • Blood flow regulation • Mouse cortex • 3D-image reconstruction • Vascular network structure

1 Introduction

The cerebral cortex consists of several layers of different types of brain cells. Each cell layer has a variable energy usage, which is due to variable cellular activity and densities [1]. This inhomogeneity of the layer-dependent energy demand should be met with well-organized vascular systems. Since oxygen is supplied through an entire pathway of the oxygen-carrier, red blood cells, that travel through cerebral microcirculation, it is important to understand the three-dimensionally (3D) organized morphometry of the cortical microvasculature from an entry point of the parenchyma (i.e., penetrating artery) to its end-point (i.e., emerging vein). Previous studies have simplified the vascular network structures to estimate oxygen exchanges between blood and tissue in functioning brains (for review [2]). However, these studies may not replicate the actual phenomenon of the brain oxygen transport, such as the inhomogeneity of cerebral microvasculature and metabolism.

In our previous study, we observed the detailed 3D microvasculature using two-photon microscopy in *in vivo* mouse cortex, and quantitatively characterized the morphological adaptation of the cortical microvasculature induced through chronic exposure to hypoxia [3]. However, the quantification of the vascular structure was limited to only a single pathway from the penetrating artery to the emerging veins due to a limited number of samples achievable by hand. To overcome this sampling bias and to resolve the layer dependencies of the cortical microvasculature, the present study aimed to develop automated image analysis methods to quantify the vascular diameter and the branching point of the penetrating arteries and emerging veins captured with two-photon microscopy.

2 Methods

2.1 Animal Experiments

Animal experimental protocols were approved by the Institutional Animal Care and Use Committee of the National Institute of Radiological Sciences. A portion of the imaging data was reanalyzed from previously published data [3]. Briefly, six C57BL/6 male mice (8–12 weeks) were anesthetized with isoflurane (3–4 % for induction, 2–3 % for surgery, and 1 % for experiments). Closed cranial window (3–4 mm in diameter) was attached on the left parietal cortex after removing the skull [4]. On the day of the imaging experiments, sulforhodamine 101 (SR101; 5 mM in saline) was injected into the animal (8 mL/kg, i.p.) to fluorescently label

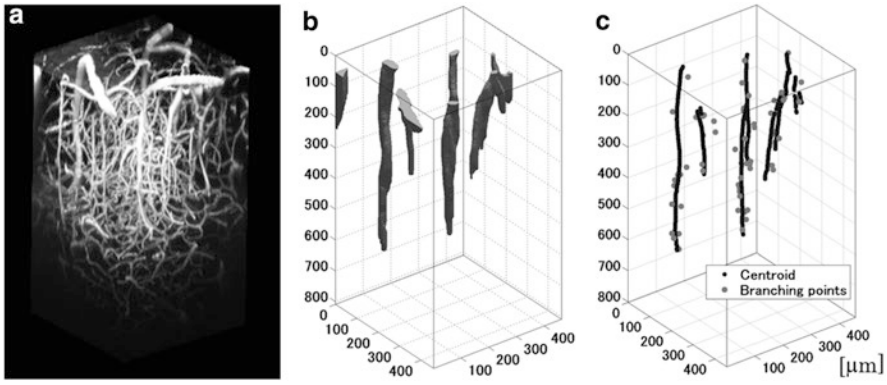

Fig. 28.1 3D reconstructed image of mouse cortical microvasculature measured with two-photon microscopy. The acquired images were three-dimensionally reconstructed (**a**). The penetrating artery and emerging vein perpendicular to the cortical surface were extracted (**b**). Finally, (**c**) the branching position (*gray dot*) and centroid position (*black dot*) of the cross-section of the extracted vessels were determined on each single-slice basis

blood plasma [5]. The cortical vasculature was then imaged through a cranial window with a two-photon microscope (TCS SP5MP, Leica Microsystems, Germany) at 900-nm excitation of Ti:Sapphire laser (MaiTai HP, Spectra-Physics, CA) and bandpass filter of 610/75 nm for detection. The pixel intensity was represented with a 12-bit gray scale and each image consisted of 1,024 by 1,024 pixels with in-plane pixel resolution of 0.45 μm. In each location, z-stack images were acquired to a depth of 800 μm from the cortical surface with a step size of 5 μm. Figure 28.1 represents a typical 3D reconstructed volume image of the cortical microvasculature.

2.2 Image Analysis

The images were first applied with median (3×3 pixels) and low-pass Gaussian filters to reduce randomized noise originating from the photomultiplier detector. Then, a morphological opening filter with cylinder shape element (12-pixel radius and 11-slice height) which preserved vessels situated in perpendicular to the cortical surface (i.e., penetrating artery and emerging vein) was applied to the 3D reconstructed image to extract only penetrating arteries and emerging veins (Fig. 28.1b). To extract the vessel areas in the image, the image was first binarized at 30 % of the signal minus background noise levels in each slice. The background noise level was a mode value measured for all pixel intensities in each image, whereas the signal was defined as the average of over 95 % of peak intensity in the image.

The single vessel was cropped manually to measure the branch numbers, and by tracing a connection of the extracted vessels to the surface vessels, the vessel was

classified as artery or vein. Then, the position of the centroid for each cross-section of the extracted vessel was determined in each slice (Fig. 28.1c). The vessel was one pixel-dilated, and the overlapped region with its branch vessel was identified. The branching point was at the center slice of the bifurcation and three slices over the branching point were excluded from the measurement of the vessel diameters because of the bifurcation that causes errors to approximate the circular cross-section of the vessel. The vessel diameter was a length of the minor axis of the ellipse that was approximated for each cross-section of the vessel in each slice image [6]. In this analysis of the vessel diameter measurements, 50 % peak intensity was used for binarization, since our preliminary experiments with fluorescent microbeads (1.1 μm) showed an accuracy of ±0.1 μm with the threshold level of 50 % peak (data not shown). Then, the diameters were measured over depths of 50–400 μm from the cortical surface. Data were represented as mean ± standard deviation. Statistical significance ($P < 0.05$) was tested with Student's t-test for comparisons between artery and vein data.

3 Results and Discussion

3.1 Vessel Diameters of Penetrating Arteries and Emerging Veins

Mean diameters of the artery and veins were similar over depths of 50–400 μm; 17 ± 5 and 15 ± 5 μm, respectively (Fig. 28.2). There were no detectable changes of the mean diameters over the depths measured, while a histogram of the diameters differed between the artery and vein. For the veins, a number of the small veins

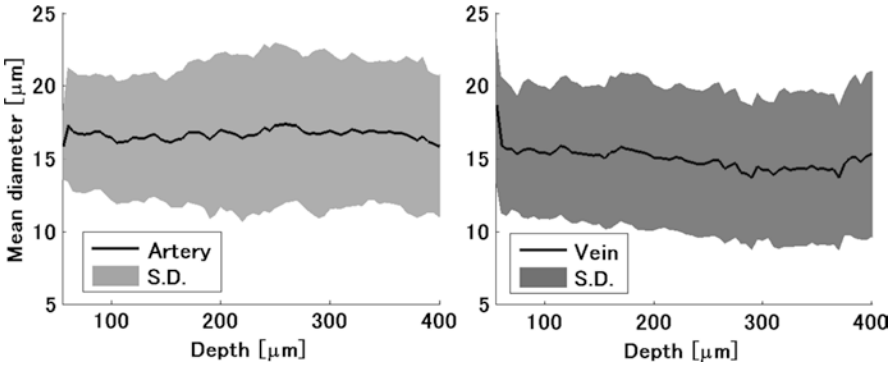

Fig. 28.2 Comparison of the vessel diameters between penetrating artery and vein. No detectable dependence of the vessel diameters on the cortical depths was observed for both artery and vein over depths of 0–400 μm from the cortical surface. Error bar: standard deviation (N = 6 animals)

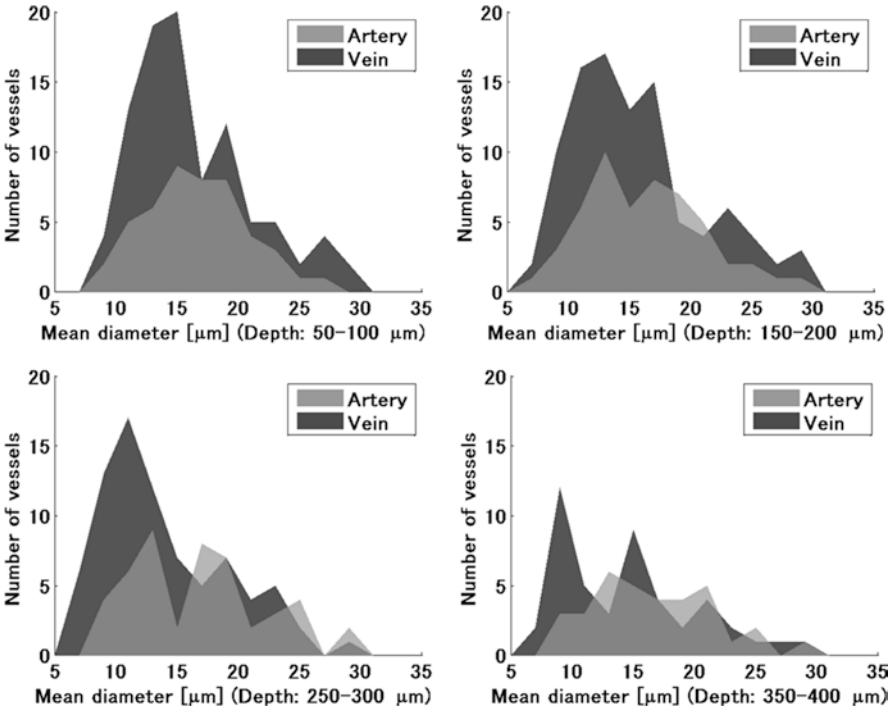

Fig. 28.3 Histogram of the vessel diameters. The measured diameters of the penetrating artery and vein were compared over depths of 50–100 μm (*top left*), 150–200 μm (*top right*), 250–300 μm (*bottom left*), and 350–400 μm (*bottom right*). Although mean diameters were similar for the artery and vein, the number of small vessels was larger for the veins than the arteries (a total of six animal data)

(e.g., less than 15 μm in diameter) was more detected relative to a large veins (i.e., positive skew) and the histogram showed a left-shifted distribution with an increase of the depths (Fig. 28.3). In contrast, the artery diameter showed a nearly symmetric distribution over the depths (Fig. 28.3).

We also observed that a ratio of the measured number of the veins to the arteries was decreased over depths; 2.00, 1.87, 1.68, and 1.35 over depths of 50–100, 150–200, 250–300, and 350–400, respectively. These values were relatively smaller than a previous report that was 2.65 measured for the mouse somatosensory barrel cortex with a histological technique [7]. The difference could be due to a counting method of the vessels. The number of the vessels will change depending on the size of the vessels included (see Fig. 28.3). In our criteria, a number of the emerging veins decreased over depths (94–46 vessels over depth 50–400 μm), but this value does not involve the number of the branched small vessels. To build a whole network of the cortical microcirculation, careful consideration of more small vessels, including capillaries, is needed in future studies.

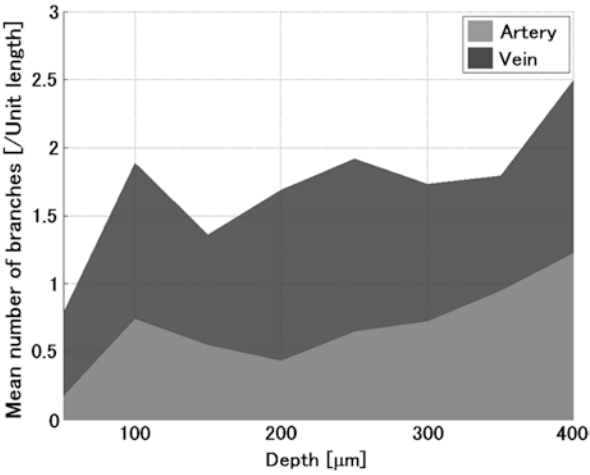

Fig. 28.4 Comparison of the number of branches per unit vessel length between penetrating artery and vein. The number of branches monotonically increased over depths of 0–400 μm for both the artery and vein (average from six animal data). About a 2.3-fold greater number of branches was observed for veins compared with arteries

3.2 Branching Points of Penetrating Arteries and Emerging Veins

The number of branches was slightly increased over 0–400 μm depths of the cortex (Fig. 28.4). For arteries, an average 1.7 ± 1.2 branches per 0.1 mm vessel length was observed, whereas a 2.2-fold greater number of branches was observed for veins; 3.8 ± 1.6 branch per 0.1 mm vessel length. A statistical significant difference was found between the numbers of arterial branches and venous branches, over depths of 50–200 μm, but not for depths of 250–400 μm. As demonstrated, the vessel diameter and branch position were successfully quantified with the present methods. Advantages of the methods are that allow for quantification of large volume data with minimum bias, and disadvantages are limitation for quantification of the capillaries. To extract entire networks of the cortical capillaries, a higher spatial resolution of imaging is further needed. With segmentalized networks of the cortical microcirculation, future works will enable us to determine the microvascular parameters that meet local energy demand, and its plasticity responding to hypoxia.

4 Conclusions

The present study characterized a depth profile of the diameters and branching points of the cortical penetrating arteries and emerging veins with automated analysis of two-photon imaging data. The methods allow for analysis of large volume data, which will contribute to the further understanding the detailed 3D morphology and blood flow structure through the complex cortical microcirculation.

Acknowledgments This study was partially supported through funding from JSPS KAKENHI (#25750400) (to K.M.), JSPS KEKENHI (#24659578) (to I.K.), and a grant from the Ministry of Health, Labor and Welfare (MHLW), Japan (to I.K.).

References

1. Zilles K, Wree A (1995) Cortex: areal and laminar structure. In: Paxinos G (ed) The rat nervous system, 2nd edn. Acadmic Press, San Diego, pp 649–685
2. Masamoto K, Tanishita K (2009) Oxygen transport in brain tissue. J Biomech Eng 131:7, 074002
3. Yoshihara K, Takuwa H, Kanno I, Okawa S, Yamada Y, Masamoto K (2013) 3D analysis of intracortical microvasculature during chronic hypoxia in mouse brains. Adv Exp Med Biol 765:357–363
4. Tomita Y, Kubis N, Calando Y, Tran Dinh A, Méric P, Seylaz J, Pinard E (2005) Long-term in vivo investigation of mouse cerebral microcirculation by fluorescence confocal microscopy in the area of focal ischemia. J Cereb Blood Flow Metab 25(7):858–867
5. Masamoto K, Tomita Y, Toriumi H, Aoki I, Unekawa M, Takuwa H, Itoh Y, Suzuki N, Kanno I (2012) Repeated longitudinal in vivo imaging of neuro-gliovascular unit at the peripheral boundary of ischemia in mouse cerebral cortex. Neuroscience 212:190–200
6. Sekiguchi Y, Masamoto K, Takuwa H, Kawaguchi H, Kanno I, Ito H, Tomita Y, Itoh Y, Suzuki N, Sudo R, Tanishita K (2013) Measuring the vascular diameter of brain surface and parenchymal arteries in awake mouse. Adv Exp Med Biol 789:419–425
7. Woolsey TA, Rovainen CM, Cox SB, Henegar MH, Liang GE, Liu D, Moskalenko YE, Sui J, Wei L (1996) Neuronal units linked to microvascular modules in cerebral cortex: response elements for imaging the brain. Cereb Cortex 6:647–660

Chapter 29
Cerebral Hemodynamic Change and Metabolic Alteration in Severe Hemorrhagic Shock

Nannan Sun, Lin Z. Li, Weihua Luo, and Qingming Luo

Abstract Understanding the biological mechanism and identifying biomarkers of hemorrhagic shock is important for diagnosis and treatment. We aim to use optical imaging to study how the cerebral blood circulation and metabolism change during

N. Sun
Britton Chance Center for Biomedical Photonics, Wuhan National Laboratory for Optoelectronics, Huazhong University of Science and Technology, Wuhan 430074, P. R. China

Key Laboratory of Biomedical Photonics of Ministry of Education, Department of Biomedical Engineering, Huazhong University of Science and Technology, Wuhan 430074, P. R. China

Molecular Imaging Laboratory, Department of Radiology, Perelman School of Medicine, University of Pennsylvania, Philadelphia, PA 19104, USA

Britton Chance Laboratory of Redox Imaging, Johnson Research Foundation, Department of Biochemistry and Biophysics, Perelman School of Medicine, University of Pennsylvania, Philadelphia, PA 19104, USA
e-mail: sunnan721@gmail.com

L.Z. Li
Molecular Imaging Laboratory, Department of Radiology, Perelman School of Medicine, University of Pennsylvania, Philadelphia, PA 19104, USA

Britton Chance Laboratory of Redox Imaging, Johnson Research Foundation, Department of Biochemistry and Biophysics, Perelman School of Medicine, University of Pennsylvania, Philadelphia, PA 19104, USA
e-mail: linli@mail.med.upenn.edu

W. Luo • Q. Luo (✉)
Britton Chance Center for Biomedical Photonics, Wuhan National Laboratory for Optoelectronics, Huazhong University of Science and Technology, Wuhan 430074, P. R. China

Key Laboratory of Biomedical Photonics of Ministry of Education, Department of Biomedical Engineering, Huazhong University of Science and Technology, Wuhan 430074, P. R. China
e-mail: qluo@mail.hust.edu.cn

H.M. Swartz et al. (eds.), *Oxygen Transport to Tissue XXXVI*, Advances in Experimental Medicine and Biology 812, DOI 10.1007/978-1-4939-0620-8_29,

the progression of severe hemorrhagic shock, especially the decompensatory stage. We used a multi-parameter (blood pressure (BP), cerebral blood flow (CBF), functional vascular density (FVD), blood oxygenation and mitochondrial NADH signal) cerebral cortex optical imaging system to observe brain hemodynamic change and metabolic alteration of rats in vivo for 4 h. Cerebral circulation and mitochondrial metabolism could be well preserved in the compensatory stage but impaired during the decompensatory stage. The changes of brain hemodynamics and metabolism may provide sensitive indicators for various shock stages including the transition from compensatory stage to decompensatory stage. Our novel imaging observations of hemodynamic and metabolic signals in vivo indicated that the rat brains under hemorrhagic shock suffered irreversible damage which could not be compensated by the autoregulation mechanism, probably due to injured mitochondria.

Keywords Brain • Cerebral circulation • Mitochondrial metabolism • Decompensatory stage • NADH

1 Introduction

Hemorrhagic shock, a condition with unmet demands of blood flow and oxygen in tissue, remains a leading cause of death among clinical trauma patients especially with an age of under 45 years [1, 2]. As the monitoring of blood microcirculation has become increasingly used in the clinical studies of shock, the parameters related to microcirculation can provide important indices of diagnosis and predictors of therapeutic effect for hemorrhagic shock [3].

In the early stage of hemorrhagic shock, various body organs activate certain protection mechanisms responding to the decline of blood volume. However, the protection mechanism of brain microcirculation generated by autoregulation may be temporary during the process of shock [2]. The abnormal perfusion of CBF, metabolic disturbance and organic damage result from the dysfunction of autoregulation when BP is lower than a threshold for a long time [4]. So understanding the dynamic process and the safety time window of protection mechanisms will be important and helpful for selecting the appropriate fluid resuscitation programs to maintain the BP as well as timely initiating cardiovascular protective measures during the process of shock.

We investigated the perfusion and response of cerebral vessels and the dynamic process of metabolism in severe hemorrhagic shock by a multi-model optical imaging system, which consists of laser speckle imaging, optical intrinsic signal imaging (OISI) and endogenous fluorescence imaging. Using this novel system we monitor visible light reflection, CBF and NADH fluorescence signals in parietal cortex of rats in vivo with high spatial resolution, large visual field and a long period of observation up to 4 h.

2 Materials and Methods

The experimental protocol was approved by the Institutional Animal Care and Use Committee of Huazhong University of Science and Technology. Twelve male Wistar rats weighing from 220 to 280 g, obtained from Hubei Center of Disease Control and Prevention, were randomly divided into two groups: shock and sham. Rats were anesthetized with an intraperitoneal injection of a mixture of α-chloralose (50 mg/kg) and urethane (600 mg/kg). Each rat was placed in a stereotaxic apparatus. A craniotomy (4 mm × 3 mm) over the parietal bone was made with a high-speed dental drill and the dura was kept intact. A PE-50 catheter was inserted into the left femoral artery for monitoring arterial pressure with a pressure transducer (RM6240, Chengdu, China). Another two catheters were inserted into the right femoral artery and vein for controllable bleeding/hemostasia or transfusion of blood and rapid resuscitation, respectively. All catheters were pretreated and flushed intermittently with saline solution containing 125 IU/mL heparin.

The experimental procedure for the shock group is presented schematically in Fig. 29.1 as described previously [5, 6]. We initiated blood pressure monitoring and optical imaging 5 min before the outset of the bleeding at 0 min. Mean arterial pressure (MAP) went down to 40 mmHg within 15 min and maintained at this level (by blood withdrawal or injection from or into the rat) for about 2 h followed by fluid resuscitation. The experimental procedure and the time line of the sham group was the same as the shock group except no bleeding and fluid resuscitation.

Cerebral hemodynamic changes and mitochondrial metabolic alteration were acquired with our home-made multimodal optical imaging system [7], which integrated fluorescence imaging, OISI and laser speckle flowmetry imaging to simultaneously monitor the changes in cerebral blood flow, vascular diameters and density, oxy-hemoglobin (HbO), total hemoglobin (HbT), deoxy-hemoglobin (HbR) and NADH fluorescence in vivo. The detail of our imaging system setup was described in previous work [7]. Under proper illumination and image acquiring protocol, a set of four images (less than 3 s for total acquisition time) were obtained with this system every half a minute. The NADH fluorescence images were acquired by a camera with a bandpass filter (475 ± 21 nm). The other three sequential images were achieved with another time-sharing CCD which employed a liquid crystal tunable filter to change the light wavelength for observation and produced the OIS images at 550 and 570 nm, and laser speckle flowmetry images at 660 nm. OIS images were used to quantify

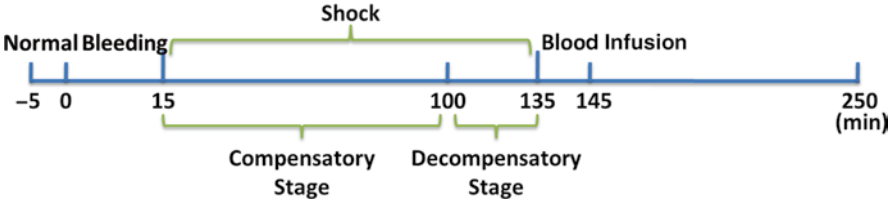

Fig. 29.1 The experimental procedure of severe hemorrhagic shock

HbO, HbT and HbR. The laser speckle flowmetry images reflected CBF and vascular perfusion and structure with high resolution comparable to that of OIS images and were obtained through online processing by laser speckle temporal contrast analysis [8–11] to obtain CBF, FVD, and the size and perfusion of specific blood vessels.

3 Results and Discussion

Figure 29.2 shows that BP, pulse pressure (PP) and heart rate (HR) dramatically declined along with the increase of bleeding during the period of rapid bleeding. After that period, the slight increase of HR suggests that autoregulation mechanism was started, although the recuperation is small limited by a decline in total blood volume of the body. The start of the decompensated stage was around 60–120 min as the blood injection into the rat was initiated to maintain the blood pressure stable. The rapid infusion was carried out half an hour later from the outset of decompensated stage so that BP went up significantly. After that, BP and PP showed a downward trend, and HR recovered slowly.

We presented typical results of various imaging parameters during severe hemorrhagic shock from a representative rat in Fig. 29.3. In the rapid bleeding period, there were negligible effects on the diameters of middle cerebral artery (MCA) and veins, but there was shrinkage of middle meningeal artery (MMA). MMA perfusion was

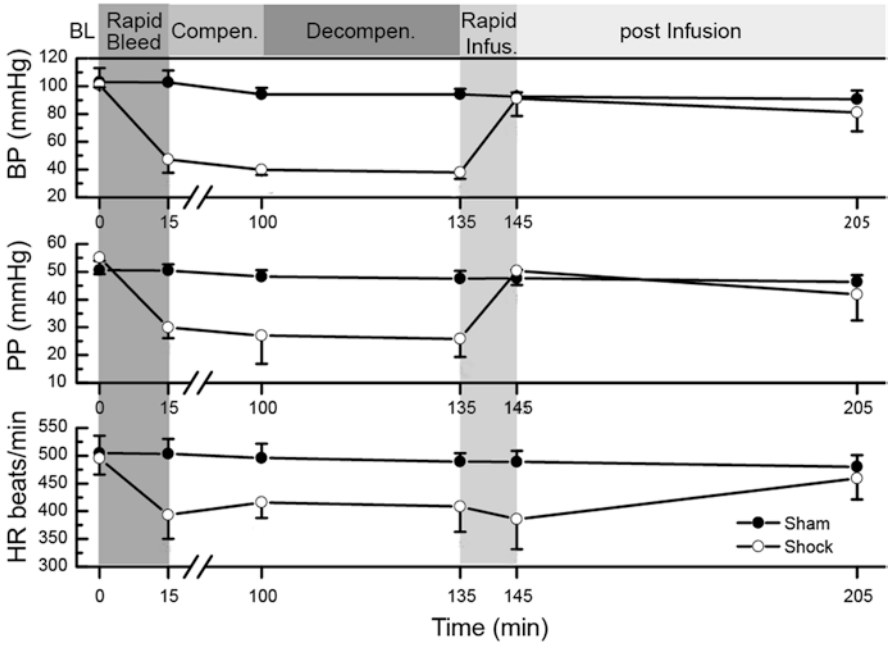

Fig. 29.2 Averaged changes of BP, PP and HR during the process of severe hemorrhagic shock

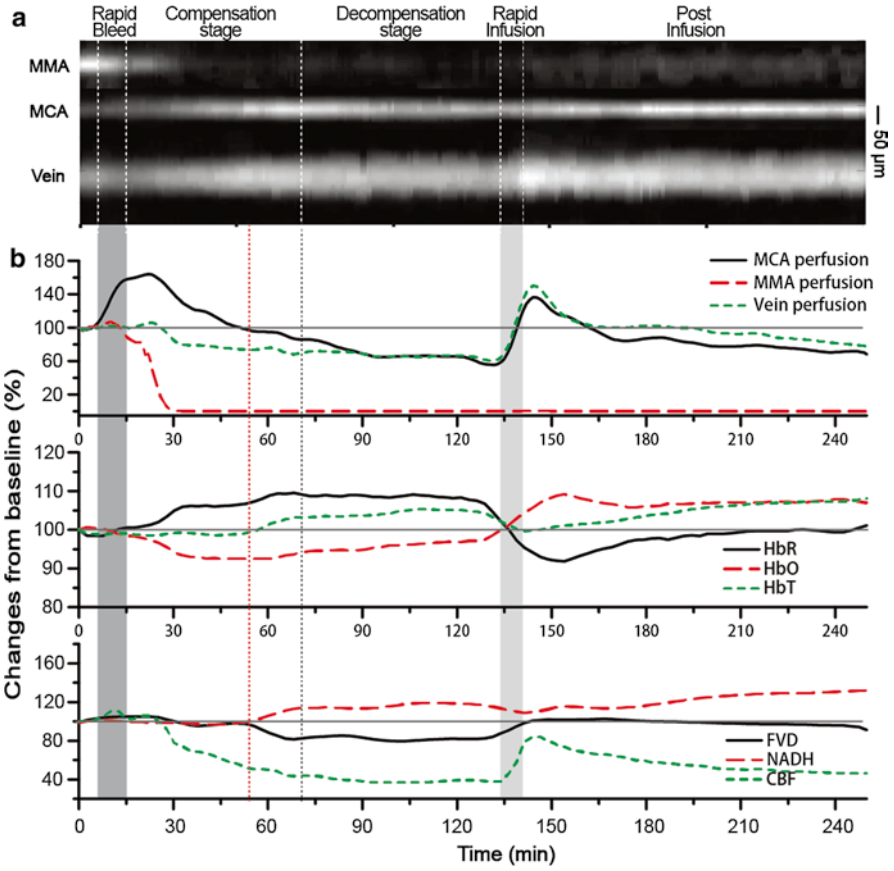

Fig. 29.3 Typical results of vascular diameter, vascular perfusion, hemoglobin concentration, FVD, NADH and CBF during the process of severe hemorrhagic shock for one rat

decreased, venous perfusion stable and MCA perfusion increased rapidly due to the autoregulation mechanism. It seems that the blood regulation system reduced the blood supply to the peripheral circulation and increased the blood supply to the interior cerebral circulation under emergency situations such as massive blood loss.

In the compensated stage (15–70 min), the diameter of MMA was decreased to undetectable and the MCA and veins showed expansion in diameters. MCA perfusion reached a maximum and then began to decline. Venous perfusion, HbO and CBF decreased rapidly. At 52 min, HbT, and NADH rose up and FVD went down at the same time, and reached a plateau at about 70 min. This may indicated that the body self-regulatory function entered a new stage. The period of 52–70 min most likely corresponds to the turning point from compensated to decompensated stage. There are not effective biomarkers to monitor the shock stages in patients in real time [5]. While the fluorescence signals of NADH, an indicator of mitochondrial metabolism, in combination with hemodynamic signals, may potentially provide a new sensitive in vivo marker for shock stages.

During the decompensated stage (about 70–135 min), the diameter of MCA shrank gradually, while the veins maintained the expansion. There were little variations in the perfusion of MCA and veins, hemoglobin-related parameters, FVD, NADH, CBF, BP and HR. The stability of all parameters before the fluid resuscitation suggested that the body might have entered the irreversible refractory stage as indicated below.

After the fluid resuscitation, MMA perfusion was still undetectable. Most of the parameters began to recover within 20 min. After that until 2 h later the perfusion of MCA and veins went down, HbO and HbT stabilized or increased, NADH significantly increased while FVD and CBF declined indicating irreversible damage to tissue function and metabolism. Three reasons may lead to these results. First of all, the blood volume is still too low during fluid resuscitation. It might not be enough if we just infuse back the original amount of blood loss. Second, there is vascular dysfunction led by massive loss of blood in a long time, which cannot be restored in a short time. Third, cellular metabolism and autoregulation function were damaged, so that the body cannot prioritize and keep up with the blood supply needed by vital organs.

The irreversible tissue damage might have begun during the decompensatory stage. We need to study more about the relationship between the optical signal changes and the underlying shock physiology in order to identify the exact time point. In the future it would also be interesting to study the effect of the timing of rapid infusion on shock recovery, which is an important factor for the shock treatment.

4 Conclusions

In conclusion, we presented for the first time simultaneous imaging of hemodynamics and mitochondrial NADH signals in vivo. This novel multi-modal optical imaging method provided clear results that the severe hemorrhagic shock suffered irreversible damage which could not be compensated by the autoregulation mechanism, probably because of injured mitochondria. The characteristic changes of hemodynamics and mitochondrial metabolism may provide sensitive markers for the tissue damage and the stages of the hemorrhagic shock.

Acknowledgments This work was supported by the National Major Scientific Research Program of China (Grant No. 2011CB910401) and the Science Fund for Creative Research Group of China (Grant No. 61121004) and the Director Fund of Wuhan National Laboratory for Optoelectronics and the Specific International Scientific Cooperation (Grant No. 2010DFR30820).

References

1. Cocchi MN, Kimlin E, Walsh M et al (2007) Identification and resuscitation of the trauma patient in shock. Emerg Med Clin N Am 25(3):623–642, vii
2. Taccone FS, De Backer D (2010) Is cerebral microcirculation really preserved in shock states? Crit Care Med 38(3):1008–1009

3. Koh IHJ, Menchaca-Diaz JL, Koh TH et al (2010) Microcirculatory evaluation in sepsis. Shock 34(Suppl 1):27–33
4. Wan Z, Sun S, Ristagno G et al (2010) The cerebral microcirculation is protected during experimental hemorrhagic shock. Crit Care Med 38(3):928–932
5. Thiemermann C, Szabo C, Mitchell JA et al (1993) Vascular hyporeactivity to vasoconstrictor agents and hemodynamic decompensation in hemorrhagic shock is mediated by nitric oxide. Proc Natl Acad Sci 90:267–271
6. Song R, Bian H, Wang X et al (2011) Mitochondrial injury underlies hyporeactivity of arterial smooth muscle in severe shock. Am J Hypertens 24(1):45–51
7. Sun X, Wang Y, Chen S et al (2011) Simultaneous monitoring of intracellular pH changes and hemodynamic response during cortical spreading depression by fluorescence-corrected multimodal optical imaging. Neuroimage 57(3):873–884
8. Jiang C, Zhang H, Wang J et al (2011) Dedicated hardware processor and corresponding system-on-chip design for real-time laser speckle imaging. J Biomed Opt 16(11):116008
9. Qiu J, Li P, Luo W et al (2010) Spatiotemporal laser speckle contrast analysis for blood flow imaging with maximized speckle contrast. J Biomed Opt 15(1):016003
10. Liu S, Li P, Luo Q (2008) Fast blood flow visualization of high-resolution laser speckle imaging data using graphics processing unit. Opt Express 16(19):14321–14329
11. Li P, Ni S, Zhang L et al (2006) Imaging cerebral blood flow through the intact rat skull with temporal laser speckle imaging. Opt Lett 31(12):1824–1826

Chapter 30
Physiological Mechanism of Increase in Deoxyhemoglobin Concentration During Neuronal Activation in Patients with Cerebral Ischemia: A Simulation Study with the Balloon Model

Naohiro Takemura, Kaoru Sakatani, Atsuo Yoshino, Teruyasu Hirayama, and Yoichi Katayama

Abstract Patients with cerebral ischemia or brain tumor have been reported to exhibit an increase of deoxygenated hemoglobin (deoxy-Hb) together with an increase of oxygenated hemoglobin (oxy-Hb). However, the physiological mechanisms underlying this hemodynamic response pattern are unclear. In this study, we performed a simulation using the balloon model (Buxton et al., Magn Reson Med 39:855–864, 1998). We hypothesized that the oxygen extraction rate during the rest period (E_0) in the patients is larger than in normal subjects, because the cerebral blood flow and the speed at which the blood passes through the brain tissues are lower in the patients. The simulation result showed an increase of deoxy-Hb as well as oxy-Hb, especially when E_0 is extremely high. Thus, the results of our simulation suggest that the increase of deoxy-Hb during activation in patients with ischemia or brain tumor is caused by an increased oxygen extraction rate at rest, compared with that of healthy adults.

Keywords Cerebral blood oxygenation • Ischemia • Near-infrared spectroscopy • Balloon model

N. Takemura (✉)
Laboratory of Integrative Biomedical Engineering, Department of Electrical and Electronics Engineering, College of Engineering, Nihon University, Koriyama, Fukushima 963-8642, Japan
e-mail: naohiro.takemura@gmail.com

K. Sakatani
Laboratory of Integrative Biomedical Engineering, Department of Electrical and Electronics Engineering, College of Engineering, Nihon University, Koriyama, Fukushima 963-8642, Japan

Department of Neurological Surgery, Nihon University School of Medicine, Tokyo, Japan

A. Yoshino • T. Hirayama • Y. Katayama
Division of Neurosurgery, Department of Neurological Surgery, Nihon University School of Medicine, 30-1 Oyaguchi-kamimachi, Itabashi-ku, Tokyo 173-8610, Japan

H.M. Swartz et al. (eds.), *Oxygen Transport to Tissue XXXVI*, Advances in Experimental Medicine and Biology 812, DOI 10.1007/978-1-4939-0620-8_30,

1 Introduction

In general, neuronal activation induces a regional increase of oxygenated hemoglobin (oxy-Hb), accompanied with a decrease of deoxygenated hemoglobin (deoxy-Hb). However, in some patients with cerebral ischemia or brain tumor, deoxy-Hb increases, as well as oxy-Hb, during neuronal activation [1–3].

The balloon model [4] is one of the physiological models used to study cerebral hemodynamics and oxygen dynamics. The model assumes that the BOLD signal or the optical signal measured by fMRI or NIRS reflects the change of venous oxy- and deoxy-Hb concentrations around the site of neuronal activation. When oxygen is metabolized in the region around a capillary vessel, blood flows into an expandable compartment in the vein. Since the increase rate of the regional cerebral blood flow (rCBF) is larger than the increase rate of oxygen metabolism, blood with high oxy-Hb concentration flows into the vein compartment and "washes out" the blood with high deoxy-Hb concentration. Consequently, the concentration of oxy-Hb in the vein increases, while the concentration of deoxy-Hb decreases. However, cerebral blood flow in patients with ischemia is smaller than normal, and consequently the oxygen extraction fraction (OEF) becomes larger [5].

In the present study, we conducted simulations with the balloon model in order to examine whether this model can reproduce the increase of deoxy-Hb concentration in ischemia patients, on the assumption that the OEF during the resting state is higher in patients with ischemia than that in healthy subjects.

2 Methods

First, the balloon model for the simulation of dynamic changes in rCBF and OEF is described. Then, the manipulation of the model for the simulation of ischemia is explained.

2.1 The Balloon Model

The balloon model [4] is a mathematical model that describes the temporal change of rCBF, rCBV and OEF. Under the assumption that all of the oxygen that leaves the capillary is metabolized and that blood flow increases are accomplished by increased capillary blood velocity rather than capillary recruitment. Increased blood flow leads to reduced oxygen extraction.

Designating rCBF that enters the vein compartment and rCBF that leaves it at time t as $f_{\text{in}}(t)$ and $f_{\text{out}}(t)$, and the OEF at time t and at rest as $E(t)$ and E_0, we can write

the temporal expansion of the deoxy-Hb content $q(t)$ and the cerebral blood volume (rCBV) in the compartment $v(t)$ as follows:

$$\frac{dq(t)}{dt} = \frac{1}{\tau_0}\left[f_{in}(t)\frac{E(t)}{E_0} - f_{out}(v)\frac{q(t)}{v(t)} \right], \tag{30.1}$$

$$\frac{dv(t)}{dt} = \frac{1}{\tau_0}\left[f_{in}(t) - f_{out}(v) \right]. \tag{30.2}$$

Note that τ_0 is the time constant, and $f_{\text{in}}(t), f_{\text{out}}(t)$, $q(t)$, $v(t)$ are relative values such that the value at the rest period is 1. $E(t)$ decreases as the blood flow increases, and is given by:

$$E(t) = E\left(f_{in}(t)\right) = 1 - \left(1 - E_0\right)^{\frac{1}{f_{in}(t)}}. \tag{30.3}$$

rCBF that leaves the compartment is dependent to the blood volume in the compartment.

$$f_{out}(v) = f_{out}\left(v(t)\right) = v(t)^{1/\alpha}. \tag{30.4}$$

Here, α is a coefficient to describe the relationship between flow and volume. The hysteresis of the flow [6, 7] is not considered here, because it is outside the scope of the present study.

2.2 Simulation of Ischemia

The parameter α is set to 0.4, following the original model [4]. The time constant is set to 2. When neuronal activation occurs, the rCBF that enters the vein compartment $f_{\text{in}}(t)$ is assumed to increase to the maximum blood flow f_a. In the present simulation, the rest duration is 10 s, task (activation) duration is 35 s, and rest duration after the task is 35 s. When the task starts, $f_{\text{in}}(t)$ increases linearly to f_a in 5 s. After the task period, $f_{\text{in}}(t)$ decreases linearly to the rest value (=1.0) in 5 s. These temporal changes of $f_{\text{in}}(t)$ are shown in Fig. 30.1a. These transient times (5 s) are chosen to ensure the convergence of the observed values (rCBV, $CMRO_2$, and deoxy-Hb) during the simulation. The time step to drive the temporal differential (30.1)–(30.4) is 0.01 s.

We conducted two simulations. First, we used a static maximum blood flow (f_{a}=0.7), following the original model [4]. Then, we simulated six cases where the OEFs at rest are as follows:

$$E_0 = \left[0.4, 0.5, 0.6, 0.7, 0.8, 0.9\right].$$

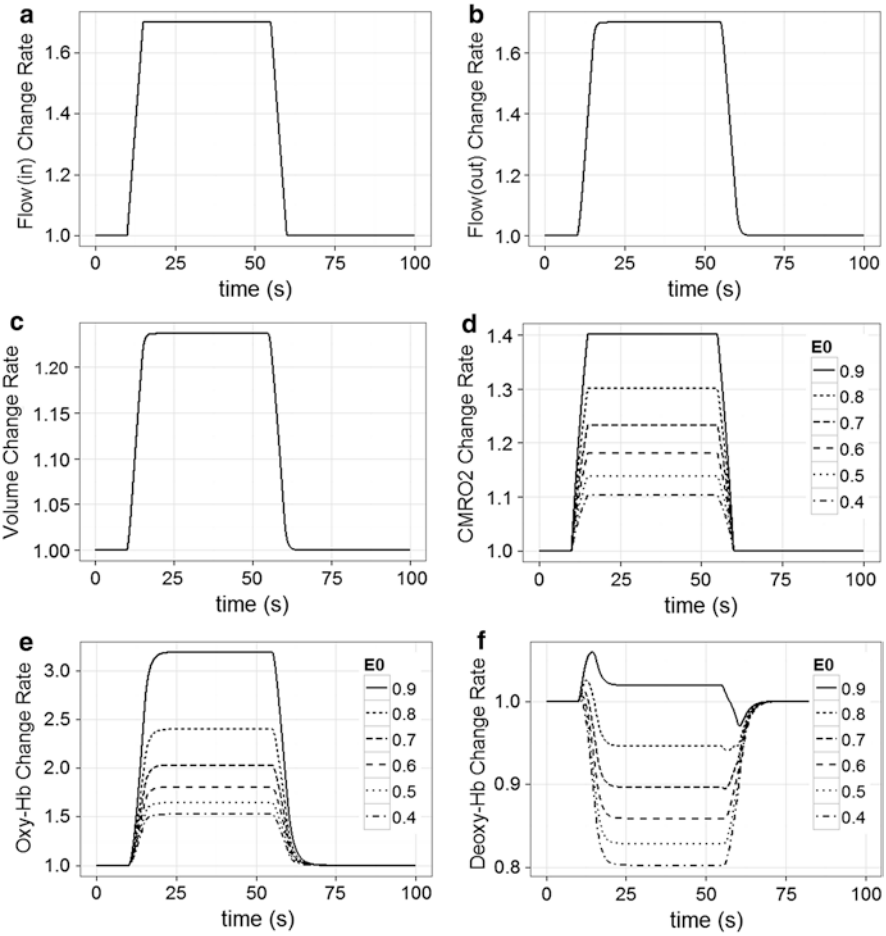

Fig. 30.1 Simulation results for the case of static maximum flow. **a**: rCBF (in-flow) change rate. **b**: rCBF (out-flow) change rate. **c**: rCBV change rate. **d**: $CMRO_2$ change rate. **e**: oxy-Hb change rate. **f**: deoxy-Hb change rate. *Dotted lines* denote the cases of larger E_0

For the second simulation, we introduced the hypothesis that, in ischemic patients, the cerebral blood vessel at the rest period is already dilated in order to compensate for the low perfusion [5], and therefore, the maximum blood flow during the neuronal activation is smaller than that in healthy subjects. We used the following six pairs of OEF at rest and maximum blood flow:

(E_0, f_a) = [(0.4, 0.7), (0.5, 0.6), (0.6, 0.5), (0.7, 0.4), (0.8, 0.3), (0.9, 0.2)].

The combination of E_0 and f_a values are determined only by increasing f_a values by 0.1 against the increase of E_0 values by 0.1 in order to how the concurrent change of these values result in the change of the rCBO. The temporal flow into the compartment in the second simulation is shown in Fig. 30.2a.

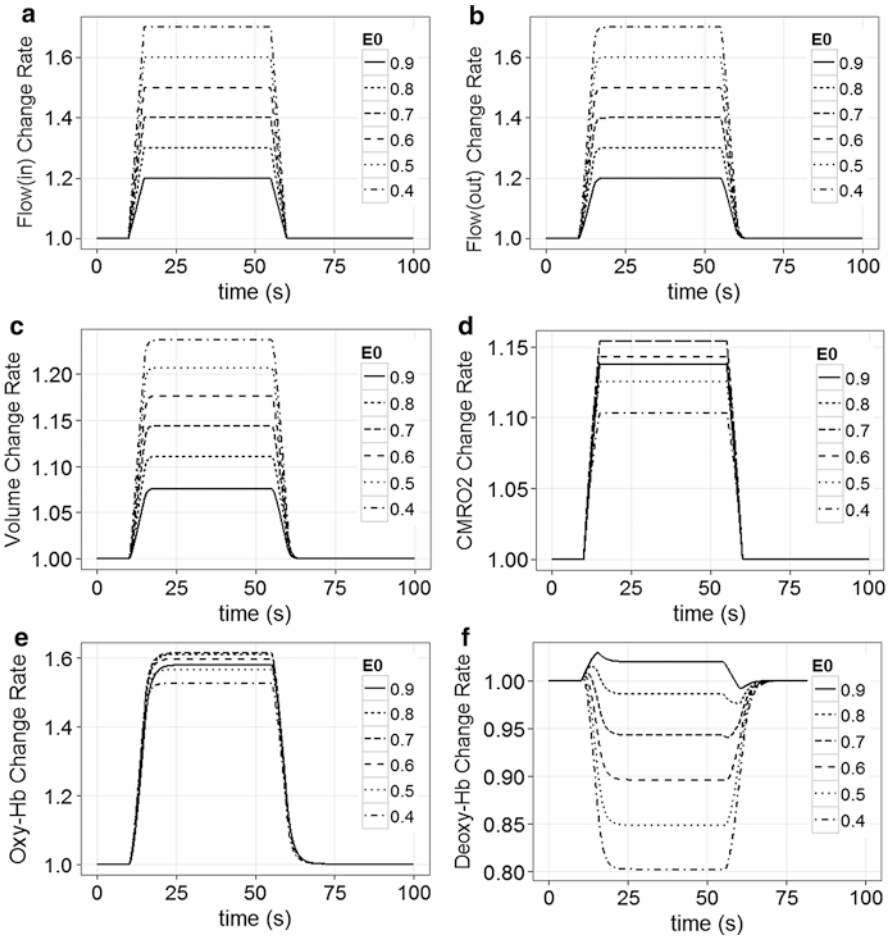

Fig. 30.2 Simulation results for the case of variable maximum flow. **a**: rCBF (in-flow) change rate. **b**: rCBF (out-flow) change rate. **c**: rCBV change rate. **d**: $CMRO_2$ change rate. **e**: oxy-Hb change rate. **f**: deoxy-Hb change rate. *Dotted lines* denote the cases of larger OEF at rest and smaller maximum flow

3 Results

The results of the first simulation are shown in Fig. 30.1. As the OEF (E_0) at rest increases, the cerebral metabolic rate of oxygen ($CMRO_2$) and the oxy-Hb during activation both increase more (Fig. 30.1c, f), and the deoxy-Hb decreases less (Fig. 30.1e). In the case of the largest E_0 (= 0.9), the deoxy-Hb even increases during activation (Fig. 30.1e). Note that the $CMRO_2$ change rate is calculated as follows:

$$CMRO_2(t) = f_{in}(t)E(t)/E_0.$$

The results of the second simulation are shown in Fig. 30.2. As the OEF (E_0) at rest increases and rCBF change rate during activation decreases (Fig. 30.2a, b), the rCBV increases less (Fig. 30.2d) and the deoxy-Hb decreases less (Fig. 30.2e). Again, in the case of large E_0 (= 0.8 or 0.9), deoxy-Hb even increases during activation (Fig. 30.2e). In this simulation, $CMRO_2$ and oxy-Hb in the case of ischemia are similar to these in healthy subjects (Fig. 30.2c, f).

4 Discussion

The simulation results reproduced the quantitative features of cerebral blood oxygenation (CBO), i.e., that the deoxy-Hb concentration increases during neuronal activation in patients with cerebral ischemia (E_0=0.9 in the simulation), while it decreases in healthy subjects. In simulation 1, the assumption that the OEF at rest is large for ischemic patients resulted in increases of $CMRO_2$ and oxy-Hb concentration. In simulation 2, on the other hand, the assumption that the OEF at rest is large and the rCBF increase rate during activation is small for ischemic patients resulted in relatively similar $CMRO_2$ and oxy-Hb concentration to those of healthy subjects.

At present, it is impossible to discuss the plausibility of these two simulations, because physiological observations of the absolute values of the CBO during activation are lacking. In general, NIRS can only measure the product of the change of the CBO and the light path length, and therefore, the absolute values of these parameters are not measurable. On the other hand, the results of the present simulation can only show the change rate of these parameters, which makes it impossible to compare the physiological measurement and the simulation result. One essential development of the present study will be to conduct simulations with absolute values of the blood flow and the blood volume. It makes it possible to compare the absolute values of the cerebral blood variables in the physiological experiments and these in the simulation. And by determining the blood flow and the blood volume, the time constant τ can also be determined, and the comparison of characteristics of the temporal development of the variables can be made.

Previous observations [2, 3], suggest that the higher the level of ischemia is, the less oxy-Hb increases during activation. The reason for this result might be either differences of the light path length between patients, or differences in the change of absolute value of the parameter. In order to investigate these possibilities, it will be necessary to measure the CBO independently of the light path length by using time-resolved near-infrared spectroscopy (TRS), and to conduct simulation using a model with absolute values of rCBF, rCBV, during resting state and activation, not relative values, of parameters. These variables are available in the literature from PET and SPECT studies. However, it is not possible to obtain these measurements simultaneously with the measurement of the CBO. Even so, we can conduct simulations based on the speculation that the characteristics of these CBF and CBV variables are preserved during the measurement of the CBO.

Acknowledgments This research was supported in part by a Grant-in-Aid from the Ministry of Education, Culture, Sports, Sciences and Technology of Japan (B23300247), and grants from Alpha Electron Co., Ltd. (Fukushima, Japan) and Iing Co., Ltd. (Tokyo, Japan).

References

1. Fujiwara N, Sakatani K, Katayama Y, Murata Y, Hoshino T, Fukaya C, Yamamoto T (2004) Evoked-cerebral blood oxygenation changes in false-negative activations in BOLD contrast functional MRI of patients with brain tumors. Neuroimage 21:1464–1471
2. Murata Y, Sakatani K, Hoshino T, Fujiwara N, Kano T, Nakamura S, Katayama Y (2006) Effects of cerebral ischemia on evoked cerebral blood oxygenation responses and BOLD contrast functional MRI in stroke patients. Stroke 37:2514–2520
3. Sakatani K, Murata Y, Fujiwara N, Hoshino T, Nakamura S, Kano T (2007) Comparison of blood-oxygen-level-dependent functional magnetic resonance imaging and near-infrared spectroscopy recording during functional brain activation in patients with stroke and brain tumors. J Biomed Optics 12:062110
4. Buxton RB, Wong EC, Frank LR (1998) Dynamics of blood flow and oxygenation changes during brain activation: the balloon model. Magn Reson Med 39:855–864
5. Powers WJ, Grubb R Jr, Raichle ME (1984) Physiological responses to focal cerebral ischemia in humans. Ann Neurol 16:546–552
6. Buxton RB, Uludag K, Dubowitz DJ, Liu TT (2004) Modeling the hemodynamic response to brain activation. Neuroimage 23(Suppl 1):S220–S233
7. Tang L, Avison MJ, Gore JC (2009) Nonlinear blood oxygen level-dependent responses for transient activations and deactivations in V1 – insights into the hemodynamic response function with the balloon model. Magn Reson Imaging 27:449–459

Chapter 31
Effect of Blood in the Cerebrospinal Fluid on the Accuracy of Cerebral Oxygenation Measured by Near Infrared Spectroscopy

J.L. Robertson, A. Ghosh, T. Correia, D. Highton, M. Smith, C.E. Elwell, and T.S. Leung

Abstract Near infrared spectroscopy (NIRS) is an optical technique used to examine the oxygenation state of tissues such as the brain in patients, including those with brain injury. We have examined the effect of a cerebrospinal fluid (CSF) contaminant, specifically haemoglobin, on the sensitivity of cerebral NIRS signals through computer simulation. Previous models of light transport in the head have shown that the clear CSF layer has a profound effect on the sensitivity profile of the NIRS signal due to its low absorbing, low scattering qualities. In subarachnoid haemorrhage, which may accompany brain injury, the principal near infrared chromophore, haemoglobin, is released into the CSF. Sensitivity was measured through forward modeling and the presence of haemoglobin within the CSF was modeled by increasing the absorption coefficient of the layer, with sensitivity quantified in terms of the partial pathlength of light within the brain. The model demonstrated that increases in the CSF absorption led to a marked decrease in the sensitivity to changes in the brain layer. This suggests that blood or other contaminants in the CSF may have a significant effect on the utility of NIRS for measurement of cerebral oxygenation, and merits further investigation.

Keywords Near infrared spectroscopy • Cerebral oxygenation • Cerebrospinal fluid • Light modelling • Haemorrhage

J.L. Robertson • C.E. Elwell • T.S. Leung (✉)
Department of Medical Physics and Bioengineering, University College London, Malet Place Engineering Building, London, WC1E 6BT, UK
e-mail: t.leung@ucl.ac.uk

A. Ghosh • D. Highton • M. Smith
Neurocritical Care, The National Hospital for Neurology and Neurosurgery, UCLH, London, UK

T. Correia
Department of Computer Science, University College London, London, UK

H.M. Swartz et al. (eds.), *Oxygen Transport to Tissue XXXVI*, Advances in Experimental Medicine and Biology 812, DOI 10.1007/978-1-4939-0620-8_31,

1 Introduction

Near infrared spectroscopy (NIRS) is a non-invasive optical technique that takes advantage of the unique properties of near infrared (NIR) light, commonly defined as wavelengths in the range from 700 to 1,400 nm. NIR light is able to penetrate into tissue where it is absorbed by physiologically important chromophores, most notably haemoglobin [1, 2]. The absorption spectrum of haemoglobin changes with its oxygenation state and, through analysis of the back-scattered light, has previously been used to perform measurements of tissue oxygenation, including cerebral oxygenation [1–3]. The sensitivity of the NIRS signal can be considered in terms of the partial pathlength of the NIR light within the brain tissue. This can also be expressed as the change in optical attenuation (A) at the detector in response to a change in the absorption coefficient (μ_a) of that layer, i.e., partial pathlength $= \partial A/\partial \mu_a$ [1]. Furthermore, the partial pathlength as a proportion of the total mean pathlength of the light passing through the head represents the specificity of the signal for the brain tissue layer.

In order for the NIRS measurements to be accurately quantified, there is a need to model the propagation of light within tissue. More recently the cerebrospinal fluid (CSF) layer that surrounds the brain, has been shown to have a profound effect on the propagation of light within the head [3–5]. Usually modeled as a low scattering medium [5], this would typically require more computationally expensive Monte-Carlo modeling. However, Custo et al. [4] suggested that the irregularity in the thickness of the CSF layer limits the average straight-line distance that a photon would travel in a region consisting of only CSF, and therefore the effective scattering coefficient is higher than that of the pure CSF. They showed that increasing the scattering coefficient to allow the use of the diffusion approximation does not significantly affect the accuracy of the model, or its validity in measuring changes in partial pathlength.

The CSF may become contaminated and discoloured following brain injuries, when it would also be desirable to use NIRS to measure cerebral oxygenation. For example, following a subarachnoid haemorrhage [6]. The CSF concentration of erythrocytes invariably rises sharply and, subsequently, as red cells lyse, haemoglobin and its breakdown products are detectable in the CSF. Free haemoglobin and its breakdown products reach peak concentrations approximately a week after haemorrhage, and remain at measurable levels long after [6]. Haemoglobin is the principal physiological absorber of NIR light, and changes in extracerebral absorption are known to affect NIRS measurements of brain tissue [7].

2 Material and Methods

2.1 The Head Model

Simulated MRI images of the head in T1, T2 and proton density (PD) modalities were obtained from the simulated MRI database BrainWeb [8]. The images were segmented using an image processing and segmentation suite, NIRview [9], and a

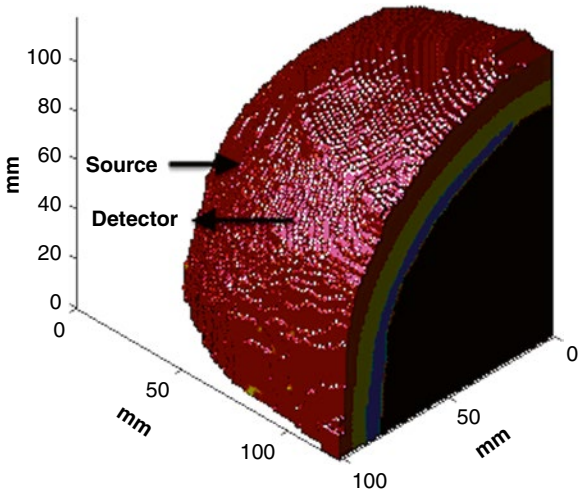

Fig. 31.1 Mesh generated from segmentation

Table 31.1 Optical properties of the head at 780 nm

Layer	Thickness (mm)	μ_a (mm^{-1})	μ_s (mm^{-1})
Scalp	6–7	0.0164	0.71
Skull	6–8	0.0115	0.91
CSF	1–3	0.0017	0.3
Brain	–	0.017	1.16

4-layer model comprising the scalp, skull, CSF and brain layers was generated. Previous studies have shown that the complex boundary geometry between CSF and the grey matter does not affect the sensitivity profile [3, 5], and so a simpler, smooth model was generated. The segmentation was stored as a 3D grey scale metaimage for use in mesh generation. NIRview was also used to define source and detector positions at 1, 2 and 4 cm separations, which were stored as 3D coordinates. The metaimage was loaded into Matlab, cropped and any holes within the image matrix were filled. A 3D mesh was generated by the "iso2mesh" Matlab toolbox [10] and can be seen in Fig. 31.1. The forward modeling was performed by the light transport modeling software suite TOAST [11].

2.2 Optical Properties of the Head and Cerebrospinal Fluid

Table 31.1 shows the absorption and reduced scattering coefficients of the head (with the exception of the increased CSF scattering coefficient) at 780 nm, obtained from [2]. Refractive index = 1.4 was used for all tissue layers. Using the grey scale image generated in NIRview these optical properties were mapped onto individual 3D image matrices, similar to the one used to generate the mesh, for use in the TOAST toolbox.

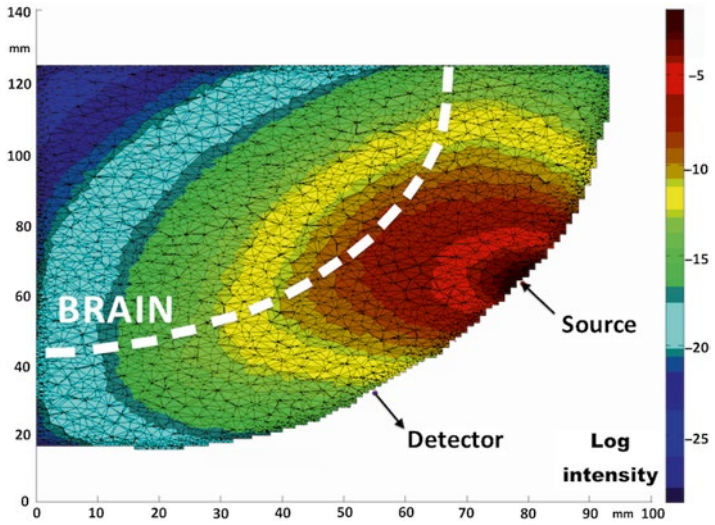

Fig. 31.2 Photon distribution (generated in TOAST)

To simulate the effect of blood contaminating the CSF, concentrations of red blood cells and haemoglobin following aneurysmal subarachnoid haemorrhage from [6] were used as a guide. A range of 0–1,000 μM CSF haemoglobin concentrations (C_{HbT}) was simulated. By comparison the haemoglobin concentration of whole blood is ~2.3 mM [12], therefore we feel this represents a reasonable range of possible values. A haemoglobin saturation (SO_2) of 70 % was assumed and the absorption coefficient of the pure CSF was also considered. For each contaminated haemoglobin concentration, the total absorption coefficient (μ_a) of the CSF in mm^{-1} was calculated as:

$$\mu_a(\lambda) = \left[\varepsilon_{HHb}(\lambda) \cdot C_{HbT} \cdot \left(1 - \frac{SO_2}{100}\right) + \varepsilon_{O_2Hb}(\lambda) \cdot C_{HbT} \cdot \frac{SO_2}{100} \times \ln 10 \times 10^{-4} + 0.0017 \right] \quad (31.1)$$

where $\varepsilon_{HHb}/\varepsilon_{O2Hb}$ is the specific extinction coefficient (OD/mM/cm with a log base of 10) for deoxy-/oxy-haemoglobin.

2.3 *Forward Modeling and Measurement of Sensitivity*

The mesh was converted into the toolbox environment, and the 3D matrices representing the optical properties mapped onto it. The source/detector positions were loaded. Forward modeling combines the mesh with the optical properties and source vector to create a map of photon fluence from the source (Fig. 31.2). This is combined with the detector vector to give the output intensity at the detector [11].

Forward modeling was carried out for each CSF haemoglobin concentration in turn. To measure the optical partial pathlength in the brain tissue layer, an initial reference intensity output was measured. Then, a 5 % change in the absorption coefficient was introduced into each layer in turn, a new intensity value measured. The change in optical attenuation from the reference value was divided by the 5 % induced absorption coefficient change to obtain a value for the partial pathlength for each layer (pathlength $= \partial A / \partial \mu_a$). This also allowed calculation of the brain tissue layer pathlength as a proportion of the total pathlength.

3 Results

Initial testing of the head model showed that values for partial pathlength in the brain and the total pathlength were comparable to those in previous studies [4, 5]. Only the 4 cm source/detector separation had an appreciable pathlength for zero CSF haemoglobin concentration within the brain, and the following results are derived from the 4 cm configuration. As shown in Fig. 31.3, when there is no CSF haemoglobin, the absolute cerebral partial pathlength is approximately 11 mm. As the CSF haemoglobin concentration increases, the cerebral partial pathlength reduces exponentially. It behaves similarly as a proportion of total pathlength, as shown in Fig. 31.4, dropping from just under 5 % in the normal model to almost nothing at the highest concentration of 1,000 μM. The reduction in the sensitivity to the brain can also be seen from Fig. 31.5 that depicts a redistribution of sensitivity to the extracerebral layers as the CSF haemoglobin concentration increases. In Wahlgren et al. [6], the maximal haemoglobin concentration was caused by a posterior cerebellar artery aneurysm, and represents the extreme maximum of the

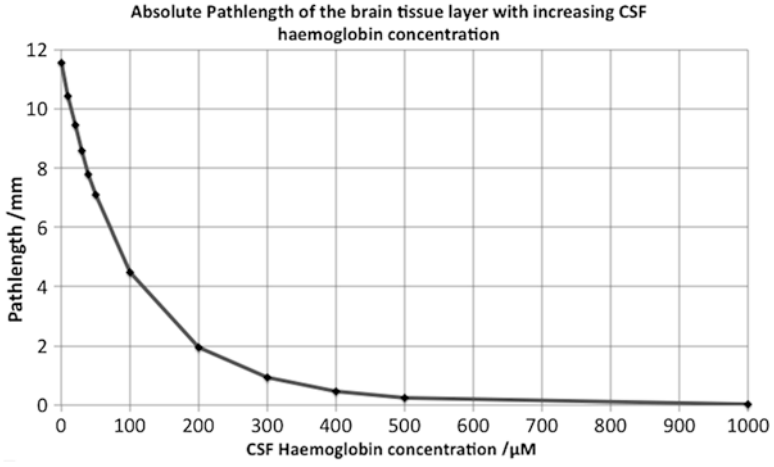

Fig. 31.3 Changes in partial pathlength in the brain tissue layer with increasing CSF haemoglobin

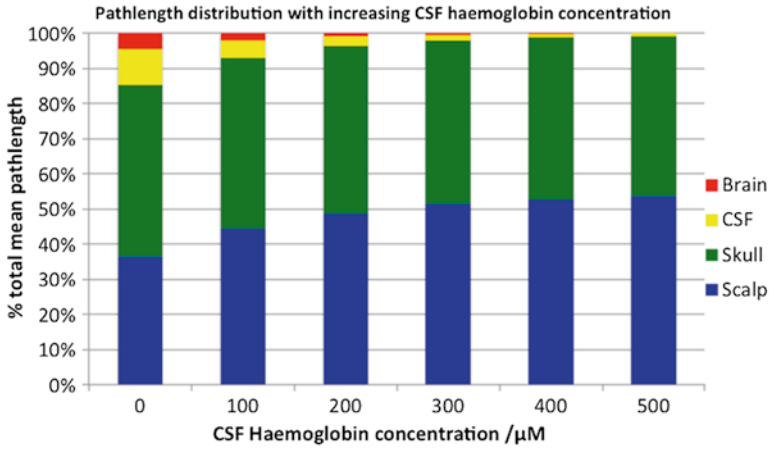

Fig. 31.4 The overall pathlength distribution with increasing CSF haemoglobin concentration

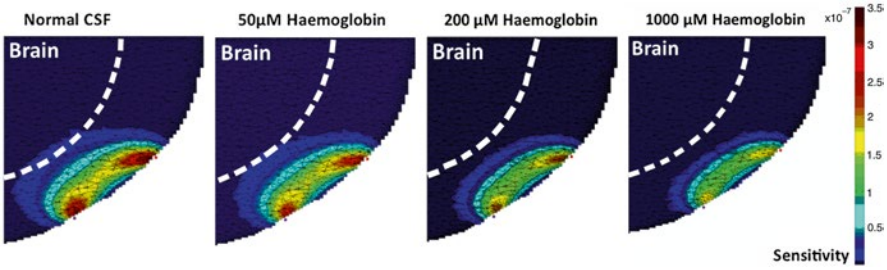

Fig. 31.5 NIRS sensitivity profiles with increasing CSF haemoglobin concentrations

range of haemoglobin concentrations detected at lumbar puncture. The reduced effect of lower concentrations implies that smaller haemorrhages will cause a smaller reduction in sensitivity or, if diffusion of blood in the CSF is limited, one more localized to the area around the haemorrhage. As a metric, from simple interpolation of Fig. 31.3, we predict a 50 % reduction in sensitivity and specificity at approximately 75 µM CSF haemoglobin concentration.

4 Discussion and Conclusion

These results clearly show that increased absorption of NIR light in the CSF layer due to haemoglobin can have a significant effect on the sensitivity profile of NIRS. However, due to the assumptions made, we are unable provide an exact quantification of any sensitivity reduction in patients.

The key limitation of this study is the assumptions made regarding CSF haemoglobin concentration. The initial values were obtained from lumbar puncture [6], and are unlikely to reflect the conditions around the brain. With this in mind the maximum-recorded values were used to create a range of feasible CSF haemoglobin concentrations. Other limitations include the fixed 70 % oxygen saturation assumed to calculate absorption coefficient values, the ignoring of any scattering effect of blood components, and a possible overestimation of the skin and CSF layers at the expense of the skull, due to poor MRI resolution of the bone layer. Similarly, cerebral oedema, which often follows brain haemorrhage and may reduce these layer thickness, was not considered. It should also be noted that breakdown products of blood, such as bilirubin, were not accounted for separately.

Despite this, we have shown that the presence of haemoglobin within the CSF has the potential to seriously reduce the sensitivity and brain specificity of NIRS. For example Figs. 31.3 and 31.4 show how at a haemoglobin concentration of 100 μM the partial pathlength of the brain drops from ~5 to ~2 %.While this may still enable measurements of brain tissue, measurement techniques and algorithms that calculate oxygenation may need to be modified to account for reduced brain specificity. However, as CSF haemoglobin concentration rises, the increasing reduction in sensitivity may preclude the use of NIRS as an imaging technique entirely.

Although previous studies have confirmed the utility of NIRS as an imaging technique in patients with SAH [13], this work suggests the potential for underestimation of measurements due to reduced sensitivity, and may help explain any abnormal or failed readings. Methods such as time-resolved spectroscopy, utilised by Yokose et al. [13], give increased depth sensitivity and may help counteract reduced specificity for the brain tissue [14]. Anatomical imaging might also be used to increase sensitivity through individualization of NIRS measurements.

Future studies in this area should aim to accurately quantify the effect of SAH on NIRS in patients through obtaining direct measurements of CSF haemoglobin following haemorrhage, and by accounting for the different absorption characteristics of bilirubin, which will determine how haemorrhage affects NIRS sensitivity in the days and weeks following SAH.

References

1. Hiraoka M, Firbank M, Essenpreis M et al (1993) A Monte Carlo investigation of optical pathlength in inhomogeneous tissue and its application to near-infrared spectroscopy. Phys Med Biol 38:1859
2. Strangman G, Franceschini M, Boas D (2003) Factors affecting the accuracy of near-infrared spectroscopy concentration calculations for focal changes in oxygenation parameters. Neuroimage 18:865–879
3. Dehghani H, Delpy D (2000) Near-infrared spectroscopy of the adult head: effect of scattering and absorbing obstructions in the CSF layer on light distribution in the tissue. Appl Optics 39:4721–4729
4. Custo A, Wells W, Barnett A (2006) Effective scattering coefficient of the cerebral spinal fluid in adult head models for diffuse optical imaging. Appl Optics 45:4747–4755

5. Okada E, Delpy DT (2003) Near-infrared light propagation in an adult head model. I. Modeling of low-level scattering in the cerebrospinal fluid layer. Appl Optics 42:2906–2914
6. Wahlgren N, Lindquist C (1987) Haem derivatives in the cerebrospinal fluid after intracranial haemorrhage. Eur Neurol 26:216–221
7. Germon T, Young A, Manara A, Nelson R (1995) Extracerebral absorption of near infrared light influences the detection of increased cerebral oxygenation monitored by near infrared spectroscopy. J Neurol Neurosurg Psychiatry 58:477–479
8. Cocosco C, Kollokian V, Kwan R et al (1997) BrainWeb: online interface to a 3D MRI simulated brain database. Neuroimage 4(2/4):S425
9. Jermyn M, Pogue B, Ghadyani H et al (2012) A user-enabling visual workflow for near-infrared light transport modeling in tissue. Biomed Optics OSA Tech Digest BW 1:A.7
10. Fang Q, Boas D (2009) Tetrahedral mesh generation from volumetric binary and gray-scale images. Proc IEEE Int Symp Biomed Image, pp 1142–1145
11. Arridge S, Schweiger M, Hiraoka M, Delpy DT (1993) A finite element approach for modeling photon transport in tissue. Med Phys 20:299–309
12. Bunn HF (2011) Approach to the anemias. In: Goldman L, Schafer AI (eds) Cecil medicine, Chap. 161, 24th edn. Saunders Elsevier, Philadelphia, PA
13. Yokose N et al (2010) Bedside monitoring of cerebral blood oxygenation and hemodynamics after aneurysmal subarachnoid hemorrhage by quantitative time-resolved near-infrared spectroscopy. World Neurosurg 73:508–513
14. Liebert A et al (2004) Time-resolved multidistance near-infrared spectroscopy of the adult head: intracerebral and extracerebral absorption changes from moments of distribution of times of flight of photons. Appl Optics 43(15):3037–3047

Chapter 32
Vessel Specific Imaging of Glucose Transfer with Fluorescent Glucose Analogue in Anesthetized Mouse Cortex

Rei Murata, Yuki Takada, Hiroyuki Takuwa, Hiroshi Kawaguchi, Hiroshi Ito, Iwao Kanno, Naotomo Tottori, Yukio Yamada, Yutaka Tomita, Yoshiaki Itoh, Norihiro Suzuki, Katsuya Yamada, and Kazuto Masamoto

Abstract The present study examined glucose transfer in the cellular scale of mouse brain microvasculature *in vivo* using two-photon microscopy and fluorescent glucose analogue (2-NBDG). The 2-NBDG was intravenously injected (0.04 mL/min) in the anesthetized Tie2-GFP mice in which the vascular endothelium expressed fluorescent protein. Time-lapse imaging was conducted on the cortical parenchyma, while the time–intensity change of the injected 2-NBDG was analysed in respective vascular compartments (artery, capillary, and vein). We observed that 2-NBDG signal increased monotonically in the vasculature during the period of the injection, and rapidly declined following its cessation. In tissue compartment, however, the signal intensity gradually increased even after cessation of the injection. Spatiotemporal analysis of the 2-NBDG intensity over the cross-sections of the

R. Murata • Y. Takada • N. Tottori • Y. Yamada
Department of Mechanical Engineering and Intelligent System,
The University of Electro-Communications, Tokyo, Japan

H. Takuwa • H. Kawaguchi • H. Ito • I. Kanno
Molecular Imaging Center, National Institute of Radiological Sciences, Chiba 263-8555, Japan

Y. Tomita • Y. Itoh • N. Suzuki
Department of Neurology, Keio University School of Medicine, Tokyo, Japan

K. Yamada
Department of Physiology, Hirosaki University Graduate School of Medicine,
Hirosaki, Japan

K. Masamoto, Ph.D. (✉)
Department of Mechanical Engineering and Intelligent System, Graduate School of Informatics and Engineering, The University of Electro-Communications, 1-5-1 Chofugaoka, Chofu, Tokyo 182-8585, Japan

Molecular Imaging Center, National Institute of Radiological Sciences, Chiba 263-8555, Japan

Brain Science Inspired Life Support Research Center, University of Electro-Communications, 1-5-1 Chofugaoka, Chofu, Tokyo, 182-8585, Japan
e-mail: masamoto@mce.uec.ac.jp

H.M. Swartz et al. (eds.), *Oxygen Transport to Tissue XXXVI*, Advances in Experimental Medicine and Biology 812, DOI 10.1007/978-1-4939-0620-8_32,

vessels further showed distinct change of the 2-NBDG intensity across the vessel wall (endothelium), which may represents a regulation site of tissue glucose influx.

Keywords Optical imaging • Glucose transporter • Vascular endothelial cell • 2-NBDG • Two-photon microscopy

1 Introduction

Brain is an organ which requires a large amount of glucose to maintain its function. A classic approach to measure brain glucose uptake is positron-emission tomography with 2-[^{18}F] fluoro-2-deoxy glucose, FDG-PET. FDG-PET allows for non-invasive measurement of the body distribution of glucose labeled with radioactive isotope. The technique is less invasive, but limited to the spatial resolution, such as to resolve the transportation to single cell. Another classic method is autoradiography that has a sufficient spatial resolution, but is only available for postmortem histology. Unlike these previous techniques, fluorescent imaging offers dynamic measurement of the glucose transfer in living brains with a high spatial resolution. 2-[N-(7-nitrobenz-2-oxa-1,3-diazol-4-yl)amino]-2-deoxy-D-glucose (2-NBDG) is the well-characterized fluorescent glucose analogue which enables us to track transport dynamics with a single cell resolution [1, 2]. The 2-NBDG is also known to bind with glucose transporters and pass through the cell membrane [3], which shares the biological characteristics of native glucose. In addition, 2-NBDG taken into the cells is phosphorylated, and the metabolite of 2-NBDG is further decomposed to a non-fluorescent derivative [4]. Using 2-NBDG, it is therefore possible to evaluate the spatiotemporal changes of the glucose transportation across the living brain cells *in vivo*.

The present study was aimed to visualize the glucose transfer in *in vivo* mouse cortex using 2-NBDG and two-photon microscopy to compare the glucose transport dynamics among the vessel types (e.g., artery, capillary, and vein). The vascular compartment was identified using genetically-engineered mice in which the vascular endothelium expressed green fluorescent protein (GFP) [5–7]. Then, the time–intensity curve of the intravenously injected 2-NBDG was measured in blood, a vessel wall, and tissue space, and compared across the vessel types.

2 Methods

2.1 Experiments

All experimental protocols were approved by the Institutional Animal Care and Use Committee of the National Institute of Radiological Sciences. To visualize the vasculature, Tie2-GFP mice (24.8–36.8 g, N = 4) in which the vascular endothelium expressed GFP [4] were used for the experiments. At least 1 week before the

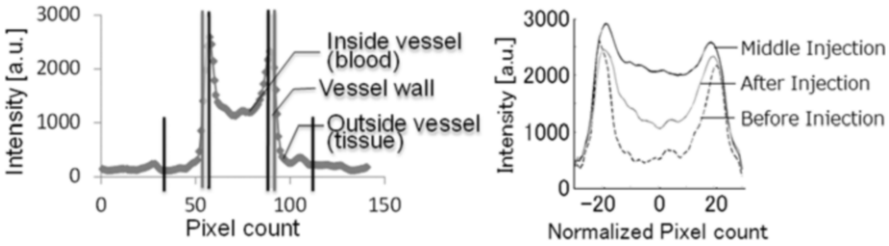

Fig. 32.1 Pixel intensity profile on the line drawn perpendicular to the vessel. *Left*: Based on the intensity profile of GFP expressed vascular endothelial cells, pixels were classified into three segments (inside of vessel, vessel wall, and outside of vessel). The edges that showed the highest intensity represent a location of the GFP expressed vascular endothelial cells. *Right*: Representative profiles of the pixel intensity changes before (*black dot*), during (*black line*), and after (*gray line*) injection of the 2-NBDG measured at the same location

experiments, the animal skull (3–4 mm diameter) over the left parietal cortex was removed and replaced with a glass cover to make a closed cranial window [8].

On the day of the experiments, the animal was anesthetized with isoflurane (2–3 % for induction, 1 % for experiments) and a cannula was inserted into one of the tail veins. The rectal temperature was maintained at 37–38 ºC, and physiological conditions (respiration rate and heart beat) were monitored with mouse Ox sensors (mouse Ox, STARR Life Sciences Corp., PA). The cortical vasculature was imaged through a cranial window with a two-photon microscope (TCS SP5MP, Leica Microsystems, Germany) at 880-nm excitation (MaiTai HP, Spectra-Physics, CA) and an emission signal was measured through a band pass filter of 506–594 nm. The 2-NBDG (2 mM in saline) was injected at a rate of 0.04 mL per min for 5 min, while the image was captured every 2–60 s for 1 h after the onset of injection. Each image consisted of 512 by 512 pixels with in-plane pixel resolution of 0.59 μm. The image was acquired at cortical surface for measurement of arteries and veins and a depth of 60 μm for capillaries sequentially in each location of the measurements for single injection.

2.2 Image Analysis

Time–intensity curve of the injected 2-NBDG was determined by measuring the pixel intensity over the single line perpendicular to the vessel in each image. The lines were drawn at ten different locations for single vessel segments. Based on the pixel intensity profile on the line before the dye injection, pixels were classified into three segments (inside vessel, vessel wall, outside vessel) (Fig. 32.1). The vessel wall (i.e., GFP-expressed vascular endothelial cells) was assigned for 3 pixels in the artery and vein, and 2 pixels in the capillaries, around the peak position of the pixel intensity on the line profile. The artery shows a thick vessel wall having dense GFP endothelial cells, whereas the vein had a thin wall and sparse distribution of the cells. The capillary was a diameter of approximately 5 μm in the image. The diameter of

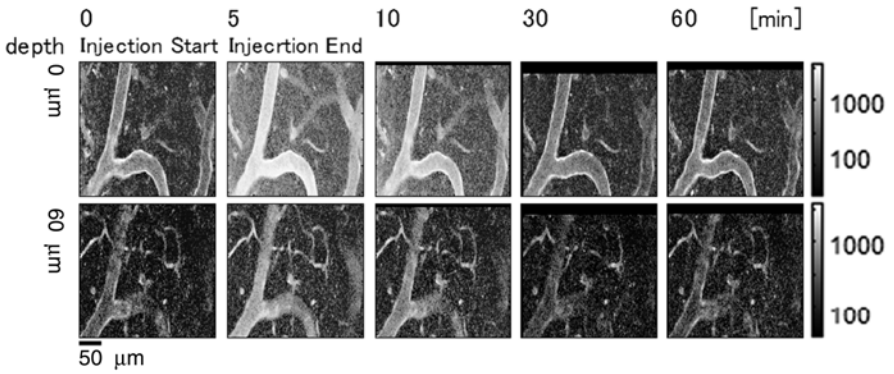

Fig. 32.2 Spatiotemporal dynamics of the pixel intensity changes following the 2-NBDG injection. The represented image showed a single frame measured at depth 0 μm (*top*) and 60 μm (*bottom*) from the cortical surface. Before injection of the 2-NBDG, vascular wall can be seen through GFP-expressed endothelial cells. Following the intravenous injection of 2-NBDG, the fluorescent intensity was detected in the vessel compartments, and then the signal gradually decreased, whereas it appeared at the tissue compartments

the vessel was normalized at the vessel wall (assigned as 20) and the center of the vessel (0). As shown in Fig. 32.1, the pre-injection baseline signal intensity differed between the measured locations, due to the background noise and GFP-expressing endothelial cells at the vessel wall. After injection of 2-NBDG, pixel intensity in the vessel (blood) clearly increased, but not tissue in vicinity of the vessel wall (Fig. 32.1). To correct the difference of the baseline level between the measured locations, the time–intensity curve of 2-NBDG was subtracted by the pre-injection baseline level, and normalized with its peak value and then averaged over the measurements in each time point.

3 Results and Discussion

3.1 Time–Intensity Curve of 2-NBDG

Following the onset of 2-NBDG injection, fluorescent intensity in the blood compartment increased over the periods of the injection (0–5 min), and after the cessation of the injection it gradually decreased (5–30 min) (Fig. 32.2). In contrast, tissue compartments showed a gradual increase of the intensity over the periods (Fig. 32.2), which continued even after cessation of the injection. The line profile across the vessel cross-section showed that there were no detectable differences in the time–intensity curve of the inside vessels among the different vessel types (Fig. 32.3a). Also, outside of the vessels had similar trend of the time–intensity curve irrespective of the vessel types (Fig. 32.3c). These findings suggest that there are no preferences for the blood to tissue glucose transportation among the vessel types (i.e., artery, capillary, and vein).

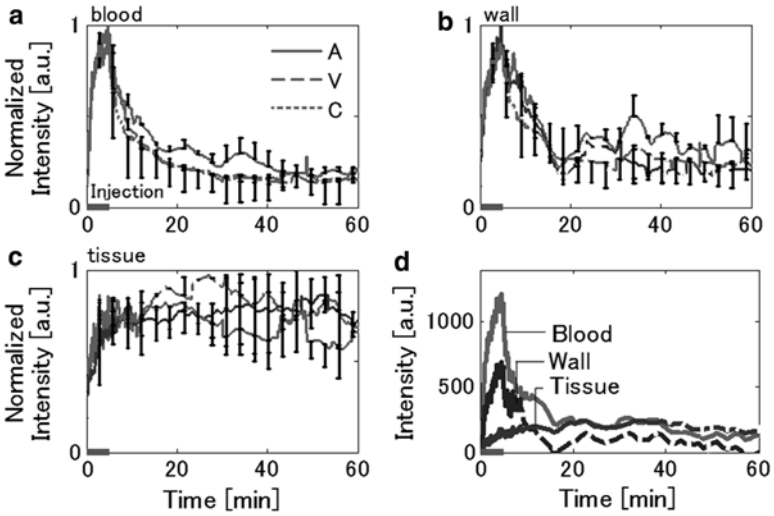

Fig. 32.3 Time-intensity curve compared across the vessel compartments. Mean time-intensity curve was compared for each segment of the inside vessel (**a**), vessel wall (**b**), and outside vessel (**c**) across the artery (*A; gray line*), vein (*V; gray dot line*), and capillary (*C; black dot line*) compartments. Y-axis represents a normalized pixel intensity relative to pre-injection baseline level and peak intensity. Similar trends of the intensity dynamic changes were observed irrespective of the vessel types. The intravenous injection of 2-NBDG were made time from 0 to 5 min. Data represent mean ± SD (N = 4 animals). (**d**) Comparison of the time-intensity curve across the three locations (inside vessel, vessel wall, and outside vessel). Y-axis represents a mean fluorescent intensity measured over the pixels within the respective locations. Mean time-intensity curve showed a fast and monotonic increase of the 2-NBDG intensity in the vessel during the periods of the injection (0–5 min), whereas the gradual signal increase was detected outside the vessel segment (0–30 min)

In addition, there were no detectable differences of the time-intensity curve measured at the vessel wall among the vessel types (Fig. 32.3b). However, the signals obtained at the vessel wall shows a mixture of the signal dynamics measured in blood and tissue compartments (Fig. 32.3d). This finding may indicate that the capillary wall is too thin to detect the signals purely originating from the vessel wall, and thus the signals originating from the both compartments may be contaminated.

3.2 Spatiotemporal Evolution of the 2-NBDG from Blood to Tissue Compartments

We observed that the spatial distribution of the 2-NBDG was greatly different at the boundary between the blood (inside vessel) and tissue (outside vessel) compartments during early phases of the injection (0–15 min after the onset of the injection) (Fig. 32.3d). Whether this 2-NBDG distribution results from control mechanisms of the vascular endothelial cells remains unclear. To resolve this question, it is needed to further improve the spatial resolution of the imaging technique and to distinguish the

differences of the 2NBDG signals at the vessel wall of the blood and tissue sides. Finally, we assumed that the measured fluorescent intensity reflects the concentration of 2-NBDG. However, the estimation of 2-NBDG concentration from the fluorescent intensity was confounded by several factors. First, self-absorption of the 2-NBDG may affect the linearity of the intensity-concentration relationships, specifically for the high concentration of 2-NBDG. Second, tissue and blood have different optical properties, such as absorption and scattering, which should be considered to compare the 2-NBDG concentrations between those two compartments.

4 Conclusions

A similar trend of the time-intensity curve of the 2-NBDG transfer to tissue was observed irrespective of the vessel types, which indicates no preferences of the glucose transportation among the vessel types. Future studies on the comparisons of glucose transporter density among the vessel walls are required to further understand the regulatory mechanism of the glucose delivery to brain tissue.

Acknowledgments This study was partially supported through funding from JSPS KAKENHI (#25750400) (to K.M.), JSPS KEKENHI (#24659578) (to I.K.), and a grant from the Ministry of Health, Labor and Welfare (MHLW), Japan (to I.K.).

References

1. Yoshioka K, Takahashi H, Homma T, Saito M, Oh KB, Nemoto Y, Matsuoka H (1996) A novel fluorescent derivative of glucose applicable to the assessment of glucose uptake activity of Escherichia coli. Biochim Biophys Acta 1289:5–9
2. Yamada K, Saito M, Matsuoka H, Inagaki N (2007) A real-time method of imaging glucose uptake in single, living mammalian cells. Nat Protoc 2:753–762
3. Yamada K, Nakata M, Horimoto N, Saito M, Matsuoka H, Inagaki N (2000) Measurement of glucose uptake and intracellular calcium concentration in single, living pancreatic beta-cells. J Biol Chem 275:22278–22283
4. Yoshioka K, Saito M, Oh KB, Nemoto Y, Matsuoka H, Natsume M, Abe H (1996) Intracellular fate of 2-NBDG, a fluorescent probe for glucose uptake activity, in Escherichia coli cells. Biosci Biotechnol Biochem 60:1899–1901
5. Motoike T, Loughna S, Perens E, Roman BL, Liao W, Chau TC, Richardson CD, Kawate T, Kuno J, Weinstein BM, Stainier DY, Sato TN (2000) Universal GFP reporter for the study of vascular development. Genesis 28:75–81
6. Itoh Y, Toriumi H, Yamada S, Hoshino H, Suzuki N (2010) Resident endothelial cells surrounding damaged arterial endothelium reendothelialize the lesion. Arterioscler Thromb Vasc Biol 30:1725–1732
7. Masamoto K, Tomita Y, Toriumi H, Aoki I, Unekawa M, Takuwa H, Itoh Y, Suzuki N, Kanno I (2012) Repeated longitudinal in vivo imaging of neuro-gliovascular unit at the peripheral boundary of ischemia in mouse cerebral cortex. Neuroscience 212:190–200
8. Tomita Y, Kubis N, Calando Y, Tran Dinh A, Méric P, Seylaz J, Pinard E (2005) Long-term in vivo investigation of mouse cerebral microcirculation by fluorescence confocal microscopy in the area of focal ischemia. J Cereb Blood Flow Metab 25(7):858–867

Chapter 33
Ischemic Pretreatment Delays Ischemic Brain Vasospasm Injury in Gerbils

Akitoshi Seiyama, Nao Yoshikawa, and Yukio Imamura

Abstract Three experiments were conducted for the present study. First, to elucidate the mechanism and functional significance underlying ischemic vasoconstriction, we investigated the relationship between arteriolar constriction and tissue energy metabolism during bilateral common carotid artery occlusion in gerbils. Second, to identify differences in the postischemic recovery of physiologic parameters between short and prolonged brain ischemia, we measured changes in regional cerebral blood flow, microvessel diameter, brain temperature, and electrophysiologic response. Third, to explore the physiological mechanism of ischemic tolerance, we studied vascular response and intracerebral oxygenation states after acute global ischemia with and without pretreatment by mild ischemic stress. Here, we identify one of the physiologic mechanisms of the ischemic tolerance caused by brief ischemic pretreatment.

Keywords Global ischemia • Cerebral blood flow • Brain temperature • Reperfusion injury • Ischemic tolerance

1 Introduction

Acute ischemia induces severe reduction of brain energy level and results in histological damage. The pathophysiological mechanism of ischemic tolerance caused by pretreatment with mild ischemic stress (MIS) is still speculative. Our previous study with bilateral carotid artery occlusion (BCO) in gerbils indicated that improvement of the tissue oxygenation state during ischemia might contribute to ischemic tolerance [1], that mismatch recovery of r-CBF and BrT after prolonged ischemia

A. Seiyama (✉) • N. Yoshikawa • Y. Imamura
Division of Medical Devices for Diagnoses, Human Health Sciences,
Graduate School of Medicine, Kyoto University, 53 Shogoin, Kawahara-cho,
Sakyo-ku, Kyoto 606-8507, Japan
e-mail: seiyama.akitoshi.7x@kyoto-u.ac.jp

H.M. Swartz et al. (eds.), *Oxygen Transport to Tissue XXXVI*, Advances in Experimental Medicine and Biology 812, DOI 10.1007/978-1-4939-0620-8_33,

initiates metabolic derangement in brain tissue, leading to the electrochemical dysfunction and mortality [2], and that pretreatment by mild ischemic stress induced improvement of the tissue oxygenation state during ischemia and contributed to the acquisition of ischemic tolerance [3]. In the present study, we aimed to clarify effects of brain temperature, energy metabolism and vasospasm on post-ischemic reperfusion injury or viability in the gerbil brain and the physiological mechanisms for acquisition of ischemic tolerance by brief ischemic pretreatment.

2 Methods

2.1 Experiment 1

Adult mongolian gerbils (weighting 50–60 g, total n = 32) were used. After pentobarbital anesthesia (50 mg/kg), a cranial window (4×4 mm^2) was prepared at 4.0 mm right and 4.0 mm caudal to the bregma. Global ischemia was induced by bilateral common carotid artery occlusion (BCO) for 5 min. Using our original microspectroscopy, the arteriolar caliber and tissue oxygenation were monitored in the cerebral cortex in vivo. After in situ freezing of the brain, adenine nucleotides, creatine phosphate (P-Cr), and lactate levels were analyzed using HPLC in vitro. Tissue damage was also assessed immunohistochemically using antibodies against microtubule-associated proteins.

2.2 Experiment 2

Mongolian gerbils were assigned to one of three groups: 5-min (G5, n = 6), 15-min (G15, n = 6), or 30-min (G30, n = 6) BCO ischemia. After pentobarbital anesthesia, a cranial window (4×4 mm^2) was prepared at 4.0 mm right and 4.0 mm caudal to the bregma. Using our original microspectroscopy system, global ischemic reperfusion was performed. Changes in regional cerebral blood flow (r-CBF), microvessel diameter, and brain temperature (BrT) were measured simultaneously. We also monitored somatosensory evoked potentials (SEPs) to evaluate electrophysiologic response.

2.3 Experiment 3

Under anesthesia, adult gerbils with sham operation (i.e., only 5 min ischemia) (S-group, n = 8) and those with pretreatment twice by global ischemia for 2 min at 3 days and 2 days before a 5 min global ischemia (MIS group, n = 8) were examined. Changes in tissue oxygenation were calculated from the absorbance changes of the

light transmitted through the brain using near infrared spectroscopy. Changes in diameter of pial arterioles were measured using our original microspectroscopy system. Seven days after the ischemic study, immunohistochemical examination was performed with an antiserum against microtubule-associated proteins.

3 Results

3.1 Effects of Ischemia on Vasoconstriction

Two phases of vasoconstriction were observed (Fig. 33.1a). Vasoconstriction was found between 1 and 2.5 min of occlusion (Fig. 33.1a–d, dark shadows. That delayed vasospasm had no additional effect on tissue energy depletion (Fig. 33.1a–d, light shadows), and imminent neuronal damage (Fig. 33.2).

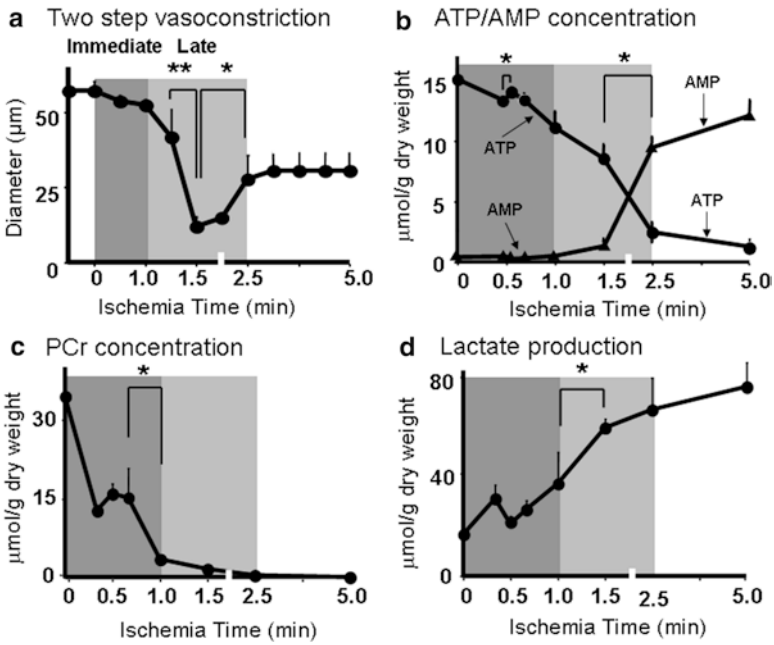

Fig. 33.1 Temporal changes in the pial arteriolar diameter and energy level during 5 min-acute ischemia. (**a**) Pial arteriolar diameter; (**b**) closed circle for ATP, closed triangle for AMP; (**c**) P-Cr; (**d**) lactate. The unit of ATP, AMP, P-Cr and lactate is pmol/μg dry weight. *Dark* and *light* zones denote the duration of immediate and late vasoconstriction, respectively. Data were modified from ref. [1]

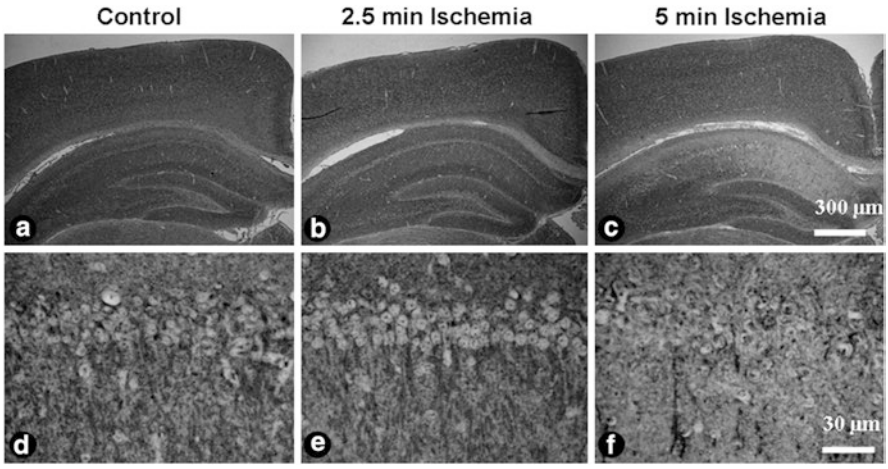

Fig. 33.2 Comparison of Hippocampus CA1 activity to immunohistochemical reaction to MAPs after reperfusion for 7 days (**a**, **d**): sham-operated control animal. Note extensive neuronal damages in the CA1 area of the hippocampus (**c**, **f**), but not in the cerebral cortex (**c**), following ischemia for 5 min. No changes were observed after ischemia for 2.5 min (**b**, **e**)

3.2 Effect of Ischemia Time on Postischemic Recovery of Physiologic Parameters

Twenty-four hours after occlusion, all G5 and G15 animals survived whereas only one of six G30 animals survived. With reperfusion after occlusion in G30 animals regional cerebral blood flow (Fig. 33.3a) rose poorly, brain temperature (Fig. 33.3b) rose almost 3 °C and electrochemical function failed to recover (Fig. 33.3c).

3.3 Effect of Ischemic Pretreatment on Tissue Oxygenation and Tissue Damage

Brief preliminary occlusions (MIS) improved tissue oxygenation during subsequent ischemia (Fig. 33.4). Seven days after reperfusion, all gerbils without preocclusion MIS (S-group) were found to have neuronal death in the hippocampus CA1 (Fig. 33.5 left), while those in the MIS-pretreated group (MIS-group) did not (Fig. 33.5 right).

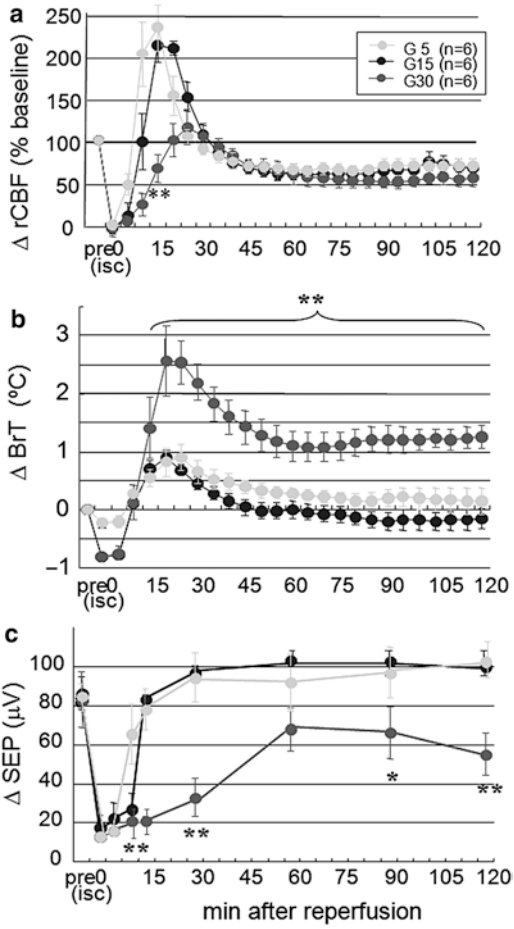

Fig. 33.3 Effect of ischemia time on the recoveries of the regional cerebral blood flow (**a**), brain temperature (**b**) and somatosensory evoked potentials (SEPs) *G5*, *G15* and *G30* denotes 5-, 15- and 30-min ischemia. Data were modified from ref. [2]

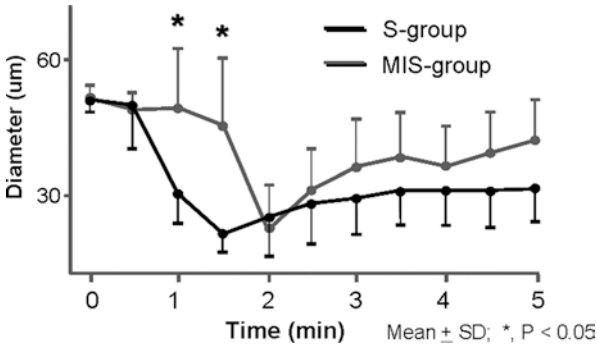

Fig. 33.4 Temporal profiles of diameter change during 5-min ischemia in the S- and MIS-groups. Note significant ($P<0.05$) differences between the S-groups and MIS-groups were observed 1.0 and 1.5 min after ischemia onset

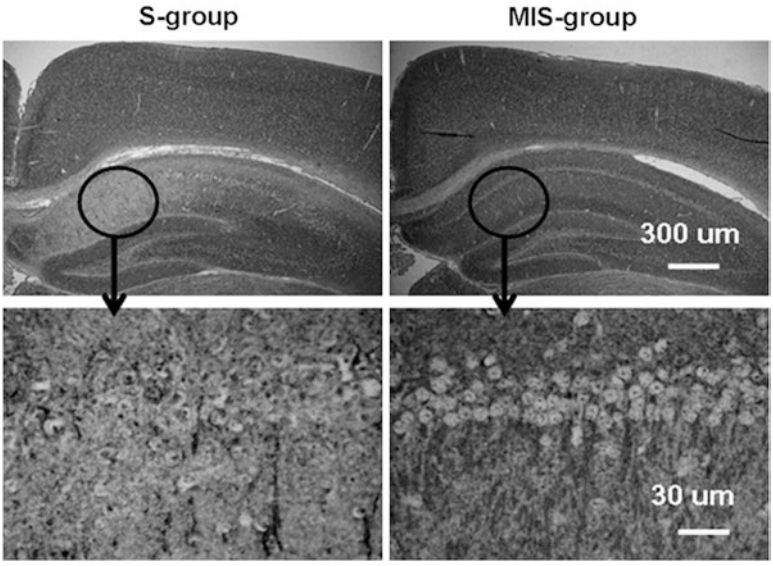

Fig. 33.5 Comparison of hippocampus CA1 activity to immunohistochemical reaction to MAPs after reperfusion for 7 days. Note extensive immuno-histochemical reactions in the S-group, but no apparent abnormality in the MIS-group

4 Discussion

Present results suggest that ischemic tolerance caused by two brief preischemic occlusions was associated with delay of ischemic vasoconstriction and thus maintenance of tissue oxygen metabolism during 5 min occlusions. Failed recovery of the cerebral blood flow and rise of brain temperature during reperfusion after ischemia initiates metabolic derangement in brain tissue, leading to brain dysfunction and mortality.

Acknowledgements The authors thank Dr. Hirokazu Ueda, Dr. Ji-Yao Li, Dr. Takehiko Yanagihara, Dr. Goro Tajima, Dr. Hiroshi Tanaka, and Dr. Hisashi Sugimoto. This study was supported in part by grants-in-aid from the Ministry of Education, Science and Culture of Japan.

References

1. Li JY, Ueda H, Seiyama A et al (2007) Ischemic vasoconstriction and tissue energy metabolism during global cerebral ischemia in gerbils. J Neurotrauma 24:547–558
2. Tajima G, Shiozaki T, Seiyama A et al (2007) Mismatch recovery of regional cerebral blood flow and brain temperature during reperfusion after prolonged brain ischemia in gerbils. J Trauma 62:36–43
3. Li JY, Ueda H, Seiyama A et al (1997) A near-infrared spectroscopic study of cerebral ischemia and ischemic tolerance in gerbils. Stroke 28:1451–1456

Chapter 34
Changes in Cerebral Blood Oxygenation Induced by Active Standing Test in Children with POTS and NMS

Ayumi Endo, Yukihiko Fujita, Tatsuo Fuchigami, Shori Takahashi, Hideo Mugishima, and Kaoru Skatani

Abstract Orthostatic dysregulation (OD) has been classified into subtypes by heart rate and blood pressure; however, the hemodynamics of brains have not yet been revealed. Therefore, we investigated changes in cerebral blood flow and oxygenation during an active standing test to clarify the pathophysiology of two subtypes: postural tachycardia syndrome (POTS) and neurally mediated syncope (NMS). We studied 31 children (15 boys, 16 girls; mean age, 14.0 ± 1.7 years) who presented with OD at the Department of Pediatrics and Child Health, Nihon University School of Medicine between 2009 and 2011. OD was diagnosed using the Japanese clinical guidelines for juvenile orthostatic dysregulation. After a 10-min resting period in the supine position, patients were asked to quickly stand up and keep upright for 10 min. Cerebral blood flow and cerebral oxygenation were measured using transcranial Doppler sonography and near-infrared spectroscopy. POTS showed a significant decrease of oxy-Hb and resistance index (RI), suggesting transient ischemia with maintainable cerebral autoregulation. NMS showed a decrease of oxy-Hb and an increase of RI, suggesting ischemia and impairment of autoregulation.

Keywords Orthostaticdysregulation • Postural tachycardia syndrome • Neurally mediated syncope • Transcranial Doppler sonography • Near-infrared spectroscopy

A. Endo, M.D., Ph.D. • Y. Fujita, M.D., Ph.D. (✉) • T. Fuchigami, M.D., Ph.D.
S. Takahashi, M.D., Ph.D. • H. Mugishima, M.D., Ph.D.
Department of Pediatrics and Child Health, Nihon University School of Medicine,
30-1 Oyaguchi-Kamicho, Itabashi-ku, Tokyo 173-8610, Japan
e-mail: fujita.yukihiko@nihon-u.ac.jp

K. Skatani, M.D., Ph.D.
Department of Neurological Surgery, Nihon University School of Medicine, Tokyo, Japan

Nihon University College of Engineering, Tokyo, Japan

H.M. Swartz et al. (eds.), *Oxygen Transport to Tissue XXXVI*, Advances in Experimental Medicine and Biology 812, DOI 10.1007/978-1-4939-0620-8_34,

1 Introduction

Orthostatic intolerance, known as orthostatic dysregulation (OD) in Japanese pediatrics, is an autonomic nervous system disorder of children and adolescents. The first OD research meeting in Japan was held in 1959 [1], where an original OD study group and proposed diagnostic criteria were developed. Patients with OD often present with various symptoms including vertigo on standing up, fainting in the standing position, and unspecific symptoms and signs in adolescents. The mechanism of these symptoms seems to be related to an imbalance between sympathetic nerves and parasympathetic nerves. The Task Force of Clinical Guidelines for Child Orthostatic Dysregulation of Japan has recently issued clinical guidelines for juvenile OD (version 1) [2], which advocates new diagnostic criteria including a modified Schellong test to classify the subtype of OD for a general pediatrician. While these diagnostic criteria are useful for speculating the pathophysiology, a more simple method for objectively evaluating hemodynamic changes, in particular, flow of central venous return, is required. In the Japanese clinical guidelines, four subsets of OD were recognized using non-invasive beat-to-beat blood pressure and heart rate monitoring: instantaneous orthostatic hypotension (INOH), postural tachycardia syndrome (POTS), neurally mediated syncope (NMS), and delayed orthostatic hypotension (delayed OH). POTS involves marked tachycardia during upright posture without obvious hypotension. The mechanisms responsible were postulated to involve loss of plasma volume, insufficient venous constriction, or hyperadrenergic response to orthostatic stress. The criteria for defining POTS are an increase in heart rate during standing of 35 beats/min or heart rate during active standing of 115 beats/min. NMS involves sudden onset of fainting/near-fainting associated with VAS depression while standing with or without bradycardia [2]. Recently, cerebral hemodynamics have been studied in orthostatic intolerance using Transcranial Doppler (TCD) sonography [3, 4] or near-infrared spectroscopy (NIRS) [5–8]. However, there are very few reports that examine cerebral circulation changes in these patients. We presumed two or more different hemodynamics of brains in each subtype. Thus, in the present study we investigated changes in cerebral blood flow and oxygenation during active standing test to clarify the pathophysiology of POTS and NMS.

2 Methods

We studied 31 children (15 boys, 16 girls) who presented with OD at the Department of Pediatrics and Child Health, Nihon University School of Medicine, between 2009 and 2011. The subset of OD was determined with the Japanese clinical guidelines for juvenile orthostatic dysregulation [2]. The patients were not treated with any drugs. We tested a conventional Schellong's orthostatic test. After a 10-min resting period in the supine position, patients were asked to quickly stand up and keep upright for 10 min. Figure 34.1 presents an overview of the experimental protocol. Blood pressure was measured with a non-invasive beat-to-beat blood pressure

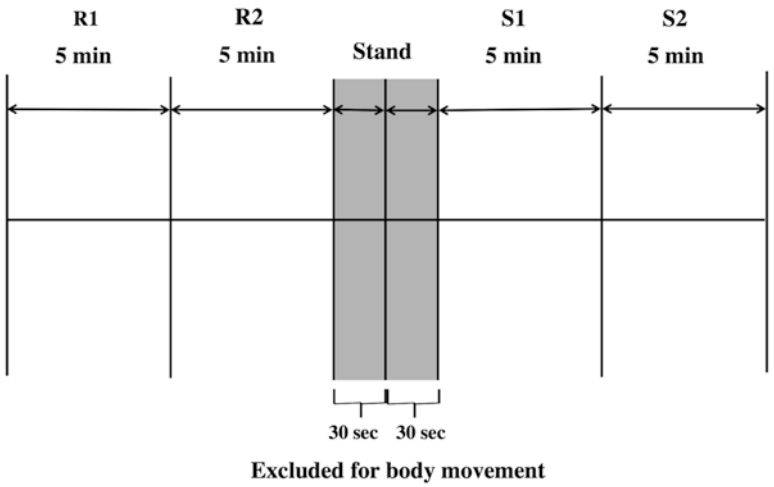

Fig. 34.1 The experimental protocol

monitor (BP-608 Evolution II CS; Omlon Colin Co., Ltd., Tokyo, Japan). Cerebral blood flow was measured by Transcranial Doppler sonography (TCD) (Companion III; Riko Trading Co., Ltd., Tokyo, Japan) and cerebral blood oxygenation was simultaneously measured by near-infrared spectroscopy (NIRS) (TRS20; time-resolved spectroscopy; Hamamatsu Photonicus Co., Ltd., Shizuoka, Japan). Nineteen patients were categorized as POTS, and 12 as NMS. The active standing tests were performed in the same quiet and temperature-regulated room by one physician and one technologist at 9:00 a.m. We terminated the test immediately when standing became impossible, or when patients became hypotensive. In TCD sonography, resistance index (RI) was calculated as a cerebral vascular resistance with the following formula: RI = Vs – Vd/Vs, where Vs and Vd represent systolic flow velocity and diastolic flow velocity, respectively in the middle cerebral artery.

The ethics committee of Nihon University Itabashi Hospital approved this study according to the revised version of the Declaration of Helsinki. Informed consent was obtained from all patients or their parents.

2.1 Statistical Analysis

Data were analyzed with statistical software (JMP8 SAS Institute Inc., Tokyo, Japan). To reduce the influence of body motion, the data for 30 s before and after standing up (for a total of 1 min) were excluded. Data were classified into four groups: R1 (first half of resting time), R2 (second half of resting time), S1 (first half of standing time), and S2 (second half of standing time) as in Fig.34.1. Based on the average value of R2, data were compared using the Dunnett's multiple comparison test. Differences were statistically significant at a P-value ≤ 0.05.

3 Results

3.1 Changes in Cerebral Blood Flow During Standing

RI data are shown in Table 34.1. During standing, RI decreased in 10 patients with POTS and increased in five patients, while RI decreased in three patients with NMS and increased in five patients.

3.2 Changes in Cerebral Blood Oxygenation

Cerebral blood oxygenation data are shown in Table 34.2. During standing, 15 patients with POTS exhibited decreased oxy-Hb, all patients exhibited increased deoxy-Hb, and 18 patients increased total-Hb. During standing, 6 patients with NMS exhibited decreased oxy-Hb, 11 patients increased deoxy-Hb, and 10 patients increased total-Hb. The summary of results is shown in Table 34.3.

Table 34.1 TCD sonography (changes of RI)

POTS					NMS				
	RI					RI			
Patients	R2	S1	S2		Patients	R2	S1	S2	
7	0.64±0.04	0.59±0.04**	0.61±0.04**	↓	22	0.58±0.02	0.54±0.03**	0.55±0.04**	↓
9	0.56±0.02	0.49±0.03**	0.50±0.04**	↓	25	0.59±0.04	0.57±0.09**	0.57±0.05**	↓
10	0.57±0.03	0.53±0.09**	0.50±0.08**	↓	31	0.50±0.04	0.48±0.13	0.50±0.06**	↓
12	0.55±0.03	0.49±0.03**	0.49±0.03**	↓	23	0.37±0.04	0.40±0.05**	0.56±0.11**	↑
13	0.60±0.04	0.58±0.04**	0.55±0.04**	↓	24	0.48±0.06	0.52±0.05**	0.61±0.11**	↑
14	0.51±0.09	0.44±0.03**	0.44±0.04**	↓	20	0.53±0.03	0.54±0.06	0.59±0.08**	↑
16	0.50±0.05	0.43±0.03**	0.42±0.03**	↓	26	0.51±0.09	0.53±0.04	0.59±0.10**	↑
8	0.44±0.04	0.43±0.04**	0.45±0.04	↓	27	0.44±0.05	0.44±0.04	0.46±0.08**	↑
11	0.52±0.05	0.51±0.07*	0.51±0.08	↓	21	0.50±0.04	0.48±0.04**	0.55±0.01**	↓↑
15	0.56±0.05	0.55±0.10	0.52±0.05**	↓	28	0.60±0.02	0.61±0.022	0.60±0.18	–
1	0.49±0.03	0.76±0.03**	0.63±0.02**	↑	29	0.57±0.05	0.56±0.04	–	–
2	0.53±0.03	0.54±0.02**	0.55±0.02**	↑	30	0.56±0.04	0.57±0.03	0.55±0.05	–
17	0.49±0.04	0.50±0.05**	0.54±0.05**	↑	–	–	–	–	–
18	0.53±0.04	0.93±0.14**	0.69±0.18**	↑	–	–	–	–	–
3	0.51±0.05	0.51±0.04	0.56±0.05**	↑	–	–	–	–	–
4	0.60±0.08	0.67±0.02**	0.56±0.01**	↑↓	–	–	–	–	–
19	0.49±0.04	0.50±0.03**	0.47±0.04**	↑↓	–	–	–	–	–
5	0.53±0.06	0.49±0.04	0.52±0.05	–	–	–	–	–	–
6	0.48±0.06	0.48±0.09	0.48±0.06	–	–	–	–	–	–

**P<0.01; *P<0.05; ↑ significantly increased; ↓ significantly decreased due to the Dunnett's multiple comparison test

Table 34.2 Change of oxy-Hb, deoxy-Hb and total-Hb

	Oxy-Hb (mean ± SD: μmol/l)				Deoxy-Hb (mean ± SD: μmol/l)				Total-Hb (mean ± SD: μmol/l)			
Patients	R2	S1	S2		R2	S1	S2		R2	S1	S2	
POTS												
1	222.3 ± 12.3	207.2 ± 13.5**	197.0 ± 11.9**	↓	84.7 ± 9.2	96.7 ± 9.6**	96.8 ± 10.4**	↑	307.0 ± 6.5	304.3 ± 2.0	303.8 ± 0	–
2	84.5 ± 2.3	82.1 ± 2.0**	82.5 ± 2.5**	↓	34.1 ± 1.3	37.4 ± 1.5**	38.4 ± 1.8**	↑	118.6 ± 1.6	119.5 ± 1.6*	120.9 ± 1.2**	↑
3	76.6 ± 1.7	74.5 ± 2.0**	73.6 ± 2.2**	↓	29.3 ± 1.2	34.1 ± 1.6**	36.3 ± 2.0**	↑	105.9 ± 1.0	108.5 ± 1.0**	109.9 ± 1.0**	↑
4	78.1 ± 3.2	74.1 ± 2.8**	69.9 ± 2.4**	↓	34.6 ± 1.9	39.5 ± 2.4**	44.8 ± 2.3**	↑	92.3 ± 1.3	96.0 ± 1.4*	97.3 ± 0.8**	↑
5	75.0 ± 2.8	73.2 ± 1.9**	73.1 ± 2.6**	↓	37.4 ± 1.7	45.2 ± 2.0**	47.4 ± 2.5**	↑	435.7 ± 127.2	627.3 ± 40.3**	638.6 ± 31.9**	↑
6	50.8 ± 12	47.0 ± 1.4**	48.6 ± 1.0**	↓	22.5 ± 0.7	28.5 ± 1.7**	30.0 ± 0.7**	↑	60.6 ± 4.3	72.9 ± 3.8**	72.9 ± 6.9**	↑
7	66.4 ± 1.1	62.8 ± 1.4**	64.7 ± 1.4**	↓	28.7 ± 0.9	32.6 ± 1.8**	33.3 ± 1.0**	↑	112.7 ± 1.8	113.6 ± 1.2**	114.7 ± 1,3**	↑
8	91.8 ± 2.4	89.9 ± 3.5**	89.2 ± 2.6**	↓	35.8 ± 1.7	41.4 ± 3.1**	44.7 ± 2.0**	↑	112.4 ± 2.0	118.4 ± 1.2**	120.5 ± 1.6**	↑
9	55.3 ± 0.9	53.5 ± 1.2**	54.4 ± 1.1**	↓	21.0 ± 0.6	22.8 ± 0.8**	23.9 ± 0.7**	↑	73.3 ± 0.6	75.5 ± 1.3	78.6 ± 0.7**	↑
10	65.6 ± 1.4	63.2 ± 1.6**	64.5 ± 1.8**	↓	35.2 ± 1.2	41.5 ± 1.7**	42.6 ± 1.5**	↑	95.2 ± 0.6	95.4 ± 1.3**	98.0 ± 0.8**	↑
11	86.0 ± 82.2	82.3 ± 2.7**	85.2 ± 4.3	↓	31.4 ± 2.3	38.8 ± 2.9**	40.1 ± 3.1**	↑	127.5 ± 1.4	131.3 ± 1.7**	133.9 ± 2.2**	↑
12	59.9 ± 1.2	59.0 ± 1.5*	60.2 ± 1.4	↓	24.3 ± 0.7	27.5 ± 1.0**	27.9 ± 1.0**	↑	76.3 ± 0.7	76.3 ± 1.0**	78.3 ± 1.0**	↑
13	66.3 ± 1.4	65.4 ± 1.4*	66.4 ± 1.5	↓	28.1 ± 0.9	32.6 ± 1.4**	34.2 ± 1.0**	↑	100.8 ± 1.4	104.7 ± 1.6**	107.1 ± 0.8**	↑
14	87.5 ± 4.1	83.2 ± 3.3**	86.0 ± 3.8	↓	50.5 ± 2.5	58.3 ± 3.1**	60.1 ± 3.0**	↑	117.4 ± 3.0	121.1 ± 2.8**	125.3 ± 2.6**	↑
15	92.2 ± 2.0	90.2 ± 1.8**	92.8 ± 2.0	↓	40.2 ± 1.1	45.0 ± 1.8**	45.7 ± 1.0**	↑	84.2 ± 0.7	86.6 ± 1.1**	88.1 ± 0.8**	↑
16	49.2 ± 1.6	49.1 ± 1.7	49.6 ± 1.5	–	31.0 ± 1.1	34.2 ± 1.9**	36.0 ± 1.4**	↑	94.4 ± 0.8	98.0 ± 1.1**	100.6 ± 1.0**	↑
17	59.1 ± 1.6	59.8 ± 1.5	59.8 ± 1.4	–	33.2 ± 0.9	35.9 ± 1.3**	37.5 ± 1.2**	↑	138.0 ± 2.3	141.5 ± 1.7**	146.1 ± 1.8**	↑
18	289.4 ± 84.2	450.4 ± 67.4**	388.6 ± 48.7**	↑	146.3 ± 63.0	177.0 ± 42.8*	250.0 ± 45.9**	↑	132.3 ± 1.4	135.2 ± 1.8**	138.6 ± 1.5**	↑
19	39.3 ± 3.7	47.2 ± 6.3**	48.4 ± 7.4**	↑	21.3 ± 2.8	25.6 ± 3.6**	24.5 ± 3.9**	↑	80.3 ± 0.8	83.2 ± 1.1**	85.6 ± 0.9**	↑

(continued)

Table 34.2 (continued)

	Oxy-Hb (mean ± SD: μmol/l)				Deoxy-Hb (mean ± SD: μmol/l)				Total-Hb (mean ± SD: μmol/l)			
Patients	R2	S1	S2		R2	S1	S2		R2	S1	S2	
NMS												
20	135.0 ± 41.1	198.4 ± 22.7**	152.0 ± 30.7	↑	48.0 ± 11.7	91.5 ± 22.5**	102.3 ± 16.4**	↑	183.1 ± 37.1	289.8 ± 7.9**	254.3 ± 36.9**	↑
21	50.4 ± 1.2	51.6 ± 1.0**	52.9 ± 2.4**	↑	24.8 ± 0.8	28.1 ± 1.0**	27.8 ± 1.3**	↑	75.2 ± 0.7	79.7 ± 0.8**	80.7 ± 1.7**	↑
22	83.1 ± 2.1	82.0 ± 2.1	84.6 ± 2.4**	↑	40.3 ± 1.4	47.2 ± 2.4**	48.7 ± 1.5**	↑	123.4 ± 1.2	129.3 ± 1.4**	133.3 ± 1.7**	↑
23	68.1 ± 13.5	67.7 ± 9.8	74.3 ± 6.0	–	28.8 ± 5.1	36.3 ± 7.5**	38.2 ± 6.2**	↑	96.9 ± 14.6	104.0 ± 10.1	112.5 ± 3.5**	↑
24	75.1 ± 2.3	74.0 ± 1.8	74.5 ± 1.6	–	32.2 ± 1.5	36.6 ± 1.4**	36.2 ± 1.5**	↑	107.3 ± 1.3	110.6 ± 1.4**	110.7 ± 1.2**	↑
25	68.7 ± 13.6	74.5 ± 12.2	63.1 ± 11.3	–	37.3 ± 7.1	45.9 ± 7.7**	40.5 ± 6.7	↑	106.1 ± 15.8	120.3 ± 13.3**	103.6 ± 10.3	↑
26	93.9 ± 14.7	74.3 ± 11.7**	64.6 ± 11.9**	↓	53.6 ± 13.5	64.1 ± 14.4	70.5 ± 13.2*	↑	147.6 ± 7.2	138.4 ± 7.4*	135.0 ± 7.5**	↓
27	64.7 ± 3.4	64.0 ± 4.2	61.1 ± 5.6**	↓	24.4 ± 2.6	27.3 ± 3.1**	30.4 ± 3.9**	↑	89.1 ± 2.1	91.3 ± 2.4**	91.5 ± 3.0**	↑
28	58.9 ± 22.0	10.8 ± 17.3**	44.5 ± 17.8**	↓	26.6 ± 9.3	9.0 ± 8.2**	27.9 ± 10.4	↓	85.6 ± 30.5	19.8 ± 22.6**	72.4 ± 26.3	↓
29	99.0 ± 2.5	91.4 ± 2.4**	91.1 ± 2.6**	↓	42.2 ± 1.4	50.2 ± 2.8**	52.9 ± 2.0**	↑	141.2 ± 1.6	141.6 ± 1.8	144.0 ± 2.5**	↑
30	81.3 ± 2.4	80.7 ± 3.9	76.7 ± 2.6**	↓	34.7 ± 1.7	40.7 ± 3.8**	45.2 ± 2.1**	↑	116.0 ± 1.2	121.4 ± 1.4**	121.9 ± 1.5**	↑
31	83.7 ± 1.8	82.1 ± 2.4**	84.7 ± 2.4	↓	34.6 ± 1.4	38.5 ± 2.2**	39.8 ± 1.9**	↑	118.4 ± 1.0	120.6 ± 2.1**	124.6 ± 1.4**	↑

**P < 0.01; *P < 0.05; ↑ significantly increased; ↓ significantly decreased due to the Dunnett's multiple comparison test

Table 34.3 Summary of results

	Oxy-Hb	Deoxy-Hb	Total-Hb	RI
POTS				
Number of increase	2	19	18	5
Number of decrease	15	0	0	10
Not significant	2	0	1	2
Others	0	0	0	2
NMS				
Number of increase	3	11	10	5
Number of decrease	6	1	2	3
Not significant	3	0	0	2
Others	0	0	0	2

The numbers denotes the difference between average values over S1 and R1

4 Discussion

POTS showed a significant decrease of oxy-Hb and resistance index (RI) and NMS showed a decrease of oxy-Hb and an increase of RI.

Postural change from supine to upright causes reduction of perfusion pressure in the cerebral artery due to negative hydrostatic pressure. An autoregulatory mechanism (autoregulation) maintains cerebral blood flow at constant levels over a blood pressure range of 60–150 mmHg. Tanaka et al. measured heart rate and blood pressure in healthy children and the parameters returned to the same level as before measurement within 20 s of standing [2]. RI and oxy-Hb are expected to recover to the same (or nearly the same) level. We did not compare RI and oxy-Hb between patients with OD and healthy children. Kim et al. [9] suggest that children in OD had impaired autoregulation of cerebral circulation during the orthostatic stress, and that this dysfunction was not directly affected by decreased systemic arterial pressure. In patients with POTS and NMS, sympathetic hyperactivity may also alter mechanisms responsible for controlling cerebral vascular resistance. TCD sonography has been used to study cerebral hemodynamics during orthostatic testing, and different patterns of cerebrovascular blood flow (CBF) velocity have been described. In POTS, patients experience cerebral hypoperfusion and excessive catecholamine effects when they stand up, which are associated with excessive reductions in systolic CBF velocity, despite maintenance of arterial blood pressure [10, 11]. Measurement of CBF velocity by means of TCD sonography has emerged as a reliable technique for assessing both blood flow and cerebral vasoreactivity [12, 13]. Therefore, in the present study we used TCD sonography to assess cerebral blood flow velocity during active standing test in patients with POTS.

Miyagawa et al. [14] performed an active standing test in 22 patients with OD and 17 normal children, and used TCD sonography to measure flow velocity of the middle cerebral artery (MCA) and anterior cerebral artery (ACA), and to calculate the pulsatility index (PI). In normal children, PI decreased during 1 min after standing, after which the decrease in PI became stabilized at approximately 10 % of the baseline in the supine position. In the patients with OD, PI increased at 15 s after

standing, and then decreased. Therefore, subjects were not classified to the subtype of OD at that time. In the present study, we calculated the RI as a measure of cerebral vascular resistance. RI decreased in 10 patients with POTS and increased in 5 patients, while RI decreased in 3 patients with NMS and increased in 5 patients. These data suggest that cerebral autoregulation was comparatively well maintained in patients with decreased RI (mainly POTS). In contrast, cerebral autoregulation will be difficult to maintain in patients with increased RI (mainly NMS), and will likely result in decreased cerebral blood flow.

The NIRS technique, which is based on the relative transparency of human tissue to near-infrared light with a modified Lambert-Beer law [15], detects changes in oxygenated Hb (oxy-Hb) and deoxygenated Hb (deoxy-Hb) in brain tissue [16, 17]. Tanaka et al. [18] previously reported impaired cerebral circulation in children with chronic fatigue syndrome using NIRS monitoring with qualitative analysis. Further, they quantified precise changes of cerebral hemodynamics during orthostatic stress in school children using NIRS. Kim et al. [9] suggested that impaired cerebral circulation associated with orthostatic intolerance may be caused by failure of autoregulation in the cerebral vessels, and that the use of NIRS during orthostatic test is a potential diagnostic tool for orthostatic intolerance. Hoshi et al. [19] assessed changes in cerebral blood volume (CBV) with NIRS during an active standing test in 17 patients with OD and 16 normal children, and reported that CBV increased in all normal children, but decreased in 10 patients (58.8 %) with OD. In contrast, Soga et al. [20] used NIRS to examine 19 patients with OD, and found that changes of cerebral circulation did not correlate with the change in systemic circulation. In brain ischemia, both cerebral arterial inflow and oxy-Hb decrease. Owing to the increase in cerebral oxygen demand, deoxy-Hb increases. Further, as cerebral blood flow decreases, total-Hb decreases.

There were very few reports that measured quantitative cerebral blood oxygenation; however, our study using TRS20 developed a quantitative study in patients with OD during an active standing test. In the present study, 15 patients with POTS exhibited decreased oxy-Hb, all patients exhibited increased deoxy-Hb, and 18 patients exhibited increased total-Hb. In contrast, 6 patients with NMS exhibited decreased oxy-Hb, 11 patients exhibited increased deoxy-Hb, and 10 patients exhibited increased total-Hb. These data suggest that transient ischemia is a likely pathophysiological mechanism of OD, while irreversible brain ischemia, which decreases total-Hb, is less likely to be so.

In summary, we investigated changes in cerebral blood flow and oxygenation during active standing test to clarify the pathophysiology of POTS and NMS. POTS patients showed significantly decreased oxy-Hb and RI, suggesting transient ischemia although maintained cerebral autoregulation. In contrast, NMS patients exhibited decreased oxy-Hb and increased RI, suggesting ischemia and impairment of autoregulation.

Acknowledgments This research was partly supported by a Grant-in-Aid from the Ministry of Education, Culture, Sports, Sciences and Technology of Japan (B23300247), and grants by Alpha Electron Co., Ltd. (Fukushima, Japan) and Iing Co., Ltd. (Tokyo, Japan).

References

1. Okuni M (1962) Orthostatic dysregulation in childhood with special reference to the standing electrocardiogram. Jpn Circ J 27:200–204
2. Tanaka H, Fujita Y, Takenaka Y et al (2009) Japanese clinical guidelines for juvenile orthostatic dysregulation version 1. Pediatr Int 51:169–179
3. Warkentin S, Passant U, Minthon L et al (1992) Redistribution of blood flow in the cerebral cortex of normal subjects during head-up postural change. Clin Auton Res 2:119–124
4. Novak V, Novak P, Spies JM et al (1998) Autoregulation of cerebral blood flow in orthostatic hypotension. Stroke 29:104–111
5. Van Lieshout JJ, Wieling W, Karemaker JM et al (2003) Syncope, cerebral perfusion, and oxygenation. J Appl Physiol 94:833–848
6. Mehagnoul-Schipper DJ, Colier WNJM, Jansen RWMM (2001) Reproducibility of orthostatic changes in cerebral oxygenation in healthy subjects aged 70 years of older. Clin Physiol 21:77–84
7. Harms MP, Colier WN, Wieling W et al (2000) Orthostatic intolerance, cerebral oxygenation, and blood velocity in humans with sympathetic failure. Stroke 31:1608–1614
8. Elwell CE, Owen Reece H, Wyatt JS et al (1996) Influence of respiration and changes in expiratory pressure on cerebral haemoglobin concentration measured by near infrared spectroscopy. J Cereb Blood Flow Metab 16:353–357
9. Kim YT, Tanaka H, Takaya R et al (2009) Quantitative study on cerebral blood volume determined by a near-infrared spectroscopy during postural change in children. Acta Paediatr 98:466–471
10. Grubb BP, Kosinski DJ (2001) Syncope resulting from autonomic insufficiency syndromes associated with orthostatic intolerance. Med Clin North Am 85:457–472
11. Sung RYT, Du ZD, Yu CW et al (2000) Cerebral blood flow during vasovagal syncope induced by active standing or head up tilt. Arch Dis Child 82:154–158
12. Aaslid R, Markwalder T, Nornes H (1982) Noninvasive transcranial Doppler ultrasound recording of flow velocity in basal cerebral arteries. J Neurosurg 57:769–774
13. Aaslid R (1986) The Doppler principle applied to measurement of blood flow velocity in cerebral arteries. In: Aaslid R (ed) Transcranial Doppler sonography. Springer, Wein, pp 39–69
14. Miyagawa M (1989) Cerebral blood flow in orthostatic dysregulation. Auton Nerv Syst 26:25–30 (In Japanese with English abstract)
15. Delpy DT, Cope M, van der Zee P et al (1988) Estimation of optical pathlength through tissue from direct of flight measurement. Phys Med Biol 33:1433–1442
16. Toet MC, Lemmers PM, van Schelven LJ et al (2006) Cerebral oxygenation and electrical activity after birth asphyxia: their relation to outcome. Pediatrics 117:333–339
17. Nagamitsu S, Nagano M, Yamashita Y et al (2006) Prefrontal cerebral blood volume patterns while playing video games – a near-infrared spectroscopy study. Brain Dev 28:315–321
18. Tanaka H, Matsushima R, Tamai H et al (2002) Impaired postural cerebral hemodynamics in young patients with chronic fatigue with and without orthostatic intolerance. J Pediatr 140:412–417
19. Hoshi Y, Shida N, Tamura M et al (1993) Study of cerebral hemodynamics in patients with orthostatic dysregulation by near-infrared spectrophotometry. J Jpn Pediatr Soc 97:692–698 (In Japanese with English abstract)
20. Soga T, Nozaki Y, Tatsuno M et al (1995) Evaluation of the cerebral blood volume in children with orthostatic dysregulation using near infrared spectroscopy. Showa Univ J Med Sci 55:392–398 (In Japanese with English abstract)

Chapter 35
Optical Imaging of Brain Activation in Gambian Infants

Marie D. Papademetriou, S. Lloyd-Fox, N.L. Everdell, M.K. Darboe, S.E. Moore, A.M. Prentice, and C.E. Elwell

Abstract We used optical topography (OT) to investigate cognitive function in infants in rural Gambia. Images of changes in oxyhaemoglobin and deoxyhaemoglobin concentrations were reconstructed using a multispectral algorithm which uses the finite element method (FEM) to model the propagation of light through scattering tissue using the diffusion equation. High quality OT data enabled us to reconstruct images with robust representation of haemodynamic changes. OT is a feasible neuroimage technology for this resource-poor setting.

Keywords Brain development • Infant undernutrition • Functional near infrared spectroscopy

M.D. Papademetriou (✉) • N.L. Everdell • C.E. Elwell
Department of Medical Physics and Bioengineering, University College London, Malet Place Engineering Building, London, WC1E 6BT, UK
e-mail: m.papademetriou@ucl.ac.uk

S. Lloyd-Fox
Centre for Brain and Cognitive Development, Birkbeck, University of London, London, UK

M.K. Darboe
MRC International Nutrition Group, MRC Keneba, Keneba, The Gambia

S.E. Moore • A.M. Prentice
MRC International Nutrition Group, MRC Keneba, Keneba, The Gambia

MRC International Nutrition Group, London School of Hygiene and Tropical Medicine, London, UK

H.M. Swartz et al. (eds.), *Oxygen Transport to Tissue XXXVI*, Advances in Experimental Medicine and Biology 812, DOI 10.1007/978-1-4939-0620-8_35,

1 Introduction

Poor nutrition is a primary health problem plaguing sub-Saharan African countries, such as The Gambia. Dietary insufficiency during the first 1,000 days of life may contribute to poor cognitive development [1]. Assessing cognitive function during infancy may reveal the impact of nutritional deficiencies and allow evaluation of the effectiveness of nutrition-specific interventions.

Optical topography (OT) is a novel non-invasive near infrared spectroscopy (NIRS) neuroimaging technique for studying functional brain activation. We previously used the technique to investigate the developing brain of UK infants by performing a range of cognitive function studies [2, 3]. OT is portable, easy-to-use and inexpensive suggesting that it should be suitable for studies in resource-poor settings. Previously, we successfully transported a dual-channel NIRS system to rural India to study the effect of Falciparum malaria on adult brain haemodynamics [4]. We are now interested in the use of OT to study brain development in Gambian infants, and specifically to deliver brain function images.

OT is based on measuring changes in absorption of near infrared (NIR) light through the intact skull [5]. NIR light is carried to and from the head via an array of optical sources and detectors, making the OT signal vulnerable to contamination from the superficial layers. Chromophore absorbers (such as melanin) present in the superficial layers can contribute to light attenuation, decreasing the signal-to-noise ratio. Conventional analysis of OT data, based on the Modified Beer–Lambert Law (MBLL), is restricted to single source-detector (channel) haemodynamic responses even if the signals are measured from source-detector pairs (channels) with multiple separations. Previously, we used a multispectral imaging algorithm to reconstruct haemodynamic responses and obtain OT images in a UK infant during visual and auditory stimulation [6]. The aim of the current study is to assess the feasibility of obtaining high quality OT data to enable us to reconstruct images of haemodynamic responses of functional brain activation in infants from rural Gambia.

2 Methods

2.1 Data Acquisition Protocol

The study was approved by the joint MRC Unit, The Gambia and The Gambia Government Scientific Coordinating and Ethics Committees. Here we present data from a single male Gambian participant, aged 4 months. Written informed parental consent was obtained prior to inclusion in the study.

The UCL OT system emitting at wavelengths of 780 and 850 nm (sampling frequency of 10 Hz), was used for data acquisition [7]. The infant wore a custom-built headgear consisting of an array of six sources (S) and four detectors (D) placed over the right temporal lobe. This array configuration enabled measurements from a total of 18 channels (12 at 2 cm and 6 at 4.5 cm S-D separations) (Fig. 35.1).

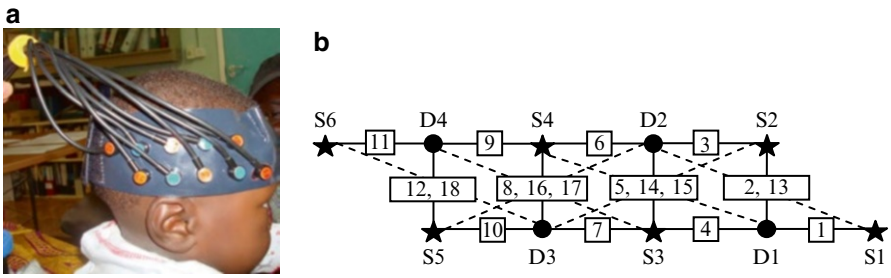

Fig. 35.1 (**a**) A Gambian infant wearing the custom-made headgear during the experiment. The headgear consists of an array of six sources (*red*) and four detectors (*blue*). (**b**) Schematic of the array showing the arrangement of sources (S) and detectors (D). This configuration allows for measurement to be taken from a total of 18 channels. Channels 1–12 at S-D separations of 2 cm and 13–18 at S-D separations of 4.5 cm

Measurements of the head circumference, the distance between right and left pre-auricular points, top of the right and left ears and nasion to inion were obtained prior to the start of the study. The headgear dimensions and S-D separations remained constant throughout the studies. The source second along from the anterior edge in the lower row of the array was aligned with the right pre-auricular point and the headband was placed in line with the top of the right ear. Photographs of the participant wearing the headgear were also obtained after the study to indicate any displacement in the headgear during the study.

The study involved measuring the response of brain activity during visual and auditory stimulation by replicating the protocols followed in the UK studies [2, 3]. The infant sat on his mother's lap while the stimuli were displayed on a screen. The stimuli alternated one after the other, beginning with a 10-s baseline condition followed by a 10-s experimental condition. Three types of experimental conditions were presented: (i) *vocal* (non-speech adult vocalizations e.g. coughing), (ii) *non-vocal* (naturalistic environmental sounds e.g. water running) and (iii) *visual-social* (human action stimuli e.g. Peek-a-boo, with no sound, performed by Gambian actors). The baseline condition consisted of videos of non-human motion.

2.2 Image Reconstruction

Intensity data at both wavelengths were low-pass filtered (cut-off frequency of 0.1 Hz) to remove physiological noise from heart and respiration rates. The signals were then separated into epochs of 24 s—consisting of 4 s pre-stimulus baseline, followed by a 10 s stimulus and a 10 s post-stimulus baseline period—representing one trial block. Each trial block was detrended using a linear fit between the last 4 s of the pre-stimulus baseline and the last 4 s of the post-stimulus baseline period to remove any effects of baseline drift throughout the experiment [8]. Trial blocks for each experimental condition were averaged for each participant. A sliding averaged window (length 4 s and overlap 75 %) was then applied to the averaged trial blocks.

The pre-processed intensity data at the two wavelengths were then used to reconstruct images of changes in HbO_2 and HHb using a linear multispectral method [6, 9]. The linear multispectral method solves the matrix equation $\Delta A_\lambda = J.\Delta C$, where $\Delta A_\lambda = \left[\Delta A_{\lambda_1} \Delta A_{\lambda_2}\right]^T$ represents the changes in the logarithm of the intensity data and $\Delta C = [\Delta(HbO_2)\ \Delta(HHb)]^T$ the chromophore concentration changes. The matrix J is the Jacobian or sensitivity matrix and was calculated using the software package TOAST (Temporal Optical Absorption and Scattering Tomography) [10]. It uses the finite element method (FEM) to model the propagation of light through highly scattering tissue using the diffusion equation, given an estimate of the medium optical properties and optode positions. The medium is considered to be a homogeneous slab with refractive index $n = 1.4$, absorption coefficient $\mu_a = 0.037$ mm^{-1} and reduced scattering coefficient $\mu_s' = 0.74$ mm^{-1} at wavelength 780 nm and $\mu_a = 0.042$ mm^{-1} and $\mu_s' = 0.71$ mm^{-1} at wavelength 850 nm [9]. A FEM mesh with 11,725 nodes, 64,045 elements and dimensions 140 mm × 60 mm × 40 mm was generated with the meshing software iso2mesh [11]. Chromophore concentration changes were obtained by solving the ill-posed inverse problem using Tikhonov regularization [6, 9].

The individual MRI volume of a 4.5 month-old infant was used to co-register the locations of the NIRS optodes on the scalp surface with the underlying cortical areas [12]. This was achieved by identifying the main anatomical landmarks (nasion, inion, right and left pre-auriculars) and then calculating the distance of the sources and detectors based on the head measurements obtained prior to the study and described in §2.1 [13]. Images of changes in HbO_2 and HHb were reconstructed at intervals of 1 s. The reconstructed images of HbO_2 and HHb at the second where the increase in HbO_2 is at maximum (activation peak) were in turn co-registered onto the cortex with the co-registered NIRS optode locations. The cortex with the projected positions of the NIRS optodes was used as the reference image and the HbO_2/HHb image reconstruction was set as the input image. A set of point pairs corresponding to the position of the optodes were chosen to infer a transformation matrix which rotates, scales and translates the input image and co-registers it to the brain image (Matlab, Mathworks Inc.).

3 Results

Figure 35.2 shows the time courses of the haemodynamic responses during the *vocal* experimental condition obtained using the conventional method of analysis, based on the MBLL. The equivalent images reconstructed for changes in HbO_2 and HHb concentrations during all three experimental conditions are shown in Fig. 35.3. The images are displayed as a function of time every 5 seconds from the onset of the stimulus and are obtained at an approximate depth of 1.5 cm. We observe an evident increase in HbO_2 associated with a decrease in HHb upon the onset of the stimulus which gradually decreases when the stimulus ceases. Figure 35.4 shows image reconstruction of HbO_2 and HHb obtained at the peak of activation co-registered on the brain.

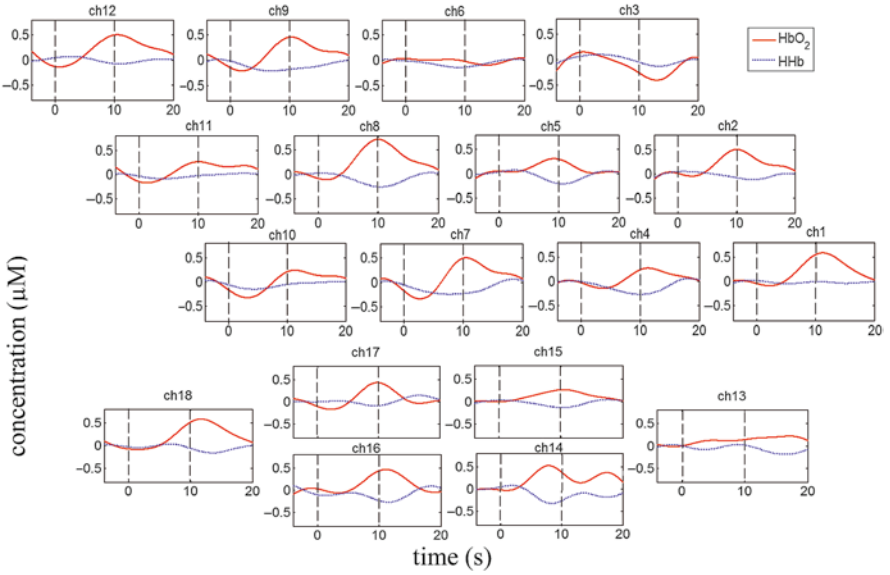

Fig. 35.2 Time courses of the haemodynamic responses for a single participant during the vocal experimental conditions. Changes in HbO_2 (*red*) and HHb (*blue*) were obtained using the Modified Beer–Lambert Law (MBLL). Responses from channels 13–18 (S-D separations at 4.5 cm) overlap in position but occur deeper than those from channels 1–12 (S-D separations at 2 cm)

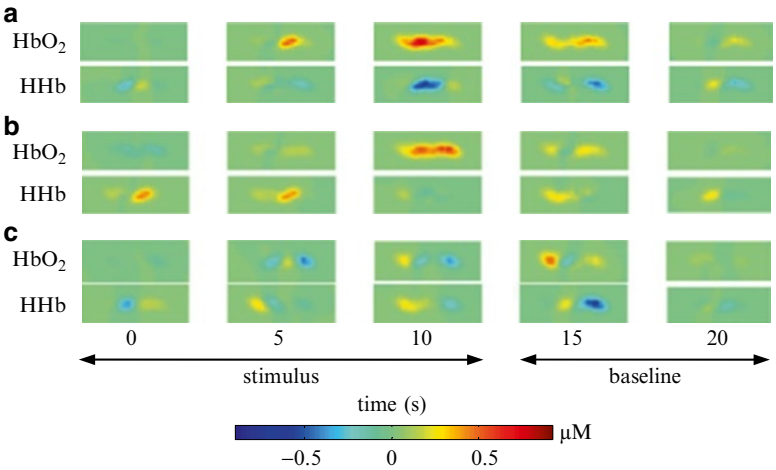

Fig. 35.3 Image reconstructions of changes in HbO_2 and HHb for a single participant during (**a**) vocal, (**b**) non-vocal and (**c**) visual-social experimental conditions. The images show the evolution of chromophore concentration changes at 5 s intervals after the onset of the stimulus

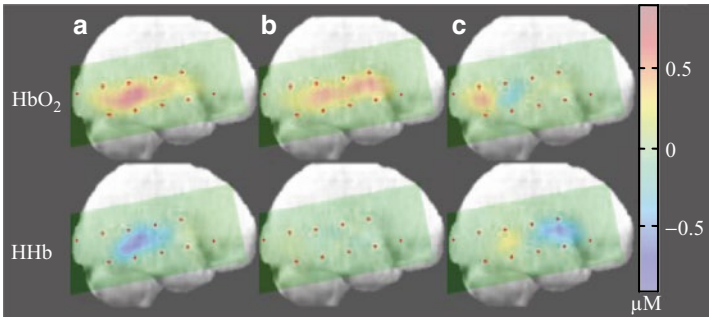

Fig. 35.4 Image reconstructions of HbO_2 and HHb at the activation peak of each of the three experimental conditions, (**a**) vocal, (**b**) non-vocal and (**c**) visual-social. The reconstructed images are from a single participant and are co-registered onto the brain of a 4.5 month-old infant. The *red dots* on the images indicate the position of the sources and detectors

Table 35.1 Changes in chromophore concentrations at activation peak for the three experimental conditions

Condition	Chromophore		Activation peak (μM)	Time (s)	ROI
Vocal	HbO_2		0.75	14	pST
	HHb		−0.56		
Non-vocal	HbO_2	1	0.55	9	pST + aST
		2	0.62		
	HHb	1	−0.04		
		2	−0.02		
Visual-social	HbO_2		0.49	11	pST
	HHb		0.00		

Time: time elapsed after stimulus onset. ROI: Cortical region activation peak; pST: posterior part of the STS region; aST: anterior part of the STS region

The quantified changes in chromophore concentrations from baseline to the activation peak are listed in Table 35.1. The images show a peak in activation over a wide area of the superior temporal sulcus region (we use the term 'STS region' to refer to regions of the superior temporal gyrus, sulcus and middle temporal gyrus extending to the temporo-parietal junction (TPJ)) during the auditory conditions. Furthermore, a second peak in activation occurs in the anterior STS region during the non-vocal condition, which is not present during the vocal condition. Finally, activation during the visual-social condition is localized in the posterior STS region.

4 Conclusions

We have demonstrated the feasibility of using OT in rural Gambia and the ability of the technique to collect high quality data from infants of African origin. We used a linear multispectral method to reconstruct images of the temporal evolution of HbO_2

and HHb during auditory and visual stimulation. Preliminary results show that activation is localised over the superior temporal lobe. Unlike the conventional method based on the MBLL, our analysis method involved reconstructing chromophore concentration using all measurements at both wavelengths simultaneously. Thus, changes are averaged over many measurements taking into account contributions from neighboring source-detector separations. This is particularly important when the optical array comprises source-detector pairs with multiple separation distances. Furthermore, reconstructed chromophore concentration changes have less contamination from surface layers and are less affected by the partial volume effect giving a more robust representation of haemodynamic changes. These data support the use of OT in a rural African setting where assessment of the impact of poor nutrition on infant neurodevelopment is of value. We have set the ground work for an on-going research with the long-term aim to use OT to establish nutrition-related biomarkers of cognitive development in undernourished children.

Acknowledgments This work is supported by a Grand Challenges Exploration Phase 1 grant from the Bill and Melinda Gates Foundation, and hosted by MRC Keneba (MC-A760-5QX00). We are grateful to the field workers at MRC Keneba, Lamin Sanyang, Saikou Drammeh and Ousman Kambi, for their help with data collection.

References

1. Geoghegan T (2012) "Nutrition in the first 1,000 days. State of the World's Mothers" Save the Children
2. Lloyd-Fox S, Blasi A, Mercure E et al (2012) The emergence of cerebral specialization for the human voice over the first months of life. Soc Neurosci 7:317–330
3. Lloyd-Fox S, Blasi A, Charman T et al (2013) Reduced neural sensitivity to social stimuli in infants at risk for autism. Proc Biol Sci 280:20123026
4. Kolyva C, Kingston H, Tachtsidis I et al (2013) Oscillations in cerebral haemodynamics in patients with falciparum malaria. Adv Exp Med Biol 765:101–107
5. Elwell CE, Cooper CE (2011) Making light work: illuminating the future of biomedical optics. Phil Trans A Math Phys Eng 369:4358–4379
6. Papademetriou MD, Richards J, Correia T et al (2013) Cortical mapping of 3D optical topography in infants. Adv Exp Med Biol 789:455–461
7. Everdell N, Gibson A, Tullis IDC et al (2005) A frequency multiplex near infrared topography system for imaging functional activation in the brain. Rev Sci Instrum 76:093705
8. Blasi A, Lloyd-Fox S, Elwell CE et al (2007) Investigation of depth dependent changes in cerebral haemodynamics during face perception in infants. Phys Med Biol 52:6849–6864
9. Correia T, Lloyd-Fox S, Everdell NL et al (2012) Three dimensional optical topography of brain activity in infants watching videos of human movement. Phys Med Biol 57:1135–1146
10. Arridge SR, Hebden JC, Schweiger M et al (2000) A method for three dimensional time-resolved optical tomography. Int J Imaging Syst Technol 11:2–11
11. Fang Q, Boas D (2009) Tetrahedral mesh generation from volumetric binary and gray-scale images. Proc IEEE Int Symp Biomed Image 2009:1142–45
12. Blasi A, Mercure E, Lloyd-Fox S et al (2011) Early specialization for voice and emotion processing in infant brain. Curr Biol 21:1220–1224
13. Lloyd-Fox S, Wu R, Richards JE, Elwell CE, Johnson MH (2013) Cortical activation to action perception is associated with action production abilities in young infants. Cerebral Cortex bht207. doi:10.1093/cercor/bht207

Chapter 36
Asymmetrical Changes in Cerebral Blood Oxygenation Induced by an Active Standing Test in Children with Postural Tachycardia Syndrome

Yayumi Kamiyama, Yukihiko Fujita, Tatsuo Fuchigami, Hiroshi Kamiyama, Shori Takahashi, and Kaoru Sakatani

Abstract Near-infrared spectroscopy enables recognition of various brain conditions based on certain factors, such as oxygenated hemoglobin (oxy-Hb). Since July 2012, we have been trying to determine the mechanisms of autonomic function in Japanese children with orthostatic intolerance (also called orthostatic dysregulation) in Nihon University Itabashi Hospital in Tokyo, Japan. A total of 23 children aged 7–16 years diagnosed with postural tachycardia syndrome (POTS), a subtype of orthostatic dysregulation, were enrolled in the study. We evaluated the relation between asymmetry in frontal cortex activity and the automatic nervous system and compared oxy-Hb changes in the right and left frontal cortices during an active standing test. We observed that during active standing oxy-Hb decreased in the frontal cortex. The oxy-Hb changes were asymmetrical, with a significantly larger decrease in the left frontal cortex than in the right frontal cortex, suggesting that tachycardia during active standing in POTS patients might be caused by activation of the right frontal cortex, which induces sympathetic nervous system activity.

Keywords Cerebral blood oxygenation • Near-infrared spectroscopy • Autonomic function • Orthostatic intolerance

Y. Kamiyama (✉) • Y. Fujita • T. Fuchigami • H. Kamiyama • S. Takahashi
Department of Pediatrics and Child Health, Nihon University School of Medicine, 30-1 Oyaguchi-Kamicho, Itabashi-ku, Tokyo 173-8610, Japan
e-mail: kyayuyayu@yahoo.co.jp

K. Sakatani
Department of Pediatrics and Child Health, Nihon University School of Medicine, 30-1 Oyaguchi, Kamicho, Itabashi-ku, Tokyo 173-8610, Japan

Nihon University College of Engineering, 30-1 Oyaguchi-Kamicho, Itabashi-ku, Tokyo 173-8610, Japan

H.M. Swartz et al. (eds.), *Oxygen Transport to Tissue XXXVI*, Advances in Experimental Medicine and Biology 812, DOI 10.1007/978-1-4939-0620-8_36,

1 Introduction

Orthostatic intolerance, known as orthostatic dysregulation (OD) in Japan [1], is failure of the autonomic nervous system. It occurs primarily in children and adolescents. Blood flow in part of their brains is abnormal, possibly because of a mismatched reaction to the cardiovascular or neurological system. Unstable regulation of brain blood flow in OD patients, however, has been evaluated by specific modalities including transcranial Doppler flowmetry and near-infrared spectroscopy (NIRS) [2–5]. Continuous-wave NIRS is based on the relative transparency of human tissue to near-infrared light using the modified Beer–Lambert law, which can detect changes in oxygenated Hb (oxy-Hb) and deoxygenated Hb (deoxy-Hb) in brain tissue. Pocket NIRS (Pocket NIRS Duo™; Hamamatsu Photonics, Shizuoka, Japan) is able to evaluate these changes in the form of a remarkable lightweight, mobile application, which can be used during exercise as well as active standing test. In the present study, we observed oxy-Hb and total-Hb changes in the right and left frontal cortices using Pocket NIRS during active standing tests in children with OD.

2 Methods

We studied 23 children or adolescents (14 boys, 9 girls), ranging in age from 7 to 17 years (mean 12.8 ± 2.6 years), who were visited at our outpatient clinic in Nihon University Itabashi Hospital from July 2012 to March 2013. Patients with organic disease were excluded. All of the patients were right-handed. We conducted a medical interview using the OD checklist (Table 36.1) [1] for all of our patients diagnosed as having postural tachycardia syndrome (POTS) based on the Japanese clinical guidelines for juvenile orthostatic dysregulation [5]. The criteria are as following; (1) the heart rate increases by >115 bpm during active standing after arising from the supine position, (2) the heart rate elevates by >35 bpm during active standing compared with that during the supine position. In addition to the patients who met the conditions of criterion (1), (2), we studied subjects whose heart rates were elevated by >21 bpm during active standing, based on Okuni's criteria [1].

The active standing test was performed in the pediatric outpatient clinic under quiet conditions. After resting for 10 min in the supine position, subjects were asked to stand up by themselves and remain standing for 10 min. During active standing, the subjects' blood pressure and heart rate were monitored with a sphygmomanometer.

Pocket NIRS can simulate the conditions of an active standing test. It is a mobile tool that includes a special system consisting of two optical probes with two channels for each and a handy wireless controller (weighing only 100 g) connected to the probes with cables. The optical probes are placed on each side of the forehead above the eyebrows. Each optical probe includes light-emitting diodes (LEDs) as sources and one photo-diode as a detector with 3 cm distance between the detector and LEDs that are able to illuminate the tissue with three wavelengths (SMC735, SMC810, SMC850; Epitex, Inc). The spectroscope continuously provides digital

Table 36.1 Checklist for orthostatic dysregulation (OD) based on Okuni's criteria

Major manifestations
A. Dizziness on standing (Frequent: including standing up slowly; sometimes: once a week; rare: less than once a week)
B. Fainting on standing (Frequent: once a week; sometimes: once a month; rare: once every 2 months)
C. Nausea when taking a hot bath (Frequent: does not enter a hot water bathtub or takes lukewarm baths; sometimes: more than half of the total; rare: once every 2 months)
D. Palpitations (Frequent: 2/3 or more when moving a little; half of the times when moving a little; rare: once every 2 months)
E. Difficulty in getting out of bed (Frequent: more than three times a week; sometimes: 1–2 times a week; rare: less than 1–2 times a week)
Minor manifestations
a. Pallor, b. Anorexia; c. Colic pain; d. Fatigue; e. Headaches (Frequent: more than three times a week; sometimes: 1–2 times a week; rare: once 2 months)
f. Car-sickness (Frequent: every time or once week or including cannot get on a car; sometimes: more than half the times; rare: once every 2 months)
Schellong test
g. Pulse pressure narrows by 16 mmHg or more during a standing test
h. A fall in systolic blood pressure of 21 mmHg or more during a standing test
i. Increase in the pulse rate of 21 beats per minute or more during a standing test
j. T_{II} depression of 0.2 mV or more on a standing EEG (When test cannot be endured, the patients are assumed to be positive)

signals from the cerebral oxy-Hb, deoxy-Hb, and total-Hb based on the modified Beer–Lambert law in which changes in hemoglobin chromophore concentrations, which is in a relation of simultaneous linear equation with light absorbance divided by the extinction coefficients of the chromophores and the optical path length in the tissue, which is the average distance that light travels between the source and detector through the tissue. The system is controlled from a standard laptop personal computer through a wireless connection provided by Bluetooth, which is enable to acquire up to 60 data per second. Time-concentration courses of cerebral oxy-Hb, deoxy-Hb, and total-Hb are monitored simultaneously on the personal computer panel while the examination is being performed. We measured changes in the oxy-Hb level and the total-Hb level in both supine and active standing postures. To evaluate laterality in both postures, the average oxy-Hb level and total-Hb level were calculated for a selected 60 s during which those variability rate was almost stable between 60 s (1 min) and 540 s (9 min). Because of avoiding terrible artifact originating from patients' motional or mental stress, we thought it was necessary to exclude unstable periods including first and last 1 min for the reasons of a tense atmosphere or getting tired. The oxy-Hb and the total-Hb were included, and the deoxy-Hb was excluded in the present study.

Data are given as the mean ± SD. The Mann–Whitney U test was used for comparison of oxy-Hb and total Hb changes between the right and left sides. A value of $p < 0.05$ was considered to indicate a significant difference. Informed consent was obtained from the patients and their legal parents.

3 Results

Oxy-Hb (Fig. 36.1, Table 36.2)

From the onset of standing, the oxy-Hb level decreased, falling markedly on the left with a mean level of –118.7 ± 72.6 μmol/L·cm (range –244.5 to 28.1 μmol/L·cm). In contrast, on the right side it fell only a mean level of –41.8 ± 56.9 μmol/L·cm (range –121.6 to 83.6 μmol/L·cm) ($p = 0.0003$).

Total-Hb (Table 36.3)

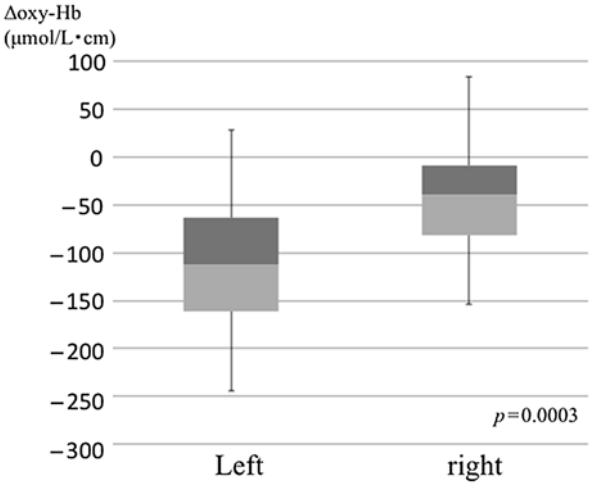

Fig. 36.1 Comparison oxy-Hb changes between the right and left frontal cortices. Oxy-Hb decreased during active standing, decreasing more markedly on the left, with a mean value of −118.7 ± 72.6 μmol/L·cm (range −244.5 to 28.1 μmol/L·cm), than on the right, with a mean value of −41.8 ± 56.9 μmol/L·cm (range −121.6 to 83.6 μmol/L·cm) ($p = 0.0003$)

Table 36.2 List of changes in oxy-Hb level

No.	Left oxy-Hb	Right oxy-Hb	No.	Left oxy-Hb	Right oxy-Hb
1	−113.6	−78.4	13	−241.8	−106.5
2	−164.3	−154.3	14	−157.7	−13.2
3	−45.3	−11.8	15	−79.7	−11.0
4	−27.0	−47.0	16	28.1	10.4
5	−54.8	83.6	17	−77.0	−15.0
6	−62.8	−6.5	18	−148.6	−107.5
7	−237.3	−12.9	19	−159.4	−70.6
8	−51.5	13.1	20	−194.4	−80.5
9	−244.5	−102.7	21	−112.6	14.0
10	−170.9	−82.8	22	−85.4	−40.0
11	−158.8	−46.1	23	−106.7	−121.6
12	−64.6	25.2	Mean	−118.7 ± 72.6	−41.8 ± 56.9

Values are expressed in μmol/L·cm

Table 36.3 List of changes in total Hb level

No.	Left total-Hb	Right total-Hb	No.	Left total-Hb	Right total-Hb
1	78.0	22.2	13	−246.7	−71.1
2	−32.1	−21.0	14	−74.0	33.2
3	4.3	24.2	15	32.5	102.4
4	55.0	22.7	16	130.3	61.4
5	−24.6	221.5	17	2.2	21.7
6	5.6	26.7	18	−47.2	−87.1
7	−259.1	32.9	19	48.5	6.1
8	−17.4	40.0	20	1.2	−20.3
9	−318.5	−113.9	21	−55.7	42.7
10	−137.0	−69.5	22	−63.3	2.7
11	−118.0	−18.0	23	54.6	−3.0
12	−18.7	65.5	Mean	−43.5 ± 110.4	14.0 ± 68.5

Values are expressed in μmol/L·cm

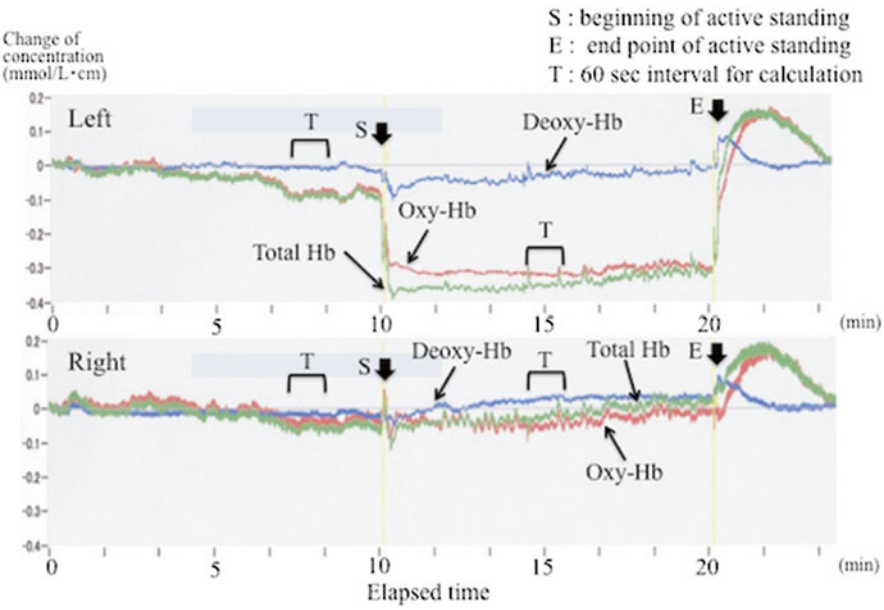

Fig. 36.2 13 Year-old male typical example of changes in NIRS parameters. Example of the variability of oxy-Hb in our study in patients with postural tachycardia syndrome. The rate of oxygen concentration changes on the *left* and *right sides* are shown in the *upper* and *lower graphs*, respectively. Oxy-Hb decreased during active standing, falling more markedly on the *left side* than on the *right. Arrow S* indicates the beginning of active standing. *Arrow E* indicates the end of active standing. Interval T with a *square bracket* means selected 60 s for calculation of oxy-Hb and total Hb level

From the onset of standing, total-Hb level on the right side slightly increased with a mean level of 14.0 ± 68.5 μmol/L·cm (range –113.9 to 221.5 μmol/L·cm). Total-Hb level on the left side decreased with a mean level of –43.5 ± 110.4 μmol/L·cm (range –318.5 to 130.3 μmol/L·cm) ($p = 0.04$).

Oxy-Hb variability rate indicated markedly clearer laterality rather than total-Hb during active standing.

4 Discussion

Changes in cerebral blood flow in patients with OD can now be determined by NIRS. Mehagnoul-Schipper et al. [6] reported that a decrease in oxy-Hb following an orthostatic change was found. Kim et al. [4] demonstrated that children with abnormal circulatory responses during active standing had significantly reduced oxy-Hb compared with their normal counterparts. However, asymmetrical changes in cerebral blood flow were not well documented in their report. We focused on bilateral cerebral oxygen levels in patients with OD during active standing.

Several NIRS monitoring systems are available clinically for evaluating cerebral oxygen levels. Because we thought that the NIRS application should be portable, lightweight and wireless during active standing, we believed that the Pocket NIRS Duo™ (Hamamatsu Photonics, Shizuoka, Japan) was best for our study. Mobile NIRS is expected to become useful in several fields. For example, it can monitor the muscle oxygenation level during exercise, which would be helpful in the sports science field. Additionally, seizure status can be monitored in infants who are in constant motion, which would be useful in brain research [7, 8]. Pocket NIRS provides data on serial changes in oxy-Hb, deoxy-Hb, and total-Hb levels as the rate of change from the beginning of the examination. Thus, it can record these levels for any turn of events. We found a significant difference in the response of oxy-Hb and total-Hb in the frontal cortices between the right and left sides, with a decreasing response during active standing. The results of oxy-Hb changes were asymmetrical, with a significantly greater decrease in the left frontal cortex than in the right frontal cortex during active standing.

We believe asymmetrical cerebral oxygen levels are related to some unstable situation during active standing. It has been reported that during mental stress tasks right frontal cortex activity plays a greater role in sympathetic nervous activity than the left frontal cortex [9–11]. Also, according to some reports describing laterality of sympathetic nervous activity, the right hemisphere plays a greater role than the left hemisphere, especially influencing cardiac performance [12–15]. We enrolled patients with POTS, in whom it is postulated that excessive blood pooling exaggerates acceleration of sympathetic nervous activity, resulting in tachycardia. In fact, we found typical asymmetrical cerebral oxy-Hb changes in patients with POTS, suggesting that the right frontal cortex during active standing by POTS patients has a greater role in cerebral regulation of the heart rate by virtue of the increased sympathetic nervous activity. Thus, tachycardia during active standing in POTS patients might be caused by activation of the right frontal cortex.

Oxy-Hb indicated major changes with typical laterality rather than total-Hb during active standing. It is said that the oxy-Hb level is better marker to evaluate cerebral oxygenation rather than total-Hb level according to some previous reports [4, 16], although total-Hb is excellent marker to estimate cerebral blood volume.

Clinical parameters including blood pressure and partial pressure of carbon dioxide in arterial blood ($PaCO_2$) might be related to our observed changes evaluated by NIRS. Tachtsidis et al. [17] reported changes in blood pressure are present in the

superficial layer of the head which is sampled when using a traditional NIRS measurement principle. On the other hand, some papers [18, 19] describe that orthostatic stress in humans can decrease $PaCO_2$ measured by end-tidal carbon dioxide. $PaCO_2$ changes effects derived from NIRS signals significantly reported by Scholkmann et al. [20]. Furthermore, the observed decreased in oxy-Hb in patients with OD might also reflect changes in systemic parameters, especially in $PaCO_2$ based on these previous studies.

4.1 Study Limitations

Because there were no controls in our study, there could be no comparison about the laterality of cerebral oxygen levels between POTS patients and normal controls. However, it might be possible to verify a causal relation between asymmetrical cerebral oxygen levels and the laterality of sympathetic nervous activity.

Although it is said that cerebral blood flow cannot be measured by NIRS application directly, the motion of cerebral blood flow corresponded to the oxy-Hb changes during active standing in this study. Thus, we believe that cerebral blood flow can be evaluated by Pocket NIRS. The Pocket NIRS device is also susceptible to superficial blood flow and oxygenation changes. We speculate that the oxy-Hb signal is only partially originating from the cortex/cerebral layers, maybe only to a very small percentage.

Acknowledgments This research was partly supported by a Grant-in-Aid from the Ministry of Education, Culture, Sports, Science, and Technology of Japan (B23300247), and grants from Alpha Electron Co., Ltd (Fukushima, Japan) and Iing Co., Ltd (Tokyo, Japan).

References

1. Okuni M (1962) Orthostatic dysregulation in childhood with special reference to the standing electrocardiogram. Jpn Circ J 27:200–204
2. Novak V, Novak P, Spies JM, Low PA (1998) Autoregulation of cerebral blood flow in orthostatic hypotension. Stroke 29:104–111
3. Miyakawa M (1989) Cerebral blood flow in orthostatic dysregulation. Auton Nerv Syst 26:25–30
4. Kim YT, Tanaka H, Takaya R, Kajiura M, Tamai H, Arita M (2009) Quantitative study on cerebral blood volume determined by a near-infrared spectroscopy during postural change in children. Acta Pediatr 98:466–471
5. Tanaka H, Fujita Y, Takenaka Y, Kajiwara S, Masutani S, Ishizaki Y, Matsushima R, Shiokawa H, Shiota M, Ishitani N, Kajiura M, Honda K, Task Force of Clinical Guidelines for Child Orthostatic Dysregulation, Japanese Society of Psychosomatic Pediatrics (2008) Japanese clinical guidelines for juvenile orthostatic dysregulation version 1. Pediatr Int 51:169–179
6. Mehagnoul-Schipper DJ, Colier WN, Jansen RW (2001) Reproducibility of orthostatic changes in cerebral oxygenation in healthy subjects aged 70 years or older. Clin Physiol 21:77–84

7. Everdell NL, Airantzis D, Kolvya C, Suzuki T, Elwell CE (2013) A portable wireless near-infrared spatially resolved spectroscopy system for use on brain and muscle. Med Eng Phys 35:1692–1697
8. Bozkurt A, Rosen A, Rosen H, Onaral B (2005) A portable near-infrared spectroscopy system for bedside monitoring of newborn brain. Biomed Eng Online 4:29
9. Sakatani K (2012) Optical diagnosis of mental stress: review. Adv Exp Med Biol 737:89–95
10. Tanida M, Katsuyama M, Sakatani K (2007) Relation between mental stress-induced prefrontal cortex activity and skin conditions: a near infrared spectroscopy study. Brain Res 1184:210–216
11. Tanida M, Sakatani K, Takano R, Tagai K (2007) Relation between asymmetry of prefrontal cortex activities and the autonomic nervous system during a mental arithmetic task: near infrared spectroscopy study. Neurosci Lett 369:69–74
12. Zamrini EY, Meador KJ, Loring DW, Nichols FT, Lee GP, Figueroa RE, Thompson WO (1990) Unilateral cerebral inactivation produces differential left/right heart rate responses. Neurology 40:1408–1411
13. Weisz J, Emri M, Fent J, Lengyel Z, Marian T, Horvath G, Bogner P, Tron L, Adam G (2001) Right prefrontal activation produced by arterial baroreceptor stimulation: a PET study. Neuroreport 12:3233–3238
14. Wittling W, Block A, Genzel S, Schweiger E (1998) Hemisphere asymmetry in parasympathetic control of the heart. Neuropsychologia 36:461–468
15. Oppenheimer SM, Gelb A, Girvin JP, Hachinski VC (1992) Cardiovascular effects of human insular cortex stimulation. Neurology 42:1727–1732
16. Terborg C, Birkner T, Schack B, Weiller C, Röther J (2003) Noninvasive monitoring of cerebral oxygenation during vasomotor reactivity tests by a new near-infrared spectroscopy device. Cerebrovasc Dis 16:36–41
17. Tachtsidis I, Leung TS, Chopra A, Koh PH, Reid CB, Elwell CE (2009) False positives in functional near-infrared topography. Adv Exp Med Biol 645:307–315
18. Hughson RL, Edwards MR, O'Leary DD, Shoemaker JK (2001) Critical analysis of cerebrovascular autoregulation during repeated head-up tilt. Stroke 32:2403–2408
19. Bjurstedt H, Hesser CM, Liljestrand G, Matell G (1962) Effects of posture on alveolar-arterial CO_2 and O_2 differences and on alveolar dead space in man. Acta Physiol Scand 54:65–82
20. Scholkmann F, Gerber U, Wolf M, Wolf U (2013) End-tidal CO_2: an important parameter for a correct interpretation in functional brain studies using speech tasks. Neuroimage 66:71–79

Chapter 37
Changes of Cerebral Tissue Oxygen Saturation at Sleep Transitions in Adolescents

Andreas J. Metz, F. Pugin, R. Huber, P. Achermann, and M. Wolf

Abstract In adults, cerebral oxy-([O_2Hb]) and deoxyhemoglobin concentrations ([HHb]) change characteristically at transitions of sleep stages. The aims were to assess these changes in adolescents and additionally to measure tissue oxygen saturation (StO_2) by near infrared spectroscopy (NIRS). Previously it was reported that in adults [O_2Hb] increased and [HHb] decreased at the transition from non-rapid eye movement sleep (NREMS) to REMS and wakefulness. Transitions to NREMS from REMS/wakefulness led to a decrease in [O_2Hb] and an increase in [HHb]. We measured [O_2Hb], [HHb] and tissue oxygenation (StO_2) with NIRS approximately above

A.J. Metz and F. Pugin are members of the Ph.D. program imMed.

A.J. Metz (✉)
Biomedical Optics Research Laboratory, Division of Neonatology,
University Hospital Zurich, Frauenklinikstasse 10, 8091 Zurich, Switzerland

Institute for Biomedical Engineering, ETH Zurich, Zurich, Switzerland
e-mail: andreas.jaakko@googlemail.com

F. Pugin
Child Development Center, University Children's Hospital Zurich, Zurich, Switzerland

R. Huber
Child Development Center, University Children's Hospital Zurich, Zurich, Switzerland

Zurich Center for Integrative Human Physiology, University of Zurich, Zurich, Switzerland

P. Achermann
Institute of Pharmacology and Toxicology, Chronobiology and Sleep Research,
University of Zurich, Zurich, Switzerland

Zurich Center for Integrative Human Physiology, University of Zurich, Zurich, Switzerland

M. Wolf
Biomedical Optics Research Laboratory, Division of Neonatology,
University Hospital Zurich, Frauenklinikstasse 10, 8091 Zurich, Switzerland

Institute for Biomedical Engineering, ETH Zurich, Zurich, Switzerland

Zurich Center for Integrative Human Physiology, University of Zurich, Zurich, Switzerland

H.M. Swartz et al. (eds.), *Oxygen Transport to Tissue XXXVI*, Advances in Experimental Medicine and Biology 812, DOI 10.1007/978-1-4939-0620-8_37,

the left prefrontal cortex in 12 healthy adolescent males (aged 10–16 years). We found comparable signs and magnitudes of changes in [O_2Hb] and [HHb] as observed in adults. StO_2 increased at the transitions from NREMS to REMS and decreased from REMS to NREMS and at sleep onset (all $p<0.01$, linear mixed effects model). Changes in oxygen metabolism during sleep transitions are similar in adolescents and adults. In addition, we show for the first time temporal changes of StO_2 at sleep transitions.

Keywords Near-infrared spectroscopy • Sleep • Sleep stage transitions • Tissue oxygen saturation

1 Introduction

Brain activity during sleep was widely studied with electroencephalography (EEG) so far. Another measure of brain activity is the cerebral oxygen metabolism [1], even though the link is not completely understood. The cerebral blood flow (CBF, as a marker of oxygen metabolism and neuronal activity [2]) was assessed by positron emission tomography (PET) [2, 3]. These data indicate that absolute global CBF is lower in non-rapid eye movement sleep (NREMS) compared to wakefulness and higher in rapid eye movement sleep (REMS) compared to NREMS. However, regional CBF changes were heterogeneous in the frontal (and parietal) areas during REMS [2, 3]. Near infrared spectroscopy (NIRS) non-invasively measures oxy-(O_2Hb), deoxyhemoglobin (HHb) and tissue oxygen saturation (StO_2) and therefore provides additional information of cerebral oxygenation compared to PET, but without spatial resolution. Several NIRS studies reported consistently an increase of [O_2Hb] and a decrease in [HHb] at the transition from sleep to wakefulness and opposite changes at transitions from wakefulness to sleep [4–9]. These studies measured hemodynamic changes approximately in the left or right (or both) prefrontal cortex. At the transition from NREMS to REMS an increase in [O_2Hb] and a decrease in [HHb] was found [8, 9] and at the transition from REMS to NREMS opposite changes were observed [8]. To our knowledge, only in one study [9] StO_2 was measured in which they reported a decrease in StO_2 in NREMS compared to wakefulness and increased levels in REMS compared to NREMS. It should be noted that this study [9] and in [4] sleep was investigated only during an afternoon nap protocol. In all studies data were recorded in adults. We aimed to examine for the first time cerebral oxygenation in adolescents and StO_2 changes at sleep state transitions.

2 Methods

2.1 Subjects

We analyzed overnight sleep recordings of 12 healthy adolescent right-handed males (age 10–16 years, mean 12.6 years). Each participant spent two nights in the sleep laboratory of the University Children's Hospital Zurich, separated by 3 weeks.

One recording was excluded due to technical difficulties. Twelve subjects with a total of 23 recordings were analyzed. The study was approved by the local ethical committee and informed consent was obtained from the legal representatives. For the detailed protocol see [10].

2.2 NIRS Measurement

OxyPrem, an in-house built continuous wave NIRS device, electronically similar to a previous device [11], measures light attenuation at three wavelengths (760, 805 and 870 nm) and at two distances (1.5 and 2.5 cm) with a sampling rate of 35 Hz. OxyPrem measures StO_2, [O_2Hb], [HHb] and total hemoglobin concentration ([tHb]) for two different areas using a self-calibrating approach [12]. Both regions cover an area of ~3 cm^2, one region being closer to electrode F3 (just below the hairline of the subject) and one closer to Fp1. The NIRS sensor was placed on the left forehead close to the electrode position Fp1 (international 10/20 system). NIRS and high density EEG with 128 electrodes were recorded simultaneously for the entire night. An accelerometer (ADXL330, Analog Devices) in the NIRS sensor also registered the subject's movements. Data were similar in both regions and we therefore only report results of the F3 region.

2.3 Post-processing

We calculated StO_2 by the diffusion approximation without accounting for water in the tissue, as described in assumption A4 in [13]. The algorithm is described in detail in [10]. [HHb] and [O_2Hb] were corrected for movement artefacts based on [14, 15]. This algorithm adapts the level after an artefact to the level before the artefact if the difference between the two levels exceeds the 95 % confidence interval of the signal (within a chosen time frame of 20 s according to [15]) prior to the artefact. Additionally, the level was adjusted to the one in periods where the signal is assumed to be correct based on the accelerometer data. From the corrected [HHb] and [O_2Hb], StO_2 was calculated as [O_2Hb]/([O_2Hb] + [HHb]) and [tHb] as [O_2Hb] + [HHb].

Sleep stages were scored according to standard criteria [16]. We focused on the following transitions: NREMS to REMS, REMS to NREMS (based on NREM-REM sleep cycles [17]), and sleep onset, which was defined as the first appearance of stage N2 (NREMS is divided into stages N1–N3, N1 being lighter sleep and N3 deep sleep). Time 0 was set at each transition and defined as center of a window of 10 min (i.e. ±5 min). We ensured that these 5 min before or after the transition contained at least 75 % of the respective states. Prior to statistical testing the signals were first low pass filtered at 0.2 Hz. Second, the mean of each 10-min window was subtracted for each time-point within the window. Third, median time courses were calculated over multiple appearances of one transition within a night, then over the two nights per subject and finally over the 12 subjects. As measure of variability, the median absolute deviation (MAD) was determined (Fig. 37.1 and Table 37.1). For display reasons the

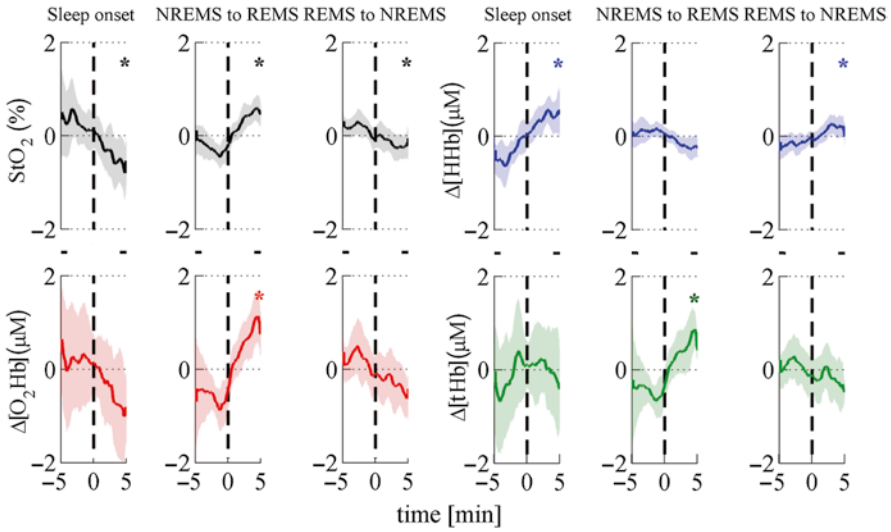

Fig. 37.1 Median time course at sleep onset and sleep state transitions for tissue oxygen saturation (StO_2, black), oxyhemoglobin ([O_2Hb], *red*), deoxyhemoglobin ([HHb], *blue*) and total hemoglobin ([tHb], *green*) in region F3. The mean of the 10 min window was subtracted from each time course. The *shaded area* depicts the median absolute deviation. Time zero represents the transition (sleep onset, first epoch of NREMS or REMS). The *horizontal black bars* between the panels delineate the data that were compared by statistical testing. Data were low pass filtered by a 1-min moving average for display reasons. NREMS: non-rapid eye movement sleep. REMS: rapid eye movement sleep. *Asterisks* mark a significant change after false discovery rate (FDR) correction. Twelve subjects contributed two nights except one and multiple transitions per night to each transition (except for sleep onset)

Table 37.1 The median difference in [O_2Hb], [HHb], StO_2 and [tHb] between the last and the first minute of the 10-min window at transitions are reported

Transition	Δ[O_2Hb] ± MAD [μM]	Δ[HHb] ± MAD [μM]	ΔStO_2 ± MAD [%]	Δ[tHb] ± MAD [μM]
NREMS to REMS	+1.80 ± 1.41*	−0.22 ± 0.40	+0.67 ± 0.47*	+1.32 ± 1.36*
REMS to NREMS	−0.65 ± 0.62	+0.45 ± 0.39*	−0.38 ± 0.32*	−0.17 ± 0.77
Sleep onset	−1.12 ± 1.95	+0.81 ± 0.91*	−0.89 ± 1.13*	+0.25 ± 2.1

Asterisks indicate a significant change (linear mixed effects model and false discovery rate correction, corrected significance level of 0.0278). MAD indicates the median absolute deviation of the difference, using Gaussian error propagation. StO_2 changes are provided in absolute per cent

median and the MAD were smoothed by a moving average of 1 min (Fig. 37.1). Data processing was performed in Matlab® (R2011b, The Mathworks®, Natick, MA, USA).

2.4 Statistics

The first and the last minute of the 10-min window were compared to test for significant changes at the transitions. To account for two nights per subject and multiple

transitions per night we applied a linear mixed effects model (function "lme" in R version 2.15.2, R Core Team, Vienna, Austria) with the fixed effects "time" (last − first minute), "night" (different nights) and "transition #" (multiple transitions within a night) and subject as random effect. To account for multiple testing (four different signals—StO_2, HHb, tHb and O_2Hb, two different regions and three different transitions) we applied the false discovery rate (FDR) correction at the 5 % significance level [18].

3 Results

StO_2, [tHb] and [O_2Hb] increased at the transition from NREMS to REMS and StO_2 decreased during the transition from REMS to NREMS. In contrast, [HHb] increased at the transitions from REMS to NREMS and at sleep onset (Table 37.1; Fig. 37.1). In total 77 NREMS to REMS, 62 REMS to NREMS transitions and 21 sleep onset periods were analyzed. At the transition from NREMS to REMS the increase in StO_2 (and [tHb], [O_2Hb]) started 72 s before the actual transition. StO_2 gradually decreased and [HHb] increased at the transition into sleep, i.e. the change started several minutes prior to sleep onset (defined as first occurrence of N2; Fig. 37.1). The changes at any of the transitions were similar in the two measured regions (data not shown).

4 Discussion and Conclusions

Our results indicate that the change in the cerebral hemodynamics and tissue oxygenation in adolescents at the sleep state transitions NREMS to REMS, REMS to NREMS and wakefulness to NREMS is similar in sign and magnitude to those reported in adults [4–9]. For the first time we showed the temporal change of cerebral StO_2 at these transitions. Although Kubota et al. [9] presented StO_2 values for different sleep stages during a nap protocol, they did not show the temporal change at transitions. Additionally, we found similar changes at the transition NREMS to wakefulness (i.e. arousal) as [8], but we excluded this transition from our analysis due to their small number of occurrence. PET literature reports that the global CBF is lower during NREMS compared to wakefulness and is elevated again during REMS to approximately the same level as in wakefulness [2, 19]. These findings point in the same direction as the NIRS findings where we also see an increase in [tHb] at transitions into REMS. [tHb] represents CBV and is related to the CBF [20]. For parts of prefrontal cortices, PET data indicate a reduction [2] of relative regional CBF in REMS compared to NREMS and thus of cortical activity; for other parts no activation or an increase was observed [21]. This may be misleading since the statistical contrast is often based on a mixture of NREMS and wakefulness or solely wakefulness whereas our findings are reflecting state transitions directly. The relative CBF change in the prefrontal cortices seen with PET may also be masked by the global change in CBF. Our findings (and the global changes found

with PET) indicate a cerebral activation during REMS and a cerebral deactivation at transitions into NREMS in the left prefrontal cortices. This interpretation is based on the assumption that the link between neuronal activity, oxygen consumption, CBF and the hemoglobin parameters (neurovascular coupling [1]) hold also during sleep. The decreased StO_2 during NREMS may be related to the reduced spiking activity in NREMS compared to wakefulness and REMS found in rats [22]. Spiking activity being responsible for ~47 % of total grey matter energy expenditure (in rodents) [23] and hence may play a cardinal role in the oxygen metabolism. Näsi et al. [8] found that the [O_2Hb] and [HHb] changes at sleep transitions (measured at 4 cm distance) were correlated to [O_2Hb] and [HHb] changes in the scalp (measured at 1 cm distance) and to heart rate using a principle component analysis. They suggested that the "cortical hemodynamic changes must correlate with systemic hemodynamic changes" but "this does not show that there are no cortical changes associated with the transitions" [8]. To avoid influences from the scalp we used a multi-distance approach [12], which removes such a bias. A possibly important variable is the CO_2, which depends on the sleep stage [24] and may influence StO_2 [25]. In the future, CO_2 should be measured additionally.

In conclusion, with NIRS we were able to non-invasively show that changes in [O_2Hb], [HHb] and [tHb] in adolescents at sleep stage transitions are similar to those in adults and for the first time we demonstrated the time course of the cerebral StO_2 at sleep transitions.

Acknowledgments This work was supported by the University Research Priority Program "Integrative Human Physiology", University of Zurich, Switzerland. The authors would like to thank Urs Bachofner and Madlaina Stauffer for their great support with data collection.

References

1. Wolf M, Morren G, Haensse D et al (2008) Near infrared spectroscopy to study the brain: an overview. Opto Electron Rev 16(4):413–419
2. Maquet P (2000) Functional neuroimaging of normal human sleep by positron emission tomography. J Sleep Res 9(3):207–231
3. Dang-Vu TT, Schabus M, Desseilles M et al (2010) Functional neuroimaging insights into the physiology of human sleep. Sleep 33(12):1589–1603
4. Spielman AJ, Zhang G, Yang CM et al (2000) Intracerebral hemodynamics probed by near infrared spectroscopy in the transition between wakefulness and sleep. Brain Res 866(1–2):313–325
5. Hoshi Y, Mizukami S, Tamura M (1994) Dynamic features of hemodynamic and metabolic changes in the human brain during all-night sleep as revealed by near-infrared spectroscopy. Brain Res 652(2):257–262
6. Shiotsuka S, Atsumi Y, Ogata S et al (1998) Cerebral blood volume in the sleep measured by near-infrared spectroscopy. Psychiatry Clin Neurosci 52(2):172–173
7. Uchida-Ota M, Tanaka N, Sato H et al (2008) Intrinsic correlations of electroencephalography rhythms with cerebral hemodynamics during sleep transitions. Neuroimage 42(1):357–368
8. Näsi T, Virtanen J, Noponen T et al (2011) Spontaneous hemodynamic oscillations during human sleep and sleep stage transitions characterized with near-infrared spectroscopy. PLoS ONE 6(10):e25415

9. Kubota Y, Takasu NN, Horita S et al (2011) Dorsolateral prefrontal cortical oxygenation during rem sleep in humans. Brain Res 1389:83–92
10. Metz AJ, Pugin F, Huber R et al (2013) Brain tissue oxygen saturation increases during the night in adolescents. Adv Exp Med Biol 789:113–119
11. Muehlemann T, Haensse D, Wolf M (2008) Wireless miniaturized in-vivo near infrared imaging. Opt Express 16(14):10323–10330
12. Hueber DM, Fantini S, Cerussi AE et al (1999) New optical probe designs for absolute (self-calibrating) nir tissue hemoglobin measurements. Proc SPIE 3597:618–631
13. Metz AJ, Biallas M, Jenny C et al (2013) The effect of basic assumptions on the tissue oxygen saturation value of near infrared spectroscopy. Adv Exp Med Biol 765:169–175
14. Scholkmann F, Spichtig S, Muehlemann T et al (2010) How to detect and reduce movement artifacts in near-infrared imaging using moving standard deviation and spline interpolation. Physiol Meas 31(5):649–662
15. Virtanen J, Noponen T, Kotilahti K et al (2011) Accelerometer-based method for correcting signal baseline changes caused by motion artifacts in medical near-infrared spectroscopy. J Biomed Opt 16(8):087005
16. Iber C, Sonia Ancoli-Israel PD, Chesson A et al (2007) The aasm manual for the scoring of sleep and associated events: rules, terminology and technical specifications. American Acedemy of Sleep Medicine, Westchester, IL
17. Feinberg I, Floyd TC (1979) Systematic trends across the night in human sleep cycles. Psychophysiology 16(3):283–291
18. Benjamini Y, Hochberg Y (1995) Controlling the false discovery rate – a practical and powerful approach to multiple testing. J R Stat Soc B Methodol 57(1):289–300
19. Braun AR, Balkin TJ, Wesenten NJ et al (1997) Regional cerebral blood flow throughout the sleep-wake cycle. An h2(15)o pet study. Brain 120(Pt 7):1173–1197
20. Grubb RL Jr, Raichle ME, Eichling JO et al (1974) The effects of changes in paco2 on cerebral blood volume, blood flow, and vascular mean transit time. Stroke 5(5):630–639
21. Maquet P, Ruby P, Maudoux A et al (2005) Human cognition during rem sleep and the activity profile within frontal and parietal cortices: a reappraisal of functional neuroimaging data. Prog Brain Res 150:219–227
22. Vyazovskiy VV, Olcese U, Lazimy YM et al (2009) Cortical firing and sleep homeostasis. Neuron 63(6):865–878
23. Attwell D, Laughlin SB (2001) An energy budget for signaling in the grey matter of the brain. J Cereb Blood Flow Metab 21(10):1133–1145
24. Shore ET, Millman RP, Silage DA et al (1985) Ventilatory and arousal patterns during sleep in normal young and elderly subjects. J Appl Physiol 59(5):1607–1615
25. Scholkmann F, Gerber U, Wolf M et al (2012) End-tidal co(2): an important parameter for a correct interpretation in functional brain studies using speech tasks. Neuroimage 66C:71–79

Chapter 38
Influence of Subjective Happiness on the Prefrontal Brain Activity: An fNIRS Study

Sayuri Oonishi, Shota Hori, Yoko Hoshi, and Akitoshi Seiyama

Abstract Focusing on the relationship between subjective happiness (SH) and emotional changes, we examined influences of SH on emotion-related prefrontal activity using multichannel NIRS. The International Affective Picture System (IAPS) was used to evoke emotional changes. Subjects were a total of 18 right-handed healthy students. Frequency of picture-induced increases in oxygenated haemoglobin (oxy-Hb) was evaluated. Subjects with a high SH score had a higher frequency of increased oxy-Hb in the left prefrontal cortex (PFC) while viewing pleasant pictures, whereas they showed a lower frequency in the right PFC while viewing unpleasant pictures. It is well known that the left PFC and right PFC are engaged in different ways in the emotional processes. Although further investigations are required, the present results indicate that the SH level influences the right-left differences in emotion-related prefrontal activity.

Keywords Subjective happiness • Emotion • Near infrared spectroscopy • Prefrontal cortex • Laterality

1 Introduction

Recently, the relationship between brain activity and levels of subjective happiness (SH) has become an attractive theme in medicine. It is reported that in persons with a high SH score, activation of the medial prefrontal cortex and ventral striatum

S. Oonishi • S. Hori • A. Seiyama (✉)
Division of Medical Devices for Diagnoses, Human Health Sciences, Graduate School of Medicine, Kyoto University, 53 Shogoin, Kawahara-cho, Sakyo-ku, Kyoto 606-8507, Japan
e-mail: seiyama.akitoshi.7x@kyoto-u.ac.jp

Y. Hoshi
The Integrated Neuroscience Research Team, Tokyo Institute of Psychiatry, Tokyo, Japan

H.M. Swartz et al. (eds.), *Oxygen Transport to Tissue XXXVI*, Advances in Experimental Medicine and Biology 812, DOI 10.1007/978-1-4939-0620-8_38,

(i.e., brain reward system) [1] and function of the immune system [2, 3] are strongly activated under normal and acute stress conditions. Therefore, it is important to investigate the relationship between brain activities and levels of SH in order to prevent mental disorders and physical illnesses.

Some external stimuli induce emotional change, but this response differs from person to person depending on individual memories, experiences and internal body conditions. On the other hand, "happiness" has been defined as consisting of three independent components: 'cognitive life satisfaction', 'positive affect' and 'negative affect' [4].

Using noninvasive techniques such as functional Magnetic Resonance Imaging (fMRI) and Positron Emission Tomography (PET) [5, 6], changes in regional brain activity in the limbic system, including the amygdala and prefrontal cortex (PFC), associated with emotional processing can be measured; however, during these measurements physical restraint is required. On the other hand, near-infrared spectroscopy (NIRS) appears more suitable because this technique is noninvasive and less physical restraint is required [7, 8].

In the present study, focusing on the relationship between SH and emotional changes, we examined influences of SH on emotion-related prefrontal activities using multichannel NIRS.

2 Methods

2.1 Subjects

Thirteen right-handed healthy student volunteers participated in the study (seven males, six females, mean age 22.9 years). Of these, five subjects (three males, two females, mean age 23.6 years) were examined again after a half year. Before the experiments, written informed consent was obtained from all participants. The Ethics Committee of Kyoto University approved the study.

2.2 Evaluation Method

2.2.1 Subjective Happiness

SH was estimated with Shimai's Japan Subjective Happiness Scale (JSHS) [9], which consists of four statements for evaluating happiness. The subject was asked to answer on a numeric scale ranging from 1 (very unhappy) to 7 (very happy) immediately prior to NIRS measurement. The total score was expressed by an average of the scores for the four statements.

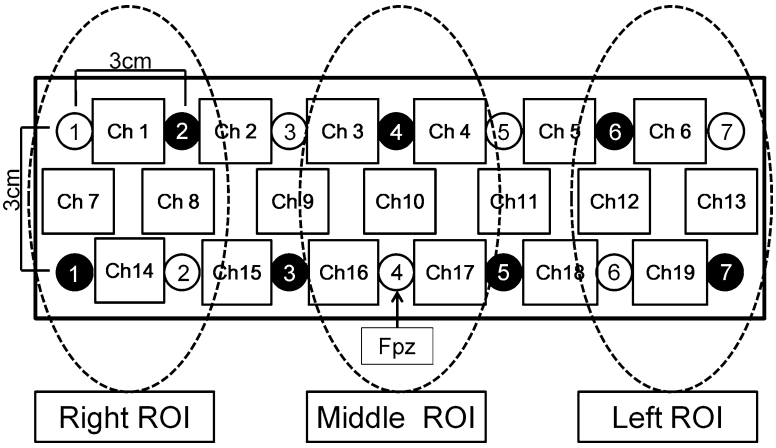

Fig. 38.1 Positions of the light guides

2.2.2 Measurements of Brain Activity

A multichannel NIRS imaging system (FOIRE-3000, Shimadzu Co., Japan) was employed for measurements. Seven pairs of illuminating (open circle) and detecting (closed circle) light guides were placed on the forehead with a distance of 3 cm between them (Fig. 38.1). This alignment of light guides measured 19 regions (channels) which covered the Brodmann's areas (BAs) 9(dorsolateral prefrontal cortex)/10(anterior prefrontal cortex))/45(pars triangularis broca's area)/46(dorsolateral prefrontal cortex). And the fourth sending illuminating light guide was positioned Fpz according to the international 10–20 system (see Fig. 38.1). The NIRS signals were sampled at every 70 ms. Original NIRS signals were analyzed without filtering.

The occurrence *f*requency of picture-induced *i*ncreases in *i*ntegrated *o*xygenated *h*aemoglobin (oxy-Hb) (FiIOH) from the value at the stimulus-onset FiIOH (t = 0 s) to a certain time FiIOH (t = T s) on each region of interest (ROI) (left and right ROI = 4 chs, middle = 5 chs, see Fig. 38.1) was evaluated. If oxy-Hb concentration integrated from 0 to t s during single task (iIOH) is more than 0, then we count iIOH = 1, else iIOH is 0. Thereby, we defined FiIOH as number of iOH > 0 during viewing 15 pictures (i.e., Minimum and maximum value of FiIOH are 0 and 15, respectively).

2.3 Experimental Procedures Stimuli

Subjects were sitting on a chair in a quiet room. The affective pictures (the IAPS) were presented on a 21.5 in. display monitor 80 cm away from each subject's face

(viewing angle 23.8°). A white cross hair was first presented at the center of a gray background for 15 s (a resting period: R) and then an affective picture was shown for 10 s (a stimulation period), which was successively followed by the second resting period. One block consisted of 15 pictures composed of equal numbers of pictures with each emotional valence (i.e., pleasant 5, unpleasant 5 and neutral 5). The order of presenting pictures was pseudo-randomized in each block. The total of two blocks was conducted with a 1-min interval. After NIRS measurements, the subjects rated their valence for all 30 pictures using the Self-Assessment Manikin (SAM) [10].

3 Results

3.1 Relationship Between NIRS Signals and SH

Figure 38.2a shows the relationship between SH and Left-FiIOH (t = 10) during pleasant picture viewing for all 18 subjects. Subjects with a high SH score (h-SH) showed significantly higher Left-FiIOH ($p < 0.05$). Figure 38.2b shows the relationship between SH and Right-FiIOH (t = 2) during unpleasant picture viewing. There was no significant correlation, but h-SH subjects showed a tendency giving less Right-FiIOH.

Figure 38.3 shows the p-value of the correlation coefficients between SH and Left-FiIOH (closed circle) and Right-FiIOH (open circle) from t = 1–10 s. As described above, Left-FiIOH gave a significant positive correlation at later time (t = 9 and 10), while Right-FiIOH gave an opposite correlation and a relatively higher correlation at an earlier time (t = 2).

Statistical analysis was performed using Pearsons product-moment correlations [11, 12] and $p < 0.05$ was considered statistically significant.

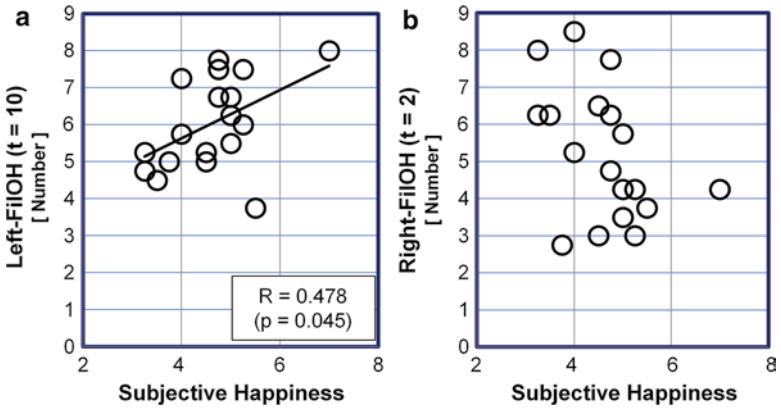

Fig. 38.2 Relationship between subjective happiness (SH) and *number* of increased integrated oxy-Hb (FiIOH). (**a**) SH vs Left-FiIOH (t = 10 s) during pleasant picture viewing. (**b**) SH vs Right-FiIOH (t = 2 s) during unpleasant picture viewing. SH scale ranging from 1 (very unhappy) to 7 (very happy)

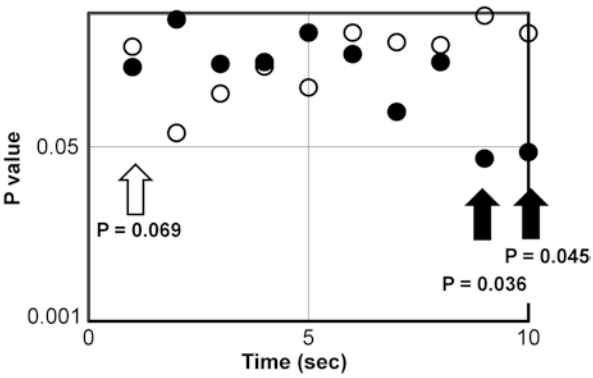

Fig. 38.3 Time variation of p-value of correlation coefficients between subjective happiness and Left and Right-FiIOH. Vertical axis is shown with logarithm. Significant value is $p<0.05$. (Left-FiIOH, *closed circle*; Right-FiIOH, *open circle*)

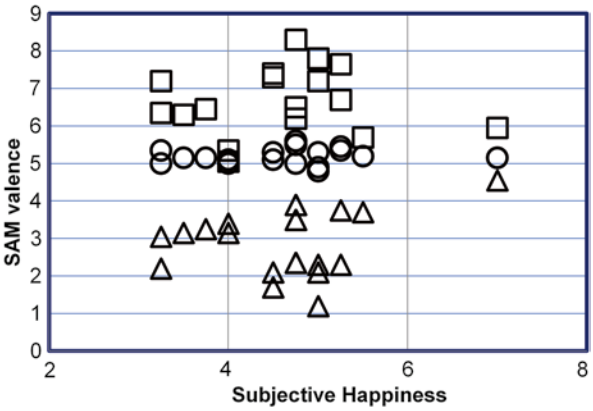

Fig. 38.4 Relationship between subjective happiness and SAM valence. *Open square*, *circle* and *triangle* denote pleasant, neutral and unpleasant pictures, respectively

3.2 Relationship Between SAM and SH

Figure 38.4 shows the relationship between SH and SAM valences. SH was not related to the valence. However, valences individually evaluated with SAM were almost consistent with the IAPS categorization.

4 Discussion

4.1 Difference Between Left and Right PFC Functions

Lesion studies have suggested that SH is related to depression [13, 14], and a melancholic tends to have pessimistic thoughts with hypoactivity in the left PFC and hyperactivity in the right PFC [15]. Our results also suggest that subjects with a low SH score showed lower activity in the left PFC and higher activity in the right PFC (Fig. 38.2). By using fMRI and/or NIRS, previous studies suggest that the left PFC

activation is associated with pleasant emotion and right PFC activation is associated with unpleasant emotion [16–18] and Hoshi et al. [8] reported that oxy-Hb increased both Left and Right VLPFCs. Further, cerebral laterality is an important feature of the negative feedback regulation, e.g., the right PFC being most directly linked to stress-regulatory systems [19]. Therefore, the present results suggest that (1) Left-FiIOH correlates with pleasant emotion and Right-FiIOH with unpleasant emotion, and (2) the h-SH correlates with high pleasant emotion and low unpleasant emotion (Fig. 38.2).

On the other hand, as shown in Fig. 38.4, SAM valence was not correlated with either SH valence or FiIOH. Several studies used self-reported anxious and mental arithmetic task have suggested that higher right than left PFC activation is associated with anxious and stress (e.g., [20, 21]). One of the possible explanations is as follows. The emotion (FiIOH) induced by IAPS does not always correlate with valence of feeling (SAM). Since h-SH subjects showed high FiIOH for pleasant pictures and low FiIOH unpleasant pictures (Fig. 38.2).

4.2 Difference in Time

It is reported that differences in the SH level affect the time course of affective priming effects induced by emotional stimulation [22]. Further, Northoff et al. [23] reported that the ventromedial PFC was activated earlier by unpleasant pictures than by pleasant ones. Our results shown in Fig. 38.3 agree with (or support) those previous reports.

5 Conclusions

In the present study, focusing on the relationship between SH and emotional change, we examined the influence of SH on emotion-related prefrontal activities using multichannel NIRS. Our present results advocate the following functional cerebral laterality: the left PFC correlates with pleasant emotion and the right PFC with unpleasant emotion. Moreover, our results suggest that the SH level influences the emotion-related prefrontal activities. Clarifying the relationships between brain activities and SH levels is important to prevent us from mental disorders and physical illnesses.

Acknowledgements This study was supported in part by grants-in-aid from the Ministry of Education, Science and Culture of Japan.

References

1. Matsunaga M, Kaneko H, Tsuboi H et al (2011) Psychosomatic approach to health from the perspective of positive psychology. Jpn Soc Psychosomat Med 51:135–140
2. Matsunaga M (2009) Associations among positive mood, brain, and cardiovascular activities in an affectively positive situation. Brain Res 1263:93–103

3. Matsunaga M, Sato S, Isowa T et al (2009) Profiling of serum proteins influenced by warm partner contact in healthy couples. Neuro Endocrinol Lett 30:227–236
4. Terasaki M, Tsunashima K, Nishimura T (1999) The structure of subjective well-being. Kawasaki Univ Medl Welfare 9:43–48
5. Fulbright RK, Skudlarski P, Lacadie CM et al (1998) Functional MR imaging of regional brain responses to pleasant and unpleasant odors. Am J Neuroradiol 19:1721–1726
6. Paradiso S, Johnson DL, Andreasen NC et al (1999) Cerebral blood flow changes associated with attribution of emotional valence to pleasant, unpleasant, and neutral visual stimuli in a PET study of normal subjects. Am J Psychiatry 156:1618–1629
7. Herrmann MJ, Ehlis AC, Fallgatter AJ (2003) Prefrontal activation through task requirements of emotional induction measured with NIRS. Biol Psychol 64:255–263
8. Hoshi Y, Huang J, Kohri S et al (2011) Recognition of human emotions from cerebral blood flow changes in the frontal region: a study with event-related near-infrared spectroscopy. J Neuroimaging 21:e94–e101
9. Shimai S, Otake K, Utsuki N et al (2004) Development of a Japanese version of the subjective happiness scale (SHS), and examination of its validity and reliability. Nihon kōshū eisei zasshi 51:845–853
10. Bradley MM, Lang PJ (1994) Measuring emotion: the self-assessment manikin and the semantic differential. J Behav Ther Exp Psychiatry 25:49–59
11. Harker LA, Keltner D (2001) Expressions of positive emotion in women's college yearbook pictures and their relationship to personality and life outcomes across adulthood. J Pers Soc Psychol 80:112–124
12. Nakahara-Gondoh Y, Fujimoto T, Sensui H et al (2013) The effects of low-frequency aerobic exercise training on psychological well-being. Bull Phys Fitness Res Inst 111:8–15
13. Kawahito J, Otsuka Y (2011) Positive self-complexity, satisfaction, happiness, and depression in university students. Jpn J Pers 20:138–140
14. Seligman ME, Rashid T, Parks AC (2006) Positive psychotherapy. Am Psychol 61:774–788
15. Okada G, Okamoto Y, Yamashita H et al (2009) Attenuated prefrontal activation during a verbal fluency task in remitted major depression. Psychiatry Clin Neurosci 63:423–425
16. Ueda K, Okamoto Y, Okada G (2003) Brain activity during expectancy of emotional stimuli: an fMRI study. Neuroreport 14:51–55
17. Schienle A, Schafer A, Pignanelli R et al (2009) Worry tendencies predict brain activation during aversive imagery. Neurosci Lett 461:289–292
18. Marumo K, Takizawa R, Kawakubo Y (2009) Gender difference in right lateral prefrontal hemodynamic response while viewing fearful faces: a multi-channel near-infrared spectroscopy study. Neurosci Res 63:89–94
19. Sullivan RM, Gratton A (2002) Prefrontal cortical regulation of hypothalamic-pituitary-adrenal function in the rat and implications for psychopathology: side matters. Psychoneuroendocrinology 27:99–114
20. Heller W, Nitschke JB, Etienne MA et al (1997) Patterns of regional brain activity differentiate types of anxiety. Abnorm Psychol 106:376–385
21. Tanida M, Katsuyama M, Sakatani K (2007) Relation between mental stress-induced prefrontal cortex activity and skin conditions: a near-infrared spectroscopy study. Brain Res 1184:210–216
22. Kotozaki Y (2012) Individual difference of the subjective well-being and automatic emotion regulation using affective priming. Jpn J Appl Psychol 37:135–136
23. Northoff G, Richter A, Gessner M et al (2000) Functional dissociation between medial and lateral prefrontal cortical spatiotemporal activation in negative and positive emotions: a combined fMRI/MEG study. Cereb Cortex 10:93–107

Chapter 39
Ginkobiloba Extract Improves Working Memory Performance in Middle-Aged Women: Role of Asymmetry of Prefrontal Cortex Activity During a Working Memory Task

Kaoru Sakatani, Masahiro Tanida, Naoyasu Hirao, and Naohiro Takemura

Abstract In order to clarify the mechanism through which extract of *Ginkgo biloba* leaves (EGb) improves cognitive function, we examined the effects of EGb on cerebral blood oxygenation in the prefrontal cortex (PFC) and on performance during a working memory task, using near-infrared spectrometry (NIRS). First, we evaluated differences in behavioral performance of the Sternberg working memory test (ST) and in the activation pattern of the PFC during ST between 15 young and 19 middle-aged healthy women. Then, we examined the effect of EGb (120 mg/day for 6 weeks) on ST performance and PFC activation pattern in the middle-aged group. The middle-aged group exhibited a longer reaction time (RT) in ST than the young group and showed a different PFC activation pattern during ST, i.e., the middle-aged group showed bilateral activation while the young group showed right-dominant activation. In the middle-aged group, administration of EGb for 6 weeks shortened the RT of ST and changed the PFC activation pattern to right-dominant, like that in the young group. The results indicate the PFC plays a role in the physiological

K. Sakatani (✉)
Laboratory of Integrative Biomedical Engineering, Department of Electrical and Electronics Engineering, College of Engineering, Nihon University, 1 Nakagawara, Tokusada, Tamuramachi, Koriyama, Fukushima Prefecture 963-8642, Japan

Department of Neurological Surgery, Nihon University School of Medicine, Tokyo, Japan
e-mail: sakatani.kaoru@nihon-u.ac.jp

M. Tanida • N. Hirao
Shiseido Research Center, Yokohama, Japan
e-mail: masahiro.tanida@to.shiseido.co.jp

N. Takemura
Laboratory of Integrative Biomedical Engineering, Department of Electrical and Electronics Engineering, College of Engineering, Nihon University, Koriyama, Fukushima 963-8642, Japan
e-mail: naohiro.takemura@gmail.com

H.M. Swartz et al. (eds.), *Oxygen Transport to Tissue XXXVI*, Advances in Experimental Medicine and Biology 812, DOI 10.1007/978-1-4939-0620-8_39,

cognitive function-enhancing effect of EGb. EGb might improve working memory function in middle-aged individuals by counteracting the occurrence of aging-related hemispheric asymmetry reduction.

Keywords Ginkobiloba • Near-infrared spectroscopy • Prefrontal cortex • Cerebral blood oxygenation • Sternberg working memory test • Reaction time

1 Introduction

A standardized preparation of extract of the leaves of the *Ginkgo biloba* tree (EGb) is well known to alleviate symptoms of many cognitive disorders, including Alzheimer's disease or multi-infarct dementia [1]. EGb also improves cognitive functions in ageing healthy populations [2] and middle-aged subjects [3]. However, the mechanism of the effect of EGb on cognitive function, particularly the role of the prefrontal cortex, remains unclear.

Here, we examined the effect of EGb on bilateral prefrontal cortex (PFC) activity associated with working memory performance, using near-infrared spectroscopy (NIRS). We focused on the hemispheric asymmetry of PFC activity to explore the cognitive function-enhancing properties of EGb. Hemispheric asymmetry of PFC activity is well known to be reduced or eliminated during ageing [4]. Employing NIRS, we evaluated the PFC activity of young and middle-aged women while they performed a Sternberg-type working memory task [5]. Then, we evaluated the effect of EGb on the age-related change in the PFC activity pattern associated with a cognitive performance task.

2 Methods

We studied 15 young (aged 20–22 years, mean 21.8 ± 0.7 years) and 19 middle-aged (aged 44–50 years, mean 46.8 ± 1.6 years) healthy women. The subjects were all deemed right-handed according to the laterality quotient questionnaire of the Edinburgh Handedness Inventory. All subjects provided written informed consent as required by the Human Subjects Committee of the Shiseido Life Science Institute.

2.1 Experimental Protocol

We employed the modified Sternberg test as a working memory task [5]. We used 2-channel time-resolved spectroscopy (TRS); the sampling rate was once per second, and the source-detector distance was 3 cm. Details of the TRS (TRS-20, Hamamatsu Photonics K.K., Japan) have been reported [6]. The concentrations of Hb were

expressed in μM. The NIRS probes were set symmetrically on the forehead; MRI confirmed that the emitter-detector was located over the dorsolateral and frontopolar areas of the PFC.

The present study consisted of two phases. First, we evaluated the difference in working memory between the young and middle-aged groups. We compared the behavioral performance on the Sternberg test and the PFC activity evoked by the Sternberg test between the two groups. We evaluated reaction time (ms) as a measure of behavioral performance in the Sternberg test. In the second phase of the study, we evaluated the effect of a putatively cognitive function-enhancing supplement on the working memory of the middle-aged women. For this, we administered SuppleX (Shiseido, Japan), which contains EGb (120 mg), for 6 weeks. After 6 weeks, we compared the behavioral performance in the Sternberg test and the PFC activity evoked by the Sternberg test between the supplement ($n=9$) and placebo ($n=10$) groups. The present study was conducted as a single blind randomized controlled trial.

2.2 Data Analysis

The evoked cerebral blood oxygenation (CBO) changes in the bilateral PFC were continuously monitored by TRS and were averaged every second during: (1) baseline conditions for 60 s; (2) the Sternberg test for 60–80 s (the period varied according to each subject's reaction time); and (3) recovery for 60 s. To analyze PFC activity in response to task performance, we calculated changes in oxy-Hb concentration during the Sternberg test. The mean baseline values (measured during 60 s) were subtracted from the mean activation values (measured during the first 60 s during task performance).

In order to determine left/right asymmetry of PFC activity during the working memory task, we calculated the right laterality score of Δoxy-Hb (right Δoxy-Hb − left Δoxy-Hb; positive values indicate greater activity of the right PFC, while negative values indicate greater activity of the left PFC.

For evaluation of the statistical significance of differences, two-way analysis of variance (ANOVA) was conducted with within-subject factors of treatment (control and Gingko supplement) and test period (pre and post).

3 Results

There was no significant difference in accuracy in the Sternberg test between the young and middle-aged groups ($p=0.47$). However, the reaction time of the middle-aged group was significantly longer than that of the young group ($p<0.0005$). TRS demonstrated increases of oxy-Hb and total Hb(t-Hb) associated with a decrease of deoxy-Hb in the bilateral PFC during performance of the Sternberg test in both the

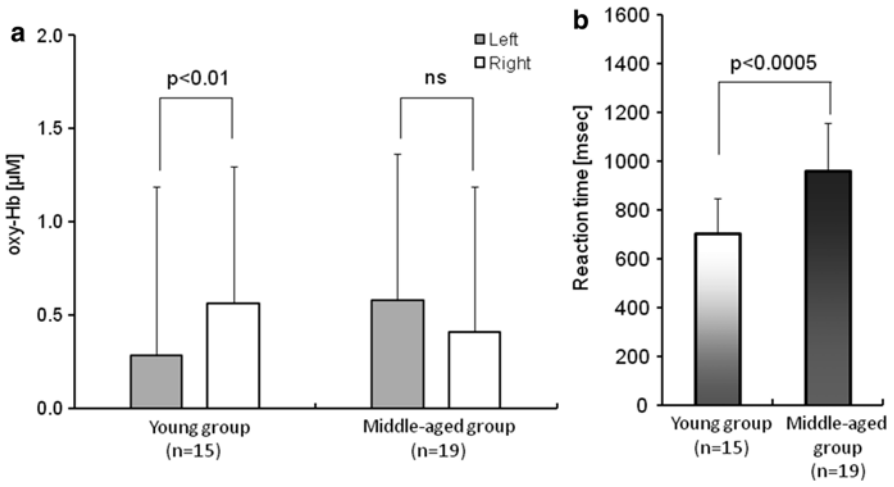

Fig. 39.1 (**a**) Comparison of oxy-Hb changes between the right and left PFC during ST in the young and middle-aged groups. The right PFC exhibited a larger change of oxy-Hb than the left PFC in the young group, but there were no significant difference in the middle-aged group. (**b**) Comparison of reaction time of 6-digit ST between the young and middle-aged groups. The middle-aged group showed a significantly longer mean reaction timethan the young group ($p < 0.0005$)

young and middle-aged groups (Fig. 39.1). There was a significant difference in the right laterality score of Δoxy-Hb between the young and middle-aged groups ($p < 0.05$).

There are significant treatment × period interactions in both RT [($F(1, 17) = 5.79$, $p < 0.05$)] and laterality ratio [($F(1, 17) = 5.47$, $p < 0.05$)]. The main effects seen in the treatment and period comparisons were as follows: Administration of the supplement significantly decreased the reaction time in the Sternberg test ($F(1, 17) = 5.47$, $p < 0.05$), while there was no significant change of reaction time in the placebo group among the middle-aged subjects ($F(1, 17) = 1.14$, $p = 0.30$) (Fig. 39.2a). In addition, the right laterality score of Δoxy-Hb was significantly increased after administration of the supplement ($F(1, 17) = 11.14$, $p < 0.005$). In contrast, the placebo group exhibited no significant change in right laterality score (Fig. 39.2b).

Finally, we evaluated the baseline concentrations of oxy-Hb, deoxy-Hb, and t-Hb before and after administration of the supplement (Table 39.1). The baseline concentrations of Hb did not change significantly after administration of the supplement ($p > 0.05$).

4 Discussion

The present findings indicate that the PFC plays a role in the physiological cognitive function-enhancing effect of EGb in humans. TRS demonstrated differences in PFC activation pattern during the Sternberg test between the middle-aged and young

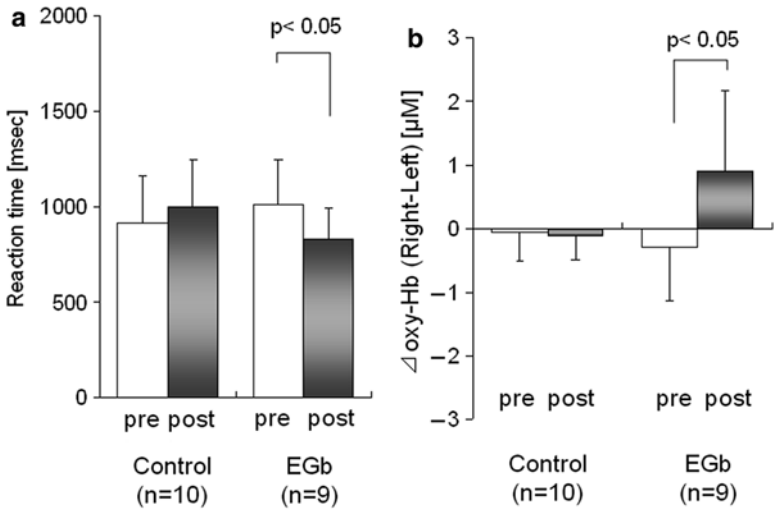

Fig. 39.2 Effects of EGb for 6 weeks on the reaction time of the Sternberg test (**a**) and the right laterality score of Δoxy-Hb in the middle-aged group (**b**)

Table 39.1 Differences in Hb concentrations under a resting condition before and after administration of the supplement

Hb concentration (μM)	Before	After
Oxy-Hb (L)	39.3 ± 4.9	39.9 ± 4.2
Oxy-Hb (R)	38.7 ± 4.8	37.8 ± 5.1
Deoxy-Hb (L)	19.8 ± 1.8	20.1 ± 2.0
Deoxy-Hb (R)	19.2 ± 1.9	19.1 ± 1.3
t-Hb (L)	59.1 ± 5.0	59.9 ± 4.4
t-Hb (R)	57.8 ± 4.5	56.9 ± 5.3

groups; the middle-aged group showed bilateral activation, while the young group exhibited right-dominant activation. It has been reported that working memory tasks cause asymmetrical PFC activation in younger adults, while older adults tended to exhibit a reduction in hemispheric lateralization (i.e., reduced asymmetry) [4]. It has also been reported that right-lateralized PFC activity is associated with more successful cognitive performance [7].

The reduction of asymmetry in PFC activity is known as HAROLD (hemispheric asymmetry reduction in older adults) [4]. Interestingly, we found that administration of the supplement changed the activation pattern of PFC in the middle-aged group during the Sternberg test to right-dominant, resembling the pattern observed in the young group. These observations suggest that EGb might improve working memory function in middle-aged subjects by counteracting the occurrence of HAROLD. However, it should be noted that such reduction of hemispheric asymmetry in older adults can be also explained by the CRUNCH (compensation-related utilization of neural circuits hypothesis) model [8].

TRS allows measurement of baseline concentrations of Hb under a resting condition. In the present study, TRS demonstrated that the baseline concentration of Hb in the PFC did not change after administration of the supplement for 6 weeks, suggesting that vascular effects such as cerebral vasorelaxation and reduction of blood viscosity [9] might not be involved in the effect of the supplement on PFC activity during the Sternberg test. Hadjiivanova and Petkov demonstrated that administration of EGb induced a significant decrease in the density of beta-adrenoreceptors in the frontal cortex and hippocampus in the rat [10]. Silberstein et al. investigated the chronic effects of EGb on steady state visually evoked potential (SSVEP) topography in healthy middle-aged subjects whilst completing an object working memory task, and found that EGb increased the SSVEP amplitude at frontal sites during the hold component of the task, suggesting that EGb may induce more efficient processing during the task performance [11]. Such neurotransmitter system effects might be involved in the cognitive enhancement in normal adults.

Finally, the limitations of the present study need to be considered. *First, we measured neuronal activity only in the PFC in the present study*. Therefore, we could not evaluate the effect of EGb on other brain regions. Second, we did not evaluate the effect of the supplement containing EGb on the young group. It is necessary to evaluate the neural correlates of EGb in normal subjects of various ages, as well as in patients with cognitive dysfunction. Therefore, it should be emphasized that further work is needed to characterize the influence of EGb on brain function.

Acknowledgements This research was supported in part by a Grant-in-Aid from the Ministry of Education, Culture, Sports, Sciences and Technology of Japan (B23300247), and grants from Alpha Electron Co., Ltd. (Fukushima, Japan) and Iing Co., Ltd. (Tokyo, Japan).

References

1. Le Bars PL (2003) Magnitude of effect and special approach to Ginkgo biloba extract EGb 761 in cognitive disorders. Pharmacopsychiatry 36(Suppl 1):S44–S49
2. Kaschel R (2009) Ginkgo biloba: specificity of neuropsychological improvement – a selective review in search of differential effects. Hum Psychopharmacol 24:345–370
3. Hartley DE, Heinze L, Elsabagh S, File SE (2003) Effects on cognition and mood in postmenopausal women of 1-week treatment with Ginkgo biloba. Pharmacol Biochem Behav 75:711–720
4. Cabeza R (2002) Hemispheric asymmetry reduction in older adults: the HAROLD Model. Psychol Aging 17:85–100
5. Tanida M, Sakatani K, Tsujii T (2012) Relation between working memory performance and evoked cerebral blood oxygenation changes in the prefrontal cortex evaluated by quantitative time-resolved near-infrared spectroscopy. Neurol Res 34:114–119
6. Oda M, Nakano T, Suzuki A, Shimizu K, Hirano I, Shimomura F, Ohame E, Suzuki T, Yamashita Y (2000) Near infrared time-resolved spectroscopy system for tissue oxygenation monitor. Proc SPIE 4160:204–210
7. Aron AR, Robbins TW, Poldrack RA (2004) Inhibition and the right inferior frontal cortex. Trends Cogn Sci 8:170–177

8. Berlingeri M, Danelli L, Bottini G, Sberna M, Paulesu E (2013) Reassessing the HAROLD model: is the hemispheric asymmetry reduction in older adults a special case of compensatory-related utilisation of neural circuits? Exp Brain Res 224(3):393–410
9. Huang SY, Jeng C, Kao SC, Yu JJH, Liu DZ (2004) Improved haemorrheological properties by Ginkgo biloba extract (Egb 761) in type 2 diabetes mellitus complicated with retinopathy. Clin Nutr 23:615–621
10. Hadjiivanova CI, Petkov VV (2002) Effect of Ginkgo biloba extract on beta-adrenergic receptors in different rat brain regions. Phytother Res 16:488–490
11. Silberstein RB, Pipingas A, Song J, Camfield DA, Nathan PJ, Stough C (2011) Examining brain-cognition effects of Ginkgo biloba extract: brain activation in the left temporal and left prefrontal cortex in an object working memory task. Evid Based Complement Alternat Med 2011:164139

Chapter 40
Bayesian Prediction of Anxiety Level in Aged People at Rest Using 2-Channel NIRS Data from Prefrontal Cortex

Yukikatsu Fukuda, Wakana Ishikawa, Ryuhei Kanayama, Takashi Matsumoto, Naohiro Takemura, and Kaoru Sakatani

Abstract The aim of this study was to predict mental stress levels of aged people at rest from two-channel near-infrared spectroscopy (NIRS) data from the prefrontal cortex (PFC). We used the State-Trait Anxiety Inventory (STAI) for the mental stress index.

We previously constructed a machine learning algorithm to predict mental stress level using two-channel NIRS data from the PFC in 19 subjects aged 20–24 years at rest (Sato et al., Adv Exp Med Biol 765:251–256, 2013). In the present study, we attempted the same prediction for aged subjects aged 61–79 years (10 women; 7 men). The mental stress index was again STAI. After subjects answered the STAI questionnaire, the NIRS device measured oxy- and deoxy-hemoglobin concentration changes during a 3-min resting state. The algorithm was formulated within a Bayesian machine learning framework and implemented by Markov Chain Monte Carlo. Leave-one-subject-out cross-validation was performed.

Average prediction error between the actual and predicted STAI values was 5.27. Prediction errors of 12 subjects were lower than 5.0. Since the STAI score ranged from 20 to 80, the algorithm appeared functional for aged subjects also.

Keywords Anxiety • Near infrared spectroscopy • Prefrontal cortex • Bayesian regression • Aging

Y. Fukuda (✉) • W. Ishikawa • R. Kanayama • T. Matsumoto
Department of Electrical Engineering and Bioscience, Waseda University, Okubo 3-4-1, Nishiwaseda Campus Building 55th N-0402, Shinjuku-ku, Tokyo 169-0072, Japan
e-mail: yukikatsu_fukuda@fuji.waseda.jp

N. Takemura
Laboratory of Integrative Biomedical Engineering, Department of Electrical and Electronics Engineering, College of Engineering, Nihon University, Koriyama, Fukushima 963-8642, Japan

K. Sakatani
Department of Electrical and Electronics Engineering, Nihon University, Tokyo, Japan

H.M. Swartz et al. (eds.), *Oxygen Transport to Tissue XXXVI*, Advances in Experimental Medicine and Biology 812, DOI 10.1007/978-1-4939-0620-8_40,

1 Introduction

Recently, mental stress has become an important issue. However, measurements of mental stress have been based on experience, and a method of obtaining objective stress measurements will have huge potential in practical usage.

Research in this field has focused on the prefrontal cortex (PFC), which is an important area involved in stress responses. Davidson et al. reported that the asymmetry of PFC activities between the right and left hemispheres was related to emotional responses; specifically, right-dominant activity was induced when the subject was in a negative mood, and left-dominant activity was induced in a positive mood [1]. These emotional responses were also associated with stress responses. The laterality index showed right-dominant activity for stressful tasks and left-dominant activity for resting states [2]. Generally, fluctuations of NIRS data are thought to play an important role in predicting mental stress level, and a default-mode network works even when the subject is resting [3]; however, the detailed neurological and physiological systems lying behind this remain unclear. A statistical prediction method employing Bayesian regression with nonlinear regression models and Markov Chain Monte Carlo (MCMC) implementations has also been reported [4]. This method used NIRS data obtained from young subjects to predict State Trait Anxiety Inventory (STAI) scores.

In this paper, we applied the same framework to aged subjects to examine the effect of aging and to investigate the properties of this method. The evaluation criteria we employed were the root-mean-square error (RMSE), the correlation coefficient, and the p-value of a two-tailed t-test between the actual and predicted STAI values of aged subjects.

Because our experimental protocol was simple and the device could easily measure near-infrared spectroscopy (NIRS) data, this approach is promising for various applications, such as preventive medicine and environmental management, and will help us to understand cerebral physiological systems.

2 Materials and Methods

2.1 Experimental Settings

We measured NIRS data from 17 subjects (10 women; 7 men), aged 61–79 years. The subjects had no history of psychiatric or neurological disorders, and had completed informed consent forms approved by the ethics committee of the Nihon University School of Medicine prior to the study.

Each subject was seated upright in a comfortable chair with their eyes open, and a two-channel pocket NIRS system (PNIRS-10, Hamamatsu Photonics K.K., Japan) was mounted symmetrically on the forehead. The NIRS probes were positioned at the midpoint between the electrode positions Fp1/Fp3 (left) and Fp2/Fp4 (right) according to the international 10–20 system.

Table 40.1 The features used in this study

No.	Variance	No.	Covariance	No.	Correlation coefficient
1	oxy(r)	5	oxy(r)/deoxy(r)	11	oxy(r)/deoxy(r)
2	deoxy(r)	6	oxy(r)/oxy(l)	12	oxy(r)/oxy(l)
3	oxy(l)	7	oxy(r)/deoxy(l)	13	oxy(r)/deoxy(l)
4	deoxy(l)	8	deoxy(r)/oxy(l)	14	deoxy(r)/oxy(l)
–	–	9	deoxy(r)/deoxy(l)	15	deoxy(r)/deoxy(l)
–	–	10	oxy(l)/deoxy(l)	16	oxy(l)/deoxy(l)

Oxy/deoxy denotes hemoglobin changes in the NIRS data, and letters "r" and "l" in parentheses denote the locations of the relevant channels. The numbers in the odd-numbered columns are feature numbers

Each subject performed one trial as described below:

Step 1. Answering STAI questionnaire. No time limit was set. The STAI results were used to measure the current anxiety level of the subjects.

Step 2. Preparation period (40 s). Subjects were allowed to move to make themselves comfortable, and the NIRS data became relatively steady within about 40 s. Parameters of the NIRS device were also set at the beginning of this period.

Step 3. Analysis period (3 min). Subjects were asked to remain relaxed and not to move during this period. No other instructions were given by the experimenters.

2.2 NIRS Data

The two-channel NIRS device acquired oxy- and deoxy-hemoglobin (Hb) concentrations. The data were a 4-dimensional matrix (right/left channels × oxy/deoxy-Hb) and 1,800 time-series values (180 s × 10 Hz sampling rate). We preprocessed the data to extract 16 second-order statistical features, namely, four variances, six covariances, and six correlation coefficients (Table 40.1). The second-order features were related in principle to the changes measured in the NIRS data.

2.3 Prediction

2.3.1 Prediction Flow

A leave-one-subject-out cross-validation (CV) was conducted. Of the NIRS and STAI datasets for the 17 subjects, one was reserved for testing, and the remaining 16 were used for training the machine. After parameters were learned with the training data, the reserved data were input to the machine for STAI prediction. One experiment consisted of repeating this procedure 17 times, once for each subject, and the final prediction results were averaged over the results of the five experiments.

2.3.2 Prediction Algorithm

Let $x^{(i)}=(x_1{}^{(i)},\ldots,x_K{}^{(i)})\in R^K, i=1,\ldots,N$, be the NIRS feature vector of the *i-th* individual and $y^{(i)}, i=1,\ldots,N$, be the STAI state scores ($K=3, N=17$). We attempted to fit the data with the following learning model:

$$P\left(y^{(i)}\mid \boldsymbol{x}_t^{(i)};\boldsymbol{\omega},\beta\right)=\sqrt{\frac{\beta}{2\pi}}\exp\left(-\frac{\beta}{2}\left(y^{(i)}-f\left(\boldsymbol{x}_t^{(i)};\boldsymbol{\omega}\right)\right)^2\right) \tag{40.1}$$

where f is the basis function, and β is unknown hyperparameter, corresponding to the magnitude of uncertainty in the STAI scores. The relationship between the NIRS data and the STAI score is expected to be nonlinear, and therefore, we employed the nonlinear basis function:

$$f\left(\boldsymbol{x}_t^{(i)};\boldsymbol{\omega}\right):=\sum_{h=1}^{H}\left[\omega_{(K+1)h}\sigma\left(\sum_{k=1}^{K}\left[\omega_{kh}x_{tk}^{(i)}\right]+\omega_{0h}\right)\right]+\omega_{(K+1)0} \tag{40.2}$$

where σ is a sigmoidal function that incorporates potential nonlinearities, and $\boldsymbol{\omega}=\{\omega_{kh},\omega_{0h},\omega_{(K+1)0}\}$, where $k=1,\ldots,K$ and $h=1,\ldots,H$ ($H=8$) are the unknown parameters associated with the basis function. All unknown parameters $\boldsymbol{\omega}$ needed to be learned from the available data $\{x^{(i)},y^{(i)}\}$. We formulated the prediction problem within a Bayesian framework, where a prior distribution was assumed about the unknown parameters incorporated into the data model in (40.1).

The prior distribution for $\boldsymbol{\omega}_k$ was $P(\boldsymbol{\omega}_k|\alpha_k)=\mathrm{N}(0,(1/\alpha_k)\boldsymbol{I})$, where $\mathrm{N}(0,(1/\alpha_k)\boldsymbol{I})$ denotes a Gaussian distribution with a mean of 0 and a covariance matrix $(1/\alpha_k)\boldsymbol{I}$, α_k is another hyperparameter to be learned, which often prevents overfitting, and $\boldsymbol{I}$ denotes the H-dimensional identity matrix. The prior distributions for α_k are set to the gamma distribution. Let $\boldsymbol{\alpha}=\{\alpha_k\},\boldsymbol{x}=\{x_t{}^{(i)}\}$ and $\boldsymbol{y}=\{y^{(i)}\}$; then the Bayes formula gives the posterior distribution:

$$P\left(\boldsymbol{\omega},\boldsymbol{\alpha}\mid\boldsymbol{x},\boldsymbol{y},\beta\right)\propto\prod\nolimits_{t,j}P\left(y^{(i)}\mid\boldsymbol{x}_t^{(i)};\boldsymbol{\omega},\beta\right)P\left(\boldsymbol{\omega}\mid\boldsymbol{\alpha}\right)P\left(\alpha\right) \tag{40.3}$$

We used a Markov Chain Monte Carlo approximation to compute (40.3).

3 Results

We examined the prediction capability with all possible combinations of features in Table 40.1, that is, four variances, six covariances, and six correlation coefficients. For example, the number of combinations of correlation coefficients was $\Sigma_{\mathrm{n}=16}^{6}\mathrm{C}_{\mathrm{n}}=63$. The best performance was observed with feature vector (14, 15, 16). Figures 40.1 and 40.2 show the results obtained with these features.

	RMSE	Correlation Coefficient	p Value
young (Sato et al.) [1]	5.2	0.687	0.00116
aged (proposed)	5.27	0.752	0.000495

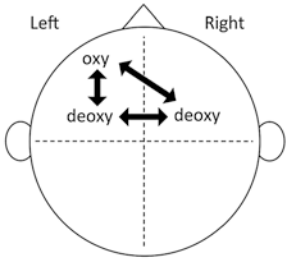

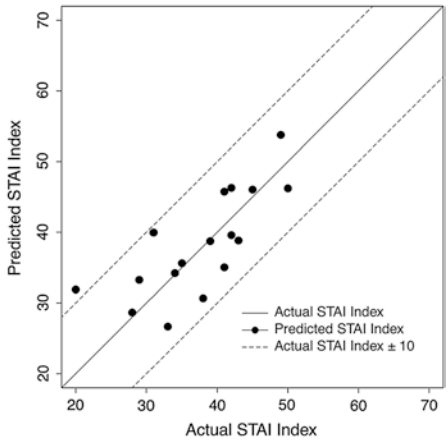

Fig. 40.1 *Top-left* table shows the root-mean-square error, the Pearson correlation coefficient, and the p-value of two-tailed t-test across 17 subjects with the feature vector (14, 15, 16). *Bottom-left* illustration shows relations of NIRS data, consisting of the feature vector (14, 15, 16) in Table 40.1. *Right graph* shows scatter plot between Actual STAI and Predicted STAI scores. *Solid line* denotes Predicted STAI = Actual STAI, and *dotted lines* denote Actual STAI ± 10

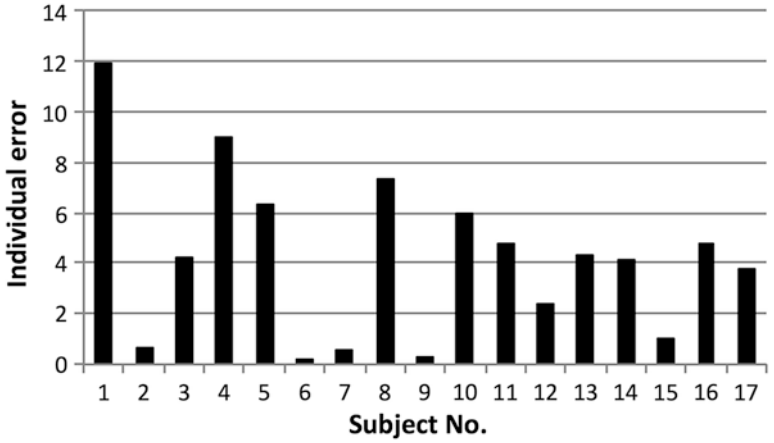

Fig. 40.2 Individual errors between the Actual STAI and Predicted STAI across 17 aged subjects with the feature vector (14, 15, 16) in Table 40.1

Figure 40.1, at the top-left, shows the average results of the 17 subjects, compared with the results of our previous study. The bottom-left illustration shows the sources of the feature vector (14, 15, 16): changes in left oxy-Hb, and changes in right and left deoxy-Hb. The right part in Fig. 40.1 shows a scatter plot of the actual STAI scores and the predicted STAI scores for all subjects, and Fig. 40.2 shows individual errors.

As seen in the top-left table in Fig. 40.1, the difference between young and aged subjects does not appear to be large in terms of RMSE and the Pearson correlation coefficients.

4 Discussion

Stress response reflected in PFC activity is an active research topic. A statistical regression method of analyzing anxiety level in normal young subjects has been reported [4], but the reproducibility with other datasets remained unclear. Therefore, in the work described in this paper, we tested the same framework with normal aged subjects to examine the effect of aging.

For the individual errors shown in Fig. 40.2, 94 % were less than 10.0, whereas 70.5 % were less than 5.0. Observe that the lowest error was 0.216; however, the highest error was 12.0, which was relatively high, and this was observed at an STAI score of 20. This error was so high because such a low STAI score was observed in only one subject, and more data at low STAI scores will be needed to achieve higher accuracy. Recall that we conducted leave-one-subject-out cross-validation, and thus the STAI score for each subject was predicted with parameters trained using the data of 16 different subjects. Therefore, there is a possibility that common features may exist among subjects, namely, the feature vector (14, 15, 16) in Table 40.1, irrespective of the influence of in-born traits or grown-up personality on current anxiety level prediction.

Although prediction models in [4] and the present paper are the same, the associated parameters are different. In [4], features 11, 12 and mean of oxy(l) were extracted by ARD [5] whereas in this study, 14, 15 and 16 were chosen by an exhaustive search as described above so that the two predictors carry different parameter sets. Figure 40.1 appears to suggest that it could be worth studying the physiological meaning associated with the correlation between changes in left oxy-Hb and right/left deoxy-Hb.

References

1. Davidson R (1998) Anterior electrophysiological asymmetries, emotion, and depression: conceptual and methodological conundrums. Psychophysiology 35(05):607–614
2. Tanida M, Sakatani K, Takano R, Tagai K (2004) Relation between asymmetry of prefrontal corte activities and the autonomic nervous system during a mental arithmetic task: near infrared spectroscopy study. Neurosci Lett 369:69–74. doi:10.1016/j.neulet.2004.07.076
3. Greicius MD, Krasnow B, Reiss A, Menon V (2003) Functional connectivity in the resting brain: a network analysis of the default mode hypothesis. Proc Natl Acad Sci U S A 100:253–258
4. Sato M, Ishikawa W, Suzuki T, Matsumoto T, Tsujii T, Sakatani K (2013) Bayesian STAI anxiety index predictions based on prefrontal cortex NIRS data for the resting state. Adv Exp Med Biol 765:251–256. doi:10.1007/978-1-4614- 4989-8_35
5. Bishop C (2006) Pattern recognition and machine learning. Springer, Heidelberg

Chapter 41
Short-Term Hypoxic Preconditioning Improved Survival Following Cardiac Arrest and Resuscitation in Rats

Kui Xu and Joseph C. LaManna

Abstract Cardiac arrest and resuscitation produces delayed mortality and hippocampal neuronal death in rats. Hypoxic preconditioning has been to shown to protect the brain from ischemic insults. We have previously reported that with chronic hypobaric hypoxia, the accumulation of hypoxic-inducible factor-1 alpha (HIF-1α) and its target genes was increased for the first several days of hypoxic exposure, and returned to baseline level by 3 weeks when angiogenesis is completed. In this study, we investigated the effect of short-term (3 days) and long-term (21 days) hypoxic preconditioning on recovery from cardiac arrest and resuscitation in rats. Our data showed that the overall survival rate was considerably improved in the short-term hypoxic preconditioning group compared to the non-preconditioned controls (86 %, 6/7 vs. 54 %, 7/13); however, the survival rate in the long-term hypoxic preconditioning group was decreased. Our data suggest that hypoxic preconditioning provides protection after cardiac arrest and resuscitation more likely through increased accumulation of HIF-1α and its target genes rather than through successful vascular adaptation as a result of hypoxia-induced angiogenesis.

Keywords Transient global ischemia • Neuroprotection • Hypoxic-inducible factor-1 alpha • Angiogenesis • Ischemic torlerance

K. Xu (✉)
Department of Neurology, Case Western Reserve University, 10900 Euclid Avenue, Robbins Building, E 732, Cleveland, OH 44106, USA
e-mail: kxx@case.edu

J.C. LaManna
Departments Physiology & Biophysics, Case Western Reserve University, Cleveland, OH, USA

H.M. Swartz et al. (eds.), *Oxygen Transport to Tissue XXXVI*, Advances in Experimental Medicine and Biology 812, DOI 10.1007/978-1-4939-0620-8_41,

1 Introduction

Cardiac arrest and resuscitation produces delayed mortality and hippocampal neuronal death in rats. For example, with 12-min ischemia, the survival rate is about 50 % and the hippocampal neuronal survival is less than 20 % at 4 days following resuscitation in the survivors. Hypoxic preconditioning has been shown to protect the brain from ischemic insults [1, 2]. Multiple mechanisms have been linked to the protection by hypoxic preconditioning, including alteration of energy metabolism and upregulation of beneficial molecules, such as hypoxic inducible factor-1 alpha (HIF-1α), erythropoietin (EPO), vascular endothelial growth factor (VEGF) [3–5]. Angiogenesis has been recognized to play an important role associated with improved outcome from stroke [6]. We have previously reported that with chronic hypobaric hypoxia, the accumulations of HIF-1α and its target genes (e.g. Epo, VEGF) were increased for the first several days of hypoxic exposure, and returned to baseline level by 3 weeks when hypoxia-induced angiogenesis (results in increased capillary density) is completed [7].

In this study, we compared the effect of short-term (3 days) and long-term (21 days) hypoxic preconditioning on recovery from cardiac arrest and resuscitation in rats to distinguish the possible relative contributions from these two mechanisms for neuroprotection, increased accumulation of HIF-1α and its target genes or increased capillary density as a result of hypoxia-induced angiogenesis. A rat model of cardiac arrest and resuscitation was used; the overall survival and hippocampal neuronal cell counts were evaluated at 4 days following cardiac arrest and resuscitation in the non-preconditioned and the hypoxia-preconditioned groups.

2 Methods

2.1 Animals and Hypoxic Preconditioning

The experimental protocol was approved by the Animal Care and Use Committee at Case Western Reserve University. Male Wistar rats (2 months old) purchased from Charles River were allowed to acclimate in our animal resource facility for 1 week before they were used in experiments. Rats were randomly assigned to non-preconditioned group, 3-day hypoxic preconditioning and 21-day hypoxic precondition groups. Hypoxic animals were kept in hypobaric chambers for either 3 days or 21 days at a constant pressure of 0.5 atmosphere (380 mmHg, equivalent to 10 % normobaric oxygen at sea level). The normoxic control rats were housed in the same room to ensure identical ambient conditions [8].

2.2 Induction of Transient Global Brain Ischemia

Transient global brain ischemia was achieved using a rat model of cardiac arrest and resuscitation as described previously [9, 10]. In brief, anesthesia was induced and

maintained with 1–2.5 % isoflurane through a nasal cone. Cannulae were placed in: (1) Ventral tail artery using polyethylene tubing (PE-50, 0.023″ i.d., 0.038″ o.d.) for the purpose of monitoring of arterial blood pressure and collecting samples, (2) External jugular vein into the right atrium using a Silastic catheter (0.025″ i.d., 0.047″ o.d.) for administration of drugs. The rats were allowed to recover for at least 1 h after surgery while restrained in plastic cages. The body temperature was maintained at 37 °C by an infrared heat lamp (250 W, 45 cm above the body) regulated by feedback from a rectal probe during the surgery and the following experiment. Cardiac arrest was induced in the conscious rat by the rapid sequential intra-atrial injection of D-tubocurare (0.3 mg) and ice-cold KCl solution (0.5 M; 0.12 ml/100 g of body weight). The animal was orotracheally intubated with a 14-gauge catheter attached to a rodent ventilator. Resuscitation was initiated at 7 min after arrest, and ventilation (100 % O_2, tidal volume: 10 cm3/kg; respiratory rate: 80 breaths/min) was begun simultaneously with chest compressions and the intravenous administration of normal saline at a rate of approximately 0.5 ml/min. Once a spontaneous heart beat returned, epinephrine (4–10 μg) was administered intravenously to bring the mean blood pressure above 80 % of pre-arrest value, the point at which animal was considered to be resuscitated. The duration of arrest was about 12 min. The ventilation was then adjusted to normal ranges of blood gases until the rats regained their spontaneous respiration. Non-arrested rats went through the same surgical procedures except cardiac arrest. Overall survival and hippocampal neuronal counts were determined at 4 days after resuscitation.

2.3 Hippocampal Neuron Counts

Rats surviving 4 days and non-arrested controls were deeply anesthetized with isoflurane, perfused through the heart with about 200 ml 0.1 M PBS, and perfusion fixed with 4 % paraformaldehyde in 0.1 M PBS (pH 7.4). The brains were removed and embedded with paraffin and sectioned on a microtome. Neuronal cell counts were made from H&E stained 5 μm coronal sections through anterior hippocampus. At the level of atlas plate 30 [11] the entire length of hippocampal pyramidal cell layer was viewed under a high-power light microscope (magnification, 400×). Neurons with rounded cell bodies and clearly visible nucleoli were considered to have survived. The number of neurons surviving was evaluated in CA1 region of hippocampus [9].

3 Results

3.1 Physiological Variables

Physiological variables were measured before cardiac arrest and 1 h post-resuscitation (see Table 41.1) in the non-preconditioned controls and the hypoxia-preconditioned groups. The pre-arrest values of body weight, mean arterial blood pressure, P_aO_2, P_aCO_2 were similar in all three groups. The rats which had hypoxic

Table 41.1 Physiological variables before cardiac arrest and 1 h post-resuscitation (mean ± SD)

	Control (non-preconditioned) (n = 13)	3-Day preconditioning (n = 7)	21-Day preconditioning (n = 7)
Body weight (g)	357 ± 28	349 ± 48	363 ± 15
MAP (mmHg)			
Pre	113 ± 6	114 ± 6	112 ± 13
1 h post	84 ± 14	96 ± 23	90 ± 10
pH (unit)			
Pre	7.41 ± 0.03	7.29 ± 0.06*	7.32 ± 0.04*
1 h post	7.35 ± 0.05	7.20 ± 0.07*	7.27 ± 0.07*
PaO_2 (mmHg)			
Pre	96 ± 17	95 ± 15	104 ± 3
1 h post	98 ± 14	95 ± 5	101 ± 7
$PaCO_2$ (mmHg)			
Pre	38 ± 3	38 ± 2	34 ± 6
1 h post	37 ± 5	33 ± 2	32 ± 2
Hematocrit (%)			
Pre	47 ± 4	58 ± 6*	66 ± 3*
1 h post	48 ± 2	60 ± 5*	67 ± 4*

MAP: mean arterial pressure; *significant difference vs. non-preconditioned group, $p < 0.05$, t-test

preconditioning seemed to have lower pH values (pre and post-resuscitation) compared to the non-preconditioned controls. The hematocrit was significantly increased in both 3- and 21-day hypoxic preconditioned groups.

3.2 Overall Survival Following Cardiac Arrest and Resuscitation

Overall survival rates were examined for 4 days following cardiac arrest and resuscitation in the non-preconditioned controls and hypoxic preconditioning groups (Fig. 41.1). At day 4 post-resuscitation, the overall survival rates were considerably higher in the 3-day hypoxic preconditioning group compared to the non-preconditioned rats (86 % survival, 6/7 vs. 54 % survival, 7/13). However, only about 20 % (2/9) of the rats with 21-day hypoxic preconditioning survived for 4 days following cardiac arrest and resuscitation. The majority of the deaths of rats occurred within the first 2 days following resuscitation.

3.3 Hippocampal Neuronal Death Following Cardiac Arrest and Resuscitation

Hippocampal neuronal counts were evaluated in non-arrested control rats and the rats that survived for 4 days after cardiac arrest and resuscitation, including

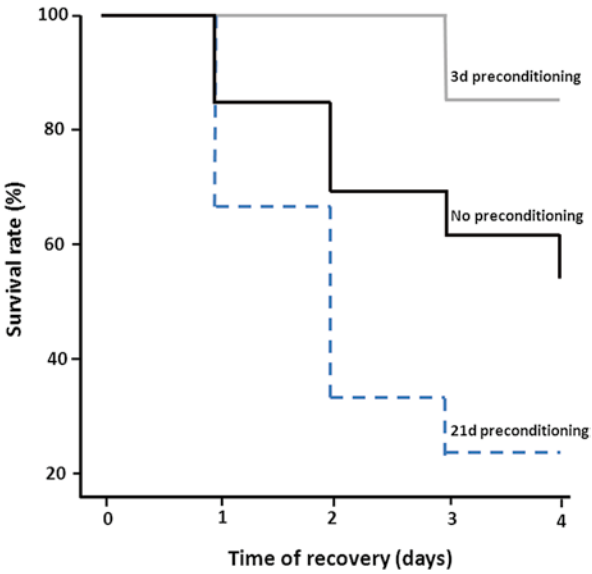

Fig. 41.1 Survival rates 4 days following cardiac arrest and resuscitation in rats without hypoxic preconditioning and rats with 3 or 21 days of hypoxic preconditioning

non-preconditioned, 3- and 21-day hypoxic preconditioned groups. At 4 days of recovery, only about 20 % of hippocampal CA1 neurons were preserved in the non-preconditioned group (mean ± SD, 21 ± 7, n = 7) compared to that of the non-arrested controls (114 ± 11, n = 7). Both preconditioning groups had similar hippocampal neuronal counts compared to the non-preconditioned group, the counts were 26 ± 10 (n = 6) and 19 ± 8 (n = 2) in the 3- and 21-day hypoxic preconditioned groups, respectively.

4 Discussion

Our group has previously developed a time course for many of the physiological and anatomical adaptations to hypoxic exposure [7, 12]. For instance, after 3 days of continuous hypobaric hypoxia HIF-1α and its target genes, such as VEGF and EPO, are upregulated, there is no significant vascular adaptation has occurred at this point of hypoxic exposure. After 21 days of chronic hypoxic exposure, the angiogenic increase in capillary density has reached its maximum. This increase in vascular density restores oxygen delivery to brain tissue and subsequently HIFs and their target genes return to baseline levels. The present study showed that at 4 days following cardiac arrest and resuscitation the overall survival was markedly improved in rats with 3-day hypoxic preconditioning compared to the rats without hypoxic preconditioning; however, rats fully adapted to hypoxia (e.g. with 21 days of exposure) seemed to be more vulnerable to the insult induced by cardiac arrest and resuscitation. Although neither 3-day nor 21-day hypoxic precondition groups showed protection on hippocampal neuronal preservation, the 3-day

hypoxic preconditioning results in higher survival rate following cardiac arrest and resuscitation. The protective effect of 3-day hypoxic preconditioning is more likely through hypoxia-induced increased accumulation of HIF-1α and HIF target genes. As HIF-1a has been described to regulate genes involved with energy metabolism and anti-apoptosis [13], its target genes such as VEGF, EPO have also been shown to protect the brain against ischemia through promoting cell survival pathways [5, 14]. Contrary to our 21-day hypoxic preconditioning results, Dunn et al. demonstrated that long-term hypoxia (3 weeks) improved the recovery outcome in rats following transient focal ischemia [15]. The discrepancy may be explained by the difference between the global or focal ischemia models. In addition, the systemic changes following long-term hypoxia may have greater impact on the recovery ability following global ischemia. Even though angiogenesis is completed around 3 weeks of hypoxia the newly grown vessels may not be fully functioning especially under the subsequent stress induced by cardiac arrest and resuscitation.

In conclusion, hypoxic preconditioning provides protection after cardiac arrest and resuscitation more likely through increased accumulation of HIF-1α and its target genes rather than through successful vascular adaptation as a result of hypoxia-induced angiogenesis.

Acknowledgments This study was supported by NIH grant NS 38632.

References

1. Emerson MR, Nelson SR, Samson FE, Pazdernik TL (1999) A global hypoxia preconditioning model: neuroprotection against seizure-induced specific gravity changes (edema) and brain damage in rats. Brain Res Brain Res Protoc 4(3):360–366
2. Gidday JM, Fitzgibbons JC, Shah AR, Park TS (1994) Neuroprotection from ischemic brain injury by hypoxic preconditioning in the neonatal rat. Neurosci Lett 168(1–2):221–224
3. Wick A, Wick W, Waltenberger J, Weller M, Dichgans J, Schulz JB (2002) Neuroprotection by hypoxic preconditioning requires sequential activation of vascular endothelial growth factor receptor and Akt. J Neurosci 22(15):6401–6407
4. Gidday JM, Shah AR, Maceren RG, Wang Q, Pelligrino DA, Holtzman DM, Park TS (1999) Nitric oxide mediates cerebral ischemic tolerance in a neonatal rat model of hypoxic preconditioning. J Cereb Blood Flow Metab 19(3):331–340
5. Bergeron M, Gidday JM, Yu AY, Semenza GL, Ferriero DM, Sharp FR (2000) Role of hypoxia-inducible factor-1 in hypoxia-induced ischemic tolerance in neonatal rat brain. Ann Neurol 48(3):285–296
6. Slevin M, Kumar P, Gaffney J, Kumar S, Krupinski J (2006) Can angiogenesis be exploited to improve stroke outcome? Mechanisms and therapeutic potential. Clin Sci (Lond) 111(3): 171–183
7. Chavez JC, Agani F, Pichiule P, LaManna JC (2000) Expression of hypoxia-inducible factor-1alpha in the brain of rats during chronic hypoxia. J Appl Physiol 89(5):1937–1942
8. Xu K, Puchowicz MA, LaManna JC (2004) Renormalization of regional brain blood flow during prolonged mild hypoxic exposure in rats. Brain Res 1027(1–2):188–191
9. Xu K, Puchowicz MA, Lust WD, LaManna JC (2006) Adenosine treatment delays postischemic hippocampal CA1 loss after cardiac arrest and resuscitation in rats. Brain Res 1071(1):208–217

10. Xu K, LaManna JC (2009) The loss of hypoxic ventilatory responses following resuscitation after cardiac arrest in rats is associated with failure of long-term survival. Brain Res 1258:59–64
11. Palkovits M, Brownstein MJ (1988) Maps and guide to microdissection of rat brain. Elsevier, New York
12. Xu K, LaManna JC (2006) Chronic hypoxia and the cerebral circulation. J Appl Physiol 100:725–730
13. Puchowicz MA, Zechel JL, Valerio J, Emancipator DS, Xu K, Pundik S, LaManna JC, Lust WD (2008) Neuroprotection in diet-induced ketotic rat brain after focal ischemia. J Cereb Blood Flow Metab 28:1907–1916
14. Digicaylioglu M, Lipton SA (2001) Erythropoietin-mediated neuroprotection involves cross-talk between Jak2 and NF-kappaB signalling cascades. Nature 412:641–647
15. Dunn JF, Wu Y, Zhao Z, Srinivasan S, Natah SS (2012) Training the brain to survive stroke. PLoS One 7(9):e45108

Chapter 42
Venular Valves and Retrograde Perfusion

Tomiyasu Koyama, Masako Sugihara-Seki, Tadahiro Sasajima, and Sinsuke Kikuchi

Abstract Forced retrograde perfusion through the venous system with arterial blood can provide adequate oxygen to peripheral tissues at rest through veno-capillary networks which is the basis for surgical restoration of blood flow by distal vein arterialization (DVA). To be successful such surgery requires disruption of valve leaflets in the veins, which can be accomplished easily in the larger vessels. However, the smallest veins (venules) of less than 100 μm in diameter, also possess valves, are distributed widely throughout all tissues and are too fine for any effective surgical interference. Thus venular valves cannot be disrupted or dissected with presently available technology. Nevertheless, clinical observations suggest that retrograde peripheral blood flow is rapidly established after DVA surgery. There is as yet no rational explanation for this phenomenon. In the present study, using Laplace's law, we attempt to elucidate the mechanical properties of venules and their valves. We speculate that the remarkably thin venular walls (and especially those of the smaller vessels which have the thinnest walls), are capable of considerable, rapid distension when subjected to increased hemostatic pressure. The increase in diameter of venules in response to the increased blood pressure renders their valve leaflets incompetent, so that the valves themselves cannot close the vessel lumen. In addition, the thin bicuspid leaflets may also be forced open retrogradely by the increased blood pressure.

Keywords Distal vein arterialization • Venular valve destruction • Retrograde perfusion • Arteriosclerosis obliterans

T. Koyama (✉)
Hokkaido University, 064-0821, Sapporo Hokkaido N-1W-25, Japan
e-mail: tomkoyamajp@yahoo.co.jp

M. Sugihara-Seki
Kansai University, Suita, Osaka, Japan

T. Sasajima • S. Kikuchi
Asahikawa Medical University, 064-0821 Sapporo, N-1W-25 Hokkaido, Japan

H.M. Swartz et al. (eds.), *Oxygen Transport to Tissue XXXVI*, Advances in Experimental Medicine and Biology 812, DOI 10.1007/978-1-4939-0620-8_42,

1 Introduction

Recent advances in distal vein arterialization (DVA) have saved many arteriosclerotic lower limbs from amputation. Following surgery, skin temperature increases quickly and pain and edema are reduced [1], while covering ulcerated areas with a skin flap encourages further recovery of the circulatory system [1].Theoretical considerations regarding improved oxygen transport to resting and exercising lower limbs related to DVA surgery [2, 3] and the effect of localized disruption of venous valves [4], together with their effects on lymphatic flow [5], have been reported previously.

DVA surgery begins with disruption of venous valves. A coronary angioplasty catheter is introduced via the plantar vein into the medial and lateral plantar veins [1] and the valves are disrupted gently, with only slight resistance being felt from them to the passage of the catheter. However, in humans many valves are present in small venous channels ("venules") of less than 100 μm diameter and even in those as small as 18 μm [6, 7]. These valves cannot be disrupted with an angioplasty catheter guide wire, since even the finest probes are too large to enter such small vessels, as sketched in Fig. 42.1. Nevertheless, soon after surgery is completed, increased blood flow through distal venous networks can be confirmed by retrograde venography [1] and skin color and temperature on the dorsal and distal skin of the foot recover quickly. The rapid rise in skin temperature after DVA suggests that venular valves do not seriously restrict retrograde blood flow. However, there is no other current evidence to support this view. In the present study we attempt to characterize the mechanical properties and behavior of venules and venular valves subjected to retrograde perfusion.

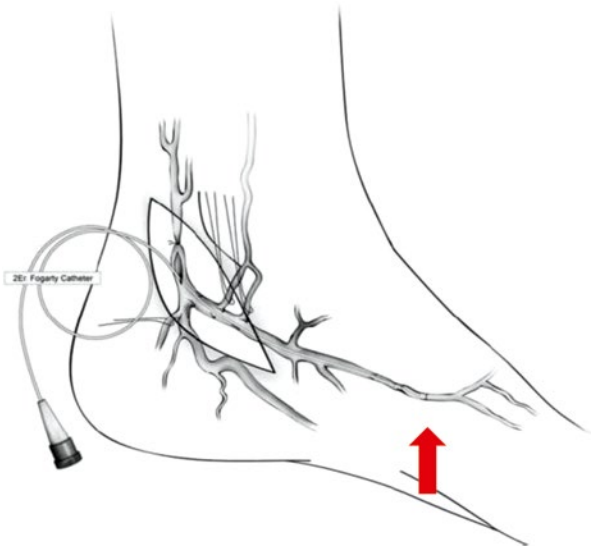

Fig. 42.1 Schematic illustration of the plantar venous system. The *arrow* indicates the inserted catheter tip: cited from [1] with permission. The coronary angioplasty guidewire can advance no further

2 Formulation for a Cylindrical Model

Consideration of the equilibrium condition for a membrane subjected to internal and external pressures, P_i[Pa] and P_e[Pa], and surface tension, T[N/m], leads to the so-called Laplace equation [8]:

$$P_i - P_e = T\left(1/R_1 + 1/R_2\right), \tag{42.1}$$

where R_1[m] and R_2[m] represent the principal radii of the curvature of the membrane, as shown in Fig. 42.2. When the membrane has a cylindrical shape of radius R[m], (42.1) can be rewritten as

$$P_i - P_e = T/R. \tag{42.2}$$

In the case of a hemisphere of radius R, (42.1) becomes

$$P_i - P_e = 2T/R. \tag{42.3}$$

Here, we consider a blood vessel of cylindrical shape of radius R and wall thickness d[m]. The distension pressure $P_i - P_e$ is balanced with the circumferential tension T in the wall. Then, we can apply (42.2) to obtain

$$T = R\left(P_i - P_e\right). \tag{42.4}$$

We express an equilibrium state of the vessel as

$$P_i - P_e = T_0/R_0. \tag{42.5}$$

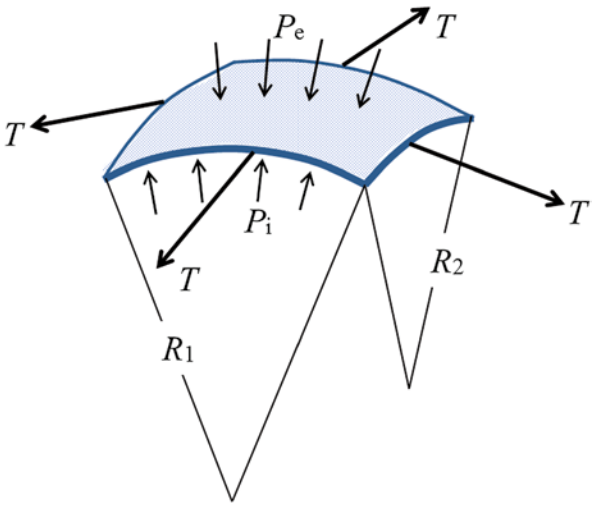

Fig. 42.2 A membrane subjected to internal and external pressures, P_i and P_e, and tensile force T

If the pressure in the vessel increases from P_i to $P_i+\Delta P$, the radius R_0 increases from R_0 to $R_0+\Delta R$, and the circumferential tension in the vessel wall also increases from T_0 to $T_0+\Delta T$, then it follows from (42.2) in the first order approximation:

$$P_i+\Delta P-P_e \approx \frac{T_0}{R_0}\left(1+\frac{\Delta T}{T_0}-\frac{\Delta R}{R_0}\right). \tag{42.6}$$

Subtracting (42.5), we have

$$\Delta T=\Delta R\left(P_i-P_e\right)+R_0\Delta P. \tag{42.7}$$

This equation may be directly obtained by differentiating both sides of (42.4).

Now, we assume a linear relationship between the circumferential stress, σ[Pa], and the strain, ε, in such a way that $\sigma=E\varepsilon$, where E[Pa] represents the elastic modulus of the vessel wall. Since $\sigma=\Delta T/d$ and $\varepsilon=\Delta R/R_0$, this assumption leads to

$$\Delta T / d = E\Delta R / R_0. \tag{42.8}$$

If the ratio of the wall thickness to the radius is defined as $\delta=d/R_0$, then from (42.7) and (42.8) we have

$$\delta=\frac{1}{E}\left(\frac{R_0}{\Delta R}\Delta P+\left(P_i-P_e\right)\right). \tag{42.9}$$

The circumferential stress is expressed as

$$\sigma=\frac{1}{\delta}\left(\Delta P+\left(P_i-P_e\right)\frac{\Delta R}{R_0}\right). \tag{42.10}$$

This expression relates the internal pressure change, the radius change and the wall thickness ratio to the circumferential stress.

3 Confirmation of the Formulation Using Published Data

The present consideration was applied to the experimental data in venules published by Lang et al. [9].

For venule 1, an increase in the inner pressure $\Delta P=+10$ mmHg increased the radius of the vessel from $R_0=72.5$ μm to 88.1 μm by $\Delta R=15.6$ μm. For venule 2, an increase in the inner pressure $\Delta P=+10$ mmHg increased the radius of the vessel from $R_0=138.0$ μm to 149.0 μm by $\Delta R=11.0$ μm. To specify the quantities of venules 1 and 2, we use superscript (1) and (2), respectively. The above experimental results indicate

$$\left\{\Delta R / R_0\right\}^{(1)}=0.22, \quad \left\{\Delta R / R_0\right\}^{(2)}=0.08. \tag{42.11}$$

If the microstructure of the two venules is the same and the pressure difference between the outer and inner pressures is the same, i.e., $E^{(1)}=E^{(2)}$ and $(P_i-P_e)^{(1)}=(P_i-P_e)^{(2)}$, then from (42.9) these values indicate

$$\delta^{(1)} < \delta^{(2)}. \tag{42.12}$$

In other words, the wall of the smaller venule 1 is relatively thinner than the wall of the larger venule 2.Furthermore, from (42.9), (42.10) and (42.11), we obtain for the circumferential stress:

$$\sigma^{(1)} > \sigma^{(2)}. \tag{42.13}$$

for the same pressure increase ΔP.

In addition, if $(P_i-P_e)^{(1)}=(P_i-P_e)^{(2)}\approx 0$, then the ratios of δ, d and σ are evaluated as

$$\delta^{(1)}/\delta^{(2)} = \left(R_0/\Delta R\right)^{(1)}/\left(R_0/\Delta R\right)^{(2)} = 0.37, \tag{42.14}$$

$$d^{(1)}/d^{(2)} = R_0{}^{(1)}\delta^{(1)}/R_0{}^{(2)}\delta^{(2)} = 0.19, \tag{42.15}$$

$$\sigma^{(1)}/\sigma^{(2)} = \delta^{(2)}/\delta^{(1)} = 2.7. \tag{42.16}$$

These results suggest that the smaller a venule the thinner its wall, and the less pressure required to expand it. The distortion tension in the wall increases with decreasing venular diameter. The distensibility of the wall by internal pressure increases with decreasing venular diameter.

4 Consideration of a Hemispherical Model for the Bicuspid Valves

As an approximation to the shape of a venular bicuspid valve, let us consider the valve leaflet as a hemisphere. Since (42.2) and (42.3) have the same form, similar mechanics can be expected. After DVA the distortion tension in the valve leaflet increases more than that in the venular wall since valves are thinner than the wall. Accordingly, the venular valves are readily made incompetent by increased blood pressure, since valve leaflets have only a simple, fragile structure.

5 Discussion

The venular wall has a basement membrane, limited smooth muscle layers and endothelial cell layers [10]. The microstructure of the venular valves is simpler and more delicate than that of the vessel wall. In the smaller venules, valve leaflets consist “of delicate connective tissue membrane lined on both sides with endothelial

cells" [10]; they do not contain the fibroblasts and myofibroblasts that are present in the leaflets of valves in larger veins [11]. Such thin venules can be distended easily by arterial blood pressure while their valve leaflets are exposed to even greater distortion than wall itself [12]. In agreement with this suggestion, Takase et al. [13] reported that even in the femoral vein valves become incompetent in 2–3 weeks after being exposed to arterial blood pressure [13, 14]. A similar observation of the development of incompetence in intact normal venous valves caused by high blood pressure, has been reported in the foot veins of humans who stand upright for 5 h [15].

Özbek et al. [12] hypothesized that venular valves cannot resist high pulsatile blood pressure, so the tissues can be perfused retrogradely. Our present calculations (considerations) show that the thinner the blood vessel the greater the distortion induced in the vessel wall by increased blood pressure. This leads to incompetence of venular valve function that is exacerbated by the fragility of the valve leaflets themselves and is consistent with our mechanistic interpretation of venular behavior during DVA.

6 Conclusion

Mechanical properties of venules and venular leaflets suggest that the thinner they are the more easily they are distended. Retrograde blood flow cannot therefore be resisted by venular valves when arterial blood is directed into the plantar vein by DVA surgery. Destruction of venous valves only in larger veins, including medial and lateral plantar veins, permits sufficient retrograde oxygen supply to the peripheral tissues of the foot through venules, despite the initial integrity of their valves, because of their fragility and mechanical properties. Thus, based on our calculations it seems reasonable to conclude that venular valves cannot resist retrograde arterial blood flow and form no practical impediment to successful DVA.

Acknowledgements The authors wish to express their thanks to Prof. Dr. Ian Silver and Prof. Dr. Maria Erecinska, Bristol University, for reading the manuscript and valuable suggestions. Thanks are also due to Elsevier Publisher and Ann Vasc Surg 2010 for the kind permission to reuse Fig. 42.1.

References

1. Sasajima T, Azuma N, Uchida H et al (2010) Combined distal venous arterialization and free flap for patients with extensive tissue loss. Ann Vasc Surg 24(3):373–381
2. Koyama T, Sasajima T (2010) Sufficient oxygen can be transported to resting skeletal muscle via arterialization of the vein: theoretical consideration in a rat model. In: LaManna JC, Puchowicz MA et al (eds) Oxygen transport to tissue XXXII (AEMB701). Springer, New York, pp 335–339
3. Sasajima T, Koyama T (2011) Biological maintenance of distal vein arterialization. In: Wolf M, Bucher HV et al (eds) Oxygen transport to tissue XXXIII (AEMB737). Springer, New York, pp 259–262

4. Koyama T, Sasajima T, Kikuchi S (in preparation) Skin temperature in lower hind limb subjected to distal vein arterialization in rats
5. Koyama T, Sasajima T (2012) Retrograde perfusion of the hind leg in diabetic patients suffering from the arteriosclerosis obliterans: theoretical considerations of oxygen supply and lymphatic flow based on rat models. In: Welch WJ, Palm F et al (eds) Oxygen transport to tissue XXXIV (AEMB765). Springer, New York, pp 245–250
6. Caggiati A, Phillips M et al (2006) Valves in small veins and venules. Eur J Vasc Endovasc Surg 32(4):447–452
7. Phillips S, Jones GT, Rii V, Zhang M (2004) Microvenous valves in the superficial vessels of the human lower limb. Clin Anat 17(1):55–60
8. Fung YC (1981) Biomechanics. Springer, New York, p 17
9. Lang DV, Johns BL (1987) Rat venule mechanical characteristics during venous pressure elevation. Am J Physiol 252:H704–H713, Heart Circ Physiol 21
10. Popoff N (1934) The digital vascular system. Arch Pathol 18:307–322
11. Braverman IM, Keh A (1983) Fibroblasts and myofibroblasts are present only in the leaflets of valves of larger veins. J Invest Dermatol 81:438–442
12. Özbek C, Kestelli M, Emrecan B, Özsöyler I, Bayatli K et al (2005) A novel approach: ascending venous arterial cardiovascularization for atherosclerosis obliterans. Eur J Endovasc Surg 29:47–51
13. Takase S, Pascarella L et al (2004) Hypertension-induced venous valve remodeling. J Vasc Surg 39:1329–34
14. Curri SB, Annoni F, Montorsi W (1987) Les microvalvulesdans les microveinules. Phlebologie 40:795–801
15. Bergan JJ, Pascarella L, Schmidt-Schönbein GW (2008) Pathogenesis of primary chronic venous disease: insights from animal models of venous hypertension. J Vasc Surg 47(1):183–92

Chapter 43
Monitoring of Filter Patency During Carotid Artery Stenting Using Near-Infrared Spectroscopy with High Time-Resolution

Takahiro Igarashi, Kaoru Sakatani, Tadashi Shibuya, Teruyasu Hirayama, Atsuo Yoshino, and Yoichi Katayama

Abstract We aimed to evaluate the usefulness of a newly developed, near-infrared spectroscopy (NIRS) device for monitoring hemodynamic changes during carotid artery stenting (CAS), as a means to detect filter obstruction due to distal embolism. We evaluated 16 patients with internal carotid artery (ICA) stenosis during the CAS procedure, using a NIRS system that can monitor not only changes in oxygenation of hemoglobin (Hb), but also the fluctuation of oxyhemoglobin (oxy-Hb) synchronized with heartbeat. The NIRS system detected a marked decrease of oxy-Hb and an increase of deoxyhemoglobin (deoxy-Hb) during ICA occlusion in patients without anterior cross circulation (ACC). Patients with ACC showed much smaller changes. The analysis of oxy-Hb fluctuation made it possible to detect occurrence of no-flow in the absence of Hb concentration changes. The amplitude of oxy-Hb fluctuation in the no/slow-flow group was significantly smaller than that in the normal-flow group. Our results indicate that the present high time-resolution NIRS device, which can measure oxy-Hb fluctuation, is superior to conventional NIRS for detecting filter obstruction.

Keywords Advanced imaging techniques • Carotid artery stenting (CAS) • Embolism • Intraoperative monitoring • Near-infrared spectroscopy (NIRS)

T. Igarashi (✉) • T. Hirayama • A. Yoshino • Y. Katayama
Division of Neurosurgery, Department of Neurological Surgery, Nihon University School of Medicine, 30-1 Oyaguchi-kamimachi, Itabashi-ku, Tokyo 173-8610, Japan
e-mail: igarashi.takahiro@nihon-u.ac.jp

K. Sakatani
Division of Neurosurgery, Department of Neurological Surgery, Nihon University School of Medicine, 30-1 Oyaguchi-kamimachi, Itabashi-ku, Tokyo 173-8610, Japan

Department of Electrical and Electronics Engineering, Nihon University College of Engineering, NEWCAT Institute, Fukushima, Japan

T. Shibuya
Department of Neuroendovascular Therapy, Sagamihara Kyodo Hospital, Kanagawa, Japan

H.M. Swartz et al. (eds.), *Oxygen Transport to Tissue XXXVI*, Advances in Experimental Medicine and Biology 812, DOI 10.1007/978-1-4939-0620-8_43,

1 Introduction

Carotid artery stenting (CAS) is a less invasive revascularization strategy than carotid endarterectomy (CEA) in patients with severe symptomatic or asymptomatic atherosclerotic carotid artery stenosis. A recently developed filter-type protection device is already widely used during CAS procedures; this device maintains blood flow in the distal internal carotid artery (ICA) [1]. However, obstruction of the filter pores by embolic particles could cause impaired distal blood flow in the ICA (i.e., no/slow flow phenomenon) [2]. According to the postmarketing prospective research in Japan, the incidence of embolic events was 17.5 % in the slow-flow group during the peri-procedural period [3]. In fact, intraprocedural embolic events are one of the factors influencing patients' outcome. Therefore, monitoring of hemodynamic changes during CAS is important to reduce adverse events.

Near-infrared spectroscopy (NIRS) has been employed to monitor changes in hemodynamic status induced by a variety of neurosurgical procedures, including CAS [4]. However, Hb concentration changes measured by NIRS are susceptible to collateral circulation and individual difference of vessel. This NIRS system has the potential to detect subtle changes in distal blood flow due to filter obstruction by measuring the fluctuation of oxy-Hb synchronized with heartbeat. Indeed, we found that this fluctuation was a more sensitive indicator of hemodynamic changes during CAS, as compared with conventional analysis of Hb concentration changes.

2 Methods

We investigated 16 patients with carotid artery stenosis (12 men and 4 women; mean age, 68.6 ± 7.8 years) who underwent CAS. We measured the hemodynamic changes in the bilateral frontal lobe using a newly developed NIRS device (Pocket NIRS, Hamamatsu Photonics K.K., Japan) (Fig 43.1a). The NIRS system uses light-emitting diodes (LEDs) of three different wavelengths (735, 810, and 850 nm) as light sources and one photo-diode as a detector; it has two channels. The common analysis of NIRS data uses the modified Beer–Lambert law. The sampling rate was 61.3 Hz. The NIRS probes were set symmetrically on the forehead with a flexible fixation pad.

CAS was performed by transfemoral catheterization with distal filter protection in all patients. Pre-stenting dilatation was performed with a controlled compliant balloon dilation catheter; the balloon was inflated at 7–10 atm for 20–30 s. Then, stent replacement was performed using a Precise® (Johnson & Johnson, Cordis, Japan). Post-balloon size was selected according to the normal luminal diameter of each ICA immediately distal to the stenotic lesion.

We evaluated the NIRS parameter changes during the CAS procedure by means of two analytical methods. First, we analyzed concentration changes of oxy-Hb, deoxy-Hb and, total-Hb by subtracting the mean value of the baseline from the mean value measured immediately after inflation and deflation of the balloon.

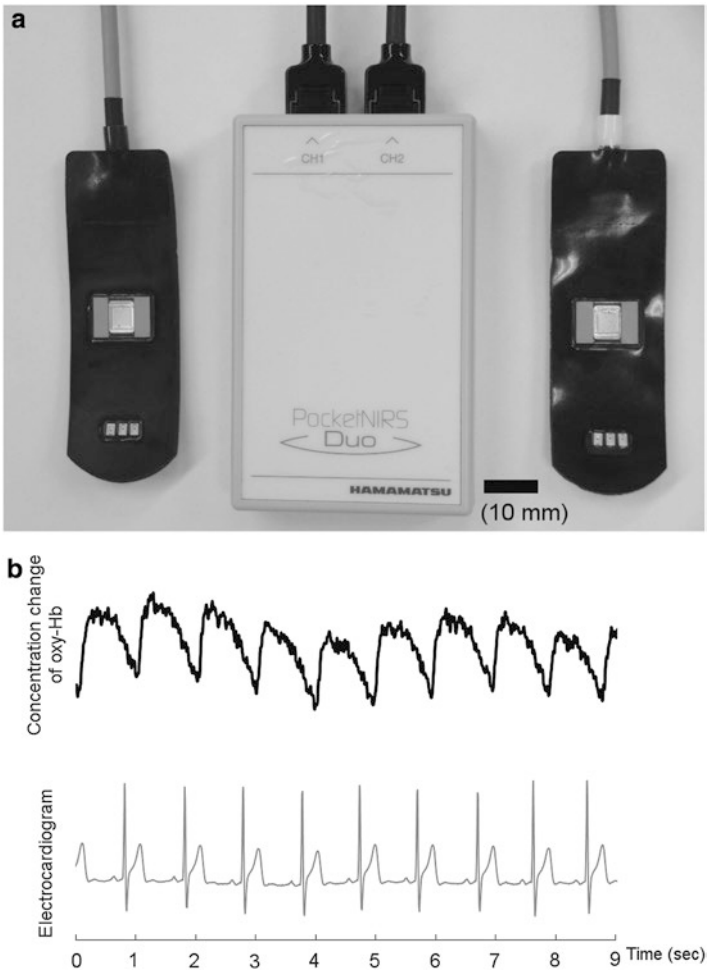

Fig. 43.1 (**a**) Appearance of the wearable NIRS device. The total weight of the controller and probes is 160 g. (**b**) Comparison of fluctuation of oxy-Hb measured by NIRS (*upper*) and ECG (*lower*). The *ordinate* indicates concentration changes of oxy-Hb in arbitrary unit (a.u.)

Second, we analyzed the fluctuation of NIRS parameters. In the preliminary study, we observed fluctuation in NIRS parameters in synchrony with heartbeat. Interestingly, oxy-Hb showed such fluctuations, while deoxy-Hb did not. Figure 43.1b compares the fluctuation of oxy-Hb and electrocardiography (ECG). We calculated the mean value of five peak-to-peak amplitudes of oxy-Hb using frequency analysis before and after stent replacement. In order to define no/slow flow and normal flow, common carotid artery angiogram was performed before and after balloon dilatation to provide information regarding transit time. Each value is

expressed as mean ± standard deviation. Statistical analysis was performed by means of an unpaired Student's t-test for comparisons involving two groups; all p values were two-tailed. Statistical analysis was performed with the SAS system (version 8.2; SAS Institute, Inc). This study was approved by the Committee for Clinical Trials and Research at Nihon University School of Medicine and Sagamihara Kyodo Hospital, Japan. All patients or their relatives gave written informed consent.

3 Results

We investigated the effect of anterior cross circulation (ACC) on Hb oxygenation change during deflation of the balloon. The patients with ACC (7 out of 16 patients) showed prominent ischemic changes. In contrast, the patients with ACC (9 out of 16 patients) exhibited much smaller changes of Hb concentrations during deflation of the balloon, compared with the patients without ACC (Fig. 43.2). Change of Hb concentration decreases by development of ACC for the blood supply from the contralateral side. Hb concentration receives an effect of ACC easily.

No/slow flow was found in 6 out of 16 patients during CAS. We compared the sensitivity of the Hb concentration changes and the fluctuation of oxy-Hb for detection of the occurrence of no/slow flow caused by filter obstruction. The analysis of oxy-Hb fluctuation could detect occurrence of no flow even when there was no

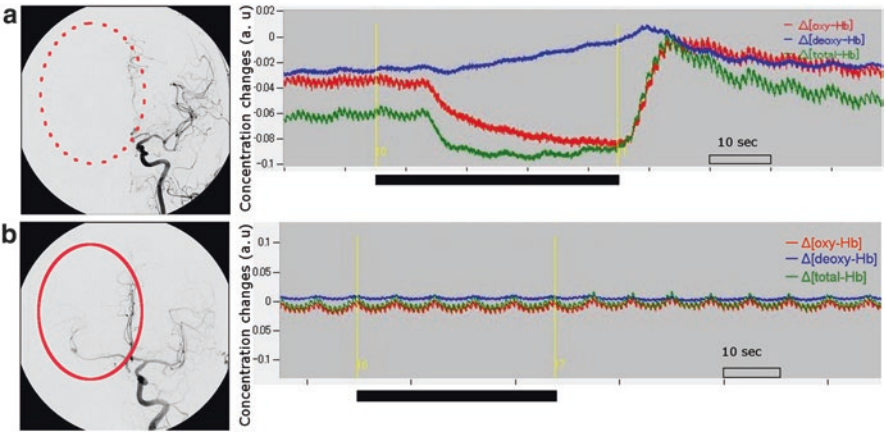

Fig. 43.2 Cerebral angiography and Hb concentration changes during right ICA occlusion. Cerebral angiography and Hb concentration changes during ICA occlusion in cases without anterior cross circulation (**a**: *dotted line*) and with anterior cross circulation (**b**: *solid line*). The *ordinates* indicate concentration changes of oxy-Hb (*red*), deoxy-Hb (*blue*), and total-Hb (*green*) in arbitrary unit (a.u.). The *abscissa* indicates time (s); *horizontal bars* indicate 10 s. *Thick black horizontal bars* indicate the period of ICA occlusion by balloon dilatation

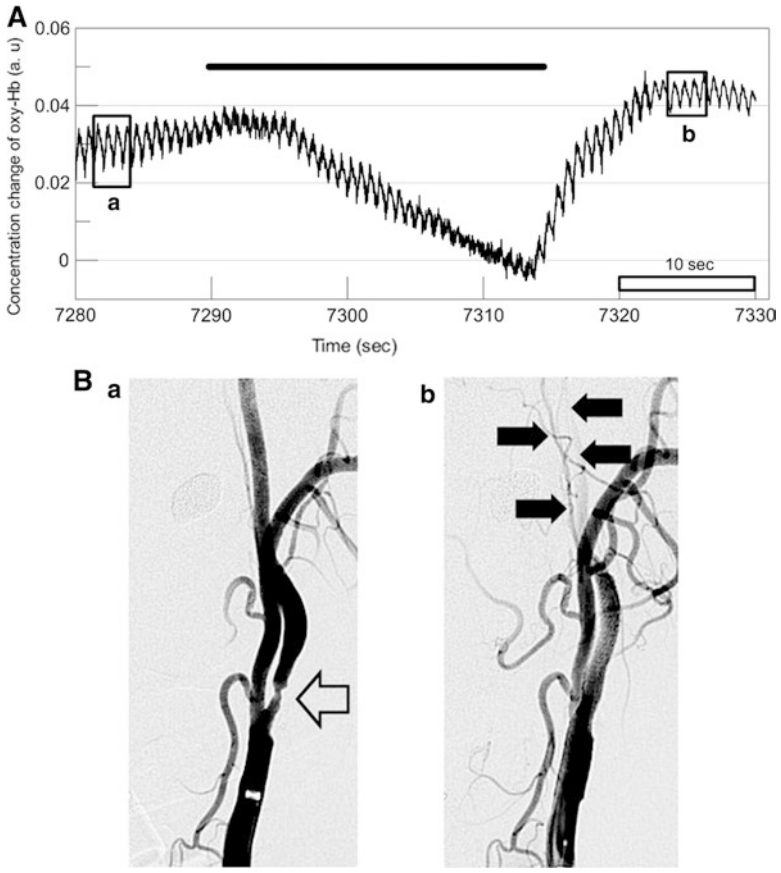

Fig. 43.3 (**A**) Changes of oxy-Hb concentration and fluctuation in patient with no flow during CAS. The *ordinate* indicates Hb concentration change (a.u.), while the *abscissa* indicates time (s). The *thick horizontal bar* indicates the period of balloon dilatation. The oxy-Hb fluctuation before balloon dilatation decreases markedly after balloon dilatation, while oxy-Hb concentration is still at control level. (**B**) Changes of common carotid artery angiogram before (**a**) and after (**b**) balloon dilatation. The *white arrow* in the angiogram (**a**) indicates severe stenosis of ICA. The *black arrow* in the angiogram (**b**) indicates no flow after balloon dilatation

apparent change in oxy-Hb concentration. Figure 43.3 shows a typical case with no flow after deflation of the balloon. It should be noted that oxy-Hb concentration increased abruptly after balloon dilatation, owing to vascular reconstruction; however, NIRS showed a decrease of oxy-Hb fluctuation 5 s after balloon deflation, while oxy-Hb concentration was still at the control level. The amplitude of oxy-Hb fluctuation in the no/slow flow groups was significantly smaller than that in the normal group ($P < 0.001$). In contrast, there was no significant difference in oxy-Hb concentration after stent replacement between the two groups ($P = 0.50$) (Fig. 43.4).

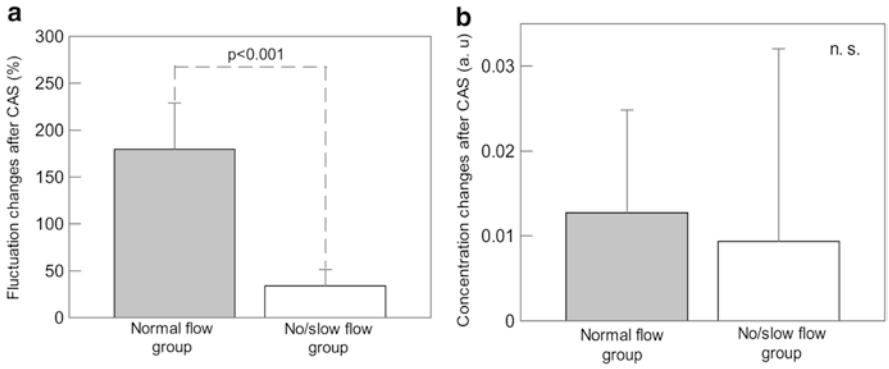

Fig. 43.4 (**a**) Changes of oxy-Hb fluctuation change after CAS in normal and no/slow flow group. The *ordinates* indicate % change of oxy-Hb fluctuation amplitude. The fluctuation amplitude of the no/slow flow group (n = 6) is significant smaller than that of the normal flow group (n = 10) (P < 0.001). (**b**) Changes of oxy-Hb concentration change after CAS in normal and no/slow flow group. The *ordinates* indicate oxy-Hb concentration change (a.u.). There was no significant difference between two groups (P = 0.50)

4 Discussion

NIRS has been employed to monitor changes in hemodynamic status induced by a variety of neurosurgical procedures, by measuring changes of Hb concentrations. For example, decreases of oxy-Hb associated with an increase of deoxy-Hb indicate ischemic changes, while increases of oxy-Hb associated with a decrease of deoxy-Hb indicate hyperperfusion following CEA.

The present findings indicate that NIRS has the potential to detect impaired distal blood flow due to filter obstruction by measuring the fluctuation of oxy-Hb synchronized with heartbeat, even when there is no change of hemoglobin oxygenation. Thus, the fluctuation analysis could detect blood flow reduction more sensitively, as compared with conventional NIRS data analysis, which measures Hb concentration change. Moreover, Hb concentration changes are susceptible to presence of ACC. No/slow flow is one of the factors influencing the patient's outcome. According to the postmarketing prospective study, the occurrence of major adverse events was 13.5 % in the no-flow group, 17.5 % in the slow-flow group, and 4.9 % in the normal-flow group [3]. Therefore, monitoring of subtle hemodynamic changes during CAS is important to reduce adverse events.

The origin of the fluctuation of oxy-Hb is not yet clear, but the following possibilities should be considered. First, the motion of the brain caused by heartbeat could cause the fluctuation of NIRS parameters. If so, all of the NIRS parameters should change; however, deoxy-Hb did not show fluctuation associated with heartbeat. Second, the pulsatile flow of cerebral arterial blood associated with heartbeat could cause the fluctuation of oxy-Hb. Changes of blood pressure could cause dilatation of the artery, resulting in an increase of oxy-Hb concentration without any change in

deoxy-Hb concentration. Indeed, deoxy-Hb exhibited little or no fluctuation. In fact, recent NIRS studies have found fluctuations of NIRS signals associated with systemic blood pressure changes in pediatric, neurosurgical and cardiac patients [5, 6]. In fact, the fluctuation of oxy-Hb was associated with no/slow flow in the ICA. These results suggest that the oxy-Hb fluctuation originated mainly in the pulsatile flow of cerebral arterial blood associated with heartbeat.

In addition, the present NIRS system is compact enough to be attached to the patient's clothes, and is equipped with telemetric data communication, so that patients can be moved freely during CAS.

5 Conclusions

The fluctuation of oxy-Hb measured by the present NIRS system appears to reflect the oscillatory wave caused by heartbeat. Our results indicate that analysis of oxy-Hb fluctuation is a more sensitive tool than monitoring of oxy-Hb concentration changes, and that it is capable of detecting impaired distal blood flow due to filter obstruction during CAS even when monitoring of oxy-Hb concentration does not detect any hemodynamic change. We conclude that this high time-resolution NIRS system is useful to monitor intraprocedural no/slow flow during CAS.

Acknowledgments This research was partly supported by a Grant-in-Aid from the Ministry of Education, Culture, Sports, Sciences and Technology of Japan (B23300247), and grants by Alpha Electron Co., Ltd. (Fukushima, Japan) and Iing CO., LTD (Tokyo, Japan).

References

1. Fanelli F, Bezzi M, Boatta E et al (2006) Techniques in cerebral protection. Eur J Radiol 60(1):26–36
2. Kindel M, Spiller P (2002) Transient occlusion of an angioguard protection system by massive embolization during angioplasty of a degenerated aortocoronary saphenous vein graft. Catheter Cardiovasc Interv 55(4):501–504
3. Taki W (2010) Memorial review celebrating the 50th year of publication of NMC–neuroendovascular therapy. Neurol Med Chir (Tokyo) 50(9):809–823
4. Matsumoto S, Nakahara I, Higashi T et al (2009) Near-infrared spectroscopy in carotid artery stenting predicts cerebral hyperperfusion syndrome. Neurology 72(17):1512–1518
5. Weerakkody RA, Czosnyka M, Zweifel C et al (2010) Slow vasogenic fluctuations of intracranial pressure and cerebral near infrared spectroscopy – an observational study. Acta Neurochir (Wien) 152(10):1763–1769
6. Yoshitani K, Kawaguchi M, Miura N et al (2007) Effects of hemoglobin concentration, skull thickness, and the area of the cerebrospinal fluid layer on near-infrared spectroscopy measurements. Anesthesiology 106(3):458–462

Chapter 44
Use of NIRS to Assess Effect of Training on Peripheral Muscle Oxygenation Changes in Elite Rugby Players Performing Repeated Supramaximal Cycling Tests

Benjamin Jones and C.E. Cooper

Abstract In most team sports, intermittent high intensity sprint efforts combined with short recovery periods have been identified as a key factor of physical performance; the ability to repeat these efforts at a sustained level is of great importance. Near-infrared spectroscopy (NIRS) has been proposed as a tool to monitor muscle oxygenation changes during such sprint efforts. The purpose of this study was to observe muscle reoxygenation rate (reoxy rate) (% s^{-1}) between sprint efforts in a repeat sprint cycle test. A two wavelength spatially resolved NIR spectrometer (Portamon, Artinis Inc.) was used to assess reoxy rate changes in the vastus lateralis of the dominant leg before and after a training stimulus. Eight UK premiership academy level rugby players were assessed (age 20.6 ± 0.9) years; height 187 ± 0.6 cm; weight 109.5 ± 8.6 kg; quadriceps skin fold 16.6 ± 4.5 mm); the subjects completed ten repeated 10-s cycle sprints interspersed with 40 s recovery, upon a Wattbike Pro cycle. Hemoglobin variables (ΔHHb, ΔtHb, ΔO_2Hb, ΔTSI %) during the sprint and the post-sprint reoxygenation rate (%TSI s^{-1}) were measured. During both cycle tests all subjects experienced a drop in muscle oxygen saturation (Pre-Δ − 12.39 ± 6.01 %), Post-Δ − 14.83 ± 3.88 %). Post-training, there was an increase in the extent of desaturation (drop in TSI %) in the group means, both for the biggest single change and the average of all ten changes. Seven out of eight players showed an increase based on the maximum change and six based on the average of their ten tests. Additionally, seven out of eight players showed a significant increase in ΔHHb (Pre-Δ + 76.80 ± 61.92, Post-Δ + 121.28 ± 69.76) ($p < 0.01$) (including the one player who did not show a significant effect on the TSI measure). Players who exercised at the highest power tended to decrease their muscle oxygenation to a greater extent. The number of bike training sessions undertaken correlated

B. Jones (✉) • C.E. Cooper
Centre for Sports and Exercise Science, University of Essex,
42 Highams Road, Hockley, Essex SS5 4DF, UK
e-mail: bjonesa@essex.ac.uk

H.M. Swartz et al. (eds.), *Oxygen Transport to Tissue XXXVI*, Advances in Experimental Medicine and Biology 812, DOI 10.1007/978-1-4939-0620-8_44,

with improvements in post-exercise recovery of oxygenation (R = 0.63). The simplest explanation for the increase in desaturation following training is an increase in muscle oxygen consumption due to an increase in mitochondrial content. This results in an increased extraction of delivered oxygen as confirmed by the HHb data. In conclusion, NIRS is able to measure positive training effects on muscle oxygen extraction, at the level of the individual elite athlete.

Keywords NIRS • Exercise • Muscle oxygenation • Rugby

1 Introduction

This exploratory training study was used to assess a portable Near-infrared Spectroscopy (NIRS) device as a tool to detect individual peripheral muscle oxygenation changes following a training stimulus. In most team sports, intermittent high intensity sprint efforts combined with short recovery periods have been identified as a key factor of physical performance [1]. These sprint efforts occur at crucial points within games, therefore the ability to repeat these efforts at a sustained level is of great importance [2]. Current research has suggested NIRS as a tool to monitor muscle oxygenation changes during sprint efforts [3]. The recovery of muscle oxygenation has also been suggested by some authors to be correlated with the recovery of phosphocreatine (PCr) resynthesis [4], an important parameter linked to repeat sprint ability [5]. The capacity to identify peripheral muscle change within individual athletes following a training period could provide the strength and conditioning coach with greater insight into an athlete's response to workload, and enable superior exercise prescription.

2 Methods

Eight academy level players from a UK premiership professional rugby team were assessed (age 20.6 ± 0.9) years; height 187 ± 0.6 cm; weight 109.5 ± 8.6 kg; quadriceps skin fold 16.6 ± 4.5 mm). A physical activity readiness questionnaire (Par-Q) was administered as a precaution to exercise contraindication, all subjects reported no history or clinical signs of cardiovascular or pulmonary disease. Subjects gave voluntary written consent to participate in the experiment.

2.1 Experimental Overview

Players were asked to complete a modified repeat sprint cycle test upon a Wattbike Pro at air brake resistance level 8. Hemoglobin changes in the vastus lateralis

muscle (NIRS) were recorded throughout the testing period. During the test players were required to produce 100 % effort on each sprint. Players were instructed to remain upright during each recovery period and distribute their weight evenly over both pedals. The warm-up procedure was 3 min in total: 3×55 s of steady pedaling interspersed with 3×5 s maximal sprints at the end of each 55 s. Players were then required to remain upright on their bikes, with their body weight evenly distributed for 3 min, to establish a baseline measurement. Then the exercise test began. At the end of the exercise there was a further 3-min recovery period, the players remaining stationary on the bike. The original intention was to assess players following an 8 week pre-season training program. However, due to player injuries, changes in training schedule and time constraints due to playing commitments, the post-test took place 16 weeks later at a mid-point in the early playing season.

2.1.1 Near-Infrared Spectroscopy Measurements

The portable NIRS apparatus (Portamon, Artinis, Medical Systems, BV, the Netherlands) used in this study was a 2-wavelength continuous system, which uses the modified Beer-Lambert and spatially resolved spectroscopy (SRS) methods. Changes in tissue oxyhaemoglobin (O_2Hb) deoxyhaemoglobin (HHb) and total haemoglobin (tHb) were measured using the difference in absorption characteristics of light at 750 and 850 nm. Values for O_2Hb, HHb and tHb are reported as a change from baseline (30-s averaging before each test) in micromolar units (μM cm). The tissue haemoglobin saturation index (TSI) expressed in % and calculated as $([O_2Hb]/([O_2Hb+HHb]))\times 100$, which reflects the dynamic balance between O_2 supply and O_2 consumption and is independent of near-infrared photon pathlength in muscle tissue [6], was calculated using SRS methods and used to assess muscle reoxygenation rate (% s^{-1}). The NIRS device was positioned on the belly of the vastus lateralis muscle, midway between the greater trochanter of the femur and the lateral femoral epicondyle. To ensure the optodes and detector did not move relative to the subject's skin, the device was fixed into position using waterproof tape and secured with a black sports support strapping to prevent contamination from ambient light. During all tests the NIRS system was connected to a personal computer by Bluetooth™ for data acquisition (1 Hz), analog-to-digital conversion and subsequent analysis.

3 Results

Table 44.1 shows that there was an increase in the extent of desaturation in the group means, both for the biggest single change and for the average of all ten changes.

Table 44.2 shows that seven out of eight players had a significant increase in ΔHHb.

Table 44.1 Data on the maximal desaturation level achieved during the pre- and post-cycle tests

	June	October	June	October
Players	MIN TSI %	MIN TSI %	Average TSI %	Average TSI %
S1	−21.98	−17.44	−20.08	−15.51
S2	−9.17	−10.02	−6.23	−8.74
S3	−14.70	−16.80	−10.40	−14.58
S4	−25.25	−25.56	−23.40	−22.15
S5	−11.68	−15.02	−6.88	−12.83
S6	−11.01	−14.05	−10.85	−12.49
S7	−13.99	−17.12	−10.07	−15.42
S8	−13.99	−18.59	−11.60	−16.96
Mean ± SD	−15.22 ± 5.66	−16.82 ± 4.43	−12.39 ± 6.01	−14.83 ± 3.88

Table 44.2 Data on individual maximal ΔHHb achieved during the pre- and post-cycle tests

Players	(June) (μM cm)	(October) (μM cm)
S1	114.4	135.36
S2	0.96	29.28
S3	95.04	152.96
S4	203.36	246.24
S5	63.84	41.12
S6	34.24	150.24
S7	49.28	132.48
S8	53.44	83.04
Mean ± SD	76.82 ± 61.87	121.34* ± 69.82

Asterisk denotes significance <0.05

Table 44.3 Change in reoxy rates and recovery half-times for all individuals

	Reoxy rate (% s^{-1})		Recovery half-time (s)	
Player	June	October	June	October
S1	0.34	0.25	33.14	34.42
S2	0.14	0.14	52.08	18.64
S3	0.32	0.20	24.96	34.78
S4	0.56	0.49	27.96	20.35
S5	0.20	0.23	37.17	22.63
S6	0.21	0.28	43.56	23.74
S7	0.22	0.08	55.52 (not used in mean)	ND
S8	0.16	0.23	27.09	34.80
Mean ± SD	0.27 ± 0.14	0.24 ± 0.12	35.13 ± 9.86	27.05 ± 7.31

Table 44.3 shows that there was no significant increase in reoxy rates post-exercise, although there was some variation between individuals. However, there was a tendency to an increase in the recovery half-time.

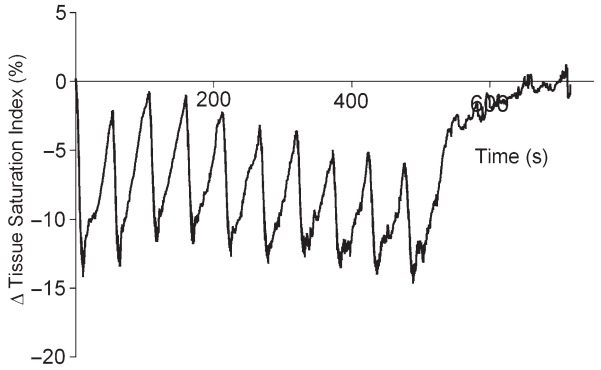

Fig. 44.1 Tissue oxygenation trend during a repeat cycling bout

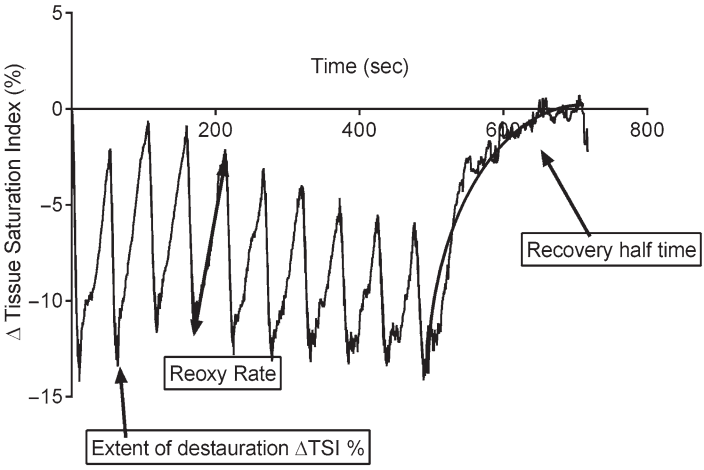

Fig. 44.2 Group post-test data illustrating how the calculations were made

Figure 44.1 shows the group averaged post-tissue saturation index (ΔTSI %) changes. As expected for this type of test, the initial effect of each sprint is a rapid drop in TSI, with recovery seen during the 40-s rest period.

Figure 44.2 depicts the calculations for extent of desaturation (ΔTSI %), interim rate of recovery (reoxy rate % s^{-1}), and recovery half time (s).

Figure 44.3 shows a strong correlation between individuals who perform sessions at a higher power output desaturate to a greater extent. Figure 44.4 suggests a possible correlation between the number of Wattbike training sessions and the oxygenation recovery (note a *lower* recovery time is a *quicker* recovery).

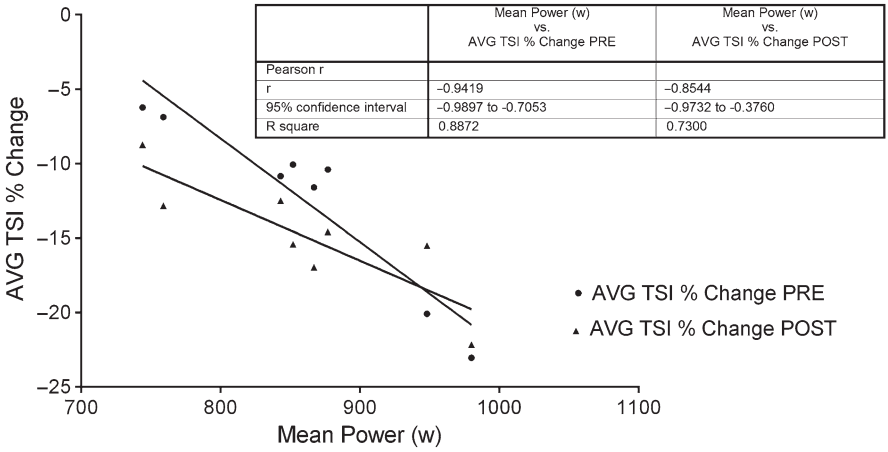

Fig. 44.3 Correlation between the mean power and tissue saturation change

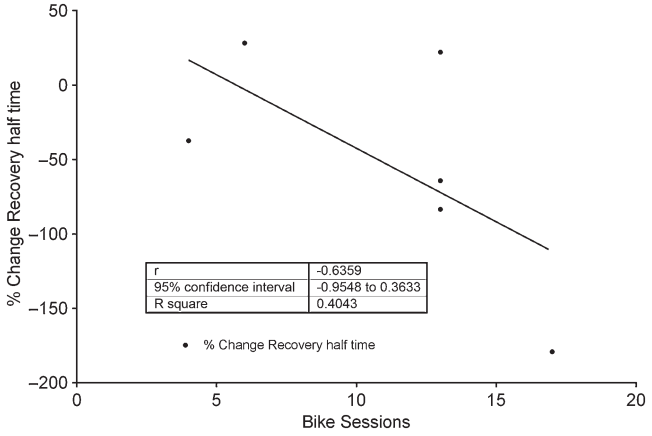

Fig. 44.4 Correlation between the number of bike sessions and recovery half-time

4 Conclusions

The simplest explanation for an increase in desaturation following training is the increase in muscle oxygen consumption due to an increase in mitochondrial content. This results in an increased extraction of delivered oxygen as confirmed by the HHb data. This mitochondrial adaptation following repeat sprint training has also been suggested by other studies [7].

It should be noted that while direct confirmation of changes in muscle oxidative capacity through biopsy would be the ideal, due to the invasive nature of the protocol this is largely impossible with elite athletes. Additionally, available research

'windows' in elite sport, the occurrence of player injury, and athlete accessibility makes it difficult to confirm that the detected NIRS changes in this study are a direct result of the repeat supramaximal cycle efforts.

In conclusion, NIRS is able to measure positive training effects on muscle oxygen extraction. Previous training studies using non-elite subjects have reported significant changes in group mean responses, but with large standard deviations and no publication of individual subject data. However, to be of practical use in elite sports teams it must be possible to rely on the data from each individual. The similar responses seen by all players in this study, suggests that NIRS may indeed be a useful tool for optimising training in individual subjects and/or monitoring muscle oxygen transport and metabolism during the course of the sporting season. The need for a more robust study, with greater control over athlete training schedules is required to further support the role of portable NIRS as a tool for exercise monitoring and prescription.

References

1. Glaister M (2005) Multiple sprint work. Physiological responses, mechanisms of fatigue and the influence of aerobic fitness. Sports Med 359:757–777
2. Buchheit M, Ufland P (2011) Effects of endurance training on performance and muscle reoxygenation rate during repeated-sprint running. Eur J Appl Physiol 111:293–301
3. Billaut F, Buchheit M (2013) Repeated-sprint performance and vastus lateralis oxygenation: effect of limited O_2 availability. Scand J Med Sci Sports 23:e185–e193
4. McCully K, Iotti S, Kendrick K et al (1994) Simultaneous in vivo measurements of HbO_2 saturation and PCr kinetics after exercise in normal humans. J Appl Physiol 77(1):5–10
5. Girad O, Mendez-Villanueva A, Bishop D (2011) Repeated-sprint ability – part 1. Factors contributing to fatigue. Sports Med 41(8):673–694
6. Wolf M, Ferrari M, Quaresima V (2007) Progress of near-infrared spectroscopy and topography for brain and muscle clinical applications. J Biomed Opt 12(6):062104–062114
7. Bailey S, Wilkerson D, DiMenna F et al (2009) Influence of repeated sprint training on pulmonary O_2 uptake and muscle deoxygenation kinetics. J Appl Physiol 106(6):1875–1887

Chapter 45
Skeletal Muscle Deoxygenation Responses During Treadmill Exercise in Children

Shun Takagi, Ryotaro Kime, Taishi Midorikawa, Masatsugu Niwayama, Shizuo Sakamoto, and Toshihito Katsumura

Abstract Muscle O_2 saturation (SmO_2) and blood volume response in activating muscles during treadmill exercise were compared between prepubertal boys (n = 9, age: 9 ± 1 years) and young men (n = 9, age: 22 ± 2 years). SmO_2 and blood volume responses were monitored continuously during the exercise at the gastrocnemius medialis muscle by near infrared spatial resolved spectroscopy. SmO_2 was significantly decreased only at peak exercise in the boys, even though a significant decrease in SmO_2 was observed at 60, 80, and 100 % of peak O_2 uptake in the men ($p < 0.05$). No significant increase in blood volume was observed in the boys, while blood volume was significantly increased in the men with increased exercise intensity ($p < 0.05$). These results suggest that both blood volume and deoxygenation response in activating muscle may be minor in prepubertal boys, compared to young men. The blunted deoxygenation response in prepubertal boys may be caused by undeveloped diffusive O_2 transport (i.e. mitochondrial respiration).

Keywords Blood volume • Muscle oxygen saturation • Near-infrared spatial resolved spectroscopy • Prepubertal boys • Young men

S. Takagi (✉) • R. Kime • T. Katsumura
Department of Sports Medicine for Health Promotion, Tokyo Medical University, 6-1-1 Shinjuku, Shinjuku-ku, Tokyo 160-8402, Japan
e-mail: stakagi@tokyo-med.ac.jp

T. Midorikawa
College of Health and Welfare, J. F. Oberlin University, Machida, Tokyo, Japan

M. Niwayama
Department of Electrical and Electronic Engineering, Shizuoka University, Hamamatsu, Shizuoka, Japan

S. Sakamoto
Faculty of Sport Sciences, Waseda University, Tokorozawa, Saitama, Japan

H.M. Swartz et al. (eds.), *Oxygen Transport to Tissue XXXVI*, Advances in Experimental Medicine and Biology 812, DOI 10.1007/978-1-4939-0620-8_45,

1 Introduction

During high intensity exercise in adults, even though an accumulation of metabolites potentially mediates intramuscular arteriolar vasodilation, muscle blood flow does not meet O_2 demand due to increasing intramuscular vascular compression and inflow occlusion secondary to muscle contraction [1, 2]. However, circulatory responses, especially during walking and running in activating muscles, have not been fully established in children. Previous studies demonstrated that children may exhibit higher muscle blood flow during exercise compared to young adults [3, 4]. Moreover, especially during walking and running exercise, the shorter leg length in children causes a shorter stride and compensatory higher step frequency [5]. In addition, the higher frequency of muscle contraction is unlikely to be attenuated by the mechanical effect during exercise [6, 7]. Therefore, these data suggest that O_2 supply to activating muscle in children may be relatively matched to O_2 utilization until high intensity exercise during walking and running exercise, compared to adults. To date, however, available data about circulation and metabolism at a muscular level in children are still limited.

The purpose of this study was to examine muscle deoxygenation responses during graded treadmill exercise in prepubertal boys, as a pilot study. We also examined the muscle deoxygenation responses in young men as reference data.

2 Methods

2.1 Subjects

Nine prepubertal boys and nine young men participated in the study (Table 45.1), which was approved by the Tokyo Medical University Local Research Ethics Committee, Japan. All subjects were healthy, non-overweight/obese [8], and non-smokers. All boys, their parents, and young men were informed of the purpose and nature of the study, after which their written, informed consent was given. Maturity stage was verified using Tanner's criteria [9].

Table 45.1 Demographic information

	Boys	Men
Age (years)	9 ± 1	23 ± 2
Height (cm)	133.8 ± 14.3	171.9 ± 9.4
Weight (kg)	34.1 ± 8.9	66.3 ± 8.4
Fat layer thickness at GM (mm)	5.16 ± 1.24	4.58 ± 1.72
Absolute peak VO_2 (ml/min)	1407 ± 335	3285 ± 429
Peak VO_2 per body weight (ml/kg/min)	42.1 ± 7.5	44.9 ± 3.9

All data are given as mean ± SD

2.2 Experimental Design

The subjects performed a graded ramp treadmill exercise (MAT-2700, Fukuda-Denshi, Tokyo, Japan), in which speed and grade of the treadmill were increased every 1 min by approximately 1 metabolic equivalent [10], until exhaustion. Pulmonary O_2 uptake (VO_2) was monitored continuously during the experiments to determine peak VO_2 with an online metabolic system (AE300S, Minato Medical Science, Osaka, Japan). In general, it is difficult for children to attain maximal effort. In this study, all boys attained respiratory gas exchange ratio >1.1 and heart rate >190 at peak exercise.

Muscle O_2 saturation (SmO_2) and relative changes from rest in oxygenated hemoglobin concentration (Δoxy-Hb), deoxygenated hemoglobin concentration (Δdeoxy-Hb), and total hemoglobin concentration (Δtotal-Hb) were monitored at the gastrocnemius medialis muscle in the left leg by near infrared spatial resolved spectroscopy (NIR_{SRS}). The NIR_{SRS} data were defined as the SmO_2 averaged over the last 10 s at rest, 20, 40, 60, 80, and 100 % of peak VO_2.

We used a two-wavelength (770 and 830 nm) light-emitting diode NIR_{SRS} (Astem Co., Japan). The probe consisted of one light source and two photodiode detectors, and the optode distances were 20 and 30 mm, respectively. The data sampling rate was 1 Hz. A previous study reported that fat layer thickness affects NIRS data because of light scattering [11]. In contrast, Niwayama et al. recently reported that the effects of fat layer thickness can be corrected in relative changes in Hb [12] or absolute value of SmO_2 [13] by normalized measurement sensitivity. In this study, we measured fat layer thickness at each measurement site in the muscles to correct these effects using an ultrasound device (EUB-7500, Hitachi Medical Corporation, Japan) by placing an ultrasound probe at the same sites as the NIR_{SRS} probes had been placed.

2.3 Statistics

All data are given as means ± standard deviation (SD). The statistical differences among values were tested using one-way repeated-measures analysis of variance. When significant difference was found, multiple comparisons were conducted using Dunnett's test to compare values at baseline and each exercise intensity. Pearson's correlation coefficient was employed to determine the relationship between variables. For all statistical analyses, significance was accepted at $p < 0.05$.

3 Results

Figure 45.1 illustrates the change in SmO_2 (A), Δoxy-Hb (B), Δdeoxy-Hb (C), and Δtotal-Hb (D) for boys and men during exercise, as a function of percent of peak VO_2. For the boys, there were significant main effects of exercise intensity in SmO_2

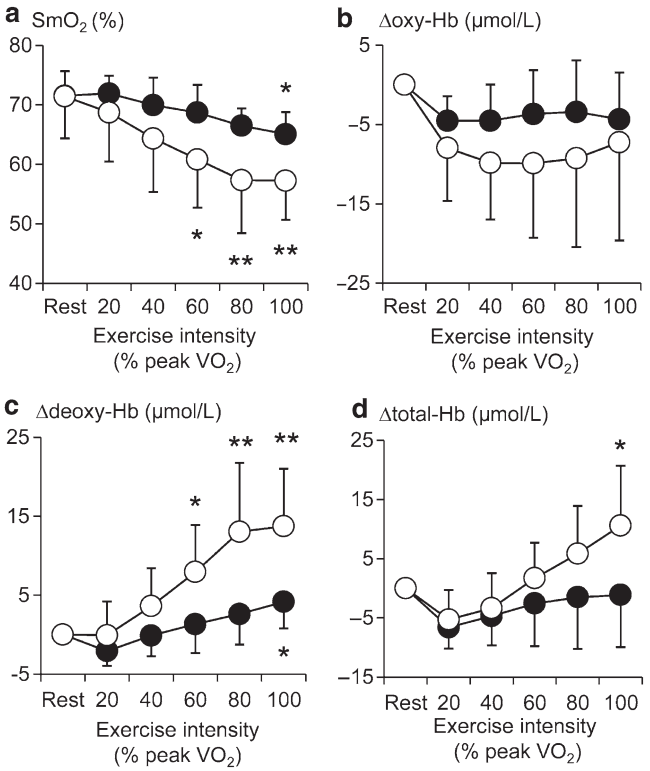

Fig. 45.1 Change in muscle O_2 saturation (SmO_2: **a**), oxygenated hemoglobin (Δoxy-Hb: **b**), deoxygenated hemoglobin (Δdeoxy-Hb: **c**), and total hemoglobin (Δtotal-Hb: **d**) responses in the gastrocnemius medialis muscle during ramp treadmill exercise in prepubertal boys (*closed circles*) and young men (*open circles*). There was a significant difference from rest (*$p<0.05$, **$p<0.01$)

($p<0.05$) and Δdeoxy-Hb ($p<0.01$), but not in Δoxy-Hb ($p=0.24$) or Δtotal-Hb ($p=0.14$). In contrast, for the men, there were main effects of exercise intensity in SmO_2 ($p<0.01$), Δdeoxy-Hb ($p<0.01$), and Δtotal-Hb ($p<0.05$), but not in Δoxy-Hb ($p=0.25$). Even though SmO_2 was significantly decreased during 60–100 % of peak VO_2 from resting value in the men, a significant decrease in SmO_2 was observed only at 100 % of peak VO_2 in the boys ($p<0.05$). Δdeoxy-Hb was significantly increased at peak exercise in the boys ($p<0.05$), while Δdeoxy-Hb response was dramatically enhanced at 60 % ($p<0.05$), 80 % ($p<0.01$), and 100 % ($p<0.01$) of peak VO_2 in men. Δtotal-Hb was not significantly changed as exercise intensity increased in the boys, although Δtotal-Hb was significantly increased at peak exercise ($p<0.05$) from rest in the men.

Even though peak VO_2 per body weight was not different between groups ($p=0.28$), absolute peak VO_2 was significantly lower in boys than men ($p<0.01$). Fat layer thickness at GM was not significantly different between groups ($p=0.41$) (Table 45.1).

4 Discussion

The present study provided two major findings. First, in the boys, we did not observe a significant change in Δtotal-Hb during exercise until exhaustion, even though Δtotal-Hb in the men was increased. Moreover, a significant increase in Δdeoxy-Hb was observed only at peak exercise in the boys, while Δdeoxy-Hb was significantly increased during moderate to high intensity exercise in the men. Second, a significant decrease in SmO_2 was observed only at peak exercise in the boys, while SmO_2 was significantly decreased from 60 to 100 % peak VO_2 in the men. These results suggest that both blood volume and deoxygenation response in activating muscle may be minor in prepubertal children, compared to adults. From our findings, we presume that dynamic O_2 balance in prepubertal children may be relatively maintained until high intensity exercise during treadmill exercise, as SmO_2 indicates the O_2 balance between supply and utilization in activating muscle.

In the present study, there was a lower deoxygenation response in the boys, compared with the men. Some previous studies reported that muscle blood flow per fat-free mass is higher in boys than young men [3, 4]. However, Berg et al. reported that children exhibit lower glycolytic enzyme activity [14]. Moreover, muscle pH during exercise is higher in children than adults [15], and lactate acidosis potentially mediates an increase in Δdeoxy-Hb via Bohr effects. In fact, in the present study, a significant increase in Δdeoxy-Hb was only observed at peak exercise in the boys. Therefore, the blunted deoxygenation response in the prepubertal children may be partly caused by undeveloped muscle energy metabolism.

Turley et al. [4] reported that children have a lower vascular resistance during exercise due to sufficient O_2 delivery to activating muscle. Moreover, systemic vascular resistance is reduced by the higher frequency of muscle contraction during dynamic exercise [7]. These data may indicate that children have a higher muscle blood volume response. However, in the present study, Δtotal-Hb response was minor until exhaustion in the boys. Because muscle hypoxia and a decrease in muscle pH cause local vasodilatory responses [1, 2], one possible reason for the minor response of blood volume may be blunted arterioles vasodilation mediated by less accumulation of metabolites.

We did not directly compare the NIRS values between the boys and the men in the present study because the lower body weight in children would most likely cause lower O_2 demand (lower VO_2) during weight bearing exercise, such as treadmill exercise, compared to higher body weight (i.e. adults). From our data, it may be speculated that the child-adult differences in muscle deoxygenation response may be mainly explained by lower O_2 demand (lower VO_2), secondary to lower body weight in children. Nevertheless, no significant relationship between body weight and Δdeoxy-Hb response was observed in the subgroups (boys: $r=-0.39$, $p=0.29$; men: $r=-0.45$, $p=0.26$), even though a marginal significant relationship was observed in all subjects ($r=0.45$, $p=0.06$). Because of the low number of subjects, this area warrants further investigation.

In conclusion, muscle deoxygenation response during exercise was minor in children until exhaustion, even though blood volume response was also blunted.

These results may be caused by undeveloped diffusive O_2 transport. Our findings indicate that muscle O_2 balance between supply and utilization in children may be relatively maintained until high intensity exercise, during walking and running exercise, compared to adults.

Acknowledgments The authors are grateful for revision of this manuscript by Andrea Hope. We also thank Masayuki Konishi and Hiroki Tabata (Waseda University, Japan) for their helpful technical assistance.

References

1. Delp MD (1999) Control of skeletal muscle perfusion at the onset of dynamic exercise. Med Sci Sports Exerc 31(7):1011–1018
2. Delp MD, Laughlin MH (1998) Regulation of skeletal muscle perfusion during exercise. Acta Physiol Scand 162(3):411–419
3. Koch G (1974) Muscle blood flow after ischemic work and during bicycle ergometer work in boys aged 12 years. Acta Paediatr Belg 28(Suppl):29–39
4. Turley KR, Wilmore JH (1997) Cardiovascular responses to treadmill and cycle ergometer exercise in children and adults. J Appl Physiol 83(3):948–957
5. Rowland TW, Auchinachie JA, Keenan TJ et al (1987) Physiologic responses to treadmill running in adult and prepubertal males. Int J Sports Med 8(4):292–297
6. Honig CR, Odoroff CL, Frierson JL (1982) Active and passive capillary control in red muscle at rest and in exercise. Am J Physiol 243(12):H196–H206
7. Gotshall RW, Bauer TA, Fahrner SL (1996) Cycling cadence alters exercise hemodynamics. Int J Sports Med 17(1):17–21
8. Cole TJ, Bellizzi MC, Flegal KM et al (2000) Establishing a standard definition for child overweight and obesity worldwide: international survey. BMJ 320(7244):1240–1243
9. Tanner JM, Whitehouse RH (1976) Clinical longitudinal standards for height, weight, height velocity, weight velocity, and stages of puberty. Arch Dis Child 51(3):170–179
10. Takagi S, Kime R, Niwayama M et al (2013) The influence of different exercise modes on muscle oxygen saturation and its relationship to peak oxygen uptake. Jpn J Clin Sports Med 21(2):388–395
11. Komiyama T, Quaresima V, Shigematsu H et al (2001) Comparison of two spatially resolved near-infrared photometers in the detection of tissue oxygen saturation: poor reliability at very low oxygen saturation. Clin Sci (Lond) 101(6):715–718
12. Niwayama M, Lin L, Shao J et al (2000) Quantitative measurement of muscle hemoglobin oxygenation using near-infrared spectroscopy with correction for the influence of a subcutaneous fat layer. Rev Sci Instrum 71(12):4571–4575
13. Niwayama M, Sone S, Murata H et al (2007) Errors in muscle oxygenation measurement using spatially-resolved NIRS and its correction. J Jpn Coll Angiol 47(1):17–20
14. Berg A, Kim SS, Keul J (1986) Skeletal muscle enzyme activities in healthy young subjects. Int J Sports Med 7(4):236–239
15. Zanconato S, Buchthal S, Barstow TJ et al (1993) 31P-magnetic resonance spectroscopy of leg muscle metabolism during exercise in children and adults. J Appl Physiol 74(5):2214–2218

Chapter 46
Development of a Hybrid Microwave-Optical Thermoregulation Monitor for the Muscle

A. Al-Armaghany, K. Tong, and T.S. Leung

Abstract This paper presents the latest development of the hybrid microwave-optical thermoregulation monitor for the muscle. It is capable of warming the muscle and measuring the subsequent blood volume changes, using a novel microwave applicator with integrated optical probes. The challenge is to measure the thermoregulation response in deep tissue while minimizing any effect from the skin layer. We have introduced a skin cooling device, an additional integrated optical Laser Doppler flow monitoring probe and a temperature sensor to measure skin blood flow and temperature, respectively. The result shows that skin cooling is essential to minimize skin flow changes during microwave warming. The hybrid probe was placed on a human thigh to measure oxy/deoxy/total haemoglobin concentration changes ($\Delta HbO_2/\Delta HHb/\Delta HbT$), skin flux and temperature upon microwave warming. Without skin cooling, the skin temperature was elevated by 4 °C and both $\Delta HbO_2/\Delta HbT$ and skin flux increased, showing microwave warming occurring in both the skin and muscle. With skin cooling, the skin temperature was kept relatively constant. While $\Delta HbO_2/\Delta HbT$ increased, the skin flux was relatively stable, showing a preferential microwave warming in the muscle, rather than the skin.

Keywords Near infrared spectroscopy • Thermoregulation • Microwave applicator • Muscle • Laser Doppler flowmetry

A. Al-Armaghany (✉) • K. Tong
Department of Electronic and Electrical Engineering, University College London, Torrington Place, London WC1E 7JE, UK
e-mail: A.armaghany@gmail.com; A.Al-Armaghany@ucl.ac.uk

T.S. Leung
Department of Medical Physics and Bioengineering, University College London, Malet Place Engineering Building, London WC1E 6BT, UK

H.M. Swartz et al. (eds.), *Oxygen Transport to Tissue XXXVI*, Advances in Experimental Medicine and Biology 812, DOI 10.1007/978-1-4939-0620-8_46,

1 Introduction

Current non-invasive thermoregulation studies are mainly on the skin which is easily accessible. The thermal response can be measured by a Laser Doppler flowmetry (LDF) probe, which can be integrated with a skin heater [1]. Vascular diseases investigated using this technique include Raynaud's phenomenon and systemic sclerosis [2]. However, assessing thermoregulation in the muscle is less straightforward. It has been performed by a microwave applicator to warm up the muscle, and measuring the muscle blood flow change using invasive/radioactive methods [3]. The aim of this work was to combine both the heat source and the blood volume monitor into a single non-invasive thermoregulation monitor. It includes a microwave applicator which raises the muscle temperature by 2–3 °C, causing blood vessels to dilate and blood flow and volume to increase. The thermoregulation responses are monitored by the two integrated optical monitors, first via near infrared spectroscopy (NIRS) to measure $\Delta HbO_2/\Delta HHb/\Delta HbT$ in deep tissue, and laser Doppler flowmetry to measure skin blood flow. The first prototype previously reported [4] warmed up both the deep tissue and the skin, and the thermoregulation response was biased towards the superficial layers. Improving upon the previous design, the present applicator includes a skin cooling device to maintain the skin temperature at a stable level, resulting in muscle dominant warming. The capability of monitoring muscle thermoregulation will aid the study of vasculature perfusion non-invasively. Potential applications include free flap reconstruction and assessment of amputation levels [5, 6].

2 Material and Methods

2.1 Microwave Applicator Design

In comparison to the previous design reported last year [4], the new applicator has a number of new features. First, the new applicator has integrated an additional optical probe and a temperature sensor for measuring skin blood flow and temperature as shown in Fig. 46.1a. Second, the new applicator is capable of maintaining the skin temperature with embedded cooling. Third, the new applicator has been carefully modeled and designed to induce electromagnetic energy (EM) inside the tissue and to minimize leakage to the surrounding. The power requirement has been reduced as the energy is more efficiently coupled to the tissue. The applicator is housed in an acetal plastic cylinder with an external diameter of 62 mm and height of 55 mm as shown in Fig. 46.1b. The hybrid applicator can be easily deployed on the human calf or arms with a elastic belt to hold the hybrid applicator in place throughout the *in vivo* measurement.

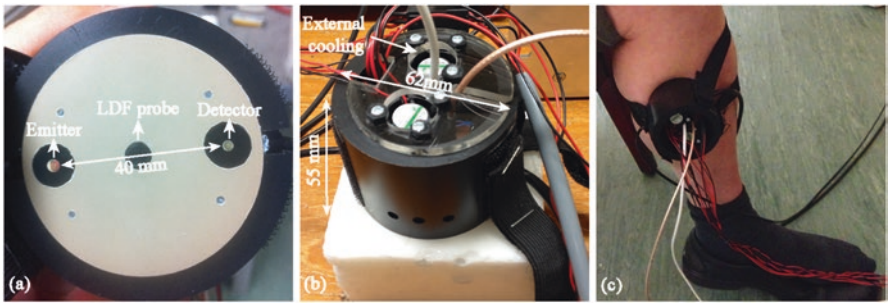

Fig. 46.1 The hybrid probe and the *in vivo* experiment: (**a**) the front view of the hybrid probe, (**b**) the back view with cooling fans (**c**) the hybrid probe securely placed on the calf

2.2 The Biological Thermal Model

The interaction of EM energy into the tissue has been modeled with an EM modeling software CST Microwave Studio 2013. The simulated tissue model consists of three layers including the skin, fat and muscle layers with the corresponding thicknesses of 2, 10 and 50 mm. The biological tissue model has the electrical and thermal characteristics of those of the human. The conversion of EM energy into heat in biological tissue was modeled by the Pennes bio-heat equation, which takes various factors into consideration, including the body temperature, metabolic heat generation and capillary blood perfusion coefficient. The simulation has open thermal boundaries at a background temperature of 20 ℃ and the simulation corresponds to 5 min after microwave exposure. The simulation model in Fig. 46.2a shows the two-dimensional transient thermal distribution in the biological tissue model without skin cooling. Two local hot spots are located at the skin fat interface with a maximum temperature of 40 ℃. A secondary local hot spot is located in deep tissue at a lower temperature of 39.3 ℃. Figure 46.2b shows the thermal distribution in the biological tissue model with skin cooling. The tissue warming is localized in the muscle alone because cooling eliminates skin hot spots. Although the peak temperature achieved in the muscle at 16.5 mm under the skin is 38.7 ℃, about 0.6 ℃ lower than the value achieved without cooling (the cooling also reduces the warming inside the muscle), this temperature is sufficient to cause vasodilation.

2.3 The Optical Probe

Optical monitors based on NIRS and laser Doppler measure physiological responses produced by the tissue warming. Both modalities have been extensively used to measure tissue oxygenation and skin blood flow in a range of applications. In this study, an in-house built NIRS monitor has been used which measures ΔHbO_2/

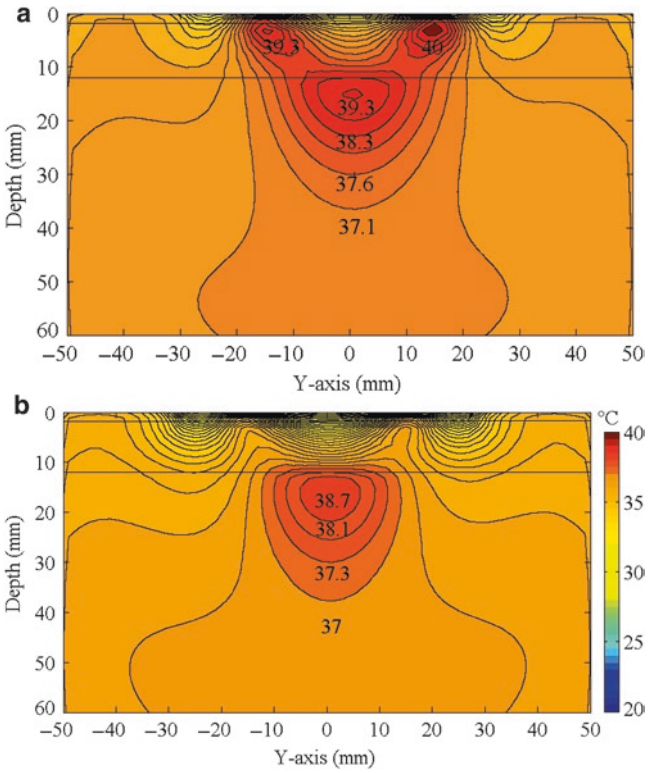

Fig. 46.2 Thermal distribution simulation: (**a**) Thermal distribution of the microwave applicator without skin cooling and (**b**) with skin cooling

ΔHHb/ΔHbT with a single detector and six laser sources operating at different wavelengths (670, 760, 780, 850, 904 and 980 nm). The source-detector separation is 40 mm for increase in light penetration in deep tissue. The differential pathlength factor (DPF) of 4.94 was used in the modified Beer–Lambert law for the conversion of the measured data [7]. In this study, the laser Doppler monitor is the commercially available moorVMS-LDF operating at a wavelength of 785 nm, used to measure the skin blood flow at approximately 1 mm of depth. In the current setup, the NIRS light source/detector and the LDF probe cannot be used simultaneously because of interference. The investigation of the skin blood flow and ΔHbO_2/ΔHHb/ΔHbT will need to be done in two separate experiments.

2.4 In Vivo *Experiment Protocol*

Initially the hybrid probe was secured on a human calf as show in Fig. 46.1c. As the skin temperature stabilized, the main experiment procedure consisted of (1) initial

rest duration of 3 min and setting the skin threshold temperature based on the stabilized value for skin cooling, followed by (2) 5 min of microwave exposure and then (3) 4 min of rest with microwave switched off. Due to the limitation of the optical monitoring mentioned in the last section, the same procedures were performed twice after the skin temperature stabilized, one with the LDF probe on (NIRS probe off) and one with the NIRS probe on (LDF probe off). The procedure was then repeated again for a new measurement of tissue warming without cooling. This study has been approved by the UCL Ethics Committee.

3 Results and Discussion

Figure 46.3 shows the measured $\Delta HbO_2/\Delta HHb/\Delta HbT$, skin flux and temperature for the two experiments: with and without skin cooling. Without skin cooling, Fig. 46.3a shows that both ΔHbO_2 and ΔHbT increased rapidly during the 5 min of microwave warming, reaching a steady state after about 4 min, while ΔHHb shows no significant change from the microwave warming, indicating that the dilation primarily occurred in the arterial vessels. After the microwave was turned off, ΔHbO_2 and ΔHbT gradually decreased for 2 min. Some confirmed movement artifacts were also seen afterwards. As shown in Fig. 46.3b, the skin temperature was approximately 29.5 °C during the rest period. When the microwave was switched on, the skin temperature increased rapidly to a peak temperature of 33.8 °C. The skin flux began to fluctuate when the skin temperature was elevated by about 1 °C, reaching a maximum flux of 22 (A.U.) from the rest period of 6 (A.U.).

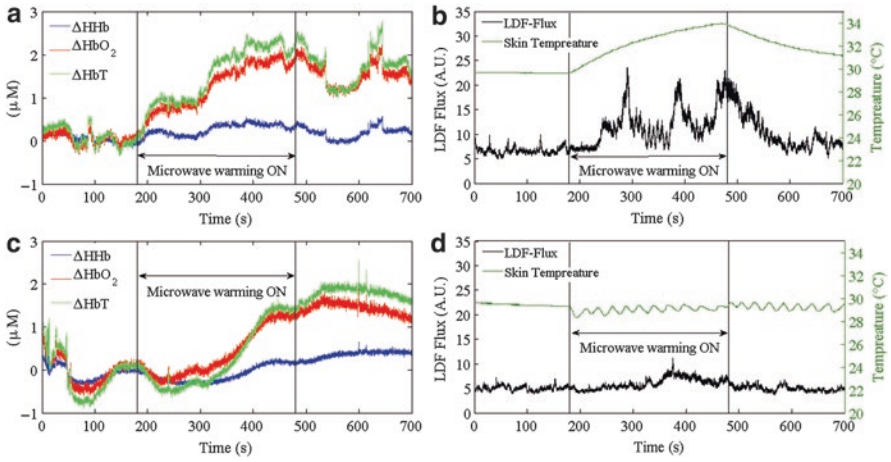

Fig. 46.3 Thermoregulation responses, without skin cooling: (**a**) $\Delta HbO_2/\Delta HHb/\Delta HbT$, (**b**) the skin flux and temperature; and with skin cooling: (**c**) $\Delta HbO_2/\Delta HHb/\Delta HbT$, (**d**) the skin flux and temperature

The skin flux fluctuation is an interesting phenomenon which deserves further investigation. After the microwave applicator was switched off, the skin temperature and skin flux decreased gradually. As predicted by the simulations in Fig. 46.2a, without skin cooling, microwaves warm up the skin as well as the deep tissue, causing increase in the skin flux. Since NIRS signals measured in this way were highly susceptible to the influence of the skin and fat layers, the changes in $\Delta HbO_2/\Delta HbT$ were likely to be dominated by the blood volume changes in the skin and fat layers. Light propagation in the muscle was simulated using a three layered diffusion model [8] to estimate the partial pathlengths in the skin, fat and muscle with typical optical properties, and skin and fat thicknesses of 1.2 and 6 mm, respectively. It was found that the $\Delta HbO_2/\Delta HbT$ signals in the skin and fat layers account for 65 % of the total signal, assuming the heat gave rise to the same amount of blood volume increase in all the three layers.

The second experiment with actively controlled skin cooling is presented in Fig. 46.3c, d with the same subject, hybrid probe placement and protocol. The haemoglobin concentration in Fig. 46.3c has larger natural variation during the rest period in comparison to the first experiment. About 2 min into microwave warming, ΔHbO_2 and ΔHbT began to rise, longer than the 25 s in the first experiment. This means that the skin cooling might have reduced the effectiveness of muscle warming. A longer warming duration was necessary to initiate the thermoregulation response from the muscle. With 5 min of exposure it was sufficient to see increases in $\Delta HbO_2/\Delta HHb/\Delta HbT$. After the microwave applicator was switched off, $\Delta HbO_2/\Delta HHb/\Delta HbT$ continued to increase for another 50 s until they gradually decreased. This delay was caused by the thermal diffusion in the muscle and slow thermal dissipation caused by the fat (a good thermal insulator). The temperature and skin flux are shown in Fig. 46.3d. The skin temperature stabilized at about 29 °C. During microwave warming, the skin cooling was switched on when the skin temperature exceeded beyond a pre-set threshold; otherwise the skin cooling was off. This mechanism led to periodic oscillations in the skin temperature of approximately ±0.4 °C. The skin flux was stable during the rest period and the early phase of the microwave warming. Approximately 3 min into the microwave warming, a small increase in the skin flux was detected which could be caused by inadequate skin cooling. After the microwave applicator was switched off, the skin flux remained stable. With minimal influence from the skin blood flow, the increases in $\Delta HbO_2/\Delta HHb/\Delta HbT$ were likely due to the deep tissue, i.e., muscle, rather than the skin.

4 Conclusions

The aim of this study was to develop a hybrid monitor to investigate the thermoregulation response in the muscle while keeping the skin temperature stable. With skin cooling, the muscle temperature can be elevated by 1.7 °C which is sufficient to cause a thermoregulation response. The hybrid monitor was used in *in vivo* experiments involving a human calf. With skin cooling, both the skin temperature

and skin flux were relatively stable, indicating that the influence of the skin was minimal. The increases in $\Delta HbO_2/\Delta HHb/\Delta HbT$ can therefore be considered predominantly from the muscle, which is the main target tissue of the hybrid monitor. To conclude, we have successfully developed a thermoregulation monitor that can warm up the deep tissue such as the muscle preferentially and measure the subsequent response in terms of $\Delta HbO_2/\Delta HHb/\Delta HbT$, as well as monitor the skin blood flow. This device has the potential to expand our understanding of vascular diseases and tissue rehabilitation such as free flap reconstruction.

Acknowledgments This work was partly funded by EPSRC (Grant Code EP/G005036/1). We would also like to thank Sonny Gunadi and Nick Everdell for building the NIRS monitor.

References

1. Johnson JM, O'Leary DS, Taylor WF et al (1986) Effect of local warming on forearm reactive hyperaemia. Clin Physiol 6(4):337–46
2. Herrick AL, Clark S (1998) Quantifying digital vascular disease in patients with primary Raynaud's phenomenon and systemic sclerosis. Ann Rheum Dis 57(2):70–78
3. Song C (1984) Effect of local hyperthermia on blood flow and microenvironment: a review. Cancer Res 44:4721s–4730s
4. Al-Armaghany A, Tong K, Leung TS (2013) Development of a hybrid microwave-optical tissue oxygenation probe to measure thermal response in the deep tissue. Adv Exp Med Biol 789: 371–377
5. Cornejo A, Rodriguez T, Steigelman M et al (2011) The use of visible light spectroscopy to measure tissue oxygenation in free flap reconstruction. J Reconstr Microsurg 27(7):397–402
6. Gebuhr P, Jorgensen JP, Vollmer-Larsen B et al (1989) Estimation of amputation level with a laser Doppler flowmeter. J Bone Joint Surg 71-B(3):514–517
7. Duncan A, Meek JH, Clemence M et al (1995) Optical pathlength measurements on adult head, calf and forearm and the head of the newborn infant using phase resolved optical spectroscopy. Phys Med Biol 40(2):295–304
8. Liemert A, Kienle A (2011) Light diffusion in N-layered turbid media: steady-state domain. J Biomed Opt 15(2):025003

Chapter 47
Evaluation of a Textile-Based Near Infrared Spectroscopy System in Calf Muscle Oxygenation Measurements

Nassim Nasseri, Christoph Zysset, Lars Büthe, Stefan Kleiser, Gerhard Tröster, and Martin Wolf

Abstract We recently introduced a novel textile-based NIRS sensor (TexNIRS). Here, we evaluate TexNIRS in ten subjects (16 legs, age 28.5 ± 2.32 years, adipose tissue thickness (ATT) 4.17 ± 1.71 mm). Three venous occlusions at 50 mmHg were performed on their calf muscle. After 3 min of occlusion, oxy/deoxy hemoglobin concentration ([O_2Hb], [HHb]) changes were 3.71 ± 1.89/1.79 ± 1.08 μM; venous oxygen saturation (SvO_2) was 75 ± 9.7 %, oxygen consumption (VO_2) was 0.02 ± 0.01 mL/100 g/min, hemoglobin flow (HF) was 0.93 ± 0.48 μmol/100 mL/min, and blood flow (BF) was 2.01 ± 1.04 mL/100 mL/min. Our results are in good agreement with the literature, but the TexNIRS enables a much higher level of comfort.

Keywords NIRS • Wearable technology • Muscle oxygenation • PVD • Calf muscle

N. Nasseri (✉) • S. Kleiser
Biomedical Optics Research Laboratory, Division of Neonatology,
University Hospital of Zürich, Frauenklinikstrasse 10, 8091 Zurich, Switzerland

Institute for Biomedical Engineering, Swiss Federal Institute of Technology,
Wolfgang-Pauli-Str. 27, 8093 Zurich, Switzerland
e-mail: nassim.nasseri@usz.ch

C. Zysset • L. Büthe • G. Tröster
Electronics Laboratory, Swiss Federal Institute of Technology,
Gloriastrasse 35, 8092 Zurich, Switzerland

M. Wolf
Biomedical Optics Research Laboratory, Division of Neonatology,
University Hospital of Zürich, Frauenklinikstrasse 10, 8091 Zurich, Switzerland

H.M. Swartz et al. (eds.), *Oxygen Transport to Tissue XXXVI*, Advances in Experimental Medicine and Biology 812, DOI 10.1007/978-1-4939-0620-8_47,

1 Introduction

Near Infrared Spectroscopy (NIRS) is a noninvasive and harmless light-based technique to measure oxygenation and hemoglobin concentration [1, 2]. NIRS was first introduced by Jobsis in 1977 and, since then, has had a wide application in the clinical environment [3]. NIRS with the ability to measure muscle hemodynamics and oxygenation is a valuable tool to study muscle metabolism [4, 5]. In 1997, Abe et al. measured the quadriceps muscle during a bicycle ergometer exercise, by NIRS; they found an oxygen utilization impairment due to a defect in mitochondrial oxidative phosphorylation [6]. In 2001 it was reported that in patients with peripheral vascular disease (PVD), tissue reperfusion after a period of ischemia, was slower than in healthy subjects [7]. A significant spatial heterogeneity of blood flow, hemoglobin flow, venous oxygen saturation, and oxygen consumption between subjects and within individual legs was reported in 2007 [8]. A systematic review on NIRS of PVD concluded that NIRS was capable of monitoring key parameters such as oxygen delivery to and oxygen consumption of the tissue [9]. In another study the area under the curve of O_2Hb measured by NIRS, during an incremental treadmill test, was significantly different in patients suffering from peripheral arterial disease (PAD) compared to healthy subjects [10]. Thus, there is increasing interest among scientists from different fields to apply NIRS as a bedside and noninvasive tool to study muscle hemodynamics and oxygenation [11–15].

Although NIRS is recognized as a noninvasive, harmless technique that provides relevant information, it still suffers from a lack of comfort for the participants. Moreover, better contact between the sensor and tissue would provide more reliable signals. Recently, we introduced a new technique to embed sensors for NIRS into textiles [16]. A textile-based NIRS system (TexNIRS) should not only provide better contact with the region of interest but also a higher level of comfort. Therefore TexNIRS can be worn or wrapped around the muscle and it measures for a long period of time. In addition, it has the possibility of measuring during physical activity.

The aim of the current study is to apply TexNIRS to venous occlusion measurement on the gastrocnemius muscle and to compare its results to the literature of conventional NIRS systems. Conducting comfortable measurements by this new technology opens new doors to the field of skeletal muscle oxygenation monitoring.

2 Materials and Methods

2.1 Textile-Based NIRS Sensor (TexNIRS)

Three types of flexible plastic strips are woven into a cotton textile. The first type includes LEDs together with transistors. The second type includes a photodiode together with a transimpedance amplifier. The third type (the so-called bus bar strip) provides connections through insulated copper wires within the textile. Two light source locations and two detectors attached on the flexible plastic strips enable to

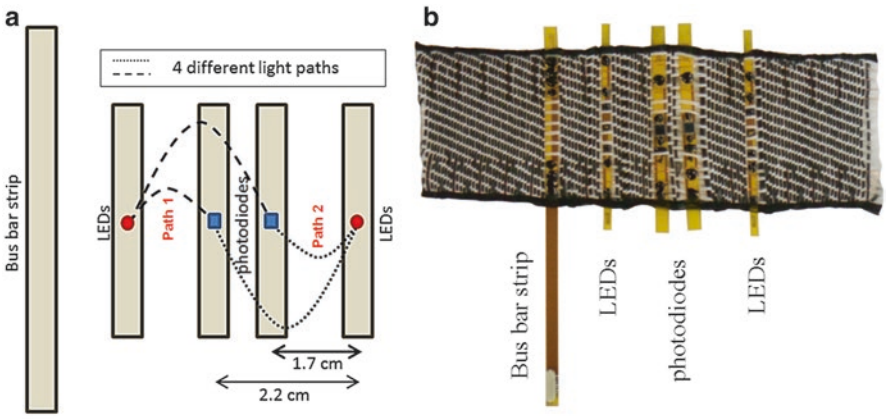

Fig. 47.1 (**a**) Schematic of the TexNIRS sensor head. (**b**) Fabricated patch

collect four light paths (Fig. 47.1). The short distance is 1.7 cm and the long distance is 2.2 cm. Each light source location consists of two LEDs with emission at 760 and 870 nm. LEDs are pulsed with a sampling frequency of 100 Hz and a maximum current of 400 mA, for 1 ms. An industrial narrow fabric weaving machine (Mueller Frick NFREQ 42) wove the plastic strips and copper wires into a cotton textile. In warp direction, eight cotton yarns were replaced by insulated copper wires to interconnect the strips within the textile. To place the plastic strip in the weft direction, the insertion of the weft yarns was blocked and the plastic strip was placed manually (after stopping the machine) in the gap which was opened due to blocking the insertion of yarns in the weft direction. The system also has a control box which handles the timing of the LEDs and provides the communication between the sensors and the host computer. Details of the system are published elsewhere [16]. The system provides four different light paths (two long and two short). In the present study only the results from the two short paths (path 1 and path 2) are presented due to the low intensity of the signals at the long distances. We calculated [O_2Hb] and [HHb] by the modified Beer–Lambert law for each light path (differential path-length factor is 6.23 at 760 nm, 5.90 at 870 nm for female and 5.05 at 760 nm, 4.77 at 870 nm for male subjects). SvO_2, VO_2, HF, and BF are calculated according to the procedure described in detail elsewhere [17].

2.2 Subjects

Ten healthy subjects participated in this study, after giving written informed consent. The measurement protocol was approved by the Ethical Committee of the ETH Zurich. Healthy subjects aged between 18 and 70 years, without any history of PVD, hypertension, hyperlipidemia, tobacco smoking, diabetes mellitus, and coronary-heart disease were included in the study. We measured 16 legs from ten different subjects.

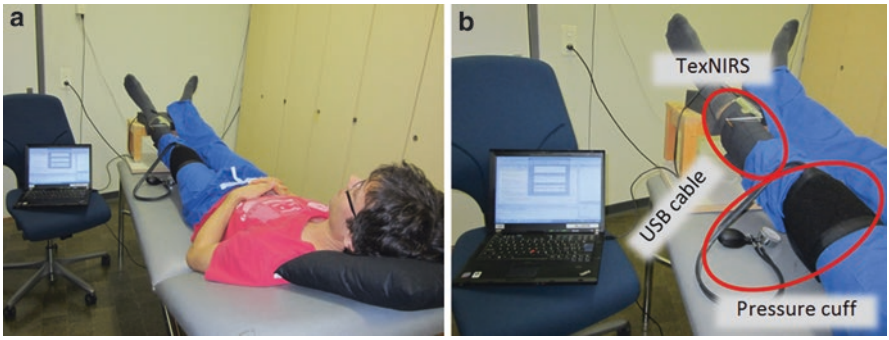

Fig. 47.2 (**a**, **b**) Calf muscle oxygenation measurement on a healthy subject, using TexNIRS

2.3 Study Protocol

All the measurements were conducted at the ETH Zurich. We started the sessions by measuring blood pressure and calf ATT (on one or both legs) by a skinfold caliper. Each subject lay on a hospital bed in supine position. His/her legs were slightly elevated to about 30º from the bed (Fig. 47.2). TexNIRS was placed over and wrapped around the gastrocnemius muscle. To reduce the effect of ambient light, all the lights were turned off during measurement and the room had no windows. The subjects were requested not to move, speak, or fall asleep during measurement. The measurement consisted of three consecutive venous occlusions at 50 mmHg. There was a 2-min period of recovery between the occlusions. The first occlusion started after 5 min of baseline recording.

3 Results

Figure 47.3 shows the result of a venous occlusion in one of the participants. Table 47.1 presents the change in parameters during each occlusion, averaged over 16 legs. The average SvO_2 was 75 ± 9.7 %, VO_2 was 0.02 ± 0.01 mL/100 g/min, HF was 0.93 ± 0.48 μmol/100 mL/min, and BF was 2.01 ± 1.04 mL/100 mL/min.

4 Discussion and Conclusion

The ability of TexNIRS to detect circulatory changes induced by venous occlusion was assessed in the human calf muscle. In agreement with the literature [8, 17, 18], immediately after occlusion was applied, there was an increase in [O_2Hb], [HHb], and [tHb]. After releasing the pressure all three parameters had returned to baseline values.

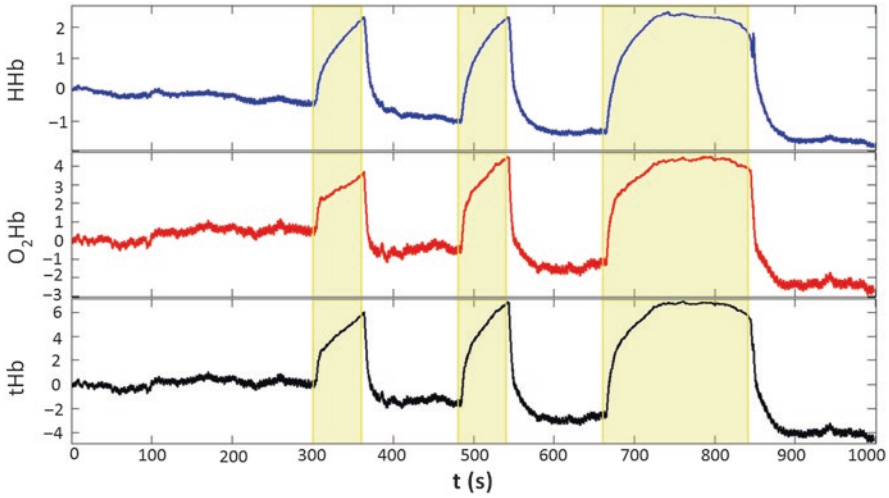

Fig. 47.3 Changes in [O_2Hb], [HHb], and [tHb] (μM), during three venous occlusion

Table 47.1 Oxy/deoxy and total hemoglobin increase at the end of the venous occlusion. Two different light paths are displayed

	First occlusion			Second occlusion			Third occlusion		
Path	O_2Hb (μM/L)	HHb (μM/L)	tHb (μM/L)	O_2Hb (μM/L)	HHb (μM/L)	tHb (μM/L)	O_2Hb (μM/L)	HHb (μM/L)	tHb (μM/L)
1	2.68 ± 1.46	1.17 ± 0.71	3.86 ± 1.96	2.8 ± 1.75	1.18 ± 0.78	3.98 ± 2.36	3.71 ± 1.89	1.79 ± 1.08	5.49 ± 2.78
2	4.4 ± 3.33	0.58 ± 0.47	4.99 ± 3.53	4.3 ± 3.56	0.4 ± 0.49	4.7 ± 3.78	5.85 ± 4.18	0.69 ± 0.7	6.54 ± 4.42

The increase in [tHb] reflects higher blood volume and occurs due to venous blockage. The increase in [HHb] reflects VO_2 which turns O_2Hb to HHb. The size of the increase in [O_2Hb], [HHb], and [tHb] varies from subject to subject and depends on ATT, i.e. the fat/muscle ratio of the measured volume, inter-individual differences in path length, resting metabolic rate, and other physiological factors. The average increases were in good agreement with the literature [8, 17, 18]. In addition also the HF, BF, SvO_2, and VO_2 were all in good agreement with the literature [17].

The current system could be improved by increasing the source-detector distance (SDD) thus providing a deeper penetration of light into the tissue. The wearability of the system could be further enhanced by replacing LEDs and detectors with optical fibers. By applying a multi-distance setup for measuring the [O_2Hb] and [HHb], instead of the modified Beer–Lambert law, the effect of superficial tissue and the coupling factors will be reduced. Unstable SDD due to the textile base of the device is the main limitation of this technique; however this error in [tHb] was less than 19 % in the present study. To conclude, we were able to reliably measure calf muscle oxygenation by TexNIRS. In contrast to the conventional NIRS devices, TexNIRS provides a high level of comfort for the subject which has always been an issue in NIRS studies.

References

1. Wolf M, Morren G, Haensse D et al (2008) Near infrared spectroscopy to study the brain: an overview. Opto Electron Rev 16:413–419
2. Ferrari M, Muthalib M, Quaresima V (2011) The use of near-infrared spectroscopy in understanding skeletal muscle physiology: recent developments. Phil Trans A Math Phys Eng Sci 369:4577–4590
3. Jobsis FF (1977) Noninvasive, infrared monitoring of cerebral and myocardial oxygen sufficiency and circulatory parameters. Science 198:1264–1267
4. Van Beekvelt MC, Colier WN, Wevers RA et al (2001) Performance of near-infrared spectroscopy in measuring local o(2) consumption and blood flow in skeletal muscle. J Appl Physiol 90:511–519
5. Binzoni T, Colier W, Hiltbrand E et al (1999) Muscle o(2) consumption by NIRS: a theoretical model. J Appl Physiol 87:683–688
6. Abe K, Matsuo Y, Kadekawa J et al (1997) Measurement of tissue oxygen consumption in patients with mitochondrial myopathy by noninvasive tissue oximetry. Neurology 49:837–841
7. Kragelj R, Jarm T, Erjavec T et al (2001) Parameters of postocclusive reactive hyperemia measured by near infrared spectroscopy in patients with peripheral vascular disease and in healthy volunteers. Ann Biomed Eng 29:311–320
8. Wolf U, Wolf M, Choi JH et al (2007) Regional differences of hemodynamics and oxygenation in the human calf muscle detected with near-infrared spectrophotometry. J Vasc Interv Radiol 18:1094–1101
9. Vardi M, Nini A (2008) Near-infrared spectroscopy for evaluation of peripheral vascular disease. A systematic review of literature. Eur J Vasc Endovasc Surg 35:68–74
10. Manfredini F, Malagoni AM, Felisatti M et al (2009) A dynamic objective evaluation of peripheral arterial disease by near-infrared spectroscopy. Eur J Vasc Endovasc Surg 38: 441–448
11. Cheng CF, Tong TK, Kuo YC et al (2013) Inspiratory muscle warm-up attenuates muscle deoxygenation during cycling exercise in women athletes. Respir Physiol Neurobiol 186: 296–302
12. Beckitt TA, Day J, Morgan M et al (2012) Calf muscle oxygen saturation and the effects of supervised exercise training for intermittent claudication. J Vasc Surg 56:470–475
13. Abraham P, Mateus V, Bieuzen F et al (2013) Calf muscle stimulation with the veinoplus device results in a significant increase in lower limb inflow without generating limb ischemia or pain in patients with peripheral artery disease. J Vasc Surg 57:714–719
14. Allart E, Olivier N, Hovart H et al (2012) Evaluation of muscle oxygenation by near-infrared spectroscopy in patients with becker muscular dystrophy. Neuromuscul Disord 22:720–727
15. Munk N, Symons B, Shang Y et al (2012) Noninvasively measuring the hemodynamic effects of massage on skeletal muscle: a novel hybrid near-infrared diffuse optical instrument. J Bodyw Mov Ther 16:22–28
16. Zysset C, Nasseri N, Buthe L et al (2013) Textile integrated sensors and actuators for near-infrared spectroscopy. Opt Express 21:3213–3224
17. Wolf U, Wolf M, Choi JH et al (2003) Localized irregularities in hemoglobin flow and oxygenation in calf muscle in patients with peripheral vascular disease detected with near-infrared spectrophotometry. J Vasc Surg 37:1017–1026
18. Boushel R, Langberg H, Olesen J et al (2001) Monitoring tissue oxygen availability with near infrared spectroscopy (NIRS) in health and disease. Scand J Med Sci Sports 11:213–222

Chapter 48
Skin Temperature in Lower Hind Limb Subjected to Distal Vein Arterialization in Rats

Tadahiro Sasajima, Shinsuke Kikuchi, Noriyuki Ishikawa, and Tomiyasu Koyama

Abstract Vascular surgery for distal vein arterialization (DVA) has been adopted clinically as a strategy for saving arteriosclerotic lower limbs from amputation. To gain more detailed information on DVA, the present study investigated the procedure in hind limbs of rats under isoflurane anesthesia. Since successful DVA requires destruction of venous valves, a coronary angioplasty catheter guidewire was used to destroy valves either solely in the femoral vein or in both femoral and popliteal veins. The femoral artery was then anastomosed to the femoral vein with sutures under binocular microsopic control. Changes in the distribution of skin blood flow in the hind limbs were studied with a thermal camera. Skin temperature increased in the thigh and knee after femoral venous valve destruction, but hyperthermia was observed in the distal leg and foot only when the valves in the popliteal vein were also disrupted. These results showed that increased arterial blood flow could be established by DVA surgery in both the proximal and distal regions of the hind limbs.

Keywords Arteriosclerosis obliterans • Distal vein arterialization • Valve destruction • Thermo camera • Skin temperature • Coronary angioplasty guide wire

1 Introduction

The arterial occlusive disease, Arteriosclerosis obliterans (AO) first affects the small sized arteries of the lower extremities. The blood flow through arteries is blocked. The peripheral tissues are finally lost because of the oxygen deficit.

T. Sasajima • S. Kikuchi • N. Ishikawa
Asahikawa Medical University, 064-0821 Sapporo, N-1W-25 Hokkaido, Japan

T. Koyama (✉)
Hokkaido University, 064-0821, Sapporo Hokkaido N-1W-25, Japan
e-mail: tomkoyamajp@yahoo.co.jp

H.M. Swartz et al. (eds.), *Oxygen Transport to Tissue XXXVI*, Advances in Experimental Medicine and Biology 812, DOI 10.1007/978-1-4939-0620-8_48,

Patients with AO often suffer severe pain, and may be treated by distal venous arterialization (DVA) in an attempt to save the distal parts of the lower limbs from amputation [1]. This procedure involves diverting an intact (non-affected) artery (posterior tibial artery or dorsalis pedis artery) and connecting it to the plantar vein below the ankle after the valves in the vein have been carefully disrupted and rendered incompetent. DVA surgery can improve the quality of patients' lives but several questions remain concerning the long-term effects of DVA, since the artificially reconstructed circulation is different from the vascular architecture of the intrinsic venous system.

The consequences of DVA on the surrounding tissue have not been well characterized. Using the Krogh's tissue cylinder to model oxygen diffusion we calculated that after DVA human skeletal muscle at rest could be supplied by retrograde perfusion of blood with a sufficient amount of oxygen [2]; basic metabolic activity of the tissue would thus be maintained by inflow of arterial blood to venular network. Our calculations also showed that when oxygen consumption increases during activity such as walking, the oxygen diffusion front would not reach the most peripheral parts of the tissue cylinder around venules [3]. However, the consequent localized hypoxia might ultimately stimulate angiogenesis, as suggested previously [4]. It is also possible that the arterial pressure applied to the venular network as a result of DVA may increase the lymphatic outflow and that this increased flow must either cause edema or be drained successfully by the existing lymphatic system [4]. Nevertheless, the more detailed effects of DVA on blood flow and distribution remain unknown. The present paper describes briefly a method for producing DVA in rat hind limbs and investigates distribution of blood flow with a thermal camera in this model. It was assumed that the skin temperature would reflect local blood flow, as has been shown previously in analysis of blood flow in Raynaud's disease [5].

1.1 Methods

Animal protocols were approved by the animal ethics Committees of Asahikawa Medical University. Female 8-week old Sprague-Dawley rats were purchased from Charles River Laboratories, Japan Inc. They were individually housed at 22 °C and 60 % relative humidity and 12 h dark and light cycles. Normal rat chow and water were accessible ad libitum.

The surgical procedure for DVA in rats is as follows. Rats were anesthetized by isoflurane inhalation and secured in a supine position. Their hind limbs were lightly stretched and fixed on a board with sticky tape. The hair was removed from the groin and medial aspect of the thigh using depilatory gel and the skin incised for 2 cm on both hind limbs to expose the femoral blood vessels distal to the femoral triangle. After clamping the left femoral vessels, 1.5 mm-longitudinal incisions were made on the superficial femoral vein and on the artery (diameter ca 0.5 mm) (Fig. 48.1).

Venous valves were destructed in the left femoral vein and, in some cases, in both the femoral and popliteal veins. This was performed as follows: (1) DVAfem: a 0.26 mm coronary angioplasty guidewire was introduced in the femoral vein and

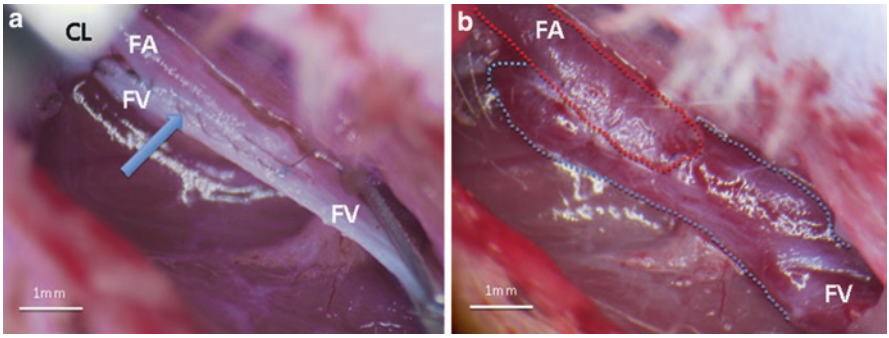

Fig. 48.1 Binocular micrographs showing the vascular anatomy and surgical procedure for DVA construction on the left femoral artery and vein in the groin area. (**a**) Clamped (CL) femoral artery and vein (FA and FV, respectively) including the anastomosis between them. The *thin black wave line* indicated with an *arrow* represents the sewing thread anastomosing FA and FV. (**b**) FA outlined by a *thin red dotted line* and FV by a *blue* one represent the increased arterial blood inflow by declamping. FV was closed on the proximal portion

advanced only to the knee, (2) DVAfem/popliteal: venous valve destruction was extended through the femoral into the popliteal vein in which the guidewire was advanced near to the ankle.

After destruction of the venous valves the incisions in the femoral vein and artery were apposed in a "side-to-side" manner and the vessels stitched together under microscopic control, using 11-0 monofilament nylon in a continuous running suture. The vein was closed in the proximal position. This procedure (complete in 10 min) formed an opening from artery to vein. The removal of the clamps caused an immediate flow of arterial blood into the femoral vein, and its dilatation. The surrounding skin became pink (Fig. 48.1).

The inflow of the arterial blood into the left distal hindlimb in DVAfem/popl rats was confirmed by an angiogram (Fig. 48.2). 0.2 ml angiographic fluid containing indocyanine green (5 %) was injected into the carotid vein through a thin catheter whose tip was placed in the carotid vein. A cine angiographic recording was started prior to the injection of the angiographic solution.

The femoral artery and vein were exposed on the right hind limb, but were not incised or anastomosed. They served as a sham-operated control.

Thermal camera (F30 NEC Avio Infrared Technologies Co. Ltd, Tokyo) observations of the skin temperatures of the medial aspects of the hind limbs were made 2, 6 or 10 weeks after the surgical operation. The distribution of the skin temperature on the hind limb was recorded from rats in a supine position under light isoflurane anesthesia. The temperature values were color-coded with blue being coolest through red to white (warmest). A color spectrum bar was shown on the thermal recording. A numerical value was automatically given from the center of the thermal sensor array plate of the visual field. The position of the center of the thermo sensor array could be selected by positioning of the sign +. The temperature sensitivity range was selected manually.

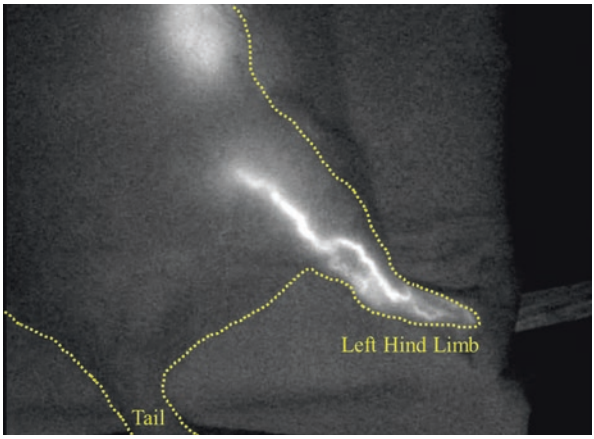

Fig. 48.2 A cine angiographic confirmation of the inflow of the arterial blood to the femoral/popliteal vein in the left distal hind limb in DVAfem/popl rat. The angiographic fluid containing indocyanine green was injected through a thin catheter whose tip was placed in the left carotid vein. The body line of the animal was traced with *dotted yellow line*

Thermographs were taken from 30 cm above the supine animal. Skin temperature was assumed to be proportional to the blood flow under the skin.

The response of the thermal camera to blood flow was checked using the skin of the right (control) leg as follows. The femoral artery was exposed in the intact right hind limb under isoflurane anesthesia. The artery was clamped for 3 min and then released. The skin temperature of the right groin and medial thigh decreased during occlusion of the femoral artery. It increased gradually after removal of the artery clip.

2 Results

2.1 Effects of DVA on Skin Temperature with Valve Destruction in the Femoral Vein only (DVAfem)

In DVAfem animals in which only left femoral vein valves were rendered incompetent (while valves in the popliteal vein below the knee remained intact) the edema of the left foot disappeared in 2 weeks after the surgery. The animals showed no claudication.

An example of the thermo camera recordings is shown in Fig. 48.3. The wide area including the groins, thighs and right foot were pinky-white. The skin temperature of the right foot read 30.0 °C. The left DVAfem foot was colored yellow showing a low temperature of 28.8 °C in this animal.

The medial aspect of the thigh showed a wide warm white area, which indicated a high skin temperature. The skin temperatures of the thigh and knee of the left DVAfem experimental hind limbs were higher than those of the right control hind limbs. Mean values and ± SD are shown in Table 48.1.

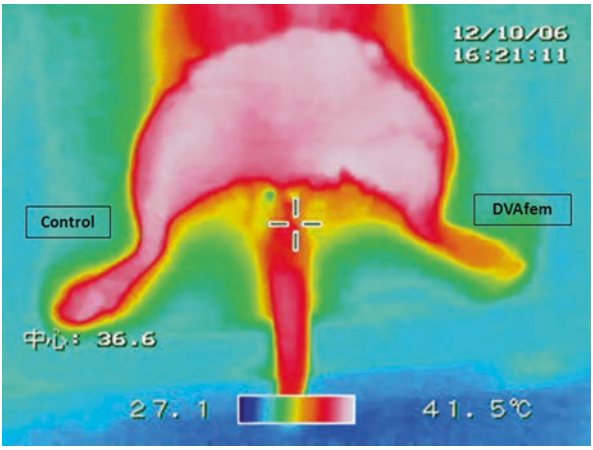

Fig. 48.3 An example of thermo camera recordings, obtained on the control foot (*right*) and DVA fem (*left*) hind limbs. A high skin temperature was observed on the right control foot (30.0 °C), compared with the left foot in DVAfem foot (28.8 °C). The position of the center of the thermo sensor array can be selected by positioning of the +

Table 48.1 Comparison of the skin temperature (°C) measured in a sham-operated control (right) and DVAfem-operated (left) hind limbs in the rats

	Thigh	Knee	Foot
Control	33.9 ± 0.5	31.7 ± 2.0	29.5 ± 2.8
DVAfem.	35.4 ± 0.7	32.6 ± 2.0	28.4 ± 2.6
Diff.	1.95 ± 0.76	1.08 ± 0.9	−1.22 ± 0.28
p-value (n = 5)	0.002	0.003	<0.001

By contrast, the foot temperature was higher in sham-operated than in DVAfem-operated hind limbs. The foot temperature difference between sham-operated and DVAfem hind limbs was small but significant by paired t-test (Fig. 48.4).

2.2 *Effects of DVA with Valve Disruption Throughout the Whole Length of the Femoral and Popliteal Veins (DVAfem/popl)*

A clear angiographic image of blood vessels was recorded only on the first frame in the left hind limb of DVAfem/popl rat (Fig. 48.2). Images on the following frames were widely spread and vague, since indocyanine green was mixed in the blood and spread in the whole body.

The clear image indicates a sharp bending of the vascular system at the knee. It required a careful handling of the guide wire for valve destruction in the popliteal vein.

Only in two animals were the venous valves disrupted from the groin to the ankle, thigh, knee, distal leg and foot. The skin temperatures were higher in the DVA fem/popl operated left hind limb than in the sham-operated right hind limb.

Low temperature was recorded on the foot of the control right hind limb (yellow). Mean values in two measurements are shown in Table 48.2.

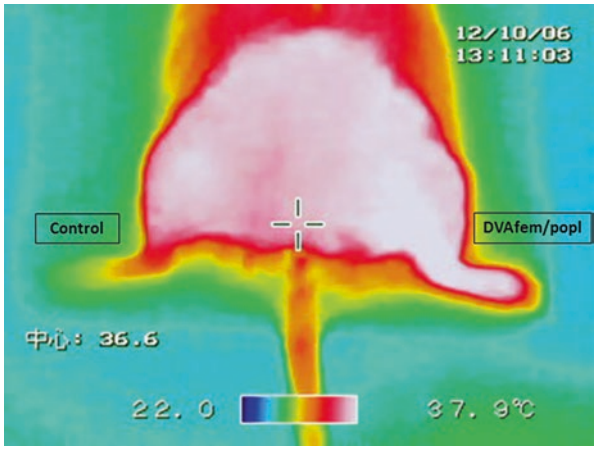

Fig. 48.4 An example of thermo camera recordings, obtained on the control foot (*right*) and DVA fem/popl (*left*) hind limbs. A high skin temperature was observed on the left DVAfem/popl foot (white 34.0 °C) compared with the right control foot (*orange* 27.3 °C)

Table 48.2 Comparison of the skin temperature (°C) measured in a sham-operated control (right) and DVAfem/popliteal-operated (left) hind limbs (mean values of two measurements)

	Thigh	Knee	Below knee	Foot
Control	34.5	32.5	29.2	27.0
DVAfem/popl	36.0	36.2	35.0	33.5
Diff.	1.5	3.7	5.8	5.5

3 Discussion

3.1 General Aspects

The thermo camera provided a color map for the skin temperature and recorded a fall in temperature during arterial occlusion and a rise following restoration of blood flow. This indicates that the camera could detect changes in the skin blood flow. However, reactive hyperemia was not observed during reperfusion of skin after ischemia, probably because of the vasodilatory effect of isoflurane [6]. The effects of arterial blood pressure on the venular microvessels remains for future study.

3.2 Skin Temperature on the Medial Thigh

It was expected that in hind limbs of animals with DVA the arterial blood would flow into the femoral vein and from there into the venular network. In confirmation of this, the skin temperature of the medial aspect of the thighs of rats with DVA was higher than that in sham-operated ones.

The hemodynamic resistance in the operated hind limbs was low because the infused arterial blood did not flow through the highly resistive arterioles. Hence, much arterial blood was able to flow directly into the venular network, which caused a rise in local skin temperature.

3.3 Skin Temperature Distal to the Knee in DVAfem

Contrary to the thigh, the skin temperature was lower distal to the knee and in the foot in DVAfem rats than in the control hind limb (Table 48.1). This result seems reasonable, since valves in the popliteal veins remained intact while the peripheral blood flow was probably reduced, most likely due to the reduced pressure in the distal section of the femoral artery.

3.4 Skin Temperature Distal to the Knee in DVAfem/popl

Conversely in DVAfem/popl rats, it seemed to be probable that skin temperature distal to the knee and in the foot was high because the destruction of venous valves in the popliteal vein allowed an increase in the inflow of arterial blood to the knee and foot (Table 48.2 and Figs. 48.2 and 48.3).

4 Conclusion

Assuming that changes in skin temperature reflect alterations in blood flow, our results suggest that the DVA procedure in rat hind limbs could provide a useful and inexpensive model for gaining more detailed information relevant to human DVA. Furthermore, it was shown that the destruction of venous valves was important for the maintenance of the retrograde blood flow.

Acknowledgments The authors wish to express their thanks to Prof. Dr. Ian Silver and Prof. Dr. Maria Erecinska, Bristol University, for reading the manuscript and valuable suggestions.

References

1. Sasajima T, Azuma N, Uchida H et al (2010) Combined distal venous arterialization and free flap for patients with extensive tissue loss. Ann Vasc Surg 24(3):373–81
2. Koyama T, Sasajima T (2010) Sufficient oxygen can be transported to resting skeletal muscle via arterialization of the vein: theoretical consideration in a rat model. In: LaManna JC, Puchowicz MA et al (eds) Oxygen transport to tissue XXXII (AEMB701). Springer, New York, pp 335–339

3. Sasajima T, Koyama T (2011) Biological maintenance of distal vein arterialization. In: Wolf M, Bucher HV et al (eds) Oxygen transport to tissue XXXIII (AEMB737). Springer, New York, pp 259–262
4. Koyama T, Sasajima T (2012) Retrograde perfusion of the hind leg in diabetic patients suffering from the arteriosclerosis obliterans: theoretical considerations of oxygen supply and lymphatic flow based on rat models. In: Welch WJ, Palm F et al (eds) Oxygen transport to tissue XXXIV (AEMB765). Springer, New York, pp 245–250
5. Ziegler S, Zöch C, Gschwandtner M, Eckhardt G, Windberger U, Minar E, Rüdiger H, Osterode W (2005) Thermoregulation and rheological properties of blood in primary Raynaud's phenomenon and the vibration-induced white-finger syndrome. Intern Arch Occup Environ Health 78(3):218–222
6. Izumi K, Akata T, Takahashi S (2001) Role of endothelium in the action of isoflurane on vascular smooth muscle of hypertension-induced venous valve remodeling. J Vasc Surg 39:1329–34

Erratum to: Oxygen Transport to Tissue XXXVI

Harold M. Swartz, David K. Harrison, and Duane F. Bruley

Errata to: H.M. Swartz et al. (eds.), *Oxygen Transport to Tissue XXXVI*, Advances in Experimental Medicine and Biology 812, https://doi.org/10.1007/978-1-4939-0620-8

The updated online versions of these chapters can be found at
https://doi.org/10.1007/978-1-4939-0620-8_22
https://doi.org/10.1007/978-1-4939-0620-8_24
https://doi.org/10.1007/978-1-4939-0620-8_25
https://doi.org/10.1007/978-1-4939-0620-8_26
https://doi.org/10.1007/978-1-4939-0620-8

H.M. Swartz et al. (eds.), *Oxygen Transport to Tissue XXXVI*, Advances in Experimental Medicine and Biology 812, DOI 10.1007/978-1-4939-0620-8_49,

Index

H.M. Swartz et al. (eds.), *Oxygen Transport to Tissue XXXVI*, Advances in Experimental Medicine and Biology 812, DOI 10.1007/978-1-4939-0620-8,